UC Santa Cruz

UC Santa Cruz Electronic Theses and Dissertations

Title

Detecting Dark Matter in the Milky Way with Cosmic and Gamma Radiation

Permalink

https://escholarship.org/uc/item/723151vx

Author

Carlson, Eric Christopher

Publication Date

2016

Copyright Information

This work is made available under the terms of a Creative Commons Attribution License, availalbe at https://creativecommons.org/licenses/by/4.0/

Peer reviewed|Thesis/dissertation

eScholarship.org Powered by the California Digital Library
University of California

UNIVERSITY OF CALIFORNIA
SANTA CRUZ

DETECTING DARK MATTER IN THE MILKY WAY WITH COSMIC AND GAMMA RADIATION

A dissertation submitted in partial satisfaction of the
requirements for the degree of

DOCTOR OF PHILOSOPHY

in

PHYSICS

by

Eric C. Carlson

June 2016

The Dissertation of Eric C. Carlson
is approved:

Professor Stefano Profumo, Chair

Professor Tesla Jeltema

Professor Robert Johnson

Dean Tyrus Miller
Vice Provost and Dean of Graduate Studies

Copyright © by

Eric C. Carlson

2016

Table of Contents

List of Figures **x**

List of Tables **xxx**

Abstract **xxxiii**

Dedication **xxxiv**

Acknowledgments **xxxv**

I Indirect Detection Fundamentals **1**

1 Introduction **2**
1.1 Evidence for Dark Matter 6
1.2 Motivations for Particle Dark Matter 11
1.3 An Overview of This Work 16

2 Indirect Detection of Particle Dark Matter **20**
2.1 Estimating Rates 20
2.1.1 Gamma-Rays and Neutrinos 21
2.1.2 Cosmic-Rays 23
2.2 Dark Matter Halo Profiles 24
2.2.1 Navarro-Frenk-White (NFW) Profile 26
2.2.2 Einasto Profile 27
2.2.3 Burkert Profile 28
2.2.4 Isothermal Profile 28
2.2.5 The Impact of Baryons 29
2.3 Indirect Detection Targets 30
2.3.1 Gamma-Ray Searches 30
2.3.2 Cosmic-Ray Searches 36
2.4 Experiments 37

2.4.1 Current and Planned Experiments . . . 38
2.4.2 Fermi-LAT Instrument Response . . . 43

3 Astrophysical Signatures of Particle Dark Matter 48
3.1 Electromagnetic Radiation From Dark Matter . . . 48
3.1.1 Gamma-rays from WIMPs . . . 49
3.1.2 X-ray Lines . . . 51
3.2 Cosmic Ray Production from Dark Matter . . . 52
3.2.1 Positrons (e^+) . . . 53
3.2.2 Antiprotons ($\bar{p}$) . . . 54
3.2.3 Antideuterons ($\bar{d}$) . . . 55
3.2.3.1 The Coalescence Model . . . 57
3.2.3.2 An Alternative Formation Model . . . 60
3.2.3.3 Antideuterons from Gravitino Decays . . . 61
3.2.4 Antihelium-3 ($^3\overline{\mathrm{He}}$) . . . 66
3.2.4.1 $A = 3$ Coalescence . . . 67
3.2.4.2 Detection Prospects for Current and Future Experiments 72
3.3 Dark Matter Interactions with Cosmic-Rays and Interstellar Matter . . . 77
3.3.1 Estimates of Expected Signals for Selected Example Models . . . 81
3.3.2 Density Distributions . . . 84
3.3.2.1 Dark Matter . . . 84
3.3.2.2 Interstellar Gas . . . 85
3.3.2.3 Cosmic-Rays . . . 88
3.3.2.4 Free Electrons . . . 90
3.3.3 Morphological Profiles . . . 92

4 Search Strategies and Statistical Methods 97
4.1 Maximum Likelihood Estimation . . . 100
4.1.1 Parameter Estimation . . . 102
4.1.2 Hypothesis Testing and Goodness of Fit . . . 104
4.2 Bayesian Methods . . . 106
4.3 Template Regression . . . 107
4.3.1 Example Templates . . . 110
4.3.2 External Fit Constraints . . . 113
4.3.3 Adaptive Point Source Masking . . . 114
4.4 Density Based Photon Clustering . . . 115
4.4.1 Cluster Significance Measure . . . 118
4.4.2 Tuning DBSCAN Parameters N_{min} and ϵ . . . 119
4.4.3 Extending DBSCAN to 3-dimensions . . . 122
4.4.4 Simulation Parameters and Clustering Properties . . . 125
4.4.5 Choosing the Temporal Search Half-Height a . . . 127
4.4.6 Summary of DBSCAN Parameter Selection . . . 129
4.4.7 Post-Processing with Boosted Decision Trees . . . 131
4.5 Sideband Subtraction . . . 134

4.6 Monte Carlo Methods . . . 137
4.6.1 Example I: The WMAP/Planck Haze . . . 137
4.6.2 Example II: The 135 GeV Line . . . 140
4.7 Blank Sky Calibration . . . 143
4.7.1 Improving the Sensitivity of Fermi to Dark Matter Annihilation in Dwarf Galaxies . . . 144
4.8 Multi-Wavelength and Multi-Messenger Studies . . . 155
4.9 ROI Optimization . . . 156
4.10 Point Source Separation Methods . . . 157
4.10.1 Wavelets . . . 157
4.10.2 Non-Poissonian Template Fitting . . . 158
4.10.3 D^{3}PO (Denoising, Deconvolving, and Decomposing Photon Observations) . . . 159

II Modeling of Galactic Cosmic and Gamma Rays 161

5 Propagation of Galactic Cosmic Rays 162
5.1 Analytic Propagation Schemes . . . 163
5.1.1 Diffusion From a Single Instantaneous Source . . . 163
5.1.2 Approximate Energy Losses for Ultra-Relativistic Electrons . . . 166
5.1.3 The Two-Zone Diffusion Model . . . 167
5.1.3.1 Nuclear Interaction Cross Sections . . . 173
5.1.4 Solar Propagation in the Force Field Model . . . 176
5.2 Numerical Propagation . . . 178
5.2.1 The Full Transport Equation . . . 179
5.2.2 Cosmic-Ray Injection . . . 180
5.2.2.1 Diffusive Shock Acceleration . . . 181
5.2.2.2 Non-Linear DSA in the Galactic Center . . . 182
5.2.3 Diffusion . . . 188
5.2.4 Convective Winds . . . 190
5.2.4.1 Galactic Winds . . . 191
5.2.4.2 Galactic Center Winds . . . 192
5.2.5 Reacceleration . . . 193
5.2.6 Energy Losses . . . 194
5.2.6.1 Inverse Compton Scattering . . . 195
5.2.6.2 Synchrotron . . . 198
5.2.6.3 Bremsstrahlung . . . 199
5.2.6.4 Ionization . . . 200
5.2.6.5 Proton-Proton Cooling . . . 200

6 Radiation From Cosmic-Rays **201**
6.1 Hadronic Emission Overview . . . 202
6.2 Leptonic Emission Overview . . . 204
6.3 γ-rays from π^0 decay . . . 210
6.4 γ-rays from Inverse Compton Scattering (ICS) . . . 214
6.5 γ-rays from Electron Bremmstrahlung . . . 217
6.6 Synchrotron from High Energy Electrons . . . 218

7 Precision Models of the Milky Way **220**
7.1 Cosmic-Ray Source Distributions . . . 220
7.1.0.6 Pitfalls of Previous Source Distributions . . . 221
7.1.0.7 Primary Cosmic-Rays from Star Forming H_2 Regions . . . 225
7.2 Interstellar Gas Distributions . . . 237
7.2.0.8 Previous Gas Models . . . 237
7.2.0.9 Pitfalls of Previous Gas Models . . . 242
7.2.0.10 New Gas Models . . . 245
7.2.0.11 Additional Notes . . . 247
7.3 Galactic Magnetic Fields . . . 248
7.4 Interstellar Radiation Fields . . . 252

III Indirect Detection Signals **256**

8 The GeV Galactic Center Gamma-Ray Excess **257**
8.1 Steady State Cosmic Rays . . . 264
8.1.1 Benchmark Models . . . 269
8.1.2 Gamma-Ray Analyses . . . 271
8.1.2.1 Data Selection . . . 273
8.1.2.2 Additional γ-ray Templates . . . 274
8.1.2.3 Global Analysis and $X_{\rm CO}$ Fitting . . . 278
8.1.2.4 Inner Galaxy Analysis . . . 283
8.1.2.5 Galactic Center Analysis . . . 284
8.1.3 Results . . . 285
8.1.3.1 Tuning the Star Formation Model . . . 290
8.1.3.2 Spectrum and Statistics at the Galactic Center . . . 304
8.1.3.3 Characterizing Residual Emission . . . 309
8.1.3.3.1 Raw Residuals . . . 309
8.1.3.4 Galactic Plane Residuals . . . 312
8.1.3.5 Radial Profiles . . . 314
8.1.3.6 Inner Galaxy Slope and Ellipticity . . . 317
8.1.3.7 Galactic Center Slope and Ellipticity . . . 321
8.1.4 Sensitivity to Diffusion Model Parameters . . . 324
8.1.5 Injection Spectrum and Enhanced Transport in the CMZ . . . 333
8.1.6 Discussion of Steady State Scenarios . . . 342

8.1.7 Summary of Steady State Cosmic-Ray Models . . . 346
8.1.8 Additional Results . . . 348
8.1.8.1 $\boldsymbol{X_{CO}}$ in the Inner Galaxy . . . 348
8.1.8.2 ROI Dependence of Fit Components . . . 352
8.1.8.3 Comparison with a Gaussian CMZ Model . . . 354
8.1.8.4 The Morphology From Ten Sky Segments . . . 357
8.1.8.5 The Galactic Center Analysis with the 1FIG Catalog . . . 359
8.2 Hadronic Cosmic Ray Bursts . . . 360
8.2.1 Analytic Estimates of Morphology . . . 361
8.2.2 Morphology from Numerical Simulations . . . 364
8.2.3 Spectral Properties of Hadronic Bursts . . . 378
8.2.4 Physical Models for the GC Excess . . . 387
8.2.4.1 A Mechanism and Evidence For GeV Spectral Breaks . . . 387
8.2.4.2 SNe Rates and Starburst Histories . . . 397
8.2.5 Discussion of the Hadronic Burst Scenario . . . 402
8.3 Leptonic Cosmic Ray Bursts . . . 404
8.4 Millisecond Pulsars . . . 407

9 The Fermi 130 GeV Gamma-Ray Line 412
9.1 Source Models . . . 420
9.1.1 Dark Matter and Pulsars Models . . . 420
9.1.2 Background Models . . . 423
9.1.3 Clustering Algorithm . . . 425
9.1.4 Photon Selection for a Gamma-Ray Analysis . . . 429
9.2 Clustering Analysis Results . . . 431
9.3 Pulsars or Dark Matter? . . . 437

10 The 3.5 keV X-Ray Line 441
10.1 Morphological Analysis . . . 446
10.1.1 Choice of Targets . . . 447
10.1.2 X-Ray Data Selection . . . 449
10.1.3 Binned Likelihood Analysis . . . 450
10.1.4 Continuum Templates . . . 451
10.1.5 Emission Line Templates . . . 453
10.1.6 Dark Matter Templates . . . 457
10.2 Results of the Morphological Analysis . . . 462
10.2.1 Residual Maps . . . 463
10.2.2 Fits and Limits for Decaying Dark Matter . . . 468
10.2.3 Cross-Correlating the 3.45-3.6 keV Emission . . . 472
10.3 Discussion of Morphological Analysis . . . 479

11 The WMAP-Planck Haze **481**
11.1 Testing the Dark Matter Origins of the Haze with Nearby Observations of Spiral Galaxies . . . 483
11.1.1 Galaxy Sample Selection . . . 485
11.1.2 The Dark Matter Haze in External Spiral Galaxies . . . 488
11.1.2.1 Dark Matter Density Profile . . . 489
11.1.2.2 Cosmic Ray Diffusion . . . 490
11.1.2.3 Galactic Magnetic Fields . . . 494
11.1.3 Monte Carlo Modeling of Systematic Uncertainties . . . 494
11.1.4 Constraints from Radio Observations . . . 499
11.1.4.1 Methodology . . . 499
11.1.4.2 Constraints from the Integrated Flux . . . 504
11.1.4.3 Constraints from Peak and Axis Fluxes . . . 507
11.1.5 Future directions . . . 511
11.1.6 Discussion . . . 512

12 Conclusions **518**
12.1 New Astrophysical Signatures . . . 518
12.1.1 Antihelium from Dark Matter . . . 519
12.1.2 Dark Matter Interactions with Cosmic Rays and the ISM . . . 520
12.2 Novel Statistical Methods . . . 521
12.3 Modeling of Diffuse Galactic γ-rays . . . 522
12.4 The GeV Galactic Center Excess . . . 523
12.4.1 GCE from Steady State Cosmic Ray Injection . . . 524
12.4.2 GCE from Hadronic Bursts . . . 526
12.5 The 130 GeV Line . . . 527
12.6 The 3.5 keV line . . . 530
12.7 The WMAP-Planck Haze . . . 532
12.8 Concluding Remarks . . . 533

Bibliography **535**

A Miscellaneous Codes **619**
A.1 GammaLike: A Fast Binned Likelihood Analysis Package for Fermi Data 619
A.2 DM production of $\overline{d}$ and $^3\overline{\mathrm{He}}$ in Pythia . . . 621
A.3 GammaCAP: A Gamma-Ray Clustering Analysis Package . . . 621
A.3.1 Description of GammaCAP Calculations . . . 625
A.3.1.1 Calculating DBSCAN Parameters . . . 625
A.3.2 Cluster Properties . . . 627
A.3.3 Simulation Tools . . . 629
A.4 Line-of-Sight Integrator with ISM Convolution . . . 629
A.5 Modified Galprop Codes . . . 631
A.5.1 Source distribution parameters . . . 631
A.5.2 Gas Model parameters . . . 632

A.5.3 Wind parameters 633
A.5.4 Debugging parameters 633
A.6 Spherical Propagation Code 633

List of Figures

1.1 The history of the Universe in the Standard Cosmological Model. Image credit to the European Space Agency. 5

1.2 Left: Stellar velocity dispersions inside three Milky Way "dwarf" satellites from Ref. [1]. Solid lines show fits which include a dark matter profile while dotted lines show fits including only the visible matter. Right: Rotational velocity curves for NGC 3198 [2] showing contributions from the visible matter disk and the fitted dark matter halo. 7

1.3 Composite image of the Bullet Cluster [3]. Blue regions of the image indicate the mass density profile as determined through gravitational lensing while red regions show the concentration of hot gas making up around 80% of the cluster's bayronic matter content. The discrepancy between the two regions shows that the vast majority of the cluster mass is made up by approximately collisionless dark matter. 9

1.4 Approaches to dark matter complementarity. The three approaches are related through crossing symmetries. 12

1.5 Evolution of the co-moving dark matter number density as the universe cools in a thermal WIMP production scenario taken from Ref. [4]. 14

2.1 Left: Common dark matter density profiles used in the Milky Way. Right: Annilhlation projected annihilation densities integrated along the line of sight for common DM profiles. Integrating this distribution over solid angle yields a J-factor. All profiles have been normalized at the solar position of 8 kpc to have a density $\rho = .4\mathrm{GeVcm}^{-3}$. 26

2.2 Schematic of tradeoffs between indfirect detection targets as well as the dark matter annihilation flux column density from the Via Lactea II simulations [5]. Stacked (joint-likelihood) analyses of dwarf galaxies enhance the J-factor while maintaining the same background uncertainties, providing even more robust constraints. 31

2.3 Left: Source sensitivity for experiments with detection capability below 10 GeV taken from [6] and flux sensitivities of high energy experiments reprinted with permission from Ref. [7] 40

2.4 Instrument Response functions (IRF) for SORCE class photons in Fermi PASS 8 release. Top, exposure time in megaseconds for the 3FGL catalog in Galactic coordinates. Bottom four panels counter-clockwise: Effective area, 68% PSF containment radius for different photon classes, 95% containment radius, and Eenrgy resolution. 44

3.1 Gamma-ray injection spectra from dark matter particles of mass m_χ annihilating to a variety of Standard Model final states. The x-axis is expresses as the ratio of the photon energy to the dark matter mass, typically denoted $x = E_\gamma/m_\chi$. 50
3.2 Positron injection spectra from dark matter particles of mass m_χ annihilating to a variety of Standard Model final states. The x-axis is expressed in terms of the fractional energy of the photon relative to the dark matter mass. Commonly called x=E_γ/m_χ. 54
3.3 Antiproton injection spectra from dark matter particles of mass m_χ annihilating to a variety of Standard Model final states. 55
3.4 Antideuteron injection spectra from dark matter particles of mass m_χ annihilating to a variety of Standard Model final states, with coalewscence momenta $p_0 = 160$ MeV. The x-axis is expressed in terms of the fractional energy of the photon relative to the dark matter mass. Commonly called x=E_γ/m_chi. 59
3.5 Comparison of $\overline{\mathrm{d}}$ injection spectra for a 100 GeV WIMP candidate annihilating to $b\bar{b}$ using either the Coalescence prescription (red), or the alternative formation model of Ref. [8](blue). Jagged lines are due to limited statistics. 61
3.6 Antideuteron injection spectra for different operators involved and different gravitino masses, as displayed in the legend. dN is the average number of antideuterons with energy dT generated in the decay of a single gravitino. In particular, we display spectra generated by the operators $\bar{u}_1\bar{d}_1\bar{d}_2$ (uds), $\bar{u}_2\bar{d}_2\bar{d}_3$ (cbs), $\bar{u}_3\bar{d}_2\bar{d}_3$ (tbs). Solid lines represent the heaviest accessible channel while dashed lines show the second heaviest. Dotted lines represent the case of a 2-body decay to b-quarks, which is often presented in antideuteron analyses. In shaded bands, we show the ranges of experimental detectability after accounting for solar modulation effects. The bands are for BESS (red), GAPS (green), AMS-02-L (blue), and AMS-02-H (gray). We have vertically offset the BESS band for readability (vertical normalizations for these bands are arbitrary). The energy range of the bands is identical for different gravitino masses, but in these coordinates the horizontal locations scale as a function of $m_{3/2}^{-1}$. 64
3.7 Injection spectra for $\bar{p}$, $\overline{\mathrm{d}}$, and $^3\overline{\mathrm{He}}$. For the latter two, uncertainty bands represent the uncertainties due to the extrapolated coalescence momentum. The $^3\overline{\mathrm{He}}$ contribution also includes contributions from Tritium which decays to $^3\overline{\mathrm{He}}$ shortly after injection. 70

3.8 Ratios of the production of ($^3\overline{\mathrm{He}}$ + $^3\overline{\mathrm{H}}$) to $\overline{\mathrm{d}}$ for Majorana dark matter annihilating to $b\bar{b}$ (left column) and W^+W^- (right column) final states integrated over the energy bands for the proposed GAPS (LDB) instrument. For each species, these bands were shifted for solar modulation according to a 500 MV Fisk potential. The solid blue vertical lines show nominal values for $p_0^{A=2}$ with uncertainties (vertical shaded) while the horizontal lines show the $A = 3$ coalescence momentum extrapolated using the nuclear binding energy (blue dashed) and heavy-ion data (black dot-dashed). White regions with no contours contained no Monte-Carlo events. 71
3.9 Flux of $^3\overline{\mathrm{He}}$ at the top of the atmosphere produced by dark matter annihilating to W^+W^- (top) and $b\bar{b}$(bottom) final states assuming an NFW dark matter density profile. Flux is multiplied by 100 for W^+W^- with m_χ =1, 2 TeV. The shaded vertical bands represent the energy-bands and proposed sensitivities for various GAPS and AMS-02 observations. Shaded uncertainty bands represent the MIN/MAX interstellar propagation models, although these are reduced to within a factor 4 of the central value after applying constraints from PAMELA measurements of the $\bar{p}$ spectrum. Nuclear physics uncertainties are not shown. 75
3.10 *Top, from left to right:* Projected emission profiles for DM (NFW profile) times the F07 gas model, PEB+NS gas model, free electrons, and, for reference a NFW^2 profile (DM annihilation) . *Bottom:* Projected profiles of DM times cosmic-ray protons and electrons for representative energies of 1 GeV (two left-most panels) and 1 TeV (right-most two panels) as calculated with the `GALPROP` package, using the Yusifov [9] distribution of primary sources. 92

4.1 The new Fermi bubbles template [10] is shown in red, and extends throughout the Galactic center region. The previous template versions [11] are shown by white contours. Also shown are the bounding windows for a typical inner Galaxy analysis (gold) and Galactic center analysis (green). The Fermi bubble's interaction with and extension into the Galactic plane are poorly understood at present. 112
4.2 Example of DBSCAN for a 3 point source Monte Carlo simulation showing in colored circles the $\epsilon-$neighborhoods for core points in each detected cluster. In this case, $N_{min} = 3$. 119

4.3 Global cluster significance S (colormap) and cluster count N_{clusters} (black contours) as a function of the DBSCAN search-radius ϵ and count threshold N_{min} for simulations of 20 point sources emitting 0,50,100 photons per source (left, center, right) in an isotropic background. Also shown is the background photon expectation (solid green) and a 3-sigma background fluctuation $N_{\text{min},\sigma}$=3 (solid red). For a large region of the ϵ and N_{min} parameter space, the correct number of clusters is found at high significance. 122
4.4 Schematic of DBSCAN3D procedure. A cylinder of height $2a\epsilon$ and radius ϵ, called the ϵ-neighborhood, is drawn around each point (small blue and red cylinders). Points are added as a cluster seed if their cylinders contain greater than N_{min} photons. All points in within the small cylinders are deemed 'density-reachable', while if they they are themselves have greater than N_{min} points, they are deemed 'density-connected'. In our implementation, the we ignore density-reachable points and the final cluster is formed by merging all points that are density-connected (roughly large-green cylinder). 123
4.5 Type-I and Type-II detection efficiencies with and without boosted decision trees. 133
4.6 Shown in black is the test statistics corresponding to adding a sliding 50 eV-wide window template to a null model consisting of 7 continuum bands (green hatched regions). In light blue we also overlay the raw XMM spectrum for the Galactic center. The 3.45-3.6 keV band is highlighted in gold. The brightest spectral line templates (with correct widths) are color coded according to the ratio of a given lines peak emissivity temperature to that of K XVIII. The TS stemming from adding a dark matter template is zero. 136
4.7 Distribution of 1.49 GHz luminosity ratio $L/L_{MW,DM}$ where L is the total integrated luminosity and $L_{MW,DM}$ is the luminosity due to dark matter for the canonical Milky Way model. The benchmark luminosity for dark matter plus cosmic rays is indicated by the vertical line. The simulated sample contains 2000 runs randomly distributed in the parameter space of tab. 4.4 with mass restricted to lie within $0.25 - 2$ times the mass of the Milky Way. We plot the contributions due to dark matter only (dot-dashed blue) and to cosmic rays only (dashed red) against extrapolated luminosities of 66 Condon Atlas galaxies meeting morphological cuts compatible with the Milky Way (solid green). Only 11.2% of the simulated dark matter-induced haze luminosities are a factor 20 smaller than our benchmark value, and only 1.42% are a factor 100 smaller. Shown in shaded green are the 7 lowest background galaxies selected from the Condon Atlas. 139

4.8 Event map of Fermi photons between 120-140 GeV (left) and a sample 3 pulsar Monte Carlo simulation (right) showing in colored circles the DBSCAN $\epsilon-$neighborhoods for core points in each detected cluster. . . . 141
4.9 Distribution of global significance of detected clusters (S) expected from both Fermi-LAT (48 photons total, left) and H.E.S.S.-II (5000 photons total, right) observations of annihilating dark matter following a NFW profile (blue dashed), flat density profile (green dashed), Einasto profile (red dashed) and decaying dark matter following an NFW profile (cyan dashed), as well as models of emission from undetected groups of one (magenta solid), two (yellow), three (black), four (blue), five (green), and six (red) pulsars, compared to the clustering properties observed in the Fermi-LAT data binned from 120-140 GeV (magenta dot dash). 142
4.10 A set of empirically driven population models for a number of gamma-ray source classes, including blazars [12], radio galaxies [13], star forming galaxies [14], and millisecond pulsars [15]. Also shown is an estimate for the distribution of dark matter subhalos, calculated as in Ref. [16] (using the mass-concentration relationship of Ref. [17]) for the case of $m_{\rm DM}$ =35 GeV and $\sigma v = 2 \times 10^{-26}$ cm^3/s to $b\bar{b}$. 146
4.11 The distribution of test statistic (TS) values for a population of 5200 randomly selected sky locations constrained to lie at a galactic latitude —b— $> 30^\circ$ and at least 1° (5°) away from point-like (extended) 2FGL sources. We show the distribution of TS values when we no additional sky regions are excluded from our analysis (red solid with shaded poisson error bars), and when we make regions that lie within 0.5° of a BZCAT source (blue dotted), within 1° of a BZCAT source (blue dotted), within 1° of a CRATES source (yellow solid), and within 1° of either the BZCAT or CRATES sources (black solid). In the case that sky locations are constrained to lie at least 1° away from any BZCAT or CRATES source, the density of TS > 8.7 locations is reduced by a factor of 2.1. 147
4.12 The ratio of the fraction of "blank sky" locations (at —b— $> 30^\circ$) with TS$>\{4, 8, 12, 16\}$ compared to that predicted by Fermi's diffuse emission model, as a function of dark matter mass (assuming annihilations to $b\bar{b}$). For all curves, the sky locations are chosen to be at least 1° (5°) from 2FGL point (extended) sources. This ratio is reduced when we further mask around BZCAT and CRATES sources, as denoted in the key. Shaded regions represent Poisson errors. By masking regions near BZCAT and CRATES sources, we can significantly reduce the fraction of the sky with TS values larger than predicted by Fermi's diffuse model. This conclusion is true for spectral shapes corresponding to wide range of dark matter masses. 149

5.1 Local interstellar positron flux due to a pulsar 100 pc away at various ages, and a high energy cutoff at $\gamma = 10^9$ and a power-law injection spectrum with index $\alpha = 2.2$. Based on the model from Ref. [18] 166
5.2 Propagation ratios $R(T) = P^{\overline{\mathrm{He}}}_{\mathrm{num}}/P^{\overline{\mathrm{D}}}_{\mathrm{num}}$ for (P_{num} in Eq. (5.21)) which show the enhancement or suppression of the antihelium flux with respect to antideuterons. MIN/MED/MAX interstellar propagation models are shown in blue/red/green for two values of the propagation cross-section: Annihilation only (solid lines) and total-inelastic (dashed lines). Also shown is the ratio of solar propagation functions in the Force Field Approximation (black solid). 171
5.3 Proton–anti-nuclei inelastic scattering cross-sections as parametrized in Ref. [19]. The non-annihilating inelastic cross-section for antideuterons is taken from Ref. [20]. Shown are the total inelastic (black), non-annihilating inelastic (red), and annihilation cross-sections for antihelium (solid) and antideuterons (dashed). 174
5.4 Summary of electron energy loss-timescales typical of the Milky Way in the disk and the Galactic center vicinity. The CMB energy density $w_{\mathrm{CMB}} = 0.26$ eV cm^{-3}, while the ($\mathrm{FIR}_{6\times10^{-3}\mathrm{eV}}$, $\mathrm{NIR}_{.3\ \mathrm{eV}}$, and $\mathrm{Opt}_{3\ \mathrm{eV}}$) radiation densities are set to (.2, .2, 0) eV cm^{-3} top-left in disk; (1, 9, 0) eV cm^{-3} top-right CMZ; (5000, 5000, 5000) eV cm^{-3} inner 1 pc bottom-left. The matter density is $n_0 = 1\mathrm{cm}^-3$ in all cases except the bottom-right where $n_0 = 100\mathrm{cm}^-3$. Figure reprinted with permission from Ref. [7]. 196
5.5 Dominant energy loss process for the radiation field densities shown in Figure 5.4. Figure reprinted with permission from Ref. [7]. 197

6.1 Model of diffuse Galactic gamma rays from the Milky Way at 22.8 GeV. The total gamma-ray emission is composed of hadronic cosmic-ray interactions with gas ($\pi^0 \to \gamma\gamma$) and leptonic interactions with the gas (bremsstrahlung) and low-energy radiation fields (inverse Compton scattering). Also clearly visible are the Fermi bubbles [21]. 201

6.2 Spectral energy distribution of accelerated protons (power-law index $\alpha_{\rm injection} = 2.0$ and cutoff at 100 TeV) and gamma rays resulting from inelastic collisions with interstellar material. The dominant emission into photons is via the decay $\pi^0 \rightarrow \gamma\gamma$ (solid brown). As can be seen, the gamma-ray spectrum follows the parent protons spectrum rather closely in the mid-energy range and the high-energy cutoff region. For all proton indices the low-energy turnover is a characteristic feature of the pion-decay emission. Also shown is the spectrum of electrons resulting from the inelastic *pp*-interactions via the decay chain $\pi^{\pm} \rightarrow \mu + \nu_{\mu} \rightarrow e^{\pm}\nu_e$ (dashed gray). For the synchrotron emission from these so-called secondary electrons a source with age $t_{\rm age} = 1000$ yrs, and B = 30μG has been assumed. The shaded gray region shows the sensitive range of current gamma-ray detectors (Fermi-LAT, IACTs). Reprinted with permission from Ref. [7] . 203

6.3 Galprop model of diffuse Galactic $\pi^0 \rightarrow \gamma\gamma$ (left) and electron bremsstrahlung emission (right) from the Milky Way at 22.8 GeV. Units are the same as Fig. 6.1 and on a $\log_{10}$ scale. 205

6.4 Spectral energy distribution of electrons at injection (light gray with $\alpha_{\rm injection} = 2.0$) and the steady state including cooling (dashed dark gray) for a source with age $t_{\rm age} = 1000$ yrs, $B = 100\mu$G, for a scenario in the inner 100 pc of our Galaxy. The cooling break in the electron spectrum at ~ 1.2 TeV is apparent in the steady-state electron distribution (dashed dark gray), in the synchrotron spectrum and in the IC spectrum. Also apparent is the turnover in the spectra at even higher energies due to KN cooling which incur catastrophic losses on the electrons. The case for a much lower B-Field of 3μG is also shown in light gray. The shaded gray region shows the sensitive range of current gamma-ray detectors (Fermi-LAT, IACTs). Reprinted with permission from Ref. [7] 208

6.5 Galprop model of inverse Compton emission from the Milky Way at 22.8 GeV from each of the three ISRF components. Units are the same as Fig. 6.1 and on a $\log_{10}$ scale. 209

6.6 Model variations in the γ-ray spectral energy distribution for cosmic-ray proton spectra following (in black) a broken power-law spectrum with $\Gamma_1 = 2, \Gamma_2 = 3$, and $p_{\rm br} = 30$ GeV (see Eq. (8.11)) and, in red, a flat power-law of index 2.82 representative of the 'sea' of Galactic protons. . 212

6.7 Feynman Diagram for inverse Compton scattering. The incoming electron has high energy while the incoming electron is a low energy photon from the interstellar radiation field. The outgoing electron loses has only 10-30% of its initial energy while the outgoing photon is a high-energy gamma-ray (with $E \sim 70 - 95\%$ of the initial electron energy). 215

7.1 **Top Left:** The azimuthally averaged surface density of cosmic-ray source distributions used in this analysis. The distribution of supernova remnants is taken from Ref. [22] (SNR CB98) and Ref. [23] (SNR G15). The Yusifov [9] and Lorimer [24, 25] distributions use pulsars as a proxy for supernovae remnants while the cosmic-ray injection morphology tracing OB Stars is taken from Ref. [26]. The best fitting cosmic-ray injection rate globally and in the inner Galaxy (with no GCE template) is an admixture with 80% of cosmic-rays tracing SNR and 20% tracing the molecular gas density ($f_{\rm H2}$ =0.2) according to the star formation prescription presented in Section 7.1.0.7 (with $n_s = 1.5$ and $\rho_c = 0.1$ cm^{-3}). All distributions have dimension of length^{-2} and are normalized in arbitrary units to have the same integrated source count. Note that the H_2 distribution contains a strong Galactic bar and spiral arms making it highly azimuthally *asymmetric*, as seen in the bottom panel. **Top Right:** Cumulative source count versus radius from the Galactic center for a variety of $f_{\rm H2}$ values, as well as the axisymmetric SNR-CB98 and Yusifov pulsar models. Also shown are observations of the fraction of the Milky Way's total cosmic-ray injection rate produced within the CMZ as computed from either the average star formation rate within the CMZ (F04 [27], YZ09 including an upper limit [28], I12 [29], L12 [30]) relative to the total Galactic SFR of 1.65 ± 0.19 M$_\odot$ yr^{-1} [31], estimates of the fractional SNR occurring within the CMZ (C11 [32]), or the fraction of Wolf-Rayet stars contained in the CMZ (R14 [33]). The F04 marker should be placed at $r = 50$ pc, though this is below the resolution of our model. **Bottom:** The primary cosmic ray source distribution derived from our star formation model for increasing values of $f_{\rm H2}$ assuming a Schmidt index $n_s = 1.5$ and a critical density $\rho_c = 0.1$ cm^{-3}. The leftmost panel corresponds to the pure SNR [22] source model while the center panels are typical of models providing improved fits to the full-sky γ-ray data. 226

7.2 **Top**: The cosmic-ray proton and electron+positron fluxes, for several representative energies, along the line-of-sight to the Galactic center ($l = b = 0^\circ$) after propagation in `Galprop`. Light to dark lines show increasing $f_{\rm H2}$. The distributions are normalized at the solar position $x = 8.5$ kpc, $y = 0, z \approx 0$ as indicated by a red '+' **Bottom**: Steady state cosmic-ray surface density for protons (left two columns) and electrons (right two columns) at representative energies for generating γ-rays over the Fermi-LAT band. The top row shows the case of $f_{\rm H2} = 0$ corresponding to the traditional axisymmetric SNR CB98 [22] source density while the bottom row shows the case of $f_{\rm H2} = 0.2$ which includes the proposed new source density model. A white '+' indicates the solar position, where the cosmic-ray densities have been normalized to unity. 232

7.3 Top row: HI (left) and H_2 (right) gas column densities (integrated over the z-direction) for the Galprop gas model after renormalizing each line of sight to the survey column density in 17 deconvolved galactocentric annuli. Bottom row: HI and H_2 gas distributions in the PEB gas model. For HI, the hydrogen spin temperature assumed here was 10^5 K and 170 K for Galprop and PEB, respectively, though it is allowed to vary in later fits. For H_2 we assume a constant CO $\rightarrow$ H_2 conversion factor $X_{\rm CO} = 2 \times 10^{20}$ cm^{-2} (K km s^{-1})$^{-1}$ in this figure and when distributing primary cosmic-ray sources. For the generation of gamma-ray maps the value of $X_{\rm CO}$ is allowed to float freely in 9 radial bins. Note that white regions are assumed to have gas densities of zero, -y corresponds to positive Galactic longitudes from the solar position at $x = 8.5$ kpc, and that the anomalous ring present in both maps between $R_\odot$ and the Galactic center with radius $R_\odot/2$ is an artifact of the velocity deconvolution. 242
7.4 Galprop's ISRF model at the Galactic center from Ref. [34]. Note that a photon energy is given by $E_{ph} = 1.24eV(1\mu{\rm m}/\lambda)$. 253
7.5 Spectrum of the Galprop ISRF model at the Galactic center from Ref. [35]. 255

8.1 The new Fermi bubbles template [10] used in this analysis is shown in red, and extends throughout the Galactic center region. The previous template versions [11] are shown by white contours. Also shown are the bounding windows for the inner Galaxy analysis (gold) and Galactic center analysis (green). 278
8.2 **Left:** Flux of the Galactic Center Excess in the inner Galaxy analysis using an NFW$_{\gamma=1.05}$ GCE template. From top to bottom rows we also vary the Schmidt index ($n_s = 1.25, 1.5, 1.75$) and the fraction $f_{\rm H2}$ of primary cosmic-ray sources distributed according to molecular gas as $Q_{\rm Primary}(\vec{x}) \propto (n_{\rm H2}(\vec{x}))^{n_s}$. The remaining fraction is distributed according to the observed azimuthally averaged surface density of supernova remnants [22]. Mod A is a benchmark model from Ref. [36]. **Center:** $\Delta\chi^2$ for the inner Galaxy analysis as $f_{\rm H2}$ is varied. Red (blue) curves show the $\Delta\chi^2$ with (without) a GCE template included, with negative values indicating a better fit than Mod A+GCE. Inset numbers indicate the statistical preference (TS) for the inclusion of a GCE template in the fit. **Right:** $\Delta\chi^2$ for the three region global $X_{\rm CO}$ fitting analysis (no GCE template is included in the global fitting). $\Delta\chi^2 = 0$ in this column corresponds to the the $f_{\rm H2} = 0$ model, with negative values indicating an improved fit. The inner Galaxy and total-global ROIs have 1.65×10^5 and 1.89×10^7 degrees of freedom respectively. 291

8.3 Pixel-by-pixel $-2\Delta\ln(\mathcal{L})$ for $f_{\rm H2} = 0.2$ against the null model $f_{\rm H2} = 0.0$, integrated over all energy bands for the global γ-ray analysis in the local($|b| \geq 8^\circ$), outer ($|b| < 8^\circ, |l| > 80^\circ$), and inner Galaxy ($|b| < 8^\circ, |l| < 80^\circ$) regions of interest, smoothed by a 0.5° Gaussian kernel. Blue regions represent an improved fit compared with the axisymmetric source distributions. The outer and inner regions have been rescaled by a factor 1/2 and 1/10, respectively and the white 'holes' are due to point source masking, where the pixels have been weighted according to Eq. (4.18). Boxes indicate the edges of each global analysis ROI, and may produce discontinuities in the residuals since different model fits are imposed. . . . 295

8.4 Inner Galaxy spectra of diffuse emission components with a GCE template (top) and without (bottom). Curves from transparent to opaque increase $f_{\rm H2}$ from 0 to 0.3 in increments of 0.05, with the $f_{\rm H2} = 0.2$ case marked by error bars. In the top panel, absolute fluxes below 10^{-7} GeV/cm^2/s/sr have been linearized in order to show negative fit values. The filled yellow error bars show correlated systematic uncertainties taken from ref. [36]. We have assumed here (with some motivation as described below) that these are comparable to the systematic errors of our new GDE models. Note that although the Fermi bubbles and isotropic spectra are allowed to float, deviations from the values determined using larger regions of interest are penalized by an externally imposed $\chi^2_{\rm ext}$, as described in Sec. 8.1.2.3. . 296

8.5 ICS flux as a function of longitude (dashed) and latitude (solid) along $b = 0$ and $l = 0$ for the cases of $f_{\rm H2} = 0$ (transparent lines) and $f_{\rm H2} = 0.2$ (opaque lines). Each line has been normalized to unity at $(l, b) = (0, 20^\circ)$. 297

8.6 Inner Galaxy $\Delta\chi^2$ as a function of energy bin for representative values of $f_{\rm H2}$ with (red) and without (blue) dark matter. The zero point is with respect to Mod A without dark matter. 298

8.7 **Left:** Flux of the GCE template, for the inner Galaxy analysis as the star formation threshold density ρ_s is varied. **Center:** $\Delta\chi^2$ for the inner Galaxy analysis with and without a GCE template included in the fit. **Right:** $\Delta\chi^2$ for the global analysis. 300

8.8 Fit statistics as star formation model parameters are varied. From left to right columns we show $\Delta\chi^2$ for the inner Galaxy with and without a GCE template (first two columns), total global $\Delta\chi^2$ with respect to $f_{\rm H2} = 0$ (third column), and the test statistic of the GCE template (right column). Lower (purple) values correspond to better fits except for the the rightmost column where purple regions indicate the minimal significance of an additional GCE component. Red '+'s indicate the Canonical model. 302

8.9 The log-likelihood fit (top) and best fit GCE spectrum (bottom) for values of $f_{\rm H2} = 0.0$ – 0.3, in models where all backgrounds are allowed to float independently in each energy bin (left), the isotropic and bubbles templates are fixed to their putative value in full sky fits to the data (center), and the isotropic, bubbles, and 3FGL point source templates are fixed to their nominal values (right). In nearly all cases a value of $\mathrm{f}_{H2} = 0.1$ is preferred by the data. We note that the NFW template remains statistically significant and maintains a consistent spectrum in all cases except for models where the 3FGL point sources are fixed to their default values, a result that is expected due to the significant degeneracy between point sources near the GC and the GCE template. 304
8.10 Same as Figure 8.9 for an analysis which masks the Galactic plane ($|\mathrm{b}| < 2^\circ$) from the $15^\circ \times 15^\circ$ ROI surrounding the GC. 305
8.11 Here we show 1σ uncertainty bands on the relative normalizations of diffuse background components in the unmasked GC analysis for fits including and excluding a GCE template, for the case of $f_{\rm H2} = 0.0$ (left) or $f_{\rm H2} = 0.2$ (right). Components include the combined π^0 and bremsstrahlung template (red), inverse Compton scattering template (ICS, blue), and isotropic background template (green). The GCE template in the Galactic center analysis is highly degenerate with the ICS template, especially in models with higher values of $f_{\rm H2}$. The isotropic template is poorly constrained over the ROI. All results are shown over the $15^\circ \times 15^\circ$ ROI of the GC analysis with no latitude mask applied. 306
8.12 Residual emission maps as $f_{\rm H2}$ is increased for the inner Galaxy analysis with no GCE template included in the fit. Red indicates under-subtracted regions while blue indicates regions where the diffuse model is overly bright. All maps have been multiplied by the Galactic plane mask, weighted according to the 3FGL point-source mask defined by Eq. (4.18), and subsequently smoothed by a Gaussian kernel of $\sigma = 0.5^\circ$. 310
8.13 Best fit flux for a window centered $\mathrm{NFW}_{\alpha=1.05}$ template as the inner Galaxy analysis is transposed along the Galactic plane. Curves from light to dark increase $f_{\rm H2}$ from 0 to 0.3 in increments of 0.05, with $f_{\rm H2} = 0.2$ case marked with error bars. The dotted lines are the 1σ (highly-correlated in energy) systematic uncertainties for residuals along the Galactic plane taken from Ref. [36]. Red '$\times$'s mark non-convergent fits. 312
8.14 Radial flux profile of the $\mathrm{NFW}_{\alpha=1.05}$ annuli at three energies representative of the Galactic center excess. Curves from light to dark increase $f_{\rm H2}$ from 0 to 0.3 in increments of 0.05, with the Canonical $f_{\rm H2} = 0.2$ model indicated by error bars. We also show arbitrarily normalized projected NFW flux profiles for inner slopes $\alpha \in \{0.5, 1, 1.25\}$. Note that (i) the inner slope of the GCE template is fixed to $\alpha = 1.05$ before subdivision into annuli, which may slightly bias results, and (ii) that the vertical axes have been rescaled by a factor 10^{-5}. 314

8.15 **Top:** Preferred morphology (ellipticity ϵ and inner-slope $\alpha_{\rm NFW}$) of the GCE template for increasing values of $f_{\rm H2}$. The left panel shows the $f_{\rm H2} = 0$ case with black '+' markers indicating the best fitting morphology for each $f_{\rm H2}$ sampled. The center two panels show the best-fitting inner Galaxy case with a GCE template and $f_{\rm H2} = 0.1$, as well as the $f_{\rm H2} = 0.2$ preferred by the global ROI. The right panel shows the preferred GCE morphology after marginalizing over $f_{\rm H2}$ – i.e. always choosing the value of $f_{\rm H2}$ which minimizes the χ^2. Here contours indicate the best fitting value of $f_{\rm H2}$, with the overall best fitting case corresponding to $f_{\rm H2} = 0.1$. **Bottom:** Same left to right columns as above, but divided into four energy bins (top to bottom) showing the energy dependence of the morphology as $f_{\rm H2}$ is increased. We note that for $f_{\rm H2} \gtrsim 0.2$, the low energy GCE spectrum becomes negative and disk-aligned, indicating that the galactic diffuse emission model is too bright along the disk near the GC. At higher energies, the GCE template prefers to extend out of the disk. 316

8.16 Spectra of the GCE template in the inner Galaxy analysis as the ellipticity ϵ and inner-slope $\alpha_{\rm NFW}$ of the GCE template is changed around our spherically symmetric Canonical $f_{\rm H2} = 0.2$ model. Disk-like models are favored at low energies where they can subtract the over-brightened disk, while higher energies favor a GCE template which is both flattened and elongated perpendicular to the disk. 317

8.17 The log-likelihood fit of our model to data in the Galactic center analysis, as a function of the inner slope of the NFW density profile for the GCE component (α) and the axis ratio for extension parallel to (<1) or perpendicular to (>1) the Galactic plane. Contours represent rings of $\Delta{\rm LG}(\mathcal{L}) = 20$. In the case of $f_{\rm H2} = 0.0$, we find that typical values ($\alpha \sim 1.0$ and an Axis Ratio of approximately unity) are favored. In the case of $f_{\rm H2} = 0.2$, this still holds, although there is some evidence for an emission component strongly elongated parallel to the Galactic plane. . . 322

8.18 Same as Figure 8.17, for a Galactic center model where the region $|b| < 2^\circ$ is masked from the analysis. Contours now represent changes of $\Delta \log(\mathcal{L}) = 10$. In the case $f_{\rm H2} = 0.0$, we find that the resulting emission profile is still roughly consistent with dark matter predictions, although profiles that are stretched parallel to the Galactic plane, and which are slightly cored near the Galactic center provide statistically better fits to the data. In the case of $f_{\rm H2} = 0.2$, the best fit profile becomes cored near the Galactic center, and prefers elongation parallel to the Galactic plane. 323

8.19 In two sets of panels, we show (top, middle, bottom) the GCE spectral variations, Inner Galaxy $\Delta\chi^2$, and Global $\Delta\chi^2$ as we vary global diffusion parameters around our Canonical $f_{\rm H2}$ model. The Canonical model parameter choice is shown in each case by a vertical pink line. **Top row**: The flux ratio in low/mid/high energy bands (0.3-1, 1-5, and 5-300 GeV) of the Galactic center excess spectrum relative to the GCE spectrum obtained using the Canonical model. Because the low-energy band (purple) is negative in the Canonical model, we reverse the slope and vertically offset the line (i.e. plot 2-Flux/Canonical) ensuring that decreasing values always indicate lower flux. **Middle Row:** Inner Galaxy $\Delta\chi^2$ with and without a GCE template. The test-statistic of the additional GCE template is indicated for each model, noting that maximal degeneracy between the GCE and the GDE model occurs when these lines are at closest approach. **Bottom Row:** Total and region-by-region global $\Delta\chi^2$ relative to the minimum over the parameter range. For $z_{\rm max}, D_0, v_a,$ and δ, we also show 1-dimensional posteriors from two Global Bayesian analysis of measurements of the local cosmic-ray spectra. Blue/gold shaded bands show 68/95% posterior ranges from Ref. [37], and dark/light-blue from Ref. [38]. Best fit parameters are indicated in each case by red lines. See also footnote 10. 325

8.20 Statistics for the Inner Galaxy when varying $f_{\rm H2}$ and $v_{\rm wind}$. **Left:** Test Statistic of the GCE template, with contours showing $\Delta\chi^2 \in \{-300, 0, 300\}$ (dot, solid, dashed) for the 'No GCE' Inner Galaxy fits. **Center:** $\Delta\chi^2$ for IG fits with No GCE template and the same contour levels, relative to the Canonical model. **Right:** Same as center, but for fits including a GCE template. In all panels, the box is comprised of 'bounds' and 'most probable' wind velocities from Ref. [39] on the vertical axis, and models which match the CMZ injection rates (See Sec. 7.1) on the horizontal. . . 337

8.21 Spectrum of the Galactic center excess as the wind velocity $v_{\rm wind}$ is varied for $f_{\rm H2} = 0.3$ which well reproduces the observed SNe rate of the CMZ. Best fitting models without a GCE prefer wind velocities from 500-1000 km/s for $f_{\rm H2} = 0.3$. In all cases the GCE is reduced very far below the GCE spectrum of Mod A. 341

8.22 Same as Figure 8.21, for a Galactic center analysis in cases where the full $15^\circ \times 15^\circ$ ROI is analyzed, as well as an analysis where the region $|b| < 2^\circ$ is masked. Note the different scales for the log-likelihood fits to the data in each analysis. In all cases, the excess remains relatively bright, similar to the default results shown in Figures 8.9 and 8.10. 342

8.23 **Top-left:** Fitted values for $X_{\rm CO}$ as $f_{\rm H2}$ is increased. **Top-right:** $X_{\rm CO}$ for $f_{\rm H2} = 0.3$ as the Galactic center wind velocity $v_{\rm wind}$ is increased. Also shown our $X_{\rm CO}$-fitted version of Mod A, as well as the commonly used $X_{\rm CO}$ profile from Ref. [40]. With the exception of the inner-most ring, all fitted values have statistical error bars $\lesssim 20\%$. **Bottom-left:** Inner Galaxy $\Delta\chi^2$ for the traditional SNR and Canonical models when limiting minimal value of $X_{\rm CO}$ (in units of 10^{20} cm^{-2}(K km s^{-1})$^{-1}$). Traditional `Galprop` models combined with γ-ray observations suggest a value around $X_{\rm CO} \approx 4 \times 10^{19}$ cm^{-2} (K km s^{-1})$^{-1}$ [41]. The impact on the Galactic center excess spectrum and significance is negligible. **Bottom-right:** Same, but for the global-inner analysis. Here the disk is unmasked and the fit quickly degrades as the minimal $X_{\rm CO}$ is increased. Models which include winds help to alleviate this problem and allow for more realistic CMZ injection rates. 349

8.24 Dependence of fit components on choice of ROI for the inner Galaxy Analysis. **Left:** GDE and GCE component normalizations (averaged over 1-5 GeV) for $f_{\rm H2} = 0$ and $f_{\rm H2} = 0.2$ as the square ROI width is increased. All ROIs include a plane mask for $|b| < 2^\circ$. **Right:** Same as left but for GCE template only. Gray lines mark the Galactic center and inner Galaxy ROIs. 354

8.25 **Top-left:** ICS emission over the Inner Galaxy ROI when adding a Gaussian cosmic-ray 'spike' of width $\sigma = 200$ and $\mathcal{N} = 1.4\%$ versus our Canonical ($f_{\rm H2} = .2$) model. **Top-right:** Latitude and longitude profiles for ICS emission running through $l = 0^\circ, b = 0^\circ$ respectively. **Bottom:** GCE Spectrum and fit statistics of the inner Galaxy ROI as the spike normalization $\mathcal{N}$ is varied in the Gaussian CMZ model. To be compared with Figure 8.2. 355

8.26 Spectrum of NFW$_{\gamma=1.05}$ template split into ten regions from Calore et al [36], with the active region indicated in red in the inset plots. Light to dark lines show the spectrum as $f_{\rm H2}$ is increased from 0 in increments of 0.05, with markers highlighting the $f_{\rm H2}$ =.2 case. The black dashed lines indicate the best fit broken power-law spectrum with low (high) energy spectral index $alpha_1$ (α_2), and a break energy $E_{\rm br}$. Note the vertical scale in units of 10^{-6} GeV cm^{-2} s^{-1} sr^{-1} 358

8.27 Same as Figure 8.9 for an analysis using the 1FIG catalog produces by [42], rather than the standard 3FGL catalog. The close comparison of these results with the results from the 3FGL point source population demonstrate the resilience of the GCE to changes in the γ-ray point source modeling. 360

8.28 The density of cosmic-ray protons, at an energy of 2 GeV, projected along the line of sight as a function of the angular distance from the Galactic center in the spherically symmetric analytic diffusion approximation. Shown in dotted blue lines is the evolution of an impulsive source after .5, 2.5, 19, 100, and 2000 Kyr from top to bottom. We also show our summed impulse model (thick black), a 7.5 Myr old continuously emitting source (thin black), and a stationary continuous source (black dashed). After a convolution with the gas density profile, the summed impulse and 7.5 Myr old continuous models have γ-ray flux profiles which approximately match that of an annihilating dark matter candidate following an NFW of inner slope $\gamma = 1.3$ (shown in dashed red for several values of γ). The shaded region shows the angular scales which are both above the Fermi-LAT point-spread function (lower-bound $\approx 0.25^\circ$) and bright enough to be differentiated from the background (upper bound $\approx 10^\circ - 15^\circ$). 363
8.29 Projected flux density at 2 GeV as a function of from a proton source at the Galactic center. For non-dark matter lines, results are derived from a full `Galprop` simulation of diffusion and subsequent neutral pion decay averaged over the north + south regions with the Galactic plane ($|b| \pm 1^\circ$) masked out upon integration. In black we show radial flux profiles for our summed impulsive (thick), a 7.5 Myr old continuous source (thin), and a steady-state continuous source (dashed). In blue-dashed and blue-dotted we show the individual impulsive sources at 100 Kyr and 2 Myr. Finally, we show NFW profiles with inner slopes 1.3 and 1.1 in solid and dashed red. Data points are taken from Daylan et al (2014) [43]. 370
8.30 Hadronic γ-ray flux density at 2 GeV from an approximately central source of high-energy protons integrated over the line-of-sight. We show impulsive sources of increasing age in all panels with the exception of the bottom-right which shows a continuously emitting source in steady state. For each map, the fluxes are normalized to the maximum. For the ease of comparing the morphology of the claimed GCE in Ref. [43] and shown in their fig. 9, we employ a linear scale in the three upper panels. The three lower panels employ, instead, a logarithmic scale to enhance the features of the emission outside the Galactic plane region. Also overlaid are reference reticles in increments of 2 degrees and indicators of the Galactic plane mask $|b| < 1^\circ$. All maps have been smoothed by a Gaussian of width $\sigma = 0.25^\circ$ to match Ref. [43]. 372

8.31 Best-fit γ-ray spectra for various analyses for the excess emission in the Galactic center region. In each panel we show three models of the underlying proton spectrum: Solid lines show the hadronic γ-ray emission for a broken power law proton injection spectrum where both indices and the energy of the spectral break are varied. Dot-dashed lines employ the same functional form, but with the break in the spectral index fixed to $\Delta\Gamma = 1$. The dotted lines represent an exponentially cutoff proton spectrum. In clockwise order and from the top left, the panels show data from Daylan et al Pass 6V11 [43], Daylan et al Pass 7V6 [43], Gordan & Macías [44], and Abazajian et al [45]. Note that the top row is normalized by the solid angle, while the bottom rows are integrated over the respective regions of interest. 381
8.32 1,2, and 3σ confidence intervals for a broken power-law proton spectrum which steepens its index Γ_1 by one above the break energy $p_{\rm br}$ (left panel), and an exponentially cutoff power law (right panel), fit to three extractions of the Galactic center excess spectrum (excluding Abazajian et al). In the top panel, the bands shaded along the x-axis represent the range of low-energy spectral indices for SNRs interacting with dense molecular clouds as measured by Fermi-LAT in Ref. [46]. The dark and dark+light shaded bands along the y-axis indicate spectral break momenta expected to occur in dense molecular clouds and more ambient molecular densities respectively. Also note that confidence regions for the two Daylan et al spectra do not include any systematic errors and hence the true confidence contours are likely to be significantly more extended. 392
8.33 Angular profile of two leptonic burst model at 2 GeV from Ref. [47] . . . 406

9.1 Event map of Fermi photons between 120-140 GeV (left) and a sample 3 pulsar Monte Carlo simulation (right) showing in colored circles the DBSCAN $\epsilon-$neighborhoods for core points in each detected cluster. . . . 425
9.2 *Global cluster significance* S (filled colored contours) and *total number of clusters* $N_{\rm clusters}$ for Fermi (ACT) simulations (above threshold $s > 1.29$ ($s > 2.0$); labeled contours) as a function of the DBSCAN search radius ϵ and core-point threshold $N_{\rm min}$. The top row corresponds to Fermi simulations of 1 (left),2 (center), and 3 (right) pulsar models while the bottom row is for ACT observations of 2 (left), 4 (center), and 6 (right) pulsar models. Results are relatively insensitive to large coincident regions in the scan parameter space for left and center columns, while the dependence on $N_{\rm min}$ increases as the number of photons per pulsar approaches the background rate. Fermi simulation DBSCAN parameters are chosen to be $\epsilon = 0.35$, $N_{\rm min} = 3$ while ACT simulation DBSCAN parameters are chosen to be $\epsilon = 0.05$, $N_{\rm min} = 8$ as a compromise between the cluster detection efficiency and the significance over background. 428

9.3 Models for the clustering properties expected from both Fermi-LAT (48 photons total, left) and H.E.S.S.-II (5000 photons total, right) observations of annihilating dark matter following a NFW profile (blue dashed), flat density profile (green dashed), Einasto profile (red dashed) and decaying dark matter following an NFW profile (cyan dashed), as well as models of emission from undetected groups of one (magenta solid), two (yellow), three (black), four (blue), five (green), and six (red) pulsars, compared to the clustering properties observed in the Fermi-LAT data binned from 120-140 GeV (magenta dot dash). The top row shows the distribution of global significance of detected clusters (S, top row). All other quantities are calculated in the subspace of clusters with significance $s > 1.29$ ($s > 2$) for Fermi (ACT) simulations. Shown is the distribution of *mean clustering radii* (2nd row), the distribution of the *total number of clusters* detected (3rd row), and the distribution of the average *number of member photons* in each cluster with $s > 2$ (bottom). 432

10.1 Representative continuum photon maps for energies in the 4.2-5.5 keV range, centered on Sgr A* in the Galactic center (left) region and on the Perseus cluster (right). Count maps have been blurred using a Gaussian kernel with $\sigma = 2.5''$ and are log-scaled to highlight distinctive spatial features. In the right panel, the x-y axes are aligned with the equatorial axes and show the angular displacement from the cluster center. In both cases, bright point sources have been masked out. 453

10.2 Morphology of 8 plasma emission lines including the 3.5 keV band surrounding the Galactic center region after subtracting off the best-fit (ML) contribution from 5 continuum bands. For illustrative purposes, we normalize maps to the variance of each template. The band from 3.45-3.6 keV is also shown in the center-right panel. A black '+' indicates the location of Sgr A* while the outer shell of the supernova remnant Sgr A East is approximately bounded by the ellipse shown, from Ref. [48]. . . . 455

10.3 Morphologies for the 8 plasma emission lines and the 3.5 keV band in the Perseus cluster after subtracting off the best-fit (ML) contribution from 5 continuum bands. The normalization prescription is as in Fig. 10.2. . . 456

10.4 $\mathcal{J}$-factors sky-maps for a decaying dark matter candidate distributed as an NFW profile convolved with the *XMM* MOS instrument response functions and exposure masks for the Galactic center field (left) and the Perseus cluster (right). 459

10.5 Comparisons between 3.45-3.6 keV residuals after subtracting the best fit continuum+isotropic templates for different models of the continuum near the Galactc Center (top row) and the Perseus cluster (bottom row). Black '+'s in the top row indicate Sgr A* while the shell of SNR Sgr A East is shown by the black ellipse [48]. Maps have been smoothed by a Gaussian kernel with $\sigma = 20'$. For the high-energy continuum model, the GC and Perseus cluster maps have been rescaled by a factor 1/2 and 1/3, respectively, in order to maintain visibility on a common scale. 464
10.6 Radial and azimuthal profiles for the Galactic center (left panels) and for the Perseus cluster's (right panels) un-smoothed residual maps shown in Fig 10.5. The shaded regions bracket alternative continuum models along with the best fitting NFW template (red), S XV Line (light blue), and Ar XVIII line (magenta). Poisson error bars are shown for our 'All' model. Azimuthal profiles rotate clockwise from the line pointing from the center (Sgr A* in the GC) to positive longitudes. In the top-right panel, we also show the steepest radial profile expected from photo-conversion of axion-like-particles (solid blue), calculated using formulae in Ref. [49] and convolved with the relevant masks and instrument response. 465
10.7 Shown in black is the test statistics corresponding to adding a sliding 50 eV-wide window template to a null model consisting of 7 continuum bands (green hatched regions). In light blue we also overlay the raw *XMM* spectrum for the Galactic center (top) and Perseus cluster (bottom). The 3.45-3.6 keV band is highlighted in gold. The brightest spectral line templates (with correct widths) are color coded according to the ratio of a given line's peak emissivity temperature to that of K XVIII. T_{peak} for K XVIII is also represented by a dashed line at 2.16 keV, visible in the Perseus plot. For both the Gaclactic center and Perseus the TS stemming from adding a dark matter template is zero. 475

11.1 The effect of variations in the nuisance parameters on the luminosity of the dark matter synchrotron haze at 1.49 GHz in units of the benchmark value, $L_{\rm MW}$. We note that variations in h_{diff} closely floow See Table 11.3 and text for more details. 492

11.2 Distribution of 1.49 GHz luminosity ratio $L/L_{MW,DM}$ where L is the total integrated luminosity and $L_{MW,DM}$ is the luminosity due to dark matter for the canonical Milky Way model. The benchmark luminosity for dark matter plus cosmic rays is indicated by the vertical line. The simulated sample contains 2000 runs randomly distributed in the parameter space of tab. 11.3 with mass restricted to lie within $0.25 - 2$ times the mass of the Milky Way. We plot the contributions due to dark matter only (dot-dashed blue) and to cosmic rays only (dashed red) against extrapolated luminosities of 66 Condon Atlas galaxies meeting morphological cuts described in Section 11.1.1 (solid green). Only 11.2% of the simulated dark matter-induced haze luminosities are a factor 20 smaller than our benchmark value, and only 1.42% are a factor 100 smaller. Shown in shaded green are the 7 lowest background galaxies selected from the Condon Atlas. 497
11.3 Distribution of 1.49 GHz luminosity ratio $L/L_{MW,DM}$ where L is the luminosity evaluated at a radius $r = 5$ kpc along the Galactic plane (dotted red), height $z = 1$ kpc above the Galactic Center (dashed blue) and $L_{MW,DM}$ is the luminosity due to dark matter for the canonical Milky Way model. The sample is identical to that of Figure 11.2 and we have repeated the integrated dark matter component (solid green). 498
11.4 Overlays of dark matter only contours from *Galprop* onto optical images obtained from the STScI Digitized Sky Survey. Units are mJy beam^{-1}. Contours are logarithmically spaced at levels $2^{n/2}$ for integer values n with outermost contours $n = -2$ for M31 and $n = -3$ for all others. With the exception of NGC 4448, which has very large distance uncertainties, the optical dimensions are similar or slightly exceed those of the lowest detectable radio contours. The diffusion zone has been matched to the estimated physical axis size. 504
11.5 10 Kpc square overlay for M31 of Condon Atlas 1.485 GHz radio contours displayed over dark matter only predictions from *Galprop*. Units are mJy beam^{-1} and the image has been corrected for distance, inclination, position angle, and beam solid angle. The colormap is linear while contours are logarithmically spaced at levels $2^{n/2}$ for integer values n with outermost contours at the same level $n = -2$. Contour limits are computed using the conservative case (outermost observed contour) lying within 10° major and minor axis (r, z). Although the integrated and peak flux measurements do set limits for M31, the contour limits are the most stringent, constraining a dark matter haze at the $\lesssim 1\%$ level, relative to that of the Milky Way. 508

11.6 20 kpc-square overlays of Condon Atlas 1.485 GHz radio contours onto dark matter only predictions from GALPROP. Units are mJy beam^{-1} and images have been individually corrected for distance, inclination, position angle, and beam solid angle. For NGC 4448, distance variations correspond to minimum and maximum NED measurements centered on the value from the Condon Atlas. For NGC 2683 and 4698, distances are allowed to vary by 1 standard deviation from the mean based on NED measurements. The colormap is linear while contours are logarithmically spaced at levels $2^{n/2}$ for integer values n with outermost contours at the same level $n = -3$. A dark matter haze should produce a fairly symmetric synchrotron signal. Here the irregular shapes of the observed contours often yield significant constraints along r, z, or both. Additionally, the peak predicted contours are often substantially higher than what is observed. . 516
11.7 Distribution of 30 and 44 GHz luminosity ratios $L/L_{MW,DM}$ where L is the total integrated luminosity and $L_{MW,DM}$ is the luminosity due to dark matter for the canonical Milky Way model at the respective frequency. Sample contains 2000 runs randomly distributed in the parameter space of Table 11.3 with the mass restricted to lie within 0.25 to 2 times that of the Milky Way. We plot the contributions due to dark matter (solid) and cosmic rays (dashed) individually. At both 30 and 44 GHz, 6.5% and 1.4% of models show suppression greater than a factor of 100 compared to the benchmark Milky Way model respectively. This indicates that higher frequency observations from Planck will produce more robust limits on dark matter origin of the haze. 517

List of Tables

2.1 Current and planned cosmic and gamma-ray experiments. 47

4.1 Monte Carlo and DBSCAN parameters relevant to the tuning of a. 126
4.2 Simulation averaged clustering properties useful for selecting correct DBSCAN parameter a. 127
4.3 Features used in boosted decision tree classification. 132
4.4 Nuisance parameters employed to estimate the range for a dark matter induced haze in external spiral galaxies. 138
4.5 A list of BZCAT and CRATES sources that lie within 1° of a dwarf spheroidal galaxy studied by Fermi-LAT team [50]. The distance to the source (in degrees) is given in parentheses. Any source detected in both catalogs is listed with the BZCAT coordinates and marked with an asterisk. 154

7.1 Definitions of annuli used by our modified Galprop gas model and used during the 3-stage global $X_{\rm CO}$ fitting described in Section 8.1.2.3. We also show the values of $X_{\rm CO}$ used in `Galprop` for the PEB and Galprop gas models after iteratively fitting our canonical model. The actual fitted values of $X_{\rm CO}$ (see Fig. 8.23) will differ between models, but the gas and source distributions induce the largest change. †We limit the *input* $X_{\rm CO}$ of the innermost ring to the, but fitting in the inner Galaxy is allowed to go to zero and generally prefers very small values. In the outer Galaxy, the outermost ring is known to be highly biased and, in the case of the PEB gas model, fits in the inner Galaxy do not converge unless the initial *input* value of $X_{\rm CO}$ is reduced. (see Sec. 8.1.8.1 for a discussion of the inner $X_{\rm CO}$ values). 240

8.1 Summary of `Galprop` parameters for our Canonical model and Mod A from Ref. [36]. *See Section 7.1.0.7 for additional details on the Star formation parameters. 272

8.2 Definitions of gas annuli used during the 3-stage global $X_{\rm CO}$ fitting described in Section 8.1.2.3. The right column shows the iteratively determined 'seed' $X_{\rm CO}$ values which are input to `Galprop` before discretely γ-ray fitting the rings to each model. 282
8.3 Summary of γ-ray analyses used in this study. 410
8.4 Properties of a few benchmark emission sources. 411

9.1 The fraction of simulations with at least 1 cluster of significance $s > 1.29$ ($n = 1$ and $s = 1.29$, corresponding to the maximum n and s_i for clusters i found in Fermi-LAT data) for Fermi-LAT simulations (column 2), the of Fermi-LAT simulations with at least 2 clusters of significance $s > 1.29$ (column 3) and fraction of simulations with at least n clusters detected at significance $s > 2.0$ with at least 10 core points for ACT simulations (columns 4-6). 435

10.1 Summary of templates used. For atomic emission lines (top), we also indicate the peak emissivity temperatures taken from the `AtomDB 2.0.2` [51]. We note that the K XVIII emission peaks at 2.16 keV (2.51×10^7 K). †This continuum band includes three weak lines from Ar XVII; the limited energy resolution of the EPIC MOS CCD's prevents the lines from being cleanly separated and they are thus treated as a single broad continuum band. 462
10.2 $\mathcal{J}$-factors for decaying dark matter profiles and limits on a sterile neutrino's lifetime and mixing angle the Galactic center and Perseus cluster *spatial* analyses using the delta-log-likelihood method at 95% confidence level. Each of the line and continuum templates were used in deriving limits. These results exclude even the smallest value of $\sin^2(2\theta)$ from Ref. [52] at 3.4 and 4.7σ for NFW and Einasto, respectively. 473

11.1 Candidate galaxies from the Condon Atlas. t, i , $v_{\rm rot}$, S, S_p, refer to the de Vaucouleurs morphological type, inclination, maximum rotational velocity, total flux, and peak flux, respectively. $\rm Rank_L$ ($\rm Rank_{2kpc}$) ranks the total (respectively, 2 kpc off disk) luminosity, in ascending order. Unless otherwise noted, inclination, type, and rotational velocity are from the HyperLeda database. 487
11.2 Distances and sizes of the candidate sample galaxies. 488
11.3 Nuisance parameters employed to estimate the range for a dark matter induced haze in external spiral galaxies. Note that we also place an additional constraint on each simulation that the diffusion height must not exceed the simulated diffusion radius. The Alfven velocity v_A and the energy dependence index, γ_D, of the diffusion coefficient are held fixed at the default values for all analyses, though the effects on the synchrotron luminosity are presented in Figure 11.1. 491

11.4 Integrated flux limits for selected galaxies at available radio frequencies from $1.49 - 15$ GHz. First and second values in parentheses represent limits corresponding to the minimum and maximum distance variations respectively. For measurements with associated flux uncertainties, $R_{\rm int}$ was computed using the 95% confidence level upper limit. Observations providing constraints are highlighted in red. 506
11.5 Contour limits for peak, major (r), and minor (z) fluxes for selected galaxies at 1.49 GHz. The first and second values in parentheses represent limits corresponding to the minimum and maximum distance variations respectively. Observations providing constraints are highlighted in red. . . 507
11.6 Fractions of random scans with luminosity suppressed by more than a factor of 20 and 100 for a randomized sample of parameter space containing 2000 galaxies with masses restricted to $.25 \leq M/M_{MW} \leq 2$. Subscript "int" indicates the total integrated dark matter luminosity and subscript r (z) indicates the luminosity evaluated at a given distance along (above) the Galactic plane. 510

Abstract

Detecting Dark Matter in the Milky Way with Cosmic and Gamma Radiation

by

Eric C. Carlson

Over the last decade, experiments in high-energy astroparticle physics have reached unprecedented precision and sensitivity which span the electromagnetic and cosmic-ray spectra. These advances have opened a new window onto the universe for which little was previously known. Such dramatic increases in sensitivity lead naturally to claims of excess emission, which call for either revised astrophysical models or the existence of exotic new sources such as particle dark matter. Here we stand firmly with Occam, sharpening his razor by (i) developing new techniques for discriminating astrophysical signatures from those of dark matter, and (ii) by developing detailed foreground models which can explain excess signals and shed light on the underlying astrophysical processes at hand. We concentrate most directly on observations of Galactic gamma and cosmic rays, factoring the discussion into three related parts which each contain significant advancements from our cumulative works. In Part I we introduce concepts which are fundamental to the Indirect Detection of particle dark matter, including motivations, targets, experiments, production of Standard Model particles, and a variety of statistical techniques. In Part II we introduce basic and advanced modelling techniques for propagation of cosmic-rays through the Galaxy and describe astrophysical gamma-ray production, as well as presenting state-of-the-art propagation models of the Milky Way.

Finally, in Part III, we employ these models and techniques in order to study several indirect detection signals, including the Fermi GeV excess at the Galactic center, the Fermi 135 GeV line, the 3.5 keV line, and the WMAP-Planck haze.

To My Parents,

John and Kristy,

Whose love, support, and generosity know no limits.

Acknowledgments

I owe a great debt to many people who have provided support, assistance, and motivation over the past five years. I would first like to thank my many collaborators which include first and foremost, Stefano Profumo and Tim Linden, who have provided invaluable guidance and incredible encouragement over my graduate career, as well as constant motivation to "converge" on all projects at all times. They possess an endless work ethic, brilliant insights, and pragmatic approaches without which I could not have progressed this far. So many others have played a crucial role including Tesla Jeltema, Christoph Weniger, Dan Hooper, Adam Coogan, Angelo Monteux, Jonathan Cornell, Andrew Strong, Alejandro Ibarra, and John Beacom. I would also like to thank those who I was not lucky enough to collaborate with, but who have provided an incredible environment for students including Jason Nielson, Bruce Schumm, Michael Dine, Robert Johnson, Howard Haber, Peter Young, Michael Bolte. I am also grateful to my undergraduate advisors David Strom and Tom Quinn.

There are too many friends to count which have influenced my scientific views and path through UC Santa Cruz including Peyton Rose, Vincent Duong, TJ Torres, Tim Linden, Jonathan Cornell, Adam Coogan, Eddie Santos, Scheena Schier, Jake Pasner, Jen Trinh, Laurel Haskins, and Ryan Reece. These people are among the best out there, and I am grateful to each of them.

Most of all, I would like to thank my parents for unending love and support, for their experience, for their encouragement of my youthful curiosity in all ways possible, for supporting my hobbies and my cultivating my interests in science, and for helping

me to develop into a functional member of society (I think...). I would never have gotten this far without them and I am forever indebted.

I would also like to thank my long-time mentors Lynn Saunders and Sally Marlino, who encouraged me to run free with ideas and projects, who taught me so much, and who poured blood, sweat, and tears into our startup company FlashTiming. My time spent there accelerated my career, expanded my knowledge, and tuned my approach to new problems. Please never stop what you are doing.

Lastly, but with the utmost enthusiasm, I want to thank my partner over the past three years, Aitana Rothfeld. She has always supported me, coped with my stress, given me new perspective, and made me laugh more than I thought possible.

Reprinting of Previously Published Material

The text of this dissertation includes modified reprints of previously published materials including:

1. *Improved Cosmic-Ray Injection Models and the Galactic Center Gamma-Ray Excess*

   E. Carlson, T. Linden, S. Profumo

   Submitted to Physical Review D March 2016 [arXiv:1603.06584]

2. *Putting Things Back Where They Belong: Cosmic-Ray Injection from Star-Forming Regions*

   E. Carlson, T. Linden, S. Profumo

   Submitted to Physical Review Letters Oct. 2015 [arXiv:1510.04698]

3. *When Dark Matter interacts with Cosmic Rays or Interstellar Matter: A Morphological Study*

   E. Carlson, S. Profumo

   Phys.Rev. D92 (2015) no.6, 063003 [arXiv:1504.04782]

4. *Where do the 3.5 keV photons come from? A morphological study of the Galactic Center and of Perseus*

   E. Carlson, T. Jeltema, S. Profumo

   JCAP 02 (2015) 009 [arXiv:1411.1758]

5. *Improving the Sensitivity of Gamma-Ray Telescopes to Dark Matter Annihilation in Dwarf Spheroidal Galaxies*

   E. Carlson, D. Hooper, T. Linden

   Phys.Rev. D91 (2015) 061302 [arXiv:1409.1572]

6. *Cosmic-Ray Protons in the Inner Galaxy and the Galactic Center Gamma-Ray Excess*

   E. Carlson, S. Profumo

   Phys.Rev. D90 (2014) 023015 [arXiv:1405.7685]

7. *Gravitino Dark Matter and Flavor Symmetries*

   A. Monteux, E. Carlson, J. Cornell

   JHEP 1408 (2014) 047 [arXiv:1404.5952]

8. *Antihelium from Dark Matter*

   E. Carlson, A. Coogan, S. Profumo, A. Ibarra, S. Wild

Phys.Rev. D89 (2014) 7, 076005 [arXiv:1401.2461]

9. *A Clustering Analysis of the Morphology of the 130 GeV Gamma-Ray Feature*

   E. Carlson, T. Linden, S. Profumo, C. Weniger

   Phys. Rev. D 88, 043006 (2013) [arXiv:1304.5524]

10. *Testing the dark matter origin of the WMAP-Planck Haze with radio observations of Spiral Galaxies.*

    E. Carlson, T. Linden, S. Profumo

    JCAP 1307 (2013) 026 [arXiv:1212.5747]

Part I

Indirect Detection Fundamentals

Chapter 1

Introduction

For more than 80 years, evidence for the existence of dark matter (DM) has accumulated into an overwhelming set of astronomical and cosmological observations. It is remarkable that this elusive matter component makes up 84% of all mass in the universe (26.8% of the total energy budget) [53], and yet has been observed *only* through its gravitational influence. And while the composition of dark matter remains mysterious, it has become a fundamental pillar of the Standard Cosmological Model, of Galaxy formation and evolution, as well as remaining the strongest evidence for particle physics beyond the Standard Model. This interdisciplinary interest gives rise to one of the most compelling open mysteries in modern Science; one which may well be solved over the coming decade.

Relatively little is known about dark matter, but much is known about what dark matter is not. Our current evidence for DM constists entirely of astronomical and cosmological observations which coherently point to a short list of fundamental concepts.

1. The gravitational influence of dark matter is observed over seven orders of magnitude in distance scale from dwarf galaxies on small $\mathcal{O}(100$ pc) scales, up to the Cosmic Microwave Background radiation (CMB) at the largest $\mathcal{O}(1$ Gpc) observable scales in the universe.

2. Above several kiloparsecs, dark matter is extremely well modelled in the ΛCDM paradigm, where the dark matter is a cold (non-relativistic) collisionless fluid in an approximately flat Friedmann-Lematre-Robertson-Walker cosmology with a positive cosmological constant. On the scales of individual Galaxy and dwarf Galaxy cores, observations deviate from simple ΛCDM predictions, but the impact of astrophysical feedback processes and/or or small DM self-interactions remain an important and open question.

3. Dark matter particles still exist today and therefore must be stable (or have lifetimes much longer than the age of the universe) and have zero, or extremely suppressed couplings to the electromagnetic and strong nuclear force – i.e. their electric and color charges must be approximately zero.

4. No Standard Model particle meets the above requirements except neutrinos. Neutrinos are both thermally under-produced as well as being relativistic at decoupling, making them 'hot' such that small scale structures cannot form. There are thus no viable SM candidates for dark matter.

5. Theoretical modifications to gravity have been unable to reproduce the success of ΛCDM across these scales simultaneously, and have failed to explain the observed

matter distributions in colliding Galaxy clusters. Compact baryonic objects such as primordial black holes or MAssive Compact Halo Objects (MACHOs) face similar difficulties and are ruled as DM candidates.

Recounting the evidence for dark matter provides a rich and informative window on the subject which simultaneously lends credence to the both the power of astronomical observations, and to the importance of understanding astrophysical uncertainties. Here we will by no means provide an exhaustive account (as in Ref.[54]), nor will we provide a historical account [55]. Instead, we will review the most compelling evidence beginning from (astronomically) small scales and working up to the size of the observable universe, providing appreciation for the depth of the mystery. The evolution of the universe in the Standard Cosmological Model is shown in Figure 1.1, and will provide a useful schematic for the following two sections. We are working backwards in terms of the formation of cosmological structure, and the reader is encouraged to consult Figure 1.1 throughout the discussion.

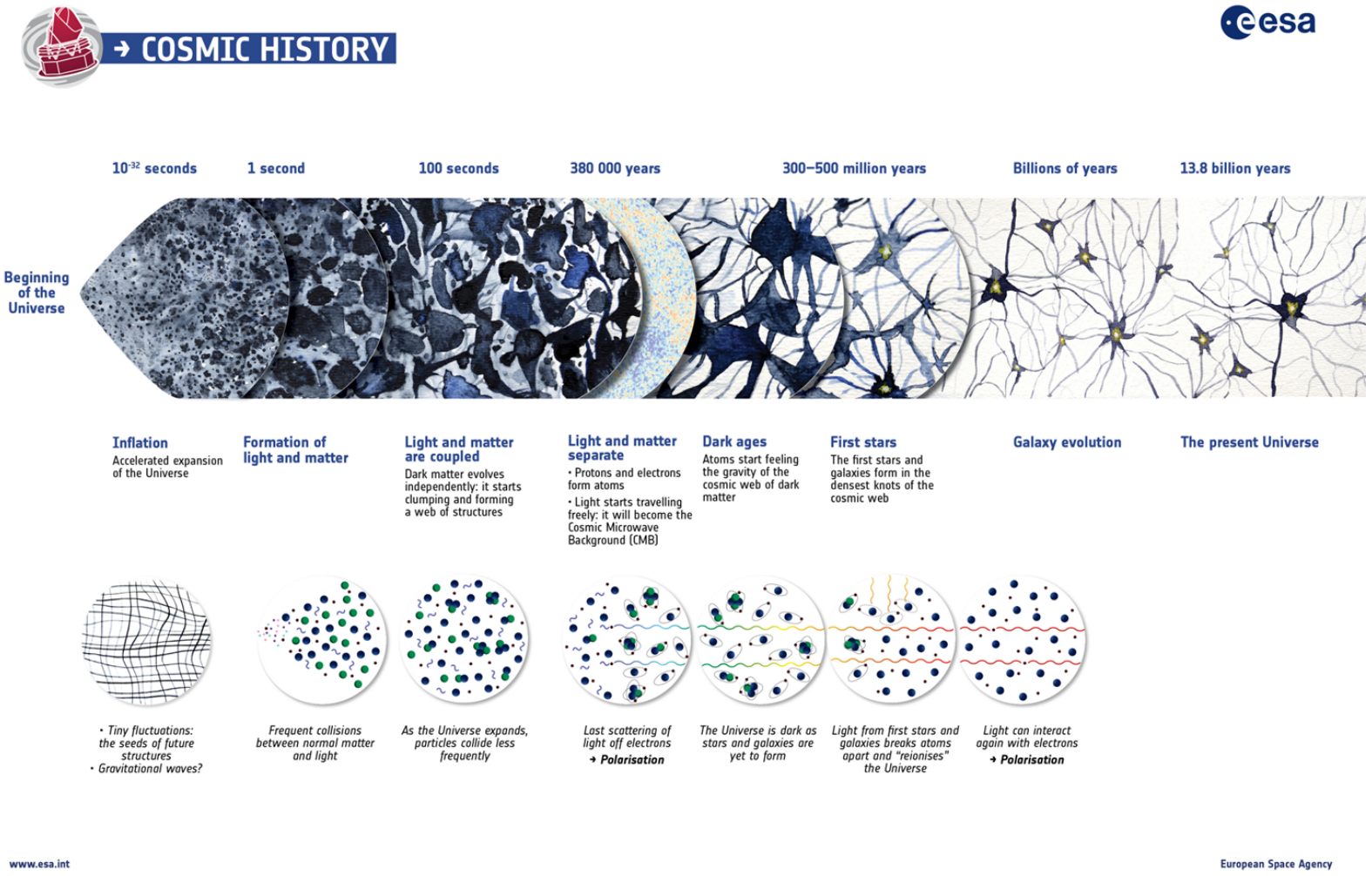

Figure 1.1: The history of the Universe in the Standard Cosmological Model. Image credit to the European Space Agency.

1.1 Evidence for Dark Matter

The smallest structures in the universe which contain both visible matter and appreciable mass fractions of dark matter are Dwarf galaxies. The Milky Way is orbited by many of these satellites which include among them the bright Large and Small Magellanic clouds (LMC and SMC). Until the turn of the century few dwarf galaxies had been detected. The advent of the Sloan Digital Sky Survey increased the count to 24 with an additional 17 "ultra-faints" detected in the first two years of operation by the Dark Energy Survey [56, 57] and an additional 6 detected using PanSTARRs and other surveys[58]. Compared to Globular clusters, these systems are characterized by their much larger half-light-radii (typically several hundred parsecs) as well as their very large mass-to-light ratios, stellar kinematics, and chemical abundances [54]. While the *total* mass of globular clusters is observed to be dominated by stars, measurements of stellar velocity dispersions inside dwarf galaxies reveal mass-to-light ratios of order ~ 100, and radial dispersion profiles which do not match the baryon content alone. Some examples are shown in the left panel of Figure 1.2 and indicate that the mass content of dwarfs is strongly dominated by dark matter by a factor of at least a few[1].

At slightly larger scales (≈ 10 kpc), we can measure the mass profile of nearby spiral galaxies by observing the rotational velocities of stars or orbiting gas clouds as a function of radius. In 1970, Vera Rubin and Kent Ford found that HII regions in the

[1]For this same reason, dwarf galaxies remain one of the most attractive indirect detection targets owing to their negligible astrophysical backgrounds. Interestingly, the DM density profiles in dwarf galaxy cores are also found (perhaps arguably) to be much less "cusped" than predicted by ΛCDM simulations[59], possibly hinting at warm dark matter, dark matter self-interactions, or just demonstrating that astrophysical feedback is yet not well understood.

outer radii of of the Andromeda Galaxy were rotating much faster than expected from the visible matter content along alone [60]. Most of the baryons are contained within the inner 10-20 kpc of the Galaxy, and bodies outside of this are expected to follow Keplarian orbits with velocities falling off as $v_{\text{orb.}} \propto 1/r$. Instead the rotation curves are observed to be flat out to very large distances showing that the baryons are embedded inside of large dark matter halos. This behavior is observed in nearly all spiral galaxies that have measured rotation curves, including the Milky Way (see e.g. right panel of Figure 1.2).

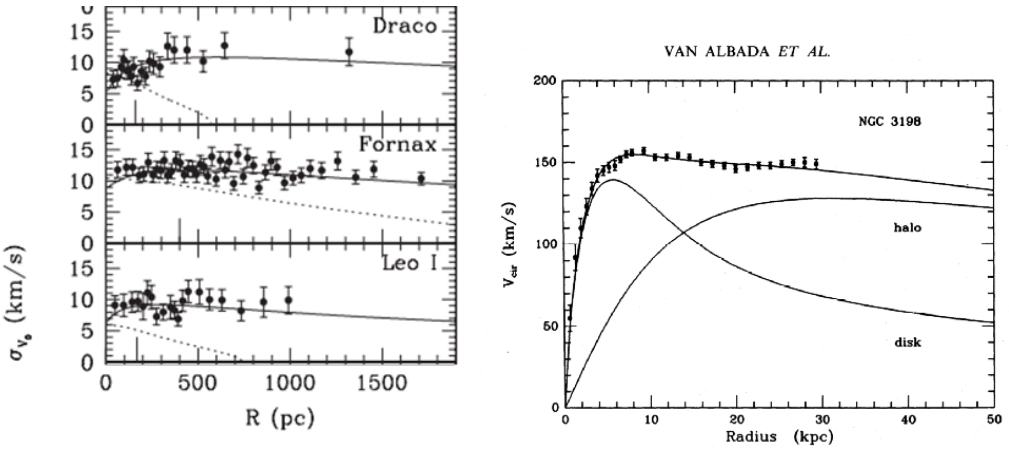

Figure 1.2: Left: Stellar velocity dispersions inside three Milky Way "dwarf" satellites from Ref. [1]. Solid lines show fits which include a dark matter profile while dotted lines show fits including only the visible matter. Right: Rotational velocity curves for NGC 3198 [2] showing contributions from the visible matter disk and the fitted dark matter halo.

On even larger scales (∼1-10 Mpc), we can look at clusters of galaxies. The first convincing evidence for dark matter (and even the name) arose here, in Fritz Zwicky's seminal 1933 paper [61]. Similar to dwarf galaxies, redshifts of individual galaxies in a cluster (here the Coma cluster) can be measured and used to determine the total gravita-

tional mass via the viral theorem – relating the average gravitational potential energy to the kinetic "temperature" of the galaxies. Zwicky found that the the measured velocity dispersions indicated a total cluster mass around 500 times more than the Galactic mass (which incidentally only makes up 20% of the baryon content of clusters, with the other 80% in the form of hot gas in the Intergalactic medium (IGM)).

Today, much more precise estimates of cluster matter density profiles can be obtained through X-ray observations of the hot ∼keV gas in the IGM along with gravitational lensing measurements, which reveal the total matter distributions by measuring the spacetime distortions of background objects. Nowhere is this more dramatically demonstrated than in the Bullet Cluster [3], shown in Figure 1.3. Here, two clusters have collided and passed through each other. The hot IGM gas has formed bow shocks and heated through the merger, while the majority of the two cluster masses are concentrated in lobes on either side of the interaction region. Since the bullet cluster discovery, at least five additional dissociative cluster mergers [62, 63] have been detected [2].

Beyond super-cluster scales, we move to cosmological probes with the majority of these being based on measurements of large scale structure formation in the early universe, and proceeding to later epochs. The non-linear structures we observe today – i.e. galaxies and clusters of galaxies – formed much earlier than is possible with baryons alone. In particular, observations of the CMB radiation reveal that substantial structure growth had already taken place by the time of CMB decoupling. In contrast,

[2]Notably, there have been recent claims [64, 65] of self-interacting dark matter causing an effective drag which displaces the collisionless stellar masses from the dark matter. At present, the uncertainties in such systems are highly underestimated, but nonetheless provide an intriguing probe of new physics.

Figure 1.3: Composite image of the Bullet Cluster [3]. Blue regions of the image indicate the mass density profile as determined through gravitational lensing while red regions show the concentration of hot gas making up around 80% of the cluster's bayronic matter content. The discrepancy between the two regions shows that the vast majority of the cluster mass is made up by approximately collisionless dark matter.

baryons, leptons, and photons remain in thermal equilibrium before recombination such that the primordial density fluctuations present at the end of inflation become washed out (due to coupling with the photon bath). Dark matter is required in order to form these deep gravitational wells early on, and promote the expedite the growth of baryon cooling and collapse after recombination. The most precise and striking measurements of the dark matter density relative to matter arise by measuring the relative heights of acoustic peaks in the power spectrum of the CMB which yield dark matter density of $\Omega_c h^2 = 0.1199 \pm 0.0022$ and a baryon density $\Omega_b h^2 = 0.02222 \pm 0.00023$ [53]. Here, the relative height of the third peak of the CMB power spectrum in particular shows that dark matter strongly enhances the the baryon compression phase by increasing the effective (gravitational) spring-constant in the acoustic oscillations [66].

After decoupling, several tracers of structure formation can be used to constrain dark matter. One technique uses two-point correlations of galaxies in large scale surveys such as SDSS to measure acoustic oscillations in the baryon-photon plasma. The structure and intensity of these Baryon Acoustic Oscillations (BAO), depend sensitively on the dark matter density. An additional probe of structure is given by the so-called Lyman-α forest. Here, redshifted photons from background quasars are absorbed by neutral hydrogen as they propagate to Earth. This creates absorption lines at different wavelengths which depends on the distance to the intervening hydrogen clouds. Performed over large regions of sky, this provides a 3D map of the baryons, and allows for one to determine the evolution of structure at very early formation epochs.

Even before recombination, the relative abundances of light nuclear species (D, ^{3}He, ^{4}He, and ^{7}Li) provide critical input to the standard cosmological picture. Big Bang Nucleosynthesis (BBN) is currently the earliest available observation of the universe (if you do not include present day production of high energy particles as early), and occurred at temperatures near the QCD phase transition $T \sim \Lambda_{\rm QCD} \approx 1 MeV$. The present day nuclear abundances are very well reproduced in the SM (except for ^{7}Li) and are sensitive to the number of relativistic degrees of freedom at these temperatures. If dark matter remains in equilibrium at these low temperatures, these abundances are not correctly replicated, implying that dark matter cannot contribute additional d.o.f. if its mass lies below $m_\chi \lesssim 5$ MeV[2] (see Ref. [67, 68] for a review on BBN and particle dark matter). Perhaps more importantly, the baryon density is constrained to be $\Omega_b \approx 0.04 \pm .02$ [69], in line with (later) measurements of the CMB. Thus, there is

a need already for dark matter at the primordial phase of the universe before stars and galaxies formed, practically eliminating the possibility of hidden baryonic objects as an explanation of DM, unless they arose from non-interacting primordial black holes (which are now almost entirely ruled out) [70].

In summary, evidence on large scales and at the earliest times, down to the highly non-linear structures we live in today all point toward the existence of dark matter. The difference in types of systems, timescales, and spatial scales provide overwhelming evidence which is extraordinarily difficult to reproduce with modified gravity, or compact baryonic objects. In the next section we explore connections between dark matter and particle physics which provides a variety of well motivated cold dark matter candidates.

1.2 Motivations for Particle Dark Matter

This overwhelming evidence for dark matter places in front of us, a mystery with only two solutions. Either we *require* new physics beyond the Standard Model, or we modify our model of gravitation. *Particle* dark matter is most strongly justified given the scale independent success of CDM cosmology, the lack of successful theories of modified gravity (and lack of external motivation for these modifications), and the knowledge that all known matter exists as particles described (at low energies) by a quantum field theory. Here we restrict our attention to cold particle dark matter candidates.

The space of suitable models is infinite, provoking the model builder to follow one or more guiding principles when positing a new theory. If other anomalous results are detected in experimental data, and can be reasonably related to dark matter, the

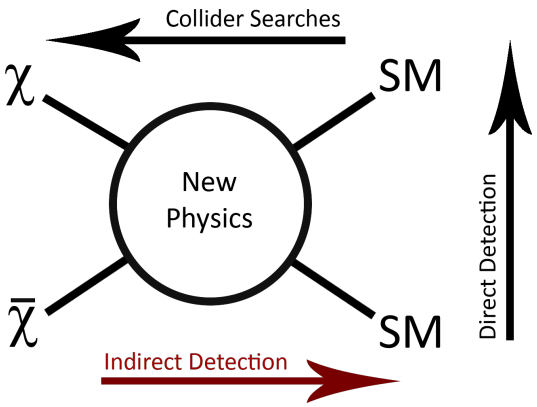

Figure 1.4: Approaches to dark matter complementarity. The three approaches are related through crossing symmetries.

most promising approach may be to construct theories which incorporate both dark matter and new other physics signals. In the absence of confident new physics signals, the phenomenologist may also have strong theoretical grounds for proposing a model, such as minimizing the new field content, utilizing "naturalness" arguments to explain model parameters, fitting models into symmetries or symmetry breaking structures. For dark matter, the most prolific class of models is by far that of Weakly Interacting Massive Particles (WIMPs), which *naturally* connects our need for additional electroweak scale physics to the correct dark matter relic abundance.

The Standard Model (SM) is plagued by the so-called hierarchy problem. Fermion loops dominated by the top-quark introduce divergences into the Higgs mass which are quadratic in the cutoff scale of the theory, either the GUT or planck scale in the SM alone. In order to reproduce the recently measured Higgs mass of 125 GeV [71, 72], the SM requires either an extraordinary fine parameter tuning (roughly 1 part in 10^{34}),

or the persence of new physics which cancels this divergence or lowers the effective cut-off. This lack of "naturalness" in the SM motivates the exploration of new physics near the electroweak scale ($\Lambda \sim m_W$) which reproduce the Higgs mass with closer to $\mathcal{O}(1)$ parameter tunings. This concept motivates many BSM theories such as supersymmetry, universal extra-dimensions or little Higgs theories, which carry natural stable, cold dark matter candidates.

One of the most remarkable coincidences (which we hope is not coincidental) is that the correct "relic-abundance" of dark matter is naturally reproduced if one assumes couplings near the Fermi coupling G_F between the dark matter and SM states, and a weak scale DM mass $m_\chi \sim m_W$. This theoretical observation is referred to as the "WIMP miracle", and the dark matter is produced thermally in the early universe.

For this this standard production scenario, matter, radiation, and DM are in equilibrium when the universe is hot relative to dark matter mass ($T > m_\chi$)[3]. As the universe expands with a scale-factor $a(t)$ and rate $\dot{a}(t)/a(t) \equiv H$, the temperature cools. Initially, the co-moving DM number density $n_{\rm eq}$ remains constant with interactions occur at a rate $\Gamma_{\rm ann} = \langle \sigma_{\rm ann} v \rangle n_{\rm eq}$, where the angle brackets represent a thermal average over the relative velocities of the dark matter profile (see Ref. [73] for a pedagogical review). $n_{\rm eq}$ is governed by a Boltzmann factor dark matter, and when the temperature of the Universe drops below m_χ, the WIMP production rate runs as $e^{-m_\chi/T}$. Soon after, when $T \approx m_\chi/20$, the DM annihilation rate is comparable to the Hubble rate H, the

[3]In other words, the diagram shown in Figure 1.4 proceed freely left to right such that particles are created and destroyed until a minimal Gibbs free energy of system is attained. Because of the precise overlap with statistical mechanics, we call this type of equilibrium *chemical equilibrium.* Equilibrium up and down on this diagram is called *kinetic equilibrium.*. When these (usually elastic) scatters between the SM and DM cease to exist we call this *kinetic decoupling* which occurs strictly after *chemical decoupling.*

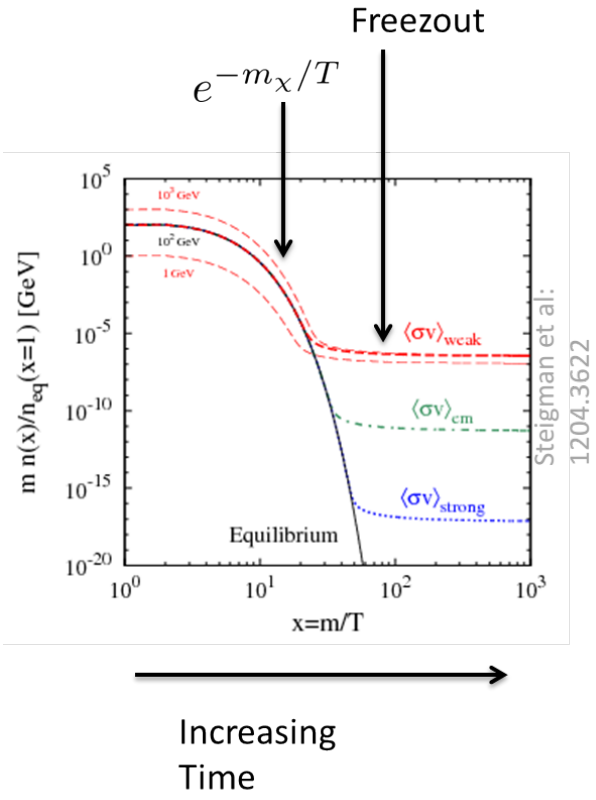

Figure 1.5: Evolution of the co-moving dark matter number density as the universe cools in a thermal WIMP production scenario taken from Ref. [4].

DM density "freezes-out", and the co-moving number density remains constant, leaving a relic abundance of DM that we hope is detectable today. At recombination, the benchmark dark matter density is given by $\Omega_c h^2 \approx 3 \times 10^{-26}$ cm^3 s$^{-1}/\langle\sigma_{\rm ann} v\rangle$, which provides a baseline cross-section for detecting WIMP dark matter today (though e.g. strongly velocity dependent cross-sections may suppress the current interaction).

These profoundly deep connections between particle physics and cosmology have led to an intense concentration of efforts around the detection of WIMPs on three frontiers: collider production, direct detection, and indirect detection. These probes

provide different lenses to test DM models and collectively comprise the framework known as "dark matter complementarity" [74]. This can be schematically represented by the different arrows of time on the Feynman diagram shown in Figure 1.4.

Collider searches aim to discover new particles through their production at either hadron colliders such as the LHC (see e.g. Reviews [75, 76, 77]) or at future e^+e^- colliders [78]. Direct detection experiments utilize large and extremely low-background underground detectors to observe the nuclear recoils following the scattering of a WIMP from the Milky Way halo off of target nuclei [79]. The final view, indirect detection, looks to the sky for signatures of dark matter pair-annihilations or decays of DM into Standard Model particles, including observations of cosmic-rays, electromagnetic radiation, and neutrinos. Ultimately, the identification of particle dark matter will require confirmation on at least two of these fronts to be confident, although a detection in any channel provides search strategies to the others.

It is important to not let theoretical preconceptions bias our view. Dark matter does not need to be a WIMP. In fact, it does not need to interact with the Standard Model at all. The lack of robust detections of new particles in direct detection and collider searches has recently led many to study alternative models for dark matter which include, for example, axions to solve the strong-CP problem, or sterile neutrinos as a solution to neutrino masses as well as a plethora of exotic candidates [80, 54]. In some models, if the dark matter self interactions are large enough to strongly modify stellar cooling, halo shapes, or cluster merger morphologies, then some hope still remains for further constraining dark matter's particle properties without direct observation. At a

basic level, it is also remarkable that our universe contains an $\mathcal{O}(1)$ ratio of dark matter to baryonic matter ($\Omega_c/\Omega_b \approx 5$) indicating that the dark sector and Standard Model Lagrangians are likely to be related at some energy scale[4]. In this thesis, we will focus almost entirely on the indirect detection of WIMP dark matter using Galactic cosmic and gamma-rays.

1.3 An Overview of This Work

In the previous section, we described a very general approach to indirect detection. In an ideal world, we would just have to design an instrument with enough sensitivity to detect an appreciable number of annihilation events. With the sole exception of heavy antimatter probes, this is far from being true. The Milky Way consists of many high energy astrophysical sources including supernovae remnants (SNR), pulsars, and a central supermassive black hole. These objects accelerate cosmic-rays to ultra-relativistic energies which propagate through the Galaxy until either escaping or interacting with interstellar gas and low-energy radiation, generating both additional cosmic-rays and bright diffuse gamma-ray emission, with additional gamma rays produced directly in pulsar magnetospheres, as well as by background starburst galaxies and blazars. These astrophysical "backgrounds" far exceed those expected from dark matter and in this regime, detecting a weak dark matter signal with any degree of confidence is a tall order, which often requires (i) new techniques for discriminating dark

[4]Some models, such as asymmetric dark matter (ADM), even use this as a starting point for the theory (see e.g. the review of Ref. [81]).

matter signals from astrophysics, and (ii) updated astrophysical models of cosmic-ray propagation, and the ensuing diffuse Galactic gamma-ray emission.

This thesis is divided into three parts which are intended to not only highlight several of our own contributions to the field, but to provide a solid foundation for both future indirect detection studies and improved modeling of Galactic cosmic and gamma-ray physics. The first two parts provide essential background, methodology for calculating/computing both signals and backgrounds, and an overview of statistical techniques and strategies for separating the two. This includes several of our own contributions, while the final part focuses on the application of these methods to several claims of indirect detection signals.

Part I, Indirect Detection Fundamentals: We present foundational knowledge for calculating and detecting indirect detection signals from dark matter. This includes targets, an overview of current and future experimental efforts, search strategies, statistical techniques, and injection spectra of standard model particles by dark matter. Our major statistical contributions include novel applications of several techniques such as clustering algorithms, new uses of multi-linear template regression, and an improved calibration of background uncertainties for dwarf galaxy searches. In addition, we perform the first calculation of anti-helium injection rates from dark matter as well as exploring models where dark matter interacts with cosmic-rays or interstellar gas.

Part II, Modeling of Galactic Cosmic and Gamma Rays: Cosmic and gamma ray back-

grounds in the Milky Way typically dominate signals from dark matter. It is crucial to understand both the uncertainties, and astrophysical possibilities before claiming detection of an excess. In *Part II* we first develop simplified cosmic-ray propagation models and apply them to cosmic-ray nuclei. We then promote the simplified models into a full precision numerical treatment of propagation including an extensive discussion of high-energy radiation (and synchrotron) emitted from cosmic-rays. We then describe in detail state-of-the-art propagation models and models of gas, cosmic-ray sources, magnetic fields, and interstellar radiation fields for the Milky Way. Our most significant contributions include developing new precision cosmic-ray source models, the use of new Galactic gas distributions, the addition of Galactic center winds to propagation simulations, the first detailed study of cosmic-ray bursts and time-dependent effects near the Galactic center, discussions of the shortcomings of modern models at the Galactic center, and new propagation methods for antihelium nuclei.

Part III, Indirect Detection Signals: Enormous leaps forward in experimental capability over the past two decades have begun to probe exciting and new astrophysics while also becoming sensitive to much of the thermal WIMP model space. These advancements have led naturally to claims of signals in excess of known astrophysical backgrounds. As we have zealously pointed out in almost every case, these astrophysical backgrounds contain large and unexplored systematic uncertainties. Here we apply the methods and models developed over the previous two *parts* toward rigorously testing the robustness of claimed indirect detection signals, including

most prominently the Fermi GeV Galactic center excess, the Fermi 135 GeV line, the 3.5 keV X-ray line, and the WMAP-Planck haze[5]. This section contains the most substantial body of work, and has been instrumental in providing a voice for astrophysical uncertainties across the indirect detection field. In studying the GeV gamma-ray excess at the Galactic center, we presented two major results: (i) Bursts of cosmic-ray injection can reproduce many of the GeV excess properties, and (ii) previous models of the Galactic center diffuse gamma-ray emission completely neglect cosmic-rays born at the Galactic center, which when added, eliminate most of excess. When examining the 135 GeV line, we employ clustering methods to eliminate the only known astrophysical background (pulsars), showing that the line must be dark matter or a systematic issue (as is the case now). In the case of the 3.5 keV line, we perform a template analysis to show that the morphology of the line signal correlates strongly with known plasma lines in the Galactic Center, and excluding a dark matter interpretation of the signal. Finally, we test the origins of the WMAP-Planck haze, showing that if due to dark matter, there must be mechanisms in place to suppress the corresponding synchrotron radiation in nearby spiral galaxies with similar properties to the Milky Way.

[5]We omit a discussion of the TeV positron excess here, although the propagation models from Parts I/II can be directly applied to these cases. Similar to most of the other signals discussed, cosmic-ray positrons generated by nearby pulsars provide an excellent fit to the data without the need for dark matter.

Chapter 2

Indirect Detection of Particle Dark Matter

2.1 Estimating Rates

If particle dark matter interacts with the Standard Model non-gravitationally, we can probe its particle properties indirectly using searches for photons, neutrinos, or charged cosmic rays which are produced during the pair-annihilation ($\chi\chi \rightarrow$ SM) or decay ($\chi \rightarrow$ SM) into SM states. From a purely observational point of view, the indirect detection signatures of dark matter model can typically be specified by three quantities [80]:

1. *Abundance:* How much dark matter occupies a given phase space in some astrophysical system? For models without a strong velocity dependent cross-section, it suffices to know the spatial density $\rho_\chi(\vec{r})$, with the number density of dark matter

given by $n_\chi = \rho_\chi / m_\chi$.

2. *Energy Scale:* What is the mass or momentum range of interest? For cold dark matter particles with velocity independent cross-sections, the dark matter mass is sufficient to specify the energy scale.

3. *SM Production:* What is the cross-section or decay rate into each SM particle (rate + branching fractions)?

At this point, the rate of injection into the interstellar medium can be calculated by a basic product of these terms. It is useful to split the discussion here into the two indirect detection cases: photons and neutrinos which travel in straight lines from their injection points, versus cosmic-rays which bend through the Galaxy's magnetic field and must be propagated using models of the Milky Way.

2.1.1 Gamma-Rays and Neutrinos

We begin by calculating the flux and spectrum for the former case, noting that γ applies equally to neutrinos.

$$\frac{d\Phi_\gamma}{dE_\gamma} = \underbrace{\int_{\Delta\Omega}\int_{l.o.s} \rho(l,b,z)^2 \; d\Omega dz}_{\mathcal{J}-\text{factor}} \underbrace{\frac{1}{4\pi}\sum_f \frac{\langle\sigma v\rangle_{\chi\chi\to f}}{2m_\chi^2}\frac{dN_\gamma^f}{dE_\gamma}}_{\text{P.P.}} \qquad \text{Annihilation} \tag{2.1}$$

$$\frac{d\Phi_\gamma}{dE_\gamma} = \underbrace{\int_{\Delta\Omega}\int_{l.o.s} \rho(l,b,z) \; d\Omega dz}_{\mathcal{J}-\text{factor}} \underbrace{\frac{1}{4\pi}\sum_f \frac{\Gamma_{\chi\to f}}{m_\chi}\frac{dN_\gamma^f}{dE_\gamma}}_{\text{P.P.}} \qquad \text{Decay} \tag{2.2}$$

Here, we have factorized the flux into two terms. The first encapsulates the astrophysics, revealing the model-independent part of the rate, integrating over the line of sight and the solid angle of the observation[1]. The second term consists of the particle physics factors. First, the isotropic emission leads to a $1/4\pi$ from the, while the summation is performed over all of the SM final states. For annihilating dark matter, the factor 2 in the denominator becomes 4 if the DM is not its own antiparticle. At this point, known physics can be used to calculate the *injection spectrum* dN_γ^f/dE of e.g. photons, given the initial SM annihilation product f (see Chapter 3).

We now have a differential flux $d\phi_\gamma/dE_\gamma$ which is usually given in units of $[\mathrm{cm}^{-2}\ \mathrm{s}^{-1}\ E^{-1}]$ and we see that the number of events can be determined by multiplication with the *effective area* of an instrument, and an *exposure time*.

$$\frac{dN_\gamma}{dE} = \mathcal{A}_{\mathrm{eff}} \cdot t_{\mathrm{exp}} \cdot \frac{d\phi_\gamma}{dE} \tag{2.3}$$

In Section 2.4, we will discuss these quantities for several ongoing and future experiments. In order to be detected, a dark matter model must have at least some events when integrated over some energy band and it must have enough events to be observable over the astrophysical background uncertainty ($N_{\mathrm{DM}} \gtrsim \sqrt{N_{\mathrm{BG}}}$). Why have we kept the flux differential in energy? Because the *spectrum* is almost always important in trying to distinguish backgrounds. Throughout this thesis we will also see that the *morphology* of a signal (i.e. the differential of $\mathcal{J}$ in solid angle) is often just as important when

[1]Note that for cross-sections $\langle\sigma v\rangle$ which are velocity independent, these cannot be factored, and the integral must be performed over the full momentum space, with $\langle\sigma(v)v\rangle$ under the integrand.

the size of the object of interest is larger than the angular resolution of our instrument. For gamma-rays and X-rays in the Galactic center for example, both the spectrum and morphology (which may or may not be energy dependent) must be used to help disentangle backgrounds.

2.1.2 Cosmic-Rays

Cosmic-rays differ from photons and neutrinos due to their propagation through the Galaxy. Because cosmic-rays are charged [2], we must calculate not only their injection, but also their motion through the Milky Way's magnetic fields, and their interactions with gas and radiation, as well as further propagation through the Solar System's magnetic field. This leads to a complicated detection strategy which requires the inversion of a very difficult partial differential equation in order to try and reconstruct the properties of the cosmic-ray source. Here we focus on calculating the injection of cosmic-rays from dark matter, and discuss these propagation model in great detail throughout Part II.

The particles of interest are those that are stable and include electrons, protons, antiprotons, positrons, as well as heavier antimatter species such as anti-deuterium ($\overline{d}$) and anti-helium-3 ($^3\overline{\mathrm{He}}$). The injection rate of a cosmic-ray species "CR" at a given spatial position is given by

$$\Gamma_{\mathrm{CR}}(\vec{r}) = \rho(\vec{r})^2 \sum_f \frac{\langle \sigma v \rangle_{\chi\chi\to \mathrm{f}}}{2m_\chi^2} \frac{dN_{\mathrm{CR}}^f}{dE} \qquad \text{Annihilation} \tag{2.4}$$

[2] Recall that free neutrons beta decay with a half-life of $\tau \approx 611$ s.

$$\Gamma_{\rm CR}(\vec{r}) = \rho(\vec{r}) \sum_f \frac{\Gamma_{\chi \to {\rm f}}}{m_\chi} \frac{dN^f_{\rm CR}}{dE} \quad \text{Decay} \tag{2.5}$$

At this point, one must propagate the injected particles through the Galaxy using an analytic, semi-analytic (i.e. Green's functions), or numerical treatment such as Galprop [82, 83, 84, 85, 86] or Dragon [87]. For antiprotons, numerical treatments are necessary due to the complex astrophysical backgrounds and tertiary scattering. For heavier species, it is usually sufficient to use two-zone diffusion models as most interactions with gas result in fragmentation or annihilation of the nucleus. The electron and positron backgrounds should be calculated with numerical treatments due to the rapid energy losses and secondary production which is sensitive to the local distribution of gas in the Galaxy. One may, however, obtain reasonable results with analytic formulae when calculating primary sources such as dark matter or nearby pulsars.

2.2 Dark Matter Halo Profiles

Our above calculation of indirect detection rates requires us to know the dark matter density. For gamma-rays, and annihilation in particular, we must understand the halo profile at the most dense points, the Centers of dwarfs or the center of the Milky Way. Detailed N-body simulations in ΛCDM cosmologies provide a wealth of information on the density of dark matter at all of these scales. However, we also know that baryonic effects, and potentially dark matter self-interactions may play an important role in these systems. In this Section we will start with the classical benchmark

halo models, and then briefly discuss the state of understanding regarding baryonic interactions. It is typical in the literature to show results for multiple halo profiles, or to generalize the models and scan parametrically when a signal is detected (as claimed in the Galactic center).

In addition to the density profile, the clumping of substructures can also play an important role, and is probed by simulations, as are the velocity distributions of the dark matter profiles. Here, the main models of interest are those s-wave dominated and are therefore independent of the DM velocity distributions. We will thus proceed under this assumption and the assumption that the DM is cold. At this point, dark matter only simulations reveal several underlying principles.

1. The halo profiles are approximately scale invariant in form, characterized from supercluster scales to Galactic subhalo scales by a single concentration parameter that depends on the formation time and mass.

2. Dark matter halos tend to be cuspy, with the inner regions running as approximately $\rho \sim r^{-1}$

3. Structure forms hierarchically from the bottom up, – i.e. first on small scales and then on larger scales.

4. Halos are triaxial ellipsoids with upto 40% enhancements along the major axis not being uncommon. Typically these halos are assumed to be spherical in indirect detection.

The focus here is on galactic sized halos, although various reviews can be found

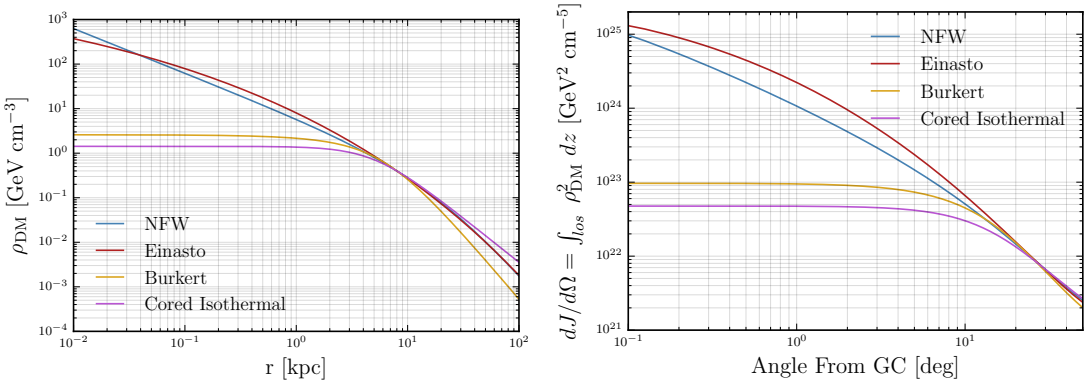

Figure 2.1: Left: Common dark matter density profiles used in the Milky Way. Right: Annilhlation projected annihilation densities integrated along the line of sight for common DM profiles. Integrating this distribution over solid angle yields a J-factor. All profiles have been normalized at the solar position of 8 kpc to have a density $\rho = .4\text{GeVcm}^{-3}$.

which discuss different mass regimes such as clusters of galaxies, or smaller subhalo structure [88]. In Figure 2.1 we show the halo profiles described below, as well as the projection of the squared profile along the line-of-sight, which yields the differential J-factor. One can immediately see that different profiles can lead to more than an order of magnitude difference in the indirect detection flux expected from the Galactic center.

2.2.1 Navarro-Frenk-White (NFW) Profile

The NFW profile [89, 90] is by far the most common used in the literature. It provides an excellent fit to halo masses over 9 orders of magnitude from globular to galaxy clusters (in DM only simulations) and has the generalized form,

$$\rho(r) = \left(\frac{r_s}{r}\right)^{\gamma} \frac{\rho_0}{(1 + r/r_s)^{3-\gamma}}, \tag{2.6}$$

where $\gamma = 1$ in the usual case and $\gamma > 1$ for contracted (more-cuspy) halos and

r_s is the halo scale-radius where the slope has an index -2 (for $\gamma = 1$). In the Milky Way, ρ_0 is typically normalized to match the locally determined dark matter density $\rho(r = 8\text{kpc}) = 0.4^{+.16}_{-.2}$ GeV cm^{-3} [91] and r_s is usually taken to be around 20 kpc. For other systems, ρ_0 is typically replaced by a *concentration* parameter c defined as the ratio of the *virial radius* and the scale radius. The following relation relates the two parametrizations.

$$M = 4\pi\rho_0 r_s^3 \left[\ln(1+c) - \frac{c}{1+c}\right] \tag{2.7}$$

where M is the *virial mass* – i.e. the mass within the virial radius which is typically defined as the radius where the dark matter density is 200 times the critical density (R_{200}). For many cluster size systems $c \approx 20$, although it is both halo mass dependent, redshift varying, and depends on the cluster core parameters (e.g. cool core or not?). For dwarf galaxies, stellar velocity measurements reveal more cored profiles and $c \approx 5$[92], and are not well fit by an NFW profile.

2.2.2 Einasto Profile

For galaxy sized halos, and for dwarf galaxies, the Einasto profile provides at least as good of a fit as an NFW. Simulations show that the log-density profile varies continuously with radius according to the differential equation

$$\frac{d\ln\rho}{d\ln r} = -2\left(\frac{r}{r_s}\right)^{\alpha} \tag{2.8}$$

with a curvature parameter $1/\alpha$ and r_s the radius at which the log-slope is -2. This is integrated to obtain the Einasto density profile [93].

$$\rho(r) = \rho_s \exp\left(-\frac{2}{\alpha}\left[\left(\frac{r}{r_s}\right)^{-\alpha} - 1\right]\right). \tag{2.9}$$

Typical scale factors for the Milky Way are r_s =20 kpc and $\alpha = 0.16$.

2.2.3 Burkert Profile

The Burkert [94] profile models highly cored profiles, and developed to provide a better fit than an NFW for dwarf galaxies, where the observed concentrations are extremely low. For the Milky Way, it is often used as a *very* conservatively low estimate of the central dark matter density. It does not posses a cusp and the scale radius is usually taken to be around 6 kpc for the Milky Way.

$$\rho(r) = \frac{\rho_0 r_s^3}{(r_s + r)(r_s^2 + r^2)}. \tag{2.10}$$

2.2.4 Isothermal Profile

Pure isothermal profiles falloff as r^{-2}, which provide a flat rotation curve. At the center of the Galaxy however, the density diverges unphysically and must be softened. The "pseudo-isothermal" profile has a cored region at the center characterized by a core radius $r_c \sim$ 1kpc. While disk dominated galaxies are fit well by isothermal and NFW profiles, low-mass galaxies have been (observationally) much better fit by pseudo-isothermal profiles [95].

$$\rho(r) = \frac{\rho_0}{1 + (r/r_c)^2} \tag{2.11}$$

2.2.5 The Impact of Baryons

Baryons dominate the gravitational potential in the central regions of galaxies such as the Milky Way. There is currently no consensus on how they impact the profile of the inner dark matter cores. Current simulations incorporating baryons and feedback processes are limited in resolution by both the gravitational softening length as well as the particle resolution and the accuracy of the subgrid physics which includes cooling and feedback mechanisms that must be phenomenologically calibrated. Two contrasting theories are often cited.

The first is known as *adiabatic contraction*. As baryons cool, they enhance the potential at the Galactic center by dragging in dark matter, both through the enhanced potential and dynamical friction. This steepens the inner DM profile [96, 97, 98]. On the other hand, this culmination of cool baryons triggers star formation or strong accretion onto the central black holes which can lead to violent bursts of feedback which expel gas from the system. This infall-feedback loop then repeats in an episodic fashion, which reduces the central potential and softens the DM density profile [99, 100, 101]. These issues are of great interest for modern simulation studies, but the balance between effects remains sensitively dependent on the implementation of sub-grid physics.

2.3 Indirect Detection Targets

In the previous section we determined concretely the rates of dark matter indirect detection signals in both photon/neutrino channels and cosmic-ray searches. We review here the potential targets for both cases[3].

2.3.1 Gamma-Ray Searches

Gamma-rays provide an excellent probe of particle dark matter for two reasons. First, *all* SM final states will produce gamma-rays[4] when the energy scale of the annihilation $m_\chi \gg m_e$. This occurs via either hadron showers ($\chi\chi \to X \to \pi^0 + X \to \gamma\gamma$) or final state radiation which both produce a diffuse spectral signature which cuts off for $E_\gamma > m_\chi$, or from direct emission ($\chi\chi \to \gamma\gamma, Z\gamma$) which produces a line-like signature at energies $E_\gamma \approx m_\chi$ or $E_\gamma \approx m_\chi(1 - m_z^2/(2m_\chi^2))$ respectively. Second, gamma-rays propagate with straight trajectories, meaning they point directly back to the source. We can therefore point our detectors toward regions of high dark matter density. As we saw in Equations (2.1-2.2), the gamma-ray flux from annihilation (decay) depends quadratically (linearly) on the dark matter density. This implies that we can set robust limits on nearly all WIMP models by performing long exposures on the cores of dwarfs, galaxies, or galaxy clusters.

[3]Owing to the identical form of Eqn. 2.4 for neutrinos and gamma-rays, most gamma-ray targets are also promising for neutrino searches. Neutrinos however, are able to travel unimposed through solid matter. For most WIMP dark matter models, the DM can be captured inside the astronomical bodies such as the Sun and Earth making them equally attractive targets for signatures of dark matter. We do not explore these neutrino-only targets here. For a recent review on the methods and status of neutrino dark matter searches see e.g. Ref. [102].

[4]Even neutrino final states can radiate a weak boson on, or off-shell.

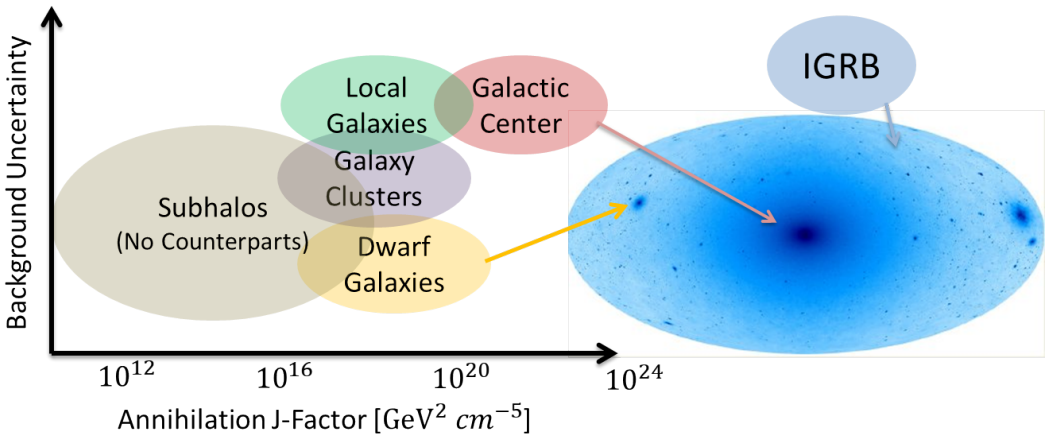

Figure 2.2: Schematic of tradeoffs between indfirect detection targets as well as the dark matter annihilation flux column density from the Via Lactea II simulations [5]. Stacked (joint-likelihood) analyses of dwarf galaxies enhance the J-factor while maintaining the same background uncertainties, providing even more robust constraints.

Fortunately, astrophysical backgrounds exist in most places[5] and one must counterbalance the background flux, complexity, and spectrum against the signal properties. In Figure 2.2, we show a schematic of common targets, although background complexity depends strongly on the energy range and annihilation spectrum of interest. Here we briefly review the pros and cons of common targets crudely ordered by in decreasing usefulness. Note that this ordering depends significantly on whether the DM annihilates or decays, as well as the energy (or more generally type of EM radiation) being observed.

Dwarf Galaxies: Among all the indirect detection targets, gamma-rays from Milky Way dwarf satellites remain the "golden channel", having essentially no astrophysical

[5]We are fortunate in this regard because cosmic-ray physics has an immense amount to teach us about high-energy astrophysical objects and environments. In PartIII, we see several examples of extraordinarily interesting systems. For this reason, one should avoid simply saying "background" without qualifying the awesomeness of the background.

background other than galaxies lying in the background along the line-of-sight[6]. Because there are now more than thirty known ultra-faints orbiting the Milky Way, several collaborations have performed joint-likelihood searches which combine (usually null) Fermi-LAT gamma-ray measurements of each galaxy while also marginalizing over the uncertain J-factors of at least 15 of the most promising targets [106] as well as teaming up with higher energy ground based Air Cherenkov telescopes such as MAGIC [107]. So far, no significant detections have arisen other the Ret II. The Fermi-LAT constraints are considered extremely robust and mark the cleanest of all indirect detection signals. They also provide cross-constraints on other purported indirect detection signals such as the GeV Galactic center gamma-ray excess.

The Galactic Center: The center of the Milky Way makes up the brightest of all gamma-ray signals. It is extremely close, lying at $d = 8$ kpc (compared to 30-200 kpc for dwarfs), and contains a very large dark matter core. These lead to an expected J-factor which is roughly 5 orders of magnitude greater than dwarfs. However, the center of the Milky Way shows signatures similar to nearby star-forming galaxies and is just becoming understood. The *Fermi* telescope is just now providing a high-resolution window at GeV energies, while radio observations from *Planck* and other multiwavelength observations are beginning to show a coherent story of cosmic-ray physics and star formation histories. In addition, the number of

[6]A gamma-ray counterpart has recently been detected in the ultra-faint galaxy Reticulum II [103] which is compatible with the Galactic center GeV excess. However, there are radio-bright galaxies overlapping that have not been conclusively disentangled as potential progenitors [104]. See also the discussion in Section 4.7 and Ref [105].

millisecond pulsars in the region is highly uncertain, providing a background at GeV energies which is nearly indistinguishable from that of dark matter. We will discuss the Galactic center GeV excess in depth throughout Chapter 8. Additional claims of detection have also arisen here inclunding the 135 GeV line, the 511 keV poistron line, the 3.5 keV line, and the WMAP-Planck haze. Each of these has proven to be astrophysical or instrumental in nature, underscoring the complexity of the backgrounds here, even in cases where the spectral signatures were originally thought to be unique to dark matter.

Galaxy Clusters: Galaxy clusters are extremely interesting objects from the perspective of cosmic-ray physics and dark matter physics, owing to their huge dark-mass fraction. While prospects for detection of any gamma-rays remains bright, no clusters have yet been detected [108], even though comparable gamma-ray intensities are expected from cosmic-rays interactions with the radiation and hot gas in the intergalactic medium. The current upper limits on the dark matter annihilation cross-section remain 1-2 orders of magnitude below the dwarf constraints [109]. For decaying DM, galaxy clusters actually outperform dwarf galaxies. Perhaps more interesting are observations at lower energies including the 3.5 keV X-ray line detected in several clusters (see Sec. 10 for a review) as well as radio constraints on dark matter to leptons via non-observation of synchrotron emission [110]. Upcoming radio observations from the Low Frequency Array (LOFAR) and Square Kilometer Array (SKA) will shed further light on these objects.

Isotropic Gamma-Ray Backgrounds (IGRB): Diffuse gamma-ray emission across the full sky can also be used to constrain dark matter models [111]. The isotropic gamma-ray background contains contributions from all unresolved point sources in the universe, which include contributions from dark matter. These backgrounds can thus be difficult to disentangle, since both are isotropic. We must also subtract the Galactic astrophysical foreground emission and the smooth Galactic DM halo contribution (which can also be used to detect DM). These constraints thus dependent on both the model of foreground, and the model of extragalactic emission assumed. They significantly under-perform dwarf constraints for annihilation signals, while remaining quite competitive for decaying DM.

Local Galaxies: Local group galaxies such as Andromeda typically contain the same problems as the Milky Way center, but are not as bright (see e.g. [112]). The cosmic-ray physics and pulsar populations are not well understood, and detection is difficult at these distances. Recently, potential excess compatible with the GeV excess has been reported by the Fermi LAT collaboration in the Large Magellenic Cloud (LMC) [113], however, similar observations in the SMC [114] have revealed no such excess, and the background models contain only very simple models for the associated diffuse emission whereas the LMC contains active star forming regions alongside only very loosely constrained cosmic-ray diffusion.

Dark Matter Subhalos: Dark matter structures form hierarchically, with the number density of a given halo mass increasing as a power-law in the mass. They are also

expected to be nearby, and bright enough to be detected, although we do not know where they are *a priori*. Recent estimates from N-body simulations [115] suggest that for a representative 40 GeV dark matter candidate annihilating to quarks, approximately 10 subhalos may have already been detected in the Fermi-LAT 3FGL catalog [116] as unassociated point sources. These appear as point-like, or very slightly extended sources with *no* multi-wavelength counterparts [117]. While these targets are intriguing, one must make dedicated multi-wavelength follow up observations before a given candidate becomes interesting, and it should be detected gravitationally via microlensing.

Globular Clusters: There has been at least one attempt [118] at detecting dark matter signals from Milky Way globular clusters. However, the mass of such systems is dominated by stars, and they contain many bright pulsars which complicate the backgrounds in the GeV regime [119]. They therefore make worse targets than Milky Way satellites for detecting dark matter.

These targets comprise the mainstream. However, new methods and models are rapidly being developed, while new experimental probes are arriving every year (see Sec. 2.4). One of the most fertile areas of new growth is the use of much more multiwavelength data to better constrain backgrounds, combined with Bayesian methods for marginalizing over unknown systematics.

2.3.2 Cosmic-Ray Searches

In order to search for dark matter using cosmic-rays, we must focus on a domain where the large astrophysical backgrounds are highly suppressed. This is not the case for cosmic-ray protons, electrons, or nuclei which are abundantly produced in the Galaxy by shock-accelerating e.g. protons and electrons in ionized plasmas. Antimatter however, is scarce in the universe. It is produced astrophysically, only through high-energy particle processes such as pair production in pulsar magnetospheres, jets of Active Galactic Nuclei (AGN), or via cosmic-ray spallation[7]. For most models of dark matter annihilation, SM particles are produced in particle-antiparticle pairs, and often decay through chains of final state radiation and/or hadronization which produce antimatter. There are two classes of cosmic-ray searches which are sensitive to these dark matter signatures: high-energy positrons and anti-nuclei searches up to atomic number 3 including $\overline{p}, \overline{d}$, and ${}^3\overline{\mathrm{He}}$.

As cosmic-rays propagate from their injection site throughout the Galaxy, they both lose energy and leak out of the diffusion halo, such that only relatively local sources can be detected. The radius of this detection neighbourhood depends strongly on both the species (e^+/e^- vs nuclei) as well as the energy.

Leptons: At the energies of interest begin at the positron mass $E = .511$ MeV, where ionization and coulomb losses restrict cosmic-rays to a very small window. At several hundred MeV, the energy loss time-scales of order 1 Gyr, but diffusion is

[7]Spallation is the interaction of a high energy cosmic ray with at-rest interstellar gas. The corresponding proton-proton collision produces many high-energy jets of particles, the most abundant of which are charged and neutral pions which produce photons, electrons, and positrons ($\pi^0 \to \gamma\gamma, \pi^\pm \to \nu_l + l^\pm$).

slow, and the particles leak from the Galaxy, limiting the window of influence to under 5 kpc. Above 1 GeV, the synchrotron and Inverse Compton losses losses are quadratic in energy, and the diffusion radius at 1 TeV is limited to several hundred parsecs of the Solar System [83].

Nuclei: For nuclear species, energy losses are not crucial for dark matter searches, and the diffusion radius at the mean residence time[8] determines the detection neighborhood. For typical energies near 1-500 GeV, this is between 5-10 kpc.

With potential exceptions for ultra-high-energy cosmic rays (UHECRs have $E \gtrsim 10^{18}$ eV), dark matter searches using cosmic-rays are therefore limited to our own Galactic dark matter halo, or very nearby dark matter substructures embedded within the Galactic DM halo, and are hardly sensitive even to the dark matter rich Galactic center region.

2.4 Experiments

Indirect detection experiments span a large and diverse array of astronomical and astroparticle datasets. The field is also rapidly evolving as searches for more exotic (non-WIMP) candidates garner attention following null detections in direct and collider searches. Here we concentrate on upcoming gamma and cosmic-ray observatories with special focus on the response characteristics of *Fermi's* Large Area Telescope (LAT). A comprehensive review of current and planned indirect detection experiments can be

[8]The cosmic-ray residence time is the lifetime of cosmic-rays living in the Galaxy before escaping the Galactic diffusion halo.

found in Ref. [120], which much of this Section is adapted from, although this review does not include less common detection methods such as radio or X-rays.

2.4.1 Current and Planned Experiments

In Table 2.4.1 we show current and planned gamma-ray and cosmic-ray experiments along with estimates of their baseline performance characteristics. It is very important to note that – for a given experiment – these characteristics are typically *strongly* dependent on both the energy range under consideration and the spatial position on the sky. Precise characteristics can be easily obtained in the technical reports for each experiment. Recall from Chapter 2 that the number of detected events from dark matter runs as

$$N \sim (4\pi)^{-1} \Gamma_{\rm DM} \; N_{\rm DM} \; \mathcal{A} \; t_{\rm exp} \tag{2.12}$$

where $\Gamma_{\rm DM}$ is the rate of annihilation or decays integrated over the volume of interest, $N_{\rm DM}$ is the number of photons falling within the detectors energy range, $\mathcal{A}$ is the effective area, and $t_{\rm exp}$ is the approximate exposure time. This allows us to quite simply estimate the magnitude of detectable events for a given model, at least in the case of electromagnetic radiation or neutrinos.

For all of their differences, cosmic and gamma-ray experiments are often purposed for both, as the detectors are typically designed to detect hadronic and electromagnetic showers. This allows us to more sensibly classify experiments in two broad categories: satellite or balloon born missions versus ground based detectors.

Satellite based detectors which have the advantage of escaping the Earth's atmosphere thereby obtaining *direct* cosmic and gamma ray measurements which are easily distinguished through for example, an external layer around the tracker designed to veto charged particles (anti-coincidence shield). Satellites are also payload limited which implies that the detector volume (and thus the effective area) must be relatively small, of order 1 m^2. However, many are designed to observe very large fields of view, if not the entire sky, and additionally compensate for this reduced area with high duty cycles as well as exposure times across the full sky on the order of years ($\pi \times 10^7$ s). Most have excellent energy resolution and the gamma-ray detectors have good angular resolution, at least below 0.5 degrees at energies above a few 10s of GeV, typically reduced to several degrees below 1 GeV, in the Compton regime.

Ground based observatories utilize the Earth's atmosphere as a calorimeter. As high energy cosmic-rays or gamma rays impact the atmosphere, either hadronic or electromagnetic showers ensue and can be detected on the ground by their Cherenkov radiation. These Imaging Air Cherenkov Telescopes (IACTs or ACTs) have the principle advantage of offering enourmous collection areas on the order of km^2 which is 10^6 times larger than space based observatories. In addition, they can easily probe extremely high energies, where the limited volume and mass of satellites cannot fully contain particles above a few TeV. However, their limited duty cycle and small field of views provide only targeted observations with typically 100-10^3 hr exposures. Furthermore, electrons and gamma-rays can not be efficiently distinguished, due to the identical EM shower profiles. Protons have distinct showers, but are very abundant and lead to large approximately

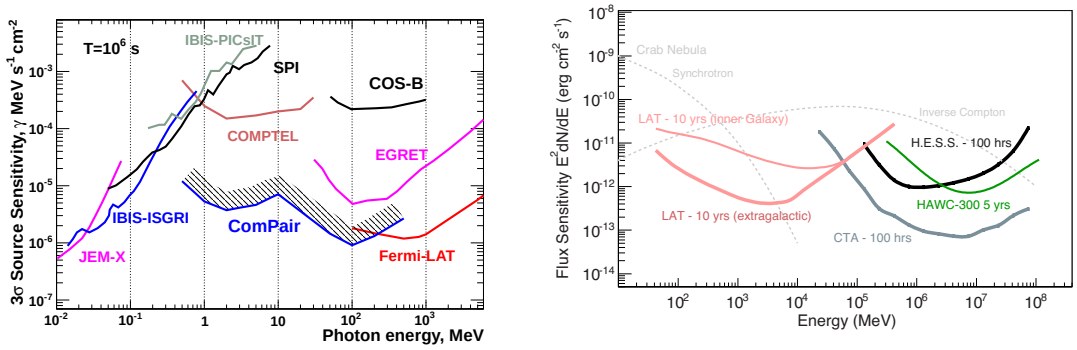

Figure 2.3: Left: Source sensitivity for experiments with detection capability below 10 GeV taken from [6] and flux sensitivities of high energy experiments reprinted with permission from Ref. [7]

isotropic background contamination. IACTs are unable to detect showers below about 25 GeV, making them unsuitable for observations in the Compton regime.

Why are we interested in energy and angular resolution? Currently dark matter searches for continuum spectra are complicated by a huge abundance of point sources and diffuse astrophysical backgrounds toward the Galactic center. This includes both systematic effects and the potential of the GeV GC excess having originated from pulsars. Enhanced angular resolution allows for clean resolution and separation of these sources so that diffuse emission can be studied independently. The angular profiles of diffuse emission also offers clues as to it's origin, allowing for example, the separation of gas correlated emission versus Inverse Compton. It may also allow for the detection of energy dependent morphologies. Energy resolution, on the other hand, is crucial to searches for gamma-ray lines.

Let us now break the gamma-ray observatories into several partly overlapping energy ranges. We show the sensitivities of the experiments discussed below in Figure 2.3.

Compton Regime ($E_\gamma \lesssim 100$ MeV): Just above X-rays, the soft gamma-ray window is the least well explored of the entire observable electromagnetic spectrum. Measurements at such low energies Are challenging, with compton scattering dominating the photon interaction cross-section at below 10 MeV, and pair-production taking over above this. Current experiements absed on silicon trackers have sensitivity only down to tens of MeV, and possess extremely large point-spread-functions that limit their scientific value at these energies. Previous observatories such as COMPTEL provided coverage over these energies, but with a very large PSF and small effective area. New efforts such as the ComPair mission [6] aim at a 2-3 order of magnitude improvement in effective area with an angular resolution of a few degrees. The dark matter applications of such an instrument are limited for WIMPs (due to the Lee-Weinberg limit, see Ch. 3), but it may provide an excellent search opportunity for decaying candidates such as heavy sterile neutrinos or more exotic spectral lines [121]. Perhaps most importantly, it will shed light on the 511 kev positron excess, and on diffuse emission associated with low-energy electrons below the π^0 production threshold, as well as a wide variety of astrophysical objects at low gamma-ray energies.

*GeV Regime (*100 MeV $\lesssim \mathrm{E}_\gamma \lesssim$ 250 GeV *)*: *Fermi* has revolutionized gamma-ray astronomy in the GeV regime and below we dedicate an entire section to understanding its performance. The scientific goals of the instrument are many, but include as a major component the detection of WIMP dark matter below 100 GeV. It's angular resolution and effective area are sufficient to probe thermal relic cross-sections, and

the survey mode allows for simultaneous pointing toward all the potential targets mentioned in Section 2.3. The most notable remaining signal is the Galactic center GeV excess, but previously there was also excitement over a gamma-ray line at 135 GeV detected toward the Galactic center. Besides the robust limits (and potential detection) placed on WIMP dark matter models, *Fermi* has provided an unprecendented view of GeV astrophysics including the detection of more than 3500 high-energy sources now in the 3FGL [116], 117 gamma-ray pulsars [122], and at least 14 supernova remnants [123], confirming them for the first time as accelerators of cosmic-rays (at least a fraction of Galactic CRs). Future comparable missions include Gamma-400 which will over above all, an order of magnitude improvement in angular resolution. This is crucial for both astrophysics, and for understanding the true nature of the GeV Galactic center excess.

*High Energy Regime (*100 GeV $\lesssim E_\gamma \lesssim$ 100 TeV*)*: At high energies, the current state of the art active instruements include HAWC, HESS, MAGIC, and VERITAS, which are similar in sensitivity. These are currently probing interaction cross-sections about 1 order of magnitude above the thermal value. The upcoming CTA proposal will have a strongly enhanced effective area and coverage of the Galactic center region which will allow the thermal cross-section to be probed for dark matter masses between 100 GeV and $\approx$ 10 TeV candidates annihilating to $b\bar{b}$. Near the Galactic center, astrophysical backgrounds above 100 GeV are not very important for setting limits, or discovery of dark matter, making the GC an extremely attractive target which is about an order of magnitude better than dwarfs. Astro-

physically, HESS will provide excellent angular resolution and sensitivity to sources in the GC region, on the Fermi Bubbles, and on pulsars and SNR throughout the Galaxy. Unfortunately, it will not shed light on the GCE excess, which lies just out of reach at the low energy edge of CTA's sensitivity.

For cosmic-rays, several ongoing experiments provide data on electrons, positrons, protons, antiprotons, and heavier nuclei including secondary to primary ratios such as B/C, up to several hundred GeV. Pamela provides excellent coverage of at lower energies, while AMS-02 has recently provided by far the most accurate CR spectra to-date. The most intriguing result is the confirmation of the rising positron fraction upto at est 450 GeV, though higher energy measurements are needed to identify the source of the excess as 1 or more pulsars, alternative cosmic-ray propagation models, or perhaps dark matter. The antiproton spectrum from AMS is marginally compatible with current numerical CR propagation models, although a very tenuous excess may be present and would be revealed by higher energy measurements. The proposed CR observatory CALET [124] will provide sensitivity at these very high energies, upto 1 TeV for positrons, protons/antiprotons, and B/C, with exploratory analysis up to several TeV.

2.4.2 Fermi-LAT Instrument Response

In order to gain further insight into the experimental side of indirect detection, and to better understand instrumental response functions, we consider here some basic building blocks for working with *Fermi* data. Thanks to the Freedom of Information Act, NASA missions are required to release their data to the public. This has led to an

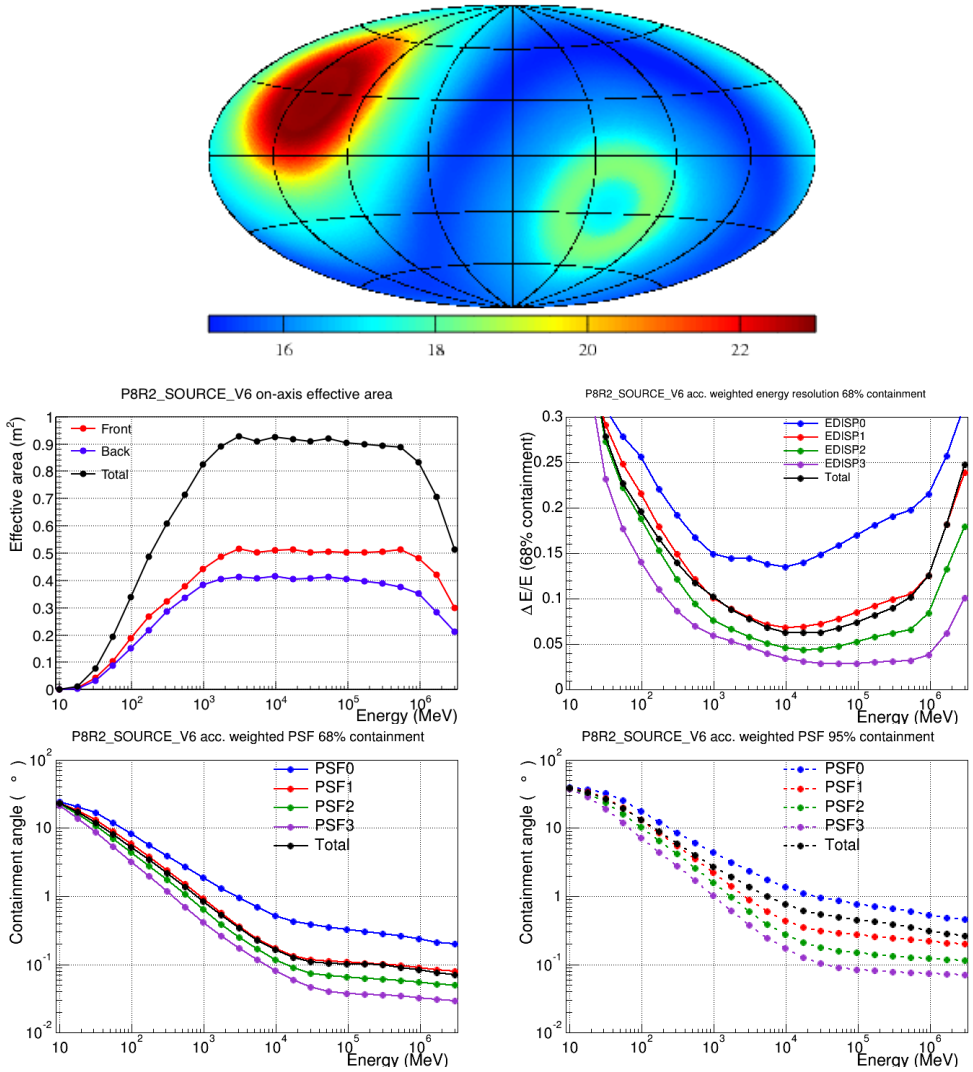

Figure 2.4: Instrument Response functions (IRF) for `SORCE` class photons in Fermi PASS 8 release. Top, exposure time in megaseconds for the 3FGL catalog in Galactic coordinates. Bottom four panels counter-clockwise: Effective area, 68% PSF containment radius for different photon classes, 95% containment radius, and Eenrgy resolution.

incredible flourishing of astrophysical and new physics analyses over the years[9].

[9]The Fermi web page http://fermi.gsfc.nasa.gov/ssc/data/analysis/documentation/ provides comprehensive documentation for running analysis using their `Fermi Science Tools`. For point source analyses, these tools are reasonably fast to use, but for large ROIs, such as fitting diffuse windows, I have developed my own binned likelihood analysis package in python called `GammaLike` which is much faster. These tools are briefly discussed in Appendix A.1.

Often we have a model for the flux of some astrophysical source, which is given as a function of angular position and energy. A flux density map ($d^2\phi/d\Omega dE$) of this sort will have units of photons/cm^2/s/sr/GeV units. In order to compare such a model against the observed data, we must convolve the model against the *instrumental response functions* (IRFs) of *Fermi*. This includes three essential elements:

1. Exposure Maps: The first quantity that must be calculated is the effective exposure on a sky segment which is the product of the effective area and the live exposure time. Although *Fermi* does survey the full sky, its acceptance is not uniform, and therefore different sky locations are exposed with different effective areas and different time exposures. The Fermi Science Tools (FST) provide tools to calculate these exposure maps which have units of [cm^2 s]. The exposure time used for the 3FGL catalog is shown in the Top panel of Fig 2.4, while the effective area as a function of energy is shown in the mid-left panel.

2. The Point Spread Function: The instrument has finite spatial resolution and we must smooth the input model using the point spread function as the convolution kernel. For diffuse sources that are relatively smooth, a Gaussian kernel of order the PSF containment radius is usually sufficient. For point sources, one must use the true PSF which can be determined using the `gtpsf` tool in the FST. Some example PSF containment radii are shown in the bottom two panels of figure 2.4, where the photons have been divided into quartiles to form different PSF classes. Note the strong energy dependence of the PSF which is approximately a power

law in containment radius below 10 GeV and nearly constant above 10 GeV.

3. Energy Dispersion: The instrument also has finite energy resolution. For *Fermi* this is strongly energy dependent, but is better than 10% over the nominal acceptance range. For smooth continuum spectra, this implies that energy convolution is not very important. However, when searching for gamma-ray lines or comparably sharp spectral features, the energy resolution must be taken into account.

For the purposes of simulating photon events, one can easily write a simple Monte-Carlo simulation with acceptance-rejection sampling, or inverse-transform sampling over these various distributions (which can be obtained from the Fermi Tools). An example of this can be found in Sections 4.4 where we model individual photons near the Galactic center. My own GammaCAP package also includes tools for simulating photon data, and the FST include their own `gtobssim` simulator[10]. Models for the gamma-ray flux are discussed in detail throughout Part III of this thesis. Methods for comparing models against Fermi photon data (which consists of an event record for each gamma-ray – i.e. location, energy, time, etc.) will be discussed throughout Chapter 4.

[10]In my personal opinion, this is so slow that it is not worth using in cases where one does not need very fine resolution. This is usually the case for dark matter where we are integrating over years, and often dealing with diffuse sources and continuum spectra.

Current:						
Experiment	Target	Energy range	$\mathcal{A}$	Angular Res.	$t_{\rm exp}$	Comments
AMS	e^+/e^-, anti-nuclei	1GeV-1TeV	0.5 m^2 sr		5 yr	Magnet Spectrometer, Running
Fermi	Photons, e^+/e^-	50MeV - 500GeV	0.9 m^2	0.3° E>10 GeV	10 yr	Pair Telescope and Calorimeter, Running
HESS	Photons, e^-	30GeV-100TeV	0.5 km^2	0.2°	100-10^3 hr	Atmospheric Cherenkov Telescope (ACT), Running
MAGIC	Photons, e^+/e^-	25GeV-30TeV	240 m^2	0.1°	100-10^3 hr	ACT, Running
PAMELA	e^+/e^-, anti-nuclei	0.4GeV-200GeV	200 cm^2		10 yr	Satellite
VERITAS	Photons, e^+/e^-	100GeV - 50TeV	10^5 m^2	0.05-0.1°	100-10^3 hr	ACT, Running
Planned:						
CALET	e^+/e^-, photons	10GeV-10TeV	1.2 m^2 sr	0.3°	5 years	Calorimeter
CTA	Photons	25GeV-100TeV	1 km^2	0.1°	100-10^3 hr	ACT
GAMMA-400	Photons	100MeV-3TeV	1 m^2	.01°	10 years	Pair Telescope
GAPS	Anti-deuterons	.1-3GeV/n	5 m^2 sr		10-21 days	TOF, X-ray and Pion detection
HAWC	Photons, e^+/e^-	100GeV-100TeV	.25 km^2	0.3°	5-10 years	Water Cherenkov, Air Shower Surface Array
CompPair	Photons	200keV-500MeV	500 cm^2	3°	5-10 yr	Compton Pair-Production

Table 2.1: Current and planned cosmic and gamma-ray experiments.

Chapter 3

Astrophysical Signatures of Particle Dark Matter

In this chapter we review the calculation of injection spectra from dark matter annihilations and decays. Having discussed already the halo profiles common to the Milky Way, understanding the injection spectrum (dN/dE in Eq. 2.1 will allow us to compute the gamma-ray flux expected at the Milky. For cosmic-rays, the injection spectrum multiplied by the annihilation or decay rate yields the source term across the Galaxy, but we cannot estimate the flux at Earth until propagation effects are taken into account (the subject of Part II).

3.1 Electromagnetic Radiation From Dark Matter

Dark matter annihilations and decays radiate in a variety of ways. The most common in indirect searches is primary, or prompt radiation, which is comprised of all the

photons originating from the location of annihilation. This includes, for example, direct annihilation into lines or virtual internal bremsstrahlung [125], or the radiation coming from electromagnetic or hadronic showering of the annihilation final state. We review the core concepts here, and point the interested reader toward good pedagogical and computational resources which exist in the literature. Depending on the level of sophistication, these calculations can be very involved, and/or computationally heavy. Barring necessary exceptions, it is recommended that precomputed tables from PPPC4DM [126] (Poor Particle Physicists Cookbook for Dark Matter) be used [1].

Secondary radiation signatures of dark matter annihilation or decay is a growing subject. Dark matter models which have significant branching fractions to leptonic species will ultimately produce an abundance of high-energy electrons. These radiate as they propagate through the Galaxy via synchrotron, inverse-Compton, and electron bremsstrahlung. These calculations are identical to those used to calculate energy losses and emission from astrophysical cosmic-rays which are described in Chapter 6.

3.1.1 Gamma-rays from WIMPs

Dark matter annihilations and decays generically produce associated gamma-rays. For any production of SM particles, the photon spectrum can be calculated using Monte Carlo codes such as Pythia [127] or Herwig [128]. In this context, these codes simulate a generic resonance, typically a spin-0 state of mass $2m_\chi$, with a single decay channel chosen by the user, such as $W^+W^-, q\bar{q}, l\bar{l}, ZZ, gg, hh, Z\gamma$. These particles are

[1] http://www.marcocirelli.net/PPPC4DMID.html

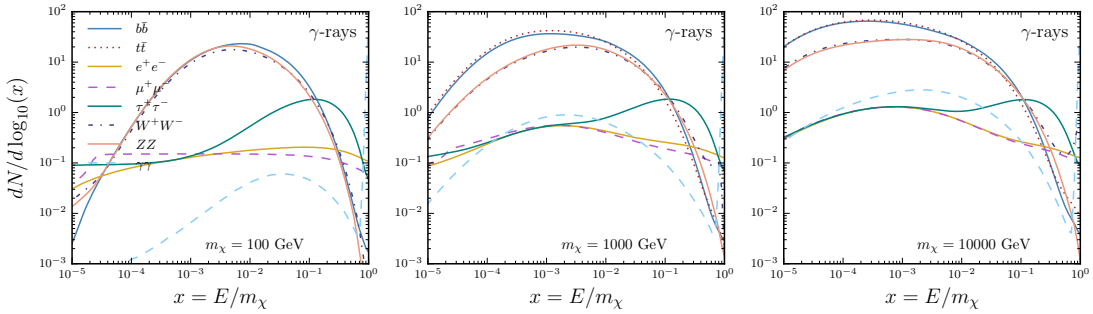

Figure 3.1: Gamma-ray injection spectra from dark matter particles of mass m_χ annihilating to a variety of Standard Model final states. The x-axis is expresses as the ratio of the photon energy to the dark matter mass, typically denoted $x = E_\gamma/m_\chi$.

then hadronized and one can examine the distribution of final state particles. An example code for such a setup can be found in example `main07.cc` in the pythia sample directory. For non-hardronic (and non-line-like) states such as e^+e^- and $\mu^+\mu^-$, analytic formulae are directly available [129]. Here, $q\bar{q}$ can be any of the quark species, although typically the quark-antiquark spectra are relatively similar, other than the top-quark which decays hadronically.

Figure 3.1 shows sample gamma-ray injection spectrum for representative dark matter masses annihilating into a variety of SM final states. Here one observes a very general difference between leptonic and hadronic final states. Hadronic final states have more rounded and lower-energy spectra compared with leptonic final states which produce hard final state radiation – particularly $\tau^+\tau^-$.

Several notes are in order regarding the use of using Monte-Carlo codes. Perhaps most importantly, HERWIG and Pythia employ different hadronization models which leads to a theoretical uncertainty on the injection spectrum. The former is based on cluster model, while Pythia is based on a color-string model, and the differences are

detailed in Ref. [126]. These uncertainties are not important for $q\bar{q}$, but they do result in a nearly factor 2 difference for gg final states and more for $\tau^+\tau^-$. Second, one should be aware that different energy regimes may demand different tunings of the hadron models. For γ-rays, this is not as important, but for nuclear cosmic-rays, this can be relevant [130]. Third, we note that for dark matter masses below about 5 GeV, these simulations break down, and one must use elaborate formalisms based on, for example, chiral perturbation theory. Finally, we note that these results pertain to two-body final states. While 1 body final states are forbidden by energy-momentum conservation, three body final states do exist, for example, in R-parity violating SUSY scenarios [131], In these cases, the hard-process must be generated in more modern Monte Carlo codes which include three-body phase space generation (such as MadGraph [132]) and then the parton level event files must be hadronized separately using Pythia.

3.1.2 X-ray Lines

Prompt radiation from dark matter can also exist at lower energies. X-ray lines can arise in a variety of particle physics scenarios via the decay of a dark sector particle which includes a photon. Many such models have arisen as potential explanations for the 511 keV line [133] and/or the 3.5 keV line [134].

Typically these X-ray signatures do not arise from WIMP candidates. However, there are scenarios such as eXcited dark matter [135], where two dark sector particle masses are almost degenerate, with a mass splitting δm_χ lying in the X-ray regime can radiate such a line after de-excitation. Similarly, there have been recent proposals for

upscattering of dark matter particles via interactions with astrophysical plasmas [121].

More traditional explanations include sterile neutrinos, which can potentially provide avenues to successful baryogenesis via leptogenesis, to the generation of the observed pattern of (active) neutrino masses and mixing, and to providing a dark matter candidate which can alleviate certain small-scale issues of cold dark matter scenarios [136]. Model building efforts were also directed toward constructing a consistent new-physics picture that could reconcile varying signal strengths across different objects, especially in the context of axion-like particles photo-converting to 3.5 keV photons in the presence of magnetic fields (see e.g. Ref. [137, 138, 139, 140, 141] for early studies of this scenario). Such signals continue to be interesting, particularly with the next generation of X-ray[2] and low-energy gamma-ray experiments such as CompPair [6].

3.2 Cosmic Ray Production from Dark Matter

Within the paradigm of Weakly Interacting Massive Particle (WIMP) dark matter, the pair-annihilation or decay of dark matter particles generically yields high-energy matter and antimatter cosmic rays. While the former are usually buried under large fluxes of cosmic rays of more ordinary astrophysical origin, antimatter is rare enough that a signal from dark matter might be distinguishable and detectable with the current generation of experiments. Antimatter searches for dark matter currently include measurements of the high-energy positron spectrum, as well as anti-nuclei such

[2]Unfortunately, the Astro-H X-ray spectrometer was to provide the most interesting contraints on X-ray lines, but was destroyed after launch by a software error which mistakenly spun the spacecraft until it broke apart.

as antiprotons, antideuterons, and antihelium, which each have their own merits. Here we review each case, applying special attention to the production of antideuterons from gravitino decays and antihelium production from dark matter candidates.

3.2.1 Positrons (e^+)

One of the oldest potential indirect detection signals is the anomalous rise in the positron fraction, first detected at high-significance by PAMELA [142] and confirmed by AMS [143]. While secondary positrons are generated through spallation of CR nuclei with interstellar gas, the spectrum is expected to be very soft, and falls off rapidly (faster than E^{-3}) above a few GeV. In contrast to this, the positron fraction is observed to rise above 10 GeV and upto at least 450 GeV, where the current detection limit stands. At these energies, positrons are confined by energy losses to within less than a kiloparsec of their production sites, leaving two possibilties: dark matter, or nearby pulsars. The latter option is explored extensively in Ref. [144], while the former has been explored in many references (see e.g. Ref. [145]). Propagation uncertainties continue to mask the true nature of the excess, but dark matter is recently looking less favorable as the statistics improve and multi-messenger constraints become stronger, namely from antiproton constraints on the annihilation cross-sections, which must be boosted well above the thermal relic value to explain such a strong positron signal.

The positron injection from dark matter is found in the same way as gamma-rays: via Monte Carlo. In Figure 3.2, we show the injection spectra from Pythia (from PPPC4DM [126]) for dark matter annihilations to a variety of Standard Model final

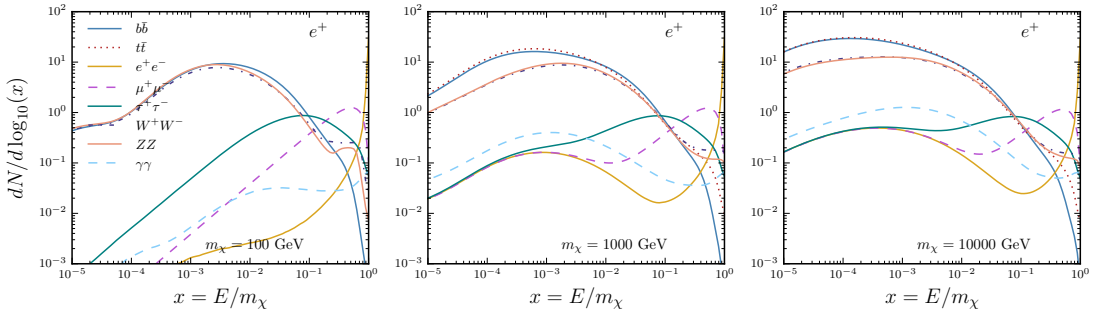

Figure 3.2: Positron injection spectra from dark matter particles of mass m_χ annihilating to a variety of Standard Model final states. The x-axis is expressed in terms of the fractional energy of the photon relative to the dark matter mass. Commonly called x=E_γ/m_χ.

states. At this point, the particles must be propagated as discussed in Sec. 5.1.

3.2.2 Antiprotons ($\bar{p}$)

While astrophysical accelerators of high-energy positrons such as pulsars' magnetospheres are well-known, observations of cosmic anti-nuclei might provide a unique window into physics beyond the Standard Model and may provide a discovery route to unveil the nature of particle dark matter.

Measurements of the cosmic-ray antiproton spectrum by BESS [146, 147, 148] and PAMELA [149] currently provide the best limits on cosmic-ray antiprotons $\bar{p}$ in excess of the astrophysical background. On a short time-scale, AMS-02 will provide the most accurate cosmic-ray proton and antiproton spectrum to date, placing stringent limits on propagation parameters and excess signals. One well motivated origin for such an excess is the annihilation or decay of WIMPs to hadronic final states – generic to models coupling WIMPs to the weak gauge bosons or quarks (e.g. W^+W^- or $b\bar{b}$).

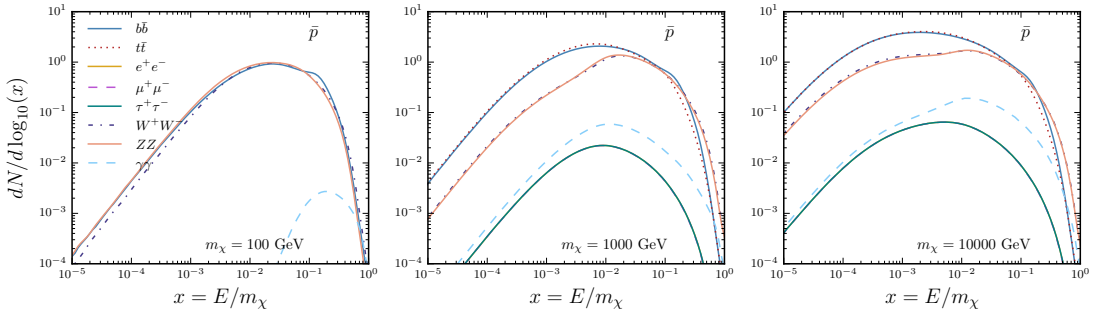

Figure 3.3: Antiproton injection spectra from dark matter particles of mass m_χ annihilating to a variety of Standard Model final states.

Similar to positrons and gamma-rays, antiproton injection spectra can be obtained directly from Pythia for standard two body final states. Sample spectra are shown in Figure 3.3. It is obvious that hadronically decaying final states produce the most robust detection prospects and limits.

While large astrophysical backgrounds often prohibit the clean disentanglement of exotic sources, a recent analysis of the 1-year AMS-02 antiproton data has produced robust constraints on WIMP annihilation to quarks which reach below the thermal-relic cross-section for dark matter masses $10 \leq m_\chi \leq 200$ GeV [150].

3.2.3 Antideuterons ($\bar{d}$)

In addition to antiprotons, Ref. [151] proposed new physics searches using heavier anti-nuclei such as antideuteron ($\overline{\mathrm{d}}$), antihelium-3 ($^3\overline{\mathrm{He}}$), or antitritium ($^3\overline{\mathrm{H}}$) forming from hadronic neutralino annihilation products. Although such production is of course highly correlated with the antiproton spectrum, the secondary astrophysical background decreases much more rapidly than the expected signal as the atomic number A is in-

creased [20]. In particular, secondary antinuclei production from the spallation of high-energy cosmic rays – i.e. the scattering of cosmic-ray protons off of cold interstellar hydrogen and helium – quickly becomes kinematically suppressed for heavier nuclei for three reasons:

(i) the constituent nucleons must lie in a small volume of phase space in order to form anti-nuclei, leading to a production suppression of roughly $10^{2A} - 10^{3A}$. While this is the case for both primary (e.g. dark matter) and secondary anti-nuclei, the secondary background is further suppressed by the rapid falloff of cosmic-ray protons at high energies. The dominant spallation processes which generate $\bar{p}$, $\overline{\mathrm{D}}$, and ${}^3\overline{\mathrm{He}}$ /${}^3\overline{\mathrm{H}}$ have production thresholds of $E_{\mathrm{p}} = 7m_p$, $17m_p$, and $30m_p$ respectively while the proton flux above 10 GeV falls as $\phi_p \propto E_{\mathrm{p}}^{-2.82}$ [152].

(ii) because of the high production threshold, the spallation products are typically highly boosted, carrying kinetic energies above 5 GeV/n (GeV per nucleon). For dark matter, the spectrum peaks instead below 1 GeV/n for annihilation channels where the hadronization frame is not boosted (e.g. $q\bar{q}$ or near threshold W^+W^-).

(iii) finally, in contrast to $\bar{p}$, $\overline{\mathrm{d}}$ and ${}^3\overline{\mathrm{He}}$ easily fragment as they undergo inelastic collisions (due to their low binding energies). This prevents efficient energy loss during interstellar transport which would otherwise redistribute the higher-energy background spectrum toward lower energies.

These three factors lead to precipitous decline in the secondary $\overline{\mathrm{d}}$ and ${}^3\overline{\mathrm{He}}$ backgrounds below ~ 5 GeV/n, enhancing the signal to background by several orders of magnitude for each increase in atomic number. Proposed anti-nuclei searches exploit this point and

are designed to observe below 1 GeV/n where the secondary/primary ratio for $^3\overline{\text{He}}$ is $\lesssim 10^{-5}$. This provides a truly zero-background channel for $A \geq 3$ at the expense of a significantly lower signal flux and it is precisely this feature which motivates dark matter searches using anti-nuclei.

Dark matter production of antideuterons and the observational prospects at AMS-02 and GAPS have been thoroughly investigated (see e.g. [151, 153, 154, 155, 156, 157, 158]). For an optimistic scenario of ∼100 GeV thermal WIMPs annihilating to $b\bar{b}$, the latter two state-of-the-art analyses predict $\mathcal{O}(0.1-10)$ $\overline{\text{d}}$ signal events – with backgrounds a factor $\mathcal{O}(10-50)$ smaller – to be measured by a GAPS Long Duration Balloon flight (LDB+). In the following subsection we detail two methods for calculating the $\overline{\text{d}}$ injection spectrum.

3.2.3.1 The Coalescence Model

In any process producing antinucleons, it is possible for antiprotons and antineutrons to bind together into a nucleus and produce antideuterons. The traditional formation model, known as the 'coalescence mechanism', was designed to empirically describe nuclei production in heavy-ion collisions based on the phase-space distributions of the constituent nucleons. It possesses a single energy-independent parameter, the coalescence momenta p_0, and assumes that if any antineutron and antiproton pair have relative invariant 4-momenta $(k_n - k_p)^2 = (\Delta\vec{k})^2 - (\Delta E)^2 \leq p_0^2$, they will fuse and form an antideuteron. The parameter p_0 is then tuned to match collider measurements of $\overline{\text{d}}$ production.

It has long been known that this model cannot accommodate the available data for a single value of the coalescence momenta to better than a factor of ~ 3. Despite this simplistic model, an improved prescription is largely hindered by limited collider data for production of antideuterons from e^+e^- collisions at high energies, as well as a lacking understanding of the underlying nuclear formation dynamics. However, recently renewed interest in antideuteron searches have led to at least two important improvements. First, it was pointed out in Ref. [156] that the isotropic nucleon distribution functions used in analytic estimates of formation rates led to an artificial suppression of the $\overline{\mathrm{d}}$ production rate at large center of mass energies. In particular, the jet structure of high-energy showers introduces significant angular correlations between nucleons. One must therefore run Monte Carlo simulations and apply the coalescence mechanism on an event-by-event basis using the simulated phase space distributions of protons and neutrons. Second, it was realized that the antideuteron wave-function is spatially localized to ≈ 2 fm and contributions to the nucleon population from long-lived baryons should be omitted, as they decay at large relative distances from the other particles in the shower. In practice, weakly decaying baryons are then excluded by stabilizing particles with a lifetime $\tau > 2\mathrm{fm/c}$ with a negligible dependence on this parameter due to the large gap between weak and hadronic timescales.

In order to fix the coalescence parameter we must choose a value which reproduces a measured rate. As previous studies have noted, a single value of the coalescence momentum cannot simultaneously reproduce rates from different underlying processes such as pp vs e^+e^-. While this can be slightly improved by tuning the hadronization

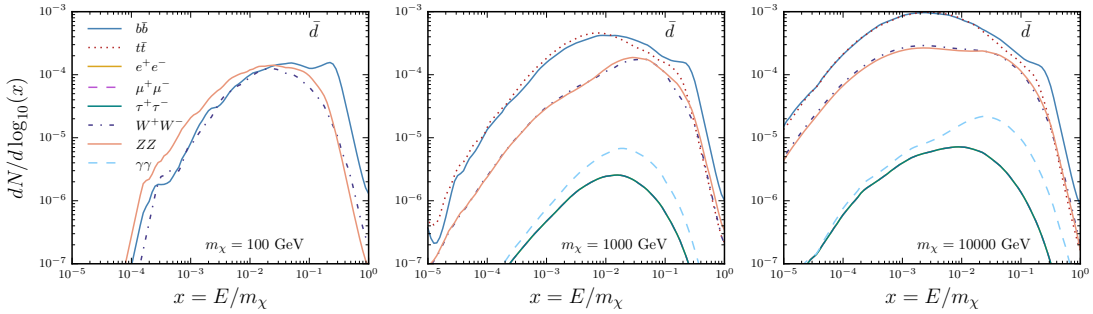

Figure 3.4: Antideuteron injection spectra from dark matter particles of mass m_χ annihilating to a variety of Standard Model final states, with coalewscence momenta $p_0 = 160$ MeV. The x-axis is expressed in terms of the fractional energy of the photon relative to the dark matter mass. Commonly called x=E_γ/m_chi.

parameters, we follow previous studies which use electron-positron collisions more likely to resemble a dark matter scenario – i.e. color singlets that are not composite. Following the approach of Refs. [158, 157, 154], we use $e^+e^- \to \overline{\mathrm{d}}$ measurements from ALEPH at the Z^0 resonance, finding $(5.9 \pm 1.8 \pm .5) \times 10^{-6}$ antideuterons per hadronic Z^0-decay with $\overline{\mathrm{d}}$ momenta 0.62-1.03 GeV/c and polar angle $|\cos\theta| < 0.95$ ([159]). We find a value $p_0^{A=2} = 0.192 \pm .030$ GeV/c consistent with Refs. [158, 157].

In Figure 3.4 we show the $\overline{\mathrm{d}}$ spectrum for WIMP annihilations to SM final states taken from PPPC4DM [126]. These models use a coalescence momentum of $p_0 = 0.16$ MeV and do not include stabilization of long-lived particles. In any case, we see similar behavior as for antiprotons, hadronic final states lead to the largest number of $\overline{\mathrm{d}}$ per annihilation event. Due to the high boost of final state particles for very heavy dark matter, the jets become more collimated and produce more $\overline{\mathrm{d}}$ per event than the more spherically symmetric angular distributions of lower mass annihilations.

A code for calculating $\overline{\mathrm{d}}$ yields with Pythia is provided in Appendix A.2, and in-

cludes both the coalescence prescription as well as alternative formation model presented in the next section.

3.2.3.2 An Alternative Formation Model

It has recently been pointed our that the coalescence model is unable to reproduce measurements of $\overline{\mathrm{d}}$ production from the ALIVE experiment at the LHC [8]. Ref. [8] have thus devised an alternative probabilistic model which produced $\overline{\mathrm{d}}$ by tallying the viable neutron capture processes, $\bar{p}\bar{n} \to \bar{d}X$ or $\bar{n}\bar{n} \to \bar{d}X$. At low relative momenta, this is dominated by radiative capture, $\bar{p}\bar{n} \to \bar{d} + \gamma$, while hadronic final states take over for center-of-mass energies larger than the pion mass (e.g. $\bar{p}\bar{p}$ or $\bar{n}\bar{n} \to \bar{d} + N\pi$). The cross-sections for each of these eight processes are parameterized [8] as a function of the invariant 4-momenta and can be used to generate antideuterons probabilistically based on the ratio of each cross-section to a total cross section σ_0, which is the only free parameter of the model. Thus $\overline{\mathrm{d}}$ are generated if, for a relative momenta k,

$$\text{Uniform Rand.}(0,1] < P(\bar{N}_1\bar{N}_2 \to \bar{d}X_i|k) = \frac{\sigma_{\bar{N}_1\bar{N}_2 \to \bar{d}X_i)}(k)}{\sigma_0}. \tag{3.1}$$

Where N_1 and N_2 are all possible combinations of $\bar{p}$ and $\bar{n}$ in the final state particle listing for each event. This leads not only to different production rates, but improves the spectral distribution of $\overline{\mathrm{d}}$ by taking into account the capture process. In Fig. 3.5 we show the antideuteron injection spectrum for a 100 GeV WIMP going to $b\bar{b}$ in both the Coalescence framework, and the alternative formation model. At energies relevant for current and future experiments, the new formation model provides approx-

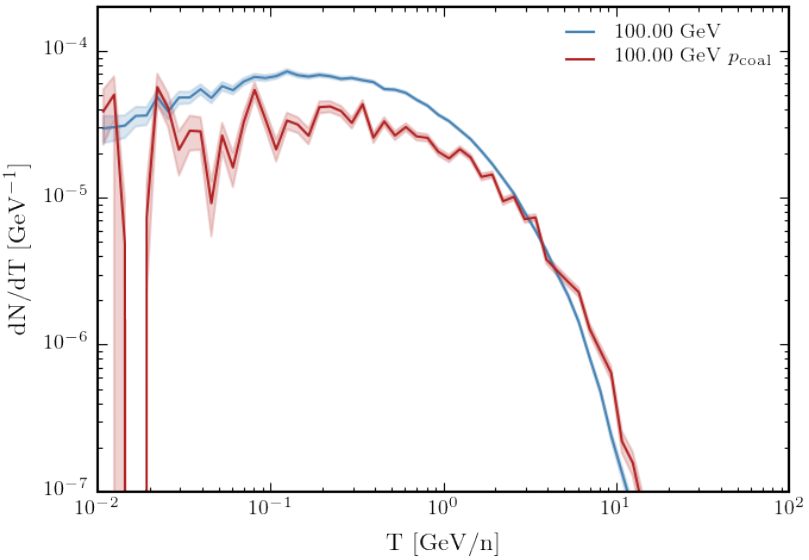

Figure 3.5: Comparison of $\overline{\rm d}$ injection spectra for a 100 GeV WIMP candidate annihilating to $b\bar{b}$ using either the Coalescence prescription (red), or the alternative formation model of Ref. [8](blue). Jagged lines are due to limited statistics.

imately a factor 2 enhancement at these dark matter masses. Since this model only changes production, the observable fluxes between the formation models and are simply rescaled (after shifting by solar modulation) versions of each other.

A code for calculating $\overline{\rm d}$ yields using this alternative formation model in Pythia 8 is provided in Appendix A.2.

3.2.3.3 Antideuterons from Gravitino Decays

In contrast to the two-body phase spaces discussed above, gravitinos in R-parity violating supersymmetry can produce antiprotons and $\overline{\rm d}$ through baryonic R-parity violating operators. Constraints on the couplings are currently competitive with those from antiprotons and are expected to improve substantially with the results of

AMS-02. While the full details can be found in Ref. [160], we provide details of the injection spectrum here in order to highlight deviations from the typical WIMP$\rightarrow$ two-body scenario.

In supersymmetric theories, R-parity[161, 162] is usually introduced to remove unwanted dimension four operators that would lead to fast proton decay; the renormalizable R-parity violating superpotential is:

$$W_{RPV} = \mu_i L_i \phi_u + \lambda_{ijk} L_i L_j \bar{\ell}_k + \lambda'_{ijk} L_i Q_j \bar{d}_k + \lambda''_{ijk} \bar{u}_i \bar{d}_j \bar{d}_k \,, \tag{3.2}$$

where the indices are generation indices, $i, j, k = 1, \ldots, 3$, and only antisymmetric combinations of i, j (respectively, j, k) are allowed in λ (respectively, λ''). The first three operators violate lepton number while the last violates baryon number, and both types of operators are involved in proton decay. It is then possible for the proton to be stable if only one type of operators is allowed, leaving B (or L) as an accidental symmetry of the theory [163, 164].

Recently, Ref. [130] provided the first antideuteron constraints for gravitinos decaying through a variety of R-parity violating operators. One novel feature of their analysis is the detailed treatment of the Monte Carlo parameters controlling the hadronization model which are tuned to reproduce a wider array of experimental antideuteron production rates. Here, much of the same production and propagation framework is used, but we do not vary the hadronization model in order to extract the model-*dependent* features of gravitino decay, and compare them to standard treatments of decaying dark matter. In doing so, we can provide simple scaling relations which allow BRPV coupling

constraints to be easily adapted from future updated measurements and more sophisticated propagation schemes that are presented in the context of two-body decays to heavy quark pairs.

For our study, we first use `Feynrules v2.0` package [165] (using a modified version of the `gld-grv` [166] and `RPV-MSSM` [167] model files) to translate our R-parity violating Lagrangian into a UFO format readable by matrix element generators. The matrix elements and phase space for the hard process $\tilde{G} \to \bar{u}_i \bar{d}_j \bar{d}_k$ are then generated using `MadGraph v5.0` and `MadEvent` [132]. Finally, these parton level distributions are fed into `Pythia 8.1` [168] for showering and hadronization.

In Figure 3.6 we show the typical antideuteron injection spectra for a gravitino decay of mass $m_{3/2}$ =10 GeV, 30 GeV, 100 GeV, 1 TeV, and 10 TeV. In solid lines, we show the spectra from the heaviest accessible channel, which is expected to dominate the decay rate in scenarios with flavor symmetries, while dashed lines show the second heaviest contribution[3]. For comparison, we also show the spectra for a standard dark-matter decay to $b\bar{b}$ in dotted lines. Shaded bands show the acceptance energies for BESS (red), GAPS (green), the low-energy band of AMS-02 (blue), and the high energy band of AMS-02 (gray). Here we assume that the spectra will be shifted to lower energies as the antideuterons propagate through the heliosphere and shift each band upward in energy due to the Fisk potential $\phi_f = 500$ MV acting on a unit electric charge in accordance with the Gleeson & Axford Force Field approximation [169]. The vertical normalization of each energy band is arbitrary and we have slightly offset the BESS band in order to

[3]In the case of the *cbs* channel at 10 GeV we observe no events.

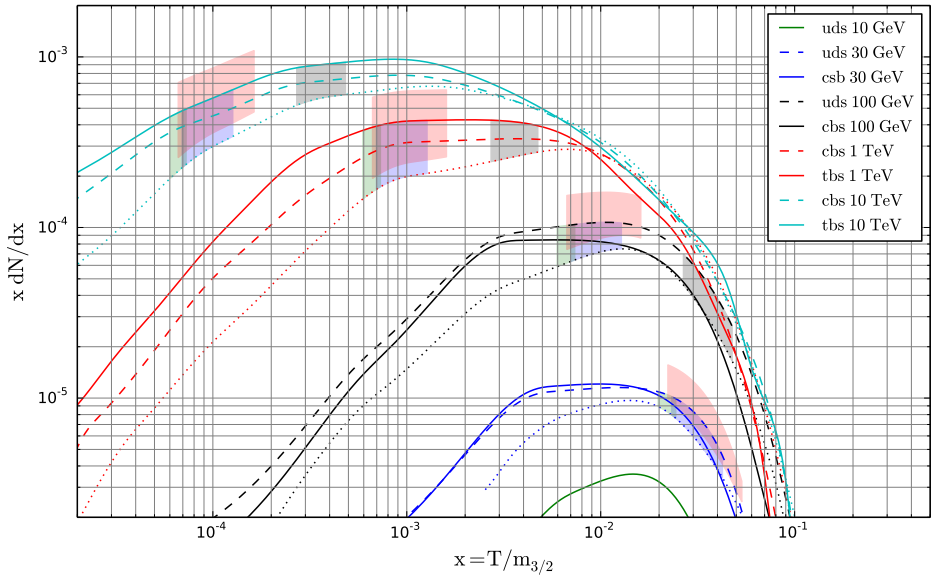

Figure 3.6: Antideuteron injection spectra for different operators involved and different gravitino masses, as displayed in the legend. dN is the average number of antideuterons with energy dT generated in the decay of a single gravitino. In particular, we display spectra generated by the operators $\bar{u}_1\bar{d}_1\bar{d}_2$ (uds), $\bar{u}_2\bar{d}_2\bar{d}_3$ (cbs), $\bar{u}_3\bar{d}_2\bar{d}_3$ (tbs). Solid lines represent the heaviest accessible channel while dashed lines show the second heaviest. Dotted lines represent the case of a 2-body decay to b-quarks, which is often presented in antideuteron analyses. In shaded bands, we show the ranges of experimental detectability after accounting for solar modulation effects. The bands are for BESS (red), GAPS (green), AMS-02-L (blue), and AMS-02-H (gray). We have vertically offset the BESS band for readability (vertical normalizations for these bands are arbitrary). The energy range of the bands is identical for different gravitino masses, but in these coordinates the horizontal locations scale as a function of $m_{3/2}^{-1}$.

keep the others visible. We note that while the energy range of each experiment is fixed, they are rescaled by a factor $m_{3/2}^{-1}$ in these dimensionless coordinates. With the injection spectra now in hand, several observations can be made:

1. Comparing between decay channels, we see that the second lightest quark mass channels have a significantly harder spectrum than the heaviest. For $m_{3/2}$ less

than a few hundred GeV, these low mass final state channels yield slightly more detectable antideuterons. Such behavior is also evidenced in Ref. [130] where the light quark channels provide the best limits on the trilinear BRPV coupling. Interestingly, this behavior reverses for $m_{3/2} \gtrsim 1$ TeV, where the heaviest quark channel dominates by a factor $\sim 20 - 30\%$ over the detectable low energies. One explanation may be the following: Increased jet multiplicity as the 2nd and 3rd generation quarks cascade down to u and d type quarks will divide the gravitino's energy. For low masses, this could sufficiently raise the threshold where heavy channels can consistently form the requisite number of protons and neutrons. When the gravitino mass is very high, each jet will contain energy $E \gg m_p$, and the 3-tiered decay of the top-quark will effectively soften the otherwise harder spectrum.

2. Compared with the 2-body decay to $b\bar{b}$, we see a significantly softer spectrum for our gravitino decay in all cases. This results in a mild enhancement in detectable antideuterons of $\mathcal{O}(50\%)$ for $m_{3/2} \approx 50$ GeV increasing to a significant factor ≈ 3 above 1 TeV. This is mostly attributed to the higher initial multiplicity of quarks in the final state of the hard process which splits the initial gravitino energy into three final states rather than two. In addition to this, the 3-body phase-space allows the hard jets to occasionally align, and thus increase the probability of a neutron and proton coalescing. In the 2-body case, jets are forced back-to-back for a decay at rest, and are therefore less likely to have cross-jet correlations.

3. The formation model used here is distinct from Ref. [130]. Notably, we use `Pythia`

for hadronization (based on the string fragmentation model) while in Ref. [130], `Herwig++` (based on the cluster hadronization model) is used. It has been shown in Ref. [170] that differences between the two different models can lead to substantially different preferred values of the coalescence momentum and variances in the spectrum of anti-deuterons produced. Furthermore, our coalescence momentum is fit to a single data-point at the Z^0-resonance while the Ref. [130] varies the parameters of the hadronization model in order to reproduce results from e^+e^- and pp collisions at 50 GeV-7 TeV. We therefore expect to see some level of disagreement at higher gravitino masses. In fact, we do find a significant enhancement in our yield (integrated over the low-energy experimental bands) of around 30% at 50 GeV up to 300% at 1 TeV. As this is an artifact of the underlying hadronization and coalescence model, it occurs independent of the two results enumerated above for which the comparison is based on a common framework.

3.2.4 Antihelium-3 ($^3\overline{\mathrm{He}}$)

In this section we discuss the coalescence model for the production of $^3\overline{\mathrm{He}}$ and calculate its formation rate relative to $\overline{\mathrm{d}}$. In Part II of this thesis we employ a simple diffusion model in order to calculate the expected flux of $^3\overline{\mathrm{He}}$ at the solar position, and the penetration of $^3\overline{\mathrm{He}}$ into the heliosphere. Here we simply take this model as is and show results for the Antihelium flux at Earth. In Section 3.2.4.2 we discuss flux scaling relations, calculate the flux, and discuss the possibility for $^3\overline{\mathrm{He}}$ observation in both the current and upcoming AMS-02 and GAPS-LDB(+) experiments, as well as a future

GAPS satellite mission. Finally, we discuss the significance of our results to the current search for cosmic-ray anti-nucleons.

3.2.4.1 $A = 3$ Coalescence

We consider a fermionic Majorana dark matter candidate of mass m_χ annihilating into the colored or color-neutral final states $b\bar{b}$ and W^+W^- through a generic, spin-0, s-channel resonance. In the absence of an analytic description of atomic nuclei formation, we employ the coalescence model described above in Sec. 3.2.3.1 as a simple, single-parameter phenomenological approach to describe the formation of light elements from the distributions of protons and neutrons in high energy collisions [171, 172]. In the antideuteron case, the coalescence model assumes that nucleons with a relative invariant four-momenta $(k_n - k_p)^2 = (\Delta\vec{k})^2 - (\Delta E)^2$ less than a coalescence momentum p_0, will bind together and form a nucleus.

For antihelium, the coalescence prescription is nearly identical. When more than three particles are involved there are two obvious ways to define the coalescence mechanism. One can either require that each of the relative momenta lie within a 'minimum bounding momentum-sphere' of diameter $p_0^{A=3}$ (dubbed MBS here), or we can require that the relative invariant 4-momenta of each particle-pair is less than $p_0^{A=3}$ (dubbed particle-pairing or PP here). If we consider a triangle with sides equal to the relative momenta of two particles, the two methods coincide for obtuse and right triangles. For acute triangles, however, the value of $p_0^{A=3}$ required to form a nucleus can be up to 15% larger than the PP case. The MBS prescription also avoids unnatural

kinks in the required value of $p_0^{A=3}$ as the inclusive angle of this triangle is varied. We therefore choose MBS which *always* underestimates the yield with respect to the particle-pairing method for identical values of $p_0^{A=3}$. From a simple Monte-Carlo which assumes an isotropic distribution of nucleon momenta, we estimate that MBS produces only approximately 6% fewer antihelium, although this difference becomes compounded exponentially for heavier elements. Without an understanding of the strong dynamics of nuclear formation, it is not important to consider one method as 'more accurate than another', but the difference should be kept in mind when comparing results between studies.

For nuclei of atomic number A, the coalescence model predicts a production rate $R(A) \propto p_0^{3(A-1)}$, making $^3\overline{\mathrm{He}}$ predictions particularly sensitive to nuclear physics uncertainties. The choice of coalescence momentum is known to have significant dependence on the details of the underlying scattering process and is measured to be larger for $A = 3$ than $A = 2$ [173]. While heavy-ion collisions provide the only available constraints on $^3\overline{\mathrm{He}}$ production, they do not resemble the dynamics of dark matter annihilation. In an attempt to bracket the effect of this uncertainty on the resulting $^3\overline{\mathrm{He}}$ spectrum, we derive values for the $A = 3$ coalescence momentum, $p_0^{A=3}$, using two different methods. In the first method, we choose to scale the antideuteron coalescence momentum, $p_0^{A=2}$, up to $p_0^{A=3}$ following the theoretically motivated scaling of Ref. [174], in which $p_0 \sim \sqrt{B}$ for total nuclear binding energy B:

$$p_0^{A=3} = \sqrt{B_{^3\overline{He}}/B_{\bar{D}}}\; p_0^{A=2} = 0.357 \pm 0.059 \text{ GeV/c}. \tag{3.3}$$

As a second method, we use heavy-ion results from the Berkeley Bevalac collider which fit $\overline{\mathrm{d}}$, $^3\overline{\mathrm{H}}$, and $^3\overline{\mathrm{He}}$ coalescence momenta for several collision species (C+C up to Ar+Pb) at incident energies from 0.4-2.1 GeV/n [173]. Averaging the measured $p_0^{A=3}/p_0^{A=2}$ (molecular targets excluded) we infer the relation

$$p_0^{A=3} = 1.28\ p_0^{A=2} = 0.246 \pm 0.038\ \mathrm{GeV/c}. \tag{3.4}$$

Without parton-level production rates, such as $pp \to {}^3\overline{\mathrm{He}}$ at the LHC we need to rely on the outlined ad-hoc schemes, which yield the largest systematic uncertainty on the final flux. In the remainder of this analysis, we use the binding energies to determine $p_0^{A=3}$.

Formation of antihelium-3 proceeds through two channels: directly through coalescence of $\bar{p}\bar{p}\bar{n}$, and through the formation and decay of tritium ($\bar{p}\bar{n}\bar{n}$). As noted in Ref. [175], the former channel is suppressed by the Coulomb repulsion of the antiprotons, while the tritium channel is not. Although it is not clear what this suppression factor is, a conservative approach ignores the direct antihelium-3 channel completely. Tritium is stable on collider timescales, and therefore we can directly study the relative production rates. Data from the Bevalac [173] and CERN-SPS [176] heavy-ion collisions indicates that the ratio of tritium to antihelium-3 production rates $\epsilon = R_{\mathrm{H3}}/R_{\mathrm{He3}}$ varies between 0 and 1, perhaps as an increasing function the center of mass energy with efficiency near unity around $\mathcal{O}(50\ \mathrm{GeV})$. For the rest of this analysis we choose $\epsilon = 1$, but one may simply rescale dN/dE (or the final flux presented later) by a factor $(1+\epsilon)/2$ to regain full generality. We note that this uncertainty is small compared to the weakly constrained coalescence momentum.

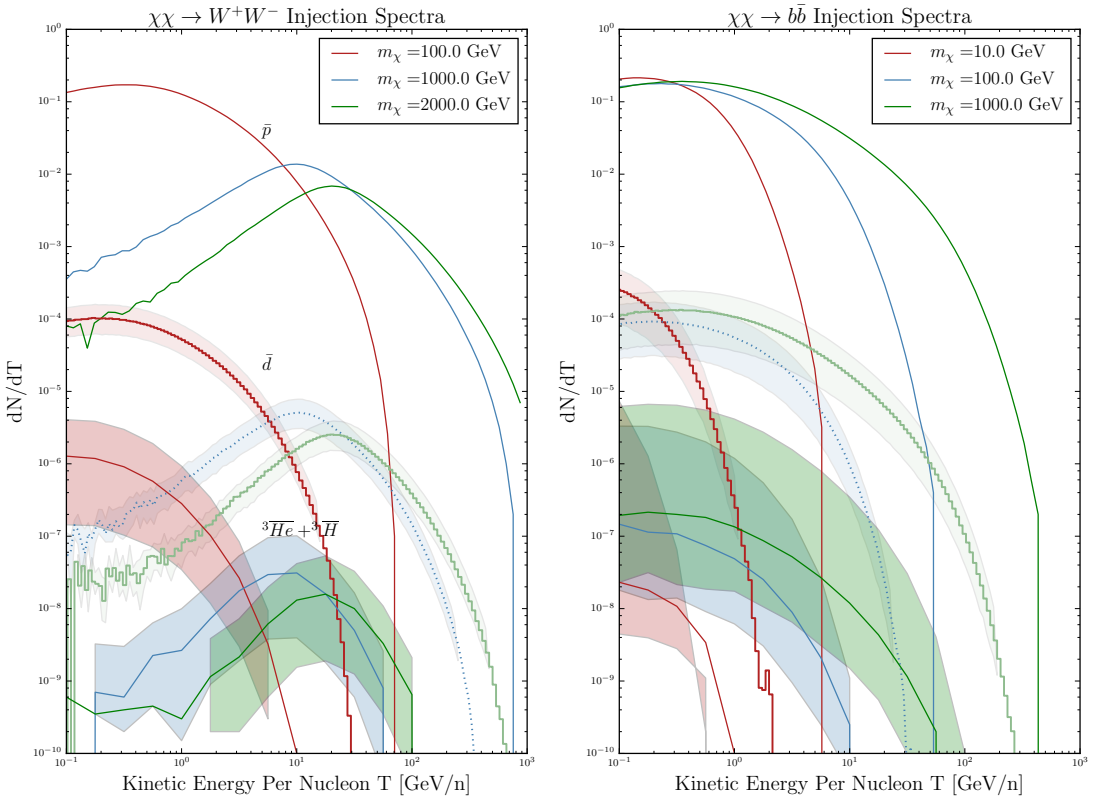

Figure 3.7: Injection spectra for $\bar{p}$, $\overline{\mathrm{d}}$, and ${}^3\overline{\mathrm{He}}$. For the latter two, uncertainty bands represent the uncertainties due to the extrapolated coalescence momentum. The ${}^3\overline{\mathrm{He}}$ contribution also includes contributions from Tritium which decays to ${}^3\overline{\mathrm{He}}$ shortly after injection.

In Figure 3.7 we show the injection spectra for $\bar{p}$, $\overline{\mathrm{d}}$, and ${}^3\overline{\mathrm{He}}$ together for representative masses and final states, along with uncertainties on the coalescence momenta discussed above. In Figure 3.8 we show ratios of the ${}^3\overline{\mathrm{He}}$ to $\overline{\mathrm{d}}$ injection spectra integrated over the energy band 0.1-0.25 GeV/n relevant for the upcoming GAPS Long Duration Balloon Flights (LDB and LDB+) as a function of the $A = 2$ and $A = 3$ coalescence momenta, for four different combinations of the dark matter pair-annihilation final state ($b\bar{b}$ in the left panels, WW in the right panels) and mass (10, 1000 and 2000 GeV). The

GAPS energy bands are quoted for kinetic energies at the top of Earth's atmosphere, after the particle momenta have been shifted by propagation through the heliosphere. Solar modulation will be discussed in detail in Section 5.1.4, but for concreteness, we integrate the $^3\overline{\mathrm{He}}$ and $\overline{\mathrm{d}}$ yields over bands shifted according to a Fisk potential of 500 MV in Figure 3.8.

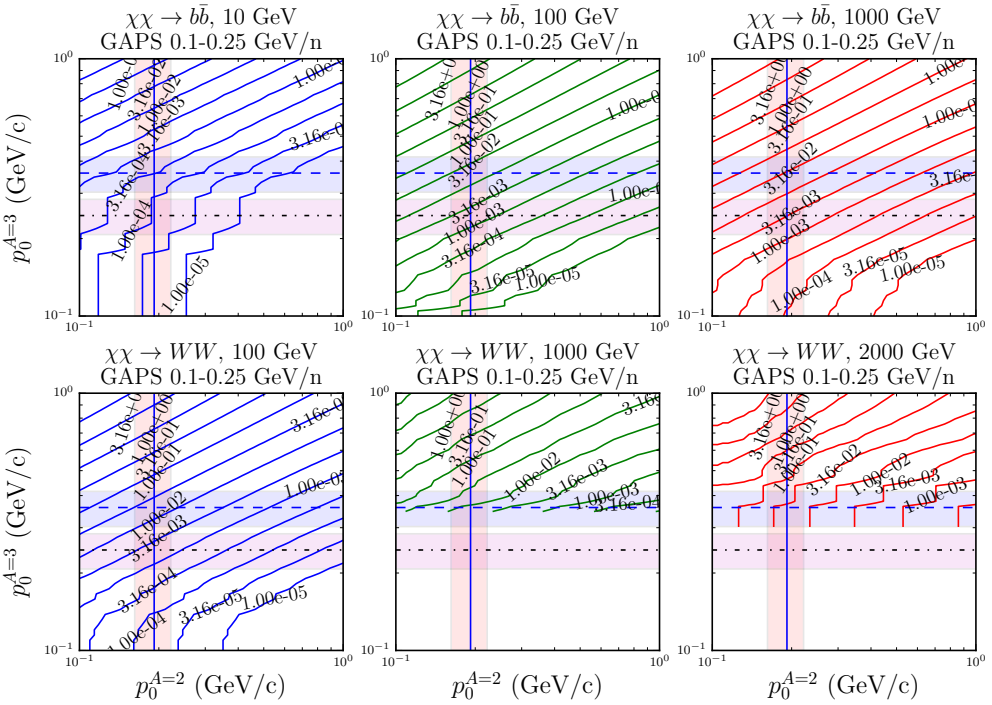

Figure 3.8: Ratios of the production of ($^3\overline{\mathrm{He}}$ + $^3\overline{\mathrm{H}}$) to $\overline{\mathrm{d}}$ for Majorana dark matter annihilating to $b\bar{b}$ (left column) and W^+W^- (right column) final states integrated over the energy bands for the proposed GAPS (LDB) instrument. For each species, these bands were shifted for solar modulation according to a 500 MV Fisk potential. The solid blue vertical lines show nominal values for $p_0^{A=2}$ with uncertainties (vertical shaded) while the horizontal lines show the $A = 3$ coalescence momentum extrapolated using the nuclear binding energy (blue dashed) and heavy-ion data (black dot-dashed). White regions with no contours contained no Monte-Carlo events.

The uncertainties on the coalescence momentum for $A = 2$ are represented by

the vertical shaded bands. For $A = 3$ coalescence momenta, the two horizontal lines in each panel represent scaling with the binding energy (blue-dashed line) and heavy-ion collisions (black dot-dashed). Regions with no visible contours produced no antihelium in the 2×10^{10} annihilation events simulated while the 'wavy' lines are due to limited Monte Carlo statistics. We see that for most masses and final states that are potentially detectable (see discussion in Section 2.4) one should expect $10^{-3} - 10^{-2}$ antihelium for each detected antideuteron. In the case of 10 GeV annihilation to b-quarks, the ratio is slightly lower as antihelium with a GAPS detectable kinetic energy requires a total energy of around 4.5 GeV. However, this quickly increases toward the higher mass results as the dark matter mass is increased away from this threshold. The effects induced by propagation of $\overline{\mathrm{d}}$ relative to $^3\overline{\mathrm{He}}$ are explored in the next section, but are sub-dominant compared with the nuclear physics uncertainties here. In Sec. 2.4 we compute the actual flux and determine the detection prospects for future experiments.

3.2.4.2 Detection Prospects for Current and Future Experiments

We have calculated injection spectra and propagation functions for $^3\overline{\mathrm{He}}$, discussed the most important differences with respect to $\overline{\mathrm{d}}$, and presented ratios for the conversion of $\overline{\mathrm{d}}$ spectrum into $^3\overline{\mathrm{He}}$. For concreteness, we reiterate the procedure here and show the most important scaling relations.

Given an antideuteron flux (or event rate) $\Phi_{\overline{D}}$, the antihelium flux is related

through the following equation:

$$\Phi_{\overline{He}}(T_{\rm TOA}) = R_{\rm IS}(T_{\rm IS}) \cdot R_{\rm solar}(T_{\rm IS}) \left(\frac{p_0^{A=3}}{\overline{p}_{A=3}}\right)^6 \times \\ \times \left(\frac{\overline{p}_{A=2}}{p_0^{A=2}}\right)^3 \cdot R_{\rm PP}(T_{\rm IS}, m_\chi, f) \cdot \Phi_{\overline{D}}(T_{\rm IS} - e\phi_F/2), \tag{3.5}$$

where $\overline{p}_{A=3} = 0.357$ GeV/c and $\overline{p}_{A=2} = 0.192$ GeV/c. Here, $T_{\rm IS} = T_{\rm TOA} + (2/3)\, e\phi_F$. $R_{\rm PP}$ is the particle production ratio, shown for GAPS energies from Fig. 3.8 for the benchmark coalescence momenta. It is only a weak function of energy for the low energies relevant to these studies. $R_{\rm IS}(T_{\rm IS})$ and $R_{\rm solar}(T_{\rm IS})$ are interstellar propagation ratios and the shifted solar ratios shown in Fig. 3.8. This expression allows one to easily take more detailed analyses of $\overline{\rm d}$ spectra, rates or counts (as found in, for example, Refs. [158, 157]) and scale them to the $^3\overline{\rm He}$ case, as well as incorporate new coalescence momentum measurements when they become available.

We then compute the flux at the top of Earth's atmosphere for a set of benchmark cases using the same dark matter models we considered in Sec. 3.2.4 and the propagation setup described in Sec. 5.1.3. In particular, we adopt $p_0^{A=2} = 0.192, p_0^{A=3} = 0.357$, MED propagation parameters, and use the slightly more optimistic "MethodANN" value for the antihelium interaction cross-section with the ISM.

In Figure 3.9 we present the flux at the top of the Earth's atmosphere for dark matter annihilating to W^+W^- and $b\bar{b}$ final states with a thermally-averaged pair annihilation cross section $\langle\sigma v\rangle = 3 \times 10^{-26}$ cm^3/s as well as propagation uncertainties. Also shown are the latest sensitivities for AMS-02, GAPS(LDB/LDB+) [177] and a GAPS(SAT) mission as proposed in Ref. [178]. We note that the propagation uncertainties largely cancel after applying $\bar{p}$ constraints from PAMELA while the uncertainty in

the $A = 3$ coalescence momentum leads to a flux uncertainty of 1-3 orders of magnitude (not-shown), independent of $\bar{p}$ constraints. The astrophysical $^3\overline{\mathrm{He}}$ background peaks with a flux of 10^{-12} [m^2 s sr GeV/n]$^{-1}$ at approximately 20 GeV/n [20]. This is off-scale over all energies shown and rapidly declines at lower energies. By 1 GeV/n the flux has already dropped by another factor 10^2. Over the low energies covered by GAPS it can be considered zero relative to the primaries.

For the case of decaying dark matter, the flux can be easily estimated from the annihilation case by modifying terms in Eq. (5.21). First, the squared terms become linear as the reaction rate now traces the dark matter density ρ_{DM} rather than ρ^2_{DM}. The numerical factor and thermal cross-section can then be replaced by finding an 'equivalent lifetime', τ, which provides an average flux equal to the annihilation case (for $\langle\sigma v\rangle = 3 \times 10^{-26}\mathrm{cm}^3/\mathrm{s}$). The term containing $\langle\sigma v\rangle$ is then replaced by (τ_0/τ). As benchmarks, for dark matter decaying to $b\bar{b}$ with mass $m_\chi^{\mathrm{dec}} = 20$ GeV we find $\tau_0 \approx 7.5 \times 10^{26} s$, while for dark matter decaying to W^+W^- with mass $m_\chi^{\mathrm{dec}} = 200$ GeV, $\tau_0 \approx 7.5 \times 10^{27} s$. Here we note that $m_\chi^{\mathrm{dec}} = 2m_\chi$.

In the case of annihilation to heavy quarks, the very recent analysis of Ref. [179] has updated antiproton constraints on WIMP annihilation to heavy quarks. Specifically, a thermal WIMP annihilating to heavy quarks is ruled out by current Fermi and PAMELA measurements up to approximately 30 GeV while AMS-02 should probe a thermal cross-section up to ∼200 GeV very soon. The antiproton flux is a very important indicator which is directly correlated to the production of heavier anti-nuclei. However, the coalescence momentum for $\overline{\mathrm{d}}$ and $^3\overline{\mathrm{He}}$ can float independently of such mea-

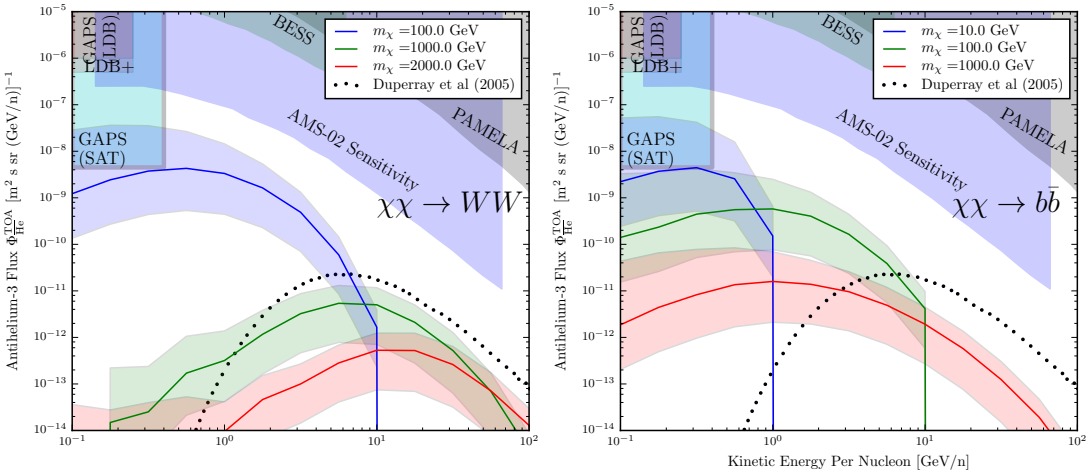

Figure 3.9: Flux of $^3\overline{\text{He}}$ at the top of the atmosphere produced by dark matter annihilating to W^+W^- (top) and $b\bar{b}$(bottom) final states assuming an NFW dark matter density profile. Flux is multiplied by 100 for W^+W^- with m_χ =1, 2 TeV. The shaded vertical bands represent the energy-bands and proposed sensitivities for various GAPS and AMS-02 observations. Shaded uncertainty bands represent the MIN/MAX interstellar propagation models, although these are reduced to within a factor 4 of the central value after applying constraints from PAMELA measurements of the $\bar{p}$ spectrum. Nuclear physics uncertainties are not shown.

surements and it is therefore not unreasonable that a $\overline{\text{d}}$ excess could be observed in-spite of an expected exclusion from antiprotons. For antihelium, an antiproton constraints are even less direct than the case of $\overline{\text{d}}$ due to the unconstrained coalescence momentum.

It is clear that the current generation of experiments is very unlikely to be sensitive to primary antihelium from dark matter annihilation. Future generation satellite born experiments using a GAPS(SAT) detector, as initially proposed in Ref. [178], could potentially be sensitive to WIMPs annihilating to W^+W^- near threshold and $b\bar{b}$ at $\lesssim$ 10 GeV. Unfortunately, higher masses quickly become undetectable, particularly in the W^+W^- case. If a convincing $\overline{\text{d}}$ signal is observed at GAPS or AMS-02, follow-

up $^3\overline{\text{He}}$ observations may be needed to confidently rule out misidentified astrophysical secondaries.

There are two important technical instrumental differences in $^3\overline{\text{He}}$ detection compared to $\overline{\text{d}}$ which are not incorporated into our analysis. GAPS works by measuring X-ray cascades emitted during the formation of exotic atoms from antimatter and the gas target. This technique requires the particle to stop completely inside the detector, and the large volume and weight required could be prohibitive for satellite based missions. This also reduces the high-energy acceptance for heavier nuclei such as helium. Finally, searches at even lower energies increase the importance of geomagnetic field effects and would require a satellite very close to the geomagnetic poles.

Due to the low production rate of cosmic-ray anti-nuclei in interstellar proton-gas interactions, the observation of such particles remains an intriguing avenue for a positive signal from dark matter annihilation. We have modeled the production rates of $A = 3$ cosmic-ray antinuclei by employing the `PYTHIA` event generator to reconstruct the angular distribution of baryons on an event-by-event basis. Noting that the larger binding energy of $^3\overline{\text{He}}$ compared to $\overline{\text{d}}$ theoretically motivates a larger coalescence momentum for $^3\overline{\text{He}}$, we have shown that the expected $^3\overline{\text{He}}$ flux at the solar position lies significantly above the "four order of magnitude" suppression of $A = 3$ anti-nuclei compared to $A = 2$ anti-nuclei, which is naively expected by the coalescence model. While it is still likely that $\overline{\text{d}}$ would be discovered well before $^3\overline{\text{He}}$, this analysis shows that observations of $^3\overline{\text{He}}$ are both technically feasible for future experiments, and may be essential to confirm that any $\overline{\text{d}}$ observation does, in fact, correspond to the discovery of

a dark matter particle.

Using the known instrumental configurations of current experiments, we have also shown that $^3\overline{\text{He}}$ is not detectable by AMS-02, or the current configuration of GAPS LDB+. However, the signal can possibly be detected by a future GAPS satellite mission. Moreover, an observation of $\bar{\text{d}}$ during either of the earlier missions will greatly constrain the parameter space of astrophysical propagation models, allowing for a more accurate forecast of the instrumental qualities necessary in order to detect the $^3\overline{\text{He}}$ signal with a future satellite mission.

3.3 Dark Matter Interactions with Cosmic-Rays and Interstellar Matter

With the advent of large-scale sky surveys at frequencies spanning most of the electromagnetic spectrum, from radio to gamma rays, our theoretical understanding of astrophysical diffuse electromagnetic emission processes is confronting the test of observation in an unprecedented and detailed way. Perhaps not surprisingly, at several frequencies diffuse emission models have, at times, fallen short of providing a satisfactory match to observations. Interestingly, in many cases such shortcomings are centered towards the inner regions of the Galaxy, a rich, and relatively poorly understood region. Over the years, some such excesses have found plausible explanations in the realm of "traditional" astrophysical processes, or in previously under-estimated emission from

populations of astrophysical objects. In some cases, however, it has also been argued that the detected excess might have a "non-traditional" origin, possibly connected with new physics.

Perhaps the longest-standing and most widely known such excess is the 511 keV line detected from a broad angular region by INTEGRAL/SPI [133]. At larger energy, COMPTEL reported an excess across the energy range between 1-20 MeV [180]. Diffuse X-ray emission from the Galactic bulge region, with an approximately thermal spectrum with a very large associated plasma temperature (around 10 keV), has also been reported from Chandra data after point-source subtraction [181][4]. At radio frequencies WMAP revealed excess microwave emission at frequencies between 23 and 61 GHz, an excess known as WMAP haze [182]. This radio "haze" has also been confirmed with Planck observations [183]. Finally, several groups have identified an extended excess of gamma rays from the Galactic center region and from the inner Galaxy, in the few GeV range [184, 185, 45], not to be confused with the Fermi Bubbles [21].

While astrophysical counterparts have been identified that might explain in part or entirely the excesses listed above, several studies have focused on the possible connection of the observed excess emissions with new physics, and specifically with particle dark matter. Dark matter pair-annihilation or decay produces electromagnetic emission both as a result of prompt photon emission from, e.g., neutral pion decay or internal bremsstrahlung or loop-mediated direct annihilation into photons, as well as from secondary mechanisms: the latter mechanism depends on how electrons and

[4]Astrophysical heating mechanisms at the Galactic center can also produce such a hot gas component as well.

positrons, produced in dark matter annihilation or decay, loose energy via synchrotron, inverse Compton, Coulomb scattering and bremsstrahlung [186, 187].

As far as the primary emission is concerned, the predicted morphology follows the integral along the line of sight of the dark matter number density (squared) for decay (annihilation, respectively). For the secondary emission, instead, the morphology is complicated by the magnetic field structure and gas and electron densities [188].

Alternately, some of the excesses listed above have been associated with slightly less trivial new physics models, where the dark matter electromagnetic emission effectively depends on the environmental cosmic-ray population. Such models include, for example, macroscopic quark nuggets [189, 190, 191, 192], which would emit via several different mechanisms: free electrons would annihilate with positrons in the nugget's electrosphere producing a 511 keV line; more energetic cosmic ray electrons would penetrate deeper and potentially produce photons in the COMPTEL energy range; cosmic-ray protons penetrating into the quark matter would produce hadronic jets potentially responsible for bremshstralung emission in the X-ray frequencies relevant for the Chandra excess; for proton cosmic rays penetrating deeper in the nugget, the complete absorption would eventually yield thermal photons with energies in the WMAP haze range (for a detailed review of all these mechanisms, see Ref. [190, 191]).

In eXcited dark matter (XDM) [135] scenarios an excited dark matter state exists at energies of a few MeV above the ground state. Such state, in the original model's incarnation, is populated by self-collisions of the dark matter particles, yielding subsequent electron-positron pairs that could explain the 511 keV line signal [135]; how-

ever, it is possible to envision modifications to the model which would entail collisions with Galactic cosmic rays, given a sufficiently large dark matter interaction with relevant cosmic-ray species. We describe one such scenario in Section 3.3.1 below.

Other scenarios where electromagnetic emission originates from elastic scattering of dark matter particles off of cosmic rays (or vice versa) were considered in Ref. [193, 194, 195], albeit no specific connection with any of the diffuse excesses was attempted. The relevant cosmic-ray populations are, in this case, high-energy cosmic-ray protons and electrons [195]. As also discussed in the next Section 3.3.1, lower-energy radiation is expected from scattering off of interstellar gas or free electrons.

We emphasize that while the models listed above, especially the macroscopic quark nugget model [189, 190], provide some motivation for our study, our results are entirely model-independent, and are intrinsically motivated by the generic possibility that dark matter interacts with cosmic rays and interstellar matter to produce diffuse electromagnetic emission. We present here detailed predictions for the morphology of *any* model where electromagnetic emission stems from interactions of dark matter with ordinary matter in the Galaxy, and the validity and scope of the present work is thus defined by this intent, and not by how compelling specific example models are. Section 3.3.1 provides quantitative estimates of the signals expected in specific example model realizations.

The generic feature of the class of models our study applies to is thus that the electromagnetic emission is proportional to the integral along the line of sight of the dark matter density times the density of a charged cosmic ray species. In this

section, we consider four classes of such cosmic ray species: (i) low-energy protons; (ii) low-energy free electrons; (iii) intermediate energy (1 GeV) cosmic-ray electrons and protons; and (iv) high-energy (1 TeV) cosmic-ray electrons and protons. We then compare the predicted average longitudinal and latitudinal intensity profiles for the four cases (in some instances we even adopt more than one model for a given case) both with the morphological prediction for dark matter annihilation and with the observed excess' emission intensity.

The remainder of this section is structured as follows: in sec. 3.3.2 we describe the dark matter and cosmic-ray densities we employ in our analysis; sec. 3.3.3 details on the calculation of the resulting emission profiles.

3.3.1 Estimates of Expected Signals for Selected Example Models

In this section we estimate rates for processes where dark matter scattering off cosmic rays or interstellar material produces radiation. Specifically, we consider (i) the antiquark nuggets model discussed extensively in Ref. [189, 190, 191, 196, 197, 192, 198], (ii) a (novel) modified version of "exciting dark matter", and (iii) models of dark matter scattering off of cosmic rays along the lines of those considered in Ref. [194].

(i) The flux of photons originating from cosmic rays interacting with antiquark nuggets has been first estimated in Ref. [189]. The rate of events per unit volume is

$$\frac{dW}{dV\ dt} \simeq \frac{4\pi R^2}{B} \cdot v \cdot n_B \cdot n_{DM} \tag{3.6}$$

with R the radius of the nuggets and B the number of nucleons in a nugget[5], and $n_{B,DM}$

[5]These two quantities are related by the typical baryon number density in a color superconducting

the baryonic and dark matter number densities, respectively. Inserting numerical values, the estimate for the flux ϕ gives [189]

$$\phi = \int dr \Delta\Omega \frac{dW}{dV\ dt} \simeq 10^{-3} \mathrm{cm}^{-2} \mathrm{s}^{-1} \left(\frac{10^{33}}{B} \right)^{1/3} \tag{3.7}$$

yielding, for the nuggets' expected baryon charge $B \approx 10^{20} - 10^{33}$ [190], fluxes adequate to explain the diffuse excesses mentioned above.

(ii) As alluded to above, it is possible to construct models of "exciting" dark matter that would also produce photons from the de-excitation of the dark matter excited state, produced by interactions of the lower-mass dark matter state with cosmic rays. To be more specific, we consider a model with two real scalar fields $\phi_{1,2}$, singlet under all Standard Model gauge interactions, with a single dimension-six effective operator describing the interactions of the new scalars between themselves and with Standard Model fermions f as follows:

$$\mathcal{L} = \mathcal{L}_{\mathrm{SM}} + \left(\sum_{i=1,2} \partial_\mu \phi_i \partial^\mu \phi_i - m_i^2 \phi_i^2 \right) + \phi_1 \phi_2 \frac{H \bar{f} f + \mathrm{h.c.}}{M^2}. \tag{3.8}$$

With the interaction term in Eq. (3.8), assuming $m_1 < m_2$, ϕ_1 is absolutely stable. The excitation process $\phi_1 + f \to \phi_2 + f$, where f is either a quark or an electron or a neutrino, leads to the subsequent decay $\phi_2 \to \phi_1 + \bar{f} f$ and the production of radiation either by radiative processes associated with f, or via standard hadronization processes and production of neutral pions if f is a quark. Note that we are not aware of any significant, model-independent collider constraints on the effective scale M of the interaction term, while model-dependent constraints might exist, but are left to further studies.

phase, $n_{CS} \simeq 3 n_0$, where $n_0 \sim (108\ \mathrm{MeV})^3$ is the nuclear saturation density, by $B \simeq \frac{4\pi}{3} R^3 n_{CS}$ [189].

The model of Eq. (3.8) leads to a collision rate per unit volume given by

$$\frac{dW}{dV\ dt} \simeq \sigma \cdot v \cdot n_f \cdot n_{DM} \tag{3.9}$$

with n_f the relevant species number density for cosmic rays or interstellar medium particles. The cross section $\sigma \approx (v/M^2)^2$, with v the Standard Model Higgs vev $v \simeq 246$ GeV. The flux resulting from the rate of Eq. (3.9) reads

$$\phi = \int dr \Delta\Omega \frac{dW}{dV\ dt} \simeq 10^{-8} \mathrm{cm}^{-2}\mathrm{s}^{-1} \left(\frac{GeV}{m_1}\right) \left(\frac{5\ \mathrm{TeV}}{M}\right)^4 . \tag{3.10}$$

As a result, there exist a variety of ranges of dark matter particle masses m_1 and interaction scales M that produce a detectable signal in the context of this framework.

(iii) Ref. [194] draws somewhat pessimistic conclusions about electroweak-interacting dark matter interacting with high-energy cosmic rays and leading to the production of a large enough radiation yield in the final state. Although it was shown there that detectable signals are possible even in the specific framework of supersymmetry, the conclusions primarily depended on two assumptions: (1) electro-weak scale and electro-weak interacting dark matter, and (2) interactions off of (relatively rare) high-energy cosmic rays. Relaxing either one of these assumptions, for example considering lighter and more strongly interacting dark matter, or considering interstellar gas as the primary target material would entirely change the conclusions. Let us be quantitative on the second case: scattering off of low-energy electrons would change the relevant flux of scattering particles

$$E\frac{d\phi_e}{dE}|_{1\ \mathrm{GeV}} \simeq \text{few} \times 10^{-1} \mathrm{cm}^{-2}\mathrm{s}^{-1} \rightarrow n_e \cdot v_{\mathrm{rel}} \simeq 10^8 \mathrm{cm}^{-2}\mathrm{s}^{-1},$$

thus increasing the expected radiative rates by around 9 orders of magnitude. Key here is that while Ref. [194] focused exclusively on gamma rays and WIMPs, a broader radiation wavelength target would yield drastically different conclusions and detectable signals.

3.3.2 Density Distributions

In this section we describe each of the matter distributions used throughout this study, including the density distribution of dark matter (sec. 3.3.2), as motivated by the results of current generation N-body simulations; the density of Galactic cosmic-rays for energies between a few hundred MeV and several TeV (sec. 3.3.2.3), as derived through numerical simulations of cosmic-ray propagation; the distributions of interstellar gas (sec. 3.3.2.3 in two recent and distinct modeling approaches; and, finally, the most up-to-date model of the Galactic distribution of free electrons (sec. 3.3.2.4). For dark matter, cosmic rays, and gas we also discuss the dominant sources of uncertainty and attempt to bracket the range of state-of-the art models.

3.3.2.1 Dark Matter

We employ as our benchmark dark matter profile a Navarro-Frenk-White (NFW) [89] profile with inner slope $\alpha = 1$ and scaling radius $r_s = 20$ kpc (see Eq.2.6). In order to assess the uncertainties due to choice of dark matter profiles, we also utilize a steeper (more 'cusped') generalized NFW with an inner slope of $\alpha = 1.2$; this is in part motivated by recent measurements of the GeV excess [184, 185, 45]; a steeper inner slope

is physically motivated in the context of halo evolution including adiabatic contraction. On the opposite extreme, we consider a cored Einasto [90] profile with $\alpha_E = 0.16$ (see Eq.2.8). We are not concerned with relative normalizations here since we are exclusively interested in the morphological predictions of the models under consideration, not the overall emission intensity. The functional forms of the two dark matter density profiles are given in section 2.2.

In Figure 3.10 we show, in the right-most top panel, the integrated line-of-sight dark matter density squared (i.e. the morphology corresponding to an annihilating dark matter candidate) for the case of the NFW profile. This morphology is of course azimuthally symmetric, and sharply centrally peaked. In the following two sections we will compare this benchmark scenario to more exotic morphologies arising from dark matter interactions with cosmic-ray protons and electrons, interstellar gas, and free electrons.

3.3.2.2 Interstellar Gas

Some models of dark matter – see e.g. Ref. [189, 190] – predict interactions with Galactic gas and/or free electrons. Both of these distributions are strongly peaked toward the Galactic center (GC), and a detailed understanding of the inner few kpc of the Galaxy are needed to formulate solid predictions for the resulting morphology.

The gas density in the Milky Way is typically described by summing contributions from three dynamically distinct components of hydrogen gas in molecular, atomic, and ionized phases. The former two overwhelmingly dominate the gas density near the

GC, and are therefore the most important here.

The three-dimensional distribution of gas in the Galaxy can be determined with excellent accuracy by combining surveys of atomic transition lines with a Galactic rotation curve. For atomic hydrogen, the hyperfine transition at 21 cm provides a direct observable. In the optically thin limit the column density is related to the observed brightness temperature by a single parameter: the hydrogen spin temperature T_S. In the case of molecular hydrogen, the lack of a permanent dipole moment requires, instead, use of a tracer gas, the CO($J = 1 \rightarrow 0$) transition, which is related to the molecular hydrogen density through a conversion factor $X_{\rm CO}$. This factor is, in principle, spatially varying.

The deconvolution technique described above relies on a relative velocity between the gas and the Solar System. In the direction of the GC, the gas is co-rotating, implying no kinematic resolution, leading to a distance degeneracy along lines of sight near Galactic longitudes $l \approx 0$. This problem is compounded by the so-called 'near-far ambiguity' which corresponds two distances to the same radial velocity in the inner Galaxy. In order to alleviate such problems, one can incorporate a model into the deconvolution procedure. For CO (H_2 by proxy), we use the gas model from Pohl, Englmaier and Bissantz (PEB), Ref. [199], which combines the survey of Dame et al [200] with a gas flow model derived from hydrodynamic simulations as well as interpolation of the spiral arms across the line-of-sight toward the GC. Not only does this provide a significant improvement in the l.o.s. gas distribution toward the Galactic center, but it importantly reconstructs a prominent Galactic bar and the intervening spiral arms.

For atomic hydrogen, Nakanishi and Sofue (NS), Ref. [201], assume, instead an analytic model of hydrodynamic equilibrium for the scale height of HI as a function of Galactic radius and uses the Leiden-Argentine-Bonn survey [202] 21 cm survey. This combination provides a high resolution model of H_2 and HI which we denote PEB+NS.

One can alternatively attempt to build a three-dimensional model based on observations of individual structures that are prominent in the region. This is the approach of Refs.[203, 204] which predicate two primary disk components in the inner 3 kpc of the Galaxy: a dense "Central Molecular Zone" approximately centered on the GC and aligned with the Galactic Plane, as well as a holed "Galactic-Bulge-disk" which is rotated at 13.5° counter-clockwise to the Galactic plane as well as having it's major axis inclined $\approx 45°$ away from the line of sight, which is notably much larger than the PEB+NS case, leading to a larger projected extent. Beyond the inner 3 kpc, we use an azimuthally averaged gas profile from Ref. [205] to describe the molecular phase, and the HI profile from Ref [206], corrected to the updated normalizations of Ref. [207]. We collectively refer to this model as Ferrière 2007 (F07).

For both the PEB+NS and F07 models, we incorporate the contributions of dark gas – i.e. molecular hydrogen not traced by CO emission, and atomic hydrogen missed due to the assumption of a uniform spin temperature – by re-normalizing the total 'analytic' HI column density along each line of sight to that of the `GALPROP` map [6]. Essentially, this involves a fitting, in addition to HI and H2, a dust template [208] to gamma-ray data. The detailed construction of this template is described in detail in

[6] rbands_hi12_v2_qdeg_zmax1_Ts150_EBV_mag5_limit.fits.gz

Refs. [209, 210].

Finally, for both models, we also include a contribution from warm, hot, and very hot phases of ionized hydrogen based on the NE2001 [211, 212] model for free electrons, described below. The specific implementation we use is described in Refs. [203, 204].

We note that the precise gas distribution in the outer galaxy is of only marginal importance due to the central peak in the dark matter (DM) density profile. Consequently, we assume both $T_s = 150K$ and $X_{\rm CO} = 2 \times 10^{20}$ cm^{-2}(K km/s)$^{-1}$ and neglect spatial dependence of either one of these quantities. Although spatial variations are certainly present in both components [40, 213], we expect the effect of this on the morphology of the Gas×DM profile to be small in the GC region of interest.

3.3.2.3 Cosmic-Rays

In order to obtain the steady state distribution of cosmic-rays in the Galaxy, we use the numerical code `GALPROP v54.r2504`[7] [85, 86], which encompasses all of the physics relevant for cosmic-ray transport through the galaxy including energy losses, primary source distributions, and re-acceleration. A detailed description of the physics can be found at the dedicated Web Site[8].

Our default diffusion setup consists the model ${}^{\rm S}{\rm L}^{\rm Z}4^{\rm R}20^{\rm T}150^{\rm C}5$ in Ref [210]. This model features a standard set of diffusion parameters fit to local observations of a variety of primary and secondary species including protons, helium, electrons, positrons,

[7] Current versions of `GALPROP` are available at http://galprop.sourceforge.net/
[8] http://galprop.stanford.edu

B/C, and ^{10}Be/^{9}Be [210]. The simulations assume cylindrical geometry with free escape boundary conditions from a diffusion halo of radius 20 kpc and half-height 4 kpc. Because the dark matter profiles are strongly centrally peaked, most of the reasonable variations related to the diffusion setup and geometry are unimportant to the final cosmic ray (CR) morphology. This includes the halo height, provided $z_{\rm max}$ is greater than a few kpc and the CR energy of interest is less than a few TeV, at which point CR propagation transitions to the rectilinear regime. Notably, since we are concerned with the morphology and not the spectrum of cosmic rays, parameters describing diffusive re-acceleration and injection spectra are irrelevant. The energy dependence of the diffusion constant will have only a very minimal effect on morphology at the very lowest and highest energies. For definiteness, we use here a diffusion coefficient $D(\mathcal{R}) = 5.3\times10^{28}{\rm cm}^2{\rm s}^{-1}(\mathcal{R}/4\ {\rm GV})^{1/3}$

Of particular interest to this analysis is the distribution of primary cosmic-ray sources. In what follows, we show predictions for four tracers of supernova remnants, believed to generate the majority of Galactic cosmic-rays. These are based on the observed surface densities of Galactic pulsars (Yusifov [9] and Lorimer [25]), OB stars [26], and supernova remnants (SNR [22]). Each of these distributions suffer from substantial uncertainties in the inner 1-2 kpc due to both statistics and systematics surrounding correction for selection effects. In fact, the latter three distributions are parametrized such that the surface density is zero at the Galactic center, while the Yusifov case is non-zero, leading to a potentially large difference in CR densities in this region. Simulations of neutron star populations in the Milky Way's gravitational potential also indicate a non-zero central density [214], with certain models predicting a strong peak. Finally,

it is difficult to rule out the possibility of a cataclysmic event, or enhanced injection of cosmic-rays at the GC, as may be evidenced by the Fermi Bubbles [215], and perhaps the Galactic Center γ-ray Excess itself (see e.g. Refs. [216, 217]). Fortunately, only for low kinetic energies – and only for very high energies for the case of $e^{\pm}$ – does this have a significant impact on the CR distributions, which become substantially smoothed after diffusion. In what follows, we do not include these more speculative CR source distributions.

3.3.2.4 Free Electrons

The density of free electrons n_e in the Milky Way has been mapped to reasonably good precision by fitting complex multicomponent models to a thousands of measurements including primarily pulsar dispersion measures (the line-of-sight integral of the n_e), temporal and angular broadening of radio pulses sensitive to variations in n_e, and emission measures (the line-of-sight integral of n_e^2). Combining this huge body of information has lead to the development of the so-called NE2001 model [211, 212].

NE2001 contains 5 component classes: (i) smooth components including a thin and thick disc as well as 4 logarithmic spiral arms, (ii) a Galactic center region consisting of a Gaussian component in radius and scale height, (iii) a 4 component local ISM region, (iv) 78 clumped HII regions, and (v) 16 void regions. The only region with high DM density is the Galactic center, and thus we only include contributions from the dense and thin (140 pc) disk, the lower density thick disk, and the small, but very dense Galactic center components. We neglect the spiral arms, which do not extend to the inner 3 kpc

of the Galaxy as well as clumps and voids which provide only weak and small angular scale ($\theta \ll 1^\circ$) perturbations to the overall density profile in the GC direction.

We also utilize a correction to the thick disk scale-height proposed in Ref. [218] after recalibrating the NE2001 model while avoiding strong HII regions in the Galactic plane. This correction roughly doubles the height of the thick disk to ≈ 2 kpc, which for our purposes leads to a substantial broadening of the expected emission to high latitudes and is therefore less disk-like and more spherically symmetric. Ref. [219] provides a recent comparison and recalibration of all models of the free electron density. Importantly, they are all based on approximately the same ingredients, with the primary differences in the smooth components being the thick disk scale-height. The model used here is the thickest, and thus offers the most optimistic scenario for fitting a DM $\times$ free electron signal to an approximately spherical excess. As we will see below, the primary motivation for modeling such emission is to explain the sharp excess observed at 511 keV by INTEGRAL/SPI and even this optimistic model is too disk-like to explain the signal.

As a final note, the next generation of free electron models are likely to incorporate all-sky surveys of the hydrogen-α emission line, perhaps leading to a significant modification of the model presented here. Under the assumption that the number density of ionized hydrogen (i.e. free protons) is equal to the number density of free electrons, the Hα intensity is directly proportional to the emission measure [220]. Unfortunately, such corrections are non-trivial and prone to large errors due to the quadratic dependence of the integrand on n_e.

3.3.3 Morphological Profiles

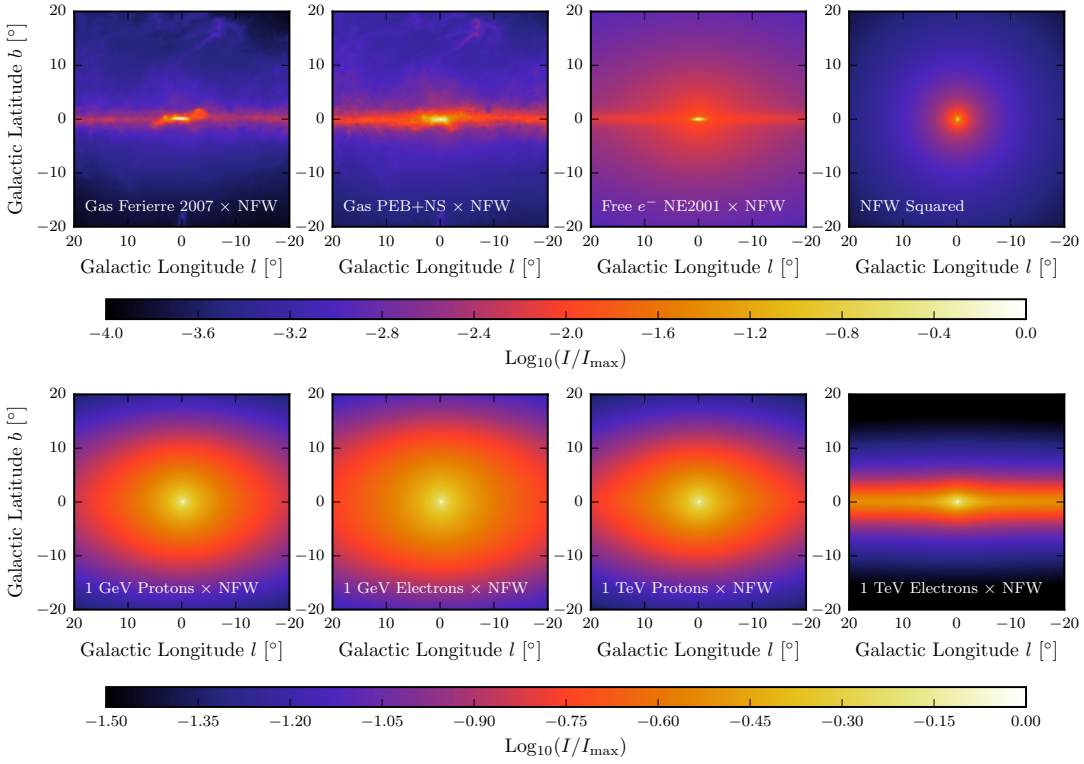

Figure 3.10: *Top, from left to right:* Projected emission profiles for DM (NFW profile) times the F07 gas model, PEB+NS gas model, free electrons, and, for reference a NFW^2 profile (DM annihilation) . *Bottom:* Projected profiles of DM times cosmic-ray protons and electrons for representative energies of 1 GeV (two left-most panels) and 1 TeV (right-most two panels) as calculated with the `GALPROP` package, using the Yusifov [9] distribution of primary sources.

With the matter distributions as specified above, we can now perform the line-of-sight convolution of dark matter with our gas models (meaning the integral along the line of sigh of dark matter times relevant cosmic ray or gas density). In the top row of Figure 7.3 we show the projected emission profiles for an NFW profile convolved with the F07 and PEB+NS gas models, the NE2001 free electron model, and a standard NFW

profile in order to compare against a standard annihilation morphology. In each case, use of either a contracted NFW or Einasto profile would lead to a slightly brighter and cuspier, or fainter and more cored profile in the innermost regions and each template has been normalized to its maximal value, with no other salient differences.

The F07 gas model possesses a very bright central core due to the highly concentrated CMZ zone surrounding the galactic nucleus (not to be confused with the even denser circum-nuclear ring [221] which occupies the innermost ≈10 pc and is below the scale probed here). Emission from the bulge disk can be seen in the diagonally oriented flares on either side. Beyond 5 degrees from the GC, the thin molecular and atomic disks dominate the emission and do not significantly extent to high latitudes making it nearly impossible to obtain a spherical excess. Similarly, the empirically derived PEB+NS model, shows a bright central disk which more smoothly falls off into the broader Galactic disks. In addition, the high latitude emission is significantly enhanced with respect to F07. Still, the overall profile lacks azimuthal symmetry and we can conclude that a truly spherical excess is not well fit by DM $\times$ gas profile.

The case of free electrons is more subtle. Here, we observe a thick disk extending beyond 2 kpc ($b \gtrsim 15^\circ$) which, combined with the DM halo produces a roughly spherical emission profile. A very bright emission disk can be observed at the Galactic center, though the angular extent is less than The thin disk, however adds a distinct elongation along the plane making the averaged longitude profile significantly less steep.

In the bottom row of Figure 7.3 we show projected emission templates for benchmark cosmic-ray protons and electrons at 1 GeV and 1 TeV, using a Yusifov

profile for the primary source distribution. For low and high energy protons, as well as low energy electrons, the CR density is relatively uniform over the region of interest, leading approximately to the same profile as would be expected from dark matter *decays*. For electrons and positrons, inverse-Compton and synchrotron energy loss timescales ($\tau_{\rm ics,sync} \propto E^{-2}$) limit the diffusion radius to $R_{\rm diff} = \sqrt{D(E)\tau_{\rm ics,sync}} \approx 7.5{\rm kpc}/E_{\rm GeV}$ for our choice of parameters, implying that the CR distributions will depend significantly on energy above a few tens of GeV as the cosmic-rays lose energy before propagating farther than a few kpc from their production region (provided the primary source distribution is not uniform). Supernova remnants are highly concentrated in the plane of the Galaxy, resulting in a full-width-half-max of only a few hundred parsecs near 1 TeV. Therefore *any* dark matter model which predicts emission due to interactions with high energy electrons or positrons will result in a significantly disk-like morphology.

An important caveat should be kept in mind before excluding models based solely on a disk-like component. Namely that most "excess" signals rely on fitting and subtracting off a complicated background model especially at low Galactic latitudes. In some cases, particularly those with gas correlated backgrounds, this fitting procedure can potentially also subtract off a disk component which was actually part of the signal. For example, the background models used to obtain the Galactic Center excess rely on fitting independent gas annuli to gamma-ray data without including any model for excess emission. Thus if the Galactic center excess actually contains a disk-like (gas correlated) component this could be 'hiding' in the artificially enhanced background normalization. One way to alleviate such issues is to fit all components simultaneously rather than

relying on residual emission alone.

Finally, we provide skymaps in FITS file format as well as Python scripts at the supplemental materials web page[9] for each combination of halo profile/gas model/free electron model, as well as logarithmically spaced templates in CR energy. Details about the files and model assumptions are provided on the same web page. We also provide example scripts demonstrating how to specify and integrate an arbitrary three-dimensional distribution against the cosmic-ray, free e^-, and gas models which may be found useful in other contexts. See also Section A.4 for additional code links.

We carried out a model-independent study of scenarios where diffuse electromagnetic emission originates from interactions of dark matter particles with the interstellar gas, free electrons or Galactic cosmic rays. We assumed that the relevant morphology depends on the integrated line-of-sight product of the dark matter particle density times the relevant gas/cosmic-ray density. The key motivation to consider such models is that a variety of large-scale diffuse excesses in the general direction of the Galactic center have been identified, at wavelengths ranging from radio to gamma rays, and that a variety of particle physics scenarios have been proposed that rely on dark matter interacting with Galactic gas or cosmic rays.

We considered a variety of state-of-the-art gas density models, and well-motivated cosmic ray models, utilizing several different assumed injection source distribution profiles. We produced the relevant latitudinal and longitudinal profiles, and we are making our results available publicly on the web.

[9] http://planck.ucsc.edu/dmcr-morphology

While our results are generic to any model that predicates diffuse electromagnetic emission from dark matter interactions with cosmic rays or with interstellar matter, our results apply to certain specific models, most notably the macroscopic quark nugget of Ref. [189, 190].

Chapter 4

Search Strategies and Statistical Methods

One of the most challenging aspects of indirect detection studies is determining methods which can robustly reject astrophysical backgrounds. In other words, if an anomalous or unexplained excess is detected in some experiment, how can we maximally differentiate dark matter from backgrounds? If no signal is detected, we would like to set upper limits on dark matter models which incorporate known astrophysical uncertainties. Many techniques have been and continue to be developed, leading to an intriguing overlap between indirect detection and statistics. Comparative analyses are always similar in structure and typically involve four basic steps: Model the signal, model the background, compare, estimate systematic uncertainties.

First we must describe the signal model. For gamma rays, X rays, or neutrinos, dark matter models are usually simple to understand since the only relevant uncertain-

ties are in the halo profile, dark matter mass, and final state[1]. All of these elements are easy to calculate using the elements presented in Chapters 2 and 3. Depending on the experiment, these signals must be convolved with the instrumental response functions (e.g. for raw *Fermi* data), while some experiments provide data which has already undergone a deconvolution with the instrument response (for example AMS-02 which provides a spectrum rather than raw events). For cosmic-ray models, the situation is more complicated and we must apply propagation in order to determine the flux at Earth. This propagation has many parameters, and therefore introduces a large signal uncertainty. For such tasks one can either pick models which bound the signal uncertainties, or preferably, utilize a Bayesian approach which uses additional observations to constrain the backgrounds.

Second, we must calculate the background models. There are at least two scenarios where the calculation of backgrounds is substantially simplified: spectral lines – where there are few or no astrophysical backgrounds and the continuum signals can be estimated directly from the data – and heavy antimatter signatures ($\overline{\mathrm{d}}$ and ${}^3\overline{\mathrm{He}}$), where the backgrounds are very far below the expected signal. For most other situations, just calculating the backgrounds requires significant domain expertise, and the uncertainties are poorly constrained, poorly understood and may involve high-dimensional parameter spaces that prohibit exhaustive exploration of uncertainties. Even dwarf searches which are thought to be a golden channel for dark matter detection, involve poorly understood

[1]In most studies, the cross section $\langle \sigma v \rangle$ is left freely floating and gets fit to the signal since it is simply directly proportional to the signal intensity (and thus only requires a multiplication of the signal). The other quantities require a full re computation of the DM signal so they are often done on a discrete grid.

backgrounds from unresolved point sources which must be calibrated using observations of 'blank sky' (see Sec 4.7).

At this point the data, signal models, and background models have been determined, and hypothesis testing must be performed. We want to choose a technique which provides the best possible statistical power in discriminating the signal from background. We always at least have spectral information, and the most common technique is to use χ^2 tests along with likelihood ratio tests (See sec. 4.1). In cases where we also have spatial information (as is usually the case with electromagnetic or neutrinos searches) the inference becomes much more powerful and we often perform multi-linear template regression, clustering, or some significance measure to separate components simultaneously in spectrum and morphology. In some cases, it may also be suitable to check for a time dependent of the signal which would indicate astrophysical origins. In cases where no signal is detected, we can use these statistical tests to set upper limits on e.g. the dark matter annihilation cross-sections.

Finally, once initial fits are performed, we are faced with understanding the systematics arising from the signal and background uncertainties, as well as instrumental and analysis uncertainties. This is typically the most difficult portion of any analysis, and is often more art than science, being far from a well constrained problem. For signal detections, one should at minimum account for the look-elsewhere effect (also called trials-factors), and try to provide bounds on uncertainties which might include three cases: a very conservative estimate of background uncertainties, a best guess at parameters, and a very strong statement if some assumptions hold. Because many indirect

detection signals have been heavily scrutinized before, the next level of analysis often involves either applying more advanced statistical techniques to the data or performing better estimations of systematic uncertainties using e.g. simulation plus Markov Chain Monte Carlo (MCMC) or importance nested sampling (MultiNest).

In this section, we provide brief descriptions of these techniques and their applications, along with references for the statistical descriptions, example usages, and codes (several of which are our own).

4.1 Maximum Likelihood Estimation

A concise, but through review of basic statistics for physicists can be found in the Particle Data Group summaries [222][2]. Here we review the most pertinent concepts for indirect detection studies.

Suppose we have a set of measurements $\boldsymbol{x}$ and a vector of parameters defining our model $\boldsymbol{\theta} = (\theta_0, ...\theta_N)$. The likelihood function is then defined as $L = P(\boldsymbol{x}|\boldsymbol{\theta})$ and proportional (not-equal) to the probability of the parameter set. While the likelihood function is not a probability distribution itself, maximizing the likelihood will provides the most probable parameters given the observed data, and is thus useful for both inference and hypothesis testing.

Computing the likelihood requires us to specify the full joint probability distribution over the data. However, if these are independently distributed (i.e. the joint PDF can be factorized) as is often the case in physics applications, then we can write

[2]http://pdg.lbl.gov/2014/reviews/rpp2014-rev-statistics.pdf

the likelihood as

$$L(\boldsymbol{\theta}) = \prod_{i=1}^{n} f_i(x_i; \boldsymbol{\theta}), \tag{4.1}$$

where $f_i(x_i; \boldsymbol{\theta})$ is the PDF corresponding to observation i. This may or may not be the same as f_{i+1} if, for example, the error bars differ for different observations, or the observations are drawn from different processes. Due to the product over PDFs, our likelihood function can quickly underflow floating point operations, and it is usually easier to work with logarithms. Since $\log(L)$ is a monotonic transformation this will not change the maximum.

Now the maximum may be found by setting the partial derivatives with respect to each θ_i.

$$\frac{\partial \log L}{\partial \theta_i} = 0, \qquad i = 1, ..., N. \tag{4.2}$$

For many problems we simply solve the optimization numerically by minimizing $-\log L$ [3]. When computing the log-likelihood here, we do not care about additive constants, and can drop anything that does not depend on $\boldsymbol{\theta}$.

As an example, suppose we have a model which predicts μ_i events in each bin as a function of θ, and we want to fit against a data set with N bins containing x_i events

[3] A great library for these types of optimization problems is iMinuit, developed at CERN which also includes tools for estimating confidence intervals. The python version is particularly easy to work with https://pypi.python.org/pypi/iminuit.

with Gaussian distributed error bars σ_i for each bin. Then the PDF for each bin is

$$f_i(x_i;\boldsymbol{\theta}) = \frac{1}{\sqrt{2\pi}\sigma_i}\exp\left(\frac{-(\mu_i - x_i)^2}{2\sigma_i^2}\right). \tag{4.3}$$

Our log-likelihood is therefore,

$$L(\boldsymbol{\theta}) = -\frac{N}{2}\log(2\pi) - \sum_{i=1}^{N}\left[\frac{1}{2}\log(\sigma_i) - \frac{(\mu_i - x_i)^2}{2\sigma_i^2}\right], \tag{4.4}$$

and we optimize $\boldsymbol{\theta}$ such that this quantity is maximised.

For counting photons, we will typically utilize the Poisson distribution rather than a Gaussian. For observed data (or bin counts) x_i, the likelihood is given by

$$L = \prod_{i=1}^{N}\frac{\mu_i^{x_i}e^{-\mu_i}}{x_i!}, \tag{4.5}$$

where μ_i is the predicted model count for bin i. Then the log-likelihood is given by,

$$\log L = \sum_{i=1}^{N}\left[-\mu_i(\boldsymbol{\theta}) + x_i - x_i\log\frac{x_i}{\mu_i(\boldsymbol{\theta})}\right]. \tag{4.6}$$

Where the last term is defined to be zero when $x_i = 0$.

4.1.1 Parameter Estimation

From a frequentist perspective, the model parameters $\boldsymbol{\theta}$ have a single value known by god. The goal of parameter estimation is to determine both a point estimator $\hat{\boldsymbol{\theta}}$ for this true value based on the data. We then would like to draw confidence intervals

around our estimator where we estimate e.g. a 95% chance of the true $\boldsymbol{\theta}$ lying in the interval. This differs from the Bayesian perspective given in Sec. 4.2.

Different estimators possess different properties, and we should choose those which best fit our situation and desired knowledge. The most important properties of interest are *consistency* (does the value of the estimator converge given more data), *bias* (does our estimator converge to the true value), *efficiency* (what is the ratio of the minimal possible variance to the estimator variance), and *robustness* (how sensitive is the estimator to deviations from assumptions or outliers etc...). Maximum likelihood estimators are the most commonly applied in physics applications because they are unbiased, are very efficient, and are reasonably robust.

The inverse covariance matrix V^{-1} for a set of maximum likelihood estimators $\hat{\theta}$ can be estimated via

$$(\hat{V}^{-1})_{i,j} = -\left.\frac{\partial^2 \log L}{\partial\theta_i \partial\theta_j}\right|_{\hat{\theta}}. \tag{4.7}$$

For an error of s-standard deviations, the contour hyper-surface of the estimator is defined around the maximum likelihood $L_{\max}$ as

$$\log L(\boldsymbol{\theta'}) = \log L_{\max} - s^2/2. \tag{4.8}$$

For systems with low covariance between parameters, the diagonal elements of the covariance matrix will provide a reasonable approximation of the variance for each θ_i. However, in many of the approaches we will see below, parameters can be extremely degenerate, and the covariances must be estimated in order to accurately reflect the uncertainties (i.e. the error ellipse is not aligned with the axis). In these high covariance

cases, confidence intervals for a given parameter are reported as the min/max parameter value taken along the error ellipse.

4.1.2 Hypothesis Testing and Goodness of Fit

A hypothesis H is a model, or range of models. We often would like to test, for example, whether one model performs better than another model, or whether some parameter lies outside/inside of a given interval. Suppose we have a null hypothesis H_0. We would like a rule for determining whether a competing hypothesis H_1 *rejects* the null at some probability α.

Suppose we have a *simple* hypothesis so that the null and test model differ only by the chosen parameter values ($H_0 : \theta = \theta_0$, $H_1 : \theta = \theta_1$). We define a statistic

$$\lambda = \frac{L(\theta_0|x)}{L(\theta_1|x)}. \tag{4.9}$$

Here, λ will be small if H_1 is much more probable and large if the H_0 is more probable given the data. We can reject the null hypothesis at a significance level α, when

$$\alpha = P(\lambda(X) \leq \eta|H_0), \tag{4.10}$$

where η must be calculated from the integral.

For our purposes, we more often have a *composite* hypothesis, where the parameters of interest are some subset of the full parameter space $\theta \in \Theta_0 \subset \Theta$. We can

then calculate the test statistic (TS) via a likelihood ratio test and Wilk's theorem

$$\mathrm{TS} = -2\log(\lambda) = -2(\log(L(H_0|x)) - \log(L(H_1|x))). \tag{4.11}$$

In the large sample size limit, TS is distributed as a χ^2 distribution with $\dim(\Theta) - \dim(\Theta_0)$ degrees of freedom – i.e. the difference in the number of parameters in the alternative model versus null model. Thus, a p-value for rejecting the null can be directly calculated via the χ^2.

In cases where the likelihood is difficult to calculate (i.e. the PDF is unknown), one can use Monte Carlo simulation to determine distributions and provide a robust estimate of p-values technique which makes no assumptions about the distribution of the test statistics (see for example the clustering case of Ch. 9).

Goodness of fit can be also be estimated from the likelihood function via Wilks' theorem. Typically we minimize the quantity $-2\log\lambda(\hat{\boldsymbol{\theta}})$, which for N bins and m parameters, obeys a χ^2 distribution with $N - m$ degrees of freedom. This is known as a Pearson's χ^2 test. If our bin counts are relatively large so that our Poisson distribution is approximately Gaussian, then we can estimate a p-value by integrating the χ^2 distribution with n_d degrees of freedom.

$$p = \int_{\chi^2}^{\infty} f_{\chi^2}(z, n_d)dz. \tag{4.12}$$

If we do not know the distribution of the bins or bin, then we can still estimate p-values via Monte Carlo methods (see Sec. 4.6).

4.2 Bayesian Methods

Much of the scientific world is gradually moving toward Bayesian methods, which provide much improved expression of uncertainties as well as the incorporation of prior beliefs, which allow us to impart expert knowledge, model constraints, or previous measurements into our final probabilistic model. The increase in computational power and efficient sampling methods is also likely responsible for this shift, which allows previously intractable models scans to be computed.

More fundamentally, the Bayesian approach to statistics demotes the parameters themselves to be random variables in contrast to the frequentist approach, which assumes the model parameters have a true value. For example, a confidence interval is now expressed as "there is a 95% probability that the parameter value is lies within our bounds" compared to "there is a 95% probability that our bounds contain the true parameter value". In other words, Bayesians believe that the model itself is probabilistic.

The fundamental expression of Bayesian statistics is Bayes' Theorem,

$$p(\boldsymbol{\theta}|\boldsymbol{x}) = \frac{P(\boldsymbol{x}|\boldsymbol{\theta})\pi(\boldsymbol{\theta})}{\int P(\boldsymbol{x}|\boldsymbol{\theta}')\pi(\boldsymbol{\theta}')d\boldsymbol{\theta}'}, \tag{4.13}$$

where all of the known information is expressed by the *posterior distribution* $p(\boldsymbol{\theta}|\boldsymbol{x})$ which is proportional to the composed of the likelihood function $P(\boldsymbol{x}|\boldsymbol{\theta})$ and the *prior* distribution $\pi(\boldsymbol{\theta})$, for the parameters. The denominator is known as the *evidence* which can be used to provide an estimate of the model fit versus model complexity, effectively implementing Occam's Razor in a quantitative way. Typically, we just want

to draw samples from the posterior, and we are less concerned with model comparison.

The prior $\pi(\boldsymbol{\theta})$ expresses the subjective beliefs about the parameter values. However, it can be formulated in an objective way, in a procedure known as *Objective Bayes*. Often we choose non-informative priors in order to express our initial ignorance. A uniform distribution is often used in practice, although one should take care to ensure that the prior is uniform in the correct space. For example, if we take a flat prior over a logarithmic parameter, then the prior itself is not uniform, but rather log-uniform, and our posterior will be highly biased. In general, a non-linear function of $\boldsymbol{\theta}$ will require a non-uniform prior in order to be non-informative. These are called Jeffreys' Priors, and they can be computed using the Fisher information matrix [222].

One of the most powerful features of Bayesian statistics is that one may iteratively draw samples from the posterior and feed back the gained information into the prior for the next sample draw. This idea leads to a variety of importance sampling and Markov Chain Monte Carlo methods which efficiently sample from the posterior distributions. These methods are commonly employed in large scans over parameter space, with the MultiNest [223] algorithm being the (current) de-facto standard in cosmology and astrophysics.

4.3 Template Regression

Above we outlined the classical (frequentist) statistical elements which are most commonly used in indirect detection. In this section we discuss *template regression* which is just a binned likelihood analysis over both spatial pixels (data morphology) and energy

bins (spectrum) and is commonly used in gamma-ray analyses. The first step is to bin our data in three dimensions: Galactic latitude, longitude, and energy bin[4].

The choice of binning should be carefully considered. The finer the binning, the less information we are throwing away, however, when we applied Wilk's theorem in the previous section, we required the assumption of Gaussian bins rather than a Poisson distribution. We should therefore make sure that we average at least 5-10 photons per bin. Furthermore, the information gain from very fine spatial binning is limited by the angular resolution of the instrument, and we may want to trade off spatial resolution for spectral resolution. In most analyses of Fermi data spatial binning than $1/8^\circ - 1/2^\circ$ is typically used, along with 10-30 logarithmically spaced energy bins over the energy range of Fermi ($\sim$100 MeV-500 GeV). However, the photon spectrum decreases rapidly and it can be useful to define an energy binning procedure which compensates for this. One choice advocated recently [36] is the recursive definition,

$$E_{j+1} = \left(E_j^{1-\Gamma} - \frac{E_{\rm min}^{1-\Gamma} - E_{\rm max}^{1-\Gamma}}{n_{\rm bins}} \right)^{\frac{1}{1-\Gamma}}, \tag{4.14}$$

for $j \in [0, 1, ..n_{\rm bins}]$. This spacing provides an equal number of photons in each bin for a power-law spectrum with index Γ. A hard index of $\Gamma = 1.45$ is a good choice to balance loss of statistics and unreasonably large bin widths at high energies [36]. This binning is also used in our analysis of the Galactic Center excess in Sec. 8.1.

[4]Over large sky segments, we often use Healpix [224] (http://healpix.sourceforge.net/) binning which provides pixels with equal area, rather than latitude longitude which shrink as we move toward the celestial poles. This healpix mapping maps the full sky's spherical surface into a one dimensional array of pixels. In the Cartesian case, we can do the same by just assigning a unique index to each pixel. We actually therefore think of 2-dimensional binning in space and energy.

Next we must choose the model components we wish to include in the template fitting which might include an isotropic emission component, models of the Galactic diffuse emission, dark matter, and/or point sources. As discussed in Sec. 2.4.2, we must transform the raw astrophysical flux models into event counts in the instrument space via convolutions with the instrumental response functions. At this point, we can fit the best linear combination of our model templates to the data. For a each template indexed by k, the model counts μ_{ij} for a given pixel i and energy bin j are given by a summing over each template count n_k times the energy dependent normalizations θ_j^k

$$\mu_{ij}(\boldsymbol{\theta}) = \sum_{k}^{N_{\text{comp.}}} \theta_j^k n_{ij}^k. \tag{4.15}$$

The normalizations θ_j^k are the parameters which must be fitted in our model. As defined above, the spectrum of each fit component is allowed to float in each energy bin. For templates or regions with high degeneracy, or low statistics, this can lead to noisy fits. In many cases we may want to reduce the number of fit parameters by fixing the spectrum or spectral form, for example, to a power-law, broken power-law, or a power law with an exponential cutoff. Commonly used spectral forms can be found on the Fermi-LAT web page [5].

Now, the χ^2 of the fit is given by,

$$\chi^2 \equiv -2 \ln \mathcal{L} = 2 \sum_{i,j} (\mu_{ij}(\boldsymbol{\theta}) - x_{ij} \ln \mu_{ij}(\boldsymbol{\theta})) \tag{4.16}$$

[5] http://fermi.gsfc.nasa.gov/ssc/data/analysis/scitools/source_models.html

where x_{ij} is the observed number of photons in pixel i and energy bin j. This defines the objective function for the optimization. Find the weights $\boldsymbol{\theta}$ which minimize χ^2. We may impose additional constraints on this objective function such as point source masking or external constraints as discussed in Sections 4.3.3 and 4.3.2 below. In the next section we present a variety of commonly used templates.

4.3.1 Example Templates

The components chosen for any template fitting procedure obviously depend on the specific problem and analysis goals. Here we review some commonly employed for fitting to Fermi gamma-ray data. However, one should also keep in mind more data-driven alternatives such as the analysis presented in Chapter 10 where empirically determined templates are used to place strong limits on dark matter origins of the 3.5 keV X-ray line.

- *Galactic Diffuse Emission (GDE):* There are three basic components to diffuse emission from the Milky Way. All arise from interactions of Galactic cosmic-rays with interstellar matter (π^0 and bremsstrahlung) and low-energy radiation fields (ICS: Inverse Compton Scattering). These components can be calculated using sophisticated numerical codes such as Galprop, but involve substantial uncertainties in the Galactic plane, particularly at the Galactic center. The entirety of Part II of this thesis is devoted to computing GDE models, and great care should be taken for analysis of diffuse sources near the Galactic plane. For gamma-ray analysis of small point-like, or slightly extended sources (less than 5 degrees), the Fermi

collaboration provides a diffuse Galactic emission model which is derived by empirically fitting templates of diffuse emission to the data and via wavelet filtering techniques[6].

- *Point Sources (PSC):* The contribution of point sources is typically based on *Fermi's* 4 year third point source catalog, 3FGL [116], which includes more than 3000 point sources and 13 extended sources. In regions containing many point sources, the spectrum and normalization of each source is often fixed to the 3FGL values and the finite angular resolution of the *Fermi-LAT* is taken into account by smearing photons according to the precise energy dependent point spread function (PSF).

  An additional note should be kept in mind: If the diffuse model in the fit is changing significantly in the fit (as it does near the Galactic plane), then the inferred point source fluxes will also change. If the ponit sources are not too dense, then one can refit sources with diffuse model. However, this often introduces a problematic number of degrees of freedom. If point sources are to be held fixed, one should perform masking as described in Sec. 4.3.3 below to reduce bias from mis-modeled point sources.

- *Isotropic Gamma-Ray Background (IGRB):* The IGRB template is composed of the population of unresolved, extra-galactic γ-ray emitters, a distribution which should be roughly isotropic over the full sky. Often this needs to be constrained

[6] A brief description of the diffuse background model can be found at http://fermi.gsfc.nasa.gov/ssc/data/access/lat/Model_details/FSSC_model_diffus_reprocessed_v12.pdf.

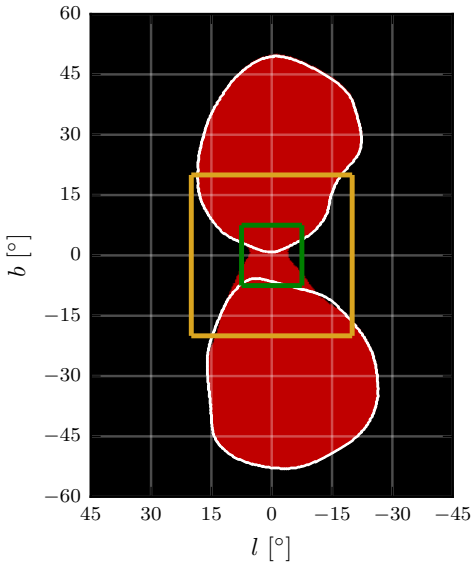

Figure 4.1: The new Fermi bubbles template [10] is shown in red, and extends throughout the Galactic center region. The previous template versions [11] are shown by white contours. Also shown are the bounding windows for a typical inner Galaxy analysis (gold) and Galactic center analysis (green). The Fermi bubble's interaction with and extension into the Galactic plane are poorly understood at present.

over small ROIs by measurements over the full sky. We refer the reader to Sec. 4.3.2 which describes such constraints. A thorough description of the isotropic gamma-ray background can be found in Ref. [225].

- *Fermi Bubbles:* The flux and spectrum of the Fermi bubbles is assumed to be spatially uniform over the region defined in Ref. [11] with more recent corrections made near the Galactic plane [10] which are shown in Figure 4.1. Typically the North and South Lobes are not modelled independently. Similarly to the isotropic template above, it is common to impose the spectrum from the latest *Fermi* Collaboration paper [226].

- *Dark Matter:* Dark matter templates in the Galactic center can be found by integrating the halo profiles presented in Section 2.2 over the line-of-sight. Often several halo models are presented, but NFW is the most common, and often different analyses scan over the inner slope. In the case of dwarf galaxies, the templates are based on the best fitting halo profiles using stellar kinematics data.

4.3.2 External Fit Constraints

In some cases, we may want to add external constraints on the template normalizations. While most optimization software allows for hard limits on the min/max values of the fit parameters, we may want to impose a more subtle penalty. For example, when analysing regions of interest (ROI) near the Galactic center, we have large scale structures such as the isotropic or Fermi Bubbles that are bigger than the ROI under analysis. Often the spectrum of these components has been measured over larger very large ROI, and is poorly constrained over a narrow window. The corresponding template normalizations should then be constrained by adding an additional penalty to Eq. (4.16) based on the *external* $\chi^2_{\text{ext.}}$ calculated from the flux and uncertainties over the larger ROI. This takes the form

$$\chi^2_{\text{ext}} = \sum_i \left(\frac{\phi_i - \bar{\phi}_i}{\Delta\phi_i} \right)^2 \tag{4.17}$$

where ϕ_i is the flux in energy bin i and $\bar{\phi}_i$ and $\Delta\phi_i$ are the mean and standard deviation. This could include for example, the IGRB flux of Ref. [225], or the Fermi Bubbles flux of Ref. [226]. Further modifications to the objective function can be imposed if one wants

to incorporate prior beliefs – in the Bayesian sense – on the fitting procedure.

4.3.3 Adaptive Point Source Masking

When analyzing diffuse emission in regions rich with point sources, the analysis results can depend significantly on the point source masking technique employed. In many cases near the Galactic plane, the inferred point source fluxes can vary significantly as the diffuse background model is changed. Ideally, one should fit each point source simultaneously to the diffuse components, but in practice this often introduces too much degeneracy and too many parameters. It is therefore common to mask point sources when studying large regions of interest.

Ref. [36] developed the weighting coefficient $w_{i,j}$ which allows for adaptive source masking based on the ratio of the point (or extended) source flux $\mu_{i,j}^{\rm PSC}$ to the diffuse flux $\mu_{i,j}^{\rm BG}$,

$$w_{i,j} \equiv \left[\left(\frac{\mu_{i,j}^{\rm PSC}}{f_{\rm PSC}\mu_{i,j}^{\rm BG}} \right)^{\alpha_{\rm PSC}} + 1 \right]^{-1}. \tag{4.18}$$

Here $f_{\rm PSC}$ and $\alpha_{\rm PSC}$ determine the point source masking threshold and transition rate from masked to unmasked pixels [36]. Good choices for Fermi data is $f_{\rm PSC} = 0.1$ and $\alpha_{\rm PSC} = 5$.

The weight coefficient can now be applied to each pixel, and Eq. 4.16 becomes,

$$\chi^2 \equiv -2\ln\mathcal{L} + \chi^2_{\rm ext} \tag{4.19}$$

$$= 2\sum_{i,j} w_{ij}(\mu_{ij} - \theta_{ij}\ln\mu_{ij}) + \chi^2_{\rm ext}. \tag{4.20}$$

with $\chi^2_{\rm ext}$ often set to zero, but potentially defined by Eq. (4.17).

4.4 Density Based Photon Clustering

In the era of publicly accessible all-sky gamma-ray surveys such as the dataset provided by the Fermi-LAT collaboration, one of the most important tasks is the identification of diffuse and point-like emission sources in sparse gamma-ray data. Unlike traditional astrophysical point-source identification, one does not have have a pixel based image built from many soft photons without significant binning which sacrifices small scale angular information that can be crucial to determining morphological properties of the emission source.

Here we explore a simple cluster Density Based Spatial Clustering for Applications with Noise (DBSCAN) as an alternative to current point source catalog 'seeding' methods such as wavelet transforms, and present our own modifications which adaptively vary the algorithm's parameters in order to account for variable density backgrounds (noise). A python Package GammaCAP has been developed in support of this goal. Details of the calculations are described below, while codes adn tutorials are described in App. A.3. **In Chapter 9 we also present a novel use of DBSCAN to discern point-like sources from diffuse sources at the Galactic center.** Other notable approaches include use of the Minimial Spanning Tree algorithms [227], however these cannot account for variable density backgrounds and must be run on small fields of view.

When photon statistics are not sparse, point source detection or 'seeding' can be done using wavelet transforms over the photon density in order to pick out point-like sources over the smoother diffuse background. This approach is used in constructing the

initial candidate source seeds for the 3FGL catalog [116]. At higher energies, the photon fields become extremely sparse and one must revert to more sensitive methods.

The seeding stage of analysis is intended to determine candidates for a maximum likelihood analysis. In addition we provide a significance measure which can also be used as a less sophisticated test-statistic. In its two dimensional incarnation, the algorithm has two free parameters which are demonstrated to be tightly correlated with the size of the PSF and the local background levels. The PSF is known precisely, and the background levels can typically be estimated to within 25% using either a map of the diffuse galactic and isotropic extragalactic backgrounds, or by directly examining photon data surrounding the region of interest. With these two free parameters correlated and constrained, one can optimize them to given choice of balance background rejection and detection efficiency. This provides the basic analysis layer which is often adequate.

If necessary, the detection threshold can be further lowered by implementing a post processing step. To this end, we construct a variety of observables for each cluster – e.g. size, eccentricity, density profile, significance, etc... – and employ machine learning classifiers to reject contamination from spurious clusters. Widely used for event identification in particle physics, Boosted Decision Trees (BDTs) are trained via Monte Carlo to cut and correlate these observables until an optimal signal/background binning is achieved. At this stage, detection and contamination efficiencies can be reevaluated and an adaptive search algorithm can be implemented on the gamma-ray sky which is robust, has deeper sensitivity, and has well defined statistical properties.

In order to classify the spatial morphology of a set of photons in a statistically

robust way, we employ the *Density Based Spatial Clustering of Applications with Noise* (DBSCAN) algorithm [228], which is capable of both distinguishing cluster points from noise and constraining the maximum connectivity size based on the instrumental point-spread function. The 2-dimensional DBSCAN algorithm possesses two input parameters, corresponding to the assumed radius (ϵ) of each cluster neighborhood and the number of points ($\mathrm{N_{min}}$) which must be contained within a neighborhood to form a new cluster or add to an existing cluster. Our implementation of DBSCAN, which is modified from the Scikit-Learn `python` package, works as follows:

1. For each photon in the input list, define the 'ϵ-neighborhood' as a circle of radius ϵ centered on the photon of interest.

2. If a photon's ϵ-neighborhood contains greater than N_{min} photons a new cluster is formed and that point is marked as a 'core point'.

3. Two core photons are considered 'density-connected' if they are mutually contained with in each other's ϵ-neighborhoods. All density connected photons are then merged into a single cluster.

4. Require any cluster to contain at least 3 core points.

Traditional DBSCAN implementations also define the notion of 'density reachable' to indicate points which are not themselves density-connected, but which lie within a core point's ϵ-neighborhood. This property is, however, not symmetric, and cluster assignment can be ambiguous depending on the input ordering of the data. Our algorithm ignores density-reachable points, thus ensuring deterministic results. We note

that a different modification of the DBSCAN algorithm has already been employed on Fermi-LAT data in the past [229].

To exemplify the use of the DBSCAN algorithm, Figure 4.2 shows the DBSCAN analysis of the Fermi-LAT photon events measured with an energy between 120 – 140 GeV (left), and of a simulated model containing two point sources near the galactic center (right). In each case, we show the DBSCAN ϵ-neighborhoods for each core point of each detected cluster. For the Fermi results, DBSCAN finds only one cluster (interestingly centered on the actual Galactic center location!), while in the 3 pulsar simulation case, the algorithm correctly identifies three clusters, at the positions corresponding to where the pulsar photons were generated. The following discussion explains in detail the procedure we employ to apply DBSCAN to γ-ray data.

4.4.1 Cluster Significance Measure

We employ the likelihood ratio proposed by Li & Ma to calculate the cluster significance, s, over the background in terms of the number of cluster photons N_s and background photons N_b:

$$s = \sqrt{2\left(N_s \ln\left[\frac{2N_s}{N_s + N_b}\right] + N_b \ln\left[\frac{2N_b}{N_s + N_b}\right]\right)}\,. \tag{4.21}$$

Here, N_b represents the expected background counts, determined either by integrating a diffuse background model over the cluster area, or by evaluating the counts in an annulus surrounding the cluster, while N_s is the total photon count (signal + background) contained in the cluster. As long as N_s and N_b are not too sparse, one can equate a cluster with significance s to an "s-standard deviation observation". Thus a cluster significance

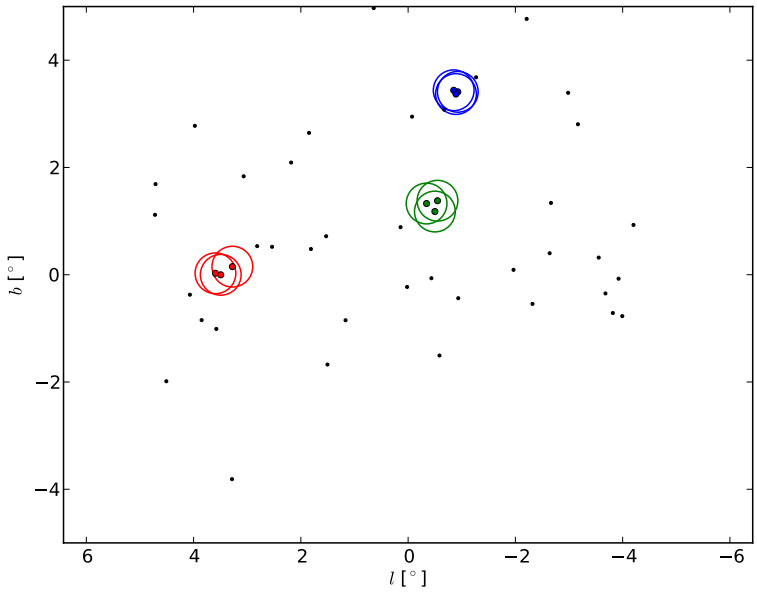

Figure 4.2: Example of DBSCAN for a 3 point source Monte Carlo simulation showing in colored circles the $\epsilon-$neighborhoods for core points in each detected cluster. In this case, $N_{min} = 3$.

$s = 2$ implies the cluster is a 2σ fluctuation above the mean background. We will use this nomenclature throughout our analysis.

With the individual cluster significance in hand, we define the *"global" significance* S as the mean significance of each detected cluster weighted by the number of photons in that cluster.

4.4.2 Tuning DBSCAN Parameters $N_{\min}$ and ϵ

We now would like to optimize the choices of the DBSCAN parameters ϵ and $N_{\min}$ such that the significance is maximized while rejecting fake clusters caused by fluctuations in the background. In choosing ϵ and $N_{\min}$, we must incorporate two important

considerations.

First, ϵ is highly constrained by the instrumental point-spread function. Choosing ϵ too large is non-physical and results in incorrect clustering properties due to the inclusion of background photons. Choosing ϵ too small is acceptable provided there are enough photons to accurately reconstruct the cluster (i.e. so that the cluster does not fragment into several sub-clusters). A satisfactory trade off is to choose ϵ equal to the 68% containment radius of the cluster, r_{68}. Long PSF tails are typical e.g. Fermi-LAT, and $\epsilon = r_{68}$ is significantly smaller than the 95% containment radius, while ensuring that the core of the cluster is still resolved. In cases where the photon densities are very high, it may be desirable to reduce this in order to more accurately reconstruct cluster properties.

Second, the background count can be estimated either by evaluating a background model at that point or by examining the background count near the cluster of interest. Thus for a given ϵ, we can choose $N_{\rm min}$ according to the level of Poisson fluctuation above the mean, $N_{{\rm min},\sigma}$, according to the following relations.

$$N_{\rm BG} = \rho_{\rm BG}\ \pi\epsilon^2 \tag{4.22}$$

$$N_{\rm min} = N_{\rm BG} + N_{{\rm min},\sigma}\sqrt{N_{\rm BG}} \tag{4.23}$$

In order to test these guidelines, we now simulate a reasonable set of point sources distributed amongst background noise. In particular, we simulate 20 point sources emitting $N_{\rm sig}$ photons with a Gaussian PSF of $r_{68} = 1$ deg. The sources are distributed over a $30^\circ \times 30^\circ$ window with an isotropic background density $\rho_{\rm BG} = 10$

photons per square degree. Next we scan over $(\epsilon, N_{\rm min})$ parameter space and examine the resulting global significance S and detected cluster count $N_{\rm clusters}$.

In Figure 4.3 we show S and $N_{\rm clusters}$ for three cases of increasing signal flux $N_{\rm sig} = \{0, 50, 100\}$ photons. The colormap shows the global significances while the black labeled contours show $N_{\rm clusters}$. Ideally, $N_{\rm clusters} = 20$ except for in the background only case, while the significance is maximized along this constraint. We also show the lines for the expected background level ($N_{{\rm min},\sigma} = 0$) and 3σ fluctuation ($N_{{\rm min},\sigma} = 3$) as detailed in Equation 4.23. The regions of high significance in the lower-right of each panel represent the case where all points in the simulation begin clustering together and are non-physical. This behavior is expected as the cluster threshold $N_{\rm min}$ drops below the background level. When the real signal is increased, regions of higher significance begin developing above the lines of $N_{{\rm min},\sigma} = 3$, where the cluster count is also found at the correct value of 20. For example, the large yellow patch in the right hand panel shows a large region where clusters are correctly identified and background noise is strongly rejected. If we move to slightly higher $N_{{\rm min},\sigma}$ (e.g. $N_{{\rm min},\sigma} = 4$) we lose some detection efficiency, but are also more robust against background fluctuations. Eventually, we will also employ cuts and boosted decision tree classifiers to further reject fake clusters based on their observed properties.

We have established simple relationships for selecting the values of the DBSCAN parameters ϵ and $N_{\rm min}$ based on two physical inputs: the point-spread function and an estimate of the local background density. With these selections in mind, we can now discuss a 3-dimensional DBSCAN where we extend the search along the time axis.

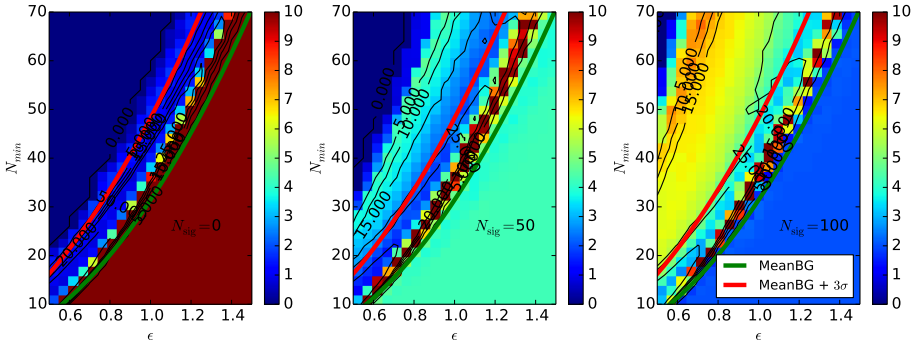

Figure 4.3: Global cluster significance S (colormap) and cluster count N_{clusters} (black contours) as a function of the DBSCAN search-radius ϵ and count threshold N_{min} for simulations of 20 point sources emitting 0,50,100 photons per source (left, center, right) in an isotropic background. Also shown is the background photon expectation (solid green) and a 3-sigma background fluctuation $N_{\text{min},\sigma}$=3 (solid red). For a large region of the ϵ and N_{min} parameter space, the correct number of clusters is found at high significance.

4.4.3 Extending DBSCAN to 3-dimensions

Beyond the 2D spatial case, DBSCAN may also be used in higher dimensions including temporal and spectral extensions, provided a metric can be found which appropriately relates these to the spatial dimensions. One such novel application is to look for transient phenomena which would otherwise be washed out by the integrated background signal. The methods mentioned above are readily extensible to this case and can potentially provide a new catalog of of interesting transient gamma-ray sources.

3-dimensional searches are performed by drawing a cylinder of radius ϵ and half-height a around each point, with the axis aligned along the time direction. The number of points is then counted and if it is larger than a threshold N_{min} then it is considered as a cluster seed. Two cluster seeds which lie within each others cylinders are called "density-connected" and are merged into a single cluster. If a point is within

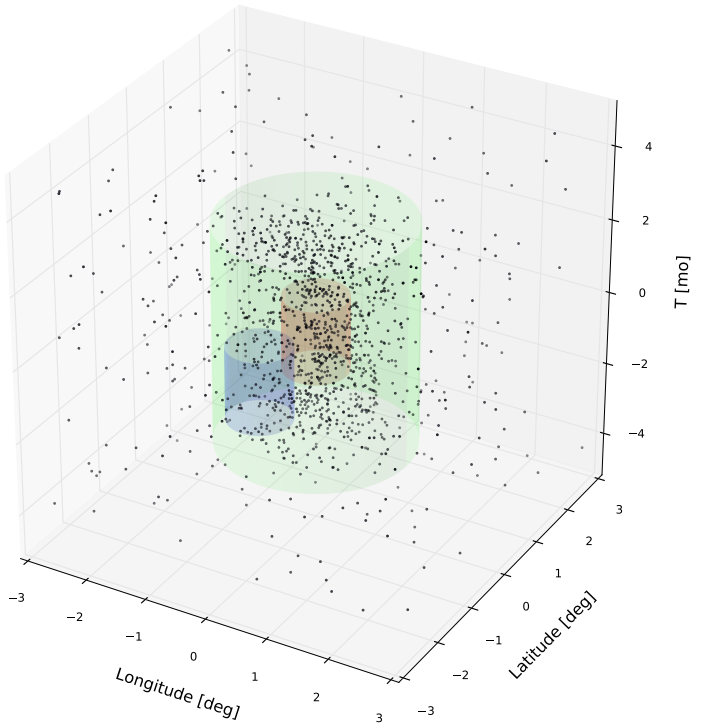

Figure 4.4: Schematic of DBSCAN3D procedure. A cylinder of height $2a\epsilon$ and radius ϵ, called the ϵ-neighborhood, is drawn around each point (small blue and red cylinders). Points are added as a cluster seed if their cylinders contain greater than $N_{\min}$ photons. All points in within the small cylinders are deemed 'density-reachable', while if they they are themselves have greater than $N_{\min}$ points, they are deemed 'density-connected'. In our implementation, the we ignore density-reachable points and the final cluster is formed by merging all points that are density-connected (roughly large-green cylinder).

the cylinder of a cluster seed, but it does not itself surpass the $N_{\min}$ threshold, then it is called "density-reachable." We show a schematic diagram of a 3-Dimensional DBSCAN search in Figure 4.4.

In traditional DBSCAN implementations, density-reachable points are included in the final cluster assignments. However, these introduce a complication. There is an ambiguity in cluster assignment when a point is density-reachable by two clusters. This introduces non-deterministic results dependent on the ordering of the input points, although this is a relatively rare occurrence for true gamma-ray sources. There are two ways to resolve this issue.

- First is the approach taken by Ref. [229] where clusters are connected through mutual density-reachable points. This fixes the ambiguity, but can lead highly asymmetrically shaped clusters. This may be desirable for diffuse source searches, or to resolve non-point-like structures.

- A second is to only use points which are density-connected as this is a symmetric property, and cluster assignment is unambiguous. In this Chapter, we are interested in point sources and thus we chose the latter which is has higher fidelity to the actual cluster center. Given that the spatial extent of point-sources is highly-constrained by the instrumental PSF, we can simply increase epsilon to account for a lower detection efficiency at the cluster boundaries.

Finally, we require a cluster to have at least 3 density-connected points to be valid. We have outlined the basic algorithm, which is quite simple. It remains to determine the choices of a, ϵ, and $N_{\rm min}$. The latter two will follow from the 2-dimensional DBSCAN case, while the first is new. First we will define several useful properties of the clusters and discuss the parameters relevant to 3-dimensional DBSCAN simulations

and searches.

4.4.4 Simulation Parameters and Clustering Properties

In this section set up an idealized Monte Carlo to simulate point sources in the presence of an isotropic background. Our goal is to discover relationships between scan parameters that will allow us to generalize and adapt DBSCAN scan realistic data where the background level varies significantly. Our simulation includes a Gaussian approximation to the Fermi PSF and simulates an isotropic background of spatial photon density $\rho_{\rm BG}$.[7] Point sources are simulated to burst $N_\gamma^{\rm sig-on}$ photons homogeneously over a period $t_{\rm burst}$ and do not emit when not bursting. The simulation volume is taken to be large enough that edge effects are negligible.

Following the 2-dimensional results, we choose $\epsilon = r_{68} = 1^\circ$ and do not consider variations on ϵ. We also note the following relationships between the background photon count $N_{\rm BG}$ expected in a DBSCAN cylinder, the 2-d (spatial) photon density $\rho_{\rm BG}$, and a parameter $N_{{\rm min},\sigma}$ which is the z-score of the background level used for DBSCAN parameter $N_{\rm min}$.

$$N_{\rm BG} = \rho_{\rm BG}\ \pi\ \epsilon^2\ \left(\frac{2\ a}{48\ \text{months}}\right) \tag{4.24}$$

$$N_{\rm min} = N_{\rm BG} + N_{{\rm min},\sigma}\sqrt{N_{\rm BG}} \tag{4.25}$$

We then take parameters listed in Table 4.1 and discretely vary them individ-

[7] 'Spatial-density' implies integration along the time axis. and the density is in counts per square degree.

ually over the range Min-Max with all other parameters held at their 'Default' value in order to understand how the cluster properties vary as a function of a.[8]

Param	Min	Default	Max	Description
ϵ	1	1	1	DBSCAN spatial search radius.
a	0.1	1	10	DBSCAN temporal search half-height.
$N_{\min,\sigma}$	2	4	5	DBSCAN $N_{\min}$ z-score over the expected background.
ρ_{BG}	1	10	50	2-D Spatial background photon Density.
$N^{\text{sig}-\text{on}}$	0	100	200	Number of signal photons in burst.
t_{burst}	1	6	12	Length of signal burst in months.

Table 4.1: Monte Carlo and DBSCAN parameters relevant to the tuning of a.

For each point in the parameter space, 96 simulations run and properties listed in Table 4.2 are computed in the following way. For each cluster in a simulation the properties are individually computed. We then average the individual quantities together using the number of points in each the cluster as averaging weights. (For N_{Members}, the significances are used as weights instead.) Finally, this is repeated for 96 simulations and the behavior averaged. The weighting allows us to focus on the actual true cluster properties rather than diluting with small false clusters. Ultimately, these false clusters will be removed in the post-processing step by feeding their properties into a boosted

[8]Because of results for DBSCAN parameters ϵ and $N_{\min}$ from the 2D case, we expect that these will generalize to the 3D case, although we do retest $N_{\min}$. Because we are now parsing data as a function of time and space, we have decreased the number of photons per $\epsilon-$neighborhood (the DBSCAN volume surrounding each point). Because we need at least three points per $\epsilon-$neighborhood, and typically many more to accurately reconstruct cluster properties, it follows that we must either increase the search volume (i.e. ϵ or a), lower $N_{\min}$, or increase the energy bin width.

decision tree classifier which will designate them as real or fake.

Metric	Description	Ideal Behavior
s	Cluster Significance (Li & Ma 1983)	Proportional to $N^{\mathrm{sig-on}}/\sqrt{N_{\mathrm{BG}}}$
R	Spatial Radius	Roughly PSF size $\sim r_{95} \approx\approx 1.5^{\circ}$
T	Temporal Length	Should be t_{burst}
N_{clus}	Number of clusters with significance $s > 2$	1 for this Monte Carlo.
N_{Members}	Number of photons per cluster	$N^{\mathrm{sig-on}} + N_{\mathrm{bg}}$

Table 4.2: Simulation averaged clustering properties useful for selecting correct DBSCAN parameter a.

4.4.5 Choosing the Temporal Search Half-Height a

The temporal search half-height a should be chosen according to three ordered conditions:

1. Large enough so that real clusters do not fragment into multiple smaller clusters. This "fragmentation threshold" is dependent primarily on the density of background photons for faint sources as these are the dominant contribution to low signal clusters. However, for sources with short, but bright light curves, this is often much too long of an interval. One must choose a such that the mean number of photons expected in an ϵ-neighborhood cylinder of volume $V = \pi\epsilon^2(2a)$ is greater than 3, which is the lowest number of photons able to form a cluster. For a total simulation time of T_{total}, which is 48 mo here, this condition can be cast in

the following inequality.

$$N^{\gamma}_{\text{expected}} = 2a\left(\frac{\rho_{\text{BG}}\ \pi\epsilon^2}{T_{\text{total}}} + \frac{0.68\ N^{\text{sig}-\text{on}}}{t_{\text{burst}}}\right) \gtrsim 3 \tag{4.26}$$

2. a should be smaller than the physical cluster size. Otherwise clusters become contaminated, linearly in a, by background photons. If looking for a 6 month long source, $a \approx 3$ is reasonable unless attempting to detect very weak signals in which case it my be necessary to slightly increase a to achieve a high enough count in each ϵ-neighborhood.

3. With the above conditions met, one should then choose a so that the cluster properties match the simulated input values, while also suppressing spurious clusters formed from background fluctuations.

When searching for low signal-to-background clusters, the background photons provide the scaffolding that enables low significance clusters to link together when the signal only slightly surpasses the clustering threshold. Therefore the value obtained through Eqn. 4.26 a should define the lower limit on a given the type of signal one wishes to search for. Given a lower cutoff on the number of signal photons, and longest burst time attempted in the search (or equivalently a minimal signal photon density), Eqn. 4.26 can be solved for the minimum a that will resolve such a signal. In our simulation, we would like to determine the thresholds of this detection method and we will therefore work in the limit $N^{\text{sig}-\text{on}} \to 0$. Inputting the parameters of our simulation, we solve Eqn. 4.26 and obtain $a = 1.5$ mo. This is the lowest usable value for a before fragmenting a low density cluster, but is not suitable for brighter searches.

Unfortunately, a cannot be chosen to simultaneously search for both short-duration bright sources and longer-duration faint sources *unless the background-only fragmentation limit provides a value of a which is satisfactorily small.* Lowering a implicitly decreases the detection efficiency for clusters with small counts. However, if there are an abundance of photons, lower a will result in the optimal reconstruction of the clustering properties, and the highest significance. Intuitively, we are increasing the granularity of the search pattern which results in a more precise discovery of the cluster properties at the expense of detection efficiency.

4.4.6 Summary of DBSCAN Parameter Selection

To summarize this section, we have derived physical relations for the three DBSCAN parameters $\epsilon, N_{\min}$, and a based on the instrumental point spread function and the background photon density. We have also shown that the scan results are robust to variations in these parameters and correctly reproduce the basic cluster properties provided that the photon population is not too sparse. We recap default parameter choices below:

- ϵ : The DBSCAN spatial search radius, ϵ, should be chosen near the 68% PSF containment radius r_{68}. Decreasing this provides more accurate cluster reconstruction at the expense of sensitivity, while substantially enlarging it leads to poor cluster reconstruction as unphysical background noise is commonly incorporated.

$$\boxed{\epsilon = r_{68}} \tag{4.27}$$

$N_{\rm min}$: The DBSCAN threshold, $N_{\rm min}$, should be chosen based upon the local background density and the size of the search region. Assuming Poisson statistics one can then choose the parameter $N_{{\rm min},\sigma} \in [3-7]$ which is the z-score of $N_{\rm min}$ with respect to the mean background. One can then adaptively vary the DBSCAN photon threshold with a single parameter based upon either a model of the diffuse background or through explicit evaluation of events surrounding the area of interest. Given a spatial background density $\rho_{\rm BG}$ and a total exposure time $T_{\rm total}$ we can choose $N_{\rm min}$ according to the following.

$$N_{\rm BG} = \rho_{\rm BG}\ \pi\ \epsilon^2\ \left(\frac{2\ a}{T_{\rm total}}\right) \tag{4.28}$$

$$N_{\rm min} = N_{\rm BG} + N_{{\rm min},\sigma}\sqrt{N_{\rm BG}} \tag{4.29}$$

a : The DBSCAN temporal search half-height, a, should be chosen as small as possible as long as it does not fragment real low-signal clusters for data with $\gtrsim 20$ photons/deg^2. Much like choosing ϵ, this ensures that cluster properties are accurately reconstructed while also preserving sensitivity to smaller bursts. This should not be chosen adaptively because it defines the lower limit on the search sensitivity. That is to say that one cannot reliably search for signals with $t_{\rm burst} \lesssim 2a$.[9] The fragmentation limit is then based on the region of lowest background density and is given by,

[9] If it is necessary to lower this, it should be accompanied by increased cuts on cluster significances so that the fragmented clusters are not included in the final sample.

$$\boxed{a = \frac{3}{2}\left(\frac{T_{\text{total}}}{\rho_{\text{BG}}\ \pi\epsilon^2}\right)} \tag{4.30}$$

4.4.7 Post-Processing with Boosted Decision Trees

DBSCAN outputs a set of cluster assignments from which we construct the properties listed in Tab. 4.2. While a major advantage of this algorithm is its high efficiency in the presence of sparse data, it is useless without a thorough understanding of the number of background contamination, and particularly, the tradeoff between efficiency and noise. When attempting to optimize the this tradeoff, it is critical to perform a post-processing step which intelligently uses the clustering properties to classify the clusters as real or false, rather than simply using parametric cuts (e.g. requiring more than N members). Ideally, such a classifier should exploit not only cuts on several parameters, but also correlations between them.

Machine learning algorithms provide a powerful solution to such a problem and have been widely implemented in a variety of information sciences, notably high-energy physics for event classification. Decision trees are one such algorithm in which a hierarchy of binary nodes classifies an an event as 'signal' or 'background' based on a vector of computed properties.

First, one must generate a training sample with both background and signal events. The training procedure then proceeds as follows. Beginning with one of the properties, an initial node is formed by picking a 'splitting value' which classifies an event as either signal or background. For each of these 'branches' another property is

used to split the sample into secondary branches. This procedure is repeated until all properties have been exhausted, ending in 'leaf' nodes. The tunings at each node are varied until an optimal classification has been achieved. 'Boosting' defines a procedure for re-weighting events that have been misclassified and subsequently generating a new tree. This is typically reiterated several hundred times and leads to significantly higher stability and robustness of the final classifier to changes in the training sample. For a detailed discussion of boosted decision trees see arXiv:0408124.

For our purposes, the decision tree is simply used as a black box which can easily be trained through mock Monte Carlo data.[10] Using the `scikit-learn` toolkit we implement a BDT using 7 cluster metrics listed in Tab. 4.3.

Param	Description
s	Cluster significance.
Members	Number of cluster members.
Size95X	95% Semi-major axis from principle component analysis.
Size95Y	95% Semi-minor axis from principle component analysis.
Size95T	95% Containment time.
MedR	Median radius from centroid.
MedT	Median temporal distance from centroid.

Table 4.3: Features used in boosted decision tree classification.

[10]Strictly speaking the decision trees are a white-box algorithm which can be easily visualized and understood. However, our objective here is simply to understand the classification efficiencies.

Next, we simulate a central point source with $r_{68} = 1^\circ$ in a $20^\circ \times 20^\circ \times 24$ mo window of background density $\rho_{\rm BG} = 10$ deg^{-2}. To showcase the power of BDTs we first simulate a 6 month long source with a variable number of photons. Clusters detected with centroids outside of the central $1^\circ \times 1^\circ$ degree window are classified as false while within this region are considered real. For each signal photon density we then use 500 simulations to train a BDT and another 500 as a test sample.

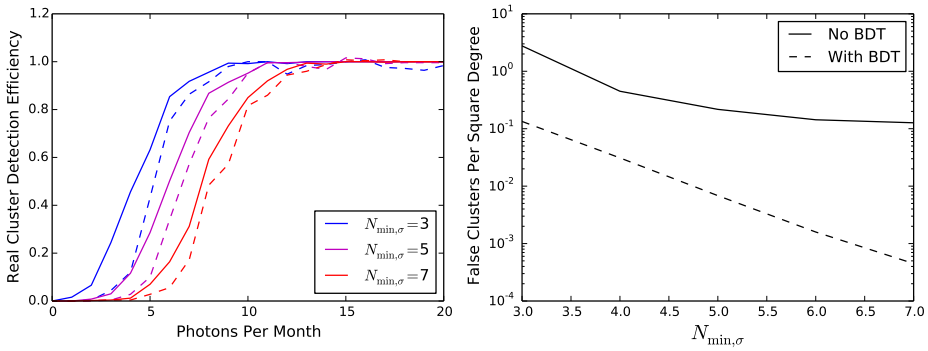

Figure 4.5: Type-I and Type-II detection efficiencies with and without boosted decision trees.

In Fig. 4.5 we show results for several values of $N_{\rm min,\sigma}$ (with $\epsilon = 1, a = 1$). The left panel shows the detection efficiency as a function of the source photon density while the right panel shows the background contamination as a function of $N_{\rm min,\sigma}$. As expected, we see that increasing $N_{\rm min,\sigma}$ results in slightly higher detection thresholds, but dramatically reduced background contamination. We also see that the decision tree does not significantly impact the detection threshold while producing at least an order of magnitude suppression of false clusters. It should be noted, however, that we have simulated a fixed length, fixed density source and thus we expect the BDT to be very

well trained to this particular signal. In realistic scenarios we would like to detect sources with variable duration and signal density.

4.5 Sideband Subtraction

The morphology of dark matter emission is well understood and should be spherically symmetric to within 20-30%. Astrophysical components near the Galactic center on the other hand, tend to possess asymmetries and are often oriented along the disk, in some bipolar configuration, or emanating from individual structures such as point sources or molecular clouds. In cases where photon sparsity is not a problem, this makes morphology an excellent method of distinguishing source classes.

Spectral lines offer an additional benefit over the template regression methods discussed above in that they allow the construction of background templates from the data itself. These continuum backgrounds can be empirically determined by looking at narrow "sidebands" on either side of the line energy and will strongly outperform theoretical models. Alternatively to template analysis, one might use other methods, such as clustering, to compare the signal morphologies of the signal and backgrounds. Several points should be considered when utilizing the sidebands.

1. The energy resolution of the instrument must be well understood, and the sideband templates must not include significant overlap with the signal region.

2. Astrophysical background morphologies are always energy dependent, due to e.g. energy dependent cosmic-ray transport, varying plasma temperatures (for X-rays),

or due to the differing spectrum of emission components. The primary assumption of sideband subtraction is that these backgrounds change slowly enough that after subtracting sidebands out of the signal region, the background residuals will be smaller than the signal in question.

3. The spectral width chosen to build the sideband template should be balanced against the rate of background energy dependence mentioned above and photon statistics. The spatial binning should be chosen so that there are many photons per pixel in order to assure that these sidebands are statistically stable (i.e. $N \gg \sqrt{N}$ for pixels in critical regions.

In addition to simply testing the residual morphology against dark matter, one can also check the compatibility of the line morphology with alternative source models or for correlations with nearby astrophysical lines. We take this exact approach when examining the morphology of the 3.5 keV line at the Galactic center and Perseus cluster throughout Chapter 10.

As an example of this sideband subtraction technique, we show in Figure 4.6 a scanning window analysis from the 3.5 keV results. The FWHM energy resolution of the instrument is about 100 eV and the 3.5 keV line is shown by the gold band. We then fit freely floating background templates (photons from the green bands) against the line data as the null hypothesis. Next, we look at the Test Statistic (TS) (see Eq. (4.11) of adding one additional template comprised of a 50 eV scanning window in energy (plotted in black). The results show that the signal region very strongly correlates with

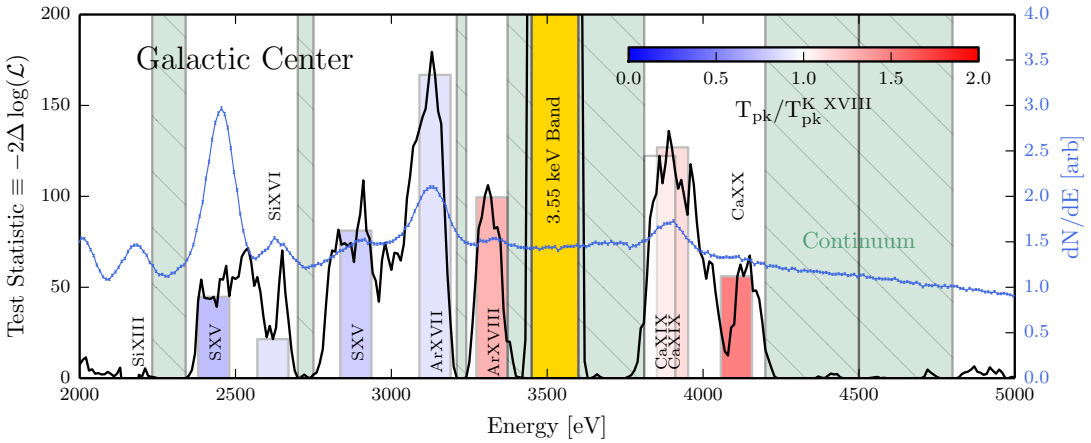

Figure 4.6: Shown in black is the test statistics corresponding to adding a sliding 50 eV-wide window template to a null model consisting of 7 continuum bands (green hatched regions). In light blue we also overlay the raw XMM spectrum for the Galactic center. The 3.45-3.6 keV band is highlighted in gold. The brightest spectral line templates (with correct widths) are color coded according to the ratio of a given lines peak emissivity temperature to that of K XVIII. The TS stemming from adding a dark matter template is zero.

nearby X-ray plasma lines, while a dark matter template does not yield any improved fit (TS= 0). This provides strong evidence against a dark matter interpretation of the 3.5 keV line at the Galactic center using a combination of template regression and sideband subtraction.

Even in the case of sparse photon fields, sidebands may provide enough statistical power to differentiate the morphologies of the continuum background and signals, although template regression is unlikely to be the most powerful approach in these cases.

4.6 Monte Carlo Methods

Given the typical coplexity of the physical systems we are studying, Monte Carlo simulation is one of the most powerful tools in the statistical arsenal. In cases where the distribution of a test statistic is *a priori* unknown, one can directly compute the PDF and determine the p-value of the data under the various hypotheses. This approach is best represented by example. Here we summarize two such analyses – testing the dark matter origins of the WMAP/Planck Haze and differentiating point sources from dark matter as progenitors of the 135 GeV line. These procedures are described in full detail in Chapters 11 and 9.

4.6.1 Example I: The WMAP/Planck Haze

The WMAP haze is a diffuse radio halo which emanates from the Galactic Center up to very high Galactic latitudes. Before detection by the Planck satellite which conclusively linked the haze morphology to the Fermi Bubbles, it was plausible that this signal was generated by synchrotron emission from high-energy leptons produced in dark matter annihilations. If indeed due to dark matter, similar halos should be detected around spiral galaxies which are physically similar to the Milky Way. Using numerical simulations of cosmic-ray physics, we can sample from the range of physical diffusion scenarios and magnetic fields for Milky-Way-type galaxies and determine what fraction of these models are compatible with the data. By doing this with and without dark matter included in the simulations, we can determine the distributions of the null and alternative hypotheses.

Parameter	[units]	$c_{\mathrm{f.f.}}$	Central	Min	Max
B_0	μG	2	60	30	120
r_0	kpc	2	4.0	2.0	8.0
z_0	kpc	2	1.8	0.9	3.6
D_0	$\mathrm{cm^2 s^{-1}}$	10	1.0 x 10^{29}	1.0 x 10^{28}	1.0 x 10^{30}
h_{diff}	kpc	10-2	16	1.6	32
R_{diff}	kpc	2	20	10	40
$u_{\mathrm{rad}}/u_{\mathrm{rad,MW}}$		5	1	.2	5
ρ_0	GeV $\mathrm{cm^{-3}}$	5	0.30	0.06	1.50
r_s	kpc	2	22	11	44
α		1.5	1.0	0.67	1.5

Table 4.4: Nuisance parameters employed to estimate the range for a dark matter induced haze in external spiral galaxies.

In Table 4.4, we show the parameter space and distribution of our simulations which include parameters for magnetic fields, diffusion, radiation field density, and dark matter profiles. Next, we generate several thousand random samples from this space, running simulations in each case with and without dark matter. We can then calculate the luminosity of the radio haze due to dark matter, compared to the radio haze due to cosmic-rays in each case and compare it against that of the Milky Way (which is about 1/20). This is shown in Figure 4.7. We calculate that the fraction less than 10% of simulated systems have such faint hazes if dark matter annihilates to pure leptons. This provides some evidence that the WMAP haze luminosity is likely too low to be from dark matter alone. Similarly, in external spiral galaxies, the hazes due to dark matter must be suppressed to be compatible.

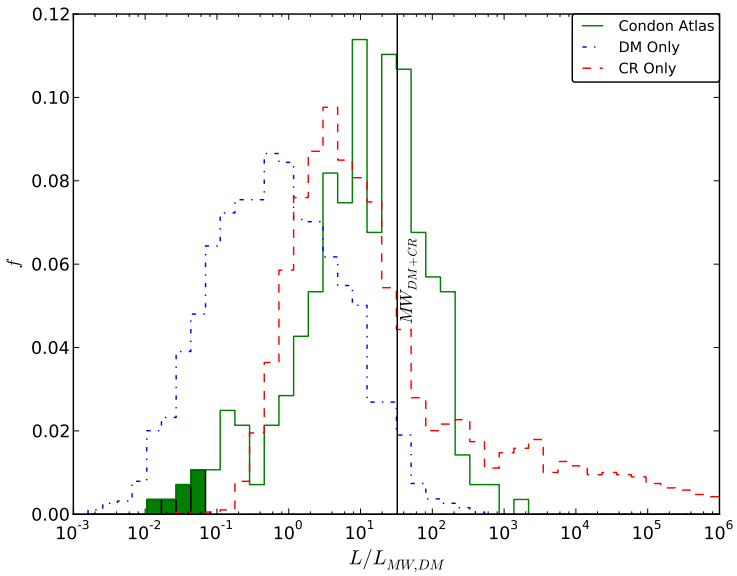

Figure 4.7: Distribution of 1.49 GHz luminosity ratio $L/L_{MW,DM}$ where L is the total integrated luminosity and $L_{MW,DM}$ is the luminosity due to dark matter for the canonical Milky Way model. The benchmark luminosity for dark matter plus cosmic rays is indicated by the vertical line. The simulated sample contains 2000 runs randomly distributed in the parameter space of tab. 4.4 with mass restricted to lie within $0.25 - 2$ times the mass of the Milky Way. We plot the contributions due to dark matter only (dot-dashed blue) and to cosmic rays only (dashed red) against extrapolated luminosities of 66 Condon Atlas galaxies meeting morphological cuts compatible with the Milky Way (solid green). Only 11.2% of the simulated dark matter-induced haze luminosities are a factor 20 smaller than our benchmark value, and only 1.42% are a factor 100 smaller. Shown in shaded green are the 7 lowest background galaxies selected from the Condon Atlas.

There are several lessons which are important here. We have chosen to sample a large dimensional parameter space randomly, but we have not specified prior distributions over the parameter spaces, which almost certainly impact the results. When sampling we should ensure that our priors are reasonable for each parameter, if not very conservative, and we should ensure that the number of samples is sufficiently large to

cover most of the sampling space. This latter problem becomes exponentially worse with the number of dimensions[11]. However, this sampling allowed us to compute a very difficult problem via simulation, even though we did not have any knowledge of the underlying distribution of the test statistic.

4.6.2 Example II: The 135 GeV Line

The 135 GeV line detected in the Galacti center by *Fermi's* Large Area Telescope drew huge attention from the particle physics community due to the lack of known astrophysical backgrounds that could produce such a narrow signal. One potential astrophysical background was proposed in which Pulsar winds could accelerate nearly monochromatic electrons which would generate gamma-ray lines through inverse Compton scattering with the thermal photons emitted from the pulsar's surface. In the energy band and spatial region of interest, only about 50 photons were detected by Fermi, so that the data is extremely sparse. The diffuse astrophysical background makes up around 75% of these photons and one must then differentiate between (i) a small number of pulsars which are point sources, or a diffuse dark matter model which follows, for example, an NFW profile.

The first step in differentiating these sources is to write Monte Carlo simulations of the photon fields. We can use acceptance rejection sampling over the signal + background models (see Ref. [222] for a review of MC methods) to determine the true location of the photons. The photon locations must then be modulated by *Fermi's* point

[11] In statistics this is known as the "curse of dimensionality".

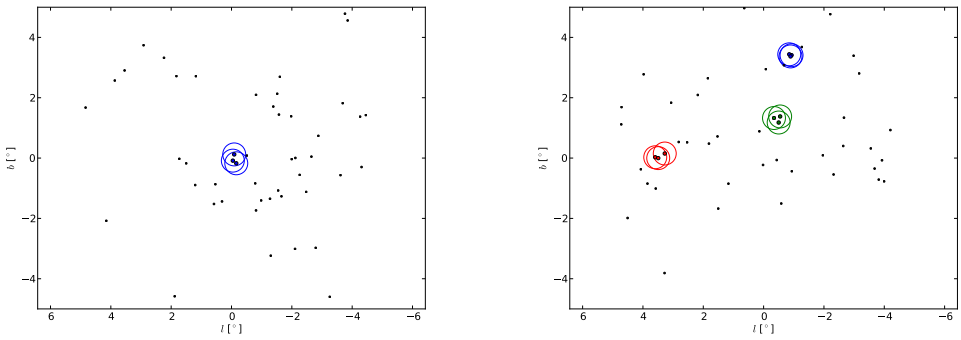

Figure 4.8: Event map of Fermi photons between 120-140 GeV (left) and a sample 3 pulsar Monte Carlo simulation (right) showing in colored circles the DBSCAN $\epsilon-$neighborhoods for core points in each detected cluster.

spread function. Now we can generate a large ensemble of realizations and look at the properties of each source model relative to the data. The goal is to rule out a small number of point sources, which would eliminate known and proposed astrophysical sources leaving only systematics or dark matter as viable candidates. Clustering algorithms are very sensitive to point sources over sparse data and therefore provide a natural fit to this problem.

In Figure 4.8 we show the data from Fermi between 120-140 GeV[12] in the left panel and a simulation containing three pulsars in the right panel. The colored rings show the results from running the DBSCAN algorithm on each case. Clearly, the clustering properties look different in these two cases, but how robust is this? How can we quantify the discriminatory ability? The answer is to determine a Test Statistic for clustering, and then look at the distribution of this statistic for each model. We define the clustering significance according to Equation (4.21), and define the *Global clustering*

[12]At this point in time the line was centered on 130 GeV, which was later shifted to 135 GeV after recalibrating the calorimetry.

significance as the weighted average of each cluster significance, weighted by the number of points in the cluster. This global significance provides our test statistic.

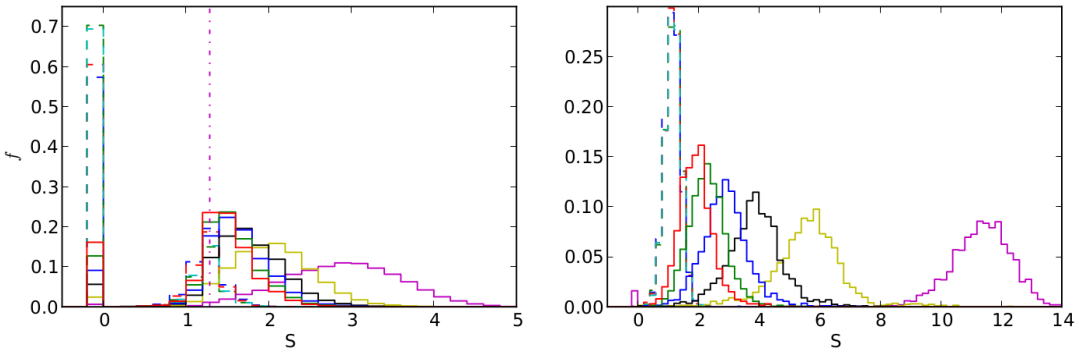

Figure 4.9: Distribution of global significance of detected clusters (S) expected from both Fermi-LAT (48 photons total, left) and H.E.S.S.-II (5000 photons total, right) observations of annihilating dark matter following a NFW profile (blue dashed), flat density profile (green dashed), Einasto profile (red dashed) and decaying dark matter following an NFW profile (cyan dashed), as well as models of emission from undetected groups of one (magenta solid), two (yellow), three (black), four (blue), five (green), and six (red) pulsars, compared to the clustering properties observed in the Fermi-LAT data binned from 120-140 GeV (magenta dot dash).

In Figure 4.9, we show the results of these simulations for dark matter and models with 1-6 pulsars in the case of Fermi-LAT observations and projected observations with IACTs. The magenta line on the left panel shows the Fermi data, which is clearly a much lower significance than the 1-2 pulsar cases. The p-value for rejecting the (null) pulsar model is given by calculating the fraction of simulations with less clustering significance than the data. This was able to rule out models with 3 or fewer pulsars at 95% confidence and shows that IACT are very effective at constraining point source origins. Recently [230], a similar Monte Carlo approach has been used to test a point source origins of the Galactic Center excess using wavelet methods as opposed to clustering. In both cases however, Monte Carlo can be used to directly compute statistical

properties with no knowledge of the distributions in question.

4.7 Blank Sky Calibration

When searching the sky for point sources, or slightly extended sources such as dwarf galaxies, it is critical to understand the systematic uncertainties of the background in order to correctly estimate the significance of the detection. For example, consider a null model, say the diffuse Galactic background and an isotropic template, and an alternative model which adds an additional template from dark matter annihilations in a dwarf Galaxy. The Poisson likelihood ratio tests discussed in Sec. 4.1 provides a purely statistical measure of the model preference, while in reality there may be substantial systematic uncertainties if, for example, there is a non-negligible contribution from unresolved point-sources in the background.

We can estimate these systematic probabilities by examining the Poisson TS over 'blank sky' positions. That is, we can choose random positions in the sky – away from known 3FGL sources for example – and determine the probability of detecting 'unresolved' point sources above a certain significance level. This then provides an empirically determined estimate of systematic uncertainties, much like Monte Carlo methods, but without having to model the backgrounds. The distribution of blank-sky TS can then be used to recalibrate the true significance measure.

In the following section we present novel methods for incorporating multi-wavelength information into the choice of blank sky positions and show that this can considerably reduce systematic uncertainties, and hence increase the estimated sensitiv-

ity of Fermi-LAT to searches for gamma-ray emission from Milky Way satellites.

4.7.1 Improving the Sensitivity of Fermi to Dark Matter Annihilation in Dwarf Galaxies

The Milky Way's dwarf spheroidal galaxies (dSphs) represent a very promising set of targets for indirect dark matter searches. Although the flux of gamma-rays from dark matter annihilating in these systems is predicted to be considerably lower than from the Galactic Center, the lower astrophysical backgrounds make dSphs comparably sensitive to annihilating dark matter. Furthermore, precision stellar rotation measurements have been used to directly constrain the dark matter density profiles of many dSphs, making it possible to predict the dark matter annihilation rate within such systems.

Several groups have analyzed dSphs as observed by the Fermi-LAT [231, 232, 233, 234, 50]. The most recent of these efforts was carried out by the Fermi-LAT collaboration, which investigated a stacked population of 25 dSphs, using four years of data [50]. The expected sensitivity of this analysis was sufficient to exclude dark matter with an annihilation cross section equal to the standard estimate for a thermal relic ($\sigma v \simeq 2 - 3 \times 10^{-26}$ cm^3/s) for masses below $m_{\rm DM} \sim 90$ GeV in the case of annihilation to $b\bar{b}$. If this expected sensitivity had been realized, the resulting limit would have been the most stringent to date, exceeding those derived from gamma-ray observations of the Galactic Center [235], galaxy clusters [236, 237], or the isotropic gamma-ray background [238, 239, 240]. However, the actual limit obtained by this analysis was significantly weaker than expected (by a factor of $\sim$4-5 for $m_{\rm DM} \simeq 10 - 100$ GeV).

The difference between the expected and actual limits was greatest for a dark matter particle of mass $m_{\rm DM} \sim 25$ GeV annihilating to $b\bar{b}$. At this mass, an excess corresponding to a test statistic (TS) of 8.7 was found. Interestingly, the normalization and spectral shape of this excess are consistent with those produced by dark matter models capable of accounting for the gamma-ray signal observed from the Galactic Center (e.g. with $m_{\rm DM} \sim$ 30-40 GeV and a cross section of $\sigma v = (1.7 - 2.3) \times 10^{-26}$ cm^{3}s^{-1} to $b\bar{b}$ [43, 241, 242, 243, 244, 245, 45, 246]).

If one assumes that the astrophysical emission models employed by the Fermi-LAT team are entirely accurate (to the level of Poisson noise), a TS=8.7 excess would correspond to a local significance of 2.95σ. This level of accuracy, however, is not expected for current astrophysical background models. In order to empirically quantify this mismodeling, the Fermi-LAT team studied 7500 random "blank sky" locations at galactic latitudes comparable to the dSph population ($|b| > 30^\circ$) and at least 1° (5°) from any point source (extended source) in the 2FGL catalog [247]. They then calculated the TS value obtained by placing a mock dSph at each location, and used the probability distribution of these residuals to convert the TS value of the dSph analysis into a significance. This method found "blank sky" locations yielding TS>8.7 to be more common (by a factor of 8.9) than predicted by the background model. When this is taken into account, the statistical significance of the measured dSph excess is reduced to a local value of 2.2σ.[13]

[13]The Fermi-LAT collaboration analysis includes a trials factor of approximately 3, due to the multiplicity of dark matter models they test. However, if dSphs are being studied in order to confirm or exclude a dark matter interpretation of the signal observed from the Galactic Center, then this trials factor is irrelevant. In this section we only consider the local significance of the dwarf excess.

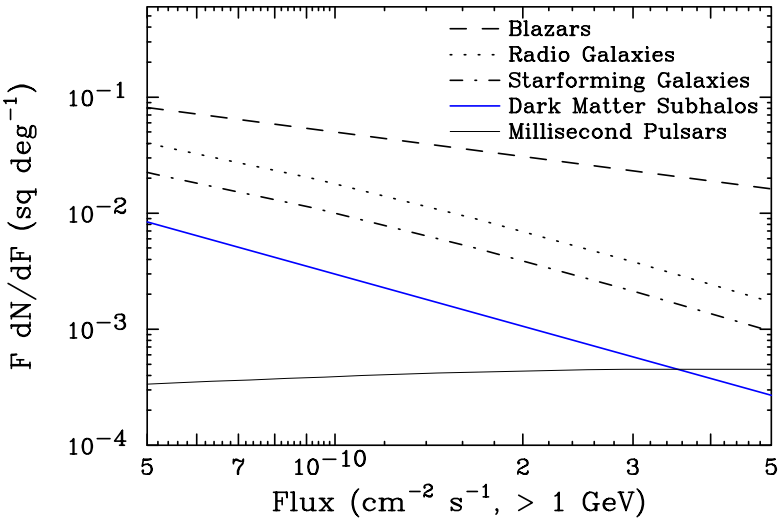

Figure 4.10: A set of empirically driven population models for a number of gamma-ray source classes, including blazars [12], radio galaxies [13], star forming galaxies [14], and millisecond pulsars [15]. Also shown is an estimate for the distribution of dark matter subhalos, calculated as in Ref. [16] (using the mass-concentration relationship of Ref. [17]) for the case of $m_{\rm DM}$ =35 GeV and $\sigma v = 2 \times 10^{-26}$ cm^3/s to $b\bar{b}$.

The Fermi Collaboration has been non-committal regarding the departures of their background model from the observed distribution, mentioning both the presence of unresolved point sources and imperfect diffuse background modeling as possible factors [50]. To estimate the contribution to this deviation from unresolved point sources, we have considered empirically constrained population models for a number of gamma-ray source classes, including blazars [12], radio galaxies [13], star forming galaxies [14], and millisecond pulsars [15]. In Fig. 4.10 we plot the flux distribution predicted for these source population models, in the range likely to lead to TS $\sim$ 8.7 departures from the background model, determined by explicitly simulating power-law point sources (dN/dE $\propto$ E$^{-2.2}$) at random high-latitude sky locations, and subsequently determining the TS values as a function of the angular offset between the true source position, and

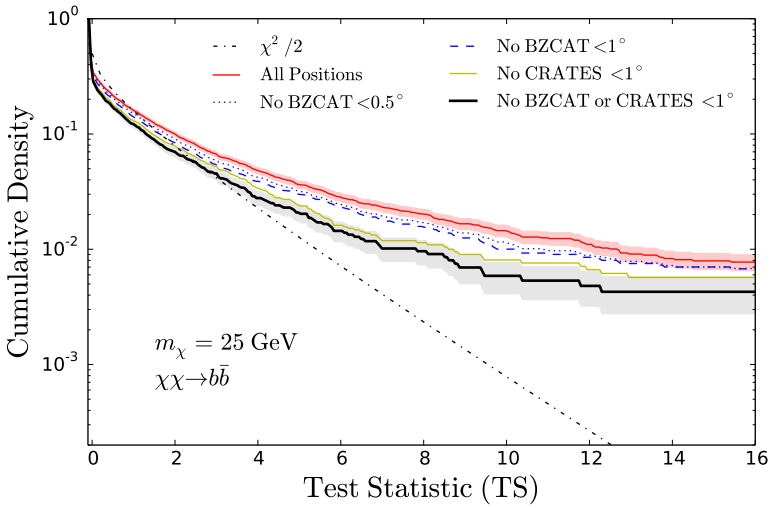

Figure 4.11: The distribution of test statistic (TS) values for a population of 5200 randomly selected sky locations constrained to lie at a galactic latitude —b— $> 30°$ and at least $1°$ ($5°$) away from point-like (extended) 2FGL sources. We show the distribution of TS values when we no additional sky regions are excluded from our analysis (red solid with shaded poisson error bars), and when we make regions that lie within $0.5°$ of a BZCAT source (blue dotted), within $1°$ of a BZCAT source (blue dotted), within $1°$ of a CRATES source (yellow solid), and within $1°$ of either the BZCAT or CRATES sources (black solid). In the case that sky locations are constrained to lie at least $1°$ away from any BZCAT or CRATES source, the density of TS > 8.7 locations is reduced by a factor of 2.1.

the analysis model position. Although radio galaxies and starforming galaxies are each predicted to provide non-negligible contributions to Fermi's unresolved source population, blazars constitute the largest number of such sources. This is not surprising given that blazars are the most numerous point sources in the high-latitude gamma-ray sky and are thought to be responsible for the majority of the anisotropy observed in the extragalactic gamma-ray background (which is dominated by sources just below the Fermi-LAT point source detection threshold) [248, 249, 250, 251, 252, 253].

To estimate the impact of these unresolved sources on the Fermi dSph analysis,

we simulated the gamma-ray signal from the unresolved source model shown in Fig. 4.10 assuming a $dN/dE \propto E^{-2.2}$ spectral shape for blazars, radio galaxies and starforming galaxies scattered uniformly at high-latitudes. We then analyzed a new random set of blank sky-locations and examined the resulting TS distribution. This simulation found that these unresolved sources could account for approximately $\sim 80 \pm 5\%$ of the TS$>$ 8.7 "blank sky" locations observed in the Fermi dSph analysis. We emphasize that the error on the above figure is purely statistical and neglects the much larger systematic uncertainties surrounding blazar, radio galaxy, and starforming galaxy population models. Nonetheless, this calculation leads us to conclude that unresolved sources are likely to be responsible for most of the observed deviations from Fermi's diffuse background model.

We can utilize multi-wavelength information to reduce the impact of unresolved sources on Fermi's dSph analysis. Notably, radio surveys have located a significant population of blazars, star-forming galaxies, radio galaxies, and pulsars which do not appear in the 2FGL catalog, but that are nonetheless likely to be significant gamma-ray emitters. Such sources will appear in the Fermi analysis as small departures from the background model.

In this letter, we utilize two multi-wavelength source catalogs. The first of these is the Roma-BZCAT Multi-Frequency Catalog of Blazars (BZCAT), which currently contains 3149 known blazar sources [254], 2274 of which are located at high galactic latitude (—b— $> 30^\circ$).[14] Second, we make use of the more than 11,000 bright

[14]The BZCAT catalog contains blazars detected by multiple surveys, and has a highly anisotropic sensitivity. For example, the catalog contains 1472 sources with b $> 30^\circ$ and only 802 sources with b $< -30^\circ$.

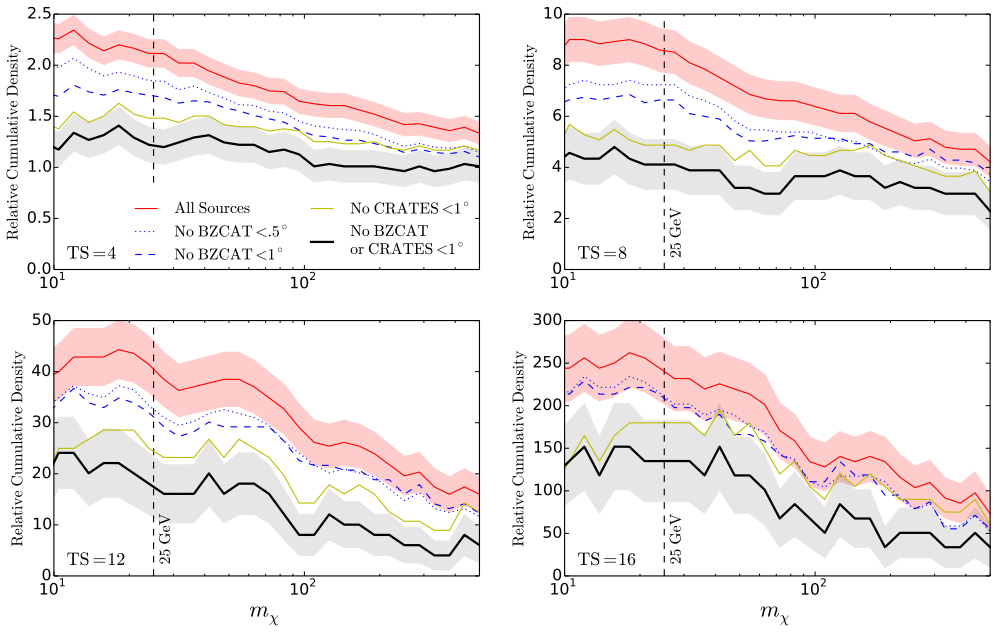

Figure 4.12: The ratio of the fraction of "blank sky" locations (at —b— $> 30°$) with TS>{4, 8, 12, 16} compared to that predicted by Fermi's diffuse emission model, as a function of dark matter mass (assuming annihilations to $b\bar{b}$). For all curves, the sky locations are chosen to be at least 1° (5°) from 2FGL point (extended) sources. This ratio is reduced when we further mask around BZCAT and CRATES sources, as denoted in the key. Shaded regions represent Poisson errors. By masking regions near BZCAT and CRATES sources, we can significantly reduce the fraction of the sky with TS values larger than predicted by Fermi's diffuse model. This conclusion is true for spectral shapes corresponding to wide range of dark matter masses.

flat-spectrum radio sources observed by the Combined Radio All-Sky Targeted Eight-GHz Survey (CRATES) [255]. CRATES claims an all-sky exposure down to 65 mJy at 4.8 GHz. While the nature of these sources is not classified, their spectra are often consistent with source classes likely to produce significant gamma-ray emission.

The strategy we propose here is to use the information provided by BZCAT and CRATES to select regions of the "blank sky" that are the least likely to contain significant emission from unresolved gamma-ray point sources. To study the impact of

such an approach, we use 4 years of Fermi-LAT data and calculate the distribution of TS values obtained for a set of 5,200 high-latitude (—b— $> 30^\circ$) blank sky locations, each chosen to lie at least $\{0^\circ, 0.5^\circ, 1^\circ\}$ from the nearest BZCAT or CRATES source. For each location, we extract the Fermi-LAT data using photons from the `P7REP_CLEAN` event class between 0.5-500 GeV, using standard analysis cuts[15].

The precise choice of masking radius will be inherently linked to the details of the point spread function. This includes the choice of event class, photon conversion type, and the low-energy cutoff[16]. Importantly, masks extending beyond 1° were found to produce no significant change to the results presented below and a detailed study of alternative photon selections is reserved for future works.

To calculate the TS for each location, we employ the `gtlike` tool utilizing the `MINUIT` algorithm to create a best fit model, including a mock point source at the chosen location, as well as all 2FGL sources and the `P7v15` and `P7REP_CLEAN_V15` diffuse and isotropic background models. We note that in the Fermi-LAT analysis, the mock sources are not point sources, but instead include 300 realizations of each dSph [50]. However, the Fermi-LAT collaboration notes that this has only a marginal effect on the calculated TS for each source. We have confirmed this result and find that our measurement falls within the statistical errors of the Fermi-LAT measurement when no BZCAT or CRATES sources are masked. In Fig. 4.11, we plot the cumulative distribution of TS values for the different masking choices, assuming that the mock sources have a spectrum equivalent to

[15] `DATA_QUAL` $= 1$ && `LAT_CONFIG` $= 1$ && `ABS(ROCK_ANGLE)` < 52

[16] In this latter case, the effective mask size is actually nearly independent of the low energy cutoff due to a balancing between the approximate power-law increase in PSF radius and the improved source localization from $N^{-1/2}$ photon statistics.

a 25 GeV dark matter particle annihilating to $b\bar{b}$, calculated using `PYTHIA 8.183` [168]. When considering only "blank sky" locations more than 1° from any BZCAT or CRATES source, the diffuse background model provides a much better description of the data. In particular, for the case shown in Fig. 4.11, the cumulative density of TS¿8.7 residuals is reduced by a factor of 2.1 after applying this cut. This effect modestly increases the significance of the TS=8.7 excess observed by the Fermi collaboration from 2.2σ to 2.5σ. In Fig. 4.12, we show the impact of these cuts as a function of the dark matter mass.

Of course, the correction described in the previous paragraph can only be self-consistently applied to the excess found in Ref. [50] if we ensure that the dSph fields are not also contaminated by BZCAT or CRATES sources. Notably, the Fermi-LAT team reanalyzed the regions of interest around each dSph, and found no new point sources within 1°, decreasing the likelihood that any bright sources are contaminating the dwarf analysis.

In Table 4.5 we list the dSphs used in the Fermi-LAT analysis which are located within 1° of at least one BZCAT or CRATES source. Of most interest are the three dSphs which dominate the excess observed by Fermi: Segue 1, Usra Major II, and Willman 1 [50]. Although, these three dSphs each have one BZCAT or CRATES source within this radius, none of these sources are particularly nearby (all are $> 0.7°$ away). In order to test the impact of these three sources, we utilize the Fermi tools and calculate their TS values to be 0.00, 4.23 and 9.71 for J100955+160223 (0.70° from Segue 1), J0854+6218 (0.91° from Ursa Major II) and J1048+5009 (0.87° from Willman 1), respectively. In order to estimate the TS value of these sources as evaluated at the

location of the dSphs under investigation, we produce 50 simulations for a location 0.7° from a simulated TS=10 source. These simulations revealed that the residual TS from the misidentification of the source is TS$\lesssim$1, corresponding to $\lesssim$10% of the actual source TS. This indicates that these three BZCAT and CRATES sources are unlikely to be responsible for a significant fraction of the dSph excess. However, we note that a more thorough re-analysis of the dSph population should investigate the potential for low-TS emission from this population.

Finally, the fraction of blank sky locations with higher than expected TS values may also include a contribution from dark matter subhalos [256, 257, 248]. Most important for the case at hand are those subhalos with masses just below those of the dSphs themselves, which are universally predicted by numerical simulations [258, 259]. These sources are expected to be distributed nearly isotropically across the sky, with an angular extent that is generally much smaller than the Fermi-LAT point-spread function. In Fig. 4.10, we show the flux distribution of such sources, as calculated in Ref. [16] (but updated using the mass-concentration relationship of Ref. [17]), for the case of $m_{\rm DM}$ =35 GeV and $\sigma v = 2 \times 10^{-26}$ cm^3/s to $b\bar{b}$. From this figure, we see that while dark matter subhalos are unlikely to dominate Fermi's unresolved source population, they may represent a significant class of unassociated gamma-ray sources, as has been noted before [256, 257, 248]. This population is qualitatively different from that of blazars or radio bright galaxies in that while the latter sources constitute a background that could be effectively eliminated using multi-wavelength information, the former corresponds to an irreducible background, with a predicted luminosity that is *directly proportional* to

that of the dSphs being investigated. The "blank-sky" background modeling employed in Fermi's dSph analysis naturally includes regions of the sky populated by such subhalos, potentially producing an excess of high-TS sources *because* of the existence of a dark matter annihilation signal, rather than in lieu of it.

In this section, we have investigated three effects that may alter the *interpretation* of the TS=8.7 excess observed in the stacked population of dSphs by the Fermi-LAT Collaboration in Ref. [50]:

- We point out the general importance of using multiwavelength catalogs to account for unresolved point source contamination in both regions of interest, and in blank sky calibrations.

- We show, in the specific case of Fermi, that more than 50% of the TS>8.7 residuals observed in blank sky locations are the result of sources identified in the BZCAT and CRATES catalogs. Recent population models of blazers, radio galaxies, and starforming galaxies lead us to expect that an even greater fraction of such residuals are the result of unresolved point sources.

- Although BZCAT and CRATES sources are found within 1° of 14 of the 25 dSphs analyzed in Ref. [50], the three dSphs most responsible for the observed excess (Segue 1, Ursa Major II, Willman 1) have no such sources within 0.7°, making them unlikely to be highly contaminated.

- For the range of dark matter masses and cross sections currently being probed by gamma-ray observations of dSphs, one expects a flux distribution of dark matter

dSph	Nearby Blazars (Distance to dSph °)
Bootes 1	J1359+1436 (.13) J1401+1350 (.74) J140136+151303 (0.80)
Bootes 3	J135948+270834 (0.71)
Canes Venatici 1	J132457+325160 (0.97)
Draco	J1715+5724 (0.85)
Hercules	J162737+121550 (0.95)
Leo 4	J1133+0015 (0.80) J113631-005250 (0.98)
Leo 5	J1131+0234 (.40) J1132+0237 (.58) J112940+021817 (0.38)
Pisces 2	J225823+051634 (0.68) J230153+060906 (0.87)
Sculptor	J0100-3337* (0.04) J010107-334758 (0.24) J005817-334755 (0.41) J005819-341957 (0.76) J010307-342458 (0.97)
Segue 1	J100955+160223 (0.70)
Sextans	J1010-0200* (0.70) J101454-005506 (0.82)
Ursa Major 1	J103034+513236 (0.77)
Ursa Major 2	J0854+6218* (0.91)
Willman 1	J1048+5009 (0.87)

Table 4.5: A list of BZCAT and CRATES sources that lie within 1° of a dwarf spheroidal galaxy studied by Fermi-LAT team [50]. The distance to the source (in degrees) is given in parentheses. Any source detected in both catalogs is listed with the BZCAT coordinates and marked with an asterisk.

subhalos that would account for ∼5-10% of the unresolved source population. Even if all astrophysical sources are accurately modeled, these subhalos will constitute an irreducible background for gamma-ray studies of dSphs.

4.8 Multi-Wavelength and Multi-Messenger Studies

Multi-wavelength studies provide excellent opportunities to separate astrophysical emitters from those of dark matter. High energy cosmic-ray electrons produced in dark matter annihilations or decays will generate potentially detectable cosmic-rays, synchrotron, inverse Compton scattering (ICS), bremsstrahlung, and potentially neutrinos from charged pion decay. Currently, synchrotron signatures are the most widely adopted multi-wavelength probe which, given a magnetic field model for the Galaxy, allows one to constrain both the spectrum and normalization of the electron cosmic-rays, helping to break the degeneracy (from gamma-rays alone) between hadronic sources or prompt emission from dark matter. Such methods will be crucial to disentangling cosmic-ray populations near the Galactic center, where radio and gamma-ray observations can be used in tandem to constrain the astrophysical scenarios. In addition, utilizing the full joint-likelihood function over radio and gamma-rays will provide powerful constraints on cosmic-ray propagation scenarios in the Milky Way, leading ultimately to a much more consistent limits on dark matter models from cosmic-rays.

Secondary radiation from dark matter annihilations in the Milky Way Galactic Center is discussed in several references [260, 261], and the basic methods will be outlined in Section 6. Ultimately, the sensitivity of these methods is limited by uncertainties in the magnetic fields and interstellar radiation fields. However, these models are ever-evolving with new astronomical datasets such as polarization data from the Planck Satellite, and massive stellar surveys such as Pan-Starrs.

Multi-messenger searches expand this scenario to include the direct detection of neutrinos and charged cosmic-rays from dark matter in complement with e.g. gamma-ray studies. Combining these measurements can often lead to extremely stringent constraints on parameter space, particularly when utilizing anti-proton constraints in combination with gamma-ray data. Before performing any indirect detection study on a specific particle model, one should check that the model is not excluded by any available constraints.

4.9 ROI Optimization

When examining sharp spectral features near the detection limit of an instrument *and* when bright astrophysical backgrounds are present, it is highly advantageous to choose select regions of interest which are optimized to the expected signal. The use of this technique was pioneered in Ref. [125] when trying first detecting the Fermi 135 GeV line.

The technique is simple: choose pixels which will optimize your signal-to-noise ratio. The method requires a candidate signal (choose a dark matter profile) and a background model. The background model can be a model, such as the Fermi diffuse model, or it can be empirically determined by integrating photons from the sidebands. For example, Ref. [125] chooses an NFW profile for the signal, and integrates photons below 40 GeV to determine the background model.

The optimal region of interest is then the one which maximizes the signal-to-noise $\mathcal{R}$ over all pixels i. Given a background count c_i and signal count μ_i, the signal-to-noise for each pixel is given by $\mathcal{R}_\rangle = \mu_i/c_i$, with the overall SNR over a set of

pixels $\mathcal{T}$ given by,

$$\mathcal{R} \equiv \frac{\sum_{i \in \mathcal{T}} \mu_i}{\sqrt{\sum_{i \in \mathcal{T}} c_i}}. \tag{4.31}$$

An efficient Greedy-style algorithm for optimizing the included pixels $\mathcal{T}$ is given in Ref. [125].

4.10 Point Source Separation Methods

The clustering algorithms described above are extremely sensitive to point-like versus diffuse emission classes when the photon statistics are sparse. At lower energies these methods are slow and more difficult to calibrate, but the photon statistics are greater, and we can typically bin data into pixels. Below, we describe three methods in the literature which can be used to discern point sources from diffuse sources on binned data.

4.10.1 Wavelets

Wavelet transform methods have long been ubiquitous in astronomical image processing [262] for the detection of point sources, and large diffuse structures. Their use on *Fermi* gamma-ray data has included both seeding for point source catalogs [116] and for discerning sub-threshold point sources in the inner Galaxy [263]. More generally, wavelets provide a very similar method to the clustering algorithms discussed earlier, but in cases where there are many photons. At the basic level, wavelet transforms allow for simultaneous localization of a signal in both spatial and frequency domains (compared

with Fourier methods which localize only in frequency). By convolving the input image against a set of wavelet basis functions, one can select out point sources by examining wavelet coefficients that are maximized for a given point-spread function.

Ref. [263] utilized these methods to show strong evidence for populations of unresolved point sources near the Galactic center in the 1-3 GeV band. By a convolution of the wavelet filter with the binned photon image, one can deetermine the significance distribution of sub-threshold (not in 3FGL) point sources in the data. Then, just as we did with clustering algorithms in Sec. 4.6 and Ch. 9, one can use Monte Carlo simulations of different source models in order to differentiate a dark-matter-like model versus a model of point source origin.

4.10.2 Non-Poissonian Template Fitting

Another alternative method for determining point source statistics at the Galactic Center is the use of Non-Poissonian template fitting (NPTF) [264]. In usual template fits, the photon statistics are emitted via a Poisson process. Specifically, the probability of a pixel i registering k photons with a mean μ_i is Poissonian, where μ_i is the sum of all templates (see Eq. 4.15).

NPTF instead assumes that a given pixel contains contributions from several sources obeying a source count distribution per flux interval F, dN_i/dF, which can be spatially varying. While the sum of two or more Poisson random variables is Poisson, the source distribution itself is not Poissonian, leading to a flux which does not obey a Poisson statistic. Three quantities must be specified: the form of dN_i/dF, the spatial

variation of dN_i/df. From here, one can calculate μ_i semi-analytically [265].

Ref. [264] uses these methods in the inner Galaxy to test for the possibility of a new millisecond pulsar component as the source of the GeV Galactic Center Excess. The source distribution dN_i/df is taken to be a broken power-law with a free break flux and high/low indices which are constant in space. The normalization of the distribution is then varied depending on the population model which includes three components: (i) an exponential disk, (ii) an isotropic point source distribution and (iii) an NFW-like pulsar distribution. One can then use Bayesian methods like MultiNest to sample from the posterior distribution. In this case, the posteriors are reduced to point estimates in the form of Bayes factors which show a preference for an NFW-like point source distribution over an NFW profile at $TS \approx 36$ (statistical only). Over such a large field of view, and with such large systematics present, this is not a large significance. Future work along these lines should also examine more than one spectral bin, spectral evolution with distance from the Galactic center, and the impact of systematic uncertainties in diffuse modelling.

4.10.3 D^{3}PO (Denoising, Deconvolving, and Decomposing Photon Observations)

In trying to separate point source from diffuse emission sources, an alternative algorithm is the D^{3}PO filter originally proposed in Ref. [266]. In order to discriminate between these morphologically different signal components, a probabilistic algorithm is derived in the language of information field theory based on a hierarchical Bayesian pa-

rameter model. The signal inference exploits prior information on the spatial correlation structure of the diffuse component and the brightness distribution of the spatially uncorrelated point-like sources. Python libraries are also included at http://wwwmpa.mpa-garching.mpg.de/ift/d3po/.

A significant advantage of this method is that it does not require a background model, which is instead estimated based on the data. A significant limitation of this algorithm is that it cannot separate between diffuse components and hence is not useful in many cases for dark matter indirect detection. However, an interesting application of such an algorithm would be toward the inner Galaxy at GeV energies where there is still uncertainty about the point source or diffuse origin of the GeV excess.

Part II

Modeling of Galactic Cosmic and Gamma Rays

Chapter 5

Propagation of Galactic Cosmic Rays

High energy charged particles are injected into the interstellar medium, either through astrophysical mechanisms – such as diffusive shock acceleration and pair-production in pulsar magnetospheres – or through exotic processes which might include production via annihilating dark matter. These cosmic-rays twist, lose energy, and escape as the propagate through the Galaxy. In this chapter we detail both analytic and numerical treatments of cosmic-ray propagation. The analytic models are limited to nearby sources of electrons and positrons as well as heavy nuclei generated from dark matter. We detail methods for the propagation of Antihelium which were not previously available in the literature, and include several python codes for performing analytic propagation.

The numerical propagation treatment of this Chapter contains the details of cosmic-ray transport in modern codes, leaving the details of radiation and models of the Milky Way to Chapter 6 and Chapter 7, respectively, where the latter contains models

for the Galactic magnetic fields, gas and cosmic-ray source distributions, and interstellar radiation fields. The content of these three chapters represents the state-of-the-art and future directions for numerical models of diffuse Galactic gamma-ray emission, which critically underlays all analyses of the Galactic center region below 100 GeV. A good understanding of these concepts and the `Galprop` code provides the reader with ample opportunity for research at the forefront of cosmic-ray physics and dark matter searches in the Milky Way.

5.1 Analytic Propagation Schemes

5.1.1 Diffusion From a Single Instantaneous Source

In this section we consider spherically symmetric diffusion from a single point-like source. We take the standard diffusion approximation which takes into account diffusion with energy-losses, but not reacceleration or convection effects. The transport equation reduces to the following form.

$$\frac{\partial \psi}{\partial t} = \frac{D}{R^2}\frac{\partial}{\partial R}R^2\frac{\partial \psi}{\partial R} + \frac{\partial}{\partial \gamma}(P\psi) + Q. \tag{5.1}$$

Here $\psi(R, t, \gamma)$ is the particle distribution function, with $\gamma = E/mc^2$. $P(\gamma) = -d\gamma/dt$ is the continous energy loss rate, which is assumed to be spatially uniform. $D(\gamma)$ is the diffusion coefficient which is energy dependent, but spatially homogeneous and isotropic. Q is the source particle injection rate. For a δ-functional source in time and space, one

can analytically solve for the full time dependent solution [18].

$$\psi(R,t,\gamma) = \frac{Q(\gamma_t)P(\gamma_t)}{\pi^{3/2}P(\gamma)R_{\rm dif}^3}\exp\left(-\frac{R^2}{R_{\rm dif}^2}\right), \tag{5.2}$$

where $\gamma_t \equiv g^{-1}(T-t)$, where $g^{-1}(T)$ is the inverse function of $g(\gamma)$

$$T = \int_\gamma^{\gamma_\star} \frac{d\gamma'}{P(\gamma')} = g(\gamma). \tag{5.3}$$

where $\gamma_\star$ is the maximal particle energy injected into the ISM (10^{15} eV/m for example). Thus γ_t is the initial energy of particles which cool to a Lorentz factor γ over time t. The effective diffusion radius $R_{\rm dif}$ for a particle of initial energy γ is given by

$$R_{\rm dif}(\gamma,t) = 2\sqrt{\Delta u}, \tag{5.4}$$

with Δu

$$\Delta u(\gamma,\gamma_t) = \int_\gamma^{\gamma_t} \frac{D(x)dx}{P(x)}. \tag{5.5}$$

Thus spherically symmetric diffusion is a Gaussian diffusion process, which is energy dependent, both through energy losses, and through the energy dependence of the diffusion coefficient.

Notice that this form is general and we have not yet specified the energy loss-function, except that it is uniform. Equation 5.2 is the Green function for sources localized in time and space. We can therefore integrate it against any source distribution.

For a stationary (continuously emitting for all time) point source, this yields,

$$\psi(R,\gamma) = \frac{1}{8\pi^{3/2}P(\gamma)} \int_{\gamma}^{\infty} \frac{Q(x)}{[\Delta u(\gamma,x)]^{3/2}} \exp\left(-\frac{R^2}{4\Delta u(\gamma,x)}\right) dx. \tag{5.6}$$

For protons above 1 GeV, the energy loss timescales are much longer than the residence time (time till escape) of the Milky Way, and can be safely neglected in this approximation. The diffusion radius at a given time then reduces to $R_{\rm dif}(\gamma) = 2\sqrt{D(\gamma)t_{\rm dif}}$. In the case of strong energy losses, $t_{\rm dif}$ becomes the energy loss timescale, providing a useful way to estimate the size of diffusion zones at different energies.

The diffusion coefficient is typically taken to be energy dependent following a power-law of index δ in rigidity $\mathcal{R}$

$$D(E) = D_0 \left(\frac{\mathcal{R}}{4GV}\right)^{\delta} = 5\times 10^{28}{\rm cm}^2/{\rm s}\left(\frac{\mathcal{R}}{4{\rm GV}}\right)^{\delta} \tag{5.7}$$

In Appendix A.6, we provide a python code for the above which is useful for calculating the positron spectrum at Earth from a nearby pulsar following the methods of Ref. [18]. More generally, this is a Green's function which can be integrated over any injection spectrum over space and time. In Figure 5.1 we show an example of the local interstellar positron spectrum for a pulsar which instantaneously injects positrons with a spectrum $dN/dE \propto E^{-2.2}$ and cutoff at $\gamma = 10^9$, and with a variable age and distance of 100 pc. A useful application of this is constraining pulsars in the distance vs. age plane as an explanation for the positron excess. We have assumed the energy loss model presented in the the following Section.

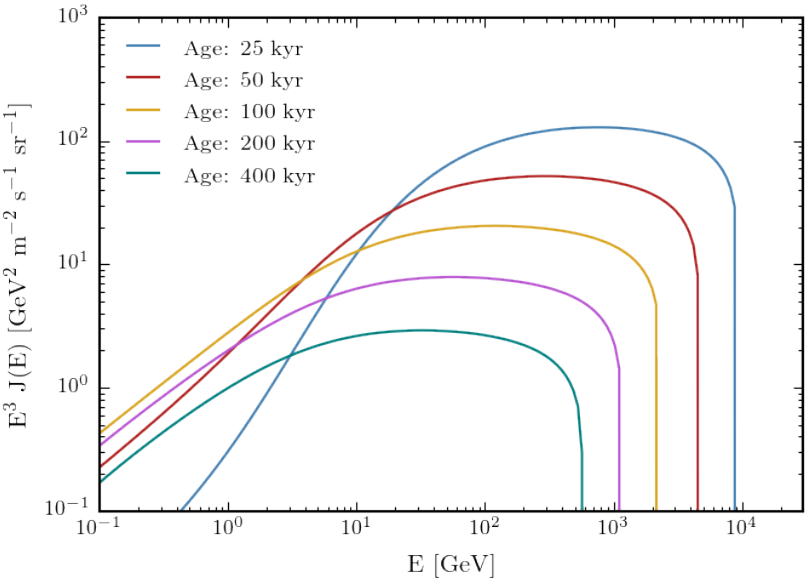

Figure 5.1: Local interstellar positron flux due to a pulsar 100 pc away at various ages, and a high energy cutoff at $\gamma = 10^9$ and a power-law injection spectrum with index $\alpha = 2.2$. Based on the model from Ref. [18]

The state of the art semi-analytic treatment of nearby lepton propagation is given in Ref. [267], which presents all details necessary for accurate calculations.

5.1.2 Approximate Energy Losses for Ultra-Relativistic Electrons

Propagating high energy electrons lose energy quickly through two mechanisms: inverse-Compton scattering and synchrotron. These energy loss rates depend on the interstellar radiation field and magnetic field strength respectively, and increase quadratically with the electron energy. This leads to extremely tight confinement at energies above a few GeV – on the order of several hundred parsecs. At lower energy, ionization losses take over, and in between, bremsstrahlung losses are non-negligible. We present full formulations in Section 5.2, but for nearby sources, such as pulsars, we can assume

simplified models. The electron energy loss rate can be approximated by [18]

$$P(\gamma) = p_0 + p_1\gamma + p_2\gamma^2. \tag{5.8}$$

Here $p_0 = 2\pi(e^2/(m_e c^2))^2 c A_i n \approx 6 \times 10^{-13} n\mathrm{s}^{-1}$ for ionization losses where A_i is a weak logarithmic function of γ. n is the neutral interstellar gas density in cm^{-3}. $p_1 \approx 10^{-15} n s^{-1}$ accounts for bremsstrahlung. Finally, $p_2 = 5.2 \times 10^{-20} w_0/(1 evcm^{-3}) s^{-1}$ includes the ICS and synchrotron contributions, where $w_0 = w_B + w_{\mathrm{CMB}} + w_{\mathrm{opt}}$ is the energy density in the magnetic field, CMB, and optical+FIR from starlight and dust reprocessing, respectively. Near the Solar System, $w_B = 0.6 ev/cm^{-3}$ for a magnetic field strength of $B_0 = 5\mu\mathrm{G}$, $w_{\mathrm{CMB}} = 0.25 ev/cm^{-3}$ uniformly through space, and $w_{\mathrm{opt}} = 0.5 ev/cm^{-3}$. The ICS losses in Eq.(5.8) correspond to the Thomson limit, which breaks down at very high energies ($\gamma \gtrsim 10^5$ is known as the Klein-Nishina Regime).

5.1.3 The Two-Zone Diffusion Model

In the absence of strong energy losses, as is the case for nuclear cosmic-ray species, interstellar propagation can be implemented via the well known stationary, cylindrically symmetric, two-zone diffusion model [268]. Two-zone diffusion consists of a thin Galactic disk of half-height $h = 100$ pm – in which cosmic-ray species interact with interstellar gas – combined with a large cylindrical diffusion halo, specified by a variable half-height L and radius of R, typically assumed to be 20 kpc.

The full model is then parametrized by an additional three components: an energy dependent diffusion constant $K(T) = K_0\ \beta\ \mathcal{R}^\delta$ with spectral index δ, $\beta = v/c$ and rigidity $\mathcal{R} \equiv p(\mathrm{GeV})/Z$ where Z is proton number, and V_c, which characterizes

Galactic wind convection. This model neglects energy losses and reacceleration terms, neither of which are expected to play an important role for nuclei. It is then possible to write the propagation in terms of the following stationary transport equation:

$$0 = \frac{\partial n}{\partial t} = \nabla \cdot (K(T,r,z)\ \nabla n) - \nabla \cdot (V_c\ \mathrm{sign}(z)\ \vec{k}\ n) - 2h\delta(z)\Gamma_{\mathrm{int}} n + Q(T,r,z). \quad (5.9)$$

Here $n(T,r,z)$ is the cosmic-ray number density and Γ_{int} is the interaction rate for the nuclei of interest with the ISM. These rates are discussed extensively in Sec. 5.1.3.1.

In the case of the nuclei injected by DM annihilation, the source term on the right hand side of the transport equation is given by:

$$Q(r,z,E) = \frac{1}{2}\langle\sigma v\rangle \frac{dN}{dE} \left(\frac{\rho(r,z)}{m_\chi}\right)^2 \quad (5.10)$$

where $\langle\sigma v\rangle$ is the thermally-averaged DM pair-annihilation cross section, dN/dE is the $\overline{\mathrm{d}}$ injection spectrum, and $\rho(r,z)$ denotes the galactic-halo DM density-distribution. For $\rho(r,z)$ we assume spherical symmetry and we adopt the profiles described in Sec 2.2 The galactocentric distance $r_\odot$ and the local DM density $\rho_\odot$ have been fixed to the following values: $r_\odot = 8.5$ kpc, $\rho_\odot = 0.39$ GeV cm^{-3}.

The transport equation may now be solved analytically via a Bessel series expansion.

$$n(r,z,E) = \sum_i N_i^E(z) J_0\left(\frac{\zeta_i r}{R}\right) \quad (5.11)$$

where J_0 is the zeroth-order Bessel function of the first kind and ζ_i are its zeros of index i. Due to the Bessel expansion, Eq. (5.9) transforms into a set of ordinary differential

equations for the functions $N_i(z|E)$ (with the energy E merely playing the role of a label), each with the following source term:

$$q_i^E(z) = \frac{2}{[J_1(\zeta_i)R]^2} \int_0^R dr\ rJ_0\left(\frac{\zeta_i r}{R}\right) q_{\bar{d}}(r, z, E) \tag{5.12}$$

where J_1 is the first-order Bessel function of the first kind. The solution at the Earth's position ($r = r_\odot$, $z = 0$) is given by:

$$N_i^E(0) = \frac{e^{-aL}\ y_i^E(L)}{B_i \sinh(S_i L/2)} \tag{5.13}$$

where we have defined:

$$a = (V_c)/(2K_0) \tag{5.14}$$

$$S_i = 2[a^2 + (\zeta_i/R)^2] \tag{5.15}$$

$$A_i = (V_c + 2h\Gamma^{\bar{d}}_{\rm ann})/(K_0 S_i) \tag{5.16}$$

$$B_i = K\ S_i[A_i + \coth(S_i L/2) \tag{5.17}$$

and where:

$$y_i^E(z) = 2\int_0^z dz'\, {\rm e}^{a(z-z')}\ \sinh\left[\frac{S_i(z-z')}{2}\right] q_i^E(z') \tag{5.18}$$

The interstellar flux can finally be expressed as:

$$\phi(E) = \frac{\beta}{4\pi} n(r = r_\odot, z = 0, E)\ =\ \frac{\beta}{4\pi}\left(\frac{\rho_\odot}{m_\chi}\right)^2 R(E)\ \frac{1}{2}\langle\sigma v\rangle \frac{dN}{dE}. \tag{5.19}$$

The spatial dependencies are captured by the "propagation function" $R_{\bar{d}}(E)$:

$$R_(E) = \sum_{i=1}^{\infty} J_0\left(\zeta_i \frac{r_\odot}{R}\right) \exp\left(\frac{V_c L}{2K}\right) \frac{y_i^E(L)}{B_i \sinh(S_i L/2)} \tag{5.20}$$

The four parameters L, K_0, δ, and V_c are then varied over the space consistent with the measured ratio of boron to carbon, with values producing the MIN/MED/MAX

flux tabulated in Ref. [269]. The resulting uncertainty in the flux spans three orders of magnitude for any nuclear species. It is notable that the Min model has now been ruled out by examining the frequency spectrum and latitudinal profile of the diffuse galactic synchrotron emission [270] which probes the lepton spectrum and density profile. These require halo-heights greater than 2 kpc.

While this uncertainty is large for all nuclear species, the propagation scenario is further constrained by the secondary flux of antiprotons. In other words the propagation setup can be constrained by assuming no additional source contributions. Now, the $\overline{\mathrm{d}}$ and ${}^3\overline{\mathrm{He}}$ fluxes are tightly correlated to $\bar{p}$, whose flux is well measured by PAMELA. The propagation uncertainty on the *maximal* $\overline{\mathrm{d}}$ (and ${}^3\overline{\mathrm{He}}$) flux allowed by the measured $p/\bar{p}$ ratio is then reduced to within a factor 4 of the MED model [158][1]. Upcoming antiproton results from AMS-02 will tighten this upper-limit and the large nuclear physics will certainly dominate in the case of antihelium. As was discussed in Section 3.2.4, the ${}^3\overline{\mathrm{He}}$ production rate (and thus flux) is sensitive to the sixth power of $p_0^{A=3}$. This is by far the dominant uncertainty, making updated collider production rates for $\overline{\mathrm{d}}$ and ${}^3\overline{\mathrm{He}}$ a crucial factor in *any* estimate of a heavy anti-nucleon flux.

The flux at the Solar System due to dark matter can now be found by numerically integrating the dark matter annihilation rates over the dark matter halo and solving the transport equation analytically. For local dark matter density $\rho_\odot$, dark matter mass m_χ, and thermal cross-section $\langle\sigma v\rangle$, the antihelium flux at the boundary of the

[1]We emphasize that propagation parameters are still fit using B/C and *not* to the measured $p/\bar{p}$ ratio which is only used to constrain the maximal propagation model.

Solar System is given by

$$\Phi^{\rm IS}_{\overline{He}}(T) = \left(\frac{\rho_0}{0.39\ {\rm GeVcm}^{-2}}\right)^2 \left(\frac{100\ {\rm GeV}}{m_\chi}\right)^2 \times \left(\frac{\langle\sigma v\rangle}{3\times10^{-26}{\rm cm}^3/{\rm s}}\right) \cdot R(T) \cdot \frac{dN(T)}{dT}, \tag{5.21}$$

where $R(T)$ is the energy dependent numerical output of the propagation code and dN/dT is the antinuclei injection spectrum from Chapter. 3. [2].

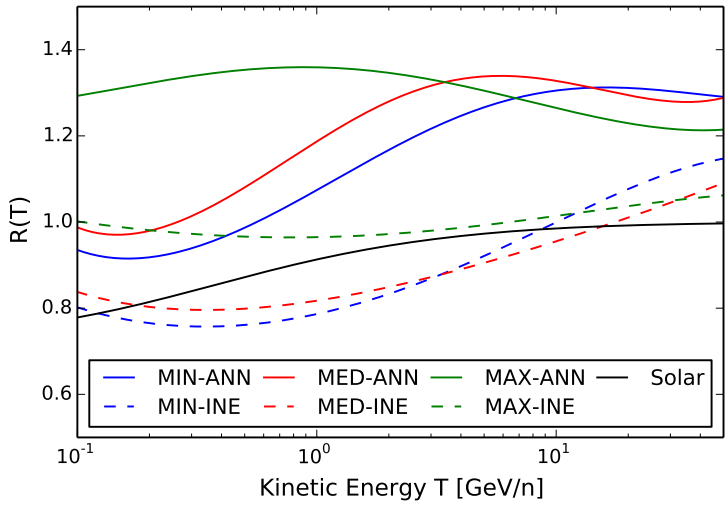

Figure 5.2: Propagation ratios $R(T) = P^{\overline{\rm He}}_{\rm num}/P^{\overline{\rm D}}_{\rm num}$ for ($P_{\rm num}$ in Eq. (5.21)) which show the enhancement or suppression of the antihelium flux with respect to antideuterons. MIN/MED/MAX interstellar propagation models are shown in blue/red/green for two values of the propagation cross-section: Annihilation only (solid lines) and total-inelastic (dashed lines). Also shown is the ratio of solar propagation functions in the Force Field Approximation (black solid).

In Figure 5.2 we show the ratio $P^{\overline{\rm He}}_{\rm num}/P^{\overline{\rm D}}_{\rm num}$ for the MIN/MED/MAX propagation models and two values of the interaction rate, $\Gamma_{\rm int}$. As we will discuss in § 5.1.3.1, uncertainty in the antihelium cross-section with interstellar gas can lead to a ∼25%

[2] For $\bar{p}$ and $\overline{\rm d}$, these propagation functions can obtained from http://www.marcocirelli.net/PPPC4DMID.html. For anti-helium, they are provided here https://github.com/erccarls/antihelium_propagation_function/blob/master/propagation_functions.pdf.

enhancement or suppression of the antihelium flux relative to that of antideuterons. Of mild importance is the higher nuclear binding energy of $^3\overline{\mathrm{He}}$ compared to the very weakly bound $\overline{\mathrm{d}}$ case. While this can more efficiently deplete the higher energy population where the non-annihilating inelastic cross-section dominates, the low energies of interest here are not significantly enhanced by tertiary contributions which are ignored in our treatment.

In-fact, the two-zone diffusion model neglects all diffusion in momentum space, the most important of which may be a proper treatment of interstellar re-acceleration. Several of these schemes, including diffusive re-acceleration, have been applied to the propagation of elements in more sophisticated numerical codes. While these attempts have been successful in reproducing otherwise anomalous peaks in the secondary to primary ratios of heavy elements such as B/C, they encounter problems for light elements. In particular, diffusive re-acceleration results in a spectral bump near 2 GeV/n for p and He which is not observed and the primary injection spectra must be artificially broken to compensate. This leads to an overestimate of the primary p and He flux by a factor $\sim$2 [271]. As we are concerned with light & low energy nuclei, and no consensus on re-acceleration has been reached for this regime, we proceed without incorporating any re-acceleration mechanism. This results in a primary spectrum within 20% of measurements at low energies [271].

5.1.3.1 Nuclear Interaction Cross Sections

In this section we discuss $^3\overline{\mathrm{He}}$ and $\overline{\mathrm{d}}$ interaction rates with the ISM. Γ_{int} in Eq. (5.9) is given by:

$$\Gamma_{\mathrm{int}} = (n_{\mathrm{H}} + 4^{2/3} n_{\mathrm{He}})\ v\ \sigma_{\overline{\mathrm{He}},p} \tag{5.22}$$

where we have assumed the H and He gas cross-sections are related by a geometrical factor $4^{2/3}$. For the Galactic Disk's interstellar hydrogen and helium densities we use $n_{\mathrm{H}} = 1\ \mathrm{cm}^{-3}$ and $n_{\mathrm{He}} = 0.07 n_{\mathrm{H}}$. v is the antihelium velocity through the ISM, and $\sigma_{\overline{\mathrm{He}},p}$ is interaction cross-section of antihelium with protons.

Direct measurements of the antihelium-proton annihilation and inelastic cross-sections needed in Eq. (5.22) are not available. Instead, we use the parameterizations in from Moskalenko, Strong, & Ormes [19] for the total inelastic, non-annihilating inelastic, and annihilation cross sections. For an atomic nucleus $(A, |Z|)$ impingent on a stationary proton with kinetic energy per nucleon T, these are given in mb by

$$\begin{aligned}\sigma^{\mathrm{tot}}_{\bar{p}A} = A^{2/3}[48.2 + 19T^{-0.55} + (0.1 - 0.18T^{-1.2})Z \\ + 0.0012T^{-1.5}Z^2]\end{aligned} \tag{5.23}$$

$$\sigma^{\mathrm{ann}}_{\bar{p}A} = \sigma^{\mathrm{tot}}_{\bar{p}A} - \sigma^{\mathrm{non-ann}}_{\bar{p}A} \tag{5.24}$$

$$\sigma^{\mathrm{non-ann}}_{\bar{p}A} = \sigma^{\mathrm{inel}}_{pA} \tag{5.25}$$

In the last equation, we assume that the non-annihilating inelastic cross-section for an antiproton-nucleus interaction is the same as the proton-nucleus interaction which can

be well-approximated by

$$\sigma_{pA}^{\text{inel}} = 45A^{0.7}\left[1 + 0.016\sin(5.3 - 2.63\ln A)\right] \times \begin{cases} 1 - 0.62e^{-T/0.2}\sin\left[\frac{10.9}{(10^3 T)^{0.28}}\right], & T \leq 3; \\ 1, & T > 3; \end{cases}$$

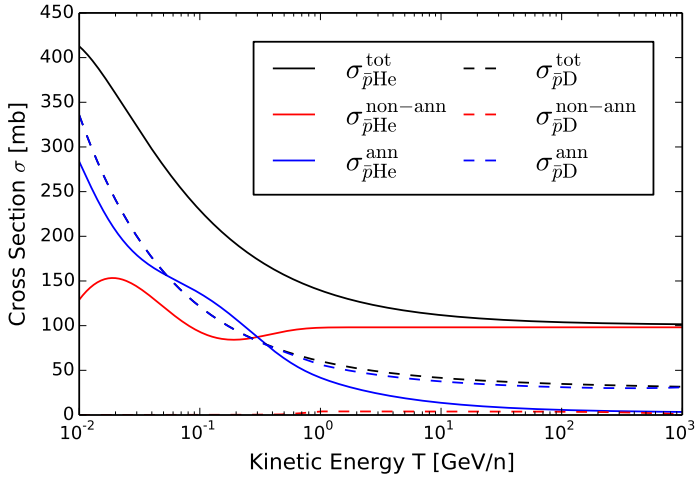

Figure 5.3: Proton–anti-nuclei inelastic scattering cross-sections as parametrized in Ref. [19]. The non-annihilating inelastic cross-section for antideuterons is taken from Ref. [20]. Shown are the total inelastic (black), non-annihilating inelastic (red), and annihilation cross-sections for antihelium (solid) and antideuterons (dashed).

In Figure 5.3 we plot the three cross-sections for antihelium and antideuterons as a function of the kinetic energy per nucleon. For the special case of $\overline{\text{d}}$, we take the parameterization from Tan & Ng [272] for total-inelastic cross-section, and an empirically determined non-annihilating inelastic cross-section which is very small due to the exceptionally low binding energy of $\overline{\text{d}}$ [20]. Peaking at approximately 4 mb, this leads to a much higher probability of annihilation during inelastic scattering than the antihelium case. We see that antihelium posesses an inelastic cross-section roughly 2

times larger than antideuterons at 1 GeV/n, while the opposite is true of the annihilation cross-sections. In principle this implies a proportionally larger tertiary contribution for antihelium, where nuclear excitations remove kinetic energy during scattering. In order to determine the relevance of this, one must also estimate the typical number of scatterings during propagation. Assuming a cosmic-ray residence time $\tau_{\rm res} \approx 5 \times 10^6$ yr [273](which is only a weak function of rigidity, scaling at most as $\mathcal{R}^{-0.6}$) [273], a mean hydrogen density $n_H = 1$ cm^{-2}, and a typical interaction cross-section $\sigma \approx 100$ mb, the number of scatters can be found by comparing the residence path length $c\ \tau_{\rm res}$ with the mean free path λ:

$$N_{\rm scatters} = \frac{c\tau_{\rm res}}{\lambda} = c\tau_{\rm res}\ n_H \sigma \approx 0.2. \tag{5.26}$$

With only a 20% chance of scattering, and given the small amount of energy removed during the inelastic process, we ignore all tertiary contributions in our semi-analytic treatment of interstellar propagation.

To bracket the impact of uncertainty in the anti-nucleus – proton cross-section, we use two methods: MethodANN and MethodINN which use the annihilation and total-inelastic cross-sections respectively in Eq. (5.22). For $^3\overline{\rm He}$, MethodINN leads to roughly a 40% lower flux than MethodANN, while for $\overline{\rm d}$, the results are nearly indistinguishable because of nearly identical total-inelastic and annihilation cross-sections. When examining the ratio of the resulting $^3\overline{\rm He}$ to $\overline{\rm d}$ flux, we see in Fig. 5.2, an enhancement (suppression) of order 25% when using the annihilation (total-inelastic) cross-sections.

Now that the dark matter properties and propagation models have been fixed and the transport equation solved, we can translate the injection spectra calculated in Sec. 3.2.4 into detectable fluxes at the top of the Earth's atmosphere.

5.1.4 Solar Propagation in the Force Field Model

The second phase of propagation is through the heliosphere and is computed using the Force Field Approximation of Gleeson & Axford [169]. The flux at the top of the atmosphere is given by

$$\Phi_{\mathrm{A,Z}}^{\mathrm{TOA}}(T_{\mathrm{TOA}}) = \left(\frac{2m_A A\ T_{\mathrm{TOA}} + A^2\ T_{\mathrm{TOA}}^2}{2m_A A\ T_{\mathrm{IS}} + A^2\ T_{\mathrm{IS}}^2} \right) \Phi_{A,Z}^{\mathrm{IS}}(T_{\mathrm{IS}}), \tag{5.27}$$

where m_A is the nucleus' mass, T_{IS} is the kinetic energy per nucleon at the boundary of the Solar System, T_{TOA} is kinetic energy per nucleon at the top of Earth's atmosphere, and $T_{\mathrm{IS}} = T_{\mathrm{TOA}} + (e\phi_F|Z|/A)$. The Fisk potential ϕ_F describes the strength of the solar modulation and varies over an 11 year cycle. Here we take $\phi_F = 500$ MV corresponding to the most optimistic detection scenario. The ratio of the $^3\overline{\mathrm{He}}$ to $\overline{\mathrm{d}}$ case is shown in Figure 5.2. The lowered rigidity of $^3\overline{\mathrm{He}}$ causes a $\sim$50% suppression at low energies relative to the $\overline{\mathrm{d}}$ modulation factor. It has been shown that at GAPS energies, the Force Field Approximation is within a factor 2 of the minimum and maximum values computed in a full numerical treatment of heliospheric $\overline{\mathrm{d}}$ transport [157]. Much of the discrepancy between analytic and numerical models should disappear when taking the ratio of modulation between antihelium and antideuterons as the first order rigidity modifications are already captured by the Force-Field Model.

More recently, the heliospheric Parker equation has been solved using numerical

and charge dependent propagation codes such as HelioProp [274]. However, these codes are not yet released to the public (though are supposedly available privately from Luca Maccione). At kinetic energies below 10 GeV, solar modulation effects impact results, and should be taken into account in most modern analyses.

5.2 Numerical Propagation

The analytic formulae of the previous sections work well for heavy nuclei, and for high energy leptons from dark matter which are confined to a roughly constant medium. While it is remarkable that these simple prescriptions work so well on cosmic-ray data, the models also contain a significant shortcomings, in particular because the Galaxy is far from homogeneous, and because the approximations break down in many cases of interest. In addition, new gamma-ray instruments are exquisitely sensitive to the Galactic diffuse emission which is produced by cosmic-ray interactions with the interstellar medium. Our measurements are therefore sensitive not just to the local cosmic-ray density, but to all cosmic-rays along a given line of sight. The power of Gamma-ray data from Fermi, and excitement over observations of the Galactic center have brought Galactic diffuse emission (GDE) modeling to the forefront, and the use of gamma-ray data in understanding Galactic cosmic-ray physics remains in its infancy.

In this section, we review the state of the art in numerical cosmic-ray propagation codes from the perspective of gamma-ray and dark matter studies. Specifically, we do not review propagation/fragmentation of heavy nuclei, nor do we present a detailed description of interaction and production cross-sections for secondary species (see [84] for details on secondary production). Instead we provide details for propagating protons, and electrons/positrons. The goal of this section and following chapters is to provide a firm understanding of numerical models, and to point out practical resources for further details, and to discuss shortcomings of the current models. In Ch. 6 we discuss radia-

tion from cosmic-rays, while in Ch. 7 we discuss the input models for the Milky Way's magnetic fields, source and gas distributions, and interstellar radiation fields, including some of our own advances.

5.2.1 The Full Transport Equation

At the heart of several, modern attempts at Galactic diffuse emission modeling lies the cosmic-ray propagation code `Galprop v54r2504` [82, 83, 84, 85, 86], as well as `Dragon` [275] which was forked from Galprop several years ago. Here, we briefly review cosmic-ray propagation in `Galprop`. Cosmic-ray transport is modeled by the following differential equation:

$$\begin{aligned}\frac{\partial \psi}{\partial t} &= q(\vec{r}, p) + \vec{\nabla} \cdot (D_{xx} \vec{\nabla} \psi - \vec{V} \psi) - \frac{1}{\tau_f} \psi - \frac{1}{\tau_r} \psi \\ &+ \frac{\partial}{\partial p} p^2 D_{pp} \frac{\partial}{\partial p} \frac{1}{p^2} \psi - \frac{\partial}{\partial p} \left[\dot{p} - \frac{p}{3} (\vec{\nabla} \cdot \vec{V}) \psi \right],\end{aligned} \tag{5.28}$$

where $\psi = \psi(\vec{r}, p, t)$ is the density per unit of total particle momentum, i.e. $\psi(p)dp = 4\pi p^2 f(\vec{p})$ where $f(\vec{p})$ indicates the phase-space density, $q(\vec{r}, p)$ is a cosmic-ray injection source term, D_{xx} is the spatial diffusion coefficient, $\vec{V}$ is the convection velocity, re-acceleration is described as diffusion in momentum space, and is determined by a diffusion coefficient in momentum space D_{pp}, and $\dot{p} \equiv dp/dt$ is the momentum loss rate. Finally, τ_f and τ_r are the time scales for fragmentation and radioactive decay.

For a given source distribution, `Galprop` solves the above transport equation numerically, assuming free escape boundary conditions at the edges of a cylindrical diffusion halo with half-height $z_{\rm halo}$ and radius $R_{\rm halo}$, using an implicit second-order

Crank-Nicholson scheme (a grid based finite-element solution). In most Galactic diffuse emission (hereafter, GDE) models, including the present one, the numerical solution proceeds until a steady state cosmic-ray density is reached (for time-dependent effects see e.g. [216, 217, 47]). We now describe the transport elements and their essential phenomenology. For a more detailed accounting of these, see Ref. [276] and references therein, as well as the `Galprop` explanatory supplement[3].

5.2.2 Cosmic-Ray Injection

In the above transport equation, a the spatial distribution of sources and their spectra are given as input. In Sec. 7.1, the spatial morphology of sources is treated. Here we briefly review the underlying ideas and discuss some environmental modifications to DSA which likely play a role in the Galactic center.

Two mechanisms are responsible for accelerating charged particles in astrophysical enviroments. The first are static-electric fields which can originate during magnetic reconnection due to the rapidly time varying magnetic fields which induce an electric field and rapidly move charges through astrophysical plasmas. This process is well understood, although the dynamics of given system are complex in practice. The second, much more common scenario, is acceleration via head-on collisions with astrophysical shocks – i.e. with magnetic turbulence. This is believed to occur most commonly in supernovae explosions, but also occurs diffusively in the interstellar medium (see our discussion of reacceleration in Sec. 5.2.5) as well as in so-called "super-bubbles" gener-

[3] http://galprop.stanford.edu/download/manuals/galprop_v54.pdf

ated by collective SNe and strong stellar winds.

5.2.2.1 Diffusive Shock Acceleration

Supernovae explosions into the interstellar medium inject approximately a fraction ϵ of their total energy (10^{51} erg) kinetically into electrons (about 0.01) and protons ($\epsilon_p 0.1$), with the velocity of the ejecta equal to [277]

$$v_{\rm ej} = 10^5 \sqrt{\frac{\epsilon}{M_{\rm ej,\odot}}} \text{ km/s}, \tag{5.29}$$

where $M_{\rm ej,\odot}$ is the mass ejected in solar mass units. The speed of sound in the ISM is given as

$$c_s = \sqrt{\gamma_g \frac{kT}{m_p}} \approx 11 \sqrt{\frac{T}{10^4 K}} \text{ km/s}, \tag{5.30}$$

for an adiabatic index $\gamma_g \sim 5/3$ and plasma temperature T. Clearly, the ejecta is highly supersonic, with Mach number

$$M_s = \frac{v_{\rm ej}}{c_s} \approx 900 \left(\frac{\epsilon}{M_{\rm ej,\odot}}\right)^{1/2} \left(\frac{T}{10^4 K}\right)^{-1/2}. \tag{5.31}$$

The ejecta therefore form a shock front, and the evolution of the shock depends strongly on the local ISM.

The shock strength is characterized by a compression ratio σ between the upstream and downstream plasmas, which is equal to the ratio of up and downstream velocities. This is related to the M_s via

$$\sigma = \frac{4M_s^2}{M_s^2 + 3}, \tag{5.32}$$

which asymptotes to $\Sigma = 4$ for strong shocks.

For first order fermi processes (Diffusive Shock Acceleration), one can solve the diffusion-convection equations [277] to obtain the distribution of particle momenta at the surface of the spherical shock which reads

$$f(p) \propto p^{-\alpha} \tag{5.33}$$

with

$$\alpha = \frac{3\sigma}{\sigma - 1}, \tag{5.34}$$

which asymptotes to $\alpha = 4$ for strong shocks. The number of particles with energy E is equal to

$$n(E)dE = 4\pi p^2 f(p) \frac{dp}{dE} dE \propto p^{-2} \tag{5.35}$$

where the last step assumes relativistic particles. Thus, DSA in the strong shock limit predicts a power-law injection spectrum with an index of 2, becoming slightly weaker for weaker shocks.

The above applied to DSA of a test particle, but in reality, the dynamics of the shock front, partially accelerated cosmic-rays, the ISM, and magnetic field are coupled, and non-linear versions of DSA come into play. This implies that the actual injected particle spectrum is environmentally dependent. In most treatments of Galactic cosmic-rays, however, the injection spectrum is treated as spatially homogeneous.

5.2.2.2 Non-Linear DSA in the Galactic Center

In DSA, shock waves propagating through ionized interstellar medium compress the plasma and transfer kinetic energy downstream through either two-body collisions, or

through collective electromagnetic effects if the collision cross section is very small. In the compressed zone preceding the shock front, resonant scattering of Alfvén waves efficiently accelerates particles until their gyro-radius $r_g = cp/(eB)$ exceeds the width of the shock layer [278]. While this test particle case assumes a fully ionized cosmic-ray precursor, the Galactic center is only partially ionized, with well over 80% of the gas content associated with neutral molecular hydrogen in the inner 200 pc, which completely engulfs the region of central starburst activity. Malkov, Diamond, and Sagdeev [279, 280] demonstrated that when the upstream edge of supernovae shocks interact with molecular clouds, ion-neutral collisions effectively damp a range of otherwise resonant Alfvén waves, severely deteriorating particle confinement within a slab of momentum space, and steepening the spectral index of protons by precisely one at an energy given in Ref. [279] as

$$p_{\rm br}/m_{\rm p}c \approx 16 B_{\mu}^{2} T_{4}^{-0.4} n_{0}^{-1} n_{i}^{-1/2}, \tag{5.36}$$

where B_{μ} is the magnetic field strength in units of μG, T_4 is the temperature of the ionized precursor in units of 10^4 K, and n_0, n_i are the neutral and ionized gas density given in in units of cm^{-3}, respectively. Similar developments in non-linear DSA have shown that over 1-10 GeV the spectrum can be as steep as $E_{\rm p}^{-4}$ depending on the shock speed and environment, flattening out again above a few TeV [281].

The mechanism described above successfully reproduces at least 6 of the 16 current Fermi-LAT observations of SNRs [282, 283, 46, 284, 285, 286], although the uncertainties associated with estimating the relevant environmental parameters are considerable. The 10 remaining observations have not yet incorporated this model into the

analysis. In Ref. [46], several SNRs observed by Fermi were shown to be interacting with molecular clouds based on radio observations of 1720 MHz OH maser emission, providing a strong indication of shocked H_2. The spectra were then reproduced by fitting the underlying proton distribution according to an exponentially cutoff power-law, as we do above.

SNRs interacting with highest density clouds were found to have low cutoff energies and hard proton spectra with $[\Gamma, E_c] = [1.7, 160\ \text{GeV}]$ and $[1.7, 80\ \text{GeV}]$ compared to the low-density cases, where [2.4,1 TeV] and [2.45,1 TeV]. For another SNR, W44, an independent analysis found that the γ-ray emission was well fit by a hard proton spectrum of index between 1.74 and 2 with a cutoff at $p_c \approx 10$ GeV/c [283]. While these examples provide a representative sample of the expected range for the low-energy spectral index and cutoff energies, we do not necessarily expect a hardened spectrum to be correlated with high gas densities. These SNR spectra match the γ radiation expected from an exponentially cutoff proton spectrum quite well, possibly indicating that the theory of Ref. [279] is underestimating the true breaking strength due to ion-neutral damping, or that an additional cutoff mechanism is at play. In either scenario, a more pointed spectral peak is predicted, and can plausibly reproduce the spectrum of the Fermi GeV Galactic Center Excess.

The Galactic center hosts a zoo of high-energy astrophysical sources including several SNRs, resolved & unresolved pulsars, pulsar wind nebulae, and the central black hole Sgr A*. Most notably Sgr A East is a $\sim 10^4 - 10^5$ year old and 10 pc wide SNR rapidly expanding into the molecular cloud M–0.02–0.07, where a half-dozen sites

show also show the 1720 MHz maser emission from shocked H_2 [287]. This complex encompasses the central black hole with most of the structure residing within a few parsecs from Sgr A* ($\lesssim 0.05^\circ$). This separation is too small to be spatially resolved by Fermi-LAT, which has a maximal angular resolution of about a quarter degree, hence it will appear as a point source, perhaps with minor spatial extension, whose spectrum cannot be differentiated from additional Galactic center sources.

An especially intriguing candidate for the recent injection of cosmic-ray protons in the inner Galaxy is Sgr A East. As an estimate of the expected flux from Sgr A East, we utilize a similar object, SNR W44. The latter is observed to have a differential flux of $\approx 1.25 \times 10^{-7}$ GeV/cm^2/s. Multiplying by the square of the distance ratio $d^2_{\rm W44}/d^2_{\rm GC} \approx (2.9 \text{ kpc}/8.3 \text{ kpc})^2$ we obtain a flux of 5×10^{-8} GeV/cm^2/s, precisely in line with the GCE residual and the Sgr A* flux reported by Abazajian et al within a $1^\circ \times 1^\circ$ box centered on the GC [45]. (Note that the the two Daylan et al fluxes reported in Figure 8.31 are normalized by the solid angle of a thin annulus at 5° from the GC). It remains to be assessed whether the spectral break energy near the Galactic center is compatible with the the results of Section 8.2.3, and whether a reasonable supernova rate is compatible with the observed flux.

The environment of Sgr A East has been studied in detail at radio and X-ray wavelengths. Unfortunately, the complicated structure and rapid gradients in density, temperature, and magnetic field strength imply that there will be no single prediction for the spectral break energy predicted by Equation (5.36), but, rather, a range of values dependent on the particular properties of the shocked region. Here we expect that

nearly all of the supernova activity will take place very close to the Galactic center, with conditions not far removed from those of Sgr A East.

The Central Molecular Zone (CMZ) is a large elliptical cloud with a gas mass fraction dominated by molecular hydrogen. It is thin and aligned with the Galactic disk, extending to a radius of approximately 150 pc from the Galactic center when projected along the line of sight[4]. This cloud makes up 5-10% of the total Galactic molecular gas and is comprised of dense clumps of H_2 as well as of a lower density ambient component which completely fills the acceleration volume for any centralized SNR. In the inner 15 pc, typical densities can vary from the ambient value of 10^2 cm^{-3} up to the dense molecular clouds at 10^5 cm^{-3} [289, 288], occasionally reaching even higher densities. The warm ionized hydrogen is significantly more extended and provides the precursor for shock acceleration. There is only weak power-law dependence of the break momentum on the density and temperature of the ionized component ($n_i^{-0.5}$ and $T^{-0.4}$). Both of these components are reasonably well measured in the Sgr A* region using X-ray observations with ion densities near 10^3 cm^{-3} and very hot plasma temperatures of 10^7 K [290].

The most important, and also the most uncertain factor in determining the break momentum, is the magnetic field strength in the shock propagation region. Zeeman splitting of OH molecules provides a measurement of the magnetic field strength along the line of sight, and indicates very strong fields in the large non-thermal radio filaments and possibly molecular clouds which can be as high as 1-4 mG [287, 291] while Faraday

[4]Interestingly, the same gas model in Ref.[288] finds a large gas bulge extending to 450 pc which is rotated 13.5° CCW from the Galactic plane when projected along the line of sight with an axis ratio of 3:1. Daylan et al found a slightly preferred fit at roughly an angle of 35°± CCW with an axis ratio of $1 : 1.4 \pm .3$, possibly indicative of gas correlated emission.

rotation measurements indicate that the surrounding medium can be somewhat lower with a strength down to several hundred μG. For an extensive review of magnetic fields in the Galactic center, we point the Reader to Ref. [291].

Efficient trapping of very low energy precursors in the very dense molecular clouds implies that these will be the primary acceleration sites for the resulting high energy cosmic-ray population, although a fraction will still originate from the surrounding lower density and lower magnetic field regions. In this case, the lower densities of the ionized and molecular components partially cancel the effect of the smaller magnetic field on the break momentum, but some broadening of the spectral peak may be expected toward lower energies. In order to estimate the range of break momenta achievable at the GC, we simply fix the least sensitive parameters to typical values, and set $n_i = 10^3$ cm^{-3}, $n_0 = 10^4$ cm^{-3}, and $T = 10^7$ K, while varying of B between 0.5 mG and 4 mG. Doing this provides a break momentum between 0.79 and 51 GeV/c with a nominal value of 12.7 GeV/c for a 2 mG field strength.

Without more accurate measurements and high-resolution 3-dimensional models of the Galactic center environment, it is extremely difficult to definitively compute the resulting cosmic-ray spectrum. If, in fact, these large magnetic fields are contained strictly to non-thermal radio filaments, or are much weaker then previously thought, as suggested in Ref. [292], the predicted momentum break would be significantly smaller, and the breaking mechanism would be disfavored as an explanation for the GCE. It is also very likely that current conditions at the Galactic center differ substantially from those of 1-10 Myr ago especially if the Fermi bubbles formed on comparable timescales.

Compounded with uncertainties in non-linear DSA in the presence of ion-neutral damping, a conclusive statement is currently not possible. Nonetheless, the observation of break energies from ten to several hundred GeV in nearby SNR indicates that such scenarios are not uncommon, and provide evidence that the description advocated above is not unrealistic.

5.2.3 Diffusion

As cosmic-rays propagate through the Galaxy, they traverse through both turbulent and regular magnetic fields. These magneto-hydrodynamic (MHD) waves and discontinuities effectively isotropize the incoming pitch angle of the CRs. In the limit that the random fluctuations at the gyro-resonant frequency are small relative to the mean regular field strength ($\delta B_{res} \ll B_{\rm reg}$), the scattering is described by a quasi-linear theory of plasma turbulence which leads to strongly enhanced (anisotropic) diffusion along the direction of magnetic field lines. On scales above $L \sim$100 pc, the magnetic fields fluctuate strongly and the random field is often several times stronger than the regular field. It is these fluctuations which make the CR arrival directions strongly isotropic to within less than 1% locally.

For a gyroradius (Larmor radius) $r_g \equiv mv_\perp/(qB)$, the diffusion coefficient when $r_g < L$ – i.e. when the gyroradius is smaller than the mean scale of coherent fields – is approximately given by

$$D_{xx} \approx \left(\frac{\delta B_{\rm res}}{B_{\rm reg}}\right)^{-2} \frac{v r_g}{3}, \tag{5.37}$$

where $\delta B_{\rm res}$ is the amplitude of the random magnetic field with wave number $k_{\rm res} = 1/r_g$

and $B_{\rm reg}$ is the regular field. The energy dependence of spatial diffusion therefore depends on the spectrum of interstellar turbulence which is observed to scale as a power-law, with spectral energy density $w(k)dk \propto k^{-2+\delta}dk$, with $\delta \approx 1/3$ for a Kolmogorov type spectrum. A typical random magnetic field in the Milky way has strength of $\delta B \approx 5\mu$G, and we can estimate,

$$D_{xx} \approx 2 \times 10^{27}\ \beta \mathcal{R}_{\rm GV}^{1/3}\ {\rm cm}^2\ {\rm s}^{-1} \tag{5.38}$$

for particle rigidities $\mathcal{R} < 10^8 GV$ above which propagation becomes rectilinear, and $\beta = v/c$. The spectrum of turbulence could be harder, with $\delta \in 0.3 \div 0.6$ being commonly expected in the literature. This is not terribly off from the commonly measured value $D_{xx} \approx 5 \times 10^{28}$ cm^2 s^{-1}, which is, however, constrained to within only about a factor 10.

Typically, isotropic diffusion is assumed. The validity of this assumption is difficult to test due to astrophysical uncertainties and the significant degeneracy between transport parameters. In general, one expects that the diffusion properties can vary considerably in different regions of the Galaxy, in particular within the Galactic center environment where strong turbulence and large scale poloidal magnetic fields likely induce strongly anisotropic diffusion [293] out of the plane. This anisotropy enhances diffusion away from the Galactic center.

Recenlty, as magnetic field models improve (including regular field components), and as simulations of cosmic-ray transport become three-dimensional and higher resolution, prescriptions for calculating the inhomogenous and anisotropic diffusion co-

efficients as a function of spatial position and energy have arisen. In addition, the free-escape boundary conditions normally implemented are realtively artificial, and it is more realistic to implement a diffusion constant which increases exponentially with the Galactic scale-height[5]. These methods may lead to much more accurate diffusion models and have recently been used to model the Galactic foreground emission (See for example Appedix A.3 of Ref. [225]).

5.2.4 Convective Winds

Galactic winds are generated through at least three processes: (i) stellar winds, SNe, and starbursts (ii) active Galactic Nuclei – supermasssive black holes at the centers of galaxies – and (iii) cosmic-ray streaming. In each case, the tight coupling between cosmic-rays, magnetic fields, and the thermal pressure leads to a coherent outflow of each of these in which cosmic rays are efficiently travelling *with* the magnetic fields that cause them to diffuse (at a speed of $v \sim 10^{-3}c$ rather than their actual near-luminal velocities. In the Milky Way, the aforementioned quantities appear to be in approximate energy equipartition, although direct evidence for Galactic winds is only observed at the Galactic center, winds play a non-trivial role in shaping the low-energy spectrum of cosmic-rays, and in particular, impacting the energy dependence of the secondary to primary ratio. In advection dominated scenarios (winds speeds greater than several few hundred km/s), transport becomes energy independent. This is in contrast to observation [276].

[5]These capabilities are not currently included in public versions of Galprop, but they are extremely easy to implement, as the diffusion tensor is already implemented as a distribution over the Galaxy. Therefore, one literally just needs to set these variables in the source code.

5.2.4.1 Galactic Winds

The collective average action of stellar winds and supernovae events in the Galactic plane drive winds which increase linearly with the height above disk at a rate of 0-50 km s^{-1}/kpc and produce adiabatic energy losses as the wind speed increases away from the disk. At the Galactic center, there is substantial evidence for very rapid outflows of order 200-1000 km/s, which dominates transport over diffusion. This GC outflow is of great importance to the Galactic center excess signal, and was first implemented in numerical codes and tested against gamma-ray data by us, as shown in Sec.8.1.5.

Two common models are employed in cosmic-ray studies of advection out of the Galactic disk. The *one zone* model consists of a linearly increasing wind speed $\vec{V} = dv/dz \times \vec{z}$ where the gradient dv/dz is a free parameter and is assumed (likely unphysically) to be independent of radius. The *two zone* model where high winds (100 km/s) are present in the Galactic halo $|z| > 1$ kpc, but not within it, where transport is purely diffusive. This acts effectively as an energy dependent diffusion height, and can reproduce several CR observables [276]. The one zone model is most typically used, with $dv/dz0 - 20$ km/s providing reasonable fits. More complex models which vary, for example, with a gradient depending on the star formation surface density along the plane have not yet been explored, but are physically motivated, do not add additional parameters, and are well tested by a gamma-ray study.

5.2.4.2 Galactic Center Winds

Winds at the Galactic center are driven by intense star formation occurring throughout the CMZ, and especially from the dense stellar clusters of the inner 10 pc. With diffusion alone, the GC is highly calorimetric. On the other hand, multiwavelength observations indicate less that more than 95% of the non-thermal injected power must be advected from the system, despite the extreme gas densities and high magnetic fields [39]. A detailed account of GC winds can be found in Ref. [39] and references therein, but is briefly reviewed here. Perhaps most significant are observations of the 'GC lobe', a rising 1° tall and $\lesssim 0.5^\circ$ radial shell of 10 GHz radio continuum emission [294] with associated mid-infrared filaments [295], X-ray shells [296], and optical and radio recombination lines which point to nested shells of ionized gas, synchrotron emission, and dust entrained in the outflow whose pressure and energetics are consistent with star formation or nuclear activity from the central 10 pc of the Galaxy [297, 295, 298]. More recent radio observations combined with multiwavelength modeling [299] have confirmed these features, finding additional X-ray counterparts and associations with the circum-nuclear disk. In addition, from the perspective of extragalactic star-forming galaxies the SFR within the CMZ is expected to drive powerful outflows in which almost 95% of cosmic-rays are likely advected from the system [39].

We first modelled these winds in Galprop as a purely radial outflow (in 3D) with constant velocity $v_{\rm wind}$ within $r_{\rm 3D} \lesssim 2$ kpc of the Galactic center, which is assumed to stall and vanish beyond this. Explicitly, we describe the wind in terms of a Fermi-Dirac distribution with a boundary width of 200 pc. A stall zone at 2 kpc is likely

conservatively small based on recent modeling [300], and, in the vertical direction, lies outside of our inner Galaxy ROI.

$$\vec{V}_{\rm wind}(r) = \frac{v_{\rm wind}\hat{r}_{\rm 3D}}{e^{(r_{\rm 3D}-2\ {\rm kpc})/0.2\ {\rm kpc}}+1} \tag{5.39}$$

where we vary the value $v_{\rm wind}$ between $0-2000$ km s^{-1}. The results shown in Sec. 8.1.5 and Sec.8.1.8.1 reveal significant gamma-ray support for such outflows at the Galactic center.

5.2.5 Reacceleration

Cosmic rays can also scatter off of propagating interstellar Alfvén waves, leading to stochastic diffusive reacceleration. This can be effectively described using momentum space diffusion [301] and is related to the spatial diffusion coefficient and Alfvén velocity, v_a, via

$$D_{pp}(\mathcal{R}) \equiv \frac{4}{3\delta(2-\delta)(4-\delta)(2+\delta)}\frac{\mathcal{R}^2 v_a^2}{D_{xx}(\mathcal{R})}. \tag{5.40}$$

Note the quadratic dependence of the momentum space diffusion on the Alfvén velocity. This strongly effects the low energy spectrum of cosmic-rays and thus also gamma-rays throughout the disk. Gamma-ray data provides an excellent probe of this parameter which is typically $v_a = 30-40$ km/s, but is expected to vary significantly throughout the Galaxy, increasing for regions with high magnetic fields and low ion density.

The effect of reacceleration is to accelerate particles at low energies as the propagate, effectively hardening the spectrum. Such effects are potentially important [47]

in relation to leptonic CR bursts at the Galactic center as an explanation for the GeV Galactic Center Excess, as they maintain a more spatially independent spectrum for ICS, which otherwise softens as the electrons age. Using cosmic-ray secondary to primary ratios as a barometer, it is observed that in the 1-100 GeV range, diffusive acceleration cannot be the primary source of acceleration throughout the Galaxy, as this would imply that higher energy particles have spent longer in the Galaxy before reaching their energy, hence the secondary abundance would increase with energy relative to primaries, which is not observed [276].

Recently, the Fermi collaboration has used a spatially varying Alfvén velocity prescription[6].

$$v_a \propto \frac{B_{\rm tot}}{\sqrt{\rho_{\rm ion}}} \tag{5.41}$$

where $\rho_{\rm ion}$ is the ion density of the ISM, and $B_{\rm tot}$ is the magnetic field. Note that here this is a propagating wave with the tensile quantity being B^2 and the inertial quantity $rho_{\rm ion}$, just as a wave velocity on a string is determined by $\sqrt{T/\rho}$. These spatially varying models have also not been publicly tested against gamma-ray data.

5.2.6 Energy Losses

Energetic cosmic-rays lose energy through interactions with (i) magnetic fields (electron and proton synchrotron emission), (ii) interstellar radiation fields (inverse Compton scattering), and interactions with interstellar gas ($p-p$ scattering, ionization, brehmstrahlung). Synchrotron, ICS and bremsstrahlung and π^0 production all

[6]See App. A.3 of Ref. [225]. Similar to many extensions of Galprop, this is extremely easy to implement into `create_transport_arrays.cc` and `propel.cc`.

produce electromagnetic radiation which is calculated in Chapter 6. Here we simply examine the energy loss-rates which can be used in numerical propagation codes, and to estimate cooling rates.

In Figure 5.4 we show the electron cooling timescales for several zones of the Milky Way. Namely the disk, and regions near the Galactic center. In Figure 5.5 we show the dominant energy loss mechanism for these same zones as a function of magnetic field strength and electron energy. Each of these scenarios are described in the following few sections.

5.2.6.1 Inverse Compton Scattering

In the Galactic disk, radiation fields are quite low, on the order of 1 eV cm^{-3}. For magnetic field strenghts above about 2μG, this implies that synchrotron will dominate the energy loss-timescales. Still, ICS is important, and in the Galactic center region, the radiation fields are expected to reach several thousand times the disk intensity, strongly influencing the electron spectrum in the immediate vicinity of the Galactic center.

A good estimate of the ICS cooling timescale is given by [7].

$$\tau_{\rm ICS} = 4 \times 10^8 f_{\rm KN}^{-1} \left(\frac{U_R}{1{\rm eV\ cm}^{-3}} \right)^{-1} \left(\frac{E_e}{\rm GeV} \right)^{-1} {\rm yr} \tag{5.42}$$

where U_R is the photon radiation field density, E_e is the electron energy and $f_{\rm KN}$ is a Klein-Nishina correction for high energies $f_{\rm KN} \approx (1 + 40 E_{e,{\rm TeV}}\ kT_{\rm eV}))^{-3/2}$ which is 1 at low energies, and proportional to $\ln(E_e/E_e^2)$ above several hundred GeV. Above 1 GeV, at least 75% of the electron's energy is transferred into the input photon, while above

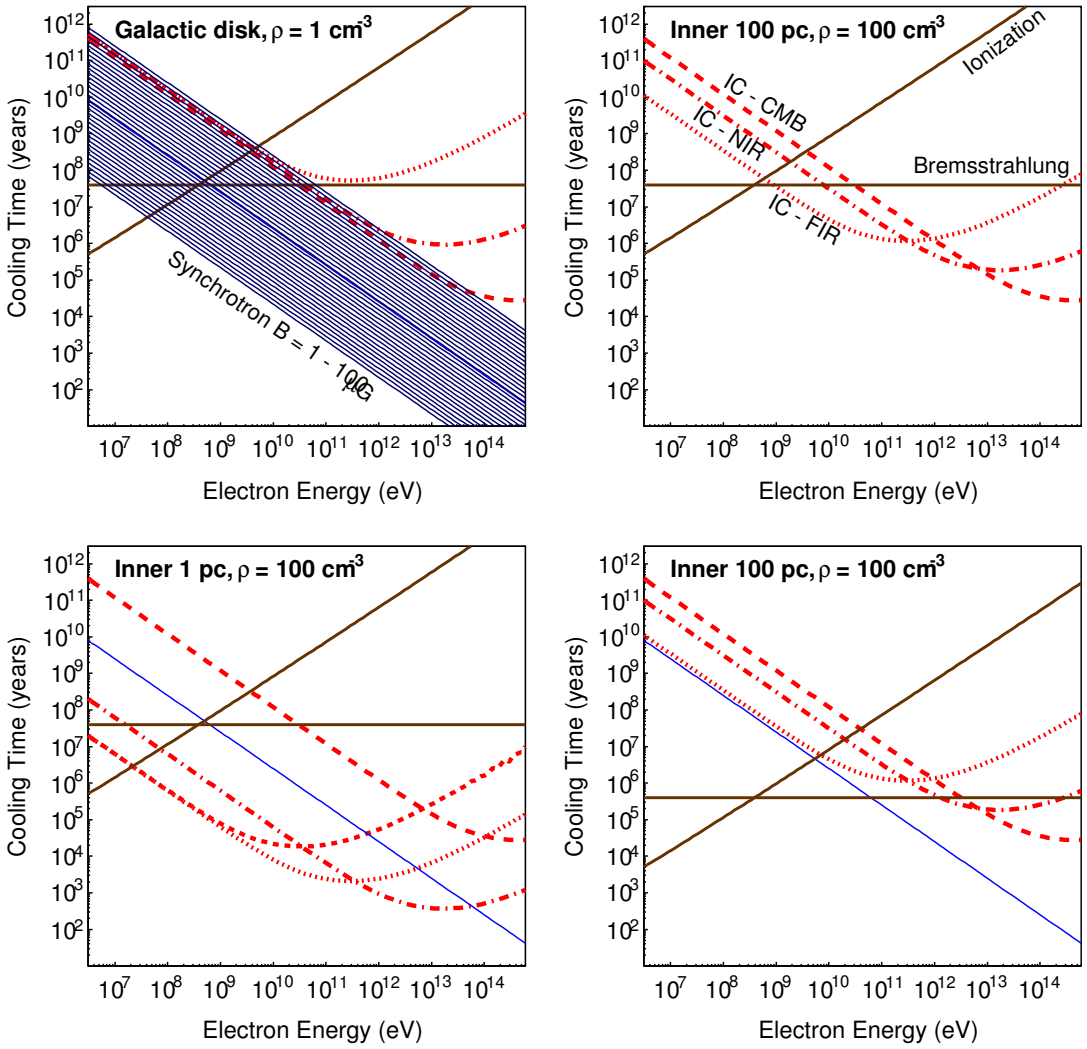

Figure 5.4: Summary of electron energy loss-timescales typical of the Milky Way in the disk and the Galactic center vicinity. The CMB energy density $w_{\rm CMB} = 0.26$ eV cm^{-3}, while the (FIR$_{6\times10^{-3}\rm eV}$, NIR$_{.3\ \rm eV}$, and Opt$_{3\ \rm eV}$) radiation densities are set to (.2, .2, 0) eV cm^{-3} top-left in disk; (1, 9, 0) eV cm^{-3} top-right CMZ; (5000, 5000, 5000) eV cm^{-3} inner 1 pc bottom-left. The matter density is $n_0 = 1$cm$^{-}3$ in all cases except the bottom-right where $n_0 = 100$cm$^{-}3$. Figure reprinted with permission from Ref. [7].

several TeV (the deep KN-regime), more than 90% of the electons input energy is gained by the photon [302], resulting in high-energy gamma-rays. In the Thompson regime, it is notable that the loss-timescale is independent of the spectrum of low-energy photons,

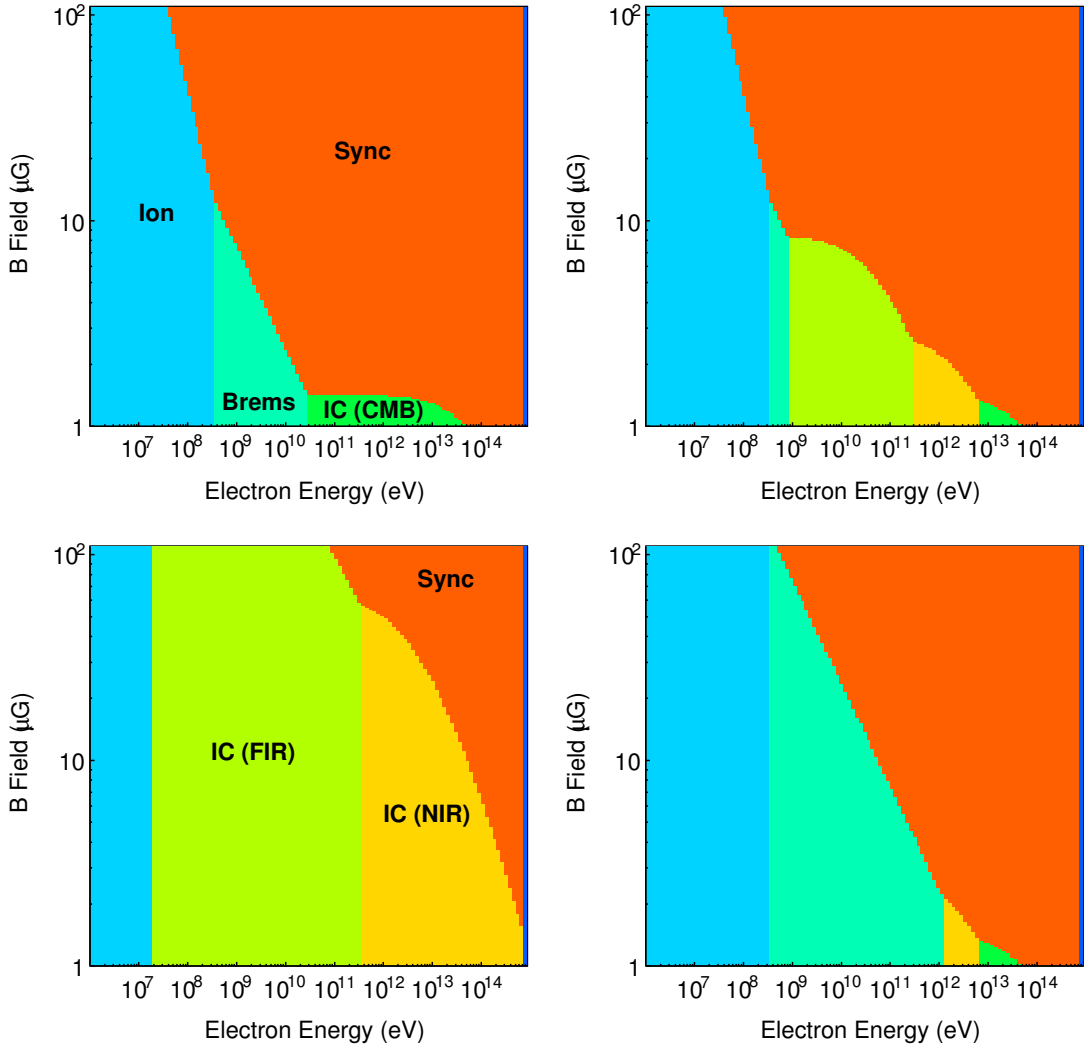

Figure 5.5: Dominant energy loss process for the radiation field densities shown in Figure 5.4. Figure reprinted with permission from Ref. [7].

while at high energies this is no-longer true.

The electron energy loss rate $b = dE_e/dt$ by Inverse Compton Scattering is

given exactly by by [261]

$$b_{\rm ICS} = 3c\,\sigma_{\rm T}\int_0^\infty d\epsilon\,\epsilon\int_{1/4\gamma^2}^1 dq\;n(\epsilon)\frac{(4\gamma^2-\Gamma_\epsilon)q-1}{(1+\Gamma_\epsilon q)^3}\left[2q\ln q+q+1-2q^2+\frac{1}{2}\frac{(\Gamma_\epsilon q)^2}{1+\Gamma_\epsilon q}(1-q)\right], \tag{5.43}$$

where $n(\epsilon, r, z)$ is the number density (per unit volume and unit energy) of photons of the ISRF, with energy ϵ, $\gamma = E/m_e$ is the relativistic factor of the electrons and positrons and $\Gamma_\epsilon = 4\epsilon\gamma/m_e$.

In the Thomson limit (valid for energies below about 100 GeV), they reduce to

$$b_{\rm ICS} = \frac{4\,c\;\sigma_{\rm T}}{3\,m_e^2}\,E^2\int_0^\infty d\epsilon\;\epsilon\;n(\epsilon,r,z) \qquad \text{[Thomson limit]}, \tag{5.44}$$

which makes the energy density in the photon bath $u_{\rm ISRF} = \int d\epsilon\,\epsilon\,n(\epsilon,r,z)$ apparent.

The ICS energy losses are *proportional to* E^2 (as evident in the Thomson expression, but also in eq. (5.43) noting that $4\gamma^2 q$ is the dominant piece at the numerator) for small E. For large E, the dependence softens.

5.2.6.2 Synchrotron

Synchrotron losses take on a similar form to ICS, with the synchrotron timescale following

$$\tau_{\rm sync} = 2.5\times10^9 B_{\mu\rm G}^{-2}E_{e,GeV}^{-1}\ \text{yr} \tag{5.45}$$

For an electron traversing a random magnetic field, the energy loss rate is given by [303]

$$b_{sync} = \frac{dE}{dt} = \frac{4\sigma_T c\gamma^2 B^2}{24\pi} \tag{5.46}$$

where σ_T is the Thomson cross-section for the corresponding particle. The magetic fields in the Galaxy range from several μG in the disk (about 8μG near the solar System) and upto several hundred μG in the inner few hundred parsecs known as the Central Molecular Zone. Some non-thermal radio filaments in this region indicate magnetic fields up to 1-2mG, though these appear to be localized to streams flowing out of the Galactic center.

5.2.6.3 Bremsstrahlung

The bremsstrahlung cooling time is energy independent, depending only on the density of interstellar gas, and is given by

$$\tau_{\rm Br} = 4 \times 10^7 n_0^{-1} \text{ yr} \tag{5.47}$$

where n_0 is the gas density in hydrogen atoms per cm^{-3}.

Most gas in the Galaxy is neutral and the cooling rate is given by [303]

$$b_{\rm Br} = 7.3 \times 10^{-16} n_e \gamma \tag{5.48}$$

where $n_e = n_p$ is an excellent approximation. One can then use a model for the galactic Gas distribution (HI and H_2) to compute energy loss rates for propagating electrons. Due to the energy independence of bremsstrahlung cooling times, the spectrum of electrons is not modified by this process.

5.2.6.4 Ionization

In gas dense regions below about 350 MeV, ionization losses dominate bremsstrahlung and the cooling time is given by

$$\tau_{\rm Ion} = 4.1 \times 10^9 E_{e,\rm GeV}((3\ln(E_{e,\rm GeV}) + 42.5)n_0)^{-1} \text{ yr} \tag{5.49}$$

and the cooling rate is given by [303]

$$b_{\rm ion} = \frac{8}{3}\sigma_0 n_e - \frac{c\gamma}{\sqrt{\gamma^2-1}}\left[22 + \log(\gamma(\gamma-1)(\gamma^2-1)) - 1.695\left(\frac{\gamma^2-1}{\gamma^2}\right) - \frac{1.39}{\gamma}\right] \tag{5.50}$$

5.2.6.5 Proton-Proton Cooling

For Galactic protons, inelastic scattering off of interstellar gas provides the strongest cooling mechanism. The hard *pp* interaction produces many seondary particles including pions, etas, and many additional light mesons. Almost 100% of the pi_0 particles decay into gamma-ray photons, while the charged pions decay weakly to neutrinos and secondary leptons. The heavier mesons have significant branching fractions to baryonic states and eventually inject secondary protons and antiprotons into the Galaxy. The total *pp* scattering cross-section σ_{pp} is nearly energy independent, making the cooling timescale also energy independent.

$$\tau_{pp} = n_0^{-1}(\sigma_{pp} f c)^{-1} = 5.3 \times 10^7 n_0^{-1} \text{ yr} \tag{5.51}$$

where f is the fraction of energy lost in a typical scatter and n_0 is the hydrogen number density in cm^{-3}.

Chapter 6

Radiation From Cosmic-Rays

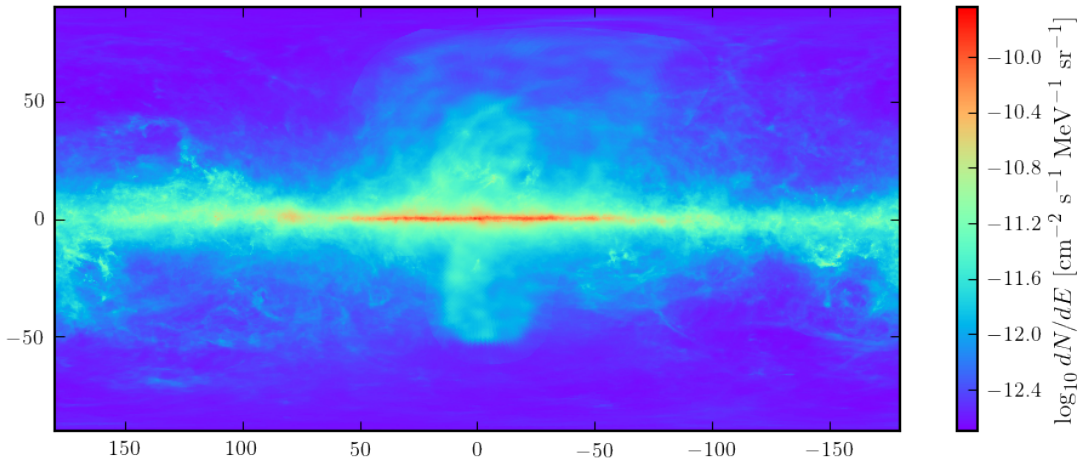

Figure 6.1: Model of diffuse Galactic gamma rays from the Milky Way at 22.8 GeV. The total gamma-ray emission is composed of hadronic cosmic-ray interactions with gas ($\pi^0 \rightarrow \gamma\gamma$) and leptonic interactions with the gas (bremsstrahlung) and low-energy radiation fields (inverse Compton scattering). Also clearly visible are the Fermi bubbles [21].

As high-energy cosmic-rays propagate the Galaxy, they emit radiation through four primary processes: Synchrotron, inverse Compton scattering, spallation (pi^0 decay), and bremsstrahlung. The latter three of these lie in the gamma-ray regime, as shown by

the composite Fermi diffuse model in Fig. 6.1, while the synchrotron emission typically peaks at radio frequencies for cosmic-ray electrons in the GeV-TeV regime. We review here the overall emisison picture for hadrons and leptons before diving into details of the gamma-ray spectrum calculations for each process. A detailed mathematical formulation of each process can be found in Ref. [304], although more recent calculations of pi^0 emission should be consulted as well (see Sec. 6.3).

We note also that the `Galprop` code provides a well tested C++ implementation of gamma-ray generation routines for a given CR spectrum, in addition to the most complete and accurate methods for secondary production. The `naima`[1] python package also provides implementations of each radiative process, as well as spectral fitting tools.

6.1 Hadronic Emission Overview

All cosmic-ray species are typically injected into the interstellar medium with a power-law spectrum and index around α which ranges from about 2-2.5 for first order Fermi processes above a few GeV. For protons, the, a single production mechanism dominates the gamma-ray spectrum due to the decay of neutral $\pi^0 \rightarrow \gamma\gamma$ processes after the high-energy protons interact with interstellar gas. The spectral energy distribution of gamma-rays from protons is shown in Figure 6.2 for several representative proton CR spectra. Note that the Galactic proton spectrum is very soft due to propagation through the Galaxy, where the injection index $\alpha \rightarrow \alpha + \delta$ after propagation (δ is the energy dependence of diffusion). However, the spectrum may be substantially harder if

[1] http://naima.readthedocs.io/en/latest/

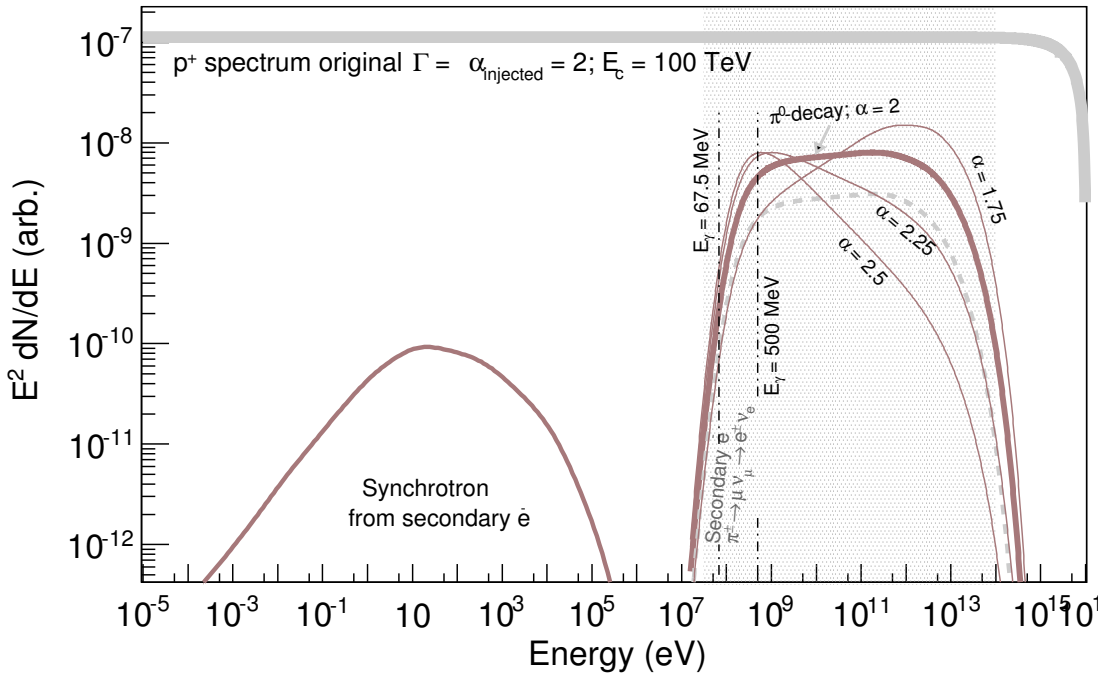

Figure 6.2: Spectral energy distribution of accelerated protons (power-law index $\alpha_{\rm injection} = 2.0$ and cutoff at 100 TeV) and gamma rays resulting from inelastic collisions with interstellar material. The dominant emission into photons is via the decay $\pi^0 \rightarrow \gamma\gamma$ (solid brown). As can be seen, the gamma-ray spectrum follows the parent protons spectrum rather closely in the mid-energy range and the high-energy cutoff region. For all proton indices the low-energy turnover is a characteristic feature of the pion-decay emission. Also shown is the spectrum of electrons resulting from the inelastic *pp*-interactions via the decay chain $\pi^{\pm} \rightarrow \mu + \nu_{\mu} \rightarrow e^{\pm}\nu_e$ (dashed gray). For the synchrotron emission from these so-called secondary electrons a source with age $t_{\rm age} = 1000$ yrs, and B = 30μG has been assumed. The shaded gray region shows the sensitive range of current gamma-ray detectors (Fermi-LAT, IACTs). Reprinted with permission from Ref. [7]

we are looking at freshly injected cosmic-rays, for example, near supernova remnants. The π^0 emission follows the parent proton spectrum very closely above 1 GeV for and peaks near 400 MeV in SED space for $\alpha \gtrsim 2$, known as the "pion-bump". As discussed in Sec. 5.2.6, cooling timescales play a minor role, with $\tau_{pp} > 10^7$ years for gas densities $n \approx 1{\rm cm}^{-3}$. Of the incident proton energy, approximately $\kappa = .17$ is converted into

gamma-rays. For $\alpha = 2.1 - -2.7$, the gamma-ray emissivitiy is $q_\gamma(> 100MeV) \approx .5 \times 10^{-13}\mathrm{s}^{-1}\mathrm{erg}^{-1}\mathrm{cm}^3(\mathrm{H-atom})^-1$ leading to an integrated flux at Earth of about [7]

$$F_\gamma(E_\gamma > 100\mathrm{MeV}) = 4.4 \times 10^{-7} \epsilon_{\mathrm{CR}} d_{\mathrm{kpc}}^{-2} \frac{n_0}{1\mathrm{cm}^{-3}} \mathrm{cm}^{-2}\ \mathrm{s}^{-1} \tag{6.1}$$

where $\epsilon \approx 0.1$ is the fraction of the supernovae energy (10^{51} erg) injected into cosmic-ray protons, d_{kpc} is the distance to a source, and n_0 is the number density of hydrogen atoms in the ISM.

In the rest frame of the π^0, the two γ's are kinematically constrained to have equal energy $E_\gamma = m_{\pi^0}/2 = 67.5$ MeV. After boosting back to the Galactic frame, the differential number-density dN/dE_γ is log-symmetric about 67.5 MeV.

Importantly, π^0 emission is correlated with the distribution of gas in the Galaxy as shown in Figure 6.3. Electron bremsstrahlung is also gas correlated, but is substantially lower in intensity. This ratio can be estimated as $q_\gamma^{\mathrm{Br}}/q_{\pi^0} \sim R3\tau_{pp}/\tau\mathrm{Br} = 4R$ where $R \approx 0.1$ is the ratio of electron to proton CRs.

Secondary electrons from the decays of $\pi^\pm$ will also emit synchrotron emission although this is typically about two-orders of magnitude lower than synchrotron from primary electrons.

6.2 Leptonic Emission Overview

The leptonic gamma-ray spectrum is more interesting, and carries several unique spectral features due to the cooling of electrons. There are three relevant emission pro-

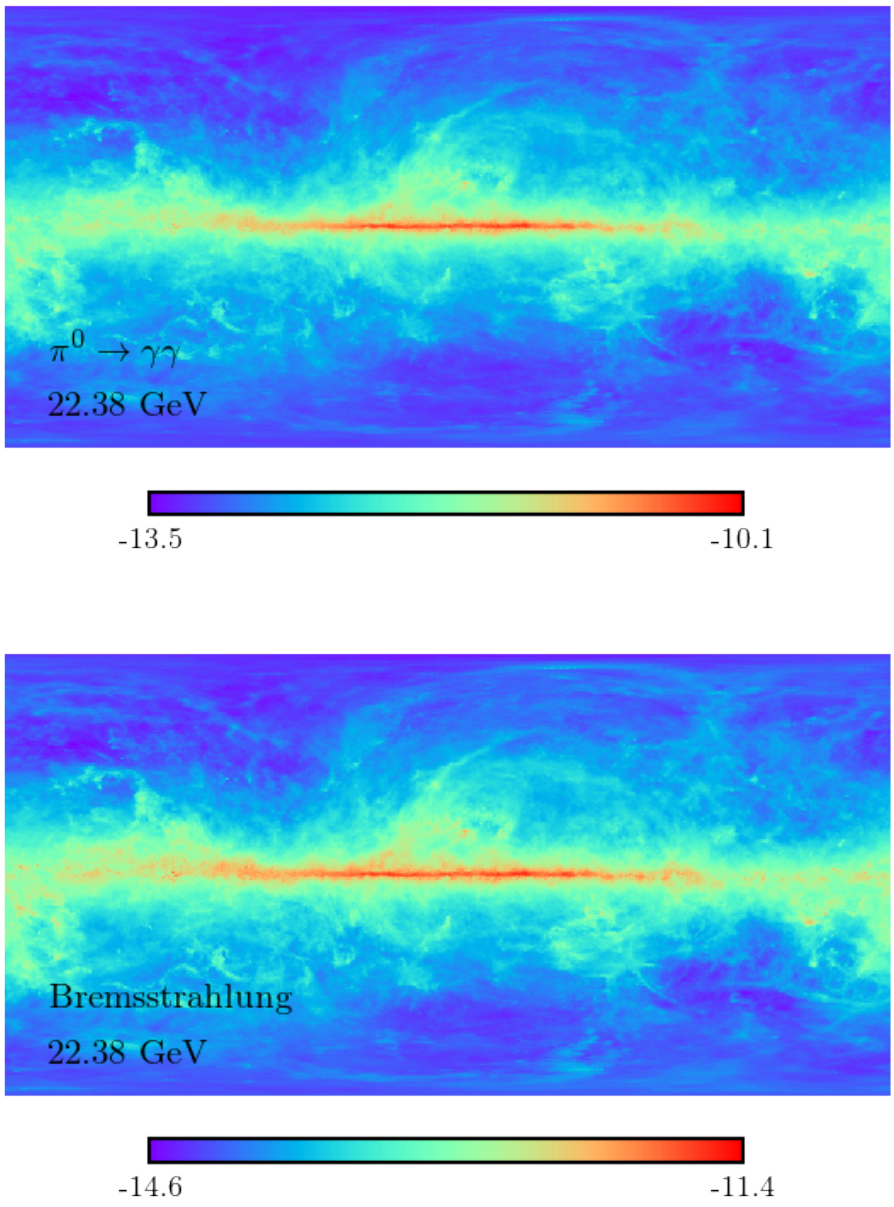

Figure 6.3: Galprop model of diffuse Galactic $\pi^0 \rightarrow \gamma\gamma$ (left) and electron bremsstrahlung emission (right) from the Milky Way at 22.8 GeV. Units are the same as Fig. 6.1 and on a $\log_{10}$ scale.

cesses: synchroton, inverse Compton scattering (ICS), and bremsstrahlung. Beginning with an $\alpha = 2.0$ injection spectrum, let us examine the behavior of each, which are

shown in Fig. 6.4.

The propagated spectrum of electrons is a flat $\Gamma = \alpha = 2$ power law up to about .01-1 TeV – depending on the environmentally dependent cooling rate and age – at which point the quadratic (in energy) losses b steepen the electron spectrum to $\Gamma = \alpha + E/b = 3$.

The synchrotron spectrum from a population of mono-energetic electrons has a characteristic frequency of [304, 7]

$$v_{\rm max} \approx \ 0.29 v_c \approx 4.6{\rm MHz}\ E^2_{\rm GeV} B_{\mu\rm G} \approx .02\ {\rm eV} B_{\mu\rm G} E^2_{\rm TeV}. \tag{6.2}$$

For a power-law electron spectrum, the synchrotron spectrum is given by

$$\Gamma_{\rm sync} = (\alpha + 1)/2. \tag{6.3}$$

Thus, the synchrotron spectrum will break by $\Delta\Gamma_{\rm sync} = 0.5$ due to the electron cooling turnover discussed above. At very high energies, catastrophic losses of electron energies occur due to Klein-Nishina effects, and the synchrotron spectrum drops off very rapidly above 10-100 MeV.

At gamma-ray energies, inverse Compton scattering of high energy electrons with the interstellar radiation field becomes relevant. This ISRF is composed of three components: the CMB radiation, dust-reprocessed starlight in the far infrared (FIR) (which often includes the NIR contribution too), and starlight in the optical regime

(Opt.). These have typical photon energies

$$E_{\rm CMB} = 10^{-3}\ {\rm eV} \tag{6.4}$$

$$E_{\rm FIR} = 10^{-2}\ {\rm eV} \tag{6.5}$$

$$E_{\rm NIR} = 10^{-1}\ {\rm eV} \tag{6.6}$$

$$E_{\rm Opt} = 1\ {\rm eV} \tag{6.7}$$

and the intensity of the FIR and optical fields vary strongly depending on the location in the Galaxy, predominantly in the GC region where massive stellar clusters produce a several thousand fold enhancement to the optical and FIR energy densities.

In the Thompson regime (below $E_e \sim 1$ TeV), an electron scattering off of a blackbody peaking at energy $E_{\rm ph}$ produces a gamma-ray spectrum peaking at

$$E_{\rm IC} = 5\ {\rm GeV} \left(\frac{E_{\rm ph}}{1\ {\rm eV}}\right) \left(\frac{E_e}{1\ {\rm GeV}}\right)^2. \tag{6.8}$$

The electron cooling from IC and synchrotron losses produces an ICS spectrum which $\Gamma_{\rm ICS} = (\alpha+1)/2 \approx 1.5$, with a steep turnover to $\Gamma_{\rm ICS} = (\alpha+1) \approx 3$ in the Klein-Nishina regime. In Figure 5.4 these spectra are shown, with the KN turnover also highlighted. Notably, this emission is correlated with the electron density times the ISRF density, which is much thicker than interstellar Gas. Thus ICS emission is responsible for most of the high-latitude gamma-ray emission in the Milky Way, competing with local gas correlated emission that appears at high latitudes due to its proximity to us (e.g. from the Gould Belt). The ICS emission from CMB, FIR, and Optical photons is shown in Fig. 6.5.

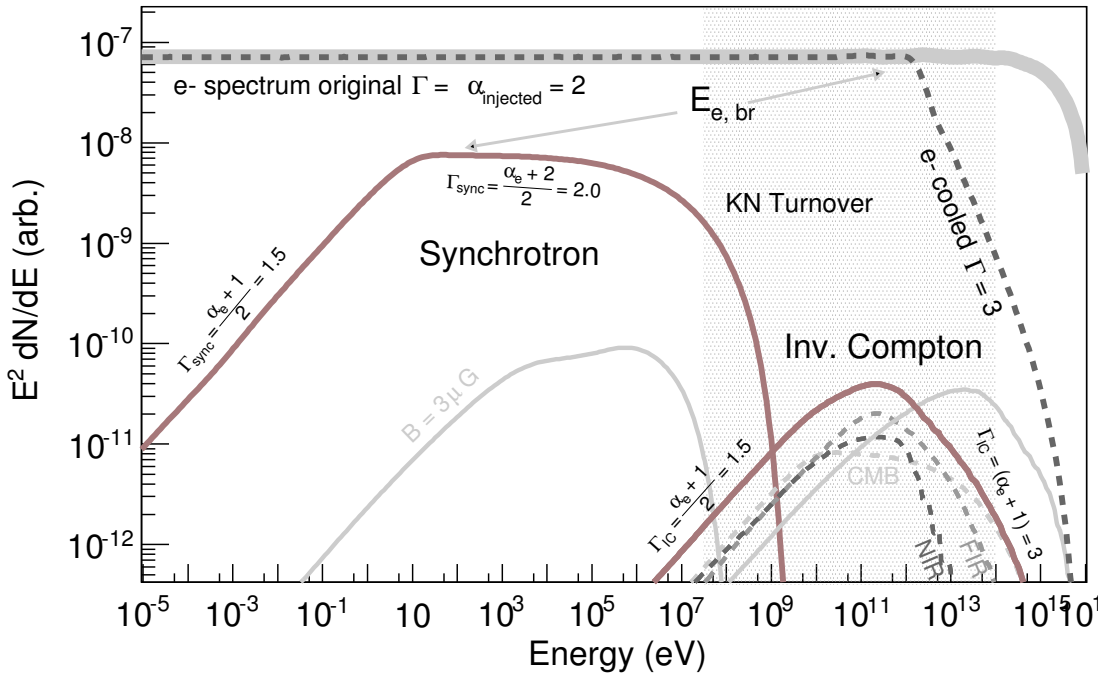

Figure 6.4: Spectral energy distribution of electrons at injection (light gray with $\alpha_{\rm injection} = 2.0$) and the steady state including cooling (dashed dark gray) for a source with age $t_{\rm age} = 1000$ yrs, $B = 100\mu$G, for a scenario in the inner 100 pc of our Galaxy. The cooling break in the electron spectrum at ~ 1.2 TeV is apparent in the steady-state electron distribution (dashed dark gray), in the synchrotron spectrum and in the IC spectrum. Also apparent is the turnover in the spectra at even higher energies due to KN cooling which incur catastrophic losses on the electrons. The case for a much lower B-Field of 3μG is also shown in light gray. The shaded gray region shows the sensitive range of current gamma-ray detectors (Fermi-LAT, IACTs). Reprinted with permission from Ref. [7]

In addition to these radiative processes, high-energy electrons will also emit non-thermal bremsstrahlung as they interact with the coulomb fields of ions and neutral atoms. This emission becomes significant at low energies, and due to the relatively small energy dependence of the interaction cross-section, follows the parent electron spectral index closely. Because the electron spectrum steepens quickly in the KN turnover, the bremsstrahlung emission is very soft above 1 GeV and is in any case suppressed by

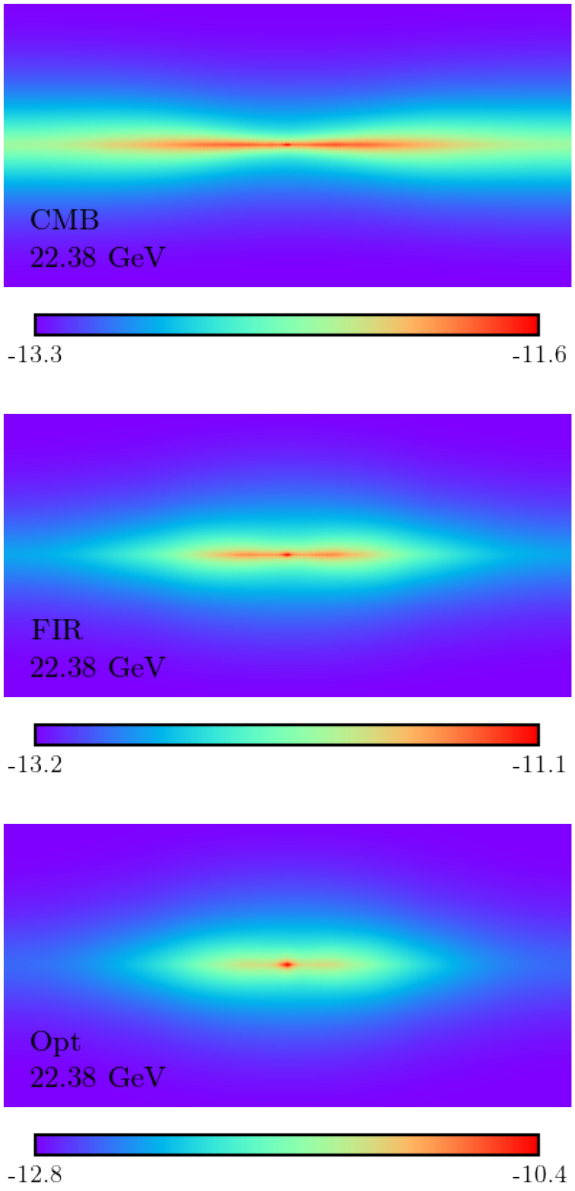

Figure 6.5: Galprop model of inverse Compton emission from the Milky Way at 22.8 GeV from each of the three ISRF components. Units are the same as Fig. 6.1 and on a $\log_{10}$ scale.

approximately 1 order of magnitude relative to the pi^0 contribution at 1 GeV. This emission is gas correlated, and is highly degenerate (morphologically) with the hadronic

gamma-ray emission.

6.3 γ-rays from π^0 decay

The γ-ray emissivity $q_\pi(E_\pi)$ of secondary neutral pions produced through inelastic scattering of cosmic-ray protons on interstellar hydrogen is given by the following expression:

$$q_\gamma(E_\gamma) = 2\int_{E_{\rm min}}^{\infty} \frac{q_\pi(E_\pi)}{\sqrt{E_\pi^2 - m_\pi^2}} {\rm d}E_\pi, \tag{6.9}$$

where $E_{\rm min} = E_\gamma + m_\pi^2/(4E_\gamma)$ and the neutral pion production term,q_π, is defined by,

$$q_\pi(E_\pi) = 4\pi n_{\rm H} \int_{m_{\rm p}}^{\infty} j_{\rm p}\left(\sqrt{E_{\rm p}^2 - m_{\rm p}^2}\right) \frac{{\rm d}\sigma_{{\rm pH}\rightarrow\pi^0}({\rm E_p}, {\rm E}_\pi)}{{\rm d}E_\pi}\ {\rm d}E_{\rm p}, \tag{6.10}$$

with $n_{\rm H}$ the target hydrogen gas density, $\sigma_{{\rm pp}\rightarrow\pi^0}$ the inclusive π^0 production cross section (p + p$\rightarrow$ π^0+ anything), and $j_{\rm p}(p_{\rm p})$ the cosmic-ray proton density as a function of the proton momentum, following recent results from Ref [305]. Note that many references use instead a proton spectrum following $E_{\rm tot}$ rather than $p_{\rm p}$ or kinetic energy $T_{\rm p}$. Although these asymptote to each other at $E \gg m_{\rm p}$, the assumption can have a non-negligible impact on the low-energy γ-ray spectrum for soft *proton* spectra $\Gamma \gtrsim 2.5$, where the low-energy protons contribute heavily. Since the cross-section falls off very rapidly below 1 GeV, this is negligible for the harder spectra of interest here. Remarkably, this cross-section is still not known to better than $\pm$10-20% near the pion production threshold of $T_{\rm p} = 280$ MeV up to a few GeV, resulting in an important systematic uncertainty when using the γ-ray spectra to probe the underlying spectrum of nuclear cosmic-rays, or *vice*

versa as is the case here. Until improved laboratory measurements are made available this remains a limiting factor in determining the global spectrum of diffuse Galactic protons using Fermi-LAT photon data [306, 307]. In this Appendix we demonstrate the systematic variations between four common models of the pion emissivity.

The first model we consider is the simple δ-function approximation for the cross section[302] as parametrized in Ref. [308]; we then consider the three numerical models implemented in `Galprop`, which use cross-sections from Kamae et al (2006) [309], Dermer (1986) [310], and a combination model of Dermer (1986) near threshold and interpolated to Kachelrieß & Ostapchenko (2013) at higher energies [311], hereafter DKO.

The simplest estimate of the pion emissivity is obtained in the delta-function approximation, where proton-proton collisions are assumed to produce only pions and hence the well known inelastic cross-section is used as a proxy for the inclusive π^0 cross section and

$$q_\pi(E_\pi) = \frac{n_{\rm H}}{\kappa_\pi}\sigma_{\rm pp}^{\rm inel}\left(m_p + \frac{E_\pi}{\kappa_\pi}\right)\; j_{\rm p}\left(\sqrt{\left(m_p + \frac{E_\pi}{\kappa_\pi}\right)^2 - m_{\rm p}^2}\right), \tag{6.11}$$

with cosmic-ray proton density $j_{\rm p}$, and with $\kappa_\pi \approx 0.17$ the mean fraction of the impinging proton kinetic energy transferred to the secondary π^0 per collision [308]. This has been adjusted empirically to provide better excellent agreement with Monte Carlo simulations above a few GeV [312]. We take the following approximation for the proton-proton inelastic cross section [312] in millibarnes:

$$\sigma_{\rm pp}^{\rm inel}(E_{\rm p}) \approx (34.3 + 1.88L + 0.25L^2)\left(1 - \left(\frac{E_{\rm th}}{E_{\rm p}}\right)^4\right)^2, \tag{6.12}$$

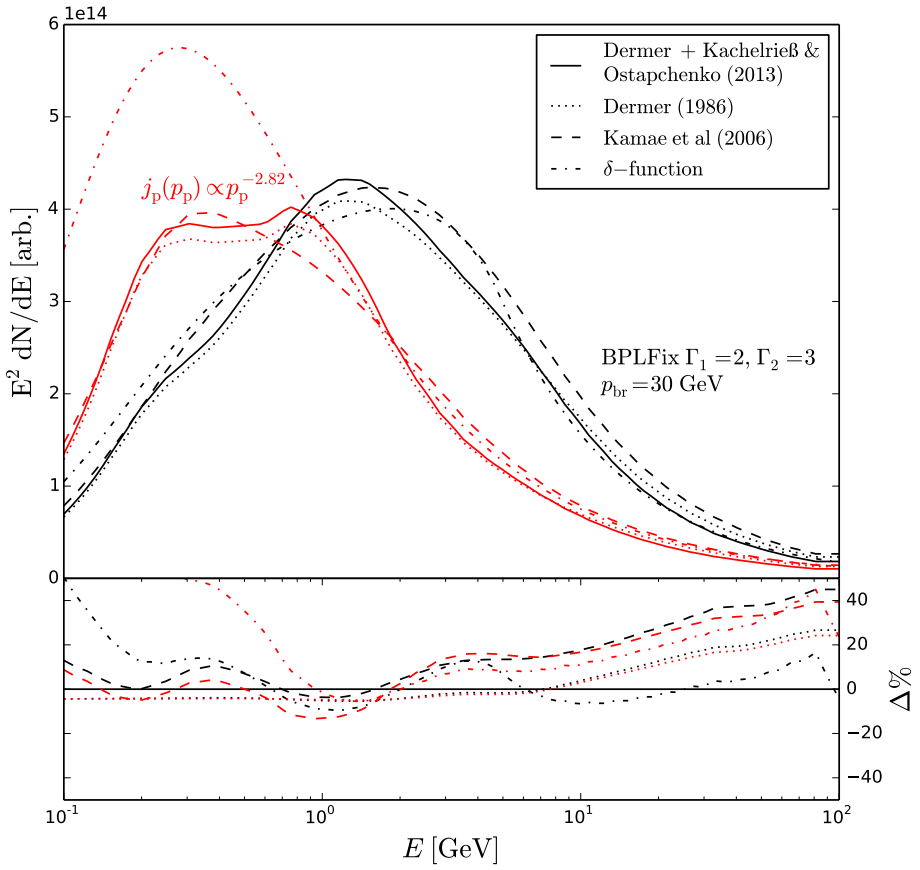

Figure 6.6: Model variations in the γ-ray spectral energy distribution for cosmic-ray proton spectra following (in black) a broken power-law spectrum with $\Gamma_1 = 2, \Gamma_2 = 3$, and $p_{\rm br} = 30$ GeV (see Eq. (8.11)) and, in red, a flat power-law of index 2.82 representative of the 'sea' of Galactic protons.

where $L = \ln(E_{\rm p}/1\ {\rm TeV})$ and $E_{\rm th} = m_{\rm p} + 2m_\pi + m_\pi^2/(2m_{\rm p})$ is the pion production threshold, below which the inelastic cross section is zero. This provides a reasonable estimate for many cases, but as can be seen in Figure 6.6, it does not provide an adequate representation of the near-threshold behavior ($T_{\rm p} \lesssim 1$ GeV). Besides integrating over the full range of proton energies (as opposed to approximating with a δ-function) the core

difference between this simplified approach and the more sophisticated calculations is a detailed parametrization of the inclusive production cross section and pion multiplicities at low energies, and sometimes Monte Carlo interpolation at high energies.

Below a few GeV, light hadronic states decaying through π^0's provide the main contribution, primarily from the $\Delta(1232)$ resonance. As the proton energy increases, heavier resonances become more important as well as secondary photons from η decays. The Dermer model includes the $\Delta(1232)$ using Stecker's isobar model [303] at low-energies with linear interpolation between 3 and 7 GeV to the scaling model of Stephens and Badhwar [313]. We note that this model relies on cross-sections originally compiled by Stecker in Ref. [314]. At higher energies, however, this model violates the Feynman scaling hypothesis, where $E\mathrm{d}\sigma/\mathrm{d}^3\mathrm{p}$ becomes independent of the center of mass energy s for $s \gg m_\mathrm{p}^2$. Kamae et al [309] instead relies on parameterizations of Monte Carlo simulations in addition to corrections for the $\Delta(1232)$, the $N(1600)$ cluster of resonances, diffractive processes, non-scaling effects, and scaling violations which provides a better fit to high-energy observations than Dermer. The mixed DKO [311] model used in Sec 8.2 combines simulation/parametrization approaches by interpolating to results from event generator QGSJET-II at energies above 30 GeV providing a better fit to available high-energy collider data. When fitting a proton spectrum to γ-ray data, Dermer provides the best fit below 1 GeV, but underestimates the higher-energy spectrum. Kamae et al has the opposite behavior, matching above 1 GeV, but overproducing photons below. The mixed model provides good fits in both regimes, and hence is the model of choice here.

In the top panel of Figure 6.6 we show in black the γ-ray spectrum resulting from the fixed broken power-law (BPLFix) model of Eq. 8.11 with $\Gamma_1 = 2, \Gamma_2 = 3$, and $E_{\rm br} = 30$ GeV as well as the background Galactic protons in red following a flat power law with index $\Gamma = 2.82$ for each of the four models. Note that the relative normalization for each of the `Galprop` models is correct while the δ-function case renormalized to match DKO at 2 GeV. In the lower panel we show the fractional variation in the spectral energy distributions of each model with respect to DKO. The two most important factors for an analysis of the Galactic center excess are the position and width of the spectral peak. The models which include the detailed low-energy characterization of Dermer produce the sharpest peak while that of Kamae et al is slightly broadened and peaks at 50% higher energy for the BPLFix model. This implies that the π^0 spectrum using Kamae et al requires slightly softer low and high-energy spectral indices than those of Dermer in order to match the GCE with a broken power law proton spectrum. Of general interest, but less importance to our analysis is the significant variation in the predicted Galactic background spectrum, where two distinctive peaks are seen in Dermer models compared to only one in the other two. It is clear that the δ-function approximation does not accurately characterize the spectrum below ≈ 1 GeV, and is hence not suitable for calculating spectra over GCE energies.

6.4 γ-rays from Inverse Compton Scattering (ICS)

Relativistic electrons transfer energy to photons in a process known as inverse Compton scattering. The ICS cross-section can be calculated from elementary QED.

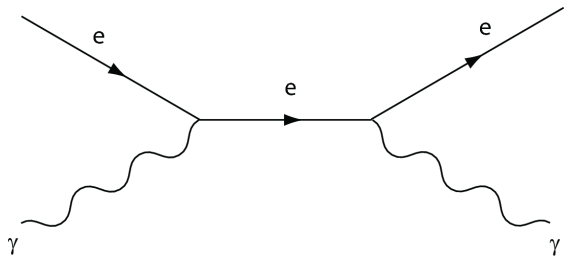

Figure 6.7: Feynman Diagram for inverse Compton scattering. The incoming electron has high energy while the incoming electron is a low energy photon from the interstellar radiation field. The outgoing electron loses has only 10-30% of its initial energy while the outgoing photon is a high-energy gamma-ray (with $E \sim 70 - 95\%$ of the initial electron energy).

The angle averaged total cross section depends only on the incoming photon energy E_{ph} and electron energy E_e and is given by [302]

$$\sigma_{\rm IC} = \frac{3\sigma_T}{8\kappa_0}\left[\left(1 - \frac{2}{\kappa_0} - \frac{2}{\kappa_0^2}\right)\ln(1+2\kappa_0) + \frac{1}{2} + \frac{4}{\kappa_0} - \frac{1}{2(1+2\kappa_0)^2}\right], \tag{6.13}$$

where $\kappa_0 = E_{ph}E_e$, with both energies in dimensionless units of $m_e c^2$. In the non-relativistic case $\kappa_0 \ll 1$ this reduces to $\sigma_{\rm IC} \approx \sigma_T(1 - 2\kappa_0)$. For $\kappa \gg 1$ we are in the ultra-relativistic Klein-Nishina regime where

$$\sigma_{\rm IC} \approx 3/8\ \sigma_T \kappa_0^{-1} \ln(4\kappa_0). \tag{6.14}$$

For a monochromatic bath of electrons in an isotropic photon bath, we can write the spectrum of outgoing gamma rays as

$$\frac{dN(E_\gamma)}{dE_\gamma} = \frac{3\sigma_T}{4E_{ph}E_e^2}\Bigg(1 + \frac{z^2}{2(1-z)} + \frac{z}{b(1-z)} - \frac{2z^2}{b^2(1-z)^2} + \frac{z^3}{2b(1-z)^2} - \frac{2z}{b(1-z)}\ln\left(\frac{b(z-1)}{z}\right)\Bigg), \tag{6.15}$$

where $b = 4\kappa_0$ and $z = E_\gamma/E_e$.

For a power-law electron spectrum with index α scattering off of a monoschromatic photon bath, this produces a power-law gamma-ray spectrum with index $\Gamma = (\alpha+1)/2$ in the Thompson regime ($4E_{ph}E_{\gamma} \ll 1$) turning over to $\Gamma = (\alpha+1)$.

More generally, this expression and Eqn.(6.14) can be integrated against the target radiation field energy density and electron spectrum to provide a full gamma-ray emissivity.

$$\frac{dq_{\rm ICS}(\vec{r}, E_\gamma)}{dE_\gamma} = c \iint n_{ph}(\vec{r}, E_{ph}) n_e(\vec{r}, E_e) \frac{d\sigma_{\rm IC}(E_e, E_{ph}, E_\gamma)}{dE_\gamma} dE_e \; dE_{\rm ph} \tag{6.16}$$

where n_{ph} and n_e are the differential ISRF and electron number densities. This emissivity must then be integrated along the line of sight and divided by 4π to obtain the flux density. Note that for diffuse sources, the $1/d^2$ reduction in flux is cancelled due to the increasing volume of the solid angle element.

There is little reason to do this analytically for anything other than simple power-law or blackbodies for the respective spectra. Galprop provides numerical codes for such an integration. Realistic target radiation fields for the Milky Way are discussed in Sec. 7.4. Even more generally, one may wish to take into account a fully anisotropic treatment of ICS [315].

A useful approximation for the energy of the outgoing gamma-ray is

$$E_{\rm IC} = 5 \text{ GeV} \left(\frac{E_{\rm ph}}{1 \text{ eV}}\right) \left(\frac{E_e}{1 \text{ GeV}}\right)^2 . \tag{6.17}$$

.

6.5 γ-rays from Electron Bremmstrahlung

The differential cross-section for an electron of energy E_e to produce a bremsstrahlung gamma-ray with energy E_γ is given by [261]

$$\frac{\mathrm{d}\sigma_i(E,E_\gamma)}{\mathrm{d}E_\gamma} = \frac{3\,\alpha_{\rm em}\sigma_T}{8\pi\,E_\gamma}\left\{\left[1+\left(1-\frac{E_\gamma}{E}\right)^2\right]\phi_1^i - \frac{2}{3}\left(1-\frac{E_\gamma}{E}\right)\phi_2^i\right\}, \tag{6.18}$$

where $\phi_{1,2}^i$ are scattering functions dependent on the properties of the scattering system.

For a completely ionized gas plasma with charge Z

$$\phi_1^{\rm ion}(E,E_\gamma) = \phi_2^{\rm ion}(E,E_\gamma) = 4(Z^2+Z)\left\{\log\left[\frac{2E}{m_e\,c^2}\left(\frac{E-E_\gamma}{E_\gamma}\right)\right] - \frac{1}{2}\right\}, \tag{6.19}$$

For neutral atomic matter the scattering functions have a more complicated dependence, but are constant in the relativistic limit of interest.

$$\begin{aligned}
\phi_1^{\rm H} &\equiv \phi_{1,\rm ss}^{\rm H} = 45.79,\\
\phi_2^{\rm H} &\equiv \phi_{2,\rm ss}^{\rm H} = 44.46,\\
\phi_1^{\rm He} &\equiv \phi_{1,\rm ss}^{\rm He} = 134.60,\\
\phi_2^{\rm He} &\equiv \phi_{2,\rm ss}^{\rm He} = 131.40,\\
\phi_{(1,2)}^{\rm H_2} &\simeq 2\,\phi_{(1,2),\rm ss}^{\rm H}.
\end{aligned} \tag{6.20}$$

The subscript $_{\rm ss}$ in this notation refers to the fact that this regime is usually called 'strong-shielding' because the atomic nucleus is screened by the bound electrons and the impinging $e^\pm$ have to force the shield.

Now we the emissivity is given by

$$\frac{dq_{\rm brem}(vecr,E_\gamma)}{dE_\gamma} = c\sum n_i(\vec{r})\int n_e(\vec{r},E_e)\frac{d\sigma_i(E_e,E_\gamma)}{dE_\gamma}dE_e \tag{6.21}$$

where n_i is the gas or ion density for species i and n_e is the differential electron number densities. This has units of $\mathrm{cm}^3/\mathrm{s}/\mathrm{GeV}$.

6.6 Synchrotron from High Energy Electrons

The synchrotron power (in erg s^{-1} Hz^{-1}) emitted in a certain frequency ν by an isotropic distribution of relativistic electrons with energy E in a uniform magnetic field is [261]

$$\mathcal{P}_{\mathrm{syn}}(\nu, E, \alpha) = \sqrt{3}\,\frac{e^3\,B\sin\alpha}{m_e\,c^2}F(x) \tag{6.22}$$

where

$$x = \nu/\nu_c', \qquad \nu_c' = \frac{1}{2}\nu_c \sin\alpha, \qquad \nu_c = \frac{3}{2\pi}\frac{e}{m_e c}B\gamma^2.$$

Here B is the strength of the magnetic field and α the angle between the line of sight and the magnetic field direction.

The synchrotron kernel $F(x)$ is

$$F(x) = x\int_x^\infty K_{5/3}(x')dx'$$

where K_n is the modified Bessel function of the second kind of order n. For a randomly oriented magnetic field the synchrotron power must be averaged over the pitch angle α:

$$\mathcal{P}_{\mathrm{syn}}(\nu, E) = \frac{1}{2}\int_0^\pi d\alpha\,\sin(\alpha)\,\mathcal{P}_{\mathrm{syn}}(\nu, E, \alpha) \tag{6.23}$$

which in the relativistic limit is equal to

$$\mathcal{P}_{\rm syn}(\nu, E) = 2\sqrt{3}\,\frac{e^3\,B}{m_e c^2} y^2 \left[K_{4/3}(y)K_{1/3}(y) - \frac{3}{5}y\Big(K_{4/3}(y)^2 - K_{1/3}(y)^2\Big)\right] \qquad (6.24)$$

with $y = \nu/\nu_c$. Integrating this quantity over ν yields the total power emitted by an electron of energy E in all frequencies, which reproduces the synchrotron energy loss term.

Next, the synchrotron emissivity has to be computed convolving the synchrotron power in eq. (6.24) with the number density of electrons per unit energy $n_e(E_e, \vec{r})$ (in cm^{-3} GeV^{-1}).

$$q_{\rm syn}(\nu, \vec{r}) = \int dE_e\ \mathcal{P}_{\rm syn}(\nu, E)\, n_e(E_e, \vec{r}) \qquad (6.25)$$

Finally, the observable in which we are interested is the intensity $\mathfrak{I}$ of the synchrotron emission (in erg cm^{-2} s^{-1} Hz^{-1} sr^{-1}) from a certain direction of observation. This is obtained by integrating the emissivity of eq. (6.25) along the line-of-sight. Schematically:

$$\mathfrak{I}(\nu, b, \ell) = \int_{\rm l.o.s.} ds\, \frac{q_{\rm syn}(\nu, \vec{r})}{4\pi} \qquad (6.26)$$

where r corresponds to the position of the parameter s along the line of observation with galactic latitude b and longitude ℓ: $r(s, \ell, b), z(s, \ell, b)$ [2].

[2] $r(s, \ell, b) = s \sin b, z(s, \ell, b) = \sqrt{r_\odot^2 + s^2 - 2\, r_\odot \cos b \cos \ell}$.

Chapter 7

Precision Models of the Milky Way

7.1 Cosmic-Ray Source Distributions

Primary cosmic rays are believed to arise from *in situ* shock acceleration of supra-thermal precursor ions and electrons. While, in principle, the source distribution depends on the species of interest, in practice, the vast majority of primary Galactic cosmic-rays are believed to originate in supernova remnants (SNR) and the source distributions of all species are typically taken to be identical, neglecting the significantly smaller contributions from millisecond pulsars and pulsar wind nebulae.

Currently, primary source distributions used in diffuse γ-ray emission modeling assume cylindrical symmetry about the Galactic rotation axis. Specifically, they (i) are spatially smooth and continuous distributions, (ii) utilize isotropic injection spectra, and (iii) are not time-dependent. It is remarkable that despite these drastic simplifications, these models reproduce most properties of the locally measured cosmic-ray

nuclei and electron spectra as well as the global spectrum and intensity of γ-rays. This provides good evidence that, on average, the cosmic-ray density in the Galaxy is reasonably smooth and uniform. On finer scales, however, these simplifying assumptions break down, as is likely to be true in the case of the significant rise in the local positron spectrum above 10 GeV [316, 317], which might point toward stochastic discrete sources in the vicinity of the Solar System. Simple three dimensional source distributions containing logarithmic spiral arms [274, 275] and a central bar [318, 319] have already been investigated in the context of cosmic-ray data. However, local cosmic-ray measurements are not sensitive to sources at the Galactic center. Gamma-rays provide a more granular probe of the three-dimensional cosmic-ray density, and the observed abundance of diffuse residuals along the Galactic plane highlight not only the difficulty of foreground modeling, but also rich ecosystem of astrophysical environments whose cosmic-ray physics deviate from the Galactic norm, with the Galactic center being the ultimate example.

7.1.0.6 Pitfalls of Previous Source Distributions

As a starting point, we delineate the four traditional cosmic-ray source distributions used in `Galprop`. Each is intended to approximate the true azimuthally averaged surface density[1] of supernovae remnants and consist of either direct observations of SNR, Pulsars, or OB type stars. Most importantly for the current study, *three of them are strictly zero at the Galactic center, and all four underestimate the CMZ injection rate by more than a factor 20.*

[1] The surface density here is defined as the three dimensional density integrated over the height (z-axis) of the Galaxy.

The first distribution, 'SNR', uses the direct observation of 178 SNR [22], of which 36 had reliable distance estimates. Distances to the remaining SNRs were estimated by fitting a model of radio surface-brightness to apparent diameter. The Galaxy was then divided into 2 kpc wide radial bins which were used to fit a gamma function,

$$f(r) = \left(\frac{r}{r_\odot}\right)^\alpha \exp\left(-\beta \frac{r - r_\odot}{r_\odot}\right). \tag{7.1}$$

In all `Galprop` models, the surface density is assumed to fall off as $e^{-|z|/z_0}$ with $z_0 = 0.2$ kpc. Ref. [22] notes that although this form suggests the surface density is zero at $r = 0$, the data indicate that this is not correct, proposing an alternative functional form to describe the inner 16.8 kpc (this distribution is not used in `Galprop`).

$$f(r) = A \sin\left(\frac{\pi r}{r_0} + \theta_0\right) e^{-\beta r}. \tag{7.2}$$

Notably, the statistical and systematic uncertainties on the central 0-2 kpc bin used to fit these distributions are 75% of the nominal value.

Since this 1998 study, the number of known SNR has now grown by almost 50% as have the number of reliable distance indicators, the calibration of surface brightness-distance relations and the understanding of selection effects. New distributions [23] have very recently become available, which are much more concentrated toward the inner Galaxy. However, as the Eq. (7.1) parameterization is still used, the models again neglect the Galactic center and still remain unsuitable for studies of the Galactic center region.

The next two distributions rely on the observed surface density of pulsars from Lorimer et al [24, 25] and Yusifov & Küçük [9]. Pulsars offer both a factor 5-10 improved

statistics as well as improved distance estimates via radio pulse dispersion, which, used in combination with a model of the free electron density provide a more reliable estimate compared with the SNR surface-brightness/diameter relations. The Lorimer model attempts to derive the underlying pulsar population by matching surveys to Monte-Carlo simulations which include survey selection effects, free electron model uncertainties, and pulsar timing. Unfortunately, the radial distribution of pulsars is still very strongly correlated with the assumed free electron density [25]. In the inner 1 kpc, this leads to an uncertainty of more than a factor two, but contains a nonzero surface density at a $2-3\sigma$ level. However, the resulting data is nonetheless fit to the functional form of Eq. (7.1), which again artificially forces the distribution to zero at the Galactic center. Similarly, the Yusifov distribution [9] is a fitted gamma function (Equation 7.1). In this case, however, r and $r_\odot$ are shifted to $r \to r - r_{\rm off}$ in order to explicitly preserve a non-zero value at the origin. This is the *only* `Galprop` source distribution which is non-zero at the Galactic center. As we will see below, our improved cosmic-ray source models still imply more than an order of magnitude more sources within 500 parsecs of the GC with respect to the Yusifov distribution, suggesting that the innermost regions of the Galaxy have a cosmic-ray injection rate which is dramatically underestimated.

The final standard cosmic-ray source distribution is based on the observed surface density of 748 regions of OB star formation regions [26] and motivated by the long-standing connection [320, 321] between cosmic-ray sources (i.e. Type II supernovae) and OB star formation. Detection and distance measurements of these regions rely on CS($2 \to 1$) molecular line surveys. Near the Galactic center this method not only

suffers from poor kinematic resolution due to the vanishing LSR velocity, but CS($2 \rightarrow 1$) provides an unreliable tracer of massive star forming regions (SFR) in the unique GC environment [322]. For these reasons, the OB distribution of Ref. [26] explicitly indicates that their focus is on the Galactic disk and neglects all sources within 10° of the Galactic center. On its own, this distribution should therefore be excluded from future studies of the γ-rays at the Galactic center, though it is included here for completeness.

These traditional `Galprop` source distributions are plagued by two additional problems that are specific to the Galactic center region:

- The first issue is due to course binning and azimuthal averaging which blend together three structures: the CMZ, central bar, and gas depleted regions on either side of the bar (see Fig 7.1 bottom panel, discussed below). Radial surface densities are derived by binning counts of SNR, pulsars, or OB stars in bins of $\Delta r \approx 1 - 2$ kpc. Between the CMZ ($r \lesssim 250pc$) and the inner spiral arms (0.25-3 kpc) the Galaxy is largely devoid of gas and significant star formation. By area, the CMZ only represents 1-2% of the central radial bin and this depletion gap at larger radii strongly suppresses the resulting fitted source density at the GC. In reality, the source density should be sharply peaked over the CMZ and bar, whose semi-major axis is ∼3 kpc and oriented within 20-40° to our line of sight [200, 323, 199]. This results in a projected central density of cosmic-ray sources which is much higher than reflected in current models.

- Second, high extinction and distance uncertainties toward the GC make both se-

lection effects and systematic uncertainties large. For example, pulsar dispersion measures only provide a reliable distance estimate when the free electron density along the line of sight is well known, and distance measures to OB star forming regions require kinematic resolution.

We have shown that the radial distributions of all current tracers of cosmic-ray sources are systematically biased toward zero in the Galactic center, primarily due to the fact that these studies have focused on large scale properties of the disk, and thus choose parametrization that explicitly force the source density to zero at $r = 0$. Additionally, the inherent observational, systematic, and statistical difficulties surrounding the Galactic center region make the reliable determination of the cosmic-ray injection rate from each existing tracer difficult. Furthermore, axial symmetry in the Galaxy is strongly broken by the central bar and spiral arms. These issues prompt the exploration of alternative models of primary cosmic-ray source distributions which more realistically reflect the geometry of the Milky Way and resolve scales below 1 kpc.

7.1.0.7 Primary Cosmic-Rays from Star Forming H_2 Regions

The connection between supernova and star forming regions is well known [320, 321]. The high-mass OB stars which precede Type II supernovae evolve on time scales of 10-30 Myr and thus produce cosmic rays on timescales similar to the typical 17 ± 4 Myr lifetimes of giant molecular clouds [324]. We therefore expect that a significant fraction of cosmic-rays in the Galaxy are accelerated in the vicinity of collapsed molecular clouds, and that the rate of cosmic-ray injection should be approximately proportional

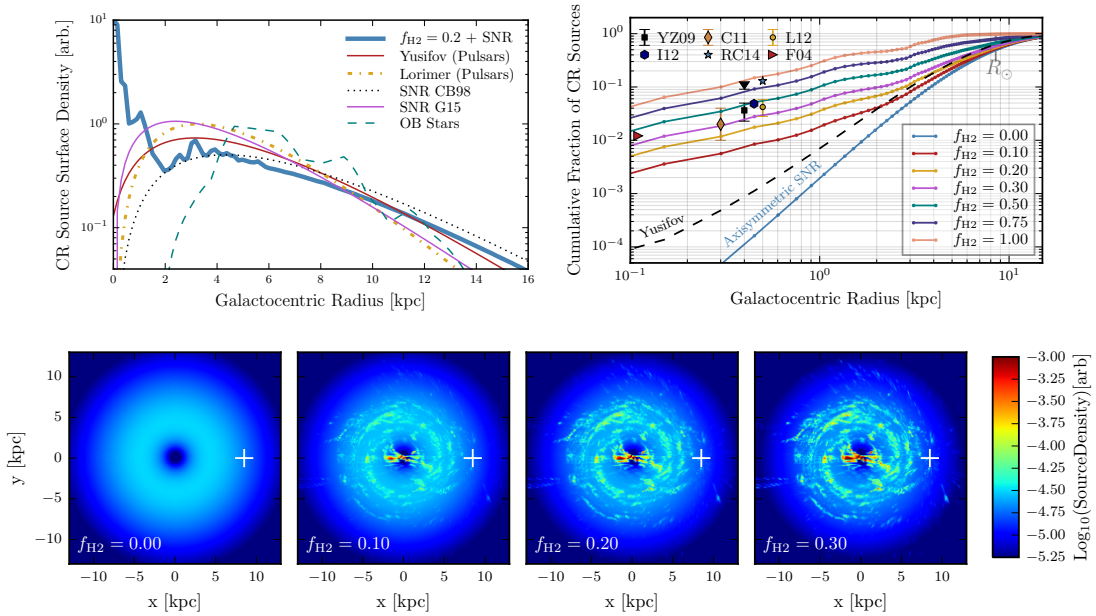

Figure 7.1: **Top Left:** The azimuthally averaged surface density of cosmic-ray source distributions used in this analysis. The distribution of supernova remnants is taken from Ref. [22] (SNR CB98) and Ref. [23] (SNR G15). The Yusifov [9] and Lorimer [24, 25] distributions use pulsars as a proxy for supernovae remnants while the cosmic-ray injection morphology tracing OB Stars is taken from Ref. [26]. The best fitting cosmic-ray injection rate globally and in the inner Galaxy (with no GCE template) is an admixture with 80% of cosmic-rays tracing SNR and 20% tracing the molecular gas density ($f_{\rm H2}$ =0.2) according to the star formation prescription presented in Section 7.1.0.7 (with $n_s = 1.5$ and $\rho_c = 0.1$ cm^{-3}). All distributions have dimension of length^{-2} and are normalized in arbitrary units to have the same integrated source count. Note that the H_2 distribution contains a strong Galactic bar and spiral arms making it highly azimuthally *asymmetric*, as seen in the bottom panel. **Top Right:** Cumulative source count versus radius from the Galactic center for a variety of $f_{\rm H2}$ values, as well as the axisymmetric SNR-CB98 and Yusifov pulsar models. Also shown are observations of the fraction of the Milky Way's total cosmic-ray injection rate produced within the CMZ as computed from either the average star formation rate within the CMZ (F04 [27], YZ09 including an upper limit [28], I12 [29], L12 [30]) relative to the total Galactic SFR of 1.65 ± 0.19 M$_\odot$ yr^{-1} [31], estimates of the fractional SNR occurring within the CMZ (C11 [32]), or the fraction of Wolf-Rayet stars contained in the CMZ (R14 [33]). The F04 marker should be placed at $r = 50$ pc, though this is below the resolution of our model. **Bottom:** The primary cosmic ray source distribution derived from our star formation model for increasing values of $f_{\rm H2}$ assuming a Schmidt index $n_s = 1.5$ and a critical density $\rho_c = 0.1$ cm^{-3}. The leftmost panel corresponds to the pure SNR [22] source model while the center panels are typical of models providing improved fits to the full-sky γ-ray data.

to the rate of star formation. Under these assumptions, we present a new primary source distribution based on high-resolution ($\sim$ 100pc) three dimensional density maps of H_2 [199] and a simple model of star formation based on the local volumetric gas density.

At the most basic level, star formation rates are thought to be governed by the gravitational collapse of these clouds, with a characteristic free fall-time $\tau_{\text{f.f.}} \propto (\rho_{\text{gas}})^{-1}$. In the absence of feedback the star formation-rate should then be proportional to the gas infall rate $\dot{\rho}_* \propto \rho_{\text{gas}}/t_{\text{f.f.}} \propto G^{1/2}\rho_{\text{gas}}^{3/2}$. This relation is known as the Schmidt law [325].

On the other hand, the Kennicutt-Schmidt law [325] encapsulates the empirical observation that the surface density of star formation scales as a power law in the gas surface density with index $1.4 \pm .15$[326]. If one assumes a constant scale-height for the gas disk, then the surface density and volume density are linearly proportional and the Kennicutt-Schmidt law is reproduced within 1σ error bars on the power law index. Of course, this scenario is highly oversimplified and one can devise much more advanced models, particularly in the context of full magnetohydrodynamic simulations [327] where not only thermodynamic quantities are known, but effects such as radiative feedback, cooling, turbulence, processes can be included [328, 329]. This can significantly alter the relationship between the Kennicutt-Schmidt (surface density) power-law index and the Schmidt (volume) index n_s. In addition to the power-law relationship between the local gas density and the star-formation rate, star-formation is observed to terminate below a critical gas density ρ_c. In our cosmic-ray simulations, we adopt a phenomenological prescription which reproduces these essential features, setting the cosmic-ray injection

proportional to

$$\dot{\rho}_{\rm CR} \propto \dot{\rho}_* \propto \begin{cases} 0 & \rho_{\rm H2} < \rho_c \\ \\ \rho_{\rm H2}^{n_s} & \rho_{\rm H2} \geq \rho_c \end{cases}, \tag{7.3}$$

where the Schmidt-index n_s is allowed to vary between 1 and 2, and $\rho_c = 0.1$ cm^{-3}, consistent with numerical simulations and theoretical expectations [327]. In Section 8.1.3.1, we will show that our results are relatively independent of ρ_c, except for extremely high values which are disfavored by our γ-ray results. One must also consider that the gas density in the Galaxy is evolving and may not reflect the distribution of cosmic-ray sources at past epochs. A benchmark diffusion rate for cosmic rays at the energies of interest for *Fermi* γ-ray studies is, $R_{\rm diff} = 2\sqrt{D_0 t} \approx 3$ kpc $t_{\rm Myr}^{1/2}$ (assuming $D_0 \sim 10^{28}$ cm^2 s^{-1}), where a few kpc is the scale at which non-axisymmetric structure in the Galaxy becomes washed out. A few Myr can also compared against the typical residence time of Galactic cosmic-ray protons, $10^7 - 10^8$ yr (depending on the height of the Galaxy's diffusion halo) [330, 331]. We should therefore expect that only a portion of cosmic rays should be represented by the current gas distribution and introduce a single additional parameter, $f_{\rm H2}$, that controls the fraction of cosmic-rays injected according to the star formation prescription. The remaining fraction (1-$f_{\rm H2}$) is then distributed according to the SNR-CB98 model, which provides the best fit of the four traditional primary source distributions.

Because H_2 molecules possess no permanent dipole moment, observations of the local H_2 density instead employ observations of a tracer molecule, chosen here to be the $^{12}{\rm CO}_{j=1\rightarrow0}$ transition line temperature, where the brightness temperature $W_{\rm CO}$

is related to the H_2 column density via a conversion factor $X_{\rm CO} = {\rm N_{H2}/W_{CO}}$. Theoretical and observational results indicate that $X_{\rm CO}$ is subject to significant spatial and environmental variations, especially in the centers of star forming galaxies in the local group [332]. For simplicity, and to reduce the computational complexity of iterating solutions, we will assume a uniform value of $X_{\rm CO} = 2 \times 10^{20}$ cm^{-2} (K km s^{-1})$^{-1}$ for propagation and cosmic-ray injection, while fitting the radial profile of $X_{\rm CO}$ in γ-ray fits (see sec. 8.1.2.3). There is reasonable evidence for a significant suppression of $X_{\rm CO}$ in the central few kpc [332, 40] and thus a suppression in H_2. In addition, CO does not provide an optimal tracer of H_2 in many cases. Nonetheless, it is the only H_2 related tracer with full sky coverage. These issues are discussed further in Appendix 8.1.8.1 and in several reviews [333, 334]. Here we will defer further study to future work, but one should keep in mind that the H_2 density in the inner few kpc of the Galaxy may be lower than modeled here, and thus our cosmic-ray injection rate may be suppressed. In contrast, we show that our best fitting models still slightly under-predict star formation in the CMZ relative to observations, a contradiction that points toward additional transport mechanisms near the Galactic center as explored in Section 8.1.5 and Appendix 8.1.8.1.

In the top-left panel of Figure 7.1 we show each of the cosmic-ray source distributions described above as well as the more recent SNR G15 parametrization [23]. We also show the azimuthal average of our proposed star-formation based model with 20% of sources distributed as $\rho_{H2}^{1.5}$ and 80% following SNR CB98. This dramatically enhances the source density within the central few hundred parsecs and generally concentrates more sources in the inner Galaxy. Additionally, this method adds significant structures

like the clearly visible spiral arm from 3-5 kpc and gas depleted region from 1-3 kpc. Our global and inner Galaxy analyses in Sec. 8.1.3 will reveal this source distribution be strongly preferred compared with any of the previous four models.

The top-right panel shows the cumulative source count for our new models as a function of Galactic radius, for different values of $f_{\rm H2}$, with the $f_{\rm H2} = 0$ case corresponding to the SNR model. Also shown is the Yusifov pulsar model which contains the largest central source density of the axisymmetric distributions. Three of the markers shown (F04, YZ09 and I12, L12) are estimates of the CMZ star formation rate averaged over periods of at least several Myr [27, 28, 29, 30]. These have then been divided by recent estimates of the total Galactic star formation rate [31] to yield the fractional SFR of the CMZ. For the C11 marker, Ref. [32] estimates the supernova rate of the CMZ to be $2\%^{+2}_{-1}$ of the Galactic total. Finally, the R14 marker estimates the fraction of Wolf-Rayet stars contained in the inner 500 pc of the Galaxy [33].

It is clear that the traditional models of primary cosmic-ray source injection *severely underestimate* the supernova rate of the inner Galaxy by at least a factor 20, while our best fitting proposed model ($f_{\rm H2} \approx 0.2$) lies just below the measured rate. In current diffusion models, the Galactic center region is highly calorimetric for both protons and electrons, and very high values of $f_{\rm H2}$ ($\gtrsim 0.50$) lead to over-luminous π^0 and inverse-Compton fluxes that are strongly disfavored by the γ-ray data. This seems to imply that cosmic-ray transport must be much more efficient near the Galactic center via some combination of strongly anisotopic diffusion driven by poloidal magnetic fields, or intense advective winds driven by either starbursts or activity from Sgr. A* [295, 39, 32].

We explore such scenarios in Sec. 8.1.4 and Sec. 8.1.5 below. In any case, only values of $f_{\rm H2} \approx 0.3 - 0.5$ are compatible with observation, providing significant prior evidence that the cosmic-ray injection rate may be even higher than most of the models explored below. In what follows, we will show that models with large values of $f_{\rm H2}$ are also favored by γ-ray observations toward the inner Galaxy ($|b| < 8^\circ$ and $|l| < 80^\circ$) and across the high-latitude sky ($|b| > 8\,{\rm deg}$).

We have implicitly assumed that the star-formation rate (in $M_\odot$ yr^{-1}) is proportional to the supernova rate. However, some observations of stellar clusters near the Galactic center [335, 336, 337] suggest that region may favor a top-heavy initial mass function (IMF). For IMF slopes $1 < \alpha < 2.35$, the number of Type II SNe per unit star-formation can increase by up to a factor ≈ 2, moving many of our SFR based lines upward. The RC14 marker is furthermore based on the relative population of Wolf-Rayet stars in the CMZ and Galactic disk. If the CMZ IMF has a slope α =1 (versus a Salpeter disk $\alpha = 2.35$), the number of Type II SNe per WR star is reduced by a factor 2, moving the marker down by $\sim$50%.

In the bottom panel of Figure 7.1 we show a top-down view of the Galaxy, plotting the surface density of cosmic-ray injection as $f_{\rm H2}$ is increased. The left panel corresponds to a pure SNR distribution, where the lack of cosmic-ray sources in the central Galaxy is readily apparent. As we increase $f_{\rm H2}$, the Galactic center becomes populated by CMZ sources while preserving the observed gas depleted regions above and below the Galactic bar ($|y| \lesssim 3$ kpc). The Galactic bar and spiral arms become visible as well as many of the largest giant molecular clouds which harbor star-formation.

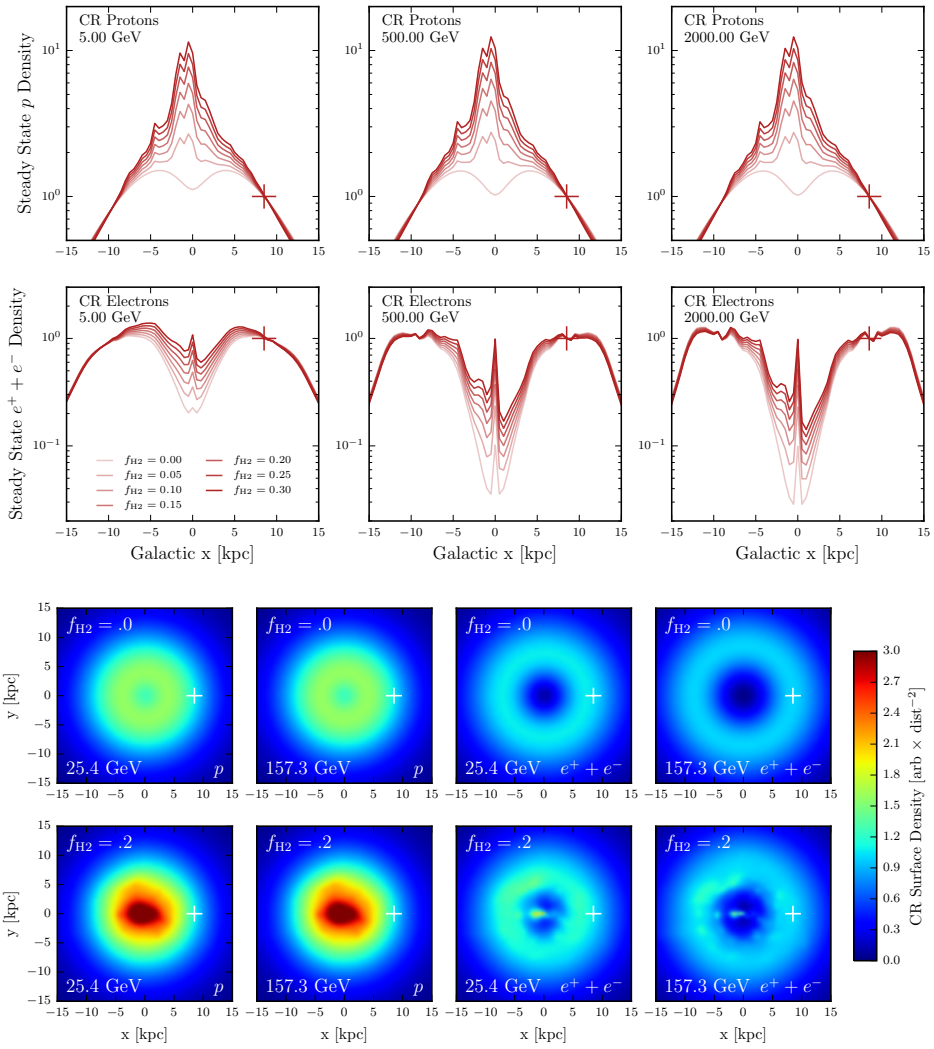

Figure 7.2: **Top**: The cosmic-ray proton and electron+positron fluxes, for several representative energies, along the line-of-sight to the Galactic center ($l = b = 0°$) after propagation in `Galprop`. Light to dark lines show increasing $f_{\rm H2}$. The distributions are normalized at the solar position $x = 8.5$ kpc, $y = 0, z \approx 0$ as indicated by a red '+' **Bottom**: Steady state cosmic-ray surface density for protons (left two columns) and electrons (right two columns) at representative energies for generating γ-rays over the Fermi-LAT band. The top row shows the case of $f_{\rm H2} = 0$ corresponding to the traditional axisymmetric SNR CB98 [22] source density while the bottom row shows the case of $f_{\rm H2} = 0.2$ which includes the proposed new source density model. A white '+' indicates the solar position, where the cosmic-ray densities have been normalized to unity.

In each case, azimuthal symmetry is strongly broken and the model introduces a wealth of new structure into the simulations.

These new cosmic-ray injection models strongly alter the steady-state (after diffusion, energy losses and secondary production are accounted for) cosmic-ray populations in the Milky Way. In the top panel of Figure 7.2, we show the resulting steady-state cosmic-ray density from `Galprop` along the line of sight to the Galactic center. For both protons and electrons, we show representative energies as $f_{\rm H2}$ is increased in our canonical diffusion model. In the bottom panel, we show the steady state surface density (integrated top-down through the Galactic disk) of cosmic-ray protons and leptons for a subset of cases with $f_{\rm H2} = 0, 0.2$ at 25 and 157 GeV.

Although much of the fine structure of the new source model is smoothed out by diffusion, the impact of an increasing $f_{\rm H2}$ on the final cosmic-ray density is dramatic. In the case of protons, the energy dependence is predictably very small from 5 GeV up to 2 TeV due to the logarithmic energy dependence of proton cooling times. The central source density is very strongly enhanced over the traditional SNR model ($f_{\rm H2} = 0$), which shows a significant 'deficit' in the central Galaxy. As was discussed in the above description of Figure 7.1, it is important to note that this does not represent a dramatic change in the total cosmic-ray power of the Galaxy due to the small relative volume of the inner Galaxy region. Also visible in the $f_{\rm H2} = 0.2$ case are features which break axial symmetry, including an elongated region of enhanced cosmic-ray density from the central bar and several large clouds to the north-west and south-east quadrants. More localized features are visible when looking at planar cross-sections of the Galaxy rather

than the full column density.

The distribution of leptons is more interesting. High energy electrons and positrons experience strong energy dependent ($dE/dt \propto E^2$) energy losses due to inverse-Compton and synchrotron cooling, which limit the diffusion radius to a size dependent on the local strength of the magnetic and interstellar radiation fields. These are strongest at the Galactic center and confine leptonic cosmic-rays on scales well below 2 kpc (under standard diffusion assumptions). The range of CRe densities at the Galactic center is stark, due to the peaked cosmic-ray injection sources within the CMZ and Galactic bar. For the SNR models, this region is systematically vacant due to the vanishing of cosmic-ray sources toward the Galactic center. Additional distinct clouds are also visible throughout the Galactic plane, particularly inside the solar circle.

The results above have two important implications for diffuse γ-ray emission modeling. First, many γ-ray analyses opt to use gas column-density templates as a proxy for the gas-correlated γ-ray emission. However, given that the cosmic-ray density can vary by much more than a factor of 2 along the line of sight (even in the $f_{\rm H2} = 0$ case) a simple gas column density template will *not* produce the correct emission morphology, and large residuals are likely to occur. Instead one should either allow for gas templates to vary in annuli around the Galactic center, or use a model of the cosmic-ray density along the line of sight to compute the full three-dimensional convolution of gas and cosmic-rays.

Secondly, one cannot arbitrarily increase the model's cosmic-ray density without over-brightening the gas-correlated emission from the disk. This 'cosmic-ray gradient

problem' is well known [84, 41, 40], and even traditional source+diffusion models require $X_{\rm CO}$ in the inner $\approx$ 2 kpc to be a factor 5 lower than in the disk. Our new source distributions exacerbate this problem and we find that plausible CMZ injection rates are not reconcilable with the range of $X_{\rm CO}$ measured in the centers of nearby spiral galaxies. Such issues can also be alleviated by efficient evacuation cosmic-rays from the inner few kpc via either enhanced anisotopic diffusion perpendicular to the disk or perhaps through high-velocity convective winds in the Galactic center (see Sections 8.1.4, 8.1.5, and Section 8.1.8.1).

An additional limitation of past and present models is that the spectrum of primary cosmic-ray injection is traditionally assumed to be homogeneous throughout the Galaxy, depending only on whether the injected particle is an electron or nuclear species. We emphasize that this is both theoretically and observationally known to be incorrect. Fermi measurements of several SNR [282, 283, 46, 284, 285, 286] expanding into dense molecular clouds provide direct evidence that cosmic-ray injection spectra at the energies of interest (1-100 GeV) can be very sensitive to environmental factors. Of particular importance at the Galactic center is the likely presence of ion-neutral damping [338, 279, 280, 281, 339]. When the upstream edge of supernovae shocks interacts with molecular clouds, ion-neutral collisions effectively damp a range of otherwise resonant Alfvén waves, severely deteriorating particle confinement within a slab of momentum space and steepening the spectral index of protons and electrons by precisely one. The energy break for this softening depends strongly on environmental parameters [279]. This mechanism was studied in detail in the context of the Galactic center

environment by two of the authors in Ref. [216], where it was shown that the corresponding π^0 emission can potentially reproduce the observed spectral features and intensity of the GCE. While we do test hardened CMZ injection spectra in Sec 8.1.5, we leave a detailed study of *broken* CMZ spectra to future work.

As a final note, we discuss the impact of our new source models on the predicted local cosmic-ray spectrum. As noted by Refs [275, 274, 318], both the primary and secondary cosmic-ray spectra depend mildly on the Solar System's proximity to Galactic spiral arms, particularly for leptons where the spectra are hardened as one moves closer to the CR source. Comparing the traditional SNR distribution against our new model (with $f_{\rm H2} = 0.2$), the proton and antiproton spectral indices are negligibly changed above 1 GeV. Below 1 GeV, measurements of the local interstellar spectra are strongly modulated by the heliosphere, but our models predict a $\approx 1\%$ hardening, well within measurement errors. The ratio $\bar{p}/p$ is enhanced by an about 7% between 10 MeV and 100 TeV, likely owing to the enhanced source density in the inner Galaxy which increases antiproton production through spallation. While this is not negligible, it is well within the systematic uncertainties since the ratio here will be directly sensitive to both the $X_{\rm CO}$ profile of the inner Galaxy and to propagation conditions (namely the convection gradient, diffusion coefficient, and halo height). The positron fraction is hardened above 1 GeV, with a 1% enhancement at 1 GeV up to a 5% enhancement at 10 GeV. Thus our changes to the injection morphologies are fully compatible with local cosmic-ray measurements. We prefer also to remain agnostic about propagation conditions throughout the rest of the Galaxy, particularly in the Galactic center region.

For both of these reasons we do not further constrain our models based on cosmic-ray measurements.

7.2 Interstellar Gas Distributions

The distribution of interstellar gas in the Milky Way is typically described by a sum of contributions from three dynamically distinct components of hydrogen gas in molecular, atomic, and ionized phases [340]. The former two overwhelmingly dominate the gas density near the Galactic disk, and are thus associated with the bulk of the γ-ray emission. This is the case even at high latitudes, where the Solar System is embedded near the center of a warm nuclear medium disk component and inside the Orion sub-arm of the Milky Way, as reflected by the inclined ring of molecular clouds and OB star-forming regions known as Gould's belt. In the following sections we discuss the standard Galprop gas model, its complications specific to the Galactic center and inner Galaxy, and then describe our new implementation based on improved survey deconvolution techniques [199, 341].

7.2.0.8 Previous Gas Models

Previous studies of the Galactic center excess using `Galprop` have relied on the gas models described in full detail in Refs. [85, 342]. We will call this setup the 'Galprop' gas model [85, 342] and review the basic details here. The gas model assumes at first azimuthal symmetry using tabulated values for the radial dependence and exponential scale-heights, which are interpolated linearly from tables. These 'analytic' gas densities

are based on collections of surveys for HI [206, 207, 343], H_2 [344, 345, 323] and for HII based on the NE2001 free electron model [346, 211, 347, 218]. For the inner 1.5 kiloparsecs of the Galaxy, HI and H_2 are based on Ref. [323] which attempts to find a model which compromises across many observations of the inner Galaxy. The result consists of two primary disk components for both HI and H_2: a dense "Central Molecular Zone" (CMZ) approximately centered on the GC and aligned with the Galactic Plane, as well as a holed "Galactic-Bulge-disk" which is rotated at 13.5° counter-clockwise to the Galactic plane as well as having it's major axis inclined $\approx 45°$ away from the line of sight. In Galprop models, this 3D distribution is azimuthally averaged and tabulated. Remarkably, we found that preserving the full three dimensional analytic gas model of Ref. [323] model resulted in only negligible differences to our gamma-ray analysis relative to the azimuthally averaged version.

At this point the Galprop model is complete for the purposes of cosmic-ray propagation – i.e. generating secondary cosmic-rays and ionization losses. Secondary hadrons represent only $\sim 10^{-4}$ of the nuclear cosmic-rays and are therefore unimportant to γ-ray studies. On the other hand, secondary leptons constitute a significant fraction of cosmic-ray leptons and their contribution to bremsstrahlung and ICS mildly sensitive to the gas distribution used for propagation. When generating gas correlated π^0 and bremsstrahlung emission, however, the impact is direct and the precise gas distribution is extremely important and one should renormalize the gas densities to survey data along each line-of-sight.

In most regions of the Galaxy, the distributions of HI and H_2 along a given line

of sight can be determined with good accuracy by using a Galactic rotation curve in combination with line Doppler shifts[2]. For atomic hydrogen, the hyperfine transition at 21 cm provides a direct observable. The HI abundance is related to the observed brightness temperature by a single spatially-varying parameter: the hydrogen spin temperature T_s, defined as the localized excitation temperature for hyperfine splitting. Although several phases of T_s exist in the interstellar medium, γ-ray studies typically adopt two values to bracket the uncertainties. Following Ref. [342], we choose $T_s \approx 150$ K and the optically thin limit $T_s \approx 10^5$ K. In the case of molecular hydrogen, the lack of a permanent dipole moment and the extreme excitation temperature for the quadrapole moment requires, instead, the use of a tracer gas. The $^{12}\mathrm{CO}(J = 1 \rightarrow 0)$ transition line[3] is related to the molecular hydrogen density through a $^{12}\mathrm{CO} \rightarrow \mathrm{H}_2$ conversion factor X_{CO}. This factor is known to be spatially (environmentally) varying, and is poorly constrained in the inner Galaxy. However, the X_{CO} conversion factor directly impacts the brightness of the Galactic disk. We reserve a dedicated discussion of X_{CO} for Section 8.1.8.1.

When generating γ-ray emission in the Galprop gas model, the Galaxy is divided into non-uniform (usually 1-2 kpc wide) annuli around the Galactic center. CO maps are first converted into H_2 densities using input X_{CO} values specified in 8.2 with power-law interpolation in radius. Next, varying the value of X_{CO} in each ring until

[2]Most ionized gas, particularly the warm ionized component, is highly correlated with the density of free electrons, n_e. For a given survey velocity element, the intensity of hydrogen-α line is proportional to the emission measure given by $\int_{l.o.s.} n_e(l,b,z)^2 dz$. This provides a possible method of indirectly determining the three dimensional ionized hydrogen density using Hα line surveys [348]. Although there exists a composite full-sky Hα map [349] constructed from three surveys [350, 351, 352], currently only the velocity integrated map is publicly available.

[3]One can also use higher level ^{12}CO or ^{13}CO transition lines under the additional assumption of a gas temperature which fixes the line ratios.

Ring Number	Radius [kpc]	Fit Region	X_{CO}^{PEB} [cm^{-2} (K km s^{-1})$^{-1}$]	X_{CO}^{Gal} [cm^{-2} (K km s^{-1})$^{-1}$]
1	$0 - 2.0$	Inner	$1.00 \times 10^{19\dagger}$	$1.00 \times 10^{19\dagger}$
2	$2.0 - 3.0$	Inner	7.97×10^{19}	8.42×10^{19}
3	$3.0 - 4.0$	Inner	1.62×10^{20}	1.61×10^{20}
4	$4.0 - 5.0$	Inner	5.39×10^{20}	1.73×10^{20}
5	$5.0 - 6.5$	Inner	1.09×10^{20}	1.72×10^{20}
6	$6.5 - 8.0$	Inner	9.39×10^{19}	1.74×10^{20}
7	$8.0 - 10.0$	Local	9.05×10^{19}	8.61×10^{19}
8	$10.0 - 16.5$	Outer	4.25×10^{20}	4.29×10^{20}
9	$16.5 - 50.0$	Outer	$1.00 \times 10^{21\dagger}$	2.01×10^{21}

Table 7.1: Definitions of annuli used by our modified Galprop gas model and used during the 3-stage global X_{CO} fitting described in Section 8.1.2.3. We also show the values of X_{CO} used in `Galprop` for the PEB and Galprop gas models after iteratively fitting our canonical model. The actual fitted values of X_{CO} (see Fig. 8.23) will differ between models, but the gas and source distributions induce the largest change. †We limit the *input* X_{CO} of the innermost ring to the, but fitting in the inner Galaxy is allowed to go to zero and generally prefers very small values. In the outer Galaxy, the outermost ring is known to be highly biased and, in the case of the PEB gas model, fits in the inner Galaxy do not converge unless the initial *input* value of X_{CO} is reduced. (see Sec. 8.1.8.1 for a discussion of the inner X_{CO} values).

the optimal fit to γ-ray data is found (see Sec. 8.1.2.3). The number and spacing of annuli depends on the gas map versions, but for computational reasons and to limit the number of X_{CO} fitting degrees of freedom we have merged 17 rings into 9, with radial boundaries given in Table 7.1. For a given latitude and longitude, the gas density integrated along the line of sight is then renormalized to survey data in each annulus. The Leiden-Argentine-Bonn survey [202] is used for HI with an angular resolution of $\sim 0.5^{\circ}$, while the Dame et al (2001) survey [200] is used for CO (H_2 by proxy) with approxi-

mately 0.25° resolution. These velocity cubes are combined with a rotation curve from Ref. [353] to assign each velocity measurement to a given annulus. We refer the Reader to Ref. [342] for additional survey and deconvolution details.

A final correction is applied to Galprop's γ-ray gas models. Gamma-ray fits to the outer Galaxy[40, 342] ($r \gtrsim 10$ kpc) are also known to be biased toward unphysically large $X_{\rm CO}$ values, possibly indicating a significant component of 'dark-gas': H_2 which is not well traced by CO lines as well as residual atomic hydrogen due to the assumption of a uniform spin temperature. In order to correct for this, Grenier (2005) [209] pioneered the use of $E(B-V)$ reddening maps from Schlegel, Finkbeiner & Davis (1998) (SFD) [208] to determine the total HI column density along each line-of-sight and generate a map of residual gas and dust that still emits in γ-rays. Ref. [342] applies a similar procedure in which a linear combination of CO and HI templates are subtracted from the SFD map in order to create a residual dust map. This residual is then distributed proportionally to HI. In regions of high-extinction, the amount of dust traced by $E(B-V)$ cannot be reliably determined and the $E(B-V)$ map is usually limited to a maximum reddening magnitude of either 2 or 5[4]

The Galprop γ-ray gas model is now defined and we show the resulting HI and H_2 surface densities in the top row of Figure 7.3.

[4]As our default gas map files we use the Galprop supplied `rbands_co10mm_v2_2001_qdeg.fits.gz` for CO and `rbands_hi12_v2_qdeg_zmax1_Ts150_EBV_mag5_limit.fits.gz` for HI. We also study the effect of changing the spin temperature and the magnitude cut on E(B-V) in Sec 8.1.4, finding that the GCE is completely insensitive to either.

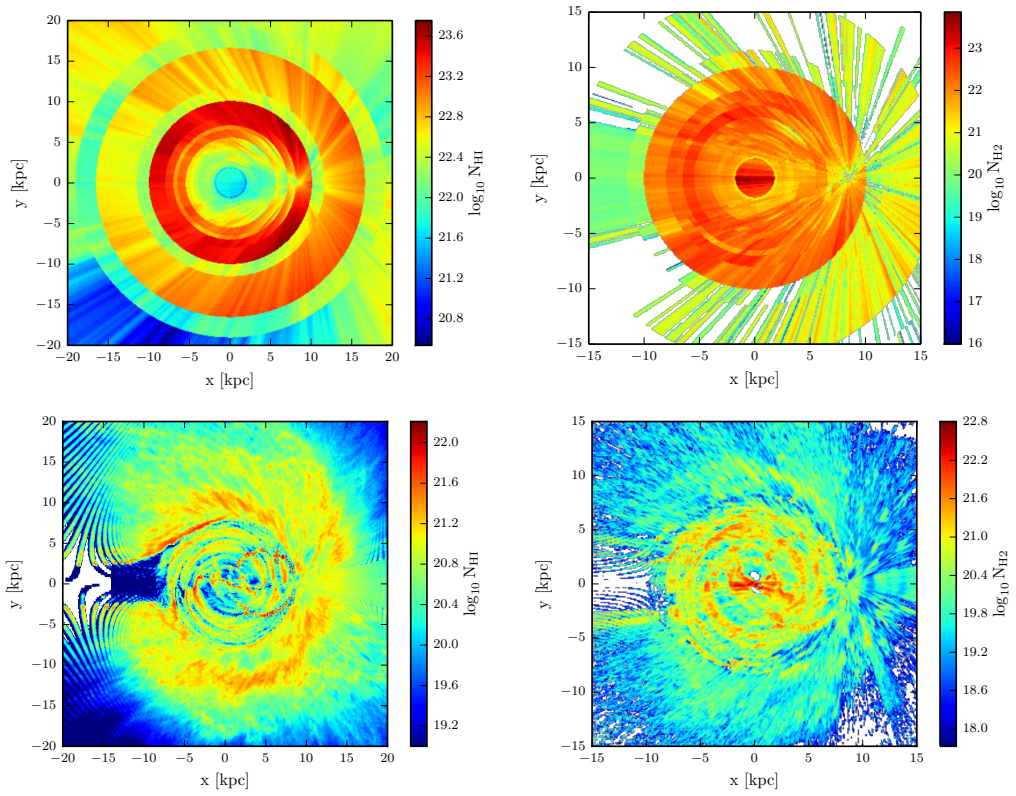

Figure 7.3: Top row: HI (left) and H_2 (right) gas column densities (integrated over the z-direction) for the Galprop gas model after renormalizing each line of sight to the survey column density in 17 deconvolved galactocentric annuli. Bottom row: HI and H_2 gas distributions in the PEB gas model. For HI, the hydrogen spin temperature assumed here was 10^5 K and 170 K for Galprop and PEB, respectively, though it is allowed to vary in later fits. For H_2 we assume a constant CO $\rightarrow$ H_2 conversion factor $X_{\rm CO} = 2 \times 10^{20}$ cm^{-2} (K km s^{-1})$^{-1}$ in this figure and when distributing primary cosmic-ray sources. For the generation of gamma-ray maps the value of $X_{\rm CO}$ is allowed to float freely in 9 radial bins. Note that white regions are assumed to have gas densities of zero, -y corresponds to positive Galactic longitudes from the solar position at $x = 8.5$ kpc, and that the anomalous ring present in both maps between $R_\odot$ and the Galactic center with radius $R_\odot/2$ is an artifact of the velocity deconvolution.

7.2.0.9 Pitfalls of Previous Gas Models

If the cosmic-ray density were uniform throughout the Galaxy, the line of sight-distribution of gas would be irrelevant. However, as we will see in the next section,

substantial gradients exist in the cosmic-ray pressure which are likely to be strongest in the Galactic center region. Therefore, the l.o.s. gas density is of the utmost importance there. As currently implemented, there are several important pitfalls to the Galprop technique which are specific to the GC region. These issues pervade all existing studies of the GCE and should be considered when discussing systematic uncertainties due to the choice of gas model.

1. *Vanishing kinematic resolution*: Line surveys sample the gas temperature as a function of latitude, longitude, and velocity relative to the Solar System. In the direction of the Galactic center and anti-center, gas is moving tangentially to the line-of-sight, implying vanishing kinematic resolution. This leads to a distance degeneracy along lines of sight near Galactic longitudes $l \approx 0$ and $l \approx 180$. In the Galprop models, each annulus is linearly interpolated from the sides (averaged over $\Delta l = 5^\circ$) between $|l| < 10^\circ$ and $|180 - l|^\circ$. The central annulus lies completely within the interpolated region, requiring a different procedure. For HI, it is assumed that the central annulus has 60% more gas than the neighboring ring while for CO all high velocity emission is assigned to the central ring as defined in Ref. [342]. Finally, each pixel in interpolated region is renormalized to the total survey column density.

2. *Large central annulus*: The innermost gas annulus extends from the GC to approximately r=1.8 kpc. This is approximately 12°, containing nearly the entire GCE region of interest. This implies that even after renormalizing the central region

to the survey derived column densities, the distribution along the line of sight is renormalized uniformly across the entire central region, even though strong CR gradients are expected across the inner 1-2 kpc, especially for CR leptons. As a result, a significant amount of structure near the Galactic center remains unresolved. This is particularly true in the case of HI, as seen in Figure 7.3 where the inner few kpc is essentially uniform and vacant. For H_2, a strong Galactic bar is present, but with uniform intensity on either side, rather than a gas depleted region as suggested by several references [323, 199].

3. *Kinematic distance ambiguity*: Two distances correspond to the same radial velocity in the entire inner Galaxy. A velocity deconvolution alone (without additional model inputs or absorption measures) cannot unambiguously assign gas to the near or far tangent point. In order to help alleviate the KDA generally – i.e. not only for resolving distances to specific molecular clouds [354] or HII regions [355] – one can incorporate additional model assumptions into the deconvolution procedure, using for example gas-flow simulations [199], or models of gas disk heights [201].

4. *Peculiar Motion and Velocity Dispersion*: Many gas clouds and the central Galactic bar have significant non-circular motion. If one can obtain independent distance estimates from e.g. absorption measures [354, 355], individual clouds can be repositioned in the gas survey. This requires a significant effort considering the large number of independent structures. Alternatively, one can model gas flow [199] in the inner Galaxy in order to kinematically resolve features with non-circular

motion. For large gas clouds, internal velocity dispersions of the gas can be a significant fraction of the bulk velocity and one needs to make assumptions about the shape and size of the cloud in order to assign the correct location.

7.2.0.10 New Gas Models

We introduce a novel gas model, which we have incorporated into the `Galprop` code version we use, which we refer to as the 'PEB' gas model, based on the improved velocity deconvolution performed by Pohl, Englemier, and Bissantz (2008) [199]. So far in the literature, the Galactic center excess has not been shown to be robust against alternative gas models other than varying $\mathrm{T_s} \in \left[150\ \mathrm{K}, 10^5\ \mathrm{K}\right]$ and $\mathrm{Mag}_{E(B-V)} \in [2, 5]$. As mentioned above, gas flow in the inner Galaxy gives rise to large non-circular motions which a pure velocity deconvolution cannot correctly reconstruct. PEB resolves this issue by employing smoothed particle hydrodynamics simulations of gas flow in a gravitational potential [356] containing 2 spiral arms and a strong central bar. The simulated gas velocity field can then be used rather than assuming pure circular motion. Not only does this more accurately resolve cloud orbits and the Galactic bar, but it provides kinematic resolution toward the Galactic center. Beyond the solar circle, the Galaxy is essentially in pure circular motion and simulations become less reliable. PEB therefore linearly interpolates between the gas flow model and pure circular motion between 7-9 kpc. Toward the anti-center, however, there is still no kinematic resolution and interpolation in longitude similar to the Galprop gas model is used between $160^\circ < l < 200^\circ$.

The starting survey data for HI [202] and CO [200] is the same as in the

Galprop gas model, although the deconvolution procedure itself is more sophisticated, iteratively determining the best fitting line-of-sight density distribution. We refer the Reader to Ref. [199] for details. The resulting gas datacube (in (r, l, b)) is output at 100 pc resolution giving more than a factor 10 resolution improvement compared with the Galprop gas model, and correctly representing the structure of the Galaxy. For the HI map [341], a uniform spin temperature of 170 K was assumed. As we do not have access to the deconvolution codes, we renormalize the *total* column density on each line-of-sight to the Galprop maps of choice in order to approximately account for varying spin temperatures and to incorporate the SFD dust corrections from Ref. [209, 342][5]. Combining all of these methods, the PEB gas model makes substantial progress toward alleviating the deconvolution issues 1-4 above.

In the bottom row of Figure 7.3 we show the surface densities of HI and H_2 for the PEB model (assuming a constant $X_{\rm CO}$). The difference relative to the Galprop gas model is striking. The spiral arms and bar are very prominent and the gas depletion in $0.3 \lesssim r \lesssim 3$ kpc surrounding the CMZ is readily apparent. In the case of the H_2 map, many individual giant molecular clouds are visible in the inner and outer Galaxy which are completely neglected in the Galprop models. In both HI and H_2 maps, a ring of radius and center $R_\odot/2 = 4.25$ kpc are observed. These artifacts are due to forbidden velocities where no distance solution can be found. This gas is automatically placed at locations with the highest radial velocity and is likely to be an indication that the gas flow

[5]Note that the SFD dust corrections are independent of the distribution of gas along the line-of-sight, and thus independent of the deconvolution procedure used. They are not, however, independent of spatial variations in $X_{\rm CO}$, since this changes to total column density of H_2.

models partially underestimate the true gas velocity in the inner Galaxy [199]. On the other side of the Galaxy kinematic resolution is lost beyond the solar circle for $|l| \lesssim 10^{\circ}$ and the gas density is underestimated. Given the thin disk and very large distance from the Sun, this will not strongly impact the inner Galaxy analysis, but may impact the Galactic center analysis where it makes up a portion of the background emission.

7.2.0.11 Additional Notes

(i) There are three additional three-dimensional survey deconvolution available in the literature. For HI and H_2, Nakanishi & Sofue [201] assume circular motion, and resolve the kinematic-distance-ambiguity in the inner Galaxy by assuming a model of hydrodynamical equilibrium in order to describe the gas disk heights as a function of Galactic radius. This is essentially the same procedure used by Ref. [357] for HI. While this does represent an improvement on the Galprop deconvolution procedure, it still assumes circular motion in the inner Galaxy and requires masking in a large region behind the Galactic center, making it unsuitable for γ-ray studies toward the Galactic center.

(ii) Several analyses of the GCE and Galactic center region have also used ultra-high-resolution gas templates as additional fit components. It is important to note, however, that template regression using gas column densities as a proxy for gamma-ray emission implicitly assumes that the cosmic-ray density is uniform across the entire projected volume of interest. At the Galactic center this is strongly violated and one should instead use a 3-dimensional model of gas and cosmic-ray pressure whenever possible and then

renormalize the modeled gamma-ray emission to their high-resolution survey according to the ratio of survey/analytic gas column densities as described above.

(iii) Within the past few years, our knowledge of dust has dramatically improved with integrated full sky dust maps from *Planck* [358] as well as three-dimensional maps of extinction (A_v) penetrating more than 10 kpc into the inner Galaxy and covering significant portions of the Galaxy [359, 360, 361]. An important next step to improving diffuse γ-ray emission models is the incorporation of this unprecedented data to resolve distance ambiguity in kinematically difficult regions by matching photometric dust measurements to CO maps, correcting for dust correlated with HI, and to use observed '$I_{\rm CO} - A_v$' relationships to determine $X_{\rm CO}$ variations in the Galaxy based on extinction [362]. The maps of Ref. [361] provide a direct photometric probe and have coverage over most of the sky.

7.3 Galactic Magnetic Fields

Magnetic fields are ubiquitous throughout the Milky Way. They play a crucial role in cosmic-ray acceleration and propagation, including impacts on diffusion through magnetic turbulence (the diffusion tensor and energy dependence), propagating of MHD waves (reacceleration), and synchrotron energy losses. For our problem, magnetic field properties at all scales above $\approx$ 1 pc are relevant. During acceleration, the presence and structure of turbulent, ordered, and random fields near the expanding SNR shock will impact the injected cosmic-ray spectrum, for example, from ion-neutral damping.

During propagation, diffusion is enhanced along ordered magnetic field directions while also being scattered off of the MHD turbulence, whose spectrum determines the energy dependence of the diffusion rate. The current state of the art grid resolution for the Milky Way is around 100 pc, and is thus not sensitive to scales below this other than through collective properties. The magnetic field strength and gas densities effect propagating MHD waves, and thus impact reacelleration.

Near the Galactic center, the model requirements become even more complex. The Central Molecular Zone (CMZ) contains the region $r < 300$ pc $|z| < 100$ pc which contains strong random magnetic fields on the order of $B \sim 100\mu$G [363] along with a strong poloidal fields which can reach much higher strengths in isolated non-thermal radio filaments. The region is also very highly turbulent and gas rich, implying that both primary acceleration and diffusive reacceleration are likely to be significantly different from the disk. In current models of cosmic-ray diffusion, these fields are essentially neglected, and require higher resolution simulations before a proper implementation can be taken into account. For cosmic-rays injected by the central black hole, even stronger mG level fields may be at play within the central 10 pc. Future studies of the Galactic center excess, for example, should attempt to take into account more realistic GC magnetic fields and interstellar radiation fields, perhaps using adaptive mesh codes rather than grids to reach the required spatial dynamic range.

Practically speaking, the magnetic field models of the Galaxy have long been crude, employing a cylindrically symmetric magnetic field model

$$B(r, z) = B_0 e^{(R_\odot - r)/r_B} e^{-|z|/z_B}, \tag{7.4}$$

where $R_\odot = 8.5$ kpc is the solar radius, and r_B and z_B are the radial and vertical scale-lengths, typically taken to range from 5-20 kpc and 1-6 kpc respectively, and being only weakly constrained, while the magnetic field strength B_0 is typically on 3-10μG.

Recently, more elaborate magnetic field models (see e.g. Ref. [364]) have been incorporated into the latest `Galprop` release [365], which may provide a promising avenue for describing more realistic spatially-varying and anisotropic diffusion. These effects include an enhanced diffusion constant along the magnetic field direction, as has been done before in studies of isotropic γ-ray emission [225].

Near the Galactic center, variations on the magnetic field strength and morphology can significantly impact the GCE spectrum [36], particularly for the new centrally concentrated source distributions described in Sec. 7.1. We present a study of these effects on the GCE in Section 8.1.4.

The best available constraints on Galactic magnetic fields are given by Faraday rotation measures and polarized synchrotron emission. These both involve taking line-of-sight integrals against free electrons, or electron cosmic-ray densities respectively, which carry their own uncertainties. Nonetheless, Ref. [365] constructs a multicomponent 3D model which is then fit to the data. For a free electron density $n_e(\vec{r})$, the rotation measure is given by

$$RM \approx 0.81 \int_{l.o.s.} \left(\frac{n_e(l)}{\mathrm{cm}^{-3}}\right) \left(\frac{B_\parallel(l)}{\mu\mathrm{G}}\right) \left(\frac{dl}{pc}\right) \tag{7.5}$$

and can be observed for a given source of true polarization angle θ_0 which is rotated to $\theta = \theta_0 + RM\lambda^2$, where λ is the observation wavelength. These measures are available

for almost 40,000 sources across the sky at several wavelengths, and provide reasonably good constraints on the line-of-sight parallel component of the magnetic field.

Polarized synchrotron radiation from non-thermal CR electrons provides sensitivity to the perpendicular component of the magnetic field.

$$j_\nu \propto n_{\rm cre} B_\perp^{(1+s)/2} \nu^{(1-s)/2} \tag{7.6}$$

where $s \approx 3$ is the electron spectral index. Given a model of electron cosmic-rays calculated from e.g. Galprop, WMAP or Planck data can be used to fit the model.

The Galactic magnetic field model of Jansson & Farrar [365] consists of 21 parameters and 4 large scale components:

Disk: The disk includes Galactic radii from 3-20 kpc with a molecular ring from $3 < r < 5$ kpc and a purely azimuthal field strength of about 0.1 μG and eight logarithmic spiral arms which subdivide the 5-20 kpc region and contain field strengths between -4 and 4 μG pointing along the spiral arms. Additional constraints are placed to conserve magnetic flux across the system. Vertically, the disk field decays exponentially with a scale height of about .4 kpc, and transitions into the halo component.

Poloidal Halo: The halo component is assumed to be axisymmetric and poloidal, forming an "X-shape" when projected onto our line of sight. The functional form is given in Ref. [365], but the strength and scale height are approximately 4.6 μG and 2.9 kpc respectively.

Toroidal Halo: The toroidal component is azimuthal with a strength of $|B| \approx 1.1 - 1.4$ μG, and a large scale height of 5.3 kpc. The field is shut off beyond 10 and 17 kpc for the north and south lobes respectively.

Striated Random Fields: These fields are assumed to be random at small scales, but their overall intensity varies in striations which are aligned with the ordered field components.

In addition, there is a purely random field component which is observable via the total (unpolarized) synchrotron emission which follows the exponential form above with similar parameters and a strength of about 5 μG.

Because this model is already implemented in galprop for synchrotron and energy losses, future 3D diffusion models should also implement reacceleration and full anisotropic inhomogeneous diffusion using the scaling discussed in Chapter 5.

7.4 Interstellar Radiation Fields

The interstellar radiation field is comprised of three main components, as described in detail in Refs. [366, 34]:

(1) cosmic microwave background radiation (CMB),

(2) starlight, which peaks in the optical band (Opt.), and

(3) a far-infrared component (FIR) arising from dust-reprocessed starlight.

The galactic ISRF model currently in Galprop is modeled as axisymmetric

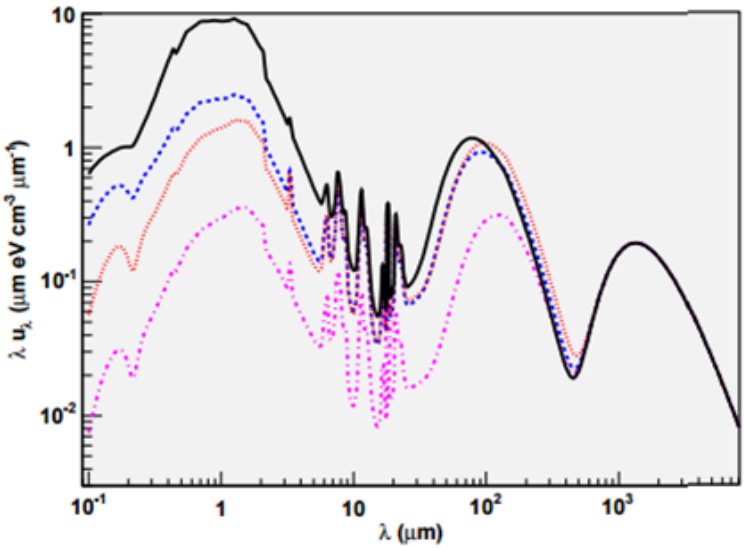

Figure 7.4: Galprop's ISRF model at the Galactic center from Ref. [34]. Note that a photon energy is given by $E_{ph} = 1.24eV(1\mu\text{m}/\lambda)$.

(with the exception of logarithmic spiral arms), and is based on the distribution of stars in the Galaxy, a dust model (distribution and properties), and a model of scattering, absorption, and remission of starlight by the dust. The spectrum at the Galactic center is shown in Figure 7.4.

The stellar model is based on the model from Ref. [367] which includes 87 stellar classes which have a local number density, scale height, number density, and spectrum in several bands. Next, these are distributed in seven components including thin and thick disks, halo, bulge, bar, ring, and spiral arms. Notably in the Galactic center, while there is a bulge component which peaks at the Galactic center, the extremely bright central stellar populations are not modeled beyond this (see discussion below). The spectra are taken from spectral libraries. Dust modeling includes a variety of organic molecules

whose grain sizes, abundances, and scattering properties can be found in Ref. [366]. The dust distributions are assumed to follow the Galprop model described in Sec. 7.2.

It is important to note the limitations of `Galprop's` current ISRF model near the Galactic center. Current models are oriented toward reproducing the global ICS component and have not yet evolved to the point of adding in individual small scale Galactic structures. This includes contributions from the stellar populations and the corresponding dust reprocessed photons in the Central Molecular Zone, where additional radiation fields will directly steepen the radial profile of ICS emission over the inner few degrees of the Galactic center. These caveats should be considered when assessing the quality of diffuse models very close to the Galactic center.

Some groups have attempted recently to model the ISRF more empirically using massive stellar surveys and photometric dust maps. In Figure 7.5, we show compare the Galprop ISRF model to more recent developments [35], which have not yet been published or incorporated into Galprop. These reveal a much more strongly peaked ISRF in the Galactic center region and rely on new 3D photometric dust maps from Green et al [361], and fits of geometric and population parameters directly against Planck and IRAS infrared measurements as well as COBE NIR measurements for starlight. These reveal not only a stronger peak toward the Galactic center, but up to an order of magnitude increase in the central ISRF intensity.

Future modeling of the Galactic center excess depends sensitively on the ISRF, and we show throughout Sec. 8.1 that the ICS signal, which is directly proportional to the ISRF intensity, is highly degenerate with the Galactic center excess properties. In

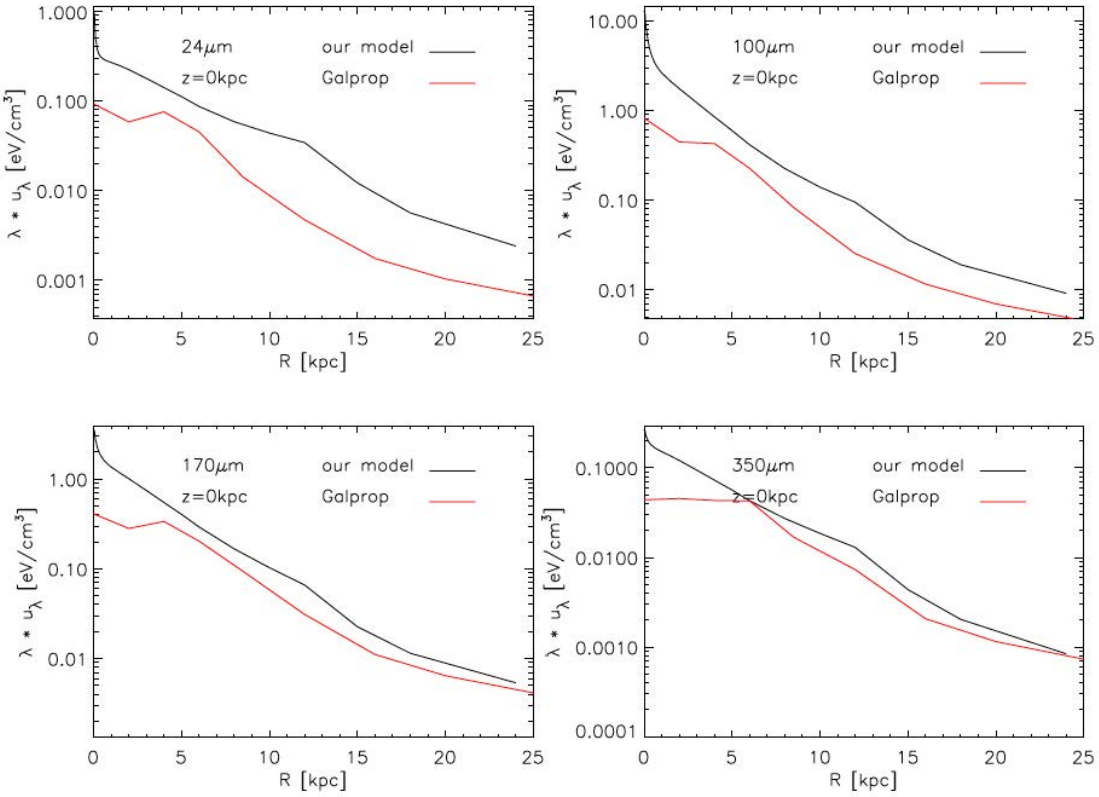

Figure 7.5: Spectrum of the Galprop ISRF model at the Galactic center from Ref. [35].

particular, the missing element is a peaked component over the inner few degrees. This could very well be due to ISRF mismodelling which, when corrected, will surely bring astrophysical models of the CMZ into better agreement with GeV gamma-ray data.

Part III

Indirect Detection Signals

Chapter 8

The GeV Galactic Center Gamma-Ray Excess

The Galactic center is a promising location to search for non-gravitational signals from particle dark matter such as gamma rays from dark matter pair annihilation. Any model for the density distribution of dark matter in the Galaxy predicts a high concentration of dark matter in the Galactic center, with a resulting large number density of dark matter particle pairs. Barring the possibility of a large, nearby dark matter "clump", the Galactic center direction is the direction in the sky where the line-of-sight integral of the dark matter density squared is maximal. As a result, the Galactic center is the location where one of the brightest photon signals from dark matter annihilation is expected.

On the downside, the center of the Galaxy hosts a complex combination of "standard" astrophysical γ-ray sources. The region contains numerous resolved and

many unresolved γ-ray point sources; in addition, the diffuse Galactic emission is brightest in the center of the Galaxy, where the largest macroscopic concentrations of gas, cosmic rays and interstellar radiation energy density are found. This dense environment copiously sources γ rays from hadronic inelastic interactions as well as from inverse Compton scattering and bremsstrahlung. Such complex background structure can be hardly reconstructed from first principles, and non-trivial extrapolations and inference often, if not always, define how the predicted background emission is calculated.

The combination of such an appealing target with such a treacherous background has contributed to much debate about the existence and nature of excess γ-ray emission from the Galactic center region. Ever since the years of the EGRET telescope, claims of an excess diffuse γ-ray emission (extending even beyond the Galactic center) have been made [368, 369], and proved premature, with several groups proposing a Galactic cosmic-ray spectra differing from local values [370, 371]. The EGRET excess was subsequently shown to be systematic in origin, relating instead to a miscalculation of EGRET's sensitivity above a few GeV [372], and was later shown to be conclusively unfounded [373] using data from the Fermi Large Area Telescope (LAT) [231].

Shortly after LAT data were made public, claims of a Galactic center Excess (GCE) have been put forward, pointing to differing particle dark matter properties (including the preferred mass, pair-annihilation rate, and annihilation pathway) depending on the background model employed in the analysis, see e.g. [241, 242, 374].

Several immediate issues have been raised following the identification of excess of γ rays over background and with associations to new physics. These include the

question of γ-ray point source modeling associated with the radio source Sgr A*, see e.g. [375, 376, 377, 378], and the role of unresolved populations of γ-ray emitters such as millisecond pulsars [379] (see however [15]).

One of the key elements in assessing the presence of a genuine γ-ray excess in the Galactic center region is, naturally, that of modeling γ-ray sources in the region. Critical to this is the role of unidentified point sources, including population models for unidentified source classes, and of sources whose spectrum and even source extension is unclear (for example the γ-ray counterpart to Sgr A*). A second key element is the diffuse γ-ray emission induced by Galactic cosmic rays. It has long been known [380, 373] that the key components of such emission, in the 0.1-100 GeV range are (i) hadronic emission from neutral pion decay produced by inelastic proton collision with the interstellar gas, (ii) inverse Compton up-scattering of background interstellar radiation by cosmic-ray electrons and positrons, and (iii) bremsstrahlung.

We review below how the two key ingredients to the background model employed to extract the Galactic center excess have been handled in the three most recent and comprehensive analyses. What we believe is a crucial point to make is that the general procedure, in those studies, has been to employ background templates that make crucial assumptions about the Galactic diffuse emission. It was pointed out in Ref. [381], that important systematic effects in extracting a diffuse γ-ray excess originate from neglecting the cosmic-ray density distribution and in utilizing templates where the diffuse hadronic emission, item (i) in the list above, follows the morphology of the target gas density. In the present study, we point out that (a) very little is known about cosmic

rays in the Galactic center region; that (b) more or less young populations of cosmic rays are likely to inhabit that region and to importantly contribute to the hadronic emission in a way that would be completely missed by a current template analysis; and, finally, that (c) such a population(s) is likely to source the claimed γ-ray excess.

Let us first briefly review three recent studies devoted to the Galactic center excess, Ref. [44], [45] and [43]. The study presented in Ref. [44] focuses on the $7^\circ \times 7^\circ$ region centered around the Galactic center (GC, $b = 0,\ l = 0$), and employs the recommended LAT Collaboration diffuse background model `gal_2yearp7v6_v0` (we will comment below on the implicit assumptions included in this model), plus isotropic backgrounds, and known γ-ray sources in the second year Fermi catalogue (2FGL). The study confirms evidence for a spherically symmetric extended source, as obtained in previous studies [243], with a spectrum consistent both with emission from millisecond pulsars and with dark matter annihilation. Ref. [44] also attempts to assess systematic uncertainties in the background modeling, concluding that such uncertainty is in the vicinity of the 20% level. In a follw-up paper [382] by the same authors, 20 cm templates tracing the molecular gas distribution were added to the likelihood analysis and were found to significantly improve the fit while still robustly detecting an approximately spherically symmetric GCE counterpart.

The analysis of Ref. [45] also considers a region of interest of $7^\circ \times 7^\circ$ centered around the GC, and employs two choices for the energy range, photon source class, pixel size, and energy binning. Ref. [45] then fits a variety of templates to the observed γ-ray data. These templates include, in addition to point sources, the recom-

mended Galactic diffuse emission model `gal_2yearp7v6_v0` and isotropic background model `iso_p7v6source`, a template (MG) that intends to map the bremsstrahlung emission associated with high-energy electrons interacting with molecular gas clouds as traced by the 20 cm radio map of the GC [292], a Galactic Center Excess (GCE) source, and a "new diffuse" component associated with a central stellar cluster, with varying spatial profiles.

The two key findings of Ref. [45] are that (i) an extended emission in the GC region associated with the GCE template is present with any combination of templates and with both choices for the pixel and energy binning etc.; and that (ii) the fluxes and spectra associated with both the γ-ray emission from the central point source Sgr A* and with the GC extended emission are significantly affected by the choice of the background model, especially in the low-energy range. The GC excess is found to have a spatial distribution consistent with a profile $\propto r^{-2.2}$.

The study of Ref. [43], which appeared less than 10 days after Ref. [45], focused on an "Inner Galaxy" region, which masks out the Galactic plane ($|b| < 1^\circ$) and includes a large region of several tens of degrees, and on a "Galactic center" region, defined by $|b| < 5^\circ$ and $|l| < 5^\circ$. Both studies use a novel cut on photon events based on the CTBCORE variable, producing higher resolution maps. In the "Inner Galaxy" analysis, Ref. [43] makes use of three templates (the Fermi collaboration `p6v11` Galactic diffuse model, an isotropic background and a uniform-brightness template matching the Fermi bubbles) plus a "dark matter" template of variable inner slope. In the "Galactic center" analysis, the templates used include a Galactic diffuse emission provided by the Fermi

collaboration (`gal_2yearp7v6_v0`, the same choice as Ref. [45]), a template tracing the 20 cm emission, along the lines of Ref. [45], an isotropic component, and all 2FGL point sources [247]. As in Ref. [45] it is found that the isotropic component needed to provide an optimal fit is considerably brighter than the extragalactic γ-ray background.

Ref. [43] indicates a strong preference for the existence of a Galactic center excess, and finds a similar preferred spatial distribution profile to Ref. [45] and, generically, a similar preferred spectral shape. Ref. [43] points out that the excess is approximately spherically symmetric. From both spectral and morphological considerations, Ref. [43] argues that a population of unresolved millisecond pulsars (MSP) in the relevant Galactic region is strongly disfavored. Also, as pointed out in Ref. [381], based on the population of *resolved* MSPs, the contribution from an unresolved population should account for less than $\sim 5-10$ % of the γ-ray excess (see also [15]).

It is apparent that a central issue to the determination of the existence of any diffuse γ-ray excess is whether or not the background model for the Galactic diffuse emission accurately reproduces the expected γ-ray emission. All recent studies reviewed above employ a diffuse Galactic model recommended by the Fermi collaboration for use with Pass 7 LAT data [383]. Interestingly, the Collaboration explicitly (and in bold face) discourages the use of one the most recent such model for Pass 7 reprocessed data "for analyses of spatially extended sources in the region defined in Fig. 1", a region which includes the Galactic center region (as noted in Ref. [43]). While the key concern is the inclusion, in the reprocessed data background model, of sources with extension more than 2°, it is also apparent that such background models are not designed with

the purpose of establishing the existence of a diffuse emission.

One of the key issues with using the diffuse model recommended by the Fermi Collaboration for the purposes of establishing a diffuse excess is the set of templates employed to reproduce the morphology of the hadronic and inverse-Compton Galactic diffuse emission. Employing gas column-density map templates to reproduce the diffuse γ-ray intensity entirely neglects the possibility of a significantly enhanced cosmic-ray abundance in the inner Galaxy, which almost certainly exists. Similarly, the inverse-Compton template is based, and sensitively depends, on specific choices for the input parameters in the `Galprop` code, most significantly source distribution, diffusive halo geometry and source spectrum (see e.g. [384]).

Other quite relevant issues with the Fermi Collaboration recommended diffuse model have been discussed and tackled in the recent studies of Ref. [45] and [43]. These include a component of bremsstrahlung emission corresponding, and traced by, molecular gas [45, 43]; a diffuse component with a density profile tracing the Milky Way Central Stellar Cluster [45]; and the so-called Fermi bubbles [43], whose intensity however quite likely deviates from the uniform-brightness assumption of Ref. [43].

With all the mentioned caveats in mind, in the present study we show that simple Galactic cosmic-ray models exist that naturally explain the observed excess, both in steady state and in burst scenarios. The origin of such cosmic rays is likely associated either with supernova remnants in the inner Galactic region, or with past activity of Sgr A*, or both. We demonstrate that there is no spectral or morphological preference for dark matter over such cosmic-ray models, whose existence in the inner Galaxy is more

than plausible. Based on Occam's razor principle, we argue that the Galactic center excess finds a much more compelling interpretation in the context of cosmic-ray models for the inner Galaxy rather than in that of dark matter annihilation.

8.1 Steady State Cosmic Rays

Gamma-ray data from observations with the Large Area Telescope on board the Fermi Gamma-Ray Satellite (Fermi-LAT) have consistently indicated the presence of a bright, extended, and spherically symmetric excess coincident with the position of the dynamical center of the Milky Way (Galactic Center, hereafter GC) [241, 242, 374, 243, 44, 245, 45, 43, 385, 36, 42]. Most notably, Ref. [43] and [36] have obtained detailed determinations of the γ-ray excess, significantly improving our understanding of its spectrum and morphology, and including an assessment of possible systematic effects in extracting the spectral and morphological details of the excess. Using the *current set of Galactic foreground models*, the key features of the GC excess are as follows:

(i) A spectrum which peaks at a γ-ray energy of $\sim$2 GeV, with a low-energy tail harder than generically expected from astrophysical π^0-decay;

(ii) A morphology which extends out to at least 10° away from the GC, with a 3D intensity falling as $r^{-2.2}$ to $r^{-2.8}$;

(iii) An approximate spherical symmetry throughout its spatial extent, and

(iv) An intensity peak centered on the dynamical position of Sgr A* to within 0.05°.

The GC excess features listed above have attracted significant attention, in

part because of their consistency with predictions from simple models where the excess is explained by the pair-annihilation of dark matter particles (see e.g.[386, 387, 388, 389, 390]). Most notably, the excess is well fit by generic dark matter models with a dark matter particle mass of around 35—50 GeV and pair-annihilates to a quark-antiquark final state with a cross-section similar to that expected for a simple thermal relic, and a density profile similar to that expected from a Navarro-Frenk-White (NFW) [89] dark matter density profile that has undergone moderate adiabatic contraction due to baryonic effects [242, 374, 391, 386].

In addition to dark matter models of the GC excess, several astrophysical scenarios have also been posited as counterparts to the excess. These include the emission from a yet-undetected population of milli-second pulsars densely concentrated near the GC and throughout the Galactic bulge [379, 243, 392, 393, 394], or an outburst originating from the position of Sgr A*, of either hadronic [216] or leptonic [217, 47] origin. At present, these astrophysical models have produced fits to the γ-ray data which are of poorer quality than dark matter models [43, 36, 15], or which appear to be in strong tension with existing constraints, especially in the case of pulsar emission models [15, 395]. However, further investigation of these models is highly warranted, due to the high Bayesian prior on the existence of unknown astrophysical emission components in the unique GC environment. Intriguingly, recent studies have tentatively shown that the excess appears compatible with a collection of (unresolved) point sources rather than with a genuinely diffuse emission [396, 230], an observation which would favor e.g. a pulsar interpretations of the GC excess. Further analyses are clearly needed in order to

assess the robustness of this conclusion. In reality, an astrophysical interpretation of the Galactic center excess is likely to involve both cosmic-ray and pulsar contributions.

The detailed features of the GC excess are prone to large systematic uncertainties stemming from bright astrophysical diffuse emission which must be removed in order to determine the excess. It is important to note that *the GC excess only accounts for approximately 10–20% of total emission within 10° of the GC, where the excess can be statistically observed.* The majority of the γ-ray emission in this region of interest (ROI) instead stems from the collision of high-energy cosmic rays with the diffuse Galactic medium. Moreover, *all existing studies of the GC excess rely on very similar (or in some cases identical) models for the diffuse Galactic background*, thus increasing the likelihood of systematic errors associated with incorrect modeling of the astrophysical diffuse emission. In particular, the majority of studies [243, 44, 245, 43, 45] have utilized the diffuse emission models provided by the Fermi-LAT collaboration[1]. While these models are based on a physically motivated model of the γ-ray sky, and should in principle provide accurate models for the diffuse Galactic γ-ray emission, these models are intended primarily to maximize the sensitivity of Fermi-LAT searches for γ-ray point sources in regions far from the GC. Thus, the Fermi-LAT team has, in some cases, added non-physical extended emission templates in order to reduce extended astrophysical excesses.

We note that several studies of the GC excess have utilized alternative models for the astrophysical diffuse γ-ray emission. The earliest studies, e.g. Ref. [241, 242, 374]

[1]The analyses of [243, 44, 43, 45] employ gal_2yearp7v6_v0.fits, while [245, 43] employ the gll_iem_v02_P6_V11_DIFFUSE.fit diffuse model for an Inner Galaxy type analysis.

utilized simple background subtraction models which assumed that the astrophysical γ-ray emission was either planer, or directly traces the molecular gas density in the GC region. More recent analyses, e.g. Ref. [36, 42] have utilized diffuse emission models based on the `Galprop` cosmic-ray propagation code, but have typically assumed that the cosmic-ray propagation parameters near the GC region are identical to those which best fit cosmic-ray data in the solar neighborhood. This introduces a similar problem as models utilizing the Fermi-LAT diffuse emission models, where the physical modeling of the GC is based on analyses tuned to fit residuals far from the GC region.

In Ref. [397] we showed that improving the physical modeling of the Galactic diffuse emission can dramatically affect the nature, and possibly the very existence, of the GC excess. In particular, in Ref. [397] we pushed the envelope of current physical models for diffuse Galactic γ rays in two distinct but complementary directions, producing:

(i) a 3-dimensional modeling of cosmic-ray propagation, and

(ii) a 3-dimensional and up-to-date choice for the Galactic gas density distribution combined with physical models for the morphology of cosmic-ray injection sources.

Specifically, we postulated that cosmic-ray injection traces regions of star formation, which is, in turn, traced by the observed molecular hydrogen (H_2) density distribution via Schmidt laws.

The key results of our study are that:

(1) diffuse emission models of the full sky strongly favor a cosmic-ray injection distribution that includes a counterpart to star-forming regions, and

(2) the features of the GC excess are significantly affected by the choice of the

cosmic-ray source distribution. In particular, we found that postulating 20-25% of the cosmic-ray injection to trace the distribution of H_2 regions improves the global fit to the observed γ-ray data, while also suppressing the GC excess and distorting its spherical symmetry. However, we note that the GC excess is still present in the best-fit models focused toward the inner Galaxy.

In this Section, we examine the parameter space of models which utilize H_2 as a tracer of cosmic-ray injection, and determine the degeneracies between the ensemble of diffusion scenarios and the properties of the γ-ray excess in various regions of interest. Our key results show that in all cases, γ-ray data toward the inner Galaxy and Galactic center statistically favor models with 10% to 15% of cosmic-ray sources tracing H_2. Notably, all fits to the γ-ray data near the GC prefer the existence of a GC excess component. However, both all-sky γ-ray fits and the observed star formation rate near the Galactic center prefer a larger fraction of H_2 distributed sources. Depending on one's confidence in these as Bayesian priors on the source distribution, we find that the intensity, morphology and spectrum of this emission component change considerably under different assumptions for the astrophysical diffuse γ-ray emission model. Finally, the preferred Galactic diffuse emission models that include physically-motivated cosmic-ray injection sources are observed to produce a significant population of low energy ($\lesssim 30$ GeV) electrons and protons, giving rise to a bright sub-GeV γ-ray emission. We find that such emission is naturally suppressed in the presence of high-velocity winds emanating from the Galactic center region – a result which brings γ-ray observations into considerably better agreement with multi-wavelength observations indicating the

existence of a strong Galactic wind [32, 298, 294, 297, 295, 298, 296, 299, 398]. We explore the interplay between the many diffuse emission processes and scenarios in the GC region in great detail, and produce an astrophysical diffuse emission model which substantially enhances our understanding of this complex region of the sky.

The outline of this Section is as follows. We then describe a set of reference benchmark models (Section 8.1.1) before delving into a detailed comparison of our newly-proposed diffuse models with γ-ray data from the Fermi telescope (sec. 8.1.2). The results of our study, especially in connection with the features of the Galactic center excess, are given in Section 8.1.3, while Section 8.1.7 summarizes and concludes. We also present additional details on the $X_{\rm CO}$ conversion factor toward the inner Galaxy (8.1.8.1), the ROI dependence of the fit results (8.1.8.2), a comparison to the Gaussian CMZ models of Ref. [399], fits of the Galactic center excess over 10 sky segments from Ref. [36], and stability of the Galactic center results when using the 1FIG point source catalog [42]. **Codes and model files associated with this project are discussed in Appendix A.1.** Details of the propagation, source injection, and gas models are given in Sections 5.2, 7.1 respectively.

8.1.1 Benchmark Models

Throughout this Section we consider three benchmark models and the effects of varying individual parameters within those models. First, we adopt reference Model A (hereafter 'Mod A') from Ref. [36] which performs better than the `P7V6` and `P6V11` Fermi diffuse models over a $40^\circ \times 40^\circ$ 'inner Galaxy' region of interest centered on the GC. The

`Galprop` parameters are quite typical for diffusion models, with the possible exception of an elevated convection gradient $dv/dz = 50$ kms^{-1}. Given the intense star formation toward the inner Galaxy, such values are not unreasonable when focusing on the Galactic center region. Furthermore, the cosmic-ray electron population is approximately doubled compared to the locally measured e^-/p flux, and the Opt.+FIR ISRF density is enhanced by $\approx 40\%$ over the `Galprop` value. Originally this model uses a step function for the $X_{\rm CO}$ gradient taken from Ref. [40], though here we have refit the radial $X_{\rm CO}$ profile to more fairly compare against our modified models. This results in a significantly better overall χ^2, but does not strongly impact any of the other GCE results below, including our profiles of fit quality versus $f_{\rm H2}$.

Next, we consider a set of "Canonical" models which take advantage of the improved features discussed above. Most importantly, the models incorporate our new source distribution with a fraction of the cosmic-ray injection tracing $f_{\rm H2}$. For propagation (energy losses and generation of secondary species) we use Galprop's analytic gas model. When generating γ-rays from π^0 or bremsstrahlung, we use Galprop's standard (survey renormalized) gas maps assuming a hydrogen spin temperature $\rm T_s = 150$ K and a reddening cut such that $\rm E(B-V) \leq 5$ magnitudes. We have also verified that varying these assumptions within the model space of Ref. [342] does not change the primary results below. Compared with Mod A, these models also possess a slightly smaller diffusion halo height, no convective wind, and a larger diffusion constant. Of less importance is the higher spatial resolution in the plane of the Galaxy, 3D diffusion, lower Opt.+FIR ISRF and a smaller vertical magnetic field scale-height. The Canonical models were

roughly optimized by hand and provide a better fit globally compared to Mod A. The model parameters are summarized in Table 8.1. Below we will consider the $f_{\rm H2}$, n_s, and ρ_c parameter space which most intensely impacts the properties of the Galactic center excess. In Section 8.1.4, we will also study the effect of varying global diffusion parameters on both the global fits and on the Galactic center excess.

8.1.2 Gamma-Ray Analyses

In order to compare our new diffuse models against *Fermi* γ-ray data, we employ three distinct maximum likelihood template regressions (See Sections 4.1 and 4.3). We first perform a 'global' γ-ray analysis over three regions (inner, outer, and local Galaxy) which collectively cover the entire sky and are used to fit the radial dependence of the CO $\rightarrow$ H_2 conversion factors $X_{\rm CO}(r)$. It is necessary to refit $X_{\rm CO}$ in this analysis due to the re-distribution of cosmic-rays and due to the variations in propagation parameters. A major benefit of global fits is the ability to statistically assess the quality of the global diffusion model rather than focusing solely on the Galactic center region. Although it is possible that diffusion in the Galactic center deviates radically from the rest of the Galaxy, it can be instructive to interpret the global likelihood (as well as the CMZ star formation rate) as a Bayesian prior toward conditions near the Galactic center, and to check that our new models remain compatible with the broader Galactic γ-ray emission.

The second analysis concerns the inner Galaxy, a 40° square region of interest centered on the Galactic center with the plane ($|b| < 2°$) masked. For this purpose we have precisely reproduced the 'inner Galaxy' analysis of Calore et al (2015) [36] which

Parameter	Units	Canonical	Mod A	Description
D_0	cm^2 s^{-1}	7.2×10^{28}	5.0×10^{28}	Diffusion constant at $\mathcal{R} = 4$ GV
δ	–	0.33	0.33	Index of diffusion constant energy dependence
$z_{\rm halo}$	kpc	3	4	Half-height of diffusion halo
$R_{\rm halo}$	kpc	20	20	Radius diffusion halo
v_a	km s^{-1}	35	32.7	Alfvén velocity
dv/dz	km s^{-1} kpc^{-1}	0	50	Vertical convection gradient
$\alpha_{\rm p}$	–	1.88 (2.39)	1.88 (2.47)	p injection index below (above) $\mathcal{R} = 11.5$ GV
$\alpha_{\rm e}$	–	1.6 (2.42)	1.6 (2.43)	e^- injection index below (above) $\mathcal{R} = 2$ GV
Source	–	SNR	SNR	Distribution of $(1 - f_{\rm H2})$ primary sources*
$f_{\rm H2}$	–	.20	N/A	Fraction of sources in star formation model*
n_s	–	1.5	N/A	Schmidt Index*
ρ_c	cm^{-3}	0.1	N/A	Critical H_2 density for star formation*
B_0	μG	7.2	9.0	Local ($r = R_\odot$) magnetic field strength
r_B, z_B	kpc	5, 1	5, 2	Scaling radius and height for magnetic field
ISRF	–	(1.0,.86,.86)	(1.0,.86,.86)	Relative CMB, Optical, FIR density
T_s	K	150	150	Hydrogen spin temperature
E(B − V)	mag	5	5	Reddening cutoff for SFD correction
dx, dy	kpc	0.5, 0.5	1 (2D)	x, y (3D) or radial (2D) cosmic-ray grid spacing
dz	kpc	0.125	.1	z-axis cosmic-ray grid spacing

Table 8.1: Summary of `Galprop` parameters for our Canonical model and Mod A from Ref. [36]. *See Section 7.1.0.7 for additional details on the Star formation parameters.

is used to characterize the extended GCE emission without significant bias from the Galactic plane.

Finally, the immediate vicinity around the Galactic center is very complex and depends sensitively on bright point sources which must be simultaneously fit to the

diffuse GCE component. This 'Galactic center' analysis is based on that of Daylan et al (2015) [43], but extends the window to a larger 15° square ROI.

We notice that the key differences with respect to previous studies of the Galactic center excess are (i) the inclusion of $X_{\rm CO}$ fitting, (ii) global likelihood results, (iii) the first analysis of the GCE using *Fermi's* Pass 8 dataset, and (iv) the use of the new *Fermi* 3FGL source catalog [116]. Below we describe the individual analyses in succession before presenting the overall analysis results.

8.1.2.1 Data Selection

In our analysis we employ 360 weeks worth of *Fermi* data using the recent Pass 8 release. We select front+back converting photons in the `P8R2_CLEAN` event class (`evclass=256, evtype=3`) using `Fermi ScienceTools v10r0p5`. Earth limb contamination is mitigated using a zenith angle cut $\theta \leq 90°$, which has been updated from the Pass 7 standard $\theta \leq 100°$. We use `gtmktime` with the standard filters `DATA QUAL>0 && LAT CONFIG==1 && ABS(ROCK ANGLE)<52`.

We note that Pass 8 provides an approximately 25% increase in effective area over Pass 7. Combined with additional exposure time this provides $\sim$ 50% increased statistics compared with Ref. [36], as well as more accurate instrumental response functions.

For analyses of the extremely dense Galactic Center ROI our event selection is identical except that we examine only events which convert in the front of the Fermi-LAT instrument, providing an enhanced angular resolution for this analysis (`evclass=256,`

`evtype=1`).

8.1.2.2 Additional γ-ray Templates

In Chapters 5 and 6, we described `Galprop's` diffuse emission components (π^0, bremsstrahlung, and ICS) arising from the sea of Galactic cosmic-rays interacting with interstellar matter and radiation. However, there are several additional γ-ray components arising from individual point and extended sources, collections of sub-threshold extragalactic sources making up the Isotropic Gamma-Ray Background (IGRB), as well as new diffuse components such as the Fermi Bubbles [11], and possibly from an additional Galactic center excess (GCE) template.

- *Point Sources (PSC):* The contribution of point sources in each of our γ-ray analyses is based on *Fermi's* 4 year third point source catalog, 3FGL [116], including the 13 extended sources. In the Global and Inner Galaxy analyses the spectrum and normalization of each source is fixed to the 3FGL values and the finite angular resolution of the *Fermi-LAT* is taken into account by smearing photons according to the precise energy dependent point spread function (PSF). Although changes to the fore/background diffuse model will inevitably change the spectrum and flux of 3FGL sources, refitting sources with the new diffuse model introduces a problematic number of degrees of freedom over the large regions of interest here. We instead fix sources to their 3FGL values and rely on adaptive masking [36] to reduce bias from mis-modeled point sources.

  In the Galactic center analysis, we utilize the 3FGL catalog, and include all point

sources within 18° of the Galactic Center. We allow any point source to vary freely in normalization if $\{|\ell|, |b|\} < 8°$, which combined with our diffuse models leaves us with 81 degrees of freedom. We note that allowing the point source normalizations to float freely in each small energy bin makes our fits independent of the global 3FGL spectral shape. We have additionally tested point source distributions based on the recently released 1FIG catalog [42], and found that the addition of these point sources has no impact on the results presented in this section, a result we show in Appendix 8.1.8.5.

- *Isotropic Gamma-Ray Background (IGRB):* In theory, the IGRB template is composed only of the population of unresolved, extra-galactic γ-ray emitters, a distribution which should be roughly isotropic throughout both the IG and GC ROIs. However, due to relatively small ROIs employed in each analysis, the IGRB template may also absorb any diffuse emission of Galactic origin which appears relatively isotropic through out the inner Milky Way (e.g. diffuse Galactic γ-ray emission from nearby sources). While the spectrum and intensity of the "true" IGRB is well constrained by observations far from the Galactic center region, the same is not true of the effective IGRB (which includes Galactic contributions), and the degeneracy between these components must be carefully treated in order to correctly model and subtract the IGRB component. In the Global analysis, the spectrum of all components is fixed and we use the *Fermi collaboration's* most recent determination of the IGRB spectrum [225], choosing Galactic foreground

Model A[2]. Like our constructed GDE models, this Model A assumes isotropic diffusion parameters throughout the Galaxy, but does not differ substantially from the IGRB spectrum inferred using alternative foreground models. As detailed in previous GCE studies [43, 36], the isotropic spectrum and flux are poorly constrained over the small ROI of the inner Galaxy analysis. We therefore opt to use the prescription of Ref. [36] whereby an external $\chi^2_{\rm ext}$ is imposed to constrain the isotropic spectrum within it's uncertainties [225] as determined from the larger regions of interest (the entire sky in this case). This takes the form

$$\chi^2_{\rm ext} = \sum_i \left(\frac{\phi_i - \bar{\phi}_i}{\Delta\phi_i} \right)^2 \tag{8.1}$$

where ϕ_i is the flux in energy bin i and $\bar{\phi}_i$ and $\Delta\phi_i$ are the mean and standard deviation of Ref. [225]'s IGRB Model A. However, *in the Galactic center analysis*, we employ a much smaller ROI, making it difficult to avoid contamination of the isotropic background by numerous diffuse Galactic sources. This is particularly true at low energies where the instrumental point spread function is large. In this case, we allow the normalization of the isotropic background to vary freely in each energy bin without an external χ^2 cost imposed. However, we will also show results produced when this template is fixed to the parameters of the physical isotropic background emission.

- *Fermi Bubbles:* The flux and spectrum of the Fermi bubbles is assumed to be spatially uniform over the region defined in Ref. [11] with more recent corrections

[2] This is not to be confused with our benchmark Galactic diffuse emission model ModA from Calore et al (2015) [36]. In all following sections, mention of ModA will always refer to the latter GDE case.

made near the Galactic plane [10] which are shown in Figure 8.1. We do not model the North and South Lobes independently. Similarly to the isotropic template above, we impose the spectrum from the latest *Fermi* Collaboration paper [226]. For the Global analysis, the spectrum is fixed (but not the overall normalization), while in the inner Galaxy, the spectrum is constrained to the form of Eq. (8.1), In the Galactic Center analysis the spectrum is allowed to float freely due to our relatively poor understanding of the Fermi bubbles in regions close to the Galactic center. We also examine scenarios where the Fermi bubble spectrum and intensity are fixed to their values far from the Galactic center, and find that our treatment of the Fermi bubbles has a negligible impact on our results of the Galactic Center analysis.

- *Galactic Center Excess:* Motivated by numerous studies observing an excess in γ-rays spherically concentrated around the Galactic center [241, 242, 374, 243, 44, 245, 45, 43, 385, 36, 42], we add and examine the properties of an additional template built to model this emission. Motivated by the reasonable fit provided by dark matter models to the morphology of the excess, we produce an additional template with a global morphology described by the integral over the line of sight of the squared Navarro-Frenk-White (NFW) density profile [89], which has a three dimensional density profile given by Eqn.(9.1).

  Based on several fits to the data, our Canonical model employs an inner slope of $\alpha = 1.05$, which is shallower than the NFW profile used in previous studies [36, 43],

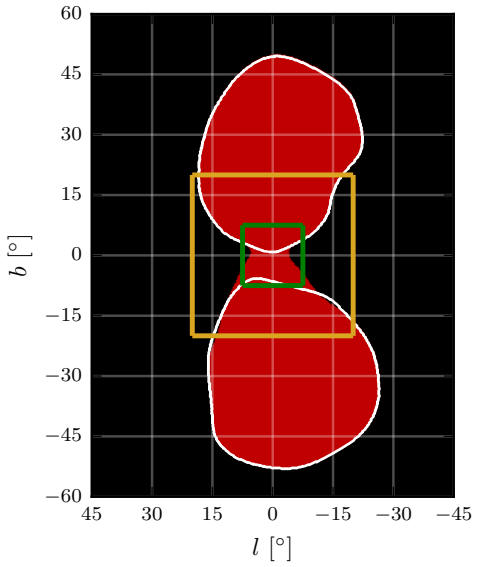

Figure 8.1: The new Fermi bubbles template [10] used in this analysis is shown in red, and extends throughout the Galactic center region. The previous template versions [11] are shown by white contours. Also shown are the bounding windows for the inner Galaxy analysis (gold) and Galactic center analysis (green).

as well as a scale radius of $r_s = 20$ kpc. In Section 8.1.3.5 we scan over different values of the inner slopes and ellipticity, in order to determine the resilience of this excess component to changes in the diffuse modeling.

8.1.2.3 Global Analysis and $X_{\rm CO}$ Fitting

After utilizing `Galprop` to generate the energy-dependent γ-ray morphology of each astrophysical model component (excepting the NFW profile and Fermi-bubbles), we construct the diffuse model by fitting the radial variations of $X_{\rm CO}$. `Galprop` outputs π^0 and bremsstrahlung templates in 9 radial annuli (defined in Tab. 8.2) for each of the gas components HI, HII, and H_2. Given the strong degeneracy between the gas-correlated π^0 and bremsstrahlung components, we merge the two into a single π^0 +

1.25 $\times$ bremsstrahlung template for each annulus and each gas component[3]. Next, we merge the HI and HII annuli into a single template whose total normalization is freely varied. The H_2 rings are kept separate in order to fit the $X_{\rm CO}$ conversion factor for each annulus. ICS emission in `Galprop` is comprised of the cosmic microwave background, optical, and far-infrared components which have their relative normalizations fixed by the model under consideration. The total ICS normalization, however, is left free. The point source template has normalizations and spectra fixed to 3FGL values. The overall normalizations for the Fermi-bubbles and isotropic component are allowed to vary with constraints from the external χ^2 described above.

Photons are spatially binned into an equal area `Healpix` [224] grid with $n_{\rm side} = 256$, providing a spatial resolution of $\sim 0.23^\circ$. Spectral binning follows the recipe of Ref. [36] consisting of four linearly spaced bins between 300-500 MeV, with $n_{\rm bins} = 20$ additional bins between $E_{\rm min} = 500$ MeV and $E_{\rm max} = 500$ GeV whose edges are defined recursively by,

$$E_{j+1} = \left(E_j^{1-\Gamma} - \frac{E_{\rm min}^{1-\Gamma} - E_{\rm max}^{1-\Gamma}}{n_{\rm bins}} \right)^{\frac{1}{1-\Gamma}}, \tag{8.2}$$

for $j \in [0, 1, ..n_{\rm bins}]$. This spacing provides an equal number of photons in each bin for a power-law spectrum with index Γ. A hard index of $\Gamma = 1.45$ is chosen to balance loss of statistics and unreasonably large bin widths at high energies [36].

Next, each diffuse emission component is smoothed by a Gaussian kernel to

[3]For the diffuse models in Ref. [36], a π^0 to bremsstrahlung ratio of 1:1.25 was found to minimize the absolute value the residuals. This precise ratio is not important even when fixed in the Galactic center analysis where the bremsstrahlung template is normally allowed to float independently. For the Global and Inner Galaxy analyses, combining these templates both improves convergence and allows us to fit a single value of $X_{\rm CO}$ for each H_2 ring.

approximate the LAT PSF in a computationally efficient manner[4]. For each energy bin, the width of the Gaussian is set to the 68% containment radius of the actual PSF, computed by averaging the PSF over the bin, weighted by the spectrum of *Fermi's* P8R2 diffuse Galactic background model. We confirm previous findings [36, 400] that the details of smoothing the diffuse emission components are not important for the inner Galaxy analysis.

For a given region of interest we use `Minuit`[5] to minimize the χ^2 in three fitting regions as defined by,

$$\begin{aligned} \chi^2 &\equiv -2\ln\mathcal{L} + \chi^2_{\rm ext} \\ &= 2\sum_{i,j} w_{i,j}(\mu_{i,j} - \theta_{i,j}\ln\mu_{i,j}) + \chi^2_{\rm bub} + \chi^2_{\rm IGRB}. \end{aligned} \tag{8.3}$$

Here $\theta_{i,j}$ is the observed number of photons in energy bin i and pixel j. The model flux $\mu_{i,j}$ is the normalization weighted sum of all model templates. In the Global analysis, the spectrum of all `Galprop` derived templates is fixed and only the total normalization over all energy bins is varied. The $\chi^2_{\rm ext}$ terms constrain the spectrum of the Fermi bubbles and isotropic components. Ref. [36] developed the weighting coefficient $w_{i,j}$ which allows for adaptive source masking based on the ratio of the point (or extended) source flux

[4] *Fermi's* PSF has substantially longer tails than a Gaussian function and one can more accurately implement the PSF by performing a spherical harmonic transform, re-weighting the coefficients, and performing the inverse transform. Unfortunately, this is only accurate if the PSF is much larger than the Healpix angular size ($\approx 0.23^\circ$) or the Healpix resolution is first up-sampled, reweighted, and downsampled, which is computationally expensive. Maps for individual point sources are still calculated using the precise Fermi PSF.

[5] See https://seal.web.cern.ch/seal/MathLibs/Minuit2/html/ and its Python interface, iMinuit http://iminuit.readthedocs.org/en/latest/ for further information.

$\mu_{i,j}^{\rm PSC}$ to the diffuse flux $\mu_{i,j}^{\rm BG}$,

$$w_{i,j} \equiv \left[\left(\frac{\mu_{i,j}^{\rm PSC}}{f_{\rm PSC} \mu_{i,j}^{\rm BG}} \right)^{\alpha_{\rm PSC}} + 1 \right]^{-1} . \tag{8.4}$$

Here $f_{\rm PSC} = 0.1$ and $\alpha_{\rm PSC} = 5$ determine the point source masking threshold and transition rate from masked to unmasked pixels [36].

With the statistical framework and templates defined, we now determine the value of $X_{\rm CO}$ for each molecular ring. In order to avoid bias from the bright Galactic plane emission, we preform subsequent fits over three sky regions as was done in Ref. [342]. A major benefit of this method is the ability to assess (via likelihood ratio tests) the quality of our new diffuse models not just in the Galactic center, but also in independent regions of the global sky. We refer to these regions as global-local, global-outer, and global-inner as defined below and summarized in Table 8.3. Annuli are defined in Table 8.2.

1. *Local Ring:* As we are embedded inside the local H_2 gas ring, the local value of $X_{\rm CO}$ is well determined by high-latitude emission which is not influenced by emission along Galactic plane. We therefore fix all of the H_2 rings except for the local ring 7 to their `Galprop` defaults and fit to the full high-latitude sky $|b| > 8^\circ$, allowing the IGRB, Bubble, π^0+bremsstrahlung, and ICS templates to vary.

2. *Outer Rings:* There are two H_2 rings in the outer Galaxy. We fix the normalizations of the Ring 7 and isotropic templates to the global-local values and proceed to fit $X_{\rm CO}$ in the outer two annuli over the region $|b| < 8^\circ |, |l| > 80^\circ$.

3. *Inner Rings:* Rings 7-9 are now fixed and the 6 remaining H_2 rings may be fit in the 'Global Inner Galaxy', defined by the region $|b| < 8°|, |l| < 80°$. The Fermi bubbles extend to $|b| \approx 50°$ and are better constrained by high-latitude fits than in the Galactic plane. We therefore fix their normalization to the value determined in the global-local fit.

Ring Number	Radius [kpc]	Fit Region	X_{CO} [cm^{-2} (K km s^{-1})$^{-1}$]
1	$0 - 2.0$	Inner	$1.00 \times 10^{19\dagger}$
2	$2.0 - 3.0$	Inner	8.42×10^{19}
3	$3.0 - 4.0$	Inner	1.61×10^{20}
4	$4.0 - 5.0$	Inner	1.73×10^{20}
5	$5.0 - 6.5$	Inner	1.72×10^{20}
6	$6.5 - 8.0$	Inner	1.74×10^{20}
7	$8.0 - 10.0$	Local	8.61×10^{19}
8	$10.0 - 16.5$	Outer	4.29×10^{20}
9	$16.5 - 50.0$	Outer	2.01×10^{21}

Table 8.2: Definitions of gas annuli used during the 3-stage global X_{CO} fitting described in Section 8.1.2.3. The right column shows the iteratively determined 'seed' X_{CO} values which are input to `Galprop` before discretely γ-ray fitting the rings to each model.

When generating γ-ray skymaps, `Galprop` uses power-law interpolation to determine $X_{CO}(r)$ from a discrete set of X_{CO} values. The final model is therefore somewhat sensitive to the initial input values unless one iteratively determines X_{CO} by feeding the

fitted values back into `Galprop` until convergence is reached [342]. In our high-resolution three-dimensional simulations, however, this approach is computationally expensive. Because $X_{\rm CO}$ is most strongly effected by the gas and source distributions, we choose to iterate our Canonical model four times. These values are then used as the input $X_{\rm CO}$ for all other models and are listed in Table 8.2. Finally, we sum the $X_{\rm CO}$ renormalized H_2 rings and add them to the HI+HII template (whose normalization is determined by the global-inner fit) to obtain a single map for π^0 and bremsstrahlung which can be used in the Inner Galaxy or Galactic Center analyses below.

8.1.2.4 Inner Galaxy Analysis

In order to model the region of the sky near the Galactic center, we define an *inner Galaxy* analysis comprised of a $40^\circ \times 40^\circ$ window centered on $l = b = 0^\circ$, but with latitudes $|b| < 2^\circ$ masked out in order to avoid bias from the bright and complex Galactic plane. The choice of a $40^\circ \times 40^\circ$ ROI balances the specificity of the model for the Galactic center against the ability to fit model components far away from regions where there may be a significant GCE contribution.

The analysis details for the inner Galaxy are identical to the global analysis with several important exceptions:

(i) each free component is now fit bin-by-bin in energy, allowing for a model independent determination of the spectrum based solely on the emission morphology;

(ii) a single π^0+1.25$\times$ bremsstrahlung template is used for all the gas correlated emission; and

(iii) we consider fits with and without a GCE template to assess the significance of a new spherical component.

The inner Galaxy analysis is thus an exact replica of Ref. [36], but using Pass 8 data and instrument response functions (versus Pass 7) as well as the 3FGL catalog (versus 2FGL). Other than point sources, every template is free to vary in each energy bin, with the Fermi bubbles and IGRB constrained by $\chi^2_{\rm ext}$.

8.1.2.5 Galactic Center Analysis

To model the γ-ray intensity and spectrum in regions very close to the GC ($15^\circ \times 15^\circ$ centered on the GC with no latitude mask), we utilize the Fermi-LAT tools to bin photons into 300×300 angular bins and 30 logarithmically spaced energy bins between 300 MeV and 300 GeV. We place photon selection cuts which are identical to all previous analyses in this section, with the exception that we select only events which convert in the front of the Fermi-LAT detector. We utilize the `gtsrcmaps` toolset to convolve all 81 model components with the Fermi-LAT PSF in each energy range, using a minimum bin size of 0.01° to calculate each source model. By producing the sourcemaps on an angular scale much smaller than our analysis scale, we avoid errors in the determination of steeply sloped emission profiles such as the NFW template in regions very close to the GC.

We then utilize the `gtlike` algorithm to calculate the best fitting normalization of each model component, fixing the spectra of each source at their default values within

the very small energy bins chosen for this study. We then calculate the resulting spectra of each emission template from the ensemble of normalizations calculated for each energy bin, and utilize `gtmodel` to determine the emission model and calculate the LG(L) of our fit to the γ-ray data. In some simulations (noted throughout the text) we add a 2° latitude mask into the Galactic Center analysis. This is done by masking the output of `gtsrcmaps`, setting both the γ-ray data and model fluxes to 0 within a given ROI. During the calculation of the likelihood function by `gtlike`, the pixels within the mask have no weight in determining the best fitting model parameters. We have tested that this strategy produces consistent results and introduces no errors into the fitting procedure. In simulations constraining the dark matter density profile and ellipticity of the NFW profile, we bin the Fermi-LAT data into 150×150 angular bins in order to decrease the computational time, and have tested that this change has no significant effect on our results.

8.1.3 Results

The diffuse emission models and methodology adopted here can be employed to address a wide variety of questions. For example, the specificity of our models to the Galactic center region make them ideal for studies of the Fermi bubbles, and the three-dimensional nature of our models makes them ideal for studies of the contribution of the spiral arms to the locally observed cosmic-ray population.

However, for the remainder of this section, we will study the impact of our improved diffuse emission models on the existence, spectrum, and morphology of the

Galactic center γ-ray excess (GCE). In this context, we also present the relevant results from the full-sky global analysis, which can be useful to inform our parameter choices, and to establish the quality of these new models.

In the following sections, we first examine the parameter space of our star-formation model, studying the resulting changes to the global diffuse γ-ray emission as well as the impact of these models on the Inner Galaxy and Galactic center ROIs and GCE properties. For the interested Reader, we quickly note the key results of our analysis:

1. Larger values of $f_{\rm H2}$ enhance the central population of cosmic rays. The CMZ electron population in particular, produces an approximately spherical, extended, and sharply peaked ICS halo surrounding the Galactic center. Depending on the value of $f_{\rm H2}$, this feature is highly degenerate with the bulk properties of the GCE.

2. When we consider only the Galactic diffuse emission model in the analysis (i.e. no GCE template), a value of $f_{\rm H2} \approx 0.1 - 0.2$ is strongly preferred by the data. Notably, larger ROIs prefer larger values of $f_{\rm H2}$; the best fit is $\sim$0.1 in the Galactic Center analysis, and 0.2 in both the Inner Galaxy analysis and the full-sky analysis.

3. Models with $f_{\rm H2} \approx 0.1 - 0.2$ still substantially underpredict the observed CMZ star formation rate (cf. Sec. 7.1). In addition, the the global-inner and global-local analyses very strongly prefer $f_{\rm H2} \approx 0.2 - 0.4$. *How the results below are interpreted depends strongly on the relative weights of these priors (toward large $f_{\rm H2}$) pitted against the statistical preference toward lower $f_{\rm H2}$ provided by the nar-*

rower inner Galaxy and Galactic center ROIs. At present, the large unknown systematics of the region, and the potential for missing model elements obfuscates an objective statistical assessment of the two possibilities. We therefore present both interpretations:

(a) When a diffuse model utilizing a value $f_{\rm H2} \approx 0.2$ is *imposed* in the Inner Galaxy analysis, it greatly affects the spectrum and morphology of the GCE, and decreases the intensity of the GCE component by approximately a factor of 3. In particular, for the Inner Galaxy ROI, we observe a marked degeneracy between the emission attributable to the γ-ray excess, and diffuse emission models. On the other hand, the GCE is relatively robust in the Galactic center analysis due to two major effects:

(i) the bright residual component within two degrees of the Galactic center which is not well fit by diffuse emission models (but is masked from the Inner Galaxy analysis), and

(ii) the smaller ROI allows the normalization of diffuse emission components to float more freely in the Galactic center analysis compared to analyses of the Inner Galaxy ROI.

(b) For all models, both the Inner Galaxy and the Galactic Center, the *inclusion of a GCE template remains statistically preferred* compared to diffuse emission models that do not include a GCE component. In these models the best fit value of $f_{\rm H2}$ is reduced to approximately 0.1 in both the Inner Galaxy and Galactic

Center analyses, and the normalization of the excess is reduced by only a factor of ∼33-50% in the Inner Galaxy analysis (and remains unchanged in the Galactic Center analysis). However, the spectrum and morphology of the GCE template can still be significantly altered by these relatively modest values of $f_{\rm H2}$, in some cases producing an unphysically hard spectrum. This appears to be a result of the GDE model becoming too bright below 1 GeV near the Galactic plane, and indicates the need for further enhancements in the diffuse emission modeling.

4. It is difficult to further reduce the residual GCE emission by varying standard diffusion parameters. In order to reconcile the large expected cosmic-ray injection rate of the CMZ with the observed γ-ray data, one must reduce the number of cosmic-ray electrons below $\sim$ 30 GeV. We find that a hardened CMZ injection spectrum cannot explain the troublesome low-energy spectrum and morphology. The remaining option is advection-dominated transport out of the CMZ. The addition of a strong Galactic center wind (i) improves the low-energy γ-ray fit, (ii) helps to reconcile CMZ injection rates with already oversaturated π^0 emission near the Galactic center (see Appendix 8.1.8.1), and (iii) prefers larger values of $f_{\rm H2}$ – which better match observed CMZ injection rates – in models with and without a GCE component.

At this point our analysis offers two distinct possible interpretations – one with a significant GCE component and one without. If one applies the full sky analysis of $f_{\rm H2}$ and adopts a strong a priori preference for $f_{\rm H2} \approx 0.2$ or higher in the Inner Galaxy

and Galactic center analysis, then the large scale emission from the GCE component is significantly mitigated, and the GCE may be interpreted as a symptom of mismodeling of the diffuse emission outside the inner-few degrees surrounding the Galactic Center. In this interpretation, some residual component is still necessary in the inner few degrees surrounding the GC, but as significant systematic uncertainties exist in this region, its interpretation would be unclear. On the other hand, one may argue that the best-fit value of $f_{\rm H2}$ in the spiral arms should not be correlated to the value of $f_{\rm H2}$ near the Galactic center and that the current CMZ injection rate lies below that of the long term average. In that case, the fit should allow the value of $f_{\rm H2}$ and the normalization of the GCE template to float freely in the fit, and our results indicate that the full log-likelihood fitting strongly prefers a lower value of $f_{\rm H2}$ along with a significant GCE component.

Ultimately, Galactic diffuse emission modeling toward the Galactic center remains a difficult and open problem whose complete, physical solution is only in its infancy. We aim here to highlight the degeneracies between the astrophysical diffuse emission and any putative dark matter emission sources, present an up-to-date analysis of the GCE in this context, and discuss avenues for improved GDE models in the Galactic center region. In these state-of-the art, yet still "simplified" models, the GCE remains an important emission component, and we will study the morphology and spectrum of the GCE in great detail using both the Galactic center and Inner Galaxy analyses. We will then study the impact of global diffusion parameters on the GCE residual, focusing especially on how they reshape the new CMZ electron cloud. CMZ specific solutions are then discussed including hardening the injection spectrum and adding strong outflowing

winds from the GC. In the appendices we also discuss the implications on $X_{\rm CO}$ and gas calorimetry at the GC, the ROI dependence of fit components, GCE fits across the 10 sky segments used in Ref. [36], comparisons to the CMZ 'cosmic-ray spike' models of Ref. [400], and robustness of the Galactic center reults against the 1FIG point source catalog [42].

8.1.3.1 Tuning the Star Formation Model

Our star formation prescription contains three parameters: the Schmidt power-law index n_s, the fraction $f_{\rm H2}$ of sources distributed according to Eq. (7.3), and ρ_c, the critical density needed to initiate star formation. In Section 7.1.0.7 we provided physical arguments describing the importance and range of each of these parameters. However, the spatial resolution of our gas map ($\sim$ 100 pc) is much lower than typical single cloud hydrodynamic simulations, making our prescription necessarily phenomenological in its modeling of the sub-grid physics. We therefore opt to explore a broad range of the parameter space initially and choose our Canonical model values as those which fit the data well over the full sky.

In this section, we show that the star formation parameters n_s and ρ_c only weakly impact the statistical fits with respect to the existence and properties of the Galactic center excess. Our star formation parameter space is approximately reduced to a single dimension aligned with $f_{\rm H2}$. We will then examine our Canonical model in great detail, focusing here on how the new GDE models ($f_{\rm H2} \neq 0$) impact the properties of the GCE.

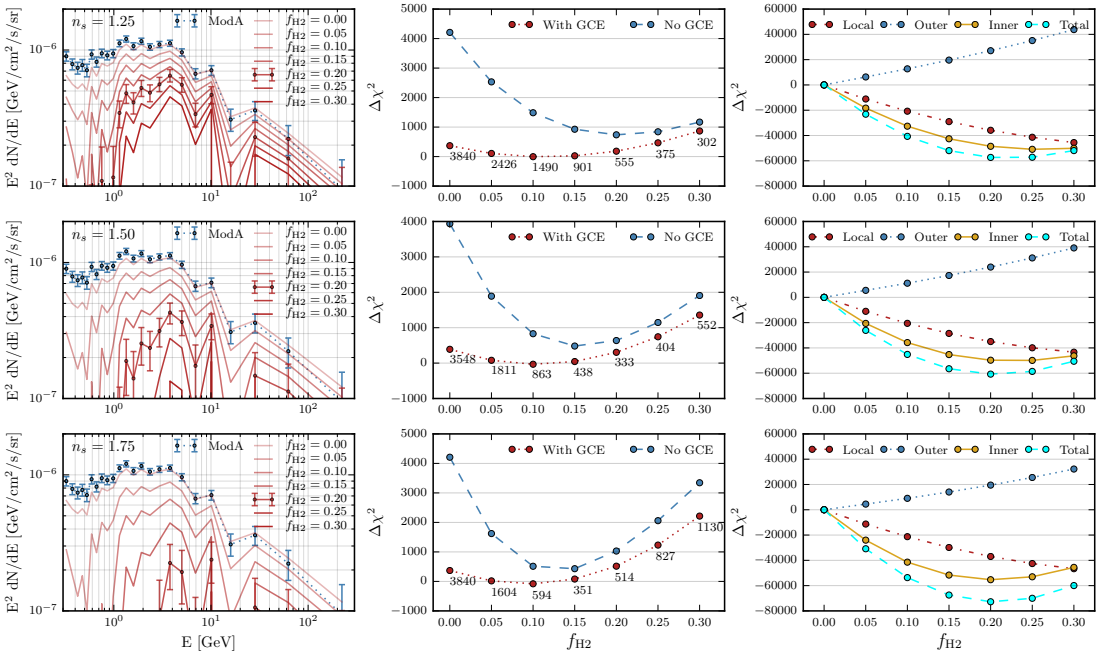

Figure 8.2: **Left:** Flux of the Galactic Center Excess in the inner Galaxy analysis using an NFW$_{\gamma=1.05}$ GCE template. From top to bottom rows we also vary the Schmidt index ($n_s = 1.25, 1.5, 1.75$) and the fraction $f_{\rm H2}$ of primary cosmic-ray sources distributed according to molecular gas as $Q_{\rm Primary}(\vec{x}) \propto (n_{\rm H2}(\vec{x}))^{n_s}$. The remaining fraction is distributed according to the observed azimuthally averaged surface density of supernova remnants [22]. Mod A is a benchmark model from Ref. [36]. **Center:** $\Delta\chi^2$ for the inner Galaxy analysis as $f_{\rm H2}$ is varied. Red (blue) curves show the $\Delta\chi^2$ with (without) a GCE template included, with negative values indicating a better fit than Mod A+GCE. Inset numbers indicate the statistical preference (TS) for the inclusion of a GCE template in the fit. **Right:** $\Delta\chi^2$ for the three region global $X_{\rm CO}$ fitting analysis (no GCE template is included in the global fitting). $\Delta\chi^2 = 0$ in this column corresponds to the the $f_{\rm H2} = 0$ model, with negative values indicating an improved fit. The inner Galaxy and total-global ROIs have 1.65×10^5 and 1.89×10^7 degrees of freedom respectively.

Remarkably, almost all of the best fitting global parameters are close to the best fit values in the inner Galaxy analysis when a GCE template is not included. In Figure 8.2 we present the most important results of this section – the GCE spectrum and the $\Delta\chi^2$ as we discretely vary $n_s \in [1.25, 1.5, 1.75]$ (top to bottom rows) and $f_{\rm H2}$. In the *left* column we show the spectrum of the NFW$_{\alpha=1.05}$ GCE template in the bin-by-

bin inner Galaxy analysis, with red lines from light to dark corresponding to increasing $f_{\rm H2}$ from 0 to 0.3. The Canonical model ($f_{\rm H2} = .2$) is highlighted with red error bars. The blue error bars show the GCE spectrum for reference Mod A[6]. The *center* column shows $\Delta\chi^2$ for the inner Galaxy analysis with (red) and without (blue) a GCE template included in the fit. Here, negative values indicate improved fit relative to Mod A+GCE, and the difference between the blue and red lines indicates the test statistic of adding the additional GCE template (24 additional degrees of freedom). Finally, the *right* column of panels shows $\Delta\chi^2$ for each of the three global fit regions, as well as the their (summed) total $\Delta\chi^2$.

As $f_{\rm H2}$ is increased from zero, which corresponds to the classic SNR source distribution, the high density of gas in the inner few hundred parsecs dramatically increases the cosmic-ray injection intensity near the Galactic center. The non-linearity of the Schmidt law (when $n_s > 1$) implies that cosmic-ray injection rate scales steeply with the H_2 density, concentrating cosmic-rays toward dense molecular clouds. Nowhere is the impact of this more dramatically realized than in the Central Molecular Zone and Galactic bar. Cosmic-rays younger than 10^5 yr remain quite close to their injection site, illuminating the giant molecular structures which generated them. As the cosmic-rays age they diffuse outward ($R_{\rm diff.}(E) = 2\sqrt{D_{xx}(E)t}$) and produce γ-rays in the ambient ISM. For electrons near the Galactic center, the magnetic fields and ISRF energy densities are sufficiently large that energy losses strongly limit the diffusion timescale,

[6]The low energy spectrum of the GCE using Mod A is substantially softer here than in the original Ref. [36]. This is due to the combined effects of switching to Pass 8 data and using 3FGL point sources. The GCE spectrum below 1 GeV remains quite sensitive to the choice of `Galprop` parameters.

leaving behind a sharply peaked, and approximately spherical inverse Compton component. Thus, as $f_{\rm H2}$ is increased, the CR population at the Galactic center is enhanced and the GCE is strongly reduced until the diffuse emission eventually over-saturates the observed emission from the inner Galaxy for high values of $f_{\rm H2}$.

As n_s is increased, cosmic-ray sources become increasingly concentrated in the most gas dense regions – e.g. the CMZ. For the inner Galaxy, the effect is quite similar to increasing $f_{\rm H2}$. Thus for larger values of n_s, the same level of GCE reduction (and CMZ injecttion rate) is achieved by smaller $f_{\rm H2}$. Statistically, this is evidenced by the compression of the $\Delta\chi^2$ versus $f_{\rm H2}$ profile as n_s becomes larger. The global γ-ray fit improves somewhat for larger values of n_s, though the difference is subdominant compared with changing $f_{\rm H2}$. Because diffusion washes out much of the peaked structures, increasing n_s adds more cosmic-rays to the densest gas clouds, effectively rescaling the action of $f_{\rm H2}$. We therefore choose $n_s = 1.5$ for the remainder of this Section and relegate further study to the future.

Without invoking an extra GCE template, the fit in the inner Galaxy analysis shows marked improvement using our star formation source model, preferring $f_{\rm H2} \approx 0.15 - 0.25$ at very high significance ($\Delta\chi^2 \approx 4000$) over the pure SNR distribution. When a GCE template is added, the fit is more agnostic to changes in $f_{\rm H2}$ and has a shallower profile which slightly prefers $f_{\rm H2} = 0.1$. The test statistic (TS) for the addition of the GCE template is given by the difference between the red and blue curves and our Canonical model with $n_s = 1.5$ and $f_{\rm H2} \approx 0.1$ reduces the significance of

the excess from TS≈4000 (in the case of Mod A), down to TS∼1000[7] These two results indicate the strong degeneracy between the GCE template and GDE models containing a cosmic-ray emitting CMZ. In addition, it is intriguing to note that the globally preferred values of $f_{\rm H2}$ are the same as those that maximally reduce the significance of the GCE. Specifically, the TS of the GCE is reduced further to TS = 333 when the best fit global model of $n_s = 1.5$ and $f_{\rm H2} \approx 0.2$ is employed, and remains highly suppressed when larger $f_{\rm H2}$ are used (as preferred by the CMZ SFR constraints). On the other hand, the statistical significance of this component is still reasonably high, motivating us to study the residual properties of the GCE in detail in Section 8.1.3.3.

Globally, our $f_{\rm H2}$ models perform much better than the default SNR case (and better than Mod A, though this is not shown). One can examine $\Delta\chi^2$ for each pixel in order to determine which regions improve as $f_{\rm H2}$ is increased. This is shown in Figure 8.3, where the delta-log-likelihoods for $f_{\rm H2} = 0.2$ versus $f_{\rm H2} = 0.0$ (null model) are presented for the three regions used in the Global analysis. Blue regions highlight lines-of-sight where the addition cosmic-ray sources tracing the H_2 density provide an improved fit relative to the axisymmetric SNR model [22].

In the global-inner Galaxy, the redistribution of cosmic rays dramatically improves the fit for $45^\circ < l < 30^\circ$. In the plane, diffuse Galactic γ-ray emission is dominated by π^0 decays following the hadronic interactions of cosmic-ray protons with *molecular* hydrogen. Because the CO$\rightarrow$ H_2 conversion factor ($X_{\rm CO}$) has been refit for each model,

[7]We note here that the $\sqrt{\rm TS}$ cannot be interpreted straightforwardly as a significance due to the large unresolved systematic uncertainties [36]. In particular, no GDE model currently describes the data even remotely close to the level of Poisson noise making an interpretation of $\Delta\chi^2$ in terms of significance difficult. A study of the (much larger) correlated systematic uncertainties along the Galactic plane can be found in ref. [36], and is used at several points below.

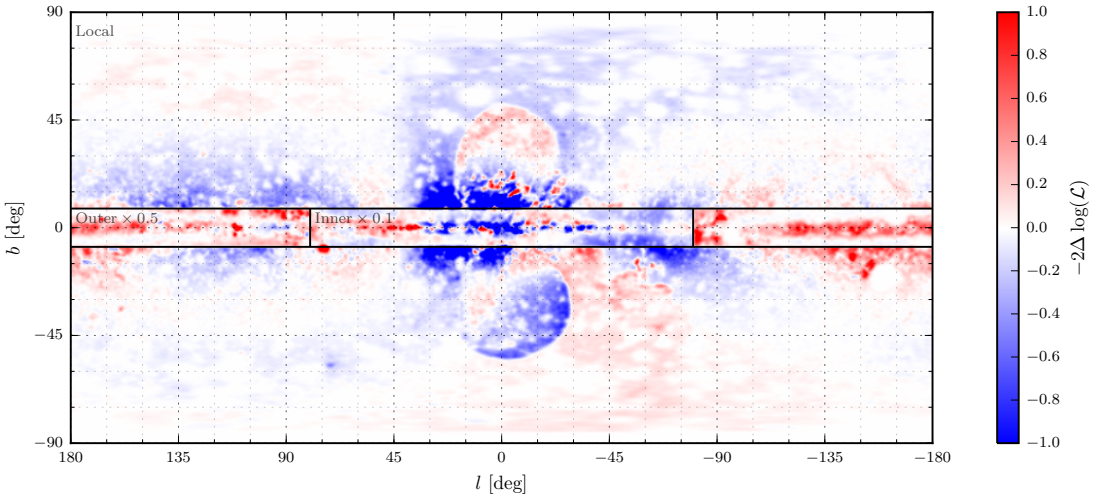

Figure 8.3: Pixel-by-pixel $-2\Delta\ln(\mathcal{L})$ for $f_{\rm H2} = 0.2$ against the null model $f_{\rm H2} = 0.0$, integrated over all energy bands for the global γ-ray analysis in the local($|b| \geq 8^\circ$), outer ($|b| < 8^\circ, |l| > 80^\circ$), and inner Galaxy ($|b| < 8^\circ, |l| < 80^\circ$) regions of interest, smoothed by a 0.5° Gaussian kernel. Blue regions represent an improved fit compared with the axisymmetric source distributions. The outer and inner regions have been rescaled by a factor 1/2 and 1/10, respectively and the white 'holes' are due to point source masking, where the pixels have been weighted according to Eq. (4.18). Boxes indicate the edges of each global analysis ROI, and may produce discontinuities in the residuals since different model fits are imposed.

the fit improvements in this region must originate from (i) non-axisymmetric features of the cosmic-ray injection morphology and/or (ii) an improved steady-state distribution of cosmic-rays which illuminate the fixed *atomic* and *ionized* Hydrogen gas components. In either case, the improved fit indicates that the new source models are resolving important cosmic-ray emitting structures toward the inner Galaxy.

The outer Galaxy analysis produces very different outcomes, with non-zero $f_{\rm H2}$ resulting in an inferior fit. However, this is likely to be a red herring, as the under-performing pixels lie above a few degrees latitude, where the thick disks of HI and HII dominate the gas density (rather than H_2). Because HI is directly observable and the

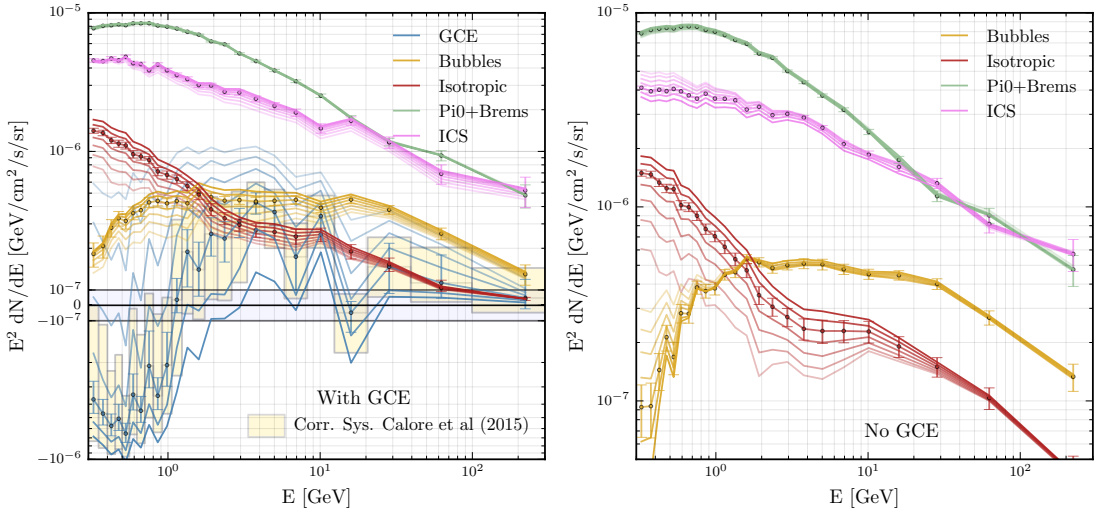

Figure 8.4: Inner Galaxy spectra of diffuse emission components with a GCE template (top) and without (bottom). Curves from transparent to opaque increase $f_{\rm H2}$ from 0 to 0.3 in increments of 0.05, with the $f_{\rm H2} = 0.2$ case marked by error bars. In the top panel, absolute fluxes below 10^{-7} GeV/cm^2/s/sr have been linearized in order to show negative fit values. The filled yellow error bars show correlated systematic uncertainties taken from ref. [36]. We have assumed here (with some motivation as described below) that these are comparable to the systematic errors of our new GDE models. Note that although the Fermi bubbles and isotropic spectra are allowed to float, deviations from the values determined using larger regions of interest are penalized by an externally imposed $\chi^2_{\rm ext}$, as described in Sec. 8.1.2.3.

conversion from 21cm line intensity to gas density is requires only a single parameter (the hydrogen spin temperature, which is typically treated as globally constant) the radial profile of atomic hydrogen is fixed. This is in contrast to H_2 where the $X_{\rm CO}$ conversion factor is allowed to vary. As we have seen in Fig. 7.2, increasing $f_{\rm H2}$ centrally concentrates the cosmic-rays causing the fixed HI and HII γ-ray emission to become dimmer. This leads to a worse fit which can only be compensated by $X_{\rm CO}$ at low latitudes. Given that the gas surveys are complete over these regions, it is notable that the outer Galaxy appears to have either a significant abundance of dark gas, or an increased population

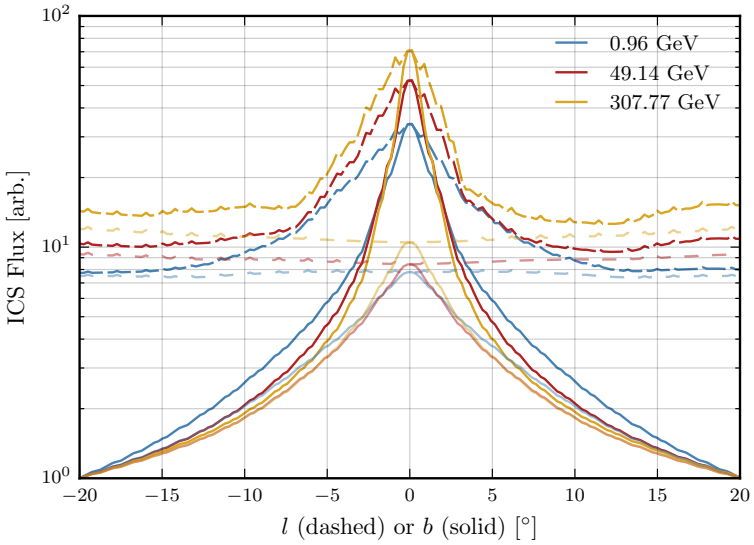

Figure 8.5: ICS flux as a function of longitude (dashed) and latitude (solid) along $b = 0$ and $l = 0$ for the cases of $f_{\rm H2} = 0$ (transparent lines) and $f_{\rm H2} = 0.2$ (opaque lines). Each line has been normalized to unity at $(l, b) = (0, 20^\circ)$.

of cosmic-ray sources relative to observations (e.g. supernova or pulsar counts). This conclusion is consistent with previous determinations of the radial $X_{\rm CO}$ profile from γ-ray data [342, 40].

In Figure 8.4 we show the spectrum of each diffuse component (omitting the fixed point source template) in the inner Galaxy analysis as $f_{\rm H2}$ is increased, with transparent to opaque lines showing $f_{\rm H2} = 0 \rightarrow 0.3$ in increments of 0.05. In the top panel, we include a GCE template in the fit and as $f_{\rm H2}$ is increased, the GCE flux is rapidly diminished at all energies, hardening at low energies and eventually becoming over-subtracted *if the DM template is allowed to take on negative values.* The yellow uncertainty bands correspond to 1σ diagonal elements of the full correlated systematic uncertainties[8] from

[8]While these were derived using a different GDE model, we show in Sec 8.1.3.4 that GCE-like residuals along the Galactic plane do not change as dramatically as the Galactic center excess with increasing $f_{\rm H2}$, implying that the errors for the $f_{\rm H2} = 0.2$ case should be comparable to those of Mod A.

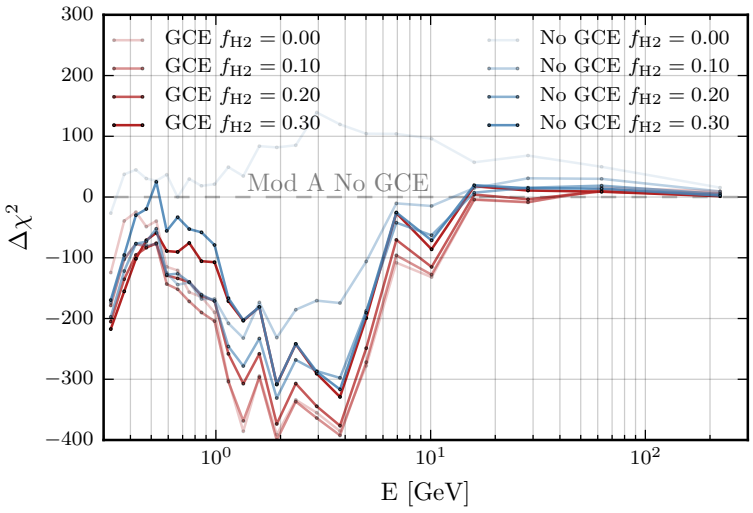

Figure 8.6: Inner Galaxy $\Delta\chi^2$ as a function of energy bin for representative values of f_{H2} with (red) and without (blue) dark matter. The zero point is with respect to Mod A without dark matter.

Ref. [36]. These are are most significant at energies $\lesssim 1$ GeV, where the *Fermi's* point spread function becomes large, making it difficult to distinguish components based on morphology alone. The ICS component, Fermi bubbles, and isotropic templates gain some power across all energies while the π^0 component is largely unchanged.

In the lower panel, we include only known astrophysical components (no GCE) in the fit. The Fermi bubbles spectrum is now very stable as a function of f_{H2} while the isotropic component changes by a factor 2-3 below 10 GeV becoming more akin to a smooth power-law for larger f_{H2}. In all cases, the isotropic and Bubbles spectra are constrained by larger ROIs. Even so, at low energies the point spread function is large, and the effective ROI of the inner Galaxy is small due to the large number of point sources in the field. The spectrum of each component is thus much more uncertain than the statistical error bars shown, and can include contributions from mismodeled point

sources, gas, or unmodeled diffuse components that are not present in other regions of the Galaxy. Finally, while the the total ICS component is reduced, this does not imply that the ICS emission is reduced near the Galactic center. In fact, models with $f_{H2} \approx 0.2$ produce a several fold enhancement within the inner few degrees compared with the pure SNR case.

In Figure 8.5 we show the longitude and latitude profiles of the ICS emission along $b = 0$ and $l = 0$ for the cases of $f_{\rm H2} = 0$ (transparent lines) and $f_{\rm H2} = 0.2$ (opaque lines). Each line has been normalized to unity at $(l, b) = (0, 20^\circ)$. Most apparent is the completely flat longitudinal profile for the traditional models, highlighting the missing CMZ contribution. As we turn on the new source distribution, a large spike appears, peaked at the Galactic center. In longitude, the old model includes a peak at $b = 0$ due to the traversal of the Galactic plane, where the electron density is large throughout. The new spike is approximately spherical (keeping in mind this figure shows the *total* ICS emission with minor elongation along the plane due to the partly disk-oriented injection morphology. It is precisely this spike component which becomes highly degenerate with the observed properties of the GCE. As will be briefly discussed later, the true ICS profile may be steeper than shown here if one includes a more realistic model of the optical and infrared radiation field morphology near the CMZ. This ISRF structure is not present, and directly impacts the morphology and spectrum of the ICS emission.

In Figure 8.6 we show $\Delta\chi^2$ as a function of the energy for different values of $f_{\rm H2}$. Increasing $f_{\rm H2}$ greatly improves the fit without a GCE template between 1 and 20 GeV where the Galactic center excess is brightest. At lower energies, the improvement is

smaller owing to the heavy PSF masking of the ROI, with only marginal improvements up to $f_{\rm H2} = 0.1$, and reversing for higher values where the GCE template becomes over-subtracted. Again, these $\Delta\chi^2$ curves are purely statistical and do not take into account the very large systematic uncertainties present below 1 GeV, where point sources in the Galactic plane can strongly influence the results, and the diffuse components become more degenerate. The greatest improvement occurs at energies near the peak of the GCE spectrum, where the number of residual photons is greatest in previous models, and the point spread function is small enough to preserve morphological details. We see that when including dark matter, the fit is only marginally improved near the peak GCE energies, compared to $f_{\rm H2} = 0.2$. The similarity of these curves points to the strong statistical degeneracy between the astrophysical ICS emission of the Canonical model and dark-matter-like GCE template.

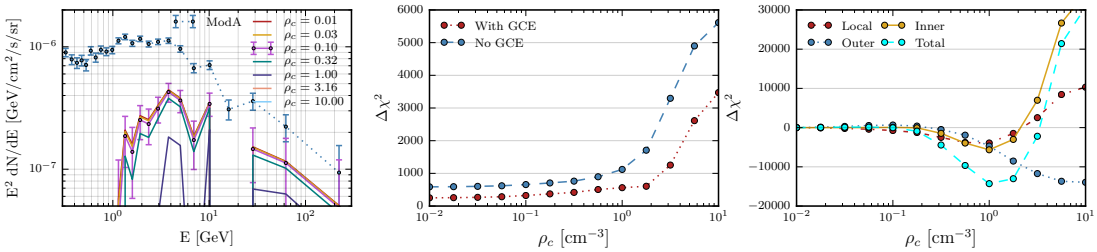

Figure 8.7: **Left:** Flux of the GCE template, for the inner Galaxy analysis as the star formation threshold density ρ_s is varied. **Center:** $\Delta\chi^2$ for the inner Galaxy analysis with and without a GCE template included in the fit. **Right:** $\Delta\chi^2$ for the global analysis.

Our star formation model has one additional parameter: the critical density, ρ_c, which sets the minimum gas threshold to initiate star formation, and thus to inject cosmic-rays. In Figure 8.7, we show variations away from the default 0.1 cm^{-3}.The

impact on the GCE negligible for $\rho_c \leq 0.1$ cm^{-3}, indicating that H_2 densities below $\rho_c = 0.1$ n$_{H2}$/cm^3 do not contribute significantly to the primary source population near the Galactic center. At higher thresholds, lower-density diffuse gas clouds contribute less. For a fixed value of f_{H2}, the number of sources in dense regions is thus increased, with an effect that is similar to increasing n_s. Globally, slightly higher thresholds $\rho_c \approx 1$ cm^{-3} are preferred, larger than those typically implemented theoretically and in hydrodynamic simulations [327], but within range of some models [401, 402]. All but the largest star forming regions are below the 500 pc resolution of our simulation and 100 pc resolution of the gas distributions, making this parameter more phenomenological than physical. Furthermore, the gas density is averaged over the lattice cell, and at sub-grid scales will contain much higher densities. The high threshold preference in the outer Galaxy is due to the redistribution of cosmic-rays to large radius, though, as mentioned above, this region appears to be biased in the γ-ray fits. Regardless of the specific value, the net effect on the Galactic center excess is to change the effective normalization of the CMZ region, since – for a given f_{H2} – excluding the low density diffuse cosmic-ray sources assigns the more sources to the very dense GC (and to the $R > 8.5$ kpc Galaxy). We therefore consider ρ_c as essentially degenerate with f_{H2}, and do not consider further variations here.

In Figure 8.8 we summarize the star formation model parameter space by showing statistics for a variety of fits in three cross-sectional planes involving f_{H2}, n_s, ρ_c. From left to right columns we show the inner Galaxy $\Delta\chi^2$ with a GCE and without a GCE template (relative to Mod A + GCE), the total Global $\Delta\chi^2$ (relative to the Canonical

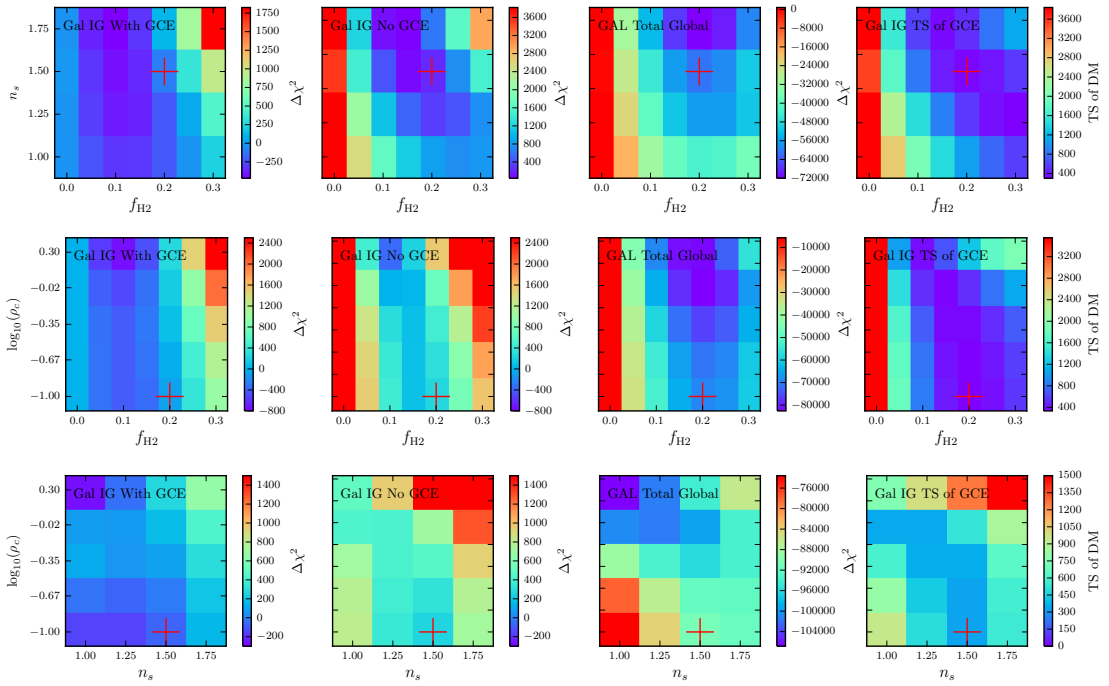

Figure 8.8: Fit statistics as star formation model parameters are varied. From left to right columns we show $\Delta\chi^2$ for the inner Galaxy with and without a GCE template (first two columns), total global $\Delta\chi^2$ with respect to $f_{\rm H2} = 0$ (third column), and the test statistic of the GCE template (right column). Lower (purple) values correspond to better fits except for the the rightmost column where purple regions indicate the minimal significance of an additional GCE component. Red '+'s indicate the Canonical model.

model with $f_{\rm H2} = 0$), and the test statistic of the GCE template in the inner Galaxy analysis. For the first three columns, lower values correspond to better fits, while in the right column, lower values correspond to lower GCE significance.

In the first row, we show the n_s versus $f_{\rm H2}$ plane. The inner Galaxy fits with and without a GCE template prefer $n_s \approx 1.5 - 1.75$ and smaller $f_{\rm H2} \approx .1 - .2$. Globally, high n_s are preferred which increases the number of sources in very dense gas regions, and decreases the fraction of cosmic-ray injection stemming from diffuse low-density sources. Because of this, a larger n_s requires a lower $f_{\rm H2}$ to achieve the same level of

structure. This inverse proportionality is clearly visible in all panels, and is especially prominent in the significance of the GCE template.

In the ρ_c versus $f_{\rm H2}$ plane, a similar story unfolds. For a fixed $f_{\rm H2}$, a larger star-formation threshold will enhance the number of sources in over-dense regions. For the CMZ in particular, the gas density is well over threshold, and an increase in ρ_c is nearly identical to increasing $f_{\rm H2}$. As we discussed in Fig 8.7, the global fit improvement at $\rho_c \approx 1{\rm cm}^{-3}$ is driven mostly by the biased outer Galaxy analysis. The inner Galaxy fit with and without a GCE template is marginally improved for $(f_{\rm H2}, \rho_c) \approx (0.1, 2\ {\rm cm}^{-3})$, but the GCE significance remains largely indifferent for similar CMZ brightnesses.

Finally, the third row shows ρ_c versus n_s. The IG fits which include a GCE template prefer a large threshold and low n_s, showing that the parameters are not completely degenerate with each other. Similarly, the global fits marginally prefer high n_s and ρ_c, again due to the improved outer Galaxy fit. With no GCE template in the IG, our Canonical model performs well. Perhaps most important is that both the IG No GCE fit and the GCE template significance are roughly constant along an elliptical ridge (blue arc moving counter-clockwise from $\log_{10}(\rho_c) = 0$ to $n_s = 1.5$). This highlights the strong degeneracy between n_s and ρ_c.

In summary, we have shown that our star formation model parameters are highly covariant with each other, and that the full model space is conveniently approximated by a single parameter $f_{\rm H2}$ over the interesting subspace. Globally, the γ-ray data strongly prefer $f_{\rm H2} \approx 0.2 - 0.25$ overall, and even higher values toward the global-local and global-inner regions. Remarkably, this parameter space is compatible with indepen-

dent measures of the CMZ SNe rate (see Fig. 7.1). When focusing only on the inner Galaxy ROI, fits including only the Galactic diffuse emission components very strongly prefer $f_{\rm H2} \approx 0.15 - 0.20$. These models produce an ICS emission spike which is highly degenerate with the properties of the GCE. However, when a GCE template is added, the fit is still significantly improved, though a lower value of $f_{H2} \approx 0.1 - 0.15$ is preferred. Below we will first study the Galactic center ROI, and will then characterize the spectrum and morphology of the residual emission in each analysis.

8.1.3.2 Spectrum and Statistics at the Galactic Center

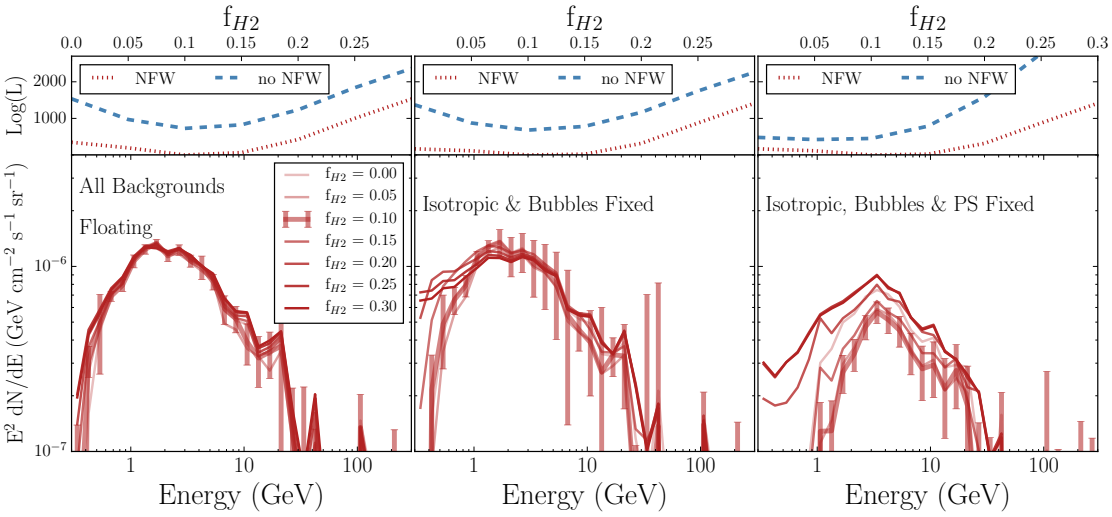

Figure 8.9: The log-likelihood fit (top) and best fit GCE spectrum (bottom) for values of $f_{\rm H2} = 0.0$ – 0.3, in models where all backgrounds are allowed to float independently in each energy bin (left), the isotropic and bubbles templates are fixed to their putative value in full sky fits to the data (center), and the isotropic, bubbles, and 3FGL point source templates are fixed to their nominal values (right). In nearly all cases a value of $f_{H2} = 0.1$ is preferred by the data. We note that the NFW template remains statistically significant and maintains a consistent spectrum in all cases except for models where the 3FGL point sources are fixed to their default values, a result that is expected due to the significant degeneracy between point sources near the GC and the GCE template.

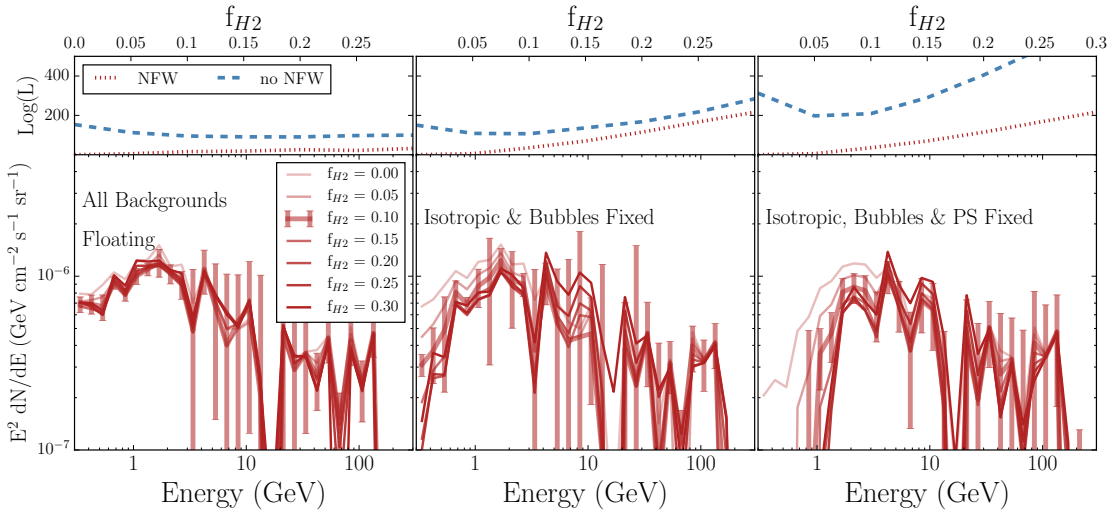

Figure 8.10: Same as Figure 8.9 for an analysis which masks the Galactic plane ($|b| < 2^\circ$) from the $15^\circ \times 15^\circ$ ROI surrounding the GC.

In this section we present results for the $15^\circ \times 15^\circ$ region surrounding the Galactic center. In this analysis, the GCE template produces a significant fraction of the total γ-ray emission throughout the entire ROI. This contrasts with the Inner Galaxy analysis, where the astrophysical emission components are, in large part, fit to the data in regions where the GCE template provides only a marginal contribution to the total γ-ray flux. Furthermore, when the bright Galactic plane is included in the analysis window, the analysis becomes sensitive to both emission along the plane, and to the GCE profile within 2 degrees of the Galactic center. For this reason, we perform fits over two analysis windows: one including the Galactic plane and one with the plane ($|b| < 2^\circ$) masked.

In Figure 8.9 we show the log-likelihood preference for the GCE template as well as the best-fitting NFW spectrum for various choices of $f_{\rm H2}$. We note two important conclusions: (1) the normalization and spectrum of the NFW template remain robust

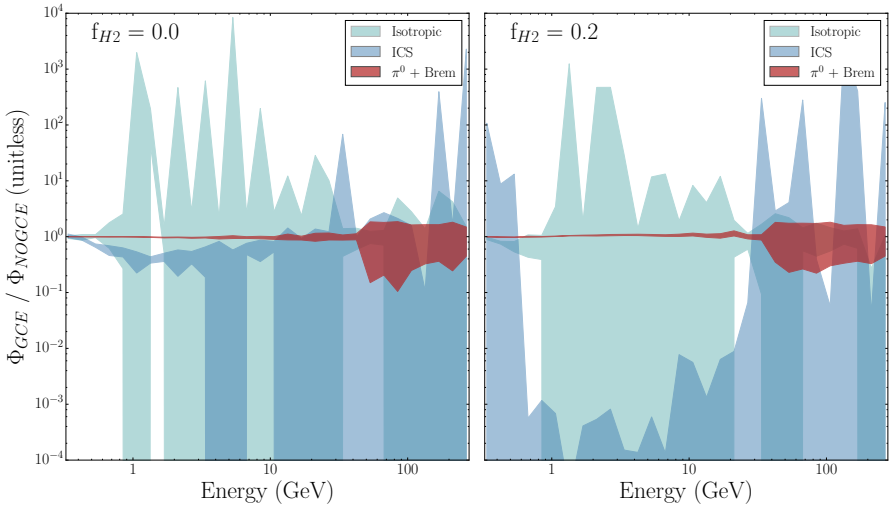

Figure 8.11: Here we show 1σ uncertainty bands on the relative normalizations of diffuse background components in the unmasked GC analysis for fits including and excluding a GCE template, for the case of $f_{\rm H2} = 0.0$ (left) or $f_{\rm H2} = 0.2$ (right). Components include the combined π^0 and bremsstrahlung template (red), inverse Compton scattering template (ICS, blue), and isotropic background template (green). The GCE template in the Galactic center analysis is highly degenerate with the ICS template, especially in models with higher values of $f_{\rm H2}$. The isotropic template is poorly constrained over the ROI. All results are shown over the $15^\circ \times 15^\circ$ ROI of the GC analysis with no latitude mask applied.

to changes in $f_{\rm H2}$, maintaining a total intensity that varies by less than 10% in the 1-10 GeV energy range for all astrophysical diffuse emission models, (2) The value of $f_{\rm H2} = 0.1$ is preferred for our standard analysis for both fits that do, or do not, include a GCE component. This result is somewhat lower than in the Inner Galaxy analysis in the case that no GCE source is present, but is consistent in the case that the GCE component remains in the analysis.

We also show the resulting spectra and normalizations of the GCE template in models where the isotropic emission component and bubbles emission component, as well as all 3FGL sources, are fixed to their standard values from analyses of larger ROIs.

We find that the spectrum and normalization of the GCE template remain robust when the isotropic and bubbles emission templates are fixed, showing the lack of degeneracy between these diffuse emission models and the GCE component in the Galactic Center ROI. However, the emission in the GCE component decreases significantly when 3FGL sources are fit to their nominal values. This is not unexpected, as there are several bright sources within $\sim 1^\circ$ of the Galactic center that are highly degenerate with the addition of an NFW template [43]. In interpretations where the GCE is a real emission component, this degeneracy is easily explained as a mismodeling of 3FGL point sources due to a miscalibration of the background diffuse emission.

However, one might worry that the robustness of the GCE in the Galactic center analysis stems from its large fractional intensity in the inner few degrees surrounding the GC. If the GCE template is highly favored close to the Galactic center, it may remain bright in a Galactic center analysis even if it provides a poorer fit to the γ-ray emission in regions several degrees from the GC. To investigate this possibility, we modify the GC analysis in order to mask regions of the sky with $|b| < 2^\circ$, identical to the mask employed in the IG analysis. In Figure 8.10 we show the resulting normalization and spectrum of the NFW profile for all choices of $f_{\rm H2}$.

We note three immediate results: (1) the best fit value of $f_{\rm H2}$ is 0.0 in scenarios where the GCE template is included. However, this result is not particularly statistically significant, and a value $\rm f_{H2} = 0.1$ is disfavored at only TS$\sim$31. (2) The best fit spectrum of the GCE component remains similar to fits over the full Galactic Center ROI, albeit with the addition of some low-energy emission that may be due to leakage

from the masked plane region, and (3) the statistical significance of the GCE component is, however, substantially reduced, from TS$\sim$1450 to TS$\sim$160. While some reduction in the TS is expected from the smaller ROI of the masked analysis, we note that cutting the region $|b| < 2^\circ$ removes only 61% of the photons above 1 GeV. Since TS is, roughly, a photon counting statistic, we would expect a similar reduction in the TS, compared to the observed 90%. Instead, this result indicates that there is a greater degeneracy between the astrophysical diffuse emission and the GCE in the region $|b| < 2^\circ$.

As mentioned above, the GCE flux is comparable to that of the astrophysical emission components over the small ROI. Thus, in the Galactic center analysis, the addition of a GCE template is likely to significantly alter the flux of astrophysical emission components, compared to models of the Inner Galaxy. In Figure 8.11 we show 1σ statistical uncertainties on relative normalization of the astrophysical diffuse background components after the addition of a GCE template in the unmasked GC analysis. The large reduction in the ICS normalization after the GCE is added shows that the ICS emission (in particular) is highly degenerate with the properties of the excess in the case where $f_{\rm H2} = 0.2$. For visual clarity, we do not show the relative normalization of the bubbles component, but note that the flux uncertainty of the Fermi bubbles component is significantly larger than its flux in nearly all energy bins, implying that the component is unimportant for fits in the Galactic center ROI. This is reasonable considering that the Fermi Bubbles template is has uniform brightness and covers almost the full GC ROI. Intriguingly, this figure depicts the Galactic center analog to the decreasing intensity of the GCE component when $f_{\rm H2}$ is increased in the Inner Galaxy analysis. In

analyses of the Galactic center ROI, the degeneracy between the GCE component and ICS component statistically favors the fit from the GCE. Turning on a GCE component thus significantly decreases the emission stemming from the ICS component, producing a spectral dip mimicking the GCE emission.

8.1.3.3 Characterizing Residual Emission

In this section we study the emission morphology and spectrum of the GCE component as determined by the Inner Galaxy and Galactic center analyses. We will first examine IG residuals as a function of $f_{\rm H2}$ (8.1.3.3.1), followed by a comparison of the GCE with residuals along the Galactic plane (Sec. 8.1.3.4). Next we will determine radial profile derived by splitting the GCE template into annuli and determining the best fit (Sec. 8.1.3.5. Then we will simultaneously vary the ellipticity and inner slope of the GCE template to determine the best fit morphology for the inner Galaxy (Sec. 8.1.3.5), and will test the energy dependence of the best-fit morphology. Finally, we perform morphological scans on the Galactic center ROI (Sec. 8.1.3.7).

8.1.3.3.1 Raw Residuals In Figure 8.12 we show residuals for the inner Galaxy analysis with no GCE template for $f_{\rm H2} = 0, 0.15,$ and 0.3 (left to right columns), integrated over low, middle, and high energy bands (top to bottom rows). The residuals have been multiplied by the weighted point source mask and smoothed by a Gaussian kernel with $\sigma \approx 0.5^\circ$. Visually, it is easy to see the disappearing excess in each energy band as $f_{\rm H2}$ is increased, eventually leading to over-subtracted (blue) regions for $f_{\rm H2} = 0.3$. For both models, the positive residual at $l \approx 10^\circ - 20^\circ$ becomes brighter

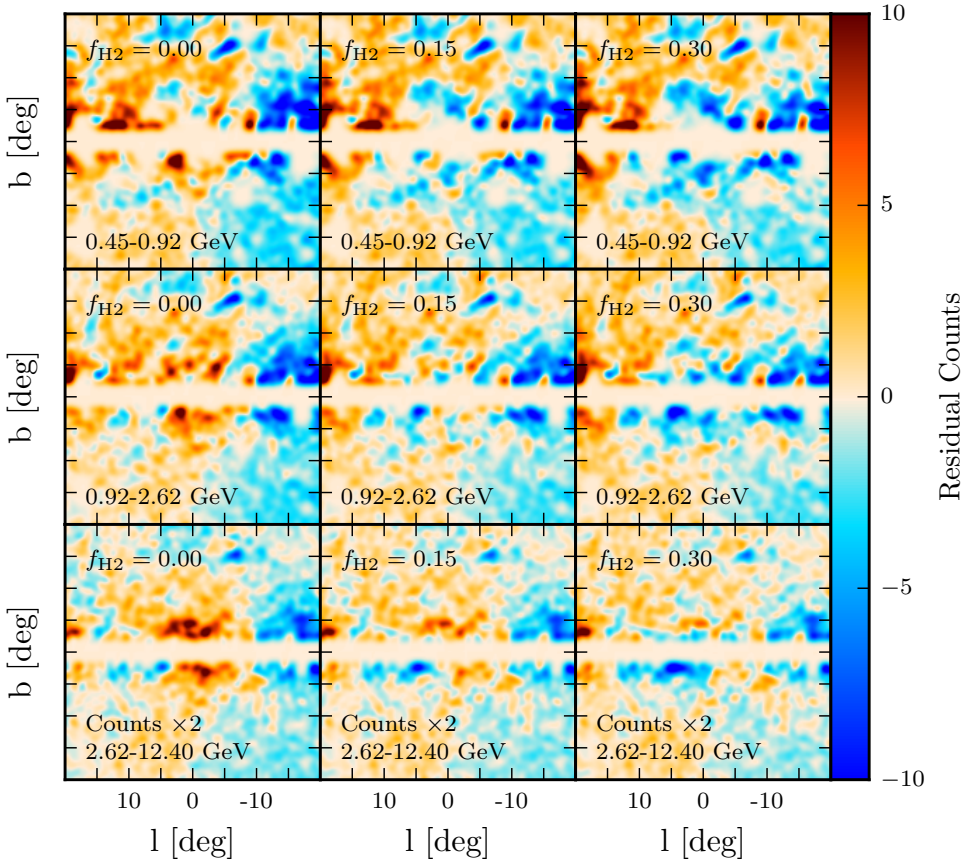

Figure 8.12: Residual emission maps as f_{H2} is increased for the inner Galaxy analysis with no GCE template included in the fit. Red indicates under-subtracted regions while blue indicates regions where the diffuse model is overly bright. All maps have been multiplied by the Galactic plane mask, weighted according to the 3FGL point-source mask defined by Eq. (4.18), and subsequently smoothed by a Gaussian kernel of $\sigma = 0.5^\circ$.

for large f_{H2}. As noted by Ref. [36], this is connected with the Aquila Rift H_2 star forming region which lies within a few hundred parsecs of the Earth. Unlike the GCE, the Aquila Rift spectrum is a smooth and soft power law, consistent with star forming regions. The residual emission associated with the Aquila Rift region falls off rapidly at higher energies. We have tried additional templates for the Aquila Rift region, where we use the PEB H2 model and sliced out the nearest 500 pc for $l > 15^\circ$ (which includes the

full AQ region). This does substantially improve the fit over the positive longitude edge of the ROI, but does not impact the flux or spectrum of the GCE. Because the inclusion of this template in fits also reduces convergence of the optimizer in many cases, we do not include it in further analyses, however, we note the utility of the PEB model [199] when generating templates for individual molecular or atomic hydrogen structures which need to be isolated along the line-of-sight.

As the diffuse emission model changes, so does inferred spectrum and normalization of point sources in the field. Although these point sources should be refit for each new diffuse model, the huge number of additional parameters make this optimization impractical for the inner Galaxy ROI. Still, γ-ray skymaps for different $f_{\rm H2}$ values vary significantly, and it is inevitable that new point sources arise and that 3FGL sources become mismodeled. To test the possibility that new point sources or leakage are significant, we compute the angular power spectra of residuals for $f_{\rm H2} = 0$ and $f_{\rm H2} = 0.3$ and examine the ratio of coefficients. We find that most of the new spectral power is picked only up at low angular frequencies while the small wavelength residual power (those below the scale of the PSF) are not changed at a statistically significant level. This provides support that the point source leakage as the diffuse model is changed is not important. We also find only very weak sensitivity to the photon PSF class for the inner Galaxy analysis. Further photon subselections are not explored further here, although we have verified that the IG and GC results presented below remain robust when using the PSF3 events class which contains 25% of the total photons with the best angular resolution.

8.1.3.4 Galactic Plane Residuals

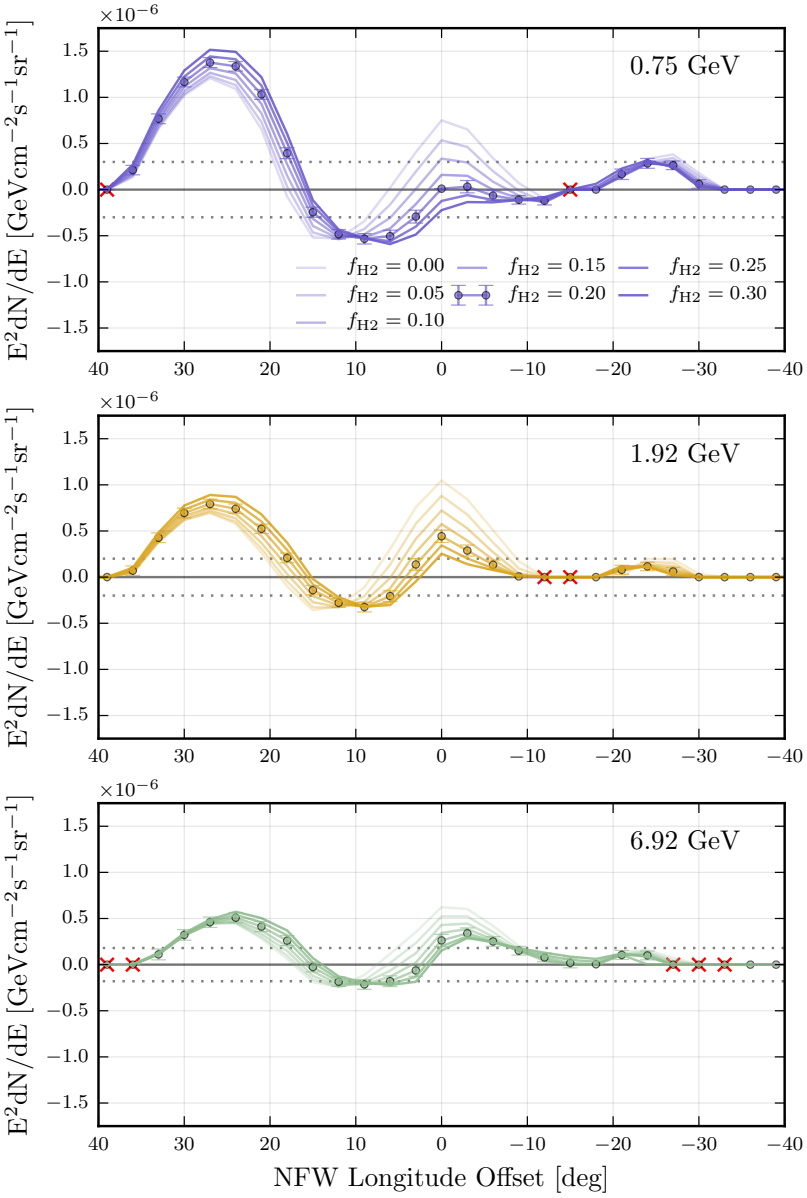

Figure 8.13: Best fit flux for a window centered NFW$_{\alpha=1.05}$ template as the inner Galaxy analysis is transposed along the Galactic plane. Curves from light to dark increase $f_{\rm H2}$ from 0 to 0.3 in increments of 0.05, with $f_{\rm H2} = 0.2$ case marked with error bars. The dotted lines are the 1σ (highly-correlated in energy) systematic uncertainties for residuals along the Galactic plane taken from Ref. [36]. Red '×'s mark non-convergent fits.

In order to compare the GCE intensity against residuals found along the Galactic plane, we follow the procedure of Ref. [36], transposing our entire inner Galaxy analysis in longitude, with the $\mathrm{NFW}_\alpha = 1.05$ GCE template centered in each offset ROI for $|l| < 40^\circ$. We do not, however, perform a full systematic study of uncertainties as done in Ref. [36]. If the plane residuals are not dramatically changed by our new source models, the systematic error bars derived in Ref. [36] should still provide a reasonable estimate of the uncertainties here.

In Figure 8.13 we show the flux of the transposed GCE template at 750 MeV, 1.9 GeV, and 6.9 GeV as f_{H2} is increased. Error bars highlight the Canonical model. The dotted lines (symmetric about zero) are the 1σ systematic error bands from Ref. [36]'s principle component analysis of Galactic plane residuals. As f_{H2} is increased we see that the Galactic center excess is reduced well below the level of the Aquila Rift star forming region at $l \approx 25^\circ$, and is comparable to the projected molecular ring at $l \approx -25^\circ$. The Canonical model is near or below the 1σ systematics in each case. The residuals along the plane do increase with increasing f_{H2}, but at a 10-20% level, indicating that $f_{\mathrm{H2}} > 0$ dominantly impacts the Galactic center excess while remaining a compatible with other regions along the Plane. It is intriguing that increasing f_{H2} enhances the Aquila Rift region ($l = 25^\circ$) given that H_2 rich regions should be made brighter, and would seemingly reduce positive residuals which have their origins in dense H_2 star forming regions. However, it is difficult to ascertain the exact cause in a template analysis since the morphology depends on emission along the full line of sight. Our new source model does improve the small residuals near $l = \pm 15^\circ$. The spectrum of the

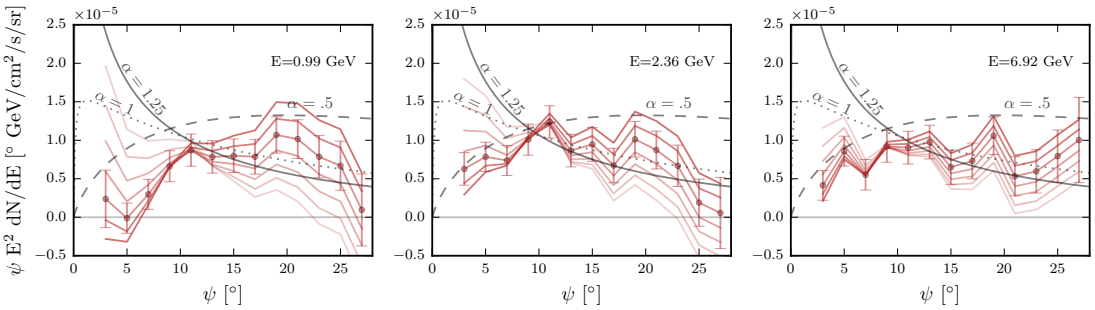

Figure 8.14: Radial flux profile of the NFW$_{\alpha=1.05}$ annuli at three energies representative of the Galactic center excess. Curves from light to dark increase $f_{\rm H2}$ from 0 to 0.3 in increments of 0.05, with the Canonical $f_{\rm H2} = 0.2$ model indicated by error bars. We also show arbitrarily normalized projected NFW flux profiles for inner slopes $\alpha \in \{0.5, 1, 1.25\}$. Note that (i) the inner slope of the GCE template is fixed to $\alpha = 1.05$ before subdivision into annuli, which may slightly bias results, and (ii) that the vertical axes have been rescaled by a factor 10^{-5}.

non-GCE residuals is essentially unchanged, following a soft power-law consistent with star-forming regions.

8.1.3.5 Radial Profiles

In addition to spectral changes to the GCE, the morphology of the Galactic center excess is also sensitive to $f_{\rm H2}$. In the case of $f_{\rm H2} = 0$, the residual is approximately spherical with a radial profile consistent with a standard NFW profile (though a slight adiabatic contraction to $\alpha = 1.05$ is statistically preferred). However, as $f_{\rm H2}$ is increased, we observe the radial profile to become much shallower and we will see that the preferred ellipticity becomes *energy dependent* and non-spherical. As an initial test of these distortions we begin with the inner Galaxy analysis and split the NFW$_{\alpha=1.05}$ template into 2° wide annuli, providing both the GCE intensity and spectrum as a function of radius.

In Figure 8.14 we show the flux as a function of the projected angle (ψ) from the Galactic center at 1, 2.36, and 6.92 GeV. Also shown, are the projected NFW profiles using inner slopes $\alpha = 0.5, 1,$ and 1.25. As $f_{\rm H2}$ is increased, we observe that the emission morphology is significantly flattened at all energies. Not only is the GCE suppressed at small radii, but it is also enhanced at large radii. This effect is most dramatic for ICS photons with $E_\gamma \lesssim 1$ GeV. At these low energies, the electron energy loss timescale is much longer, and the electrons diffuse farther away from the CMZ. Eventually, the diffuse emission becomes too bright and saturates $\psi \lesssim 5^\circ$. This suppresses the entire ICS template, including the high latitude ICS from the disk. At large radii, the GCE template brightens to compensate. At higher energies, larger $f_{\rm H2}$ would further reduce the excess, but more efficient transport is also needed so that electrons above 30 GeV can propagate to larger radii over the same energy loss time-scale. In Appendix 8.1.8.4, we show the GCE spectrum over the 10 IG regions defined by Calore et al [36], in which similar conclusions can be drawn.

Most importantly, the remaining excess is too flat to match any non-cored NFW emission profile. As shown in Fig 7.1, models with $f_{\rm H2} < 0.3$ still under-predict the supernovae rate in the CMZ, and the results shown here may be conservative. On the other hand, low $f_{\rm H2}$ models with a GCE component are still statistically preferred, and one must make a choice about which prior weights to apply on the value of $f_{\rm H2}$.

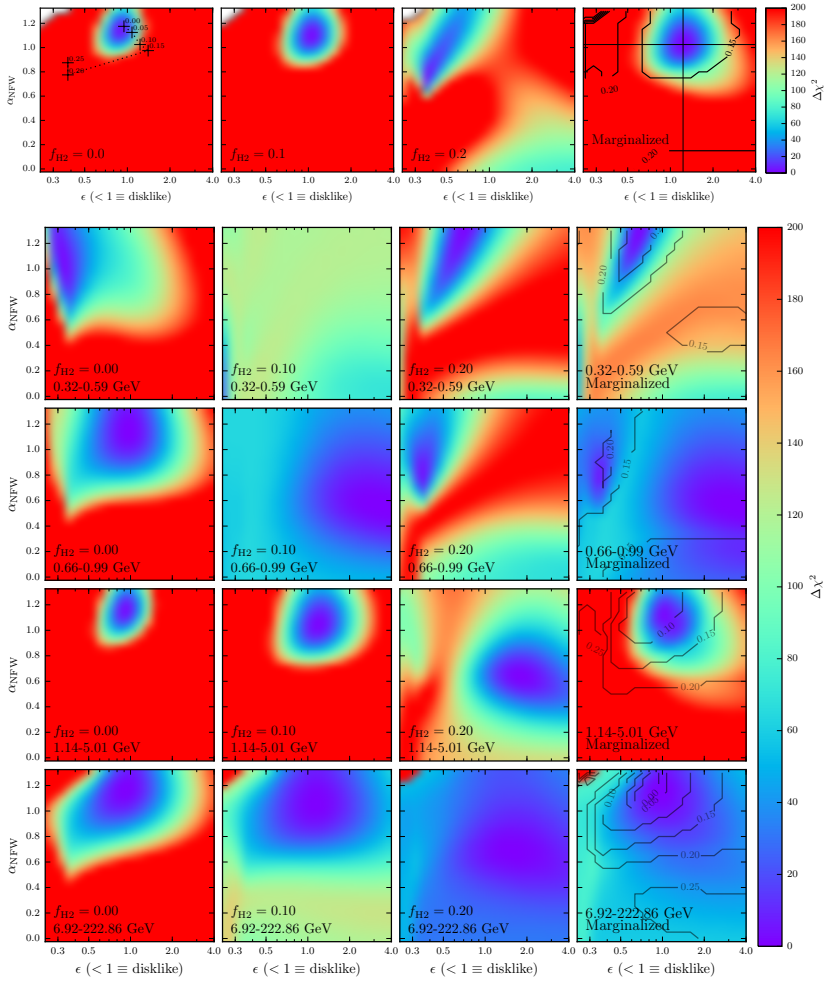

Figure 8.15: **Top:** Preferred morphology (ellipticity ϵ and inner-slope $\alpha_{\rm NFW}$) of the GCE template for increasing values of $f_{\rm H2}$. The left panel shows the $f_{\rm H2} = 0$ case with black '+' markers indicating the best fitting morphology for each $f_{\rm H2}$ sampled. The center two panels show the best-fitting inner Galaxy case with a GCE template and $f_{\rm H2} = 0.1$, as well as the $f_{\rm H2} = 0.2$ preferred by the global ROI. The right panel shows the preferred GCE morphology after marginalizing over $f_{\rm H2}$ – i.e. always choosing the value of $f_{\rm H2}$ which minimizes the χ^2. Here contours indicate the best fitting value of $f_{\rm H2}$, with the overall best fitting case corresponding to $f_{\rm H2} = 0.1$. **Bottom:** Same left to right columns as above, but divided into four energy bins (top to bottom) showing the energy dependence of the morphology as $f_{\rm H2}$ is increased. We note that for $f_{\rm H2} \gtrsim 0.2$, the low energy GCE spectrum becomes negative and disk-aligned, indicating that the galactic diffuse emission model is too bright along the disk near the GC. At higher energies, the GCE template prefers to extend out of the disk.

8.1.3.6 Inner Galaxy Slope and Ellipticity

We have shown above that the intensity and radial profile of the residual emission are highly sensitive to $f_{\rm H2}$, with larger values resulting in a pronounced flattening. The properties of the excess must now be evaluated in terms of the new preferred morphology. We therefore perform a new scan in the parameter space of inner slope $\alpha_{\rm NFW}$ vs ellipticity ϵ for several values of $f_{\rm H2}$.

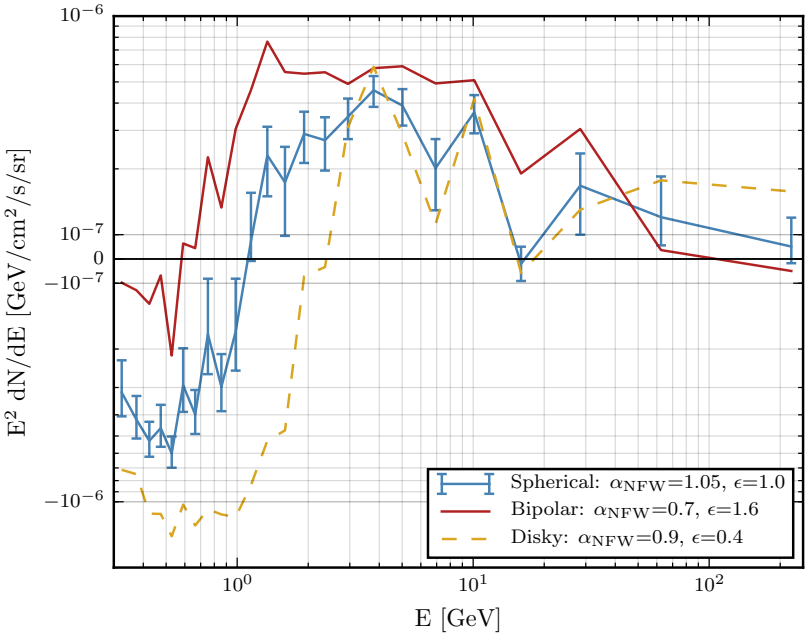

Figure 8.16: Spectra of the GCE template in the inner Galaxy analysis as the ellipticity ϵ and inner-slope $\alpha_{\rm NFW}$ of the GCE template is changed around our spherically symmetric Canonical $f_{\rm H2} = 0.2$ model. Disk-like models are favored at low energies where they can subtract the over-brightened disk, while higher energies favor a GCE template which is both flattened and elongated perpendicular to the disk.

In the top panel of Figure 8.15, we present the IG $\Delta\chi^2$ in the $\alpha_{\rm NFW}$ vs ϵ plane for three values of $f_{\rm H2}$. The left panel contains the standard case of $f_{\rm H2} = 0$ which shows a highly spherical profile and a steep inner slope $\alpha_{\rm NFW} \approx 1.15$. In black '+'

markers, we show the evolution of the best fitting profile as $f_{\rm H2}$ increases. As observed in the morphological tests above, we find the profile parametrically becomes elongated and flattened as $f_{\rm H2}$ increases, up to $f_{\rm H2} = 0.15$. In the second column we show the case of $f_{\rm H2} = 0.1$ which is the best fitting case for the Inner Galaxy with a GCE template included. Interestingly, in this case, we find that a peaked, and roughly spherically symmetric profile is still preferred overall. The third panel shows our Canonical model, which is the preferred fit in both the full sky data, as well as the Inner Galaxy when no GCE template is included. Here, two islands form which are either highly disk oriented or prefer an ellipticity extending out of the disk. Here the energy dependence of the GCE is manifest, and it is clear that we can not rely on an energy averaged view alone. If the CMZ star formation rate and global γ-ray analysis are taken as a strong priors toward $f_{\rm H2} \geq 0.2$ in the inner Galaxy, then a dark-matter-like profile ($\alpha_{\rm NFW} = 1$, $\epsilon = 1$) is ruled out by $\Delta\chi^2 \approx 133$, with larger values of $f_{\rm H2}$ even more strongly disfavoring a dark matter interpretation.

In the right panel, we marginalize[9] over $f_{\rm H2}$ by choosing the best fitting case for each ($\alpha_{\rm NFW}$, ϵ), and represent this best fitting $f_{\rm H2}$ via overlaid contours. Intriguingly, the best fits to the inner Galaxy (with a value of $f_{\rm H2} = 0.1$) remains consistent with the standard assumptions for an NFW profile motivated by dark matter annihilation ($\alpha = 1.0$, Axis Ratio $= 1.0$) at the level $\Delta\chi^2 = 34$. For dark matter interpretations of the GCE, this remains the most important result of the present work. Using vastly improved

[9]Typically, marginalizing implies integrating out the nuisance parameter. Here the likelihood function is usually quite sharp in $f_{\rm H2}$ for a given choice of morphology and it suffices to just select the best fitting value.

and more realistic diffuse emission models for γ-ray generation near the GC, models with a GCE component motivated by dark matter annihilation remain compatible with the data.

More important than the energy *averaged* morphology is to examine the energy dependence as $f_{\rm H2}$ is increased (left to right). In the bottom pane of Figure 8.15, we show the preferred morphology split into four bins of increasing energy (top to bottom columns). For the $f_{\rm H2} = 0$ models which have no CMZ, the morphology is spherical except for the lowest energy bin where a disky profile is favored by $\Delta\chi^2 \approx 80$. Before adding CMZ cosmic-rays, the energy independent GCE mophology provides an indication that – for a cosmic-ray interpretation of the GCE to succeed – CR transport near the Galactic center must be dominated by energy *independent* mechanisms such as advection, rather than energy *dependent* diffusion.

For $f_{\rm H2} = 0.1$, the GCE flux below 1 GeV is near zero, and the instrumental PSF is large. This results in only weak low-energy constraints on the morphology, with a slight preference toward very flat $\alpha_{\rm NFW} \lesssim 0.6$ profiles elongated out of the disk. Above 1 GeV, the profile remains spherical and steep. These models remain compatible with a dark matter interpretation, but still dramatically underestimate the CMZ injection rate.

For $f_{\rm H2} = 0.2$, the CMZ injection rate is somewhat low, and the morphology is already becoming highly energy dependent. Below 1 GeV, the GCE template normalization is *negative*. Thus, the preferred morphology is not reflecting a residual, but rather parts of the GDE model which are over-saturated. In this case, the disk-aligned GCE morphology clearly implies that γ-ray emission near the disk is too bright in our

Canonical model. Above 1 GeV, where the residual still remains positive and fairly bright, the GCE morphology strongly prefers a flat ($\alpha_{\rm NFW} = 0.6$) and highly elliptical ($\epsilon = 2$) GCE morphology out of the disk. This trend continues for larger values of $f_{\rm H2}$. The dual preference for a negative, steep, and disky profile versus a positive, flat, and perpendicular profile is also to be expected if the true GCE is somewhat bipolar. Similar morphological features have recently been noted in Ref. [403], and would be prevelent if a bipolar Galactic center wind is present which would both clear out low-energy electrons from the disk and elongate the ICS model vertically. In the marginalized column, large, disk oriented $f_{\rm H2}$ is preferred at below 1 GeV, while the peaked emission remains spherical above 1 GeV.

As the morphology of the GCE template is adjusted to the preferred morphologies, the spectrum of the excess must be re-evaluated. In Figure 8.16 we show the GCE spectrum for our Canonical background model for a variety of different morphologies. In solid blue we show the typical spherical profile. In dashed-yellow we see that disky GCE profiles become even more negative at low energies. For these 'disky' models, this improves the fit substantially by allowing the normalization of ICS to increase $\sim 20\%$ below 1 GeV, but requires an unphysical subtraction of the central disk by the negative GCE template. As we flatten the profile and elongate the GCE template vertically out of the plane, the low energy GCE flux moves back to zero, with less GCE flux gained above 1 GeV. Overall, we find that low energies in particular, are extremely sensitive to the GCE template morphology. This seems to strongly disfavor a dark matter interpretations of the GCE for models with realistic cosmic-ray injection rates.

8.1.3.7 Galactic Center Slope and Ellipticity

We attempt a similar exercise in the Galactic center, distorting both the inner profile slope and the axis ratio of the NFW template which produces the GCE emission component. We note that these simulations are conducted at a slightly lower angular resolution of 0.1°, and we have checked that this only negligibly affects our results. In Figure 8.17 we find that ratios near the nominal value for dark matter motivated interpretations of the GCE are preferred, with a best fit $\alpha \sim 1.15$ and an axis ratio of unity. When $f_{\rm H2}$ is increased to 0.2, this best fit value remains robust, although there is also some preference for a new γ-ray emission component which is strongly stretched along the Galactic plane. These results closely mirror our analysis of the Inner Galaxy ROI, and indicate that the morphology of the GCE very near the Galactic Center is not degenerate with the injection of cosmic-rays tracing the local H_2 density in regions very near the Galactic center.

As noted in Section 8.1.3.2, the strong preference for spherical symmetry and a $\alpha = 1.0$ NFW profile in the Galactic center analysis may stem solely from the very high preference for this γ-ray morphology in the inner degree or two surrounding the GC. Thus, in Figure 8.18 we repeat the above exercise, but mask out regions with $|b| < 2°$. In this case, we find a small (though statistically significant) preference for slightly flatter NFW emission profiles ($\gamma = 0.8$—1.0), and for some alignment parallel to the Galactic plane (Axis ratio 0.6—1.2). These results become more pronounced as f_{H2} is increased from 0.0 to 0.2. However, we note that the statistical significance of these results has also decreased greatly after masking the Galactic plane, and standard

values ($\gamma = 1.0$, Axis Ratio $= 1$) are only in tension with the best fit results at the level of $\Delta\chi^2 = -2\Delta\mathrm{LG}(L) \sim 20$. While the origin of this new emission morphology is unknown, it may correlate with either the treatment of point sources very close to $|b| = 2^\circ$ (regions which are masked in the Inner Galaxy analysis), or the modeling of the bubbles component, which is highly uncertain near the Galactic plane.

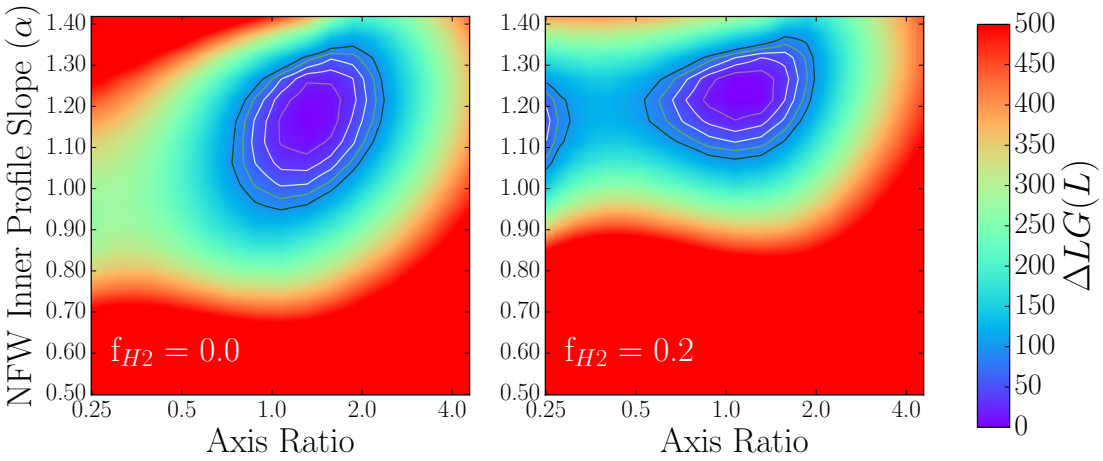

Figure 8.17: The log-likelihood fit of our model to data in the Galactic center analysis, as a function of the inner slope of the NFW density profile for the GCE component (α) and the axis ratio for extension parallel to (<1) or perpendicular to (>1) the Galactic plane. Contours represent rings of $\Delta\mathrm{LG}(\mathcal{L}) = 20$. In the case of $f_{\mathrm{H2}} = 0.0$, we find that typical values ($\alpha \sim 1.0$ and an Axis Ratio of approximately unity) are favored. In the case of $f_{\mathrm{H2}} = 0.2$, this still holds, although there is some evidence for an emission component strongly elongated parallel to the Galactic plane.

In summary of the residual analysis, we have shown that as f_{H2} is increased, the GCE becomes suppressed in the inner Galaxy. Transposing our analysis along the Galactic plane shows that the GCE template flux which remains is reduced well below the level of nearby Galactic plane residuals, albeit with a distinct peaked spectrum. This level of reduced residuals occurs uniquely at the Galactic center. Splitting the GCE tem-

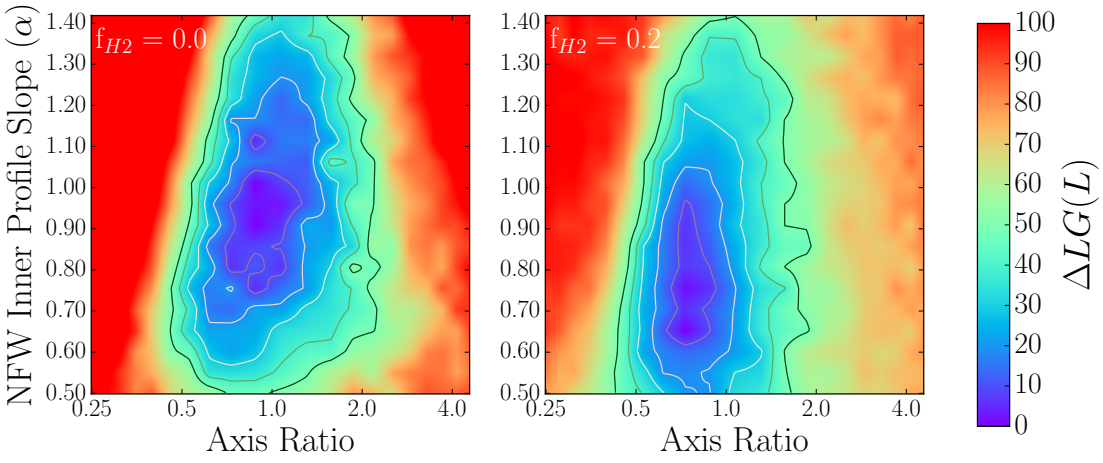

Figure 8.18: Same as Figure 8.17, for a Galactic center model where the region $|b| < 2^\circ$ is masked from the analysis. Contours now represent changes of $\Delta \log(\mathcal{L}) = 10$. In the case $f_{\rm H2} = 0.0$, we find that the resulting emission profile is still roughly consistent with dark matter predictions, although profiles that are stretched parallel to the Galactic plane, and which are slightly cored near the Galactic center provide statistically better fits to the data. In the case of $f_{\rm H2} = 0.2$, the best fit profile becomes cored near the Galactic center, and prefers elongation parallel to the Galactic plane.

plate into annuli reveals that the radial profile of the GCE strongly flattens as $f_{\rm H2}$ is enhanced, with the inner 5° becoming oversubracted below 1 GeV, and indicating an overabundance of electrons below $\sim$30 GeV in the Canonical model. We then scanned the ellipticity and inner slope of the GCE template, finding that the preferred emission morphology becomes highly energy dependent for increasing $f_{\rm H2}$ but remaining compatible with a dark matter interpretation for $f_{\rm H2} \leq 0.1$. The spectrum and flux of the GCE were then shown to depend sensitively on the chosen GCE template morphology. For the Galactic center analysis, a bright, spherical, and highly peaked feature remains in the inner 2° surrounding the GC, regardless of the value of $f_{\rm H2}$, indicating that the current models do not provide an explanation for these extreme inner regions. When masking the Galactic plane, the inner profile flattens considerably and becomes disk aligned, but

remains compatible with a dark matter interpretation at the level of $\Delta\chi^2 \approx 50$.

8.1.4 Sensitivity to Diffusion Model Parameters

Globally and in the inner Galaxy, the new source distribution represents a genuine quantitative improvement compared with the azimuthally symmetric case, with a $\Delta\chi^2$ comparable to that of changing between the diffusion parameters, gas distributions, or source distributions over the model space of Refs. [342, 36]. In this Section we show how the inner Galaxy GCE spectrum, inner Galaxy $\Delta\chi^2$, and Global $\Delta\chi^2$ change depending on the parameters of the `Galprop` model. Galprop's potential parameter space is large, and long computation times prohibit a full multi-dimensional exploration of the models. Instead, we simply vary our Canonical model along each direction of the parameter space individually. Our aim is to show (i) that the globally preferred parameter space also maximally reduces the Galactic center excess, (ii) that adding our new source distribution improves the global and inner Galaxy fits by an amount comparable to the changing most of Galprop's major parameters (within reasonable ranges inferred by local cosmic-ray measurements), and (iii) to explore how the GCE spectrum is impacted by changing global diffusion conditions.

Below we group the discussion into related parameters which include the standard diffusion parameters (D_0, $z_{\rm max}$, v_a, δ, dv/dz) as well as source and gas distributions, ISRF variations, and magnetic field properties. We also show the impact of global anisotropic diffusion perpendicular to the plane. In most cases the results are similar to the findings of Ref. [36], where the diffusion parameters do not strongly change the GCE

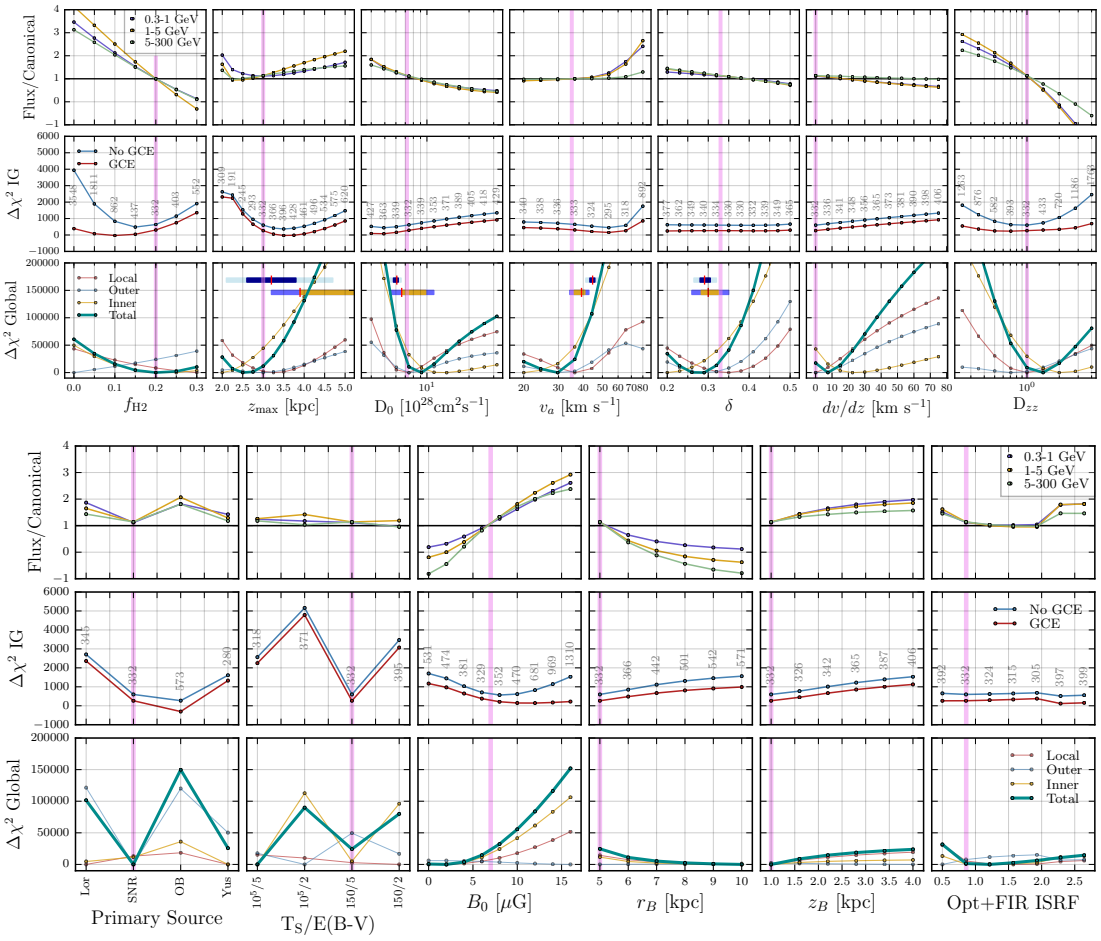

Figure 8.19: In two sets of panels, we show (top, middle, bottom) the GCE spectral variations, Inner Galaxy $\Delta\chi^2$, and Global $\Delta\chi^2$ as we vary global diffusion parameters around our Canonical $f_{\rm H2}$ model. The Canonical model parameter choice is shown in each case by a vertical pink line. **Top row**: The flux ratio in low/mid/high energy bands (0.3-1, 1-5, and 5-300 GeV) of the Galactic center excess spectrum relative to the GCE spectrum obtained using the Canonical model. Because the low-energy band (purple) is negative in the Canonical model, we reverse the slope and vertically offset the line (i.e. plot 2-Flux/Canonical) ensuring that decreasing values always indicate lower flux. **Middle Row:** Inner Galaxy $\Delta\chi^2$ with and without a GCE template. The test-statistic of the additional GCE template is indicated for each model, noting that maximal degeneracy between the GCE and the GDE model occurs when these lines are at closest approach. **Bottom Row:** Total and region-by-region global $\Delta\chi^2$ relative to the minimum over the parameter range. For $z_{\rm max}, D_0, v_a,$ and δ, we also show 1-dimensional posteriors from two Global Bayesian analysis of measurements of the local cosmic-ray spectra. Blue/gold shaded bands show 68/95% posterior ranges from Ref. [37], and dark/light-blue from Ref. [38]. Best fit parameters are indicated in each case by red lines. See also footnote 10.

spectrum except occasionally at low energies. However, several parameters reshape the *new* CMZ cosmic-ray population, and the morphology of the resulting γ-ray emission depends on the diffusion conditions and energy losses at the Galactic center. Here we limit our discussion to changing diffusion parameters *globally*, emphasizing that these changes effect both the CMZ electron cloud *and* the Galactic foreground emission.

In Figure 8.19 we present a large grid of three-panel sets for each parameter. The top row shows the ratio of the GCE spectrum to the Canonical model in three energy bands (0.3-1, 1-5, and 5-300 GeV), derived by averaging the individual bins (weighted by their inverse variance). Because the low energy band is negative in the Canonical model, we have plotted this 0.3-1 GeV line as 2-flux/Canonical. The sign-flip ensures that all decreasing trends correspond to lower (possibly negative) flux, and the offset allows for comparison with the mid/high energy bands so that one can observe the spectral reshaping. However, this also shifts the line of zero flux to +2 for the low-energy band. In the second row, we show the $\Delta\chi^2$ for the inner Galaxy analysis, with and without a GCE template. In the bottom row, we show the global $\Delta\chi^2$ for each region relative to the best fit. For several of the standard diffusion parameters ($z_{\rm max}, D_0, v_a,$ and δ), we plot 1-dimensional Bayesian posteriors obtained by fitting `Galprop` models against a variety of nuclear cosmic-ray spectra [37], and more recently, AMS-02 measurements of B/C and protons [38]).

Before iterating through our parameters individually, several notes are in order regarding the global $\Delta\chi^2$ and posteriors. First, the spectrum in our global fits is fixed to the `Galprop` output, and we have not marginalized over injection spectra, implying that

our global $\Delta\chi^2$ could be slightly biased by an improved spectral fit rather than morphological fit for some parameters (this is not the case for $f_{\rm H2}$). Second, the cosmic-ray posteriors shown are based on the cosmic-ray spectrum in the Solar System and may not reflect populations throughout the Galaxy, where e.g. turbulence, magnetic fields, or injection spectra differ from the local ISM. Third, the results here are 1-dimensional, while many cosmic-ray parameters are notoriously degenerate. This is particularly true when using primary-to-secondary ratios, where $D_0/z_{\rm max}$ are nearly perfectly correlated[10].

$f_{\rm H2}$: For comparison, we recast the $f_{\rm H2}$ results from Section 8.1.3.1. Globally, the improvement going from $f_{\rm H2} = 0$ to $f_{\rm H2} = 0.2$ is very significant, particularly if one added additional sources to the outer Galaxy. Relative to the global $\Delta\chi^2$ of other diffusion parameters explored here, the $f_{\rm H2}$ profile is of the same order of improved $\Delta\chi^2$, noting that for most of the parameters, the shown range is much larger than the range allowed by cosmic-ray observations. In the IG ROI, the impact of increasing $f_{\rm H2}$ on the GCE template significance is matched by no other parameter or obvious combination of parameters. Similarly, the fit quality without a GCE improves more than any other parameter, other than the Gas distributions (which provide an orthogonal improvement). Spectrally, increasing $f_{\rm H2}$ decreases the GCE steadily at all energies, and more than any other single parameter.

$z_{\rm max}$ and D_0: Using only cosmic-ray primary to secondary ratios, the ratio of these

[10]Ref. [38] breaks some of this degeneracy using the proton spectrum observed by AMS-02, loosely constraining $z_{\rm max}$, but tightly constraining $D_0/z_{\rm max}$. In the D_0 panel of Figure 8.19 we show the posterior based on our chosen $z_{\rm max} = 3$ kpc, though the marginalized posterior would be much wider.

parameters is typically constant. Here however, it appears that the global γ-ray data strongly breaks this degeneracy (the $\Delta\chi^2$ are not linearly proportional) and is directly sensitive to the distribution of cosmic-rays out of the plane. The inner and outer Galaxy in particular prefer thin diffusion halos which quickly leak out cosmic-rays. Given that we have hugely increased the cosmic-ray density in the inner Galaxy, this might be expected, and we observe strong preferences toward efficient transport out of the plane with each of the related parameters (D_0, dv/dz, and D_{zz}). The local ring includes high latitudes ($|b| > 8^\circ$), and is provides a relatively clean gauge of the local diffusion halo size, preferring $z_{\rm max}$ between 2.75 and 4 kpc.

Importantly, the spectrum of the GCE is strongly reshaped by changes in $z_{\rm max}$, with very thin halos enhancing the low energy GCE spectrum (which was previously oversubtracted) and suppressing the other bands. Models with $z_{\rm max} = 2.25$ kpc reduce the GCE significance to a mere TS=191 (adding 24 d.o.f. to the fit) over the entire inner Galaxy ROI, and reduce the GCE flux far below other Galactic plane residuals at all energies (recall that for the low-energy band, a GCE flux of zero corresponds to flux/canonical=+2 due to our offset). This is the only cosmic-ray propagation parameter which reshapes the GCE spectrum in this way. Above a few tens of GeV, the strong energy losses at the GC mostly confine the cosmic-ray electrons below 2 kpc and thinning the diffusion halo has little impact. At lower energies, however, the electrons can reach the boundary of the diffusion halo and escape freely. This reduces the low-energy electron and proton populations which are otherwise confined, and correspondingly reduces the ICS emission below 1 GeV. (This was over-subtracted in the baseline Canonical model).

It is not clear why the thin halo models are disfavored by the IG ROI by $\Delta\chi^2 \approx 2000$, though this is likely related to the foreground profile, noting that the global-local ROI favors thicker halos.

Enhancing the isotropic diffusion constant D_0 simply broadens the width of the ICS profile as electrons at all energies diffuse to larger radii before losing their energy. This has relatively little impact on the statistics of the IG. The GCE spectrum at all energies is reduced as the ICS spike becomes wider. At low energies however, the ICS becomes even more oversubtracted, making large D_0 disfavoured in the IG.

Alfvén Velocity $\mathbf{v_a}$: Diffusive reacceleration of cosmic-rays is quadratic in the Alfvén velocity (cf. Eq (5.40)). By fractional of their kinetic energy gained, low energy particles are most strongly accelerated, and the particle spectrum is hardened. For our chosen injection spectral index, fairly typical values between 30-50 km/s are preferred globally, in line with cosmic-ray data. The GCE is not strongly effected until very high values $v_a > 60$ km/s are reached at which point the low energy electrons produce harder ICS emission and do not regain some of the energy lost to synchrotron and IC cooling. The dimmer low-energy ICS enhances the GCE spectrum in the 0.3-1 GeV band (good), but also in the 1-5 GeV band (bad), while leaving the high energy ICS unchanged. Diffusive reacceleration in the context of leptonic burst models for the GCE are discussed further in Ref. [47], where very large values were required to preserve the hard electron spectrum far from the GC in the presence of strong energy losses.

δ: The energy scaling of the diffusion constant is globally quite important, as it shapes the energy dependence of both the cosmic-ray residence time and the diffusive smoothing

scale that smears our source distribution. Overall, we find good agreement with the previous cosmic-ray studies, strongly disfavoring $\delta \gtrsim 0.4$. The inner Galaxy prefers very low values of δ which enhances CR diffusion at low energies. The GCE significance is basically unaffected, while the GCE spectrum decreases for larger δ as low energy cosmic rays are more confined and high energy cosmic-rays have enhanced diffusion. Over the small energy range of interest to the GCE, this effect is weak relative to other parameters.

Convection Gradient dv/dz: The convection gradient is globally preferred to be zero for the local-global and outer Galaxy, while higher values from 20-40 km/s are preferred toward the inner Galaxy. Once again, we see a preference for enhanced low-energy cosmic-ray evacuation from the inner Galaxy. This is not unreasonable given the higher star formation rate of the inner Galaxy which generate the strong Galactic winds. The GCE statistics and spectrum are not strongly affected.

Anisotropic Diffusion $\mathbf{D_{zz}}$: Here we set the vertical diffusion coefficient equal to $D_{zz} \times D_0$, so that diffusion out of the plane is enhanced for $D_{zz} > 1$. In the local and outer Galaxy, the data prefer highly isotropic diffusion ($D_{zz} \approx 1$). In the global-inner Galaxy, there is a strong preference for D_{zz} =2-3, driven by the large population of central cosmic-rays. Quasi-linear theory predicts that diffusion should be enhanced along ordered magnetic field lines such as the strong poloidal fields near the Galactic center [364]. In the IG ROI, the statistical significance of the GCE template is minimized for $D_{zz} = 1$. Above and below unity, the electron cloud of the CMZ becomes elliptically skewed with a major axis stretched perpendicular or along the plane. This causes the

relatively spherical GCE template to regain significance. The GCE spectrum is unilaterally suppressed by enhancing D_{zz}. Similar to increases in f_{H2}, this can eliminate the mid/high energy excess, but the low energy ICS remains much to bright, forcing the GCE to be negative. Note that our modelling here concerns only globally anisotropic diffusion and we have not studied the impact of anisotropic diffusion at the GC alone.

Primary Sources: The primary source distribution used for the axisymmetric (1-$f_{\rm H2}$) fraction of sources is globally extremely important for the outer Galaxy, with the SNR model providing the best fit there and overall. In Figure 7.1, we showed that of all the distributions, the SNR CB98 contains the most sources outside the solar circle, and better illuminates the outer Galaxy. The significance of this is very apparent here, with Yusifov models providing the second largest outer Galaxy source population. Toward the inner and local Galaxy the SNR distribution is only weakly disfavored with the Yusifov and Lorimer pulsar based models providing slightly better fits as they concentrate cosmic-rays toward the inner Galaxy. Tracers based on OB stars are strongly disfavored in all regions as it does not populate either the inner or outer Galaxy. For the IG results, we see that models containing no sources in the Galactic center (OB) *increases* the GCE significance, while models with the largest number of central sources (Yus) *minimizes* the GCE significance. This underlines Sec. 7.1, which stated that existing source models systematically underestimate the population of cosmic-rays at the Galactic center. The spectrum is somewhat sensitive to the source distribution, with the softest GCE occurring for pulsar models and the hardest GCE arising from our chosen SNR models.

Gas Distributions: We show all combinations of the assumed hydrogen spin temper-

ature $T_s \in [100, 10^5]$ K and the reddening cut for dust corrections E(B-V)$\in [2, 5]$ mag. These distributions are clearly globally important with a strong preference given to models with maximum reddening E(B-V)=5 mag, which allows more gas to be assigned to regions of high-extinction – i.e. the inner Galaxy. The outer Galaxy also prefers large hydrogen spin temperatures, which populate HI's triplet state and assigns a higher HI number density to a given 21 cm line temperature. While the total fit quality of the IG ROI is highly sensitive to the the gas distribution, the GCE significance and spectrum are essentially unaffected.

Magnetic Fields: Our magnetic field model is simply an exponential with scale radius r_B, height z_B, and random field intensity B_0. In the global-inner and local Galaxy, low field intensities are strongly preferred, perhaps due to the reduced confinement of cosmic-ray electrons to the plane where the HI correlated π^0 emission is already very bright. In the outer Galaxy, the situation is reversed, corroborating this interpretation given that our models are under-luminous in γ-rays across the outer Galaxy. The global data is rather agnostic to the magnetic field shape only mildly preferring large scale radii and small scale heights. Such small values of z_b are not totally inconsistent with more modern models [364], which contain a thin disk plus a toroidal halo with thin/thick scale heights of 0.4/4-6 kpc and radii of 10-15 kpc. B_0 varies in these models between 1-5μG in these models. The GCE spectrum is very sensitive to the magnetic field shape and intensity which dictate the shortest energy loss time-scale. The scaling radius is much larger than the CMZ so that r_B has little impact on GC electrons. However, r_B does control the energy loss timescale of the foreground disk electrons which are

important near the plane. The scale height z_B will impact *both* electrons at the GC and in the foreground. Larger values of any of these three both parameters shrink the the effective foreground ICS scale height. At the GC, B_0 and z_B shape the central CRe population. Larger values of either lead to stronger confinement toward the GC, and the GCE intensity becomes larger. We also note that the strong CMZ magnetic fields [363] are not present in our models here, though they are likely to play an important role very near the GC.

ISRF Intensity: Here we globally vary the strength of the optical and FIR components of the interstellar radiation field relative to the CMB, with a value 1 corresponding to the default `Galprop` model. Globally, the `Galprop` model appears to fit well. In the inner Galaxy, results are not significantly changed until very high values begin to further confine the CMZ electrons. The foregrounds are also effected, and like the magnetic fields, it is difficult to disentangle the two effects using simple template regression here.

8.1.5 Injection Spectrum and Enhanced Transport in the CMZ

Although the GCE significance is reduced from TS=3800 to 333 by the Canonical model, we have seen that the ICS emission below 1 GeV is too bright and too broadly distributed, such that it must be compensated at high latitudes by increased isotropic template emission. This results from an over-abundance of $E \lesssim 30$ GeV electrons. *If our goal is to produce a self-consistent cosmic-ray model compatible with the GCE then we must reduce the central population of low-energy electrons via either (i) a hardened electron injection spectrum for the CMZ, or (ii) enhanced transport at low energies.*

For protons, saturated π^0 emission toward the inner Galaxy forces $X_{\rm CO}$ to be unphysically low when realistic CMZ injection rates are imposed, and additional elements are needed to remove low energy protons from the otherwise calorimetric environment (See App. 8.1.8.1).

The *global* electron spectrum and abundance are not critical to the GCE spectrum due to the freely floating ICS in each energy bin. However, the ICS template morphology toward the GC does depend on the ratio of cosmic-ray electrons in the CMZ versus the Galactic disk. A hardening of the CMZ injection spectrum should dim the low-energy ICS spike. Such an injection spectrum is motivated by the hadronic γ-ray spectrum of the GC ridge as measured by HESS [404] and VERITAS [405], which have TeV photon spectral indices Γ =2.05-2.29 that are substantially harder than the typical Galactic γ-rays.

We test these models by hardening the injection spectrum of both protons and electrons (above $\mathcal{R} > 11.5$ and 2 GV respectively) at the CMZ ($r_{\rm 2D} < 300$ pc) by $\delta\alpha$. Even for $0 < \delta\alpha < 1$, the resulting GCE spectrum and significance are negligibly effected. Apparently, the central photon morphology drives the GCE and ICS template normalizations much more than the disk emission, such that the entire ICS template is renormalized. This results in little change in the GCE properties from spectral hardening of the CMZ alone. These combined factors leave one obvious option for reconciling the Galactic center excess with a steady state cosmic-ray population: enhanced transport at the GC.

Enhanced cosmic-ray transport comes in several flavors, but those explored in

Sec. 8.1.4 each come with caveats when attempting to explain the full GCE spectrum. While a very thin diffusion halo in the Galactic center can help reduce the unphysically-negative low-energy GCE, the overall inner Galaxy fit becomes significantly worse. Alternatively one can enhance diffusion out of the plane ($D_{zz} > 1$) or add a large vertical convection gradient dv/dz. However, these stretch the CMZ electron cloud vertically and the corresponding ICS profile becomes less spherical, resulting in a larger GCE significance. One can also increase the isotropic diffusion constant D_0, but this simply broadens the width of the ICS spike, decreasing the mid/high energy GCE, but further exacerbating the low-energy problem. Decreasing δ reduces the energy dependence of diffusion, but does not have much effect over the small energy range of interest here. Altering the ISRF energy densities only impact high-energy electrons by reshaping their effective diffusion radius while changing the magnetic field model cannot correctly reshape the spectrum. Large Alfvén velocities strongly increase diffusive reacceleration and harden the low energy particle spectrum. And although this this produces less low energy ICS without effecting the high energy band, it cannot sufficiently suppress the GCE peak between 1-5 GeV.

No obvious combination of the above seems to solve our problem, leaving one potential cosmic-ray transport solution: high velocity winds emanating from the Galactic center region. In order to compete with diffusion, the wind velocity must be at least several times 100 km/s (10^3 km/s $\equiv$ 1 kpc/Myr). In the advection dominated regime, particle transport is energy-independent. With an appreciable mixture of diffusion, the winds dominate low energy transport where the diffusion rate is lowest, and diffusive

transport dominates at high energies, where large particle rigidities lead to faster propagation. In addition to the transport rate enhancement and energy independence, the radial profile of a constant velocity advective wind is geometrically fixed to r^{-2}, whereas diffusion from a point-like stationary injection source results in a shallower $\sim$1/r profile over the inner kiloparsec. These features make strong winds a natural solution to our problem.

Winds at the Galactic center are driven by intense star formation occurring throughout the CMZ, and especially from the dense stellar clusters of the inner 10 pc. With diffusion alone, the GC is highly calorimetric. On the other hand, multiwavelength observations indicate less that more than 95% of the non-thermal injected power must be advected from the system, despite the extreme gas densities and high magnetic fields [39]. A detailed account of GC winds can be found in Ref. [39] and references therein, but is briefly reviewed here. Perhaps most significant are observations of the 'GC lobe', a rising 1° tall and $\lesssim 0.5^\circ$ radial shell of 10 GHz radio continuum emission [294] with associated mid-infrared filaments [295], X-ray shells [296], and optical and radio recombination lines which point to nested shells of ionized gas, synchrotron emission, and dust entrained in the outflow whose pressure and energetics are consistent with star formation or nuclear activity from the central 10 pc of the Galaxy [297, 295, 298]. More recent radio observations combined with multiwavelength modeling [299] have confirmed these features, finding additional X-ray counterparts and associations with the circum-nuclear disk. In addition, from the perspective of extragalactic star-forming galaxies the SFR within the CMZ is expected to drive powerful outflows [39].

We consider here the addition of such a wind, modelled as a purely radial outflow with constant velocity $v_{\rm wind}$ within $r_{\rm 3D} \lesssim 2$ kpc of the Galactic center, which is assumed to stall and vanish beyond this. Explicitly, we describe the wind in terms of a Fermi-Dirac distribution with a boundary width of 200 pc. A stall zone at 2 kpc is likely conservatively small based on recent modeling [300], and, in the vertical direction, lies outside of our inner Galaxy ROI.

$$\vec{V}_{\rm wind}(r) = \frac{v_{\rm wind}\hat{r}_{\rm 3D}}{e^{(r_{\rm 3D}-2\ {\rm kpc})/0.2\ {\rm kpc}}+1} \tag{8.5}$$

where we vary the value $v_{\rm wind}$ between $0 - 2000$ km s^{-1}.

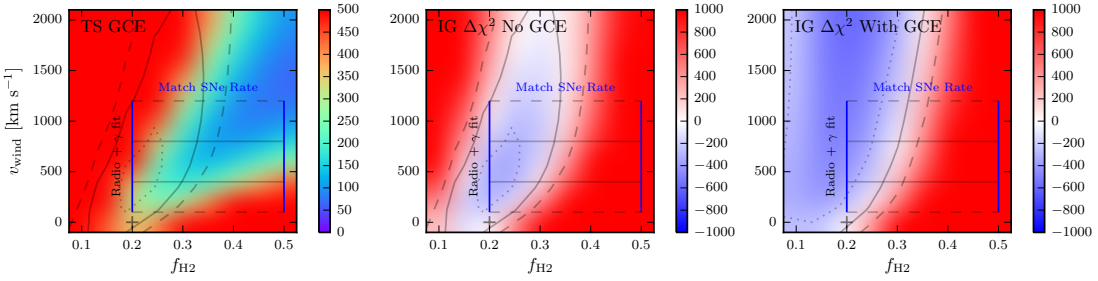

Figure 8.20: Statistics for the Inner Galaxy when varying $f_{\rm H2}$ and $v_{\rm wind}$. **Left:** Test Statistic of the GCE template, with contours showing $\Delta\chi^2 \in \{-300, 0, 300\}$ (dot, solid, dashed) for the 'No GCE' Inner Galaxy fits. **Center:** $\Delta\chi^2$ for IG fits with No GCE template and the same contour levels, relative to the Canonical model. **Right:** Same as center, but for fits including a GCE template. In all panels, the box is comprised of 'bounds' and 'most probable' wind velocities from Ref. [39] on the vertical axis, and models which match the CMZ injection rates (See Sec. 7.1) on the horizontal.

Although the wind is expected to be bipolar we do not explicitly model an opening angle here, leaving such studies to future work. In modeling the GC wind, we also increase the simulation's planar resolution to $dx = dy = 250$ pc and set $dz = 100$ pc.

In Figure 8.20, we show the statistics of the IG fit at the Galactic center as we simultaneously vary $f_{\rm H2}$ and $v_{\rm wind}$. Specifically we show the TS of the GCE template (left panel), the $\Delta\chi^2$ for fits with no GCE template, and the $\Delta\chi^2$ for fits with a GCE template. The inset box shows the range of wind velocities compatible with radio observations of the GC Lobe and TeV γ-ray observations of the HESS region [39]. Alternative modelling assumptions [398] suggest potentially higher wind speeds depending on the magnetic field strength of the CMZ. Horizontal bands highlight values of $f_{\rm H2}$ which approximately match the observed SNe rates at the Galactic center assuming typical SNR cosmic-ray acceleration efficiencies (See Sec. 7.1).

In the left panel, we see clearly that a simultaneous increase of the injection rate and wind speed leads to strong reduction of the GCE significance, with reasonable parameters (from multi-wavelength data) reducing the entire GCE template to TS$\approx$100. On the other hand, models which reduce the GCE significance the most are not strongly preferred by the inner Galaxy fits, and the GCE significance can only be reduced to TS$\approx$ 250 while also providing an improved IG fit. As the wind velocity increases, the low-energy electron cloud becomes both dimmer in ICS and more sharply peaked, with electrons above 50 GeV remaining unaffected by the wind. This sharply reduces the negative low-energy residuals picked up by the GCE template in windless models.

Examining the center panel we see that the addition of a GC wind not only reduces the GCE significance, but can also improves the inner Galaxy fit by up to $\Delta\chi^2 = -375$ over the Canonical zero-wind model. Although these are not fully overlapping parameter spaces, a mutual reduction of the GCE and improved fit in the inner

Galaxy is achieved over a substantial portion of the parameter space. Importantly, the preferred parameter space overlaps well with multi-wavelength expectations and statistically excludes a purely diffusive transport at $\Delta\chi^2 \approx 350$ for only two additional parameters[11]. The right panel shows that even with the addition of the GCE template, a non-zero wind velocity is still favored, and is highly degenerate with the GCE template up to 2000 km/s provided that $f_{\rm H2} \lesssim 0.3$. As we show in Appendix 8.1.8.1, these models also provide more reasonable values for the inner Galaxy $X_{\rm CO}$ conversion factor as they remove low energy protons which otherwise saturate the gas-correlated γ-ray emission.

In Figure 8.21 we show the GCE spectrum as the wind velocity is increased for models which correctly reproduce the CMZ supernovae rate ($f_{\rm H2} = 0.3$). The addition of winds strongly reduces the low-energy electron and proton populations at the GC which in turn (i) more sharply peaks the associated ICS emission, and (ii) reduces π^0 emission associated with the thick atomic and ionized hydrogen disks (which cannot be compensated by adjusting $X_{\rm CO}$). This strongly reduces the negative normalization of the GCE template while only weakly impacting emission above 5 GeV. Thus the spectrum and morphology of cosmic-rays at the GC are reshaped in precisely the way needed to further reduce the Galactic center excess. `Galprop` allows us to directly examining the electron spectrum at the Galactic center and reveals that the wind induces a broad break in the steady-state spectrum between 10-50 GeV (depending on the wind velocity). Assuming a CMZ magnetic field strength $B \gtrsim 100\ \mu G$, this break energy is

[11] It is important to note that this is a purely statistical significance and that systematic uncertainties are much larger, in particular due to the magnetic-field and ISRF uncertainties from the CMZ, and the transport parameters discussed in Sec. 8.1.4.

nearly equivalent to that inferred from the 1 GHz spectral break in the Galactic ridge synchrotron spectrum [39].

In Figure 8.22 we show results for the same diffuse emission models applied in our Galactic center analysis, utilizing both the full $15^\circ \times 15^\circ$ ROI as well as an analysis which masks the region $|b|<2^\circ$ from the Galactic plane. In the analysis of the full-sky ROI, we find that, similar to the analysis of the IG region, models with non-zero wind velocities are statistically preferred in the data. Specifically, we find the data to be best fit by a wind velocity of 2000 km/s both in models that include, or ignore the GCE component. However, we note that wind velocities of 600 km/s are disfavored by only a ΔLG(L) of 10 (48) in the case that the GCE component is included (not included) in the model. A model with no winds, however, is disfavored by a ΔLG(L) of 288 (372). In an analysis that masks the region $|b| <2^\circ$, models with no winds are slightly preferred by the data, but at a level of only ΔLG(L) of 11 (33) compared to a model with 600 km/s winds.

Unlike for models with non-zero winds in the Inner Galaxy analysis, the spectrum and intensity of the GCE component appears to be unaffected by the presence of strong GC winds, similar to our results for models with varying values of $f_{\rm H2}$ in the Galactic Center ROI. The effect of the addition of the GCE template in the Galactic Center ROI is to significantly suppress the normalization of the ICS emission template.

The results above show that for any realistic value of $f_{\rm H2}$, *Fermi GeV data toward the inner Galaxy strongly favor the presence of a Galactic center wind based on the morphology of the low energy ICS emission.* Furthermore, the presence of this

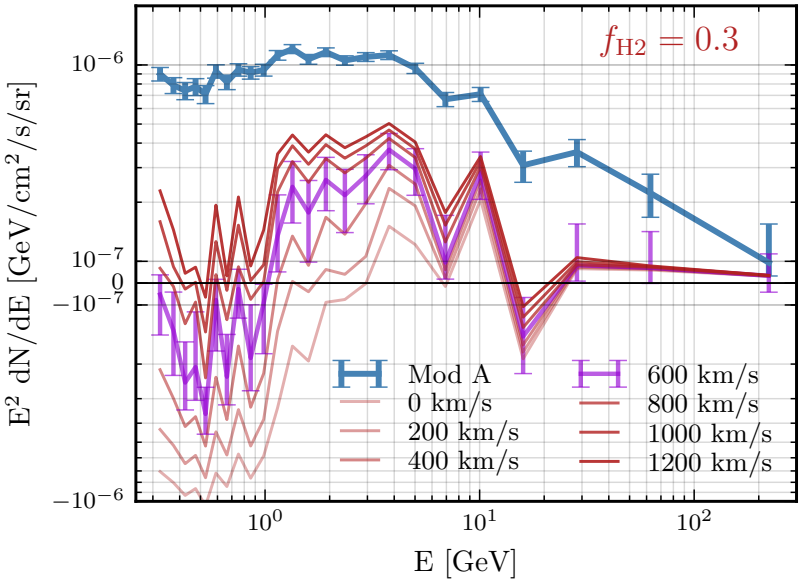

Figure 8.21: Spectrum of the Galactic center excess as the wind velocity $v_{\rm wind}$ is varied for $f_{\rm H2} = 0.3$ which well reproduces the observed SNe rate of the CMZ. Best fitting models without a GCE prefer wind velocities from 500-1000 km/s for $f_{\rm H2} = 0.3$. In all cases the GCE is reduced very far below the GCE spectrum of Mod A.

wind increases the degeneracy between the peaked central ICS emission and templates for a GCE component. In the Galactic Center ROI we also see some evidence for Galactic center winds in the overall fit to the γ-ray data, but do not find any degeneracy between the strength of the GC winds and the normalization and spectrum of the GCE component. In Appendix 8.1.8.1 we provide additional evidence for Galactic center winds based on the over saturation of $E \sim 1$ GeV π^0 emission in the central 2 kpc of the Galaxy.

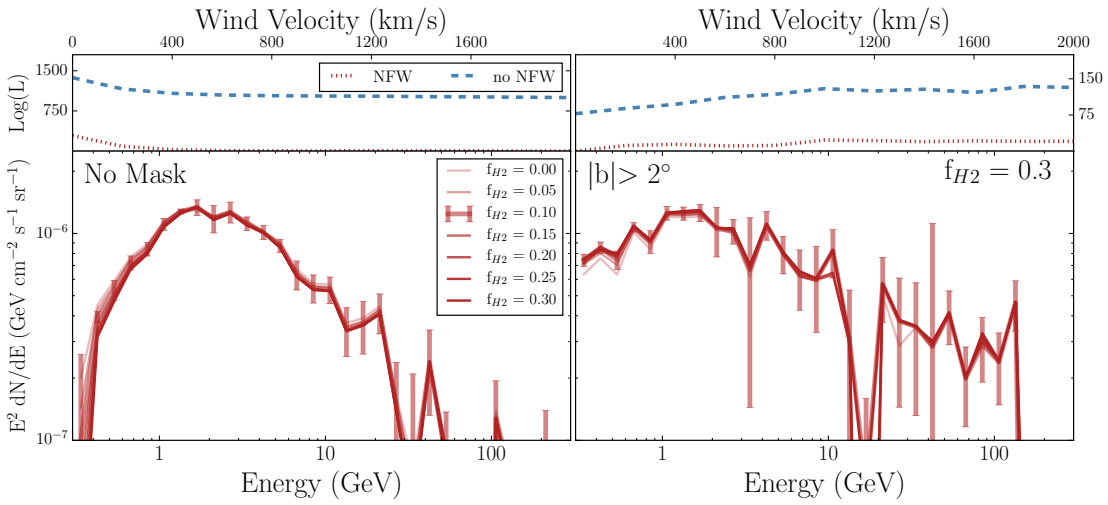

Figure 8.22: Same as Figure 8.21, for a Galactic center analysis in cases where the full $15^\circ \times 15^\circ$ ROI is analyzed, as well as an analysis where the region $|b| < 2^\circ$ is masked. Note the different scales for the log-likelihood fits to the data in each analysis. In all cases, the excess remains relatively bright, similar to the default results shown in Figures 8.9 and 8.10.

8.1.6 Discussion of Steady State Scenarios

In Chapter 7.1 we presented novel, physically-motivated, and significantly improved models for Galactic diffuse γ-ray emission in the Milky Way, focusing on understanding the diffuse sources of $\sim$GeV γ-ray emission in the complex Galactic center region. In contradiction with multi-wavelength observations, previous models of the Galaxy's diffuse Galactic emission have neglected cosmic-rays from the Central Molecular Zone, which is known to harbor a significant fraction of the Milky Way's supernova power (and thus cosmic-ray injection). Here, we have rigorously examined the robustness, spectrum, and morphology of the GeV Galactic Center excess in the presence of this new CMZ associated γ-ray emission. Our primary results can be condensed into three key findings:

1. There exists a clear degeneracy between the intensity, spectrum, and morphology of the GCE and the ICS emission following from realistic cosmic-ray injection near the Galactic center.

2. Models with $f_{\rm H2} = 0.2$—0.25 both reproduce the correct CMZ injection rate and provide the best fit to the γ-ray data in regions far from the Galactic center (i.e. the full sky, and the inner Galaxy fits with no GCE template). When these models are employed in the Inner Galaxy analysis, they substantially decrease the intensity and significance of the Galactic center excess, and also distort its morphology and spectrum. When fitting these models in the Galactic Center ROI, the spectrum and intensity of the GCE remain high, but the statistical significance of the excess decreases drastically if the region $|b| < 2^\circ$ is masked.

3. When including a GCE template, fits in the Inner Galaxy and Galactic center analyses statistically prefer $f_{\rm H2} \approx 0.1 - 0.15$. For these models, the intensity of the GCE component generally decreases by $\sim$30%, while the morphology and spectrum remain consistent with previous results – i.e. compatible with a dark matter interpretation.

These results can thus be interpreted in two ways. If global γ-ray fits and the multi-wavelength evidence for large cosmic-ray injection in the CMZ are accepted as priors on the value of $f_{\rm H2}$, then the low-intensity, hard spectrum residual that remains may be potentially viewed as a systematic issue of uncertain origin. On the other hand, if these priors are taken to be weak against the statistical preference for lower $f_{\rm H2}$ in

the narrower Inner Galaxy and Galactic center ROIs, then the resilience of the GCE in light of our new models reaffirms previous determinations of the GCE properties. Large and presently unknown systematic uncertainties from both analysis procedures and from GDE modeling make it difficult to objectively balance the weights of the high $f_{\rm H2}$ priors against the low $f_{\rm H2}$ IG+GC likelihood function. Ultimately, the properties of the GCE depend sensitively on these assumptions and its remains an open question.

In addition to the results above, we find that GDE models with appreciable CMZ injection rates predict overly bright γ-ray emission below $\sim$1 GeV near the plane. This strongly impacts the spectrum of the low-energy GCE, and the inferred $X_{\rm CO}$ conversion factor toward the inner Galaxy. We discuss multiple possible systematics that could produce this signal, and show that the majority of (global) diffusion parameters can not alleviate these issues.

Motivated by substantial multi-wavelength evidence, we implement a radially outflowing wind at the Galactic center. For wind speeds $\gtrsim$ 500 km/s, our models are improved simultaneously in three separate ways: (i) low-energy cosmic rays are advected from the region so that the low-energy GCE spectrum is no longer compensating an oversaturated GDE model, allowing for more realistic values of $X_{\rm CO}$ in the inner Galaxy; (ii) Inner Galaxy and Galactic Center fits (both with and without a GCE template) are substantially improved; (iii) the best fit value of $f_{\rm H2}$ in the Inner Galaxy ROI is increased, bringing the preferred model space into better agreement with the full-sky γ-ray data and with the observed CMZ supernovae rate. Furthermore, when both $f_{\rm H2}$ and the wind velocity are large, the GCE can be even further suppressed. However, we again find that

the models which best fit the γ-ray data in both the Galactic Center and Inner Galaxy ROIs include a significant GCE component with a spectrum and intensity consistent with previous analyses.

There remain multiple avenues worth of future exploration, and additional modeling improvements are necessary to fully understand diffuse γ-ray emission from regions near the Galactic center. At present, our models employ ISRFs and magnetic field energy densities that are not consistent with multiwavelength observations of the CMZ. Specifically, radio surveys find that 50—200μG magnetic fields permeate the CMZ [363, 32], while stellar populations spanning the inner few degrees [406, 407] and the dense nuclear star clusters surrounding Sgr A* indicate ISRF energy densities in the inner 10 pc which are several orders of magnitude higher than current `Galprop` models [408, 409, 337]. A realistic model of diffuse γ-ray emission will need to investigate both:

(i) the short electron cooling timescales indicated by these observations, as well as

(ii) utilize a detailed model of the stellar (and dust-reprocessed FIR) ISRF in order to determine the precise morphology of ICS γ-rays in the inner few degrees surrounding the GC.

Finally, gas maps for both γ-ray generation, and for our our H_2 based source model, may be improved using more recent molecular line surveys of the CMZ, such as MOPRA [410], which samples multiple organic species in order to better probe the variety of gas phases that are not well traced by CO alone. Alongside the improved γ-ray predictions (which also include the TeV regime), more precise models can be better

constrained by cosmic-ray calorimetry and synchrotron emission modeling.

8.1.7 Summary of Steady State Cosmic-Ray Models

The conclusive determination of the existence of genuinely *excess* diffuse emission from the inner regions of the Galaxy depends crucially on the use of *reliable* and *physically motivated* models for the Galactic diffuse emission. It is clear that in studies thus far available a critically important population of cosmic rays in the region has been neglected, with potentially dramatic implications for the determination of both the existence and the properties of any excess emission.

In a recent short note, Ref. [397], we proposed a physically well-motivated model for the three-dimensional Galactic cosmic-ray injection source distribution, based on a fraction $f_{\rm H2}$ of such sources being associated with relatively recent injection in star-forming regions. We employed observational data on the density of H_2 alongside a simple prescription for star-formation efficiency, and showed that the resulting Galactic diffuse emission models with $f_{\rm H2} \sim 0.1-0.3$ are *statistically strongly favored* by the γ-ray data over models with $f_{\rm H2} = 0$.

The present extensive study explores in detail the implications of our original finding [397] on models for the diffuse Galactic emission, and the resulting impact on the existence and properties of any Galactic center "excess". We found that the new cosmic ray population is consistent with the CMZ supernova rate (as determined by multi-wavelength observations) and produces a significant γ-ray emission that is degenerate with many properties of the γ-ray excess. The choice of the region of interest impacts

the details of this degeneracy. Specifically, without employing a GC excess template there is a strong preference for $f_{\rm H2} \sim 0.1$ in the (narrower) Galactic Center analysis, and for $f_{\rm H2} \sim 0.2$ in the (broader) Inner Galaxy and in the full-sky analyses. Including a GC excess template, but utilizing a value $f_{\rm H2} \sim 0.2$ as a *prior* in the Inner Galaxy analysis, the GC excess is strongly affected, while the Galactic Center analysis still favors the existence of a bright residual emission. *In all cases, we find a clear statistical preference for the existence of a Galactic Center Excess residual emission template, but with an intensity, spectrum, and morphology which are sensitive to* $f_{\rm H2}$.

An additional important finding of the present study is that low-energy ($E \lesssim$20 GeV) protons and electrons are over-produced in the GC region, as determined by the negative γ-ray residuals below 1 GeV. We explored possible solutions to this issue, and argue that the most plausible solution is the addition of significant advective winds which remove the excess electron and proton populations from the central Galactic regions. We showed that the existence of such winds is physically well-motivated. The inclusion of strong galactocentric winds significantly improves our fit to the γ-ray data both in models that include (exclude), a GCE component, at the level of $\Delta\chi^2$=605 (375) in an Inner Galaxy type analysis. For models which include a GCE component, the addition of strong Galactic winds removes the negative residuals typically absorbed by the GCE template, producing a GCE γ-ray spectrum which is physically realistic over the full energy range.

We believe that the models for the diffuse Galactic emission discussed here present a clear step forward in the current state of the art in this field. Additionally, it

is clear that a solid determination of the properties of a Galactic center excess, and its association with new physical phenomena such as dark matter annihilation, hinges on further improving our modeling of the Central Molecular Zone. At present, a precision determination of diffuse emission in the Galaxy remains the most significant barrier to using high-energy gamma rays as a probe of new physics at the Galactic center.

8.1.8 Additional Results

8.1.8.1 $X_{\rm CO}$ in the Inner Galaxy

Previous studies of the Galactic center excess have neglected variations on the $H_2 \rightarrow$ CO conversion factor $X_{\rm CO}$. However, understanding the radial $X_{\rm CO}$ provides an important indicator of the hadronic cosmic-ray density and calorimetry toward the Galactic center. Here, we (i) briefly comment on the empirical and theoretical understanding of $X_{\rm CO}$ toward the centers of star-forming galaxies similar to the Milky Way, (ii) show that for realistic cosmic-ray injection rates from the CMZ, the gas-correlated γ-ray emission is over-saturated (assuming an SNR-like injection ratio $q_p/q_e \approx 10$), and (iii) demonstrate that advective outflows at the Galactic center help to alleviate this problem.

Theoretical and observational results indicate that $X_{\rm CO}$ is subject to significant spatial and environmental variations, especially in the centers of local group star forming galaxies [332]. Comparisons of the total dust opacity to the CO-inferred gas density in local group spiral galaxies shows that $X_{\rm CO}$ is relatively flat throughout Galactic disks, but decreases on average by a factor more than 2 in the central regions. In 3 of the

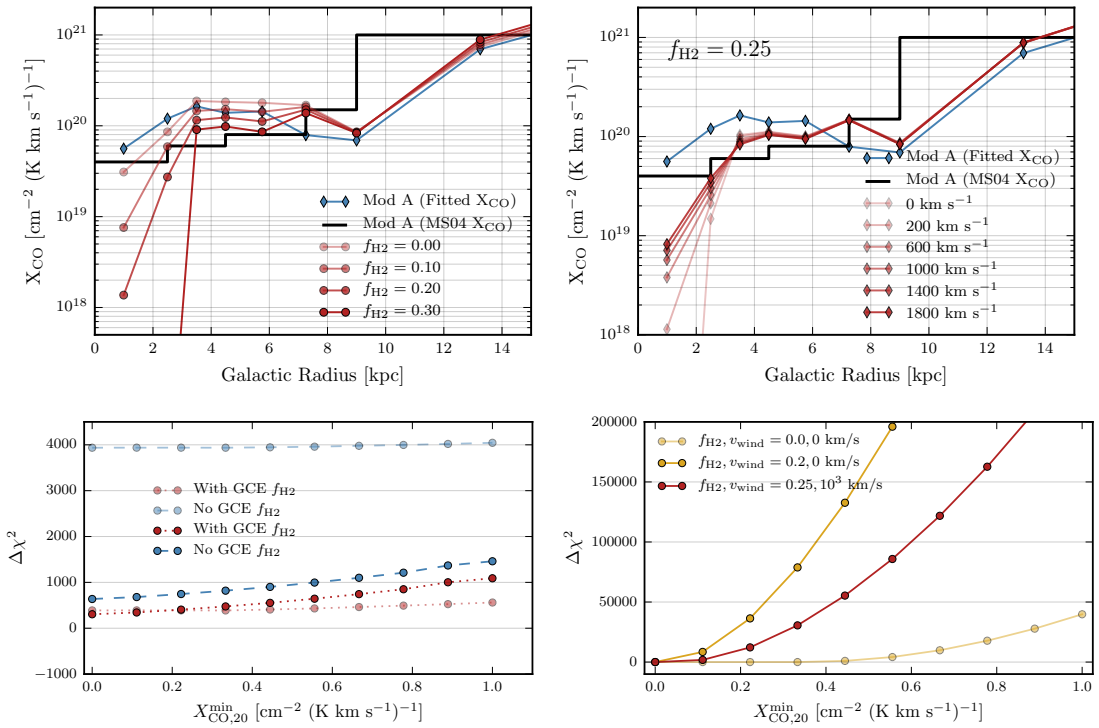

Figure 8.23: **Top-left:** Fitted values for X_{CO} as f_{H2} is increased. **Top-right:** X_{CO} for $f_{H2} = 0.3$ as the Galactic center wind velocity v_{wind} is increased. Also shown our X_{CO}-fitted version of Mod A, as well as the commonly used X_{CO} profile from Ref. [40]. With the exception of the inner-most ring, all fitted values have statistical error bars $\lesssim 20\%$. **Bottom-left:** Inner Galaxy $\Delta\chi^2$ for the traditional SNR and Canonical models when limiting minimal value of X_{CO} (in units of 10^{20} cm^{-2}(K km s^{-1})$^{-1}$). Traditional `Galprop` models combined with γ-ray observations suggest a value around $X_{CO} \approx 4 \times 10^{19}$ cm^{-2} (K km s^{-1})$^{-1}$ [41]. The impact on the Galactic center excess spectrum and significance is negligible. **Bottom-right:** Same, but for the global-inner analysis. Here the disk is unmasked and the fit quickly degrades as the minimal X_{CO} is increased. Models which include winds help to alleviate this problem and allow for more realistic CMZ injection rates.

16 Galaxy cores surveyed in Ref. [332], X_{CO} was at least a factor of 10 below the Milky Way average $X_{CO} = 2 \times 10^{20}$ cm^{-2} (K km s^{-1})$^{-1}$. X_{CO} was found to have a strong inverse correlation with the interstellar radiation intensity and surface densities of star formation, stellar mass, and dust mass, all of which are much higher in the

Milky Way center than the disk (see Sec. 7.1). $X_{\rm CO}$ is also believed to increase sharply with decreasing metallicity for $Z \lesssim Z_{\odot}/2$ [334], which can severely alter the inferred gas density in chemically enriched regions of the Galaxy, such as the Galactic Center. Finally, fitting EGRET [40] and Fermi [342] data to models of the Milky-way's diffuse γ-ray emission requires $X_{\rm CO}$ in the inner 2 kpc to be a factor $\sim$4 lower than the rest of the Galaxy. In addition to this, we have shown throughout this Section that *status quo* cosmic-ray models have dramatically underestimated the injection rate from the CMZ, implying that either $X_{\rm CO}$ must be reduced even farther, or that transport in the inner Galaxy must be enhanced.

In the top-left panel of Figure 8.23, we show the fitted $X_{\rm CO}$ profile as $f_{\rm H2}$ is increased. We also show the $X_{\rm CO}$ profile from Moskalenko & Strong (2004) [40] (MS04) which has previously been used for Ref. [36]'s Mod A. As cosmic-ray injection is enhanced toward the inner-Galaxy, $X_{\rm CO}$ must simultaneously be reduced to maintain the same level of hadronic γ-ray emission. Nowhere is this more important than the for the innermost Galactocentric ring ($r < 1.8$ kpc) which, for $f_{\rm H2} = .2$, becomes suppressed by more two-orders of magnitude relative to the local value. In the top-right panel, we add the advective wind discussed in Sec. 8.1.5 and show that while the outer Galaxy is relatively unaffected, as the wind velocity is increased the best-fitting $X_{\rm CO}$ returns to potentially physical values. All models remain biased to very high values in the outer Galaxy, consistent with previous studies [40, 342]. We note that the MS04 profile was obtained from EGRET data, and does not employ point source masking. Interestingly, we find that our $X_{\rm CO}$ profiles inside the Solar circle are quite sensitive to the adopted

point source masking, and that masking systematics should be understood for future studies of $X_{\rm CO}$ utilizing γ-ray data.

In all of the previous model fits, we have allowed the values of $X_{\rm CO}$ to float freely when performing global fits. Here we enforce a lower limit on $X_{\rm CO}$ in order to gauge the maximal allowed value. In the bottom panels of Figure 8.23 we show $\Delta\chi^2$ for the inner Galaxy and global-inner fits. The statistics of the inner Galaxy are hardly effected until $X_{\rm CO}$ rises well above historical determinations [40, 342]. This is to be expected in the inner Galaxy analysis where masking of the plane hides most of the H_2 emission near the Galactic center. For the global-inner fits, the plane is not masked and the fit rapidly worsens as the lower limit on $X_{\rm CO}$ is increased, which forces the inner H_2 rings to oversaturate. For our Canonical model, physically likely values of $X_{\rm CO}$ are very strongly disfavoured by the data, with statistical penalties outweighing even major changes to Galactic diffusion parameters. We find that $X_{\rm CO}$ *must* be substantially more than a factor 10 smaller than the Milky-way average in order to support the expected CMZ injection rates without Galactic center winds or much stronger vertical convection gradients.

The gas-correlated γ-ray saturation toward the inner Galaxy is driven mostly by π^0 emission below a few GeV where the number of photons is largest. Stronger winds blow low-energy protons and bremsstrahlung generating electrons away from the gas-rich CMZ. This allows $X_{\rm CO}$ to increase to more physical levels for wind velocities of at least several hundred km/s. Alternative transport options are such as enhanced or anisotopric diffusion at the GC could also help alleviate the gas saturation. However, none of these

alternatives alone is likely to fully reconcile the expected CMZ injection rates with the observed level of π^0 emission. We take this point as significant evidence in favor of strong GC winds. Future modeling of gas in the CMZ should include combinations of improved molecular-line surveys tracing H_2 – such as the MOPRA CMZ survey [410] – which are less prone to environmental variations than CO. Improved gas modelling is crucial in order to better constrain proton populations and winds at the GC, and can aid in discriminating between leptonic, hadronic, or mixed cosmic-ray injection models in the future.

8.1.8.2 ROI Dependence of Fit Components

In Section 8.1.3.2 we showed that the GCE is not strongly reduced in the Galactic center analysis, compared with a strong reduction in the Inner Galaxy, and that the morphology of the GDE template in the IG and GC analyses differs. The dependence of these results on the analysis windows implies that the GCE (or GDE templates) do not fully describe the residual data when cosmic-rays are added to the CMZ. In Figure 8.24 we show the average raw normalizations, from 1-5 GeV, of each template in the inner Galaxy analysis (with a GCE template) as the fitting region is increased from $10^\circ \times 10^\circ$ to $60^\circ \times 60^\circ$. We omit the π^0+bremsstrahlung template which remains flat to within $< 10\%$ for all ROIs. The Bubbles and isotropic spectrum normalizations are with respect to the original source spectra (see Sec.8.1.2), while the DM spectrum is relative to Ref. [36]. The ICS normalization is relative to the `Galprop` predictions of the respective models.

As the ROI is expanded, the isotropic and ICS components remain flat until

eventually the isotropic template increases by more than 50% beyond 50°. The origin of this is not clear, but the smooth increase is a likely indication that the isotropic template prefers to be larger over all ROIs, but is constrained by the $\chi^2_{\rm ext}$, which has reduced weight as the ROI grows. Because of the large latitudes involved, this is likely related to uncertainties in the foreground ICS rather than the GCE, which carries little weight over a 60° window. The Fermi bubbles template used here is essentially isotropic over the central 5 degrees of the ROI before becoming bipolar at higher latitudes. For $f_{\rm H2} = 0.2$, windows between 20° and 50° result in a brightened bubbles template, but *only* in fits which include a GCE. In fits that do not include the GC template, the bubbles template varies by less than 10% above 1 GeV, for all values of $f_{\rm H2}$ (see Fig. 8.4). In other words, the presence of the GCE template changes the inferred spectrum of the Fermi bubbles near the Galactic center (though the template morphology in this region is not well understood).

The most dramatic change is the GCE template normalization (Fig. 8.24 right). For $f_{\rm H2} = 0$, the GCE spectrum is stable to within about 20% over all ROIs. As we increase $f_{\rm H2}$ 2, overall normalization drops across all ROI sizes above 20°, eventually reducing near zero for $f_{\rm H2} = 0.2 - 0.25$. For ROIs under 20°, however, the reduction saturates around $f_{\rm H2} = .1 - .15$ at about half the original brightness. The sharp decline of GCE template as the ROI increases indicates that the radial profile of the template is mismatched to the residual. In particular, the ICS spike is too shallow to fully reproduce the inner few degrees. When the ROI is small, ICS is suppressed and the GCE template is bright. As the ROI becomes larger, the ICS template brightens and the GCE becomes

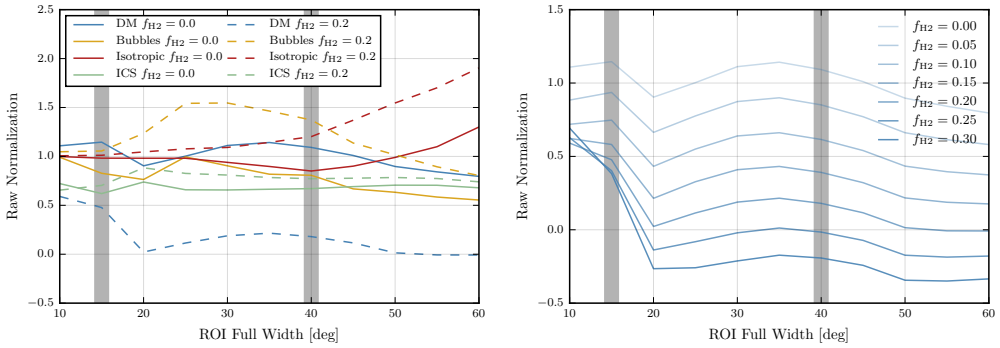

Figure 8.24: Dependence of fit components on choice of ROI for the inner Galaxy Analysis. **Left:** GDE and GCE component normalizations (averaged over 1-5 GeV) for $f_{\rm H2} = 0$ and $f_{\rm H2} = 0.2$ as the square ROI width is increased. All ROIs include a plane mask for $|b| < 2°$. **Right:** Same as left but for GCE template only. Gray lines mark the Galactic center and inner Galaxy ROIs.

suppressed by the lack of excess emission far from the GC. This is in agreement with the findings of Sec. 8.1.3.2 and could relate to a number of factors including poor CMZ ISRF modeling, limited resolution of the simulations or injection gas maps, or be indicative of a very young injection of cosmic-rays as indicated by HESS observations of the Galactic center [404].

8.1.8.3 Comparison with a Gaussian CMZ Model

Recently, Gaggero et al [399] noted that previous GDE models have neglected cosmic-ray sources at the Galactic center. They proceeded to add a spherically symmetric Gaussian cosmic-ray source at the position of the Galactic center in order to account for the CMZ. For cosmic-ray 'spikes' of width 200-400 pc (constrained by the size of the CMZ), they found that such models could reproduce the bulk properties of the GCE, and strongly reduce the significance of the GCE. Our findings fully support this conclusion,

but using a physical model and empirical inputs for the size and shape of the spike. In addition, our star formation prescription correctly reproduces the normalization of the spike based on both the measured SNe rate of the CMZ *and* based on global fits to Fermi γ-ray data. Their model is parametrized by a Gaussian width σ and a normalization $\mathcal{N}$, which represents the fraction of total Galactic cosmic-ray injection contained in the CMZ ($r < 300$ pc). Here we reproduce this models for $\sigma = 200$ pc and using Mod A ($X_{\rm CO}$ fixed to MS04 profile) in order to make direct comparisons.

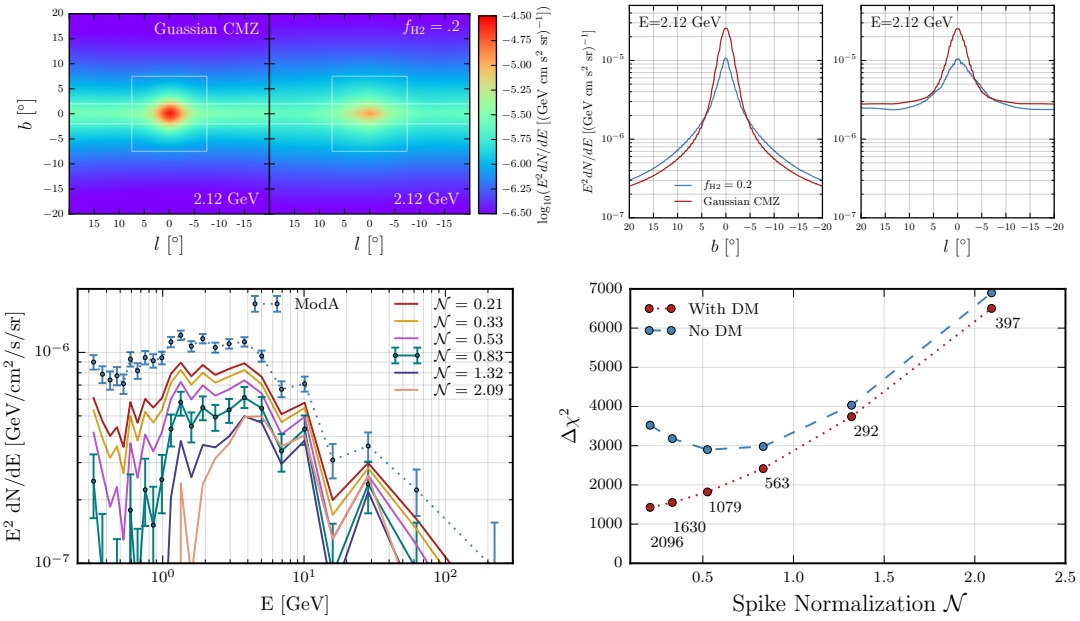

Figure 8.25: **Top-left:** ICS emission over the Inner Galaxy ROI when adding a Gaussian cosmic-ray 'spike' of width $\sigma = 200$ and $\mathcal{N} = 1.4\%$ versus our Canonical ($f_{\rm H2} = .2$) model. **Top-right:** Latitude and longitude profiles for ICS emission running through $l = 0°, b = 0°$ respectively. **Bottom:** GCE Spectrum and fit statistics of the inner Galaxy ROI as the spike normalization $\mathcal{N}$ is varied in the Gaussian CMZ model. To be compared with Figure 8.2.

In the top-left panel of Figure 8.25 we show the ICS emission for the $\mathcal{N} = 1.4\%$ model and our Canonical star-formation based model over the inner Galaxy ROI at

the peak GCE energy. In the top-right panels, we show latitude and longitude profiles through $l = 0$ and $b = 0$, respectively. Several features differentiate the two models. First, the excess Gaussian CMZ spike is completely spherically symmetric (as is expected for an isotropic diffusion tensor), while the $f_{\rm H2} = 0.2$ model is elongated along the plane (in reality, the height of the CMZ is very thin with FWHM$\approx$45 pc [323], and not 200 pc as taken in Ref [399]), and contains an axisymmetric structure from the bar which extends toward positive longitudes. Second, both the latitude and longitude profiles of the spike are substantially steeper than our Canonical model at 2 GeV, which may be driven by both the improved simulation resolution (thus injection resolution) afforded by the cylindrical simulations, or by the higher resolution of the gas model, which is an analytic model compared with our more limited $dx = dy = 100$ pc empirical gas model. We expect that our models produce a more realistic model of the CMZ shape and foreground emission as indicated by the much improved overall IG fit.

In the bottom panels of Figure 8.25, we show the GCE spectrum and statistics for the IG analysis. Both quantities are remarkably similar to our findings in Section 8.1.3.1, and show that the GCE is highly degenerate with the new ICS profile. The minimum TS for the added GCE template is comparable to our results. A major difference is that the best-fitting model without a GCE template provides a much worse fit than our Canonical model. This is not due to $X_{\rm CO}$ fitting, or differences in diffusion parameters, but to axisymmetric and non-Gaussian features present in the injection morphology. Our optimal no-DM fits not only provide a minimal GCE significance, but improve the IG fit by $\Delta\chi^2 \approx 4000$, compared to less than 600 here. Finally, the fit

improvement offered by the Gaussian CMZ model is limited to the inner 10-20 degrees, and does not improve the global γ-ray fits in a significant way, whereas our models provide an improved fit comparable to major changes to diffusion parameters in all regions except the outer Galaxy.

8.1.8.4 The Morphology From Ten Sky Segments

In Figure 8.26 we divide the $\mathrm{NFW}_{\alpha=1.05}$ GCE template into ten regions over the inner Galaxy ROI (defined in ref. [36]) and show the spectrum as f_{H2} is increased. We also show the best fit broken power law spectrum (for $f_{\mathrm{H2}} = 0.2$) with black-dashed lines, where the break energy and high/low energy spectral indices are allowed to vary. The low energy spectrum is observed to very hard near the Galactic center ($\alpha_1 \lesssim 1$), with a gradual softening at larger radii. As we will see below, this low energy over-subtraction appears to be unphysical, and vanishes when the GCE template inner slope and radial profile are changed to their better fit values. A strong flattening and vertical elongation of the GCE profile is evident at all energies, with the sideband regions (regions VII and VIII) depleting much more significantly than the vertical regions (V & VI). The left sideband (fourth row left). Note that the low energy spectrum of Region VII is heavily contaminated by the soft-spectrum residual from the Aquila Rift star-forming region. In each region, we find that a broken power law provides an extremely good fit ($\chi^2/d.o.f. \approx 0.2$), even without including the larger systematic uncertainties.

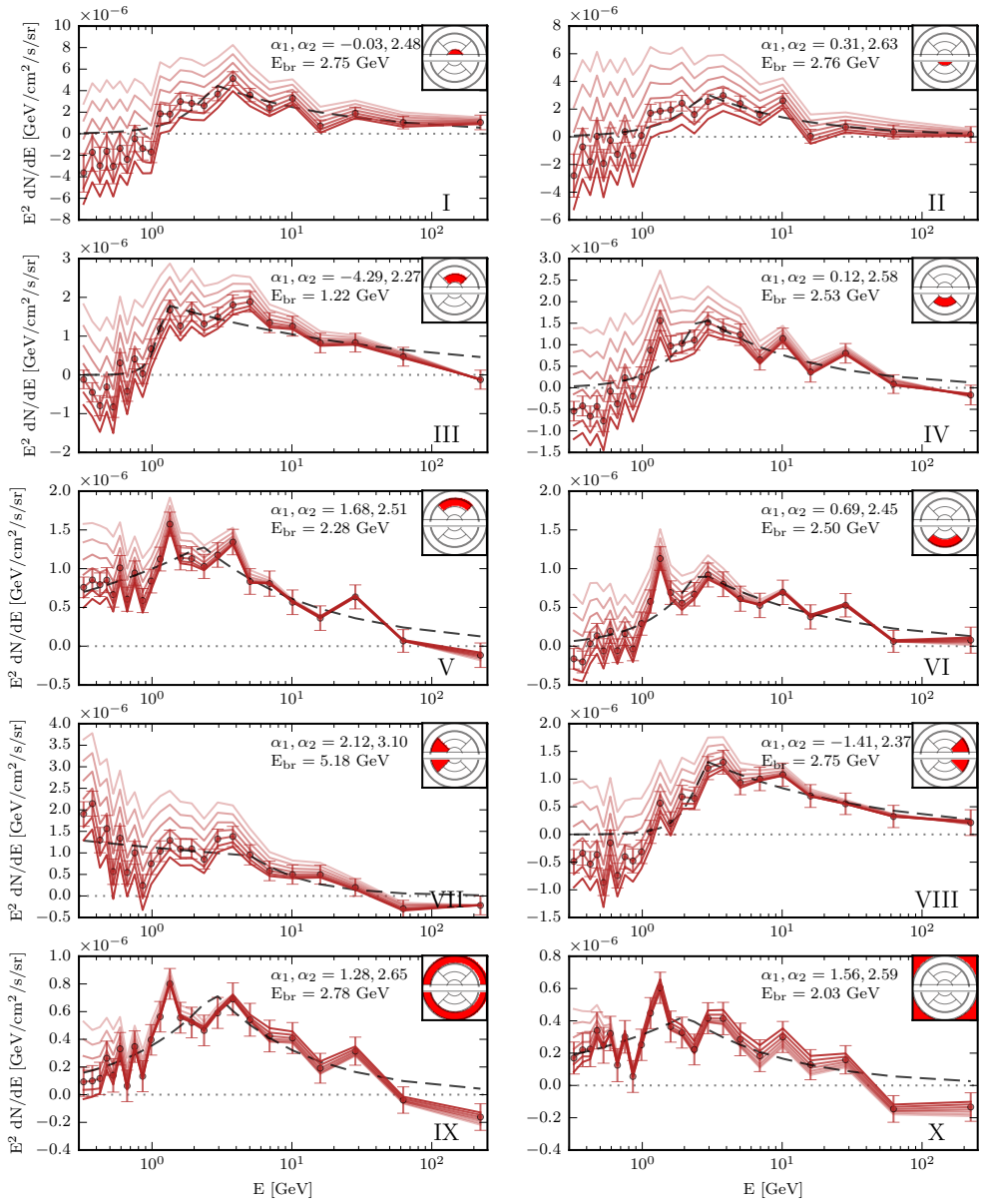

Figure 8.26: Spectrum of $\text{NFW}_{\gamma=1.05}$ template split into ten regions from Calore et al [36], with the active region indicated in red in the inset plots. Light to dark lines show the spectrum as f_{H2} is increased from 0 in increments of 0.05, with markers highlighting the $f_{\text{H2}} = .2$ case. The black dashed lines indicate the best fit broken power-law spectrum with low (high) energy spectral index $alpha_1$ (α_2), and a break energy E_{br}. Note the vertical scale in units of 10^{-6} GeV cm^{-2} s^{-1} sr^{-1}

8.1.8.5 The Galactic Center Analysis with the 1FIG Catalog

Recently, the Fermi-LAT collaboration produced an analysis of the $15^\circ \times 15^\circ$ region surrounding the Galactic center, utilizing new diffuse models and a new point source catalog to determine the properties of the Galactic Center excess [42]. While the diffuse emission models are not currently publicly available, the locations of 1FIG sources are. Using this source list, and again letting the normalization of all sources float independently in each energy bin (as in the case of 3FGL sources above). In Figure 8.27 we show the resulting spectrum and intensity of the GCE component in models using the 1FIG catalog, finding that our results are in very close agreement with models utilizing the 3FGL catalog. Since there are substantial differences between the 1FIG and 3FGL catalogs, this result illustrates a point made previously by [43] among several other results — that the observed γ-ray point source populations do not appear degenerate with the properties of the GCE component.

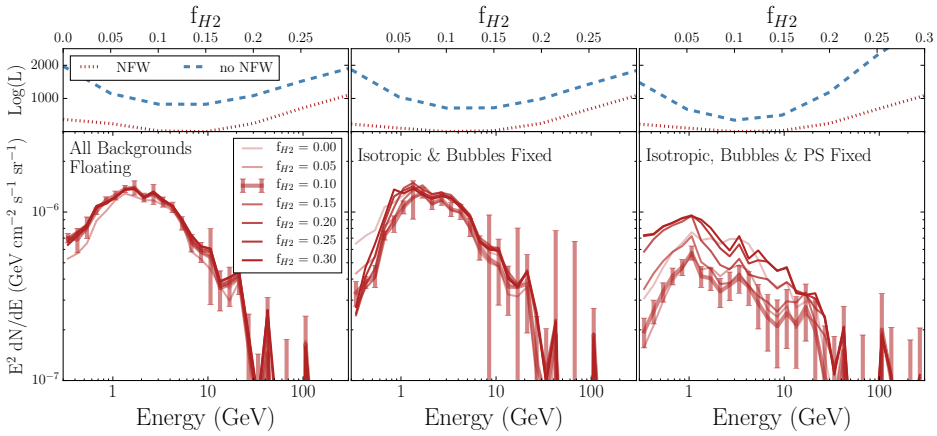

Figure 8.27: Same as Figure 8.9 for an analysis using the 1FIG catalog produces by [42], rather than the standard 3FGL catalog. The close comparison of these results with the results from the 3FGL point source population demonstrate the resilience of the GCE to changes in the γ-ray point source modeling.

8.2 Hadronic Cosmic Ray Bursts

There exist two key potential sources of cosmic rays in the inner Galaxy within the energy range relevant here: (i) supernova remnants and (ii) past activity of the central supermassive black hole associated with the radio source Sgr A*. For simplicity, we assume that both sources injected cosmic rays at the center of the Galaxy ($l = 0,\ b = 0$) at one or more points in time in the past. We will assume both an impulsive and a continuous injection for the sources, the former arguably more plausible for Sgr A* or for isolated star-formation bursts, and the latter closer to what expected for a population of supernova remnants. We first feature a qualitative analytic discussion (sec. 8.2.1), and we then present detailed results obtained with a full cosmic-ray propagation simulation with the `Galprop` package (sec. 8.2.2).

8.2.1 Analytic Estimates of Morphology

In the case of an impulsive source, the spatial distribution of the protons after a time t_i can be approximated as follows [302]:

$$f(r) \propto \frac{\exp[-r^2/R_{\rm dif}^2(t_i)]}{R_{\rm dif}^3(t_i)}, \tag{8.6}$$

where the diffusion radius

$$R_{\rm dif}(E,t) = 2\sqrt{D(E)t\frac{\exp[t\delta/\tau_{\rm pp}]-1}{t\delta/\tau_{\rm pp}}}, \tag{8.7}$$

with $D(E) = D_0(E/4\ {\rm GeV})^\delta$, and where $\tau_{\rm pp}$ is the approximately energy-independent proton cooling time. For timescales $t \ll \tau_{\rm pp}$, $R_{\rm dif} \approx 2\sqrt{D(E)t}$, indicative of a purely Brownian process. Note that the particle spectrum clearly depends on position unless $\delta = 0$, since the quantity $R_{\rm dif}$, driving the spatial dependence, depends on energy. In the narrowly peaked energy range of interest for the Galactic Center excess, such effect is, however, limited. For example, to first order and for $\delta \sim 0.33$, $R_{\rm dif} \propto E^{0.16}$ which is less than a factor 1.5 difference from 10 GeV to 100 GeV.

The counterpart to Eq. (8.6) for a continuous source is given by

$$f(r) \propto \frac{{\rm erfc}[r/R_{\rm dif}]}{r}, \tag{8.8}$$

where erfc is the error-function, and with the same $R_{\rm dif}$ as in Eq. (8.7) but with t, this time, referring to the time at which the continuous cosmic-ray source started injecting particles. In the limit $r \ll R_{\rm dif}$, the cosmic-ray flux saturates to a density $\propto 1/r$.

For a diffusion coefficient $D(E) = D_0(E_{\rm p}/4\ {\rm GeV})^\delta$, with $D_0 = 6.1\times10^{28}\ {\rm cm^2 s^{-1}}$, we then consider a variety of impulsive and continuous sources, with ages listed in Ta-

ble 8.4 along with their physical and angular diffusion radii at 2 GeV, where the GCE peaks.

In Figure 8.28 we show the projected density of cosmic-ray protons for the putative impulsive and continuous sources listed in Table 8.4. In particular, we show the evolution of a single impulsive source over the times from Table 8.4 as well as the continuous models C1 & C2 along with a representative superposition of impulsive sources (Im4+10×Im5) which we will employ in what follows. The overall normalization is left arbitrary for the sake of illustration. It is crucial to note that this is the *cosmic-ray proton* density, and that it must be multiplied with the spatially varying target gas density in order to obtain spatial distribution of the γ-ray flux. As a guideline, we also show the prompt γ-*ray* flux for an annihilating dark matter candidate following an NFW profile of inner-slope γ between 1.1 and 1.3 and scale-length $r_s = 24$ kpc. These two values bracket the signal morphology resulting from the analyses of Ref. [45, 43].

As we will demonstrate in the next section, the Im4 + 10 × Im5 and the C1 models have the correct proton densities to reproduce the GCE after convolution with the gas profile and are reshaped to closely match the $\gamma = 1.3$ profile[12]. In the plot, the shaded region indicates the angular region of interest, bounded at low angular scales ($\approx 0.25^\circ$) by the point-spread function of Fermi-LAT, and at the approximate angular scales ($\approx 12^\circ$) where statistical and systematic uncertainties currently render the excess invisible over backgrounds. It is important to note that the recent bursts (Im1, Im2, Im3 and Im4), or superposition thereof, provide highly concentrated populations of cosmic-

[12]The other values of γ shown will be used in a later discussion of dust template modulation.

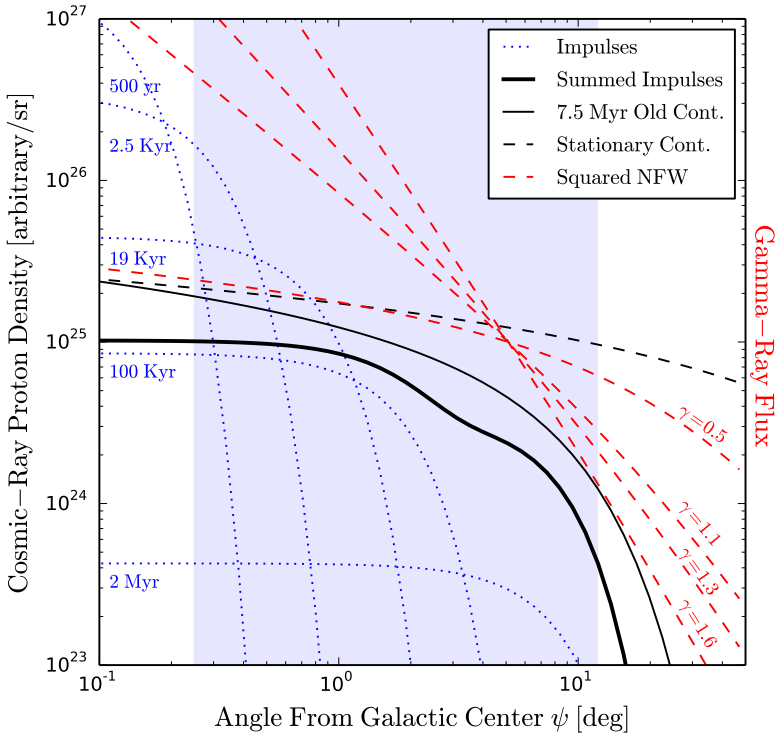

Figure 8.28: The density of cosmic-ray protons, at an energy of 2 GeV, projected along the line of sight as a function of the angular distance from the Galactic center in the spherically symmetric analytic diffusion approximation. Shown in dotted blue lines is the evolution of an impulsive source after .5, 2.5, 19, 100, and 2000 Kyr from top to bottom. We also show our summed impulse model (thick black), a 7.5 Myr old continuously emitting source (thin black), and a stationary continuous source (black dashed). After a convolution with the gas density profile, the summed impulse and 7.5 Myr old continuous models have γ-ray flux profiles which approximately match that of an annihilating dark matter candidate following an NFW of inner slope $\gamma = 1.3$ (shown in dashed red for several values of γ). The shaded region shows the angular scales which are both above the Fermi-LAT point-spread function (lower-bound $\approx 0.25^\circ$) and bright enough to be differentiated from the background (upper bound $\approx 10^\circ - 15^\circ$).

ray protons in the Galactic center, possibly yielding a bright, centralized, and spherically symmetric γ-ray emission.

Note that the time-scales we employ in the present estimates are not accidental:

for example, model Im5 is close to the age of the Fermi bubbles, as estimated e.g. by Ref. [411] and Ref. [412] to be around 1-3 Myr, while model Im4 is also close to another alternate age estimate for the bubbles, 4×10^5 yr, obtained by Ref. [21], as well as matching age estimates of $10^4 - 10^5$ yr for the supernovae remnant Sgr A East at the Galactic Center. Also notice that for the time-scales listed above we are never in the regime where $t_1 \gg \tau_{\rm pp}$ with the exception of the stationary continuous source, where protons are replenished over the region of interest anyway.

8.2.2 Morphology from Numerical Simulations

The hadronic γ-ray emission from π^0 decay traces both the density of cosmic-ray protons and the spatial distribution of the target interstellar gas. While the discussion above shows that with one or more burst injections, a variety of cosmic-ray density profiles can be obtained (including highly centrally concentrated ones), the present discussion must include the target density for hadronic inelastic processes. We note again that the template analyses of Refs. [43, 45] are predicated on a uniform distribution of cosmic-ray protons, and therefore neglect any gradients introduced by sources and by a non-trivial cosmic-ray morphology in the region of interest such as those shown in Fig. 8.28.

In order to simulate in detail the γ-ray emission from the region and to assess the role of the cosmic-ray distribution, we employ the code `Galprop v54.1.2423` [413][13] which provides a 3+1-dimensional numerical solution to cosmic-ray transport along with

[13] Available at http://sourceforge.net/projects/galprop/

empirically calibrated semi-analytical models of atomic, molecular, & ionized hydrogen (HI, HII, H^+) gas in the Galaxy, in addition to a sophisticated treatment of pion production and decay.

For simulations longer than 50 Kyr we employ a `Galprop` simulation consisting of a 10×10 kpc box centered on the Galactic plane with the x-axis defined by the Sun-GC line. The half-height along the z-direction is 4 kpc with a lattice spacing of 200 pc along each axis. For shorter simulations, the box-size is reduced to a sufficiently large cube of dimension 4 kpc with lattice spacing reduced to 50 pc. A source of cosmic-ray protons is then defined as a narrow sub-grid Gaussian localized at the Galactic center. In the case of impulsive source models, the `Galprop` code has been modified to inject protons in time following a δ-function centered at $t = 0$. Cosmic-ray transport is then solved forward in time with the `Galprop` code, using 'explicit-time mode' with step sizes of $\Delta t = 10^2, 10^3$ yr for sources younger and older than 50 Kyr, respectively.

As in the previous section, we assume an isotropic diffusion tensor with diagonal entries $D(E) = D_0(E/4 \text{ GeV})^{+0.33}$ and a diffusion constant $D_0 = 6.1 \times 10^{28}$ cm^{2}s^{-1}. For our morphological study of impulsive sources, we have explicitly verified that the diffusion constant and the diffusion time (the "age" of the source) are approximately degenerate for the quantity $D_0 t_{\text{diff}}$ held constant. This is expected in the limiting case of Eq. (8.6) where the diffusion time is much shorter than the proton cooling timescale. In other words, holding the quantity $D_0 t_{\text{diff}}$ constant will preserve the shape of the diffusion cloud, although the flux scales as D_0^{-1}. This implies that if the diffusion constant differs in the Galactic center our results will still hold, but diffusion timescales will change, as

will the energetics in the case of a continuous source.

The region of interest under consideration here extends to ± 1.5 kpc at 10 degrees, while the height of the diffusion zone is much larger and set to ± 4 kpc. Unless this half-height is reduced to $h_{\rm dif} \lesssim 2$ kpc, variations in the height of the diffusion zone are also of negligible impact, and are thus not considered. Diffusive reacceleration is incorporated using a Kolmogorov spectrum for interstellar turbulence ($\delta_{\rm turb} = 1/3$) and an Alfvén velocity of 30 km/s.

At the small Galactic latitudes of interest, low-speed ($\lesssim 15$ km/s) convective winds out of the Galactic disk have been confirmed to be negligible, via explicit simulations, and are set to zero. Notably, recent studies [414, 415, 416, 398] have presented extensive multi-wavelength evidence for very fast ($\gtrsim 150$ km/s) global outflows from the Galactic center region. Driven by intense and approximately constant star-formation, this energy independent advective transport provides a good fit over radio, GeV, and TeV observations and it is suggested that such a component could, in fact, dominate over diffusive transport. A detailed model of outflows is beyond the scope of the present study, but should not alter our overall conclusions. The narrow energy range of the GCE implies that diffusive transport is effectively energy-independent, and spherically symmetric advection should produce a comparable morphology in the inner galaxy, albeit with somewhat different time scales and energetics. However, it should be kept in mind that at the level of morphological detail required for template analysis, such effects are important and could significantly change the quality of fit compared to templates derived using diffusion alone.

As mentioned at the beginning of this section, a crucial ingredient that a full cosmic-ray simulation allows us to test is the role of the interstellar gas distribution in predicting the morphology of the diffuse γ-ray emission. In our simulations, the interstellar gas consists of three components: molecular, atomic, and ionized hydrogen. In `Galprop`, the first two components are modeled as independent, cylindrically symmetric distributions of seven galactocentric rings derived from surveys of HI & CO, where the latter is used as a tracer of molecular hydrogen [417]. These surveys are then combined with distance information derived from the line-of-sight velocity distributions and Galactic rotation curves to assign a gas density to each ring as a function of height. Finally column densities from the analytic model are renormalized to agree with the survey gas column densities, breaking the cylindrical symmetry and reproducing the observed asymmetric gas structures. Using this gas model, `Galprop` propagates the cosmic-ray protons and convolves the resulting density with the gas model in order to produce a projected map of the γ-ray flux. The smallest resolvable scales are thus ultimately limited by the gas map resolution. In the case of HI and H_2, this amounts to an angular resolution of 0.5° and 0.25° respectively. Notably, the latter is approximately of the same characteristic size as the Fermi PSF above a few GeV.

Within the Galactic plane, the mass fraction of ionized hydrogen is only a few percent when compared with the other two components. For the sake of comparison with the 'inner-Galaxy analysis' of Ref. [43], we focus on Galactic latitudes $|b| > 1^\circ$ where the ionized Warm Interstellar Medium (WIM) makes up a significant portion of the diffuse γ-ray signal. In `Galprop`, the WIM is based on the commonly used NE2001 model of

Cordes & Lazio [346, 212] with scale-heights doubled to 2 kpc to ensure consistency with recent pulsar dispersion data as described in Gaensler et al 2008 [418].

We emphasize that our gas model is nearly identical to that used to derive the hadronic component of the Fermi-LAT Collaboration's Galactic Diffuse Model, although the Fermi diffuse model also includes inverse Compton scattering and bremsstrahlung contributions from high-energy electrons, which are not of interest in testing possible issues with the hadronic component of the diffuse emission. For a thorough description of the gas model we discussed above, see Ref. [342] and enclosed references. One difference of limited importance in our implementation of the scale-factor $X_{\rm CO}(R)$. This parameter captures the ratio between the survey-derived integrated CO line intensity and the H_2 column density. In contrast to the fixed value used by the Fermi-LAT team, we choose this ratio to increase as a function of Galactic radius, in accordance with the findings of Ref. [41]. As this function is nearly flat in the inner Galaxy, this change is not expected to play a significant role.

The gas model and diffusion setup are now defined and we thus proceed to a morphological comparison between centralized proton sources and the measured Galactic center excess. In the analyses of Refs. [45, 43], the basic features of the excess emission show an approximately spherical shape with flux approximately 3% of the brightness of the Fermi diffuse model in the central $5^\circ \times 5^\circ$ window [45] centered on the GC. We define three benchmark cases of interest:

(i) a continuously emitting central source of high-energy cosmic-ray protons, which has reached steady state over $\gtrsim 10^9$ year timescales,

(ii) a continuous source which was started injecting protons 7.5 Myr ago, a time-scale consistent with ages proposed for the Fermi-bubbles, and

(iii) a two-component impulsive source where protons were injected at ages of 19 Kyr, 100 Kyr, and 2 Myr, summed with free relative normalizations.

In what follows, we calculate the γ-ray emission profile of our models as a function of the projected distance from the Galactic center. We then fit this profile to the GCE to determine statistical compatibility and study the remaining spatial properties.

In Figure 8.29 we plot the projected γ-ray flux, integrated along the line-of-sight and assuming a solar position of $r_{\odot}$ =8.5 kpc, for each model as a function of radius from the Galactic center and compare against the 'concentric ring' analysis of Daylan et al (2014) [43] (black data-points). In practice, we use the same convention for this figure as in Ref. [43]: specifically, we average the line-of-sight integrated flux over circular annuli of increasing radius and a full-width of 1 degree, with the masked Galactic plane regions excluded. Also shown for comparison are NFW profiles of inner slopes 1.1 and 1.3, as suggested in Ref. [43]. In order to fit each model to the data, we choose normalizations using a (logarithmic) least-squares fit weighted by the (log) inverse variances of each of the nine points. We then calculate the chi-squared per 9-2 degrees of freedom. For the NFW models fit in Ref. [43], the normalization and slope were free parameters. For our proton source models, the normalization is allowed to vary and source ages were chosen by hand to provide a reasonable fit. Both of these parameters are included when counting degrees of freedom. In case (iii), i.e. the summed impulsive model, we do not include the 19 Kyr component since its contribution is negligible outside of the masked region

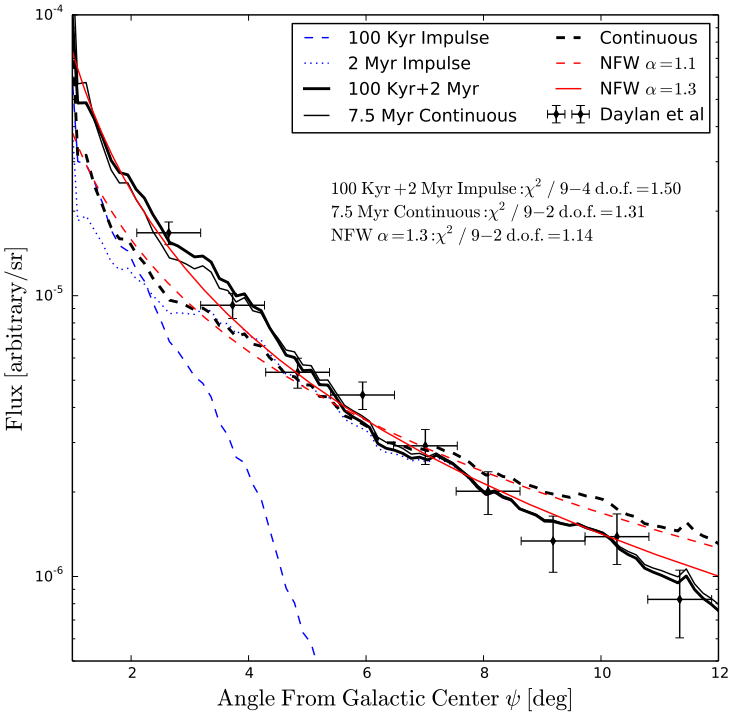

Figure 8.29: Projected flux density at 2 GeV as a function of from a proton source at the Galactic center. For non-dark matter lines, results are derived from a full `Galprop` simulation of diffusion and subsequent neutral pion decay averaged over the north + south regions with the Galactic plane ($|b| \pm 1°$) masked out upon integration. In black we show radial flux profiles for our summed impulsive (thick), a 7.5 Myr old continuous source (thin), and a steady-state continuous source (dashed). In blue-dashed and blue-dotted we show the individual impulsive sources at 100 Kyr and 2 Myr. Finally, we show NFW profiles with inner slopes 1.3 and 1.1 in solid and dashed red. Data points are taken from Daylan et al (2014) [43].

(although it could be important to match the Galactic center analysis in the central few degrees, as we will show below). We then sacrifice an additional degree of freedom and allow the normalization of the 100 Kyr and 2 Myr components to float independently. Thus the summed model includes 2 ages and 2 normalizations. The energetics of the normalizations are assumed arbitrary at this point. We will explore how reasonable the

resulting normalization values we infer actually are in section 8.2.4.2 where a concrete astrophysical scenario is discussed.

The profile slope of the continuous source in steady-state appears to be slightly too flat to match the observed emission and does not provide a particularly good fit to the data (χ^2/d.o.f. = 6.15). However, if this emission were initiated at an age of $\mathcal{O}$(5-10) Myr, the corresponding diffusion radius would be approximately 10 degrees. In this case, the resulting emission profile is significantly steepened, providing a very good fit – χ^2/d.o.f. = 1.31 – compared to the $\alpha = 1.3$ NFW profile where χ^2/d.o.f. = 1.14. Our best fitting model is the 100 Kyr+2 Myr impulsive model with χ^2/d.o.f. = 1.50. We find that for the summed impulse model, the best-fit injection luminosities have relative normalization 1:10, the larger corresponding to an event at 2 Myr. Although this precise ratio depends on the relative ages of the two components, this fact does indicate that two events with relatively comparable energetics provides good agreement with the observed excess and may indicate that events of similar nature and origin might have fueled the two cosmic-ray bursts needed to explain the observed morphology.

In Figure 8.30 we investigate the overall spatial distribution of the emission from a new population of cosmic-ray protons injected in the Galactic center region. The Figure shows the γ-ray flux associated with a central proton source for the benchmark impulse times of 0.5, 2.5 and 19 Kyr (upper panels) and of 100 Kyr, 2 Myr and continuous (lower panels). We use a linear scale in the three upper panels to help the Reader visually compare our results with what shown e.g. in Fig. 9, right panels, of Ref. [43]. To the end of emphasizing the emission outside the Galactic plane, we instead employ a logarithmic

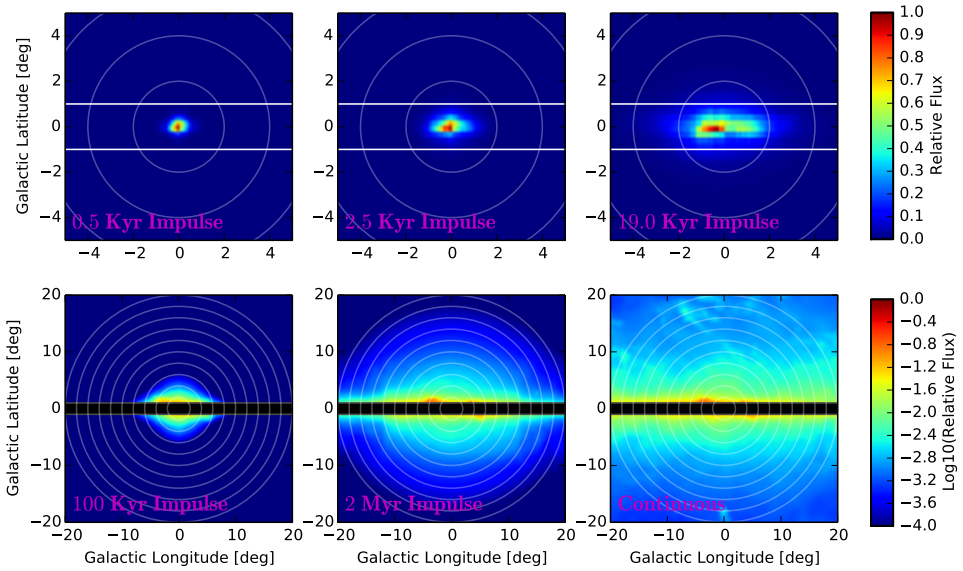

Figure 8.30: Hadronic γ-ray flux density at 2 GeV from an approximately central source of high-energy protons integrated over the line-of-sight. We show impulsive sources of increasing age in all panels with the exception of the bottom-right which shows a continuously emitting source in steady state. For each map, the fluxes are normalized to the maximum. For the ease of comparing the morphology of the claimed GCE in Ref. [43] and shown in their fig. 9, we employ a linear scale in the three upper panels. The three lower panels employ, instead, a logarithmic scale to enhance the features of the emission outside the Galactic plane region. Also overlaid are reference reticles in increments of 2 degrees and indicators of the Galactic plane mask $|b| < 1°$. All maps have been smoothed by a Gaussian of width $\sigma = 0.25°$ to match Ref. [43].

scale for the older bursts and continuous sources in the lower panels. In each case, the fluxes are rescaled such that the maximum flux equals unity. The Galactic plane mask ($|b| < 1°$) is bounded by white lines (or is masked out) and reference reticles have been overlaid at radial increments of 2°.

The top three panels show that a recent (from a fraction of a Kyr to tens of Kyr) impulsive cosmic-ray proton injection event in the Galactic center region yields

a highly spherically symmetric and concentrated source, with morphological properties very closely resembling and matching those found in the Galactic center analysis of Ref. [43] (see their Fig. 9, right panels), as well as in the GCE source residuals shown in the bottom panels of Fig. 1 in Ref. [45], and in the residual found in Ref. [44] and shown in Fig. 3. As long as the injection episode is recent enough, the morphology primarily traces the distribution of cosmic-ray protons, and is relatively insensitive to the details of the target gas density distribution — the diametrically opposite regime from what assumed in the diffuse Galactic emission background models of Ref. [43, 45, 44].

It is evident that the sub-Myr simulations show a significant degree of spherical symmetry outside the masked regions. Also, an excess with the same morphological aspect as in in fig. 9, right panels, of Ref. [43] can be easily reproduced by young or very young sources, as shown in the three upper panels. As the diffusion time increases to to several Myr, the emission profile becomes more elongated and spherical symmetry is degraded. At higher latitudes ($|b| \gtrsim 2^\circ$), most of the spherical symmetry is, however, restored as the molecular and atomic gas distributions fall off, and the ionized component produces a more isotropic emission. In the template analyses of Refs. [45, 43], a portion of this residual ridge emission may also be absorbed by the Fermi diffuse model, although it is difficult to exactly pinpoint this effect without repeating the full maximum likelihood analysis. It is also evident that gas structure is mostly washed out for recent impulsive sources, and that it becomes increasingly more prominent for older sources and for the continuous emission cases. Finally, we note that if a substantial portion of the inner excess is due to unresolved millisecond pulsars, much of the Galactic ridge would remain

at a lower relative luminosity.

Quantitatively examining the angular profile for each source at a variety of different radii shows that within $\pm 45^\circ$ of the north and south Galactic poles, there is a high degree of spherical symmetry with typical (positive) variations on the order of 20% with respect to the flux at Galactic north. At larger angles, however, the flux rapidly rises as one approaches the Galactic plane to values many times larger than the Galactic north flux. Although this does significantly illuminate the Galactic plane, it is unclear how important a role this plays in the analysis of Daylan et al [43], where spherical symmetry was tested by scanning the axis ratio of the (now ellipsoidal) dark matter template. Their analysis found a strong statistical preference in both the inner Galaxy and Galactic center analyses for an axis ratio of approximately $1 : 1 \pm 0.3$. While this template distortion does provide a simple test, its geometry is not physically motivated and does not correctly probe the bar+sphere shape expected from a central hadronic source.

In Appendix C of Ref. [43], the authors examine the excess in two regions: north/south, defined by angles within the 45° of the poles, and east/west, defined as the complementary region dominated by the Galactic disk. While both regions exhibit an excess, the E/W template shows a significantly enhanced peak of the signal compared to a flatter N/S spectrum [43]. This seems to indicate that either the Fermi-bubbles template absorbs much of the excess N/S emission, or that the emission is, in fact, more extended along the disk, as is seen in our benchmark models with a central cosmic-ray proton source. In further testing the axis-ratio, Ref. [43], again, uses ellipsoidal

projections of the NFW emission, this time allowing the template to rotate (there is still no test for a rectilinear disk component), finding a small statistical preference for an axis ratio of 1 to 1.3-1.4 elongated at an angle of $\approx 35^\circ$ counter-clockwise from the Galactic disk. It is possible that this component of the excess is in fact a component of an extended central molecular gas bulge, as advocated e.g. in Ref. [288], which is oriented at $\sim 14^\circ$ CCW and is not modeled by the cylindrically symmetric `Galprop` gas model and that, as a result, is therefore not included in Fermi Diffuse Galactic template.

In Appendix 4 of Ref. [43] the hypothesis of an excess proton density is tested by adding an additional template based on the Schlegel-Finkbeiner-Davis dust map [419]. The gas-correlated dust map is then spatially modulated so that the resulting template is given by

$$\text{Modulation} = \text{SFD}(\tilde{\text{r}}) \times \frac{\int_{\text{l.o.s.}} \rho^2_{\text{NFW}}(\tilde{\text{r}})}{\text{g}(\tilde{\text{r}})} \tag{8.9}$$

where the NFW profile's inner slope was scanned to maximally absorb the emission, preferring an inner slope $\gamma = 1.1$. The functional form for $g(|l|, |b|)$ was then assumed to be the product of a latitudinal linear $\times$ exponential function and a longitudinal Gaussian. This function was then fit over $|b| < 45^\circ$ and $|l| < 70^\circ$ to also maximally absorb residuals. It was found that the modulated dust absorbed a significant component of the excess when an additional NFW template was omitted. However, when the NFW template was included in the analysis, it absorbed nearly the entire excess and the modulated dust map appears uncorrelated with the excess. It was concluded that gas-correlated emission does not provide a suitable description of the GCE. We disagree with this conclusion for the following reasons:

1. The morphology of the underlying population of cosmic-ray protons which reproduces the GCE is shown by the 7.5 Myr continuous source shown in Figure 8.28 and is clearly *very* different from any of the NFW profiles shown. In the modulated dust template analysis, the functional forms chosen for $g(\vec{r})$ would need to be drastically different in order to reproduce distribution of protons matching that of Figure 8.28. In particular, any analysis must consider that the target gas density already falls off as one moves away from the Galactic center, and that the dust map should be initially modulated by the expected proton density, *not* proportionally to a projected NFW profile. For example, if one takes $g(r) = 1$ in Eq. 8.9, the resulting γ-ray template would fall off much faster than r^{-3} when integrating over unmasked regions as was done for Fig. 8.29. As can be seen in Fig. 8.28, within the inner few degrees of the Galactic center, our 7.5 Myr continuous hadronic source would correspond approximately to a dust profile modulated by an NFW profile of inner slope $\gamma \approx 0.45$, which would then be required to steepen to more than $\gamma = 1.6$ by 10° in order to not severely overestimate the flux at large radii.

2. As seen in Figure 8.30, the gas-correlated emission from cosmic-ray populations younger than a few hundred Kyr remains highly spherically symmetric at high latitudes. Only in substantially older sources ($\gtrsim$ 1 Myr) does the gas structure of the Galaxy become completely dominant in shaping the γ-ray morphology. In particular, this indicates that much of the dust structure lies at radii intermediate between the Earth and the Galactic center, whereas protons from a young cosmic-ray source have only reached the inner-most rings. Our simulations take this 3-

dimensional structure into account using gas velocity measurements to construct a model of Galactic structure and indicate that a 2-dimensional map of the column-density simply cannot account for a non- uniform cosmic-ray density.

3. If astrophysical in nature, the residual is likely to be the result of several emission sources. A substantial emission component in the inner few degrees naturally needs to be attributed to unresolved MSPs [420] which exhibit an approximately spherically symmetric, or slightly ellipsoidal profile (see however [15]). Such an addition would inevitably alter the preferred templates in the unmasked Galactic center analysis.

To summarize this section, we have used the cosmic-ray propagation code `Galprop` to simulate the γ-ray emission associated with neutral pion decay as cosmic-ray protons from a central proton source diffuse and interact with interstellar gas. Using a gas model identical to that of the Fermi-LAT Galactic diffuse template, we studied a variety of continuous and impulsive proton injection histories. Under standard assumptions for the diffusion setup, it was shown that one can reasonably reproduce the spatial morphology of the observed Galactic center excess using source histories that are potentially correlated with past Galactic activity. Specifically, the radial flux profile can be very closely matched if a continuous proton source turned on within the past 5-10 Myr, or if two or more events of comparable energy occurred at ages of around 0.1 and 2 Myr, although these simple benchmarks only represent a few possible scenarios. The spatial distribution of these source's γ-ray emission may be somewhat more extended

along the Galactic plane compared to the observed GCE, although without repeating the full likelihood analysis, a direct comparison is difficult. Indeed, a repeated likelihood analysis using the hadronic templates derived here is key to helping rule out a hadronic origin for the GCE and will be studied in detail in follow-up work. The spatially concentrated excess found in the 'Galactic center' analysis of Ref. [43] is reproduced by young impulsive sources active from a fraction to a few Kyr ago in the center of the Galaxy, or perhaps even by efficient trapping of the 100 Kyr cosmic-ray population in sub-resolution molecular clouds at the GC. At Galactic latitudes above 2-3 degrees emission from the Galactic ridge becomes no longer dominant and at angles within $\approx \pm 45^{\circ}$ of the Galactic poles, our sources exhibit a very high degree of spherical symmetry while the projected gas structure is left largely unresolved relative to the steady-state Galactic diffuse model. Finally, we discussed possible correlations of the GCE with unmodeled gas components in the Galactic center as well as pointing out important issues with the modulated dust template analysis in Ref. [43]. In the next sections we turn to a study of the spectral characteristics of the GCE.

8.2.3 Spectral Properties of Hadronic Bursts

Three independent recent analyses of the GCE have found spectra which share a characteristic peak near 2 GeV, with little excess emission over background either below a few hundred MeV or above 10 GeV. Although the location of the spectral peak is relatively robust, the shape of the excess is very sensitive to the modeling of point sources in the field, with additional systematic uncertainties such as the Galactic diffuse

emission, and with differing "regions of interest", leading to a large variation in the reported low and high energy spectral slopes. While most models are relatively well fit by a hard exponentially cut-off power law for the *photon* spectrum (and, as a result, reasonably well fit by dark matter models), we show below that a power-law *proton* spectrum with a break at energies of $\approx$ 10 GeV also provides good fits to the excess spectrum.

A crucial feature of the differential γ-ray spectrum produced through the inelastic scattering of astrophysical high-energy protons on interstellar gas, is a characteristic maximum flux at 100 MeV induced by the rapid downturn of the inclusive π^0 production cross-section below 1 GeV. Importantly, in the spectral energy distribution representation, $E_\gamma^2 dN/dE_\gamma$, this peak is shifted to $\approx$ 1GeV where both pulsar spectra and the GCE approximately peak. It is thus a remarkable and unfortunate coincidence that the claimed GCE spectrally peaks at $\approx$ 2GeV, where the likelihood of confusion with astrophysical sources is maximal.

Here, we consider three reference spectral models for the underlying cosmic-ray proton population, and thus for the resulting γ-ray spectrum. The first cosmic-ray spectrum we consider is a power-law with an exponential cutoff (PLExp) where the proton spectrum at momentum $p_{\rm p}$ is given by,

$$n_{\rm p}(p_{\rm p}) \sim \; p_{\rm p}^{-\Gamma} \; \exp[-p_{\rm p}/p_{\rm c}]. \tag{8.10}$$

The second and third models have a broken power-law injection of protons of

the following functional form:

$$n_{\rm p}(p_{\rm p}) \sim \begin{cases} (p_{\rm p}/p_{\rm br})^{-\Gamma_1} & : p_{\rm p} < p_{\rm br} \\ (p_{\rm p}/p_{\rm br})^{-\Gamma_2} & : p_{\rm p} > p_{\rm br}, \end{cases} \tag{8.11}$$

where we allow the second index to be arbitrary in one case (BPL), and where we fix it to $\Gamma_2 = \Gamma_1 + 1$ in the other (BPLFix). The BPLFix model will later be motivated by the possibility of proton acceleration by supernova remnants taking place inside dense and partially ionized molecular clouds. We then calculate the resulting γ-ray spectrum using one of `Galprop's` newest models, employing the detailed low-energy parameterizations of Dermer (1986) [310] with interpolation to the Monte-Carlo studies of Kachelrieß & Ostapchenko (2013) which better fit available collider data at high energies [311] (see App. 6.3 for details).

We then take data from the two analyses of Daylan et al (2014) [43], where different versions of the Fermi-LAT Galactic Diffuse Model were used to extract the GCE spectrum (using the template from the `P6v11` and `P7v6` releases, respectively), from Abazajian et al (2014) [45], and from Gordan and Macías (2013) [44]. We perform a maximum likelihood fit for each of our three spectral models, and compute the reduced χ^2 for $f = N - M$ degrees of freedom where N is the number of data points and M=3 for PLExp and BPLFix and 4 for the general BPL.

It is crucial to note that Daylan et al [43] do not provide an estimate of the systematic uncertainties (which are expected to be relatively large), nor do we attempt to include any such estimate. The error bars quoted in the analysis of Ref. [43] arise

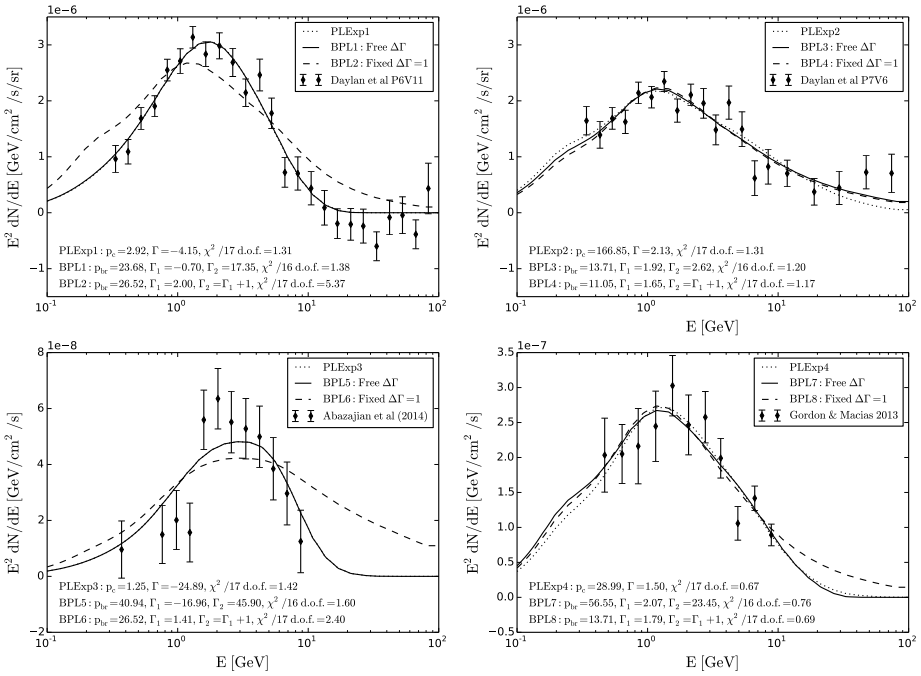

Figure 8.31: Best-fit γ-ray spectra for various analyses for the excess emission in the Galactic center region. In each panel we show three models of the underlying proton spectrum: Solid lines show the hadronic γ-ray emission for a broken power law proton injection spectrum where both indices and the energy of the spectral break are varied. Dot-dashed lines employ the same functional form, but with the break in the spectral index fixed to $\Delta\Gamma = 1$. The dotted lines represent an exponentially cutoff proton spectrum. In clockwise order and from the top left, the panels show data from Daylan et al Pass 6V11 [43], Daylan et al Pass 7V6 [43], Gordan & Macías [44], and Abazajian et al [45]. Note that the top row is normalized by the solid angle, while the bottom rows are integrated over the respective regions of interest.

purely from counting statistics. Abazajian et al [45] do estimate the relative systematic error Galactic diffuse model based on variations in the spectral form chosen for the GCE, but they do not provide a specific number. Based on their Fig. 8, we estimate the error (conservatively small) as 1×10^{-8} GeV/cm^2/s, and combine this in quadrature with the statistical errors for each point. Gordan & Macías [44] provide the most rigorous test

of systematic uncertainties related to the Galactic diffuse model by looking at residuals as a window is scanned along the Galactic plane in regions with no contaminating point sources. This results in an estimated $\approx$ 11% standard deviation from Fermi's diffuse background model. However, if we combine their statistical and systematic errors in quadrature, the fit is very poorly constrained. We therefore use only systematic uncertainties (which are typically larger) for this case. Below we discuss the results of Figure 8.31, but one can already see from the substantial variations between the four extracted spectra that estimating the systematic uncertainties is a highly non-trivial issue. We thus urge caution when interpreting the reduced χ^2 values we quote, which should be taken only as a rough indicator of fit quality.

Figure 8.31 shows the best fits for each of the three spectral models. In the top-left panel is the Daylan et al analysis which uses the the non-reprocessed `P6v11` diffuse model. The excess is very well fit by the PLExp model which closely matches the prompt emission from a light dark matter candidate. The BPL model also provides an exceptionally good fit, although the pre-break index is unphysically steep, at $\Gamma_1 = -0.7$ while the second index converges to a value $\Gamma_2 \approx$17 with a relatively large break energy $E_{\rm br} = 23.7$ GeV, effectively mimicking the PLExp model (the two lines are in fact hardly distinguishable in the figure). Of more interest is our BPLFix model, which provides a reasonable, though not optimal, fit to the data considering the underestimated error bars. The best-fit low-energy index Γ_1=2 is intriguingly equal to the canonical value $\Gamma \approx 2$ expected from the theory of linear diffusive shock acceleration (DSA) thought to drive supernovae and black-hole acceleration processes. Note that there exist systematic

uncertainties arising in the low and high-energy ranges from modeling of the inclusive $pp \to \pi^0 +$ anything cross section, as is discussed in App. 6.3 and Ref. [314]. Such uncertainties can be as large as 15% below 1 GeV up to 40% above 100 GeV, and thus affect any conclusion of the precise values needed for the cosmic-ray proton injection spectrum.

The top-right panel shows the Daylan et al `P7v6` analysis, which includes a Fermi-LAT model of the bubbles in the Galactic diffuse template in addition to the independent Finkbeiner bubble template. Unlike the `P6v11` analysis, which used mismatched photon data from the `P7` release, this model is appropriately calibrated to the full `P7` event data. Compared to the `P6v11` analysis, this approach yields a substantial flattening of the spectrum, with all models providing equally good fits, with nearly identical γ-ray spectra. Γ_1 is found to vary between 1.65 and 2.13 and in both BPL models $\Gamma_2 \approx 2.6$. The similarity between the BPL and BPLFix models is remarkable, given the significant difference in their initial spectral index. This indicates a weak spectral dependence on Γ_1 due to the natural 'GeV-bump' associated with pion decay. This is also observed for in the fits to the other analyses, where the initial index can have completely unphysical values $\gamma_1 \gtrsim 15$ with only a very small change in the log-likelihood. Later we will show contour plots for the BPLFix model which indicate a strong covariance between the break momentum and the low-energy spectral index, and acceptable values of Γ_1 over the large range 1.25-2.5.

In the bottom-left panel we show spectra taken from the full model of Abazajian et al (Figure 3), Ref. [45], with statistical errors added as discussed above. Even our

conservative estimate of the systematic error leads to large uncertainties in the spectrum, and all of our models provide acceptable fits. Although the BPLFix model does not appear to fit the data particularly well, we encourage the reader to review Figure 8 of Ref. [45] where a range of GCE spectra are shown depending on the spectral model used in the likelihood fit. The data shown here is for the measured residual – as opposed to what results from a specific dark matter template – and corresponds approximately to the most strongly peaked model. The "mean model" of Fig. 8 in Ref. [45] has a significantly softer low-energy spectrum. The fit is also severely impacted by the asymmetrically small number of data points above the bump.

Finally, in the lower-right panel we show data from Gordan & Macías (2013) which we found, again, to be well fit by all models, with a preference for a slightly hardened low-energy index of Γ_1=1.73 for the BPLFix model and a break energy of 13.7 GeV.

Collectively, our results reveal two characteristic features: Firstly, in most cases there is a slight preference for the PLExp model; the BPL with free indices typically tend to converge towards a PLExp form. One exception is the `P7v6` fit from Daylan where the BPLFix model is actually preferred. The BPLFix models provide a reasonable fit throughout, with the exception of Daylan et al's `P6v11` which, however, does not include any treatment of systematic uncertainties. Second, for a flat $p_{\rm p}^{-2}$ proton spectrum, the γ-radiation from π^0 decays naturally peaks at $\approx$1.25 GeV, slightly below the observed excess peak at $1.5-2$GeV. In order to shift the peak to these higher energies we prefer a slightly harder initial spectral index Γ_1 between approximately 1.6 to 2, although there

is low sensitivity to this parameter. The placement of the spectral break is typically near $p_{\rm br} = 10 - 50$ GeV and provides an effective control of the width of the spectral peak while the second index Γ_2 controls the cutoff rate as is expected from the nearly flat π^0 production cross-section above 1 GeV given in Eq. (6.12). The preference for a slightly hardened spectral index could arise naturally if the emission is a combination of e.g. SNR accelerated protons with index ≈ 2 and MSP emission which can easily have Inverse-Compton spectra harder than 1.5.

As an additional cautionary note, we reiterate that the theoretical predictions for the γ-ray spectra from proton-proton collisions are affected by significant systematic uncertainties associated to the modeling of the $pp \to \pi^0+$ anything production cross section. Such uncertainty feeds into the inferred spectral properties for the cosmic-ray populations associated with a given γ-ray emission. We discuss and evaluate quantitatively such uncertainties in the App. 6.3. For now, it is important to note that any conclusion on the nature of the GCE based on spectral considerations alone ought to include this source of systematic uncertainty as well.

In addition to the 'GeV bump' feature of the pion-decay spectrum, we point out the discussion of Section 4.2.3 in Ref. [302], which describes the temporal evolution of the spectrum of a cosmic-rays which are accelerated inside a molecular cloud, where large gas densities and magnetic fields can trap low-energy protons on timescales of 10^5 yr. For an impulsive accelerator and a cloud of very high density, high energy-protons can suffer substantial energy losses and propagate in a more rectilinear fashion, allowing escape while the low-energy protons remain inside. The cloud is thus illuminated with a

spectral energy distribution peaked at a few GeV with a steepened high-energy falloff at ages greater than 10^4 years. The low-energy index remains virtually unchanged unless the source is very young and brehmstrahlung from secondary electrons is contributing strongly. By 10^5 yr the cloud's peak flux decreases by 2 orders of magnitude and becomes part of the diffuse background. Although this produces gas-correlated emission that could potentially be resolved, very close to the Galactic center the spatial resolution of Fermi-LAT is limited to scales larger than about 30 pc, larger than most of the (many) molecular clumps orbiting in the central few parsecs. Such sources cannot thus be spatially differentiated from the central point source with γ-ray observations. If the escaping high-energy emission is already suppressed, as in our BPLFix model, this would appear as an additional spectral break at approximately the same energy. This very scenario may be realized at the Galactic center for the $\sim 10^4 - 10^5$ year old supernova remnant, Sgr A East, which we discuss in detail later. Almost certainly, molecular clouds are trapping protons at the Galactic center on scales unresolvable by Fermi-LAT and effectively reproducing the morphology of a younger source.

In summary, we proposed three models for the spectrum of a new population of cosmic-ray protons which could explain the GCE: an exponentially cutoff power law, and two broken power laws with free and fixed ($\Delta\Gamma = 1$) changes to the spectral index, respectively. We calculated the γ-ray spectra resulting from inelastic collisions of the protons on interstellar gas, noting that nearly all physically reasonable proton injection spectra exhibit a bump near ≈ 1 GeV in the γ-ray $E^2 \mathrm{d}N/\mathrm{d}E$ distribution. For each model we performed a maximum likelihood fit to each of the four GCE residuals and

found good fits in all cases over a broad range of parameter values. We concluded that *the core spectral features of the GCE* – namely a hard low-energy spectral index, a peak between 1-3 GeV, and a rapid decline above a few GeV – *can be naturally produced by an additional population of cosmic-ray protons in the inner Galaxy.* In the next section, we provide theoretical and phenomenological evidence that such a population is likely to exist in the Galactic center.

8.2.4 Physical Models for the GC Excess

In this section we demonstrate that the needed luminosity and spectral properties for the cosmic ray population we invoke to explain the GCE have sound physical motivations. In particular, we explain in Sec. 8.2.4.1 how the spectral breaks in the cosmic-ray proton spectra we consider might have arisen in the Galactic center region, and related observational evidence; we then estimate in Sec. 8.2.4.2 the energetics required by a cosmic-ray interpretation of the GCE, and argue that the time-scales and energy scales are plausible and in line with observations and theoretical expectations.

8.2.4.1 A Mechanism and Evidence For GeV Spectral Breaks

For half a century, the bulk of Galactic cosmic rays has been thought to originate from supernova remnants (SNRs) which inject 3-30% of the total supernova energy ($E_{SN} \approx 10^{51}$ erg) into protons and other light nuclei [421]. A detailed theory of diffusive shock acceleration is still incomplete, but simplified linear models predict that supernova shocks propagating through an ionized gas precursor can accelerate protons and

other nuclei up to 10^{15} eV with a resulting proton spectrum of $p_{\rm p}^{-2}$ at the source [422]. When combined with sophisticated models of nuclear propagation through the Galaxy and Solar System, this source spectrum successfully reproduces the locally measured spectrum of cosmic-ray nuclei. Direct confirmation of this acceleration model was provided only very recently (2013) by the Fermi-LAT collaboration following the detection of γ radiation characteristic of π^0-decay in association with two known SNRs, IC443 and W44 [421].

In order to postulate a viable astrophysical model for the Galactic center residual – i.e. without invoking new particle physics – we require either a substantial reduction in the 10^{15} eV high-energy cutoff, or a strong spectral break near ≈ 10 GeV which renders the signal invisible over that of the diffuse sea of background cosmic-rays where the γ spectrum is roughly $\propto E_\gamma^{-2.7}$. In what follows, we describe recent proposals that modify the canonical theory of DSA in the presence of dense molecular clouds which surround the inner Galaxy, as well as actual realizations of this scenario as seen in recent Fermi SNR observations showing significant breaks at $\mathcal{O}(10$ GeV) in the underlying proton spectrum. It is thus possible to provide a natural explanation for the spectrum, energetics, and morphology of the GCE requiring only the assumption of an enhanced central supernova activity over the past few million years.

In DSA, shock waves propagating through ionized interstellar medium compress the plasma and transfer kinetic energy downstream through either two-body collisions, or through collective electromagnetic effects if the collision cross section is very small. In the compressed zone preceding the shock front, resonant scattering of Alfvén waves efficiently

accelerates particles until their gyro-radius $r_g = cp/(eB)$ exceeds the width of the shock layer [278]. While this test particle case assumes a fully ionized cosmic-ray precursor, the Galactic center is only partially ionized, with well over 80% of the gas content associated with neutral molecular hydrogen in the inner 200 pc, which completely engulfs the region of central starburst activity. Malkov, Diamond, and Sagdeev [279, 280] demonstrated that when the upstream edge of supernovae shocks interact with molecular clouds, ion-neutral collisions effectively damp a range of otherwise resonant Alfvén waves, severely deteriorating particle confinement within a slab of momentum space, and steepening the spectral index of protons by precisely one at an energy given in Ref. [279] as

$$p_{\rm br}/m_{\rm p}c \approx 16 B_{\mu}^{2} T_{4}^{-0.4} n_{0}^{-1} n_{i}^{-1/2}, \tag{8.12}$$

where B_{μ} is the magnetic field strength in units of μG, T_4 is the temperature of the ionized precursor in units of 10^4 K, and n_0, n_i are the neutral and ionized gas density given in in units of cm^{-3}, respectively. Similar developments in non-linear DSA have shown that over 1-10 GeV the spectrum can be as steep as $E_{\rm p}^{-4}$ depending on the shock speed and environment, flattening out again above a few TeV [281].

The mechanism described above successfully reproduces at least 6 of the 16 current Fermi-LAT observations of SNRs [282, 283, 46, 284, 285, 286], although the uncertainties associated with estimating the relevant environmental parameters are considerable. The 10 remaining observations have not yet incorporated this model into the analysis. In Ref. [46], several SNRs observed by Fermi were shown to be interacting with molecular clouds based on radio observations of 1720 MHz OH maser emission, provid-

ing a strong indication of shocked H_2. The spectra were then reproduced by fitting the underlying proton distribution according to an exponentially cutoff power-law, as we do above.

SNRs interacting with highest density clouds were found to have low cutoff energies and hard proton spectra with $[\Gamma, E_c] = [1.7,160\text{ GeV}]$ and [1.7,80 GeV] compared to the low-density cases, where [2.4,1 TeV] and [2.45,1 TeV]. For another SNR, W44, an independent analysis found that the γ-ray emission was well fit by a hard proton spectrum of index between 1.74 and 2 with a cutoff at $p_c \approx 10$ GeV/c [283]. While these examples provide a representative sample of the expected range for the low-energy spectral index and cutoff energies, we do not necessarily expect a hardened spectrum to be correlated with high gas densities. These SNR spectra match the γ radiation expected from an exponentially cutoff proton spectrum quite well, possibly indicating that the theory of Ref. [279] is underestimating the true breaking strength due to ion-neutral damping, or that an additional cutoff mechanism is at play. In either scenario, a more pointed spectral peak is predicted, and as a result the fit to the residual GCE spectrum in Section 8.2.3 is generally improved.

The Galactic center hosts a zoo of high-energy astrophysical sources including several SNRs, resolved & unresolved pulsars, pulsar wind nebulae, and the central black hole Sgr A*. Most notably Sgr A East is a $\sim 10^4 - 10^5$ year old and 10 pc wide SNR rapidly expanding into the molecular cloud M–0.02–0.07, where a half-dozen sites show also show the 1720 MHz maser emission from shocked H_2 [287]. This complex encompasses the central black hole with most of the structure residing within a few

parsecs from Sgr A* ($\lesssim 0.05^\circ$). This separation is too small to be spatially resolved by Fermi-LAT, which has a maximal angular resolution of about a quarter degree, hence it will appear as a point source, perhaps with minor spatial extension, whose spectrum cannot be differentiated from additional Galactic center sources[14]

An especially intriguing candidate for the recent injection of cosmic-ray protons in the inner Galaxy is Sgr A East. As an estimate of the expected flux from Sgr A East, we utilize a similar object, SNR W44. The latter is observed to have a differential flux of $\approx 1.25 \times 10^{-7}$ GeV/cm^2/s. Multiplying by the square of the distance ratio $d^2_{\rm W44}/d^2_{\rm GC} \approx (2.9 \text{ kpc}/8.3 \text{ kpc})^2$ we obtain a flux of 5×10^{-8} GeV/cm^2/s, precisely in line with the GCE residual and the Sgr A* flux reported by Abazajian et al within a $1^\circ \times 1^\circ$ box centered on the GC [45]. (Note that the the two Daylan et al fluxes reported in Figure 8.31 are normalized by the solid angle of a thin annulus at 5° from the GC). It remains to be assessed whether the spectral break energy near the Galactic center is compatible with the the results of Section 8.2.3, and whether a reasonable supernova rate is compatible with the observed flux.

The environment of Sgr A East has been studied in detail at radio and X-ray wavelengths. Unfortunately, the complicated structure and rapid gradients in density, temperature, and magnetic field strength imply that there will be no single prediction for the spectral break energy predicted by Equation (8.12), but, rather, a range of values dependent on the particular properties of the shocked region. Here we expect that

[14]For reference, the template analysis of Daylan et al, which uses large photon statistics and an event selection which optimizes PSF, finds the most likely position for the GCE to be centered within about 3 arcmin of Sgr A*. The next generation of ground-based γ-ray telescopes is likely to resolve these structures at energies above 50 GeV.

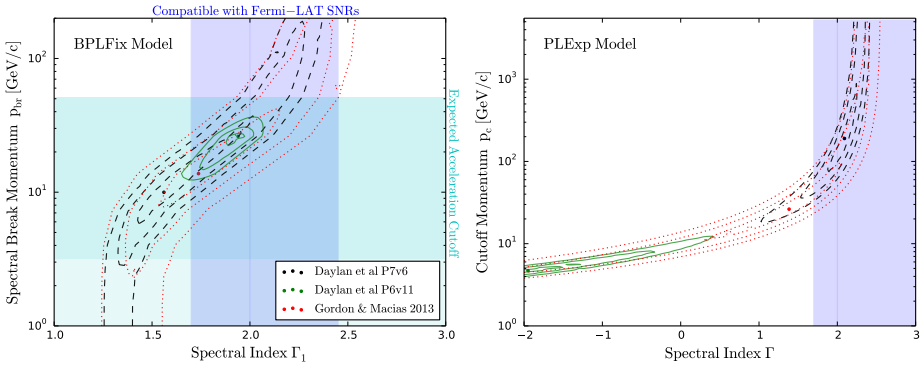

Figure 8.32: 1,2, and 3σ confidence intervals for a broken power-law proton spectrum which steepens its index Γ_1 by one above the break energy $p_{\rm br}$ (left panel), and an exponentially cutoff power law (right panel), fit to three extractions of the Galactic center excess spectrum (excluding Abazajian et al). In the top panel, the bands shaded along the x-axis represent the range of low-energy spectral indices for SNRs interacting with dense molecular clouds as measured by Fermi-LAT in Ref. [46]. The dark and dark+light shaded bands along the y-axis indicate spectral break momenta expected to occur in dense molecular clouds and more ambient molecular densities respectively. Also note that confidence regions for the two Daylan et al spectra do not include any systematic errors and hence the true confidence contours are likely to be significantly more extended.

nearly all of the supernova activity will take place very close to the Galactic center, with conditions not far removed from those of Sgr A East. The goal of the current study is to determine whether the conditions can plausibly reproduce the GCE, while a detailed environmental model and statistical treatment of uncertainties is reserved for future work.

The Central Molecular Zone (CMZ) is a large elliptical cloud with a gas mass fraction dominated by molecular hydrogen. It is thin and aligned with the Galactic disk, extending to a radius of approximately 150 pc from the Galactic center when projected along the line of sight[15]. This cloud makes up 5-10% of the total Galactic molecular gas

[15]Interestingly, the same gas model in Ref.[288] finds a large gas bulge extending to 450 pc which is

and is comprised of dense clumps of H_2 as well as of a lower density ambient component which completely fills the acceleration volume for any centralized SNR. In the inner 15 pc, typical densities can vary from the ambient value of 10^2 cm^{-3} up to the dense molecular clouds at 10^5 cm^{-3} [289, 288], occasionally reaching even higher densities. The warm ionized hydrogen is significantly more extended and provides the precursor for shock acceleration. There is only weak power-law dependence of the break momentum on the density and temperature of the ionized component ($n_i^{-0.5}$ and $T^{-0.4}$). Both of these components are reasonably well measured in the Sgr A* region using X-ray observations with ion densities near 10^3 cm^{-3} and very hot plasma temperatures of 10^7 K [290].

The most important, and also the most uncertain factor in determining the break momentum, is the magnetic field strength in the shock propagation region. Zeeman splitting of OH molecules provides a measurement of the magnetic field strength along the line of sight, and indicates very strong fields in the large non-thermal radio filaments and possibly molecular clouds which can be as high as 1-4 mG [287, 291] while Faraday rotation measurements indicate that the surrounding medium can be somewhat lower with a strength down to several hundred μG. For an extensive review of magnetic fields in the Galactic center, we point the Reader to Ref. [291].

Efficient trapping of very low energy precursors in the very dense molecular clouds implies that these will be the primary acceleration sites for the resulting high energy cosmic-ray population, although a fraction will still originate from the surrounding

rotated 13.5° CCW from the Galactic plane when projected along the line of sight with an axis ratio of 3:1. Daylan et al found a slightly preferred fit at roughly an angle of 35°± CCW with an axis ratio of $1 : 1.4 \pm .3$, possibly indicative of gas correlated emission.

lower density and lower magnetic field regions. In this case, the lower densities of the ionized and molecular components partially cancel the effect of the smaller magnetic field on the break momentum, but some broadening of the spectral peak may be expected toward lower energies. In order to estimate the range of break momenta achievable at the GC, we simply fix the least sensitive parameters to typical values, and set $n_i = 10^3$ cm^{-3}, $n_0 = 10^4$ cm^{-3}, and $T = 10^7$ K, while varying of B between 0.5 mG and 4 mG. Doing this provides a break momentum between 0.79 and 51 GeV/c with a nominal value of 12.7 GeV/c for a 2 mG field strength.

Without more accurate measurements and high-resolution 3-dimensional models of the Galactic center environment, it is extremely difficult to definitively compute the resulting cosmic-ray spectrum. If, in fact, these large magnetic fields are contained strictly to non-thermal radio filaments, or are much weaker then previously thought, as suggested in Ref. [292], the predicted momentum break would be significantly smaller, and the breaking mechanism would be disfavored as an explanation for the GCE. It is also very likely that current conditions at the Galactic center differ substantially from those of 1-10 Myr ago especially if the Fermi bubbles formed on comparable timescales. Compounded with uncertainties in non-linear DSA in the presence of ion-neutral damping, a conclusive statement is currently not possible. Nonetheless, the observation of break energies from ten to several hundred GeV in nearby SNR indicates that such scenarios are not uncommon, and provide evidence that the description advocated above is not unrealistic.

In Figure 8.32 we show confidence intervals for the low-energy spectral index

and break energy for the BPLFix and PLExp models of the *proton* spectrum as fitted to the two Daylan et al GCE residuals as well as that extracted by Gordon & Macías. We do not show the results of the fits to the Abazajian et al results due to the previously mentioned asymmetry in the number of points below and above the spectral peak which forces a very hard spectrum that clearly does not fit the rapid falloff above 2 GeV seen in the other datasets. While the *residual* found by Abazajian et al is indeed very hard at low energies, when an additional GCE template and spectral form is included as part of the fit, the low-energy index softens significantly becoming very similar to the other analyses. This behavior is clearly delineated in Fig. 8 of Ref. [45] and the enclosed discussion.

In the left panel, the shaded regions along the x-axis show the range of the low-energy proton index which are compatible with Fermi-LAT observations of SNRs interacting with molecular clouds taken from Refs. [283, 46], highlighting the canonical index $\Gamma_1 = 2$ predicted by linear DSA. In the shaded y-axis regions, we show expectations for the position of the spectral break in conditions typical of the very dense molecular clouds (dark cyan) and in the ambient lower density environment (darker+lighter cyan). It is promising that these contours are fully compatible with one-another when fitting to the BPLFix model. Clearly, if one assumes the BPLFix model, the parameter values are in line with those expected from SNR interacting with molecular clouds in the Galactic center.

In the right panel we show similar regions shaded along the x-axis representing the range of the spectral indices compatible with Fermi-LAT observations where fitting

the underlying proton spectrum used an exponentially cutoff power-law model [282, 284, 286]. Although these studies also indicate GeV-TeV scale cutoff energies, it is unclear how such cutoff scales should change in the Galactic center environment without a theoretical understanding of the cutoff mechanism itself. In contrast to the BPLFix model, a PLExp spectrum reveals less compatibility among the three GCE residuals, with the main `P6v11` analysis of Daylan et al requiring an unphysically hard spectral index. Interestingly, two of the GCE datasets show a rapid upturn in the contour as the spectral index rises above $\Gamma = 2$. In this region, the fit is almost completely insensitive to the cutoff energy up to at least ≈ 10 TeV. Notably, a spectral index softer than 2 is commonly invoked when modeling radio and γ-ray emission from AGN in the context of hadronic injection. Although the relatively low momentum cutoff would still need to be explained, the insensitivity here could allow for a variety of possibilities, and warrants additional study.

To summarize, we find that the occurrence of a break in the spectrum of cosmic-ray protons in the specific environment of the Galactic center is well-motivated. Observations of the γ-ray spectrum of several SNR with the Fermi LAT point to cosmic-ray proton spectral features aligning precisely with those needed to fit the spectrum of the GCE; the location of a spectral break in the accelerated cosmic-ray protons in the presence of dense molecular clouds in the inner Galaxy also falls squarely in the range that optimally fits the inferred γ-ray spectrum of the GCE. We thus conclude that the spectra we invoked to fit the GCE are well motivated by both theory and observation.

8.2.4.2 SNe Rates and Starburst Histories

In this section we explore the energetics required to produce the GCE with cosmic-ray protons injection at the center of the Galaxy. In the previous section, we showed that the flux measured from SNR W44 corresponds to the approximate luminosity needed to explain the GCE in the inner Galaxy. At radii larger than 1 degree, the GCE signal decays rapidly as shown in Fig. 8.29. In Section 8.29 we showed that such a radial flux profile could be achieved rather naturally by the diffusion of protons injected at the Galactic center in several different episodes – for example, impulsive injection over 2-3 different epochs ($\approx 10^4, 10^5,$ and 10^6 yr) or continuously if the source was turned on around 7.5 Myr ago. Previously, we ignored the normalization of the flux and were only concerned with the relative normalization of the summed impulsive models This revealed that the 100 Kyr + 2 Myr summed model preferred relative normalizations of, respectively, 1:10. The energetics of these long-timescale events is more constrained than for more recent outbursts.

We compute the γ-ray flux due to protons assuming a nuclear injection spectrum of index $\Gamma_1 = 2$ breaking to $\Gamma_2 = 3$ at 10 GeV. We find that the 100 K and 10^6 summed impulsive model requires a total injection of $\mathcal{O}(10^{52})$ erg into protons with energies above 100 MeV in order to produce flux compatible with the GCE consistent with the very recent findings of [398]. For continuous sources only a few million years old, the required energy is approximately 10^{38} erg/s, or a few 10^{48} erg/century, while continuous sources in steady-state are an order of magnitude less and comparable to the rates needed to maintain the current molecular gas temperatures near the Galactic

center [423].

Stellar densities at the Galactic center are extremely high rising from a mass density of 10^4 $M_\odot/\mathrm{pc}^{-3}$ at a radius of 10 pc to over 10^6 $M_\odot \mathrm{pc}^{-3}$ in the central parsec (compared to the local density $\ll 1$ $M_\odot/\mathrm{pc}^3$). Measurements of the infrared luminosity near the Galactic center provide an indirect probe of the star formation rate. If this has not changed dramatically over short stellar evolution timescales (10^8 yr), the expected supernova rates are 0.01-0.1 per century [39] each injecting $\epsilon_p 10^{51}$ erg where ϵ_p is the fraction of the supernova energy channeled into proton acceleration, often taken to be near 0.1 [302]. This implies an average continuous injection rate of $10^{48} - 10^{49}$ erg/century, compatible with the observed excess signal. For impulsive sources, the same value of ϵ_p would require bursts of 10-100 supernovae to occur within a timescale relatively short – 10^4 to 10^5 yr – with respect to the diffusion timescale. While any realistic scenario would likely be an admixture of continuous and burst-like injections, the supernova rates required to reproduce the observed GCE flux in either case are well within the possible histories of the Galactic center Region.

Star formation rates within the central hundred parsecs of the Galaxy is a subject of hot debate. Over $\sim$10 Gyr timescales, several studies[414, 415, 416] suggest that the star formation rate has been approximately stable, with long-lived bulge stars formed during the Milky Way's last major merger event and relatively quiescent activity since. On much shorter timescales the situation is less clear. Highly variable and intense star-formation producing tens to thousands heavy stars over a few Myr, cannot be ruled out. High ionization rates, severe shocks, and the large scale inflow/outflow accompa-

nying molecular cloud collisions or cataclysmic events, such as star-bursts or activity from the central supermassive black hole, can trigger periods of rapid star-formation taking place inside the densest molecular clouds[16]. In contrast to self-collapsing molecular clouds, such external compression mechanisms are believed to induce significantly heavier initial mass functions, producing O/B type stars which evolve over $10^6 - 10^7$ years before going supernova [425]. While many of the Galactic center conditions can also inhibit star formation, observations indicate at least 100 high mass stars with ages estimated around several Myr, indicating that an era of high star-formation rates may have occurred $\sim 10^7$ yr ago which has since halted.

It is notable that the orbital time period for a typical molecular cloud at a radius of 1 pc is 10^5 years providing ample opportunity for interactions with other clouds, or with the accretion disk surrounding the central black hole [425]. Alternatively, this could be taken as possible evidence of intense supernovae or Sgr A* activity several million years ago in which shocked molecular clouds became highly compressed, initiating star-formation. Supernovae bursts have also been proposed as a driver of the Fermi bubbles on Gyr timescales [39] and as a mechanism to explain the extremely hot plasma temperatures in the Galactic center where gas in excess of up to 10^8 K are observed, hotter than the Galactic escape energy, implying extraordinary energy injection event(s) with total energy 10^{53} erg and a lifetime of order 10^5 yr in order to remain contained near the Galactic center [290]. Such extreme events have comparable timescales and energetics to produce the scenarios explored earlier.

[16]For a recent review of massive star formation in the Galactic center, see Ref. [424]

Another possibility which has been previously considered is the injection of protons directly from the central black hole [426, 427, 428]. Our morphological analysis of Section 8.2.2 is substantially blind to the spectrum over the very narrow energy range under consideration. Spectrally, the situation is more difficult as such low-energy cutoffs in the proton spectrum do not seem typical of active galaxies[17]. It is possible that a yet unknown mechanism is responsible for producing a cutoff proton spectrum from Sgr A*. Such a scenario was in fact considered in Ref. [429]. In this case, the black hole is taken to be in a quiescent state with a very hard proton spectrum $\Gamma = 1$ exponentially cut off at 5 GeV. Secondary electrons produced in the hadronic interactions are of low enough energy to preserve their spectral shape and emit very hard infrared and millimeter synchrotron spectra, matching radio observations of Sgr. A*. In such a scenario, the soft protons could diffuse to large radii while the hard synchrotron emission would be confined to the confined to the ultra high magnetic fields in the immediate vicinity of the central black hole.

A very recent result [398] examined the compatibility of radio and GeV/TeV γ-ray observations with predictions from two models of starburst galaxies based on the interactions of cosmic-rays (of supernova origin) in the Central Molecular Zone. Particularly careful attention was paid to the relevant astrophysical parameters, which are fully consistent with what we employed here. For each model, the average magnetic field strength, convective wind speed, ionized gas density, and free electron absorption

[17] Although many AGN spectra do have breaks in the γ-ray spectrum near 5 GeV, this results from absorption in the so-called 'broad-line region' within a few hundred Schwarzschild radii of the central black hole and does not provide a viable mechanism for *extended* emission peaked in the GeV range.

fraction were allowed to vary in order to find optimized fits to data. The results strongly favor ion densities between 50 and 100 cm^{-3} and magnetic fields between 100 and 350 μG throughout the *entire* ambient CMZ cloud. While radio and TeV observations are well fit, a GeV excess still persists. The addition of additional populations of either protons or electrons is then considered. In the case of protons, a soft spectral index $\Gamma \approx 3.1$ and a supernova rate enhanced by a factor ~ 100 are found to be consistent, but are dismissed from further analysis based on the required SNe rate. For electrons, the energetics are more compatible, but the spectral indices predicted for radio and γ-rays are found to be inconsistent with observations. We note that in our analysis, this is precisely the proton spectral index we predict above a ~ 10 GeV and that the required SNe rate is substantially reduced due to our much harder $\Gamma = 2$ low-energy spectrum (which also matches the GeV excess in much greater detail than what considered in Ref. [398]). We find it remarkable that a completely independent analysis of the conditions required to fit starburst models to observations of the CMZ can naturally motivate an SNR explanation for the GCE at such a detailed level.

To summarize, in this section we have presented observational and theoretical evidence for spectral breaks in the cosmic-ray spectrum when protons undergo diffusive shock acceleration by supernovae remnants which are inside or strongly interacting with partially-ionized molecular cloud complexes. This ion-neutral damping mechanism then predicts a break in the power-law index Γ of precisely $\Delta\Gamma = 1$ occurring at an energy parametrized by the local magnetic fields, ion/neutral number densities, and the temperature of the ionized precursor. We then discussed the conditions in the Galactic

center environment needed to produce plausible break energies which were found to be of the correct order to explain the GCE if magnetic fields in the acceleration region are of approximately mG strength. Allowing the spectral index and break energy to float, we presented confidence contours for our fit to the Galactic center excess and showed that the preferred parameter space is spectrally compatible with an interpretation in terms of protons originating from GC SNR. Next, the energetics required to match the GCE were calculated, finding that each impulsive event requires tens to hundreds of supernovae (total energy 10^{52} erg) to occur on timescales somewhat smaller than the age of the outburst, or that quasi-continuous sources inject protons at a rate of order 10^{38} erg/s. Finally, we discussed evidence for sporadic increases in star-formation and supernovae rates in the Galactic center on the timescales relevant explain the extension of the GCE in terms of cosmic-ray diffusion and subsequent γ-rays of hadronic origin. Very large uncertainties plague each step of such an analysis and estimate. Nonetheless, the combination of spectral compatibility along with reasonable energetics and a plausible Galactic history provide a crucial background to any analysis of $\sim$GeV γ-ray data at the Galactic center.

8.2.5 Discussion of the Hadronic Burst Scenario

We presented a case for high-energy cosmic-ray protons injected in the Galactic center region as a plausible explanation to the reported Galactic center γ-ray excess over the expected diffuse background. Our study focused on whether such an explanation meets the required (i) morphology, (ii) spectrum and (iii) energetics.

We demonstrated that cosmic rays injected on the order of a mega-year ago explain the observed spherical symmetry reported from the "inner Galaxy" analysis of Ref. [43], while a more recent (on the order of a few kilo-years old) episode would possess the same morphology obtained for the innermost portions of the Galaxy in the "Galactic center" analysis of Ref. [43]

We showed that the γ-ray spectrum predicted by cosmic-ray proton energy distributions responsible for the emission observed from supernova remnants (such as broken power laws with specific spectral indexes, and exponentially suppressed power laws) provide excellent fits to the observed Galactic center excess. We pointed out that the preferred range for the break of the power law and for the spectral indexes inferred from the observed excess fall squarely in the ranges inferred from observations of supernova remnants, as well as in the general range expected from theory considerations. We also pointed out the importance of systematic effects in spectral reconstruction due to hadronic cross sections impacting the predictions for the γ-ray spectrum from inelastic proton-proton collisions.

Finally, we inspected the time-scales, spectrum and energetics we invoked to reproduce the morphology and spectrum of the Galactic center excess in the context of one or more additional populations of cosmic-ray protons in the region. We demonstrated that the existence of such populations is motivated by a variety of observational and theoretical reasons, which we reviewed in detail.

To conclude this Section, we gave proof of existence of a well-motivated alternative to dark matter annihilation or milli-second pulsars as an explanation to the reported

Galactic center γ-ray excess. Our results indicate that conclusively claiming a signal of New Physics from γ-ray observations of the inner regions of the Galaxy must contend with a variety of additional astrophysical processes. In particular, we highlighted that one or more previously unaccounted-for populations of cosmic-ray protons in the Galactic center could potentially produce a γ-ray emission with a spectrum, morphology and intensity closely resembling those of the Galactic center γ-ray excess.

8.3 Leptonic Cosmic Ray Bursts

In addition to the steady state and hadronic burst scenarios discussed in the previous two sections, two groups have examined the possibility of the GCE originiating from purely leptonic outbursts of cosmic-rays at the Galactic center. Such models are well motivated for two reasons: (i) the additional ICS emission is much more spherically symmetric since the ISRF is diffuse and more uniform (or at least relatively spherical) near the Galactic center compared to a more planar distribution of gas (excepting the ionized component); (ii) leptonic bursts are well motivated from central AGN jets, and activity from the central black hole of the Milky Way may provide a similar accelerator. These models were first explored analytically in Ref. [393], and later were explored numerically using Dragon simulations in Ref. [47]. We briefly review the main findings of Ref. [47].

The essential premise is that one or more historical injections of cosmic-rays at the Galactic center could produce a signal which is compatible with the Galactic center excess. If this is leptonic, the uniformity of the ISRF scattering medium produces a

reasonably spherical halo of ICS emission which approximately traces the prjected distribution of electrons. Instantaneous bursts with ages upto 10^6 years. Analytic analysis showed that it is difficult to reproduce the bulk GCE properties such as uniformity of the spectrum and the radial profile due, in particular, to electron cooling which softens the spectrum at large radii, and steepens the radial profile at an energy dependent rate. In the case of Ref. [47], the numerical approach allows for the incorporation of reacceleration, convection, and of anisotropic diffusion.

Using the same 'inner-galaxy analysis' as our analysis above (described in Sec. 8.1), Ref. [47] explores a systematic scan over propagation parameters, using the Bayesian importance sampling code MultiNest and utilizing the full systematic covariance matrices from Ref. [391] in order to compute the likelihood function. The fit parameters include a spectral index of injected electrons, a cutoff energy, a diffusion coefficient D_0, and energy dependence δ, anisotropic diffusion in the vertical direction D_{zz}/D_{xx}, a variable Alfvén velocity, and a burst age. Each have linear flat prior except for anisotropic diffusion which is log-flat.

Models with 1 and 2 bursts are then considered. The parameters are then scanned to find the best fitting single and double outburst models. The single models are unable to fit the GCE well, while models with two outbursts, very high reacceleration (150 km/s compared with typical Galactic values of 35 km/s), and very hard injection spectra ($\alpha \sim 1$) are able to fit the excess well other than the innermost 2 degrees. The bursts would have occurred approximately 1 Myr and 100 kyr ago and possess differing high-energy cutoffs at 60 and 20 GeV respectively, which ensure that the older burst

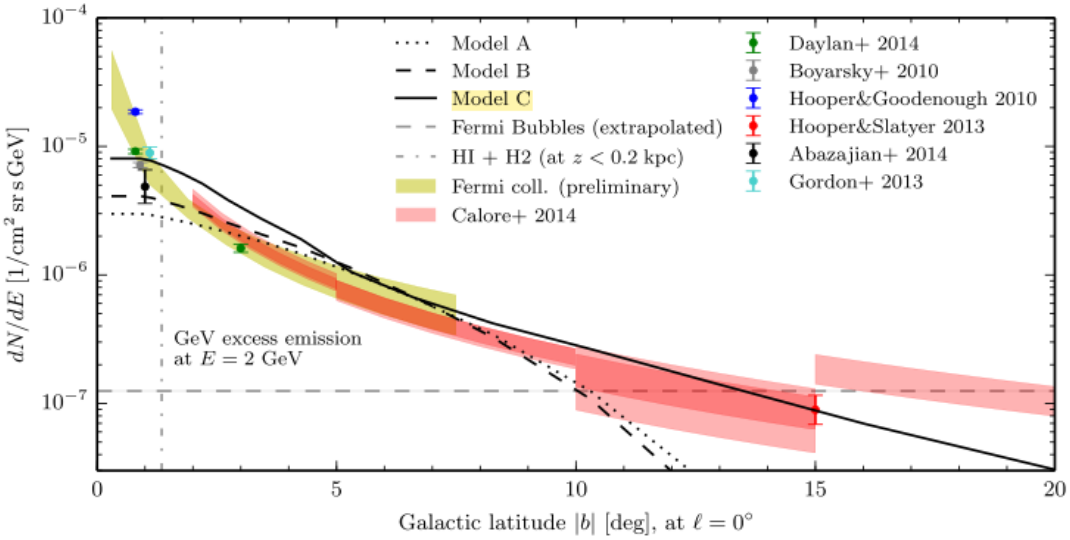

Figure 8.33: Angular profile of two leptonic burst model at 2 GeV from Ref. [47]

possesses a similar spectrum to the younger after cooling. The radial profile of this model is shown in Figure 8.33 along with several different groups measurement of the Galactic center excess.

In the Galactic center region, the two burst scenario cannot accommodate the observed flux. However, given the ISRF uncertainties in Sec. 7.4, and given evidence over the HESS region of a young, several kiloyear old high energy CR burst, this region is dominated by systematics, and poorly modeled at present. Thus, the leptonic burst scenarios as an explanation cannot be ruled out as a possibility, but the models require significant tuning of energetics, propagation parameters, injection, and burst timing, making them probably unlikely in isolation. However, it is very likely that some combination of MSP, steady state, and episodic injection comprises the real physical system at play in the Galactic center.

8.4 Millisecond Pulsars

An alternative, or more likely complementary, interpretation of the Galactic center excess is comprised of emission from a yet-undetected population of milli-second pulsars densely concentrated near the GC and throughout the Galactic bulge [379, 243, 392, 393, 394]. Intriguingly, recent studies have tentatively shown that the excess appears compatible with a collection of (unresolved) point sources rather than with a genuinely diffuse emission [396, 230], an observation which would favor e.g. a pulsar interpretations of the GC excess. There are both evidences against and for such an interpretation, which are summarized below, though the primary motivation for these models is the remarkable (or unremarkable if from MSPs) spectral similarity between the GCE and known millisecond pulsars (MSP).

Refs. [396, 230] both employ point source discrimination techniques in order to test for potential contributing populations in the direction of the Galactic center. Both reference make an important assumption as a staring point: *assume* a 3D radial distribution of the point sources which falls off like the steepened NFW profile ($r^{-2.5}$). Such a population might be plausibly generated by evolving massive stars in the very dense central stellar clusters which after going supernova, kick pulsars out with a velocity $v_{\rm kick} \approx 450$ km/s. Approximating the potential as spherical (a bad approximation for a region fed by a strong bar) this produces a profile which is roughly geometrically constrained to r^{-2} or steeper if the potential is strong. Because the GCE signal is constrained to be highly spherical, an interesting project would be to test the possible

sphericity of the pulsar distribution in realistic Galactic potentials.

Ref. [396] employs the non-Poissonian template fitting procedure discussed in Section 4.10.2, finding that such templates are preferred by $TS \approx 36$ compared with the purely diffuse template. This significance is statistical only and is small relative to changes in the Galactic diffuse model, which remains an untested effect. Similarly, Ref. [230] runs a wavelet kernel over the binned photon map and examines the distribution of source significances, determining (via Monte Carlo techniques) that an additional point source population is preferred at 10σ. This is somewhat more robust against the diffuse model, but is still likely to be strongly impacted by additional CR populations at the GC as discussed above in Sec 8.1. Two issues are missing from these studies which are (i) the extension of the analyses to more than a single energy bin – in order to study the collective spectral properties of these unresolved point sources – and (ii) to test the robustness against Galactic emission models.

It is also important to note the contrasting evidence against a pulsar interpretation of the GCE, which relies on known pulsars detected by Fermi [15, 395]. Both the luminosity distribution, maximum luminosity cutoff must be reconciled against future observations of gamma-ray pulsars, radio surveys, and X-ray observations of Low-mass X-ray binaries. The large flux of the GCE implies that several hundred to several thousand MSPs must contribute at current levels, while Fermi has observed very few at such high luminosities. The future is bright in studying these areas. Of crucial importance in any GCE interpretation is the incorporation of multi-wavelength data in both constraining pulsars, and in constraining CR populations in the region. Ultimately, both of

these astrophysical sources must exist at the Galactic center, our current models remain in their infancy, and much more must be learned about the astrophysics and history of the Galactic center region.

Analysis	Template	Fixed
Global-Local	π^0+ 1.25 Bremss. (HI+HII)	No
	π^0+ 1.25 Bremss. (H_2 Ring 7)	No
ROI – $\|b\| > 8^\circ$	π^0+ 1.25 Bremss. (H_2 Ring 1-6,8,9)	Yes
Pixel Type – Healpix Nside=256	Inverse Compton Scattering	No
Binning – 24 bins .3-500 GeV Ref.[36]	Isotropic (Ext. χ^2)	No
Events – P8 Clean Front+Back	Fermi Bubbles (Ext. χ^2)	No
Spectra Fixed to Galprop/3FGL	Point Sources (3FGL)	Yes (To 3FGL)
Global-Outer	π^0+ 1.25 Bremss. (HI+HII)	No
	π^0+ 1.25 Bremss. (H_2 Ring 1-6)	Yes
ROI – $\|l\| > 80^\circ, \|b\| < 8^\circ$	π^0+ 1.25 Bremss. (H_2 Ring 7)	Yes (From Local)
Pixel Type – Healpix Nside=256	π^0+ 1.25 Bremss. (H_2 Ring 8,9)	No
Binning – 24 bins .3-500 GeV Ref.[36]	Inverse Compton Scattering	No
Events – P8 Clean Front+Back	Isotropic	Yes (From Local)
Spectra Fixed to Galprop/3FGL	Point Sources (3FGL)	Yes (To 3FGL)
	π^0+ 1.25 Bremss. (HI+HII)	No
Global-Inner	π^0+ 1.25 Bremss. (H_2 Ring 1-6)	No
ROI – $\|l\| < 80^\circ, \|b\| < 8^\circ$	π^0+ 1.25 Bremss. (H_2 Ring 7)	Yes (From Local)
Pixel Type – Healpix Nside=256	π^0+ 1.25 Bremss. (H_2 Ring 8,9)	Yes (From Outer)
Binning – 24 bins .3-500 GeV Ref.[36]	Inverse Compton Scattering	No
Events – P8 Clean Front+Back	Isotropic	Yes (From Local)
Spectra Fixed to Galprop/3FGL	Fermi Bubbles	Yes (From Local)
	Point Sources (3FGL)	Yes (To 3FGL)
Inner Galaxy	π^0+ 1.25 Bremss.	No
ROI – $\|l\| < 20^\circ, 2^\circ < \|b\| < 20^\circ$	Inverse Compton Scattering	No
Pixel Type – Healpix Nside=256	Isotropic (Ext. χ^2)	No
Binning – 24 bins .3-500 GeV Ref.[36]	Fermi Bubbles (Ext. χ^2)	No
Events – P8 Clean Front+Back	Point Sources (3FGL)	Yes (To 3FGL)
Bin-by-Bin Spectral Fit	GCE $NFW_{\alpha=1.05}$	No
Galactic Center	π^0+ 1.25 Bremss.	No
ROI – $\|l\| < 7.5^\circ, \|b\| < 7.5^\circ$	Inverse Compton Scattering	No
Pixel Type – Cartesian $0.05^\circ \times 0.05^\circ$	Isotropic	No
Binning – 0.119-300 GeV 34 Log-Spaced	Fermi Bubbles	No
Events – P8 Clean Front	Point Sources (3FGL)	No
Bin-by-Bin Spectral Fit	GCE $NFW_{\alpha=1.05}$	No

Table 8.3: Summary of γ-ray analyses used in this study.

Name	Type	Age	$R_{\rm diff}(2\ {\rm GeV})$	
Im1	Impulse	.5 Kyr	18 pc	0.12°
Im2	Impulse	2.5 Kyr	40 pc	0.28°
Im3	Impulse	19 Kyr	110 pc	0.76°
Im4	Impulse	100 Kyr	250 pc	1.7°
Im5	Impulse	2 Myr	1.13 Kpc	7.8°
C1	Continuous	7.5 Myr	2.19 pc	15°
C2	Continuous	$\gtrsim 1$ Gyr	∞	∞

Table 8.4: Properties of a few benchmark emission sources.

Chapter 9

The Fermi 130 GeV Gamma-Ray Line

The launch of the Fermi Large Area Telescope (LAT) in 2008 has allowed for a greatly expanded view of the γ-ray sky, including a significantly enhanced energy and angular resolution, compared to previous missions [430]. These characteristics have allowed, in particular, for a thorough investigation of the extremely dense population of high-energy γ-ray sources in the Galactic center (GC) region [431]. The GC region is known to host such diverse γ-ray sources as supernova remnants [432], highly ionized gas [433], dense molecular clouds [434], massive O/B stars [435], both young and recycled pulsar populations [436], as well as being the densest region of dark matter in the Galaxy [437]. Notably, no other location in the sky is expected to provide a signal from dark matter annihilation which is as bright as the GC (for a recent general review of gamma-ray searches for signals from dark matter annihilation see Ref. [438]). While this makes the GC region an extremely interesting location for a multitude of scientific studies, it also means that additional information, such as characteristic spectra for each

source class, must be carefully considered in order to separate the desired signal from the bright background.

Recently, [125] and [439] found indications for a unique spectral signature in observations of the region surrounding the GC, which is consistent with dark matter annihilation. Specifically, in sky regions optimized for large signal-to-noise ratios for various dark matter density profiles, they observed an excess of photons with an energy spectrum resembling a 130 GeV γ-ray line[1], smeared by the finite energy resolution of the Fermi-LAT telescope. The significance of this excess was found to be 3.2σ globally [439] – enough to make the feature interesting on statistical grounds. The feature is strongest when using regions of interest that have been optimized for dark matter density distributions following: (1) a Navarro-Frenk-White (NFW) profile [89], (2) an Einasto profile [440], and (3) a generalized NFW profile, with a radial slope governing the dark matter density profile ($r^{-\alpha}$) set to $\alpha = 1.15$, similar to what could result from adiabatic contraction [441, 442]. The reported feature is much weaker for profiles where the dark matter density is cored near the GC.

A monochromatic γ-ray line has been long considered the "Holy Grail" for dark matter indirect detection, given the difficulty of producing a high-energy monochromatic signal with ordinary astrophysical processes. Thus, this observation prompted a number of follow-ups. [443] noted that the observation of a monochromatic γ-ray signal could be qualitatively mimicked by an additional power-law component which breaks strongly

[1]Note that upon the release of Pass 8 Fermi data, the line energy was shifted to 135 GeV after recalibration of the calorimeter. This analysis uses Pass 7 data, and we therefore work under the premise of the line being at 130 GeV throughout.

at an energy of 130 GeV, and posited the Fermi bubbles [444] as a possible source for this excess (although rather strong breaks are required to fit the data, see Ref. [438]). Most notably, [445] localized the emission to within approximately 5° of the GC, finding a 6.5σ (5.0σ after including a trials factor) preference for a line signal following an off-center Einasto profile compared to the assumption of a simple power-law background (see also [446]). This finding disputes the implication of the Fermi bubbles as a source for the excess, as the latter are observed to extend over a much larger emission region. The off-centered nature of the dark matter profile is at the moment only marginally statistically significant [447, 448]. However, if confirmed, an off-center peak would pose a challenge to traditional models of the Galactic dark matter density which assume the largest dark matter density to fall on top of the peak of the baryonic mass density[2]. However, a recent analysis by [449] found that the peak in the dark matter density may, in fact, be displaced by hundreds of parsecs from the dynamical center of the Galaxy - although this scenario might be incompatible with the assumption of a cusped profile.

More data are needed to clarify whether the 130 GeV feature in the data persists with larger statistics or if it is only a statistical fluke. Since the observation of a γ-ray line is extremely sensitive to inaccuracies in the energy-reconstruction of γ-rays observed by Fermi-LAT, a great deal of interest has also focused on searching for possible instrumental abnormalities affecting the photons belonging to the γ-ray line. The most notable characteristic of any such instrumental effect would be the observation of line activity either across the entire sky, or across a certain region of instrumental

[2]Which we assume, here, to be identical to the position of Sgr A*, and call the GC throughout this Chapter.

phase space. Interestingly, some early results found an excess of 130 GeV events in observations of the Earth-limb [445, 450, 451]. This is troubling, as the vast majority of limb photons are known to result from the di-photon π^0 decay spectrum created as cosmic-ray protons interact with the upper layers of the Earth's atmosphere. There is no conceivable model in which dark matter annihilation could create a γ-ray line in this region [445]. However, this line activity was not detected along the Galactic plane, which provides significantly more photons than the GC, and inhabits similar regions of instrumental phase space. A comprehensive study by [450] did not find any significant evidence for systematic features in the energy reconstruction of the Fermi-LAT, which would be able to artificially produce a γ-ray line (see however Refs. [452, 453, 454]).

Follow up analyses by the Fermi-LAT team are currently ongoing, but have revealed two noteworthy results. At the time of the initial discovery of the γ-ray line, efforts were already ongoing to improve the energy normalization of the Fermi-LAT data, accounting for a decrease in the calculated energy of γ-rays over time due to radiation damage to the calorimeter. This effect linearly increased the reconstructed energy of high energy photons, moving the line signal from 130 GeV up to approximately 135 GeV. However, this reprocessing did not greatly affect any other signature of the posited line analysis. We note that throughout the rest of this chapter, we refer to the "130 GeV line", as we are using a version of the Fermi-LAT data which has not been reprocessed. However, all results shown here are very nearly applicable to an analysis of the 135 GeV line observed in the reprocessed data.

Additionally, the Fermi-LAT analysis did uncover one troubling aspect of the

posited γ-ray line. Employing a parameter CTBBestEnergyProb (which is not publicly available), they investigated the confidence they had in the energy reconstruction of each photon belonging to the γ-ray line. In the case where a true γ-ray line feature is present in the data, this should increase the statistical significance of the observation, as the proceedure adds additional statistical weight to the line photons which are most likely to have a correctly measured energy. However, when this analysis was applied to the observed photon data, the statistical significance of the line feature was found to decrease moderately. This signals that the line feature has photons with a somewhat poorer energy resolution than would generally be expected[455]. However, further inquiry of these systematic issues is required, as none of the systematics can clearly account for the entire statistical strength of the line feature.

If interpreted as a signal of particle dark matter annihilation or decay, the large observed intensity of the 130 GeV γ-ray line (along with strong constraints on the total continuum emission from additional hadronic states [456]) has proved a difficult, though by no means intractable, particle physics problem. Numerous models have already been posited to "brighten" the γ-ray line [457, 458, 459, 460, 461, 462, 463, 464, 465, 466, 467, 468, 469, 470, 471, 472, 473, 474, 475, 476, 477, 478, 479, 480, 481, 482, 483, 484, 485, 486]. Summarizing the myriad particle physics details of these models lies beyond the scope of the present chapter.

Although often characterized as a "smoking gun" signature for the annihilation or decay of particle dark matter, tentative observations of the 130 GeV line have spurred the question of whether any traditional astrophysical mechanism might mimic a line

in the relevant energy range. [487] argued that the only plausible mechanism for the creation of an astrophysical γ-ray line is through inverse Compton scattering of ambient photons by a jet of nearly monoenergetic electrons and/or positrons, occurring in the deep Klein-Nishina regime. If the latter kinematic regime holds, the photon acquires nearly the entire energy of the incoming lepton, allowing for a nearly monoenergetic lepton spectrum to efficiently transfer into a sharply peaked γ-ray feature.

One possible class of astrophysical objects that possesses the potential to host the needed leptonic monochromatic "jet", as well as the ambient photons in the needed energy range (here, a few eV) is *cold ultrarelativistic pulsar* (PSR) *winds* [487]. It is important to note that this scenario presents a potential difficulty in explaining the observed spread of 130 GeV photons beyond a single point source, as different PSRs would be expected to exhibit γ-ray lines at different energies. One way to test this one astrophysical background is therefore to study whether the morphology of the observed 130 GeV photons can be reproduced with a small number of point sources or not. This is the key objective of the present study.

Several other approaches have tested the dark matter nature of the 130 GeV photons. For example, any dark matter interpretation of the 130 GeV line implies additional regions of interest for follow up searches, where the so-called J-factor (the line-of-sight integral of the dark matter density squared, smeared over the instrumental point-spread function) is expected to be largest. Most importantly, dwarf spheroidal galaxies and galaxy clusters have been singled out as promising regions to search for a dark matter signal. Observations of Milky Way dwarfs have not uncovered any evidence

of a 130 GeV signal [488]: this is not unexpected, as the estimated annihilation cross-section to $\gamma\gamma$ implied from GC observations predicts less than one photon to arrive from the population of dwarf spheroidal galaxies. Interestingly, [489] argued for an observation of a 130 GeV line in a population of nearby galaxy clusters. However, it should be noted that this signature is only significant when very large ROIs of $\sim 8^{\circ}$ are considered, which is much larger than the expected angular size of the galaxy clusters under investigation.

Using a similar method, [490] investigated the population of unassociated Fermi-LAT point sources – that is, point sources detected by the Fermi-LAT instrument which have not been identified at other wavelengths. They found a statistically significant detection for a double 130 GeV and 111 GeV line, with 14 unassociated sources showing evidence of a line photon. Furthermore, they found no significant detection of γ-ray line emission in the control sample of Fermi-LAT point sources that have already been associated with various astrophysical phenomena. This caused them to conclude that some portion of the unassociated point-source sample may contain previously unknown dark matter substructures. However, [491] argue against this conclusion, noting that each unassociated source is identified primarily based on its continuum emission between energies of 100 MeV-10 GeV, rather than based on the detection of a single line photon. The intensity and spectrum of this continuum emission can then be compared to the signal from dark matter annihilation to any final state producing a γ-ray continuum, and is expected in order to produce the thermal relic abundance of dark matter. They find that for at least 12 of the 14 indicated unassociated point sources, the continuum emission is not compatible with any dark matter annihilation pathway. Furthermore,

they argue that the latitude distribution of the identified sources is not consistent with that expected from any model of dark matter subhalo formation. A second analysis by [492] argued that while these 14 sources remain unidentified, at least 12 of the sources (not identical to those from [491]) are spectrally strongly consistent with AGNs.

In addition to considering the energy signature of the 130 GeV line, understanding the morphology of the photons belonging to the source class producing the observed feature will be key to elucidate the physics behind the line phenomenon. Notably, the point-spread function of front-converting events at energies near 100 GeV approaches 0.1° [430], which is significantly smaller than the $\sim 5^\circ$ region of interest implicated by [445], allowing for the actual morphology of the line emission to be closely mirrored by Fermi-LAT observations. To first order, observations indicating a morphology consistent with widely accepted dark matter density profiles would provide additional evidence for a dark matter interpretation (the data indeed points to that direction, see e.g. Fig. 3 of Ref. [438]), while measurements consistent with either a population of point sources, or a significantly flattened profile may point to other astrophysical or instrumental interpretations.

In this Chapter, we examine the morphology of photons belonging to the γ-ray line more closely, analyzing with a sound statistical approach the distribution of the arrival direction of photons by employing a clustering algorithm to pinpoint the correlation between the arrival directions of photons putatively belonging to the line feature. We then compare these results against simulated models where the line is produced by dark matter annihilation or by an astrophysical process associated with

a few point sources (for example a handful of PSRs). The key result of our study is that *current data disfavor a scenario where the line photons stem from 4 or fewer point sources*. Given how unlikely it is that 4 or more pulsars produce a gamma-ray line at exactly the same energy (within the LAT energy resolution), our study disfavors the PSR scenario over a truly diffuse and un-clustered origin for the photons.

In Section 9.1 we describe the data employed in our observations of the γ-ray line feature, the specifics of the algorithms used to determine the photon morphology, our models for both the annihilation of dark matter and emission from PSRs, and the diffuse background in the region. In Section 9.2 we present the results of our study both for current Fermi observations, and for projections for upcoming observations of the GC with the Atmospheric Cherenkov Telescope (ACT) H.E.S.S.-II. Finally, in Section 9.3 we discuss the interpretation of the results, and present our conclusions.

9.1 Source Models

9.1.1 Dark Matter and Pulsars Models

In order to establish a quantitative measure for the clustering properties of γ-rays due to either dark matter or one or more point-sources in the GC region, we produce Monte Carlo simulations of the expected positions of photons stemming from each model.

In the case of PSRs, we examine models featuring between 1 and 6 point sources to explain the excess 130 GeV emission. We randomly pick the distribution of each point

source following a surface density distribution $\rho(\mathrm{r}) \propto \mathrm{r}^{-1.2}$, as motivated by the observed density distribution of O/B stars in the inner Galaxy [493] and we produce an excess number of photons which are distributed randomly (assuming equal brightness) between the simulated pulsars.

In the case of dark matter annihilation, we predict the annihilation signal to follow the integral over the line of sight of the square of the dark matter density. We choose two independent dark matter density profiles motivated by models of dark matter structure formation. We first examine a generalized Navarro-Frenk-White [89] profile, with a density profile

$$\rho(r) \propto \left(\frac{r}{r_s}\right)^{-\alpha} \left(1 + \frac{r}{r_s}\right)^{-3+\alpha} . \tag{9.1}$$

In our standard analysis we choose $\alpha = 1$ and $\mathrm{r}_s = 22$ kpc fitting the best numerical results from the Aquarius simulation [440]. In order to evaluate the effect of changing the dark matter density profile, we also consider an Einasto profile with a density distribution [440]:

$$\rho(r) \propto \exp\left[-\frac{2}{\alpha}\left(\left(\frac{r}{r_s}\right)^{-\alpha} - 1\right)\right], \tag{9.2}$$

assuming, here, that $\alpha = 0.17$ [440]. In each case, we assume that the annihilation rate is proportional to $\rho^2(\mathrm{r})$, and then integrate over the line of sight from the solar position $\mathrm{R}_\odot = 8.3$ kpc [494] in order to generate the dark matter morphology that would be observed by the Fermi-LAT.

We additionally consider two alternative profiles. First, the case of decaying

dark matter following the NFW profile given in Eq. (9.1), with the decay rate now proportional to ρ(r). Second, the case of isotropic emission, i.e. a uniform surface profile. Since the clustering properties of the source are highly dependent on the number of observed photons, we calculate for Fermi-LAT (H.E.S.S.-II), 10^5 (2000) realizations of 48 (5000) photons following the distribution assumed in each of these cases over a 10° (4°) square window. For H.E.S.S.-II observations, we estimate the number of photons from a relatively short exposure time, on the order of 6 hours, using an effective area given for the H.E.S.S.-II telescope with the flux in the 130 GeV energy range measured by the Fermi-LAT.

In each case, we must also consider the smearing of target photons based on the point-spread function of the Fermi-LAT telescope. In order to accomplish this accurately for observations at the GC, we employ the Fermi tools to estimate the point-spread function for photons entering both the front and back of the instrument at different θ-angles. Specifically, we employ the *gtpsf* tool developed by the Fermi-LAT collaboration in order to calculate the effective PSF given the total exposure of the GC region from all locations in the Fermi-LAT instrumental phase space (i.e. how much was the GC viewed from different spacecraft orientations). For the selected observation period, the average (68%, 95%) containment radius over the observation is (0.124°,0.529°) for front-converting events ($\sim$ 56% of exposure area) and (0.258°,0.907°) for rear converting events ($\sim$ 44% of exposure area). The resulting PSF for each photon (signal and background) is randomly chosen based on this weighted average of instrument coordinates and the incoming photon is smeared based on the given PSF. In the case of Atmospheric

Cherenkov Telescope (ACT) simulations, the PSF depends somewhat sensitively on the angle of incidence of the incoming photons. Following Aharonian *et al* [495] we approximate the H.E.S.S. point-spread function as an energy independent, two-component Gaussian with the probability density of an event smearing to radius θ given by,

$$P(\theta) = A\theta \left[\exp\left(-\frac{\theta^2}{2\sigma_1}\right) + A_{rel} \exp\left(-\frac{\theta^2}{2\sigma_2}\right) \right] , \tag{9.3}$$

where $\sigma_1 = 0.046$, $\sigma_2 = 0.12$, and $A_{rel} = 0.15$ and an overall normalization A.

9.1.2 Background Models

In order to characterize the morphology of the expected diffuse background we follow the detailed PASS 7 Galactic Diffuse Model, which contains both spectral and morphological information generated by observations of both HI and CO line surveys, which constrain the distribution of interstellar gas. The γ-ray morphology and spectrum are then generated by convolving these maps with the modeled cosmic-ray densities utilizing the Galprop code [413], and calculating the expected γ-ray emission from processes including π^0-decay, bremsstrahlung emission, and inverse-Compton scattering. Utilizing these simulations, we then generate a Monte Carlo population of background γ-rays following a morphology compatible with observations across the γ-ray spectrum.

In the case of the Fermi-LAT telescope, we assume zero cosmic-ray contamination, since we are considering only the GC region, which is very bright in γ-rays. Given the calculated intensity of the γ-ray line, we calculate an average of 12 signal, and 36 background photons between an energy of 120–140 GeV. In each simulation of the

Fermi-LAT data, we allow the strength of this signal to float using Poisson statistics, setting the mean intensity to be 12 signal photons. For Fermi-LAT observations we model a 10° square window around the GC.

In the case of ACT observations, we note that cosmic-ray contamination is a much larger issue, since hadronic showers dominate the data collected by these telescopes. Extrapolating the cosmic-ray and γ-ray signals from recent low-energy H.E.S.S. observations at 300 GeV [496] and using the best estimates for the H.E.S.S.-II instrumental characteristics [497], we find that 86% of the total background signal will stem from cosmic-ray backgrounds. Thus, for ACT observations we create a simulation composed of 4.35% signal photons, 13.15% diffuse background photons (following the Fermi PASS-7 Galactic diffuse model) and 82.5% isotropic background photons. As in the case of Fermi-LAT observations, we allow the total number of signal photons to float using Poisson statistics, and maintain a background which is 86% isotropic, and 14% diffuse. For H.E.S.S.-II observations we model a 4° square window around the GC, consistent with the smaller field of view of ACT instruments.

The background model described above is also used to estimate the average background count N_b during the computation of the cluster significances. N_b is calculated by integrating the background template, normalized to the correct background count over the 95% containment area of the cluster members (100% containment in cases with fewer than 20 cluster members). This allows for a statistical measure which traces the local morphology of the background and is thus minimally dependent on its anisotropic structure, reducing the significance of 'hot-spots' in the background which may be falsely

identified as true clusters.

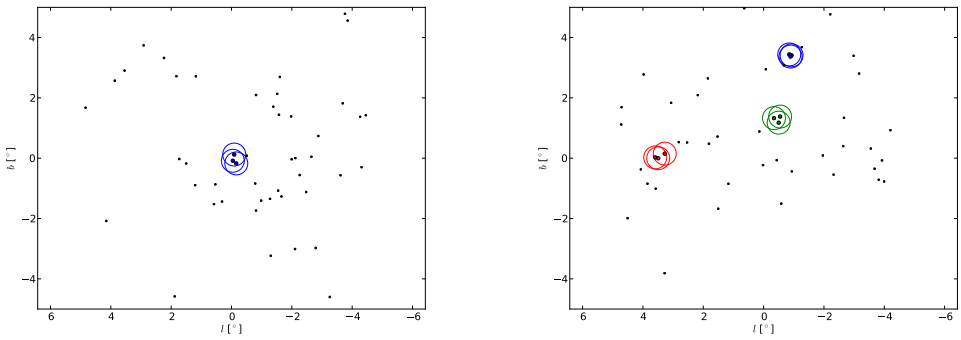

Figure 9.1: Event map of Fermi photons between 120-140 GeV (left) and a sample 3 pulsar Monte Carlo simulation (right) showing in colored circles the DBSCAN $\epsilon-$neighborhoods for core points in each detected cluster.

9.1.3 Clustering Algorithm

In order to classify the spatial morphology of photons in a statistically robust way, we employ the *Density Based Spatial Clustering of Applications with Noise* (DBSCAN) algorithm [228], which was described in Sec. 4.4. This algorithm is capable of both distinguishing cluster points from noise and constraining the maximum connectivity size based on the instrumental point-spread function.

To exemplify the use of the DBSCAN algorithm, Figure 9.1 shows the DBSCAN analysis of the Fermi-LAT photon events measured with an energy between 120 – 140 GeV (left), and of a simulated model containing two point sources near the galactic center (right). In each case, we show the DBSCAN ϵ-neighborhoods for each core point of each detected cluster. For the Fermi results, DBSCAN finds only one cluster (interestingly centered on the actual Galactic center location!), while in the 3 pulsar simulation

case, the algorithm correctly identifies three clusters, at the positions corresponding to where the pulsar photons were generated. The following discussion explains in detail the procedure we employ to apply DBSCAN to γ-ray data.

To quantitatively compare our models against *Fermi* data, we follow [229] and employ the likelihood ratio proposed by [498] to calculate the cluster significance, s, in terms of the number of cluster photons N_s and background photons N_b:

$$s = \sqrt{2\left(N_s \ln\left[\frac{2N_s}{N_s + N_b}\right] + N_b \ln\left[\frac{2N_b}{N_s + N_b}\right]\right)}\,. \tag{9.4}$$

Here, N_b represents the expected background counts, determined by integrating a diffuse background model (discussed in Subsection 9.1.2), while N_s is based on the total photon count contained in the cluster; we effectively adopt $\alpha = 1$ in the notation of Ref. [498]. According to Ref. [498], as long as N_s and N_b are not too sparse, one can equate a cluster with significance s to an "s-standard deviation observation". Thus a cluster significance $s = 2$ implies the cluster is a 2σ fluctuation above the mean background as computed in Subsection 9.1.2. We will use this nomenclature in our analysis. With the individual cluster significance in hand, we now define the *"global" significance* S as the mean significance of each detected cluster weighted by the number of photons in that cluster. We then optimize the choices of the DBSCAN parameters ϵ and $N_{\rm min}$ for ACT simulations by maximizing the global significance for the clustering results from our pulsar simulations. Finally we explain why this optimization procedure does not work with the limited Fermi photon count at 130 GeV and choose appropriate DBSCAN parameters based on the Fermi spatial point spread function.

The value of ϵ must be large enough that true cluster elements are not excluded, but small enough that noise is not included. The variable ϵ, as a result, is closely tied to the physical size of the instrumental PSF. One must additionally choose a value $\mathrm{N_{min}}$ large enough such that the background does not easily fluctuate above this number, but low enough that one has a high efficiency of finding real clusters. To this end, we use simulations of 1, 2, and 3 pulsar models for Fermi simulations, and 2, 4, and 6 pulsar models for ACT observations to determine a region of $(\epsilon, N_{\mathrm{min}})$ parameter space which simultaneously optimizes the significance and detection efficiency. Displayed in the top row of Figure 9.2 is the global clustering significance (shown in filled contours) and number of detected clusters with $s > 1.29$ (inset, labeled contours) for 48 photon Fermi simulations of 1, 2, and 3 pulsars as a function of the DBSCAN parameters ϵ and N_{min}. In the bottom row, we again plot the global clustering significance and number of detected clusters with $s > 2$ for 5000 photon ACT simulations with columns from left to right corresponding to 2, 4, and 6 pulsar models. We note that we apply a firm cut that N_{min} must be at least 3, as this represents the lowest possible non-trivial clustering which may be analyzed by the DBSCAN algorithm.

Inspection of the all three columns for both Fermi and ACT simulations reveals that the clustering algorithm detects clusters at high significance over large coincident regions of DBSCAN parameter space. In the case of ACT observations where the clusters are better differentiated from the background, we also see that these regions also detect the correct number of clusters until the number of pulsars becomes too large to reliably detect all true clusters. This indicates that the results are robust for most reasonable

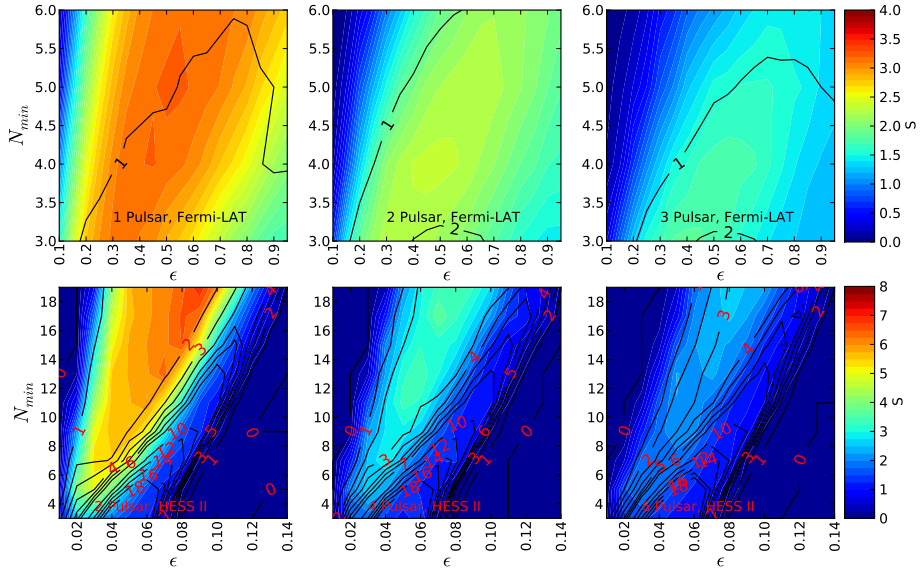

Figure 9.2: *Global cluster significance* S (filled colored contours) and *total number of clusters* N_{clusters} for Fermi (ACT) simulations (above threshold $s > 1.29$ ($s > 2.0$); labeled contours) as a function of the DBSCAN search radius ϵ and core-point threshold N_{min}. The top row corresponds to Fermi simulations of 1 (left),2 (center), and 3 (right) pulsar models while the bottom row is for ACT observations of 2 (left), 4 (center), and 6 (right) pulsar models. Results are relatively insensitive to large coincident regions in the scan parameter space for left and center columns, while the dependence on N_{min} increases as the number of photons per pulsar approaches the background rate. Fermi simulation DBSCAN parameters are chosen to be $\epsilon = 0.35$, $N_{\text{min}} = 3$ while ACT simulation DBSCAN parameters are chosen to be $\epsilon = 0.05$, $N_{\text{min}} = 8$ as a compromise between the cluster detection efficiency and the significance over background.

choices of scan parameters while in the case of 6 pulsars, the number of detected clusters is somewhat more sensitive to parameter choices. For these ACT simulations, we see that choosing N_{min} too small or ϵ too large can lead to the identification of extra (false) clusters which lowers the overall significance.

We choose our scan parameters based on the 6 pulsar simulations (bottom right) which have the lowest signal to noise ratio among the models we consider here.

These considerations motivate a choice of $\epsilon = 0.35^\circ$, $N_{\rm min} = 3$ for Fermi simulations and $\epsilon = 0.05^\circ$, $N_{\rm min} = 8$ for ACT projections as a balance between preserving significance and detecting most of the clusters at $s > 2$. We note that detailed studies on the behavior of DBSCAN settings applied to Fermi-LAT data at lower energies have found qualitatively comparable optimization regions for DBSCAN parameters [229].

In summary, for ACT observations we expect ∼5000 photons for a 6h exposure, and use our significance measure balanced against the number of detected clusters to optimize the DBSCAN parameters. We find $\epsilon = 0.05^\circ$ and $\mathrm{N_{min}} = 8$. For Fermi observations, we choose $\epsilon = 0.35^\circ$ and $\mathrm{N_{min}} = 3$, which represents the lowest level of non-trivial clustering. We note that there are only 48 photons in our sample, and thus we do not expect to be able to identify more than a few clusters corresponding to point sources with our analysis technique.

9.1.4 Photon Selection for a Gamma-Ray Analysis

In order to analyze the population of photons stemming from the putative γ-ray line emission, we must make a photon selection which isolates the line photons from those correlating to background events. We follow here the same photon selection employed in Ref. [499], which provides the location of observed Fermi-LAT photons in three energy bands, 70-110 GeV, 120-140 GeV, and 150-300 GeV over a 10° square window centered on the GC. Since the Fermi-LAT energy resolution is approximately 10% at 130 GeV, we assume photons in the 120-140 GeV band to encompass the photons related to the γ-ray line observation, while photons in the low and high energy bands correspond to

background events not associated with the γ-ray line observation. Below, a power-law fit to the sidebands will be used to fix the background rate in our 120-140 GeV simulations while the remainder of the photon excess will make up the signal. We note that there is some evidence for a second line at energies of around 111 GeV [445], however the weak significance of that feature makes its impact on the population of 70-110 GeV γ-rays negligible.

In comparing the photon morphology from the line region against the "sideband" photons, we assume that the background morphology remains approximately invariant throughout the 70-300 GeV energy range. This assumption is warranted in light of observations indicating that the primary component of diffuse emission through this region stems from π^0-emission tracing the Galactic gas [500, 456]. While some unresolved point-sources may also be present, it is unlikely that any given source contributes multiple photons to the observed high-energy γ-ray emission, making the spectral features of each individual source irrelevant.

Before proceeding with the description of the clustering algorithm we employ in this analysis, we describe in the following sections the simulated data sets we use to validate our analysis. Section 9.1.1 details the simulated line events from both dark matter annihilation scenarios with different dark matter density profiles, and scenarios with one or more point sources. Section 9.1.2 details the simulated background events. Finally, sec. 9.1.3 describes the clustering algorithm we employ in the present study.

9.2 Clustering Analysis Results

In order to compare our models of the expected 130 GeV line signal produced by both dark matter and pulsars, we first calculate the clustering properties of the actual Fermi dataset in the energy range of 120-140 GeV using the DBSCAN algorithm. We find only one detected cluster with a significance of $s = 1.29$, an angular scale of 0.22° (defined as the mean pairwise distance of each pair of cluster members), and 3 member photons (see Fig. 9.1, left).

We first define the parameters useful for differentiating different emission classes and then compare to current Fermi data and projections for upcoming H.E.S.S.-II observations. In addition to the global significance, S, we define three quantities in the space of clusters with significance $s > 1.29$ for Fermi and $s > 2$ for ACT observations. The quantities we employ are chosen to best capture the results of each simulation based on the output of DBSCAN, and provide useful information on the clustering properties of each source model. Specifically, we use:

1. the *mean clustering radius*, $r_{\rm cluster}$, defined as the average of the mean pairwise distance (angular scale) of each cluster above threshold, weighted by the cluster's significance;

2. $N_{\rm clusters}$ defined as the *total number of clusters* detected above threshold with at least 3 (10) cluster members for Fermi (ACT), and

3. $N_{\rm members}$ defined as the *mean number of photons* of clusters above threshold, weighted by each cluster's significance. The significance weighting is used sim-

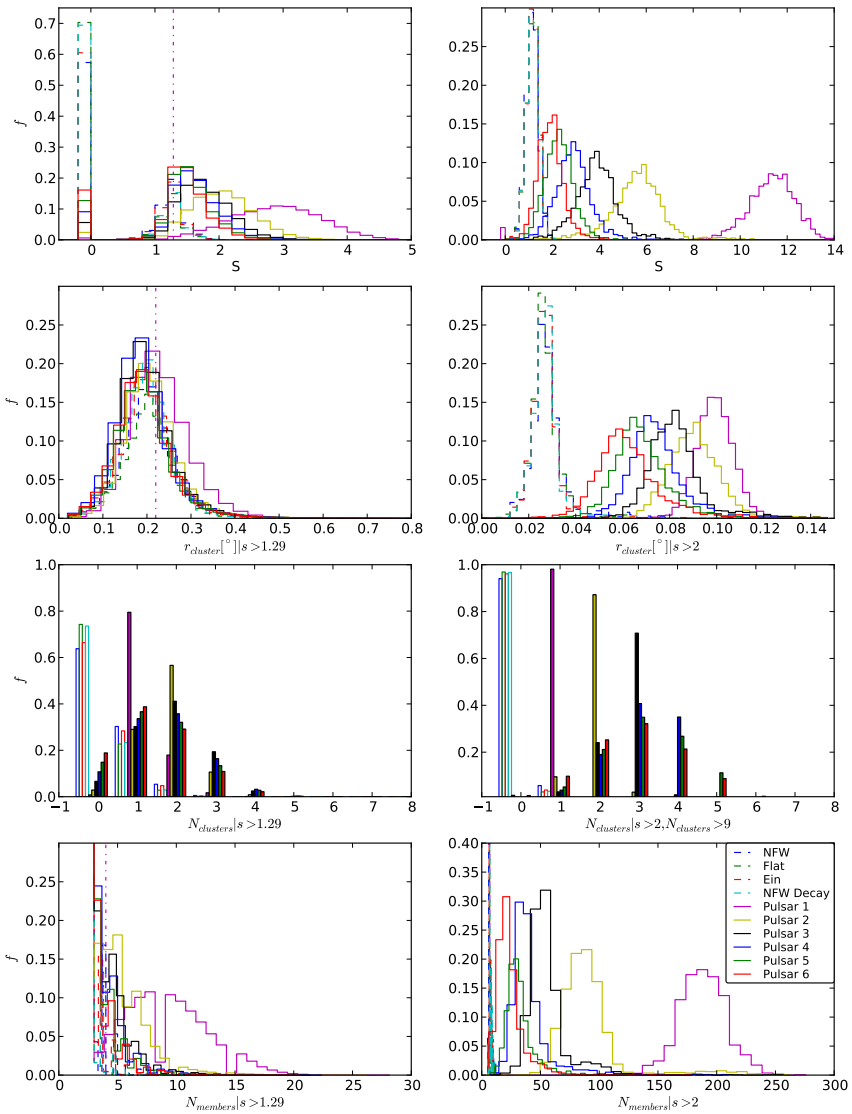

Figure 9.3: Models for the clustering properties expected from both Fermi-LAT (48 photons total, left) and H.E.S.S.-II (5000 photons total, right) observations of annihilating dark matter following a NFW profile (blue dashed), flat density profile (green dashed), Einasto profile (red dashed) and decaying dark matter following an NFW profile (cyan dashed), as well as models of emission from undetected groups of one (magenta solid), two (yellow), three (black), four (blue), five (green), and six (red) pulsars, compared to the clustering properties observed in the Fermi-LAT data binned from 120-140 GeV (magenta dot dash). The top row shows the distribution of global significance of detected clusters (S, top row). All other quantities are calculated in the subspace of clusters with significance $s > 1.29$ ($s > 2$) for Fermi (ACT) simulations. Shown is the distribution of *mean clustering radii* (2nd row), the distribution of the *total number of clusters* detected (3rd row), and the distribution of the average *number of member photons* in each cluster with $s > 2$ (bottom).

ply to suppress the influence of clusters which are likely background fluctuations.

In Figure 9.3 we show the results of the DBSCAN algorithm applied to both the Fermi data (vertical dashed-dotted line), compared to results from Monte Carlo simulations of dark matter and point source emission from pulsars for 48 photons (left; resembling Fermi-LAT observations) and 5000 photons (right; resembling ACT observations). The dashed lines correspond to diffuse dark matter annihilation models – NFW (blue dashed), Einasto (red dashed), NFW decay model (cyan dashed) and a flat distribution (green dashed). Pulsar models are represented by solid lines – 1 (magenta), 2 (yellow), 3 (black), 4 (blue), 5 (green), and 6 (red). Each histogram is normalized and if no clusters are found, the significance defaults to zero. We thus see that it is much less likely for diffuse models to produce clusters dense enough to be picked up by DBSCAN, indicating that our combination of ϵ and $N_{\min}$ are reasonably efficient at rejecting spurious background clusters, especially in the ACT case.

The *global cluster significance* S (top row of Figure 9.3) provides the strongest metric for differentiating point-source from diffuse emission. Diffuse models should possess virtually identical clustering properties as the extent of any true structure is much larger than the instrumental point spread function. Thus, diffuse sources should only occasionally produce low significance, loosely grouped clusters due to background fluctuations. One possible exception for dark matter models is the identification of a single point source at the GC where the dark matter annihilation rate can be very large. It is notable that the single cluster found in the Fermi data lies precisely on the galactic center. We see in the case of Fermi simulations (top left panel) that there is a fairly

sharp cutoff in the fraction of models with global significance $S \lesssim 1$. This lower bound is set by DBSCAN's minimum cluster detection requirements, as well as the location of the cluster with respect to the background template, which determines the number of background photons in that region. Because the cluster detected in the Fermi data is loose, we expect the single detected Fermi cluster to be close to the effective cutoff ($S = 1.29$ for the detected cluster).

The second row of Figure 9.3 shows the *mean clustering radius*. For ACT observations there is a clear division between the point source and smaller diffuse emission scales. However, the Fermi-LAT simulations do not offer any useful discrimination between models with such low photon counts. For point sources, this distribution is governed by the average value of the PSF and possesses an asymmetric tail at larger scales due to the inclusion of background photons and events whose true position is determined by the long PSF tails. For diffuse models, the distribution is governed dominantly by the ϵ DBSCAN parameter until the background density becomes dominant.

Displayed in the third row is the distribution of the *total number of clusters*, N_{clusters}, found with significance s > 1.29 (s > 2). In the case of ACT observations we also require clusters to have at least 10 core points to be included whereas we required only 3 for Fermi. We expect to be able to discern *at most* N_{sig}/N_{min} point sources if the signal photons happen to distribute themselves evenly between sources. Even in this case, these true clusters may still lie below the significance threshold. It is realistic to identify only 2-3 true clusters with 12 signal photons (48 total) if they in fact have point source progenitors. This is reflected here. For diffuse sources, only a fraction the

Model	$f^{\text{Fermi-LAT}}_{s>1.29}$	$f^{\text{Fermi-LAT}}_{s>1.29}$	$f^{\text{ACT}}_{s>2.0}$	$f^{\text{ACT}}_{s>2.0}$	$f^{\text{ACT}}_{s>2.0}$
	$n=1$	$n=2$	$n=1$	$n=2$	$n=3$
NFW	0.362	0.059	0.060	0.002	0.0
Einasto	0.335	0.052	0.039	0.001	0.0
NFW Decay	0.264	0.031	0.034	0.001	0.0
Flat	0.257	0.030	0.031	0.001	0.0
1 Pulsar	0.992	0.197	0.984	0.003	0.0
2 Pulsars	0.971	0.681	0.997	0.902	0.030
3 Pulsars	0.934	0.631	0.998	0.967	0.726
4 Pulsars	0.897	0.556	0.997	0.956	0.769
5 Pulsars	0.851	0.485	0.993	0.942	0.730
6 Pulsars	0.811	0.424	0.985	0.888	0.635

Table 9.1: The fraction of simulations with at least 1 cluster of significance $s > 1.29$ ($n = 1$ and $s = 1.29$, corresponding to the maximum n and s_i for clusters i found in Fermi-LAT data) for Fermi-LAT simulations (column 2), the of Fermi-LAT simulations with at least 2 clusters of significance $s > 1.29$ (column 3) and fraction of simulations with at least n clusters detected at significance $s > 2.0$ with at least 10 core points for ACT simulations (columns 4-6).

detected clusters pass the significance cut. As the number of events is increased, this significance cut could be increased to maintain a high acceptance/rejection ratio, though it is clear that for diffuse models, we typically obtain either zero clusters or one cluster per simulation with our current significance cuts, while still efficiently detecting several clusters in the case of pulsar models.

Finally, the fourth row contains the distribution of the *mean number of cluster*

members, N_{members}. For a random distribution of events between pulsars, we expect a Poissonian distribution with a mean of approximately $N_{sig}/N_{pulsars}$ (contributions from the background should typically be <1 photon for Fermi, but the number of signal photons can fluctuate significantly during Poisson sampling). For Fermi-LAT observations we expect 12 ± 3.5 signal photons distributed between $N_{pulsars}$. In the case of ACT observations, we expect 232 ± 15 photons. Occasional spurious clusters will force this distribution downwards, although this effect is reduced by the significance weighting and because we only consider "core points" to be cluster members, thus rejecting those lying on the cluster boundaries.

In order to quantify in how confidently point-source or diffuse models for the 130 GeV excess can be rejected, we count the fraction of simulations which are incompatible with Fermi-LAT data for each tentative source class. A simulation is deemed incompatible if at least 1 cluster is detected at significance $s > 1.29$ corresponding to the maximum number and significance of clusters detected in the Fermi-LAT data. The first column of Table 9.1 shows the fraction of simulations for each model with at least one cluster ($n = 1$) with $s_i > 1.29$. In column 3 we show the fraction of simulations which have two clusters detected with a significance of $s_i > 1.29$ in Fermi-LAT simulations, which further demonstrates the vast statistical separations between the clustering properties of diffuse and point-source models. In the subsequent columns we show similar data for the H.E.S.S.-II telescope, which also requires a cluster to have at least 10 core points, and clearly provides an ever greater ability to differentiate between source classes producing the γ-ray line.

Our statistical approach shows that Fermi-LAT data already rule out models where the 130 GeV γ-ray line is produced by 1, (2, 4) or fewer pulsars at the 99% (95%, 90%) confidence level (CL). Specifically, only one cluster was detected in the Fermi-LAT data with a significance $s = 1.29$, while a cluster with a larger significance is observed in more than 90% of simulations with any ensemble of less than 4 point sources. Due to the greatly increased effective area of the H.E.S.S.-II telescope, we find an even greater statistical separation between our models of diffuse and point source emission. This indicates that H.E.S.S.-II will be able to conclusively differentiate models of the 130 GeV line using purely statistical properties.

9.3 Pulsars or Dark Matter?

If confirmed, the tentative detection of a γ-ray line in the Fermi data might potentially turn into one of the most important breakthroughs on physics beyond the Standard Model, pointing towards the mass of the dark matter particle. Key future developments include the analysis of Fermi γ-ray events with the forthcoming Pass 8 version of the Fermi-LAT analysis software, which will include a major overhaul of the energy reconstruction algorithm [501]. It will also be crucial to identify whether the excess events at 130 GeV from the Earth's limb are indeed a statistical fluke. This question will be answered by increased exposure, which will increase the current statistical sample [445, 455].

At present, barring instrumental effects, a 130 GeV line could be ascribed to

either new physics, presumably a dark matter particle decaying or pair-annihilating into a 2γ (or γZ, γh etc.) final state, or to one or more pulsars featuring a cold wind with electrons with an energy at, or very close to, 130 GeV. This latter possibility, it is argued in [487], is the only "traditional" astrophysical process envisioned thus far that could produce a sharp gamma-ray line in the energy regime of interest. It is therefore of the utmost importance to discriminate between a cold pulsar wind scenario and a dark matter scenario, if indeed the line is resilient to future tests and observations.

Discriminating dark matter and pulsar interpretations of the 130 GeV line may not be possible based solely on the spectral characteristics of the Fermi-LAT data. In the present study we sought to use morphological information, i.e. the 130 GeV events' arrival direction, to establish whether the signal is likely due to multiple point sources as opposed to a truly diffuse origin. This is a meaningful question, since the signal region is much larger than the instrumental angular resolution, and it should be thus possible to discriminate a finite number of point sources, as expected in the pulsar case, from a distribution that follows a diffuse morphology, such as what expected from dark matter annihilation or decay.

To quantitatively approach the issue of discriminating pulsars versus dark matter on a morphological basis, we employed the DBSCAN algorithm which distinguishes clusters from background noise based on the local photon density. We defined a statistical significance measure, and we optimized the algorithm's two physically well-constrained parameters in order to reconstruct as accurately as possible the potential "clusters" producing the observed γ-ray events.

As a result of our analysis of the available Fermi-LAT data, we concluded that at the 99%, 95%, 90% confidence level the data need at least 2, 3, 5 or more point sources, respectively, while the events' morphology is perfectly consistent with various dark matter density profiles. We conclude that the data strongly disfavor the hypothesis of a small number of pulsars as the origin of the signal. If the pulsar scenario is indeed the culprit for the 130 GeV events, it is necessary to postulate a relatively large population of pulsars (likely at least 4) with cold winds featuring electrons with exactly, to within the instrumental energy resolution, the same energy. This appears, to say the least, quite problematic. A diffuse origin seems therefore the most likely scenario for the 130 GeV photons. Our clustering algorithm approach, clearly, is not optimized to discriminate between different diffuse morphologies: in fact, on the basis of our results, we find that we cannot discriminate between different diffuse morphologies (like dark matter annihliation vs. decay).

Present and future observatories have the potential to shed additional light on the presence and characteristics of the 130 GeV line [502]. Improvements to the H.E.S.S. telescope (H.E.S.S.-II) have reduced the γ-ray threshold to around 50 GeV, allowing for the independent determination of a line signal from the GC region. This is especially important, as the 10^4 m^2 collecting area of the H.E.S.S. telescope will quickly alleviate the low-statistics issues involved in Fermi-LAT studies [487]. Furthermore, future instruments such as Gamma-400 [503] and CTA [504] are likely to provide the necessary effective area and energy-resolution to definitively and conclusively test the existence and nature the 130 GeV line feature.

However, in the near future, the most important contribution is expected to come from Fermi-LAT itself: Additional data taken since last year, and the continuous accumulation of more data over the next years, will show whether the signature persists or is a rare statistical fluke. Simultaneously, the availability of pass 8 events, based on a set of completely rewritten event reconstruction algorithms for the LAT, will allow a fresh look on possible instrumental systematics.

Chapter 10

The 3.5 keV X-Ray Line

Recently, an unidentified spectral line at 3.55-3.57 keV was reported by Bulbul et al [134] using *XMM-Newton* observations of galaxy clusters. The signal was detected in five independent samples, including observations both of single objects and stacked cluster spectra. Subsequently, the presence of an unidentified line at ~ 3.52 keV was confirmed by a re-analysis of *XMM* data of the Perseus cluster, and also reported from an analysis of *XMM* observations of M31 in Ref. [52]. *XMM* blank-sky observations do not reveal any evidence for any feature at the energy of interest [52]. Furthermore, when detected in clusters, the line is observed to have a redshift consistent with that of the host cluster, helping to rule out an obvious instrumental origin [134].

Two possible explanations have dominated the ensuing debate over the origin of this mysterious signal. The first was initially put forth by Ref. [134], proposing the exciting possibility that the line is due to the decay of sterile neutrino dark matter. The second possibility is astrophysical, suggesting that the size and impact of uncertainties

in modeling the complex multi-phase plasma structure in clusters had been previously underestimated, and that one or more weak plasma transition lines could in fact be responsible for the signal [505]. Below we summarize these ongoing developments and present a novel spatial analysis method which aims to discriminate the two scenarios using existing archival *XMM* X-ray data.

Self-consistency of the unidentified X-ray line across different objects and for different X-ray instruments (*XMM* MOS, PN and Chandra) has appeared problematic from the start. For example, the precise spectral location of the line[1] has been difficult to pin down and the line flux for a given object were found to vary substantially even between different instruments on the same telescope. Interpretations of the signal in terms of a standard decaying dark matter candidate are also troubling due to the observed strength being inconsistent across different objects [134].

The possibility of explaining the 3.5 keV signal with new physics prompted vigorous activity especially in the model-building community, and a variety of possible particle physics scenarios have been proposed. In particular, models with sterile neutrinos can potentially provide avenues to successful baryogenesis via leptogenesis, to the generation of the observed pattern of (active) neutrino masses and mixing, and to providing a dark matter candidate which can alleviate certain small-scale issues of cold dark matter scenarios [136]. Model building efforts were also directed toward constructing a consistent new-physics picture that could reconcile varying signal strengths across different objects, especially in the context of axion-like particles converting to 3.5 keV

[1] In what follows, we will refer to the energy of the line simply as 3.5 keV for brevity.

photons in the presence of magnetic fields (see e.g. Ref. [137, 138, 139, 140, 141] for early studies of this scenario).

In the dark-matter decay picture the relative signal strength is easily calculated, scaling as the dark matter density integrated over the line of sight. It thus became clear that a confirmation of the non-standard and possibly dark-matter-related origin of the unidentified line might come from observations of nearby targets such as the Galactic center (GC), or nearby dark-matter-dominated systems, such as local dwarf spheroidal galaxies (dSph), where no plasma emission line background is expected.

Ref. [506] proceeded to analyze Chandra data of the Galactic center, finding no evidence for an excess 3.5 keV line after including known plasma emission lines. This study produced constraints on a decaying dark matter scenario in clear tension with such an interpretation of previous results, but it was not clear from this work if the measured line fluxes near 3.5 keV were consistent with those expected from plasma lines.

While relevant, Chandra observations of the Galactic center are significantly shallower than available archival *XMM* observations. In Ref. [505], two of us (TJ & SP) analyzed *XMM* observations of the center of the Galaxy, and discovered a line at an energy of about 3.5 keV. We pointed out that the detected line signal was compatible, at face value, with a dark matter decay origin, and calculated the corresponding preferred sterile neutrino lifetime and mixing angle[2]. However, we also showed that, given the fluxes of other bright plasma emission lines, the flux of the detected 3.5 keV line is compatible with two atomic lines from K XVIII at 3.47 and 3.51 keV, making astrophysical

[2]This aspect of our study appears to have been under-appreciated in the recent literature on the topic.

plasma emission a natural explanation of the 3.5 keV feature.

In Ref. [505] we also re-analyzed, in the 3-4 keV energy range, archival *XMM* data from M31, and found no statistical evidence for a line at 3.5 keV. In addition, we pointed out that the procedure employed in Ref. [134] to predict the K XVIII line flux and the flux of other atomic transition lines was not, contrary to what was stated in that paper, maximally conservative. We argued that the multi-temperature models employed there were biased towards excessively large temperatures which artificially suppress, for example, the expected K XVIII line intensity[3].

Two key subsequent observational analyses of other sources also found no confirmation of an exotic origin for the 3.5 keV line (or any line at that energy whatsoever): Ref. [508] analyzed stacked observations of dwarf galaxies, while Ref. [509] analyzed Chandra and *XMM* observations of two large samples of galaxies and groups of galaxies, which should exhibit tenuous, if any, plasma emission features. Both results robustly rule out a dark matter decay interpretation of the 3.5 keV line observations reported by Ref. [134] and by Ref. [52].

Finally, a recent study utilized deep Suzaku observations of Perseus, Coma, Virgo and Ophiuchus, to test the dark matter decay hypothesis for the 3.5 keV line [510]. While confirming the existence of a 3.5 keV signal in Perseus, Ref. [510] did not find any evidence of an associated signal, with the appropriately rescaled intensity, in the other three clusters, robustly ruling out a dark matter interpretation for the 3.5 keV

[3]We further demonstrate this point in Ref. [507], where we show that the Ca XX to Ca XIX ratio indicates temperatures inconsistent with the multi-temperature models employed in Ref. [134]: for example, in the case of the "all-clusters" MOS sample, the large temperatures employed in Ref. [134] produce *under*-estimates of the K XVIII line flux by factors between more than 4 and more than 10.

line observed from Perseus; also, Ref. [510] points out that the radial variation of the 3.5 keV signal in Perseus is in tension with what expected from dark matter decay, and finds evidence that the Perseus signal could be potentially explained by elemental lines, as we had originally suggested in Ref. [505].

Following our analysis of the GC data in Ref. [505], two comments, Ref. [511, 512], appeared regarding our paper, as well as an analysis of *XMM* data of the Galactic center, which confirmed our discovery of a 3.5 keV line [513]. While these comments debate some details of the analysis in Ref. [505], we show in Ref. [507] that none of our conclusions are substantially affected or challenged by the points raised. This ongoing discussion highlights the difficulty in assessing the origin of (and in the case M31, the existence of) such a weak spectral feature amongst a background rich in astrophysical emission.

Previous studies have argued that a final word on the origin of the 3.5 keV line might possibly come from future high-resolution instruments such as Astro-H. In this work, we show that it is possible to assess the nature of the 3.5 keV line by using available archival data in a completely independent context compared with the spectral analyses performed thus far: we show that a *morphological* analysis of the 3.5 keV emission allows for a critical evaluation of the physical nature of the source, and conclude that the 3.5 keV line is highly unlikely to originate from dark matter decay, or from axion-like particle conversion. We also derive the most constraining limits to-date on the lifetime of a putative radiatively decaying dark matter particle producing a monochromatic 3.5 keV line.

In this Chapter we carry out an extensive morphological analysis of two of the most tantalizing locations where the 3.5 keV line has been conclusively detected: the Galactic center and Perseus cluster. As the 3.5 keV line is quite tenuous compared to the continuum emission, the choice and determination of the continuum model is important. We thus consider a broad sample of continuum emission models, and assess possible systematic effects associated with modeling the morphology of the continuum using different assumptions. We then study the morphology of plasma emission lines observed at different energies, and assess the radial and azimuthal behavior of the residual emission at 3.5 keV. We compare this residual emission with the morphology of line emission templates as well as with dark matter templates. Finally, we study the cross-correlation of the 3.5 keV morphology with a sliding-window template, and calculate the resulting constraints on any emission sharing the morphology expected from dark matter decay models for both the Galactic center and Perseus.

10.1 Morphological Analysis

In this section, we introduce the two targets we focus on in the present study, we describe our *XMM* data selection, the details of the binned-likelihood analysis, the "sideband" templates for nearby spectral lines and continuum emission, and finally, the generation of sky-maps for decaying dark matter based on several choices for the dark matter halo model.

10.1.1 Choice of Targets

The present study focuses on the Galactic center [505], and on the Perseus cluster [134, 52]. The proximity of the Galactic center and the inherent asymmetry of the expected astrophysical emission makes it an especially compelling target for a morphological study; the Perseus cluster's 3.5 keV line has been robustly detected with several X-ray instruments (including *XMM* MOS but not PN, Chandra ACIS-S and ACIS-I, and Suzaku) and the cluster has a large enough extension in the sky, compared to the instrumental angular resolution, that a morphological study is also possible.

If the 3.5 keV line indeed arises from the decay (or annihilation, or conversion of the decay products) of particle dark matter, the spatial morphology of any excess emission must be both roughly spherical[4] and declining with growing distance from the center of the halo. On the other hand, the flux from atomic emission lines should trace the distribution of the astrophysical plasma as the product of atomic abundance and emissivity, the latter of which possesses a strong dependence on the local plasma temperature.

The X-ray emission from the Galactic center is dominated by resolved and unresolved X-ray point sources as well as thermal emission from the hot gas. In addition to hot plasma and high gas densities, the Galactic center region is densely packed with feedback sources, including the central black-hole, Sgr A*, supernova remnants such as Sgr A East, and stellar clusters. This environment leads to an extremely complex

[4] A possible exception, which we discuss in what follows, is the case of the Galactic center for axion-like-particle conversion.

and spatially varying multi-temperature plasma structure, as well as to strong gradients in the atomic abundances of each radiating species, making it difficult to conclusively spatially correlate strong emission lines [514, 515, 516].

X-ray emission from galaxy clusters originates from the hot intergalactic medium heated during gravitational collapse. With very different cooling and feedback processes compared to the Galactic center, such systems provide an independent lens for spectrally *and* morphologically differentiating dark matter emission from that of ∼keV plasma emission lines. Already, there is substantial tension between the 3.5 keV line fluxes detected within the stacked and unstacked observations of clusters [134], perhaps providing an indication of differing multi-phase plasmas, or more exotic dark matter candidates, such as an Axion-Like-Particle with a photo-conversion rate dependent on the cluster's magnetic field structure.

Categorically, clusters fall into two groups. 'Cool-core clusters' are stable virialized structures with no recent major-mergers, whereas in 'non-cool-core' clusters recent collisions have inhibited dynamical relaxation. Radiative cooling timescales are $\sim 10^8 - 10^9$ yr, creating a flow of hot (~ 7 keV) dispersed gas to into the cool (~ 3 keV) cluster center. AGN feedback eventually halts the inflow and maintains temperatures of about a few keV [517]. Perseus is a prototypical cool-core cluster with a complicated core structure, where the plasma has clearly been affected by feedback from the bright central AGN, offering an excellent test case for a comparative study of DM versus gas-correlated emission. Unfortunately, due to the relatively low flux of the spectral line in question, all but the most prominent of the detailed core structures in Perseus are unre-

solved, making a morphological analysis potentially less stringent than in the Galactic center. A prominent spatial feature associated with the cluster core would, however, provide a strong handle for differentiating exotic emission from that associated with the cool core [518, 519, 517] (see also Ref. [510]).

10.1.2 X-Ray Data Selection

We employ archival observations from *XMM* for both the Galactic center and the Perseus cluster. We restrict our analysis to using the two EPIC MOS detectors which have both higher spatial resolution and fewer instrumental chip gap features than the EPIC PN detector. While in principle the Chandra Observatory would offer better spatial resolution, the smaller field-of-view and lower effective area of Chandra make *XMM* the better choice. In addition, given the small 3.5 keV line flux, we employ a binning that is in any case larger than the inherent instrumental angular resolution.

For the Galactic center we use the same observations as listed in Table 1 of Ref. [505]. This set has been chosen to eliminate observations with either strong particle background flaring or significant flaring from Sgr A*. For the Perseus cluster we utilize the same two *XMM* observations as in Ref. [134]. The basic data reduction follows Ref. [505]. All observations were reprocessed using the `emchain` task in *XMM* SAS version 13.5.0. Particle background flares were then removed using the `mos-filter` task in the *XMM* `ESAS` package [520, 521]. The energies of all photons in the Perseus field-of-view are then blue-shifted by the current NED value[5] $z = 0.0179$.

[5] http://ned.ipac.caltech.edu

For each observation, we also created a mask to remove regions containing bright point sources, including Sgr A* in the Galactic center and the central AGN in Perseus, as well as low exposure regions due to chip gaps and bad columns on the detector. Masks were generated with the `ESAS` task `cheese` run on broad-band (0.4-7.2 keV) images. These masks are applied consistently to all images generated as described below. To appropriately include the detector response when modeling the possible dark matter contribution (see Sec. 10.1.6), we also created exposure maps in the 3-4 keV band for each observation.

10.1.3 Binned Likelihood Analysis

In order to quantify the contributions of various templates to the 3.45-3.60 keV band, we perform a pixel-by-pixel binned likelihood analysis (See. Sec 4.1 and 4.3. Photons are binned into 20" square pixels over the $\approx 0.5^{\circ}$ diameter field of view of *XMM*'s MOS1 & MOS2 imagers. This choice provides an average of several photons per pixel for the weak detectable emission lines (after subtracting off continuum emission), and happens to be only slightly larger than the *XMM* MOS point-spread function, implying that little would be gained with finer resolutions. We verified that the main conclusions reached by the present analysis are largely independent of this specific choice of binning, with only minor changes to e.g. limits. In these cases, we have ensured that the results presented here reflect the most conservative values. The templates employed are described in the following three sections.

10.1.4 Continuum Templates

We select 5 continuum emission bands at energies between 3.19 and 4.8 keV[6]. The lower-energy sideband includes photons from 3.19 and 3.27 keV. Although partially overlapping with the bright Ar XVII line at 3.14 keV, this band is included to provide continuum photons at low energies, where dense line structure prohibits a single band of wide energy (and also prohibits the selection of line-free continuum at energies below 3 keV). The second low-energy continuum band is also selected to be very narrow, ranging from 3.373-3.45 keV, but provides a reasonable background sample immediately neighboring our spectral region of interest. For the next neighboring continuum band, we choose 3.6-3.811 keV which also includes a series of three weak and tightly-packed Ar XVII lines. The limited energy resolution of the *XMM* MOS sensors make it difficult to separate such lines, and we include them as a single wide-band contribution. Finally, two additional high-energy bands from 4.2-4.5 keV and 4.5-4.8 keV provide a region which is effectively free of emission lines.

While the continuum templates are visually difficult to distinguish, it is clear from the likelihood analysis that they do supply linearly independent degrees of freedom, and that the inclusion of each additional continuum template improves the model fit to photons in the 3.5 keV band at high-significance. In Figure 10.1 we show log-scaled continuum count maps at high binning resolution (2.5") for the photons between 4.2 and 5.5 keV in both the Galactic center and Perseus fields. The GC is reveled to be very asymmetrically-structured, while the Perseus cluster is significantly smoother and more

[6]See also Fig. 10.7, where we show the bands we employ as vertical green bands above 3 keV.

spherically symmetric (i.e. virialized). A similar trend is observed in the morphology of emission lines, although in the Perseus cluster different plasma lines show different characteristic radii depending of the temperature at which their emissivity peaks.

When analyzing the morphology of the residual emission (i.e. the emission not associated with continuum templates), when performing dark matter fits, and when computing limits, we consider three different continuum models with the intent of probing the sensitivity to the background model. The set of continuum models we employ is as follows:

- '*All*', utilizes all five continuum templates
- '*Neighboring*' uses the two templates bracketing our 3.45-3.6 keV band of interest plus a single high-energy band (4.2-4.5 keV), and
- '*High-energy*' uses only the two high-energy bands.

While it is naively preferable for the 'Neighboring' model to include only the neighboring two bands, these are both contaminated by Ar line structures that are substantially brighter near Sgr A* than the nearby continuum. In addition, when we fit the 3.5 keV photons using this background model, inspection of the covariance matrix reveals near degeneracy between fitting the normalization of the two neighboring sidebands in both Perseus and the Galactic Center. We therefore (minimally) add the 4.2-4.5 keV band in order to provide at least one clean ("line-free") continuum sample. It is important to note that this continuum template does not resemble a dark matter profile (Fig. 10.1) while improving the fit dramatically in each system.

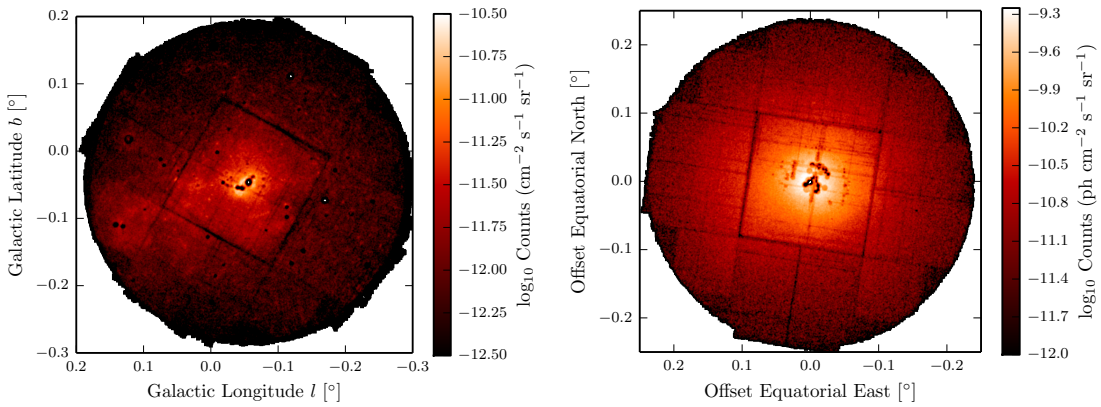

(a) Galactic center

(b) Perseus cluster

Figure 10.1: Representative continuum photon maps for energies in the 4.2-5.5 keV range, centered on Sgr A* in the Galactic center (left) region and on the Perseus cluster (right). Count maps have been blurred using a Gaussian kernel with $\sigma = 2.5''$ and are log-scaled to highlight distinctive spatial features. In the right panel, the x-y axes are aligned with the equatorial axes and show the angular displacement from the cluster center. In both cases, bright point sources have been masked out.

10.1.5 Emission Line Templates

In order to search for qualitative correlations between the 3.5 keV exess and known plasma emission lines, we create templates for 8 spectral lines between 2 and 4.1 keV by selecting photons within ±50 eV of each line's central energy[7]. The complete list of lines we consider is in the first column of the left panel of Table 10.1, along with the corresponding central energies and peak emissivity temperatures (the electron temperature for which the line intensity is maximal). In Figure 10.2 we show the line templates, as well as our 3.45-3.6 keV band of interest, with the best fitting 'All' continuum model subtracted off in order to highlight the characteristic morphology of each line. A black

[7]The Full-Width-Half-Maximum (FWHM) energy resolution of the MOS CCDs is approximately 100 eV$\sqrt{E_\gamma/3.5\text{ keV}}$. Performance characteristics for *XMM* used throughout this section are taken from http://xmm.esac.esa.int/external/xmm_user_support/documentation/uhb_2.1/node1.html.

'+' and ellipse indicate the location of Sgr A* and the shell of the supernova remnant (SNR) Sgr A East, from Ref. [48].

It is important to note that because some of the lines are weak with respect to the continuum emission, and because our continuum is slightly energy dependent, it is difficult to unambiguously separate 'line photons' from 'continuum photons'. For most of the lines listed in Table 10.1, the line flux is a substantial or even dominant fraction of the total emission, excepting the 3.45-3.6 keV band and some weaker lines in Perseus, which contribute only a few percent of the total flux. Later in our analysis we refer to 'line' templates in two contexts: for qualitative comparisons we will subtract off the best fitting continuum model, and thus most of the residual should be characteristic of that spectral line. When setting limits on the dark matter decay lifetime we include *all* photons in the respective line energy. In each case where the line templates are used, one should keep the above caveats in mind, though we do not expect either the continuum or line emission to trace emission from dark matter.

Figure 10.2 shows a clear common feature observed across all lines whose emissivities peak at relatively low plasma temperatures, which exhibit a negative (oversubtracted) residual concentrated near SNR Sgr A East, which increases into a bright, 0.2° diameter lobe extended toward positive galactic longitudes. In contrast, the lines which peak at higher plasma temperatures[8] are seen to be more centrally concentrated around Sgr A* and Sgr A East. The 3.45-3.6 keV band shows a distinct quadrapolar morphology with positive residuals in the north/south oriented lobes. Visually, this 'residual'

[8]We urge caution in strictly interpreting emission in terms of temperature, as varying relative elemental abundances also play an important role in the morphology.

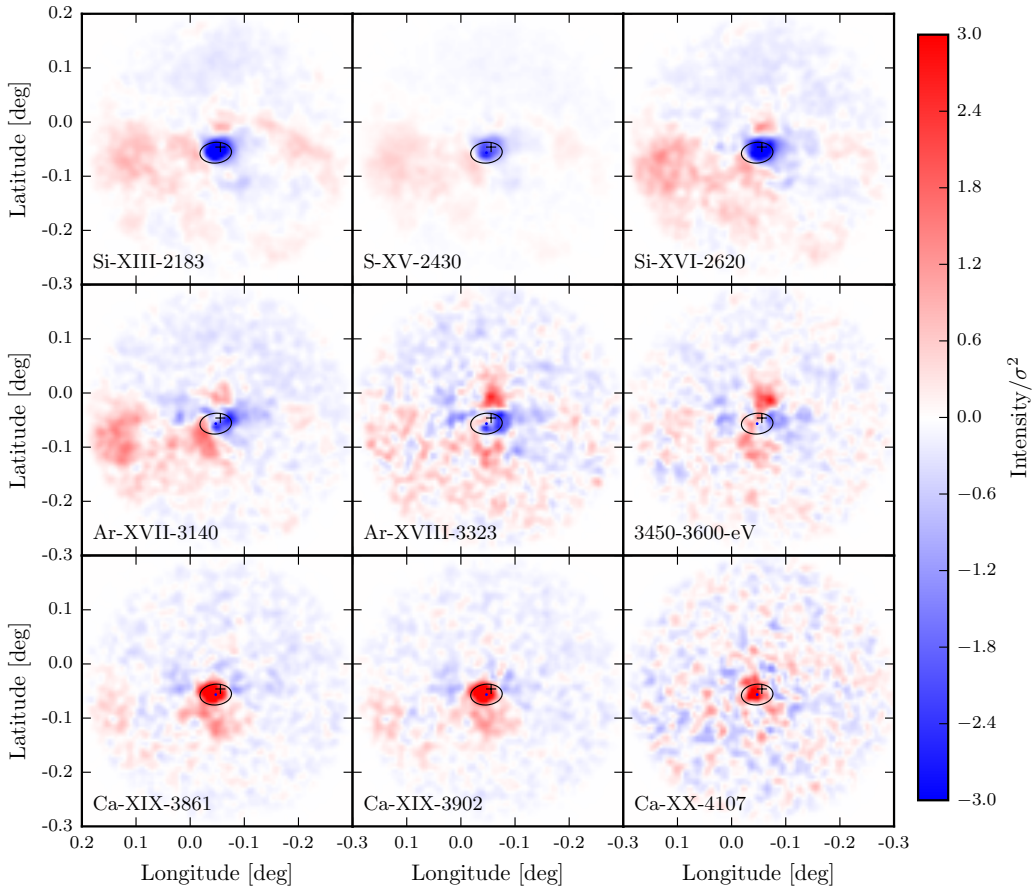

Figure 10.2: Morphology of 8 plasma emission lines including the 3.5 keV band surrounding the Galactic center region after subtracting off the best-fit (ML) contribution from 5 continuum bands. For illustrative purposes, we normalize maps to the variance of each template. The band from 3.45-3.6 keV is also shown in the center-right panel. A black '+' indicates the location of Sgr A* while the outer shell of the supernova remnant Sgr A East is approximately bounded by the ellipse shown, from Ref. [48].

emission most closely resembles the Ar XVIII line at 3.32 keV. If this residual is representative of the line morphology (rather than mis-modeling of the energy dependent continuum), then it is evident that this emission profile is qualitatively incompatible with that expected from dark matter. We quantify this statement accurately in what follows.

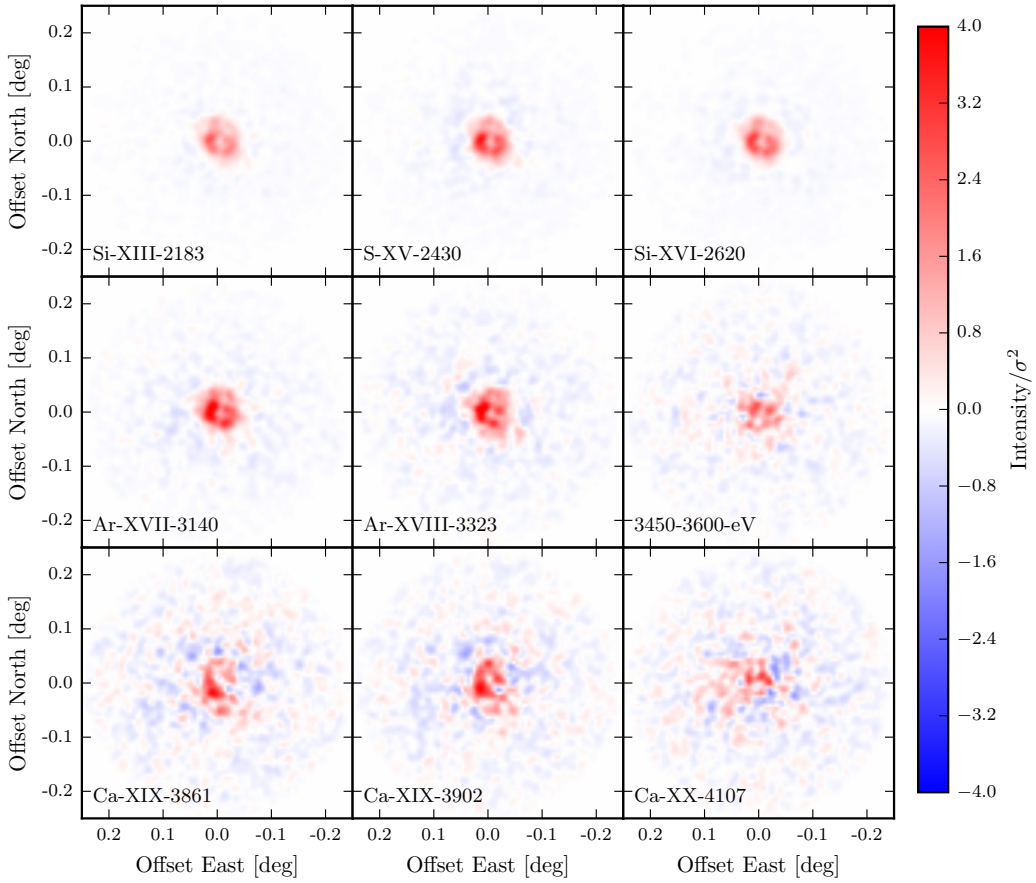

Figure 10.3: Morphologies for the 8 plasma emission lines and the 3.5 keV band in the Perseus cluster after subtracting off the best-fit (ML) contribution from 5 continuum bands. The normalization prescription is as in Fig. 10.2.

In Figure 10.3, we exhibit the same set of lines for the Perseus cluster. At our binning resolution and exposure depth, many of the detailed asymmetric features in the cluster are unfortunately washed out, and one is left with an approximately spherical distribution of X-rays for both the continuum and the lines. Still, the two well-known 'ear-like' features (see e.g. Ref. [519]) are visible in the central regions, keeping in mind that point source masking and exposure maps induce some distortions. Clearly, cooler

emission lines are more concentrated in the cool cluster core, with a characteristic radius $\lesssim 2.5'$, while emission lines associated with hotter, higher-dispersion plasmas extend well beyond the core. The 3.5 keV band appears, here, to be associated both with the core, perhaps from residual low-energy continuum emission, as well as exhibiting a small extended component tracing the morphology of emission lines that peak at higher temperatures ($T_{\rm peak} \gtrsim 3$ keV). It is important to note that in the case of Perseus, the 3.5 keV line is (even globally) quite weak. Thus a large, or even dominant portion of the residual emission in this band could be related to errors in continuum modeling. In Section 10.2.1 we discuss potential systematic effects associated with the continuum model for the 3.5 keV band.

10.1.6 Dark Matter Templates

The differential flux of photons from dark matter decay factorizes into two components: one containing the particle physics (P. P.) factors and one associated with the particle-physics-model-independent astrophysics.

$$\frac{d\Phi_\gamma}{dE_\gamma} = \underbrace{\frac{1}{4\pi} \sum_f \frac{\Gamma_f}{m_\chi} \frac{dN_\gamma}{dE_\gamma}}_{\rm P.P.} \underbrace{\int_{\Delta\Omega} \int_{l.o.s} \mathcal{A}(l,b) \cdot \rho(l,b,z) \; d\Omega dz}_{\mathcal{J}-{\rm factor}} \qquad \text{Decay} \quad (10.1)$$

In the above equations, the first terms represent the particle physics for final-states f, dark matter mass m_χ, and model-independent decay rate $\Gamma \equiv 1/\tau$. The modification of Eq. (10.1) above for the case of annihilation is trivial. In our primary model of interest, a sterile neutrino decays at loop level to a standard neutrino, radiating

a nearly monochromatic photon with energy $E_\gamma \approx m_\chi/2$ in the process. The lifetime is independent of the particular sterile neutrino model and is given in terms of a mixing angle θ with active neutrinos [522].

$$\tau = 7.2 \times 10^{29} \text{ s } \left(\frac{10^{-4}}{\sin(2\theta)}\right)^2 \left(\frac{1 \text{ keV}}{m_\chi}\right)^5. \tag{10.2}$$

The double integral term in Eqn. 10.1 is known as the $\mathcal{J}$-factor, with units GeV cm^{-2} for decaying dark matter. The mask $\mathcal{A}(l, b)$ represents an efficiency factor due to gaps between CCDs, masked point source regions, defective pixels, and the off-axis effective area. The mask $\mathcal{A}$ takes values between 0 to 1 and is generated by summing the individual aligned observation and exposure masks, weighted by their Good exposure Time Intervals (GTIs). Note that $\mathcal{A}$ itself is also an isotropic emission template which can be used to subtract the contribution of isotropic backgrounds such as galactic foreground and extragalactic background emission which are focused through the telescope. For a cosmic-ray induced isotropic background template $\mathcal{A}_{\text{flat}}$, we can use $\mathcal{A}$ without exposure masking (but including point-source and chip-gap masks), since these events are not focused through the telescope. The majority of each of these isotropic events should be compensated by the sideband templates. However, this couples the relative isotropic normalizations to the continuum emission. We therefore include these templates when explicitly indicated, although this has little quantitative impact in practice.

For the Galactic center field of view, we take three dark matter profiles including an NFW [89], an Einasto profile [90], and the paradigmatically cored Burkert [94] profile, which serves as a conservative (low) estimate of dark matter emission from the inner

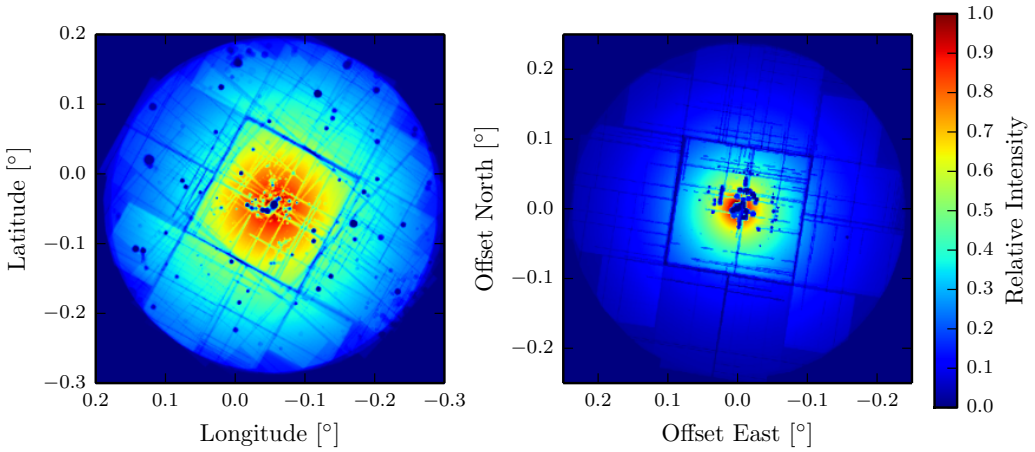

Figure 10.4: $\mathcal{J}$-factors sky-maps for a decaying dark matter candidate distributed as an NFW profile convolved with the *XMM* MOS instrument response functions and exposure masks for the Galactic center field (left) and the Perseus cluster (right).

Galaxy. The functional form of the dark matter density profiles are defined as follows:

$$\rho(r) = \left(\frac{r_s}{r}\right)^{\alpha} \frac{\rho_0}{(1 + r/r_s)^{3-\alpha}}, \qquad \text{NFW} \tag{10.3}$$

$$\rho(r) = \rho_0 \exp\left(\frac{-2}{\alpha}\left[\left(\frac{r}{r_s}\right)^{-\alpha} - 1\right]\right), \qquad \text{Einasto} \tag{10.4}$$

$$\rho(r) = \frac{\rho_0 \; r_s^3}{(r_s + r)(r_s^2 + r^2)}, \qquad \text{Burkert} \tag{10.5}$$

where the scaling radius $r_s = \{20, 20, 6\}$ kpc, $\alpha = \{1, .16, \mathrm{N/A}\}$, and the normalization factors[9] are chosen such that the local dark matter density $\rho(R_\odot) = 0.4$ GeV cm^{-3} is reproduced at the solar radius $R_\odot = 8.5$ kpc.

For the Perseus cluster we employ an NFW profile, with inner slope $\alpha = 1$ and

[9]The overall normalization is obviously irrelevant for our template analysis.

a scaling radius derived using the mass-concentration relation of Ref. [523],

$$c_{\rm vir} = 9 \left(\frac{M_{\rm vir}}{10^{14} M_\odot h^{-1}} \right)^{-0.172}, \tag{10.6}$$

where $c_{\rm vir} = R_{\rm vir}/r_s$. The virial overdensity is taken to be 200, with $M_{200} = 10.8^{+.46}_{-.41} M_\odot h^{-1}$ and $r_{200} = 2.66 \pm 0.04$ Mpc [524], yielding NFW parameters $r_s = 445 \mp 3$ kpc and $\rho_0 = 0.0217 \pm .001$ GeV cm^{-3}. Following Ref. [52], we assume that Perseus lies at redshift $z = 0.0179$ ($d = 72$ Mpc).

Once the $\mathcal{J}$-factors are calculated for each pixel, the skymap is smeared by the *XMM* MOS point-spread function (PSF), taken to be a Gaussian with $\sigma = 15''$, and normalized according to the total GTI of the field and assuming an on-axis effective area of 750 cm^2 for MOS1+MOS2 which is corrected off-axis using generated exposure maps. In Figure 10.4, we show example templates for decaying NFW dark matter in the Galactic center and in the Perseus cluster.

In addition to the instrumental effects discussed above, one may worry about the effects of X-ray absorption by the dense interstellar medium near the Galactic center. In order to assess the impact of this, we have utilized high-resolution velocity integrated[10] radio observations from the ATCA HI Galactic center survey [525]. One can then relate the integrated line brightness to the HI column density, N_H (see e.g. Ref [526]). We then employ the absorption model of Wilms et al [527] which provides an optical depth per

[10] In principle, one should not include absorption behind the GC region. Unfortunately, converting velocity cubes into positional space is extremely difficult in the direction of the Galactic center as the velocity relative to the Sun vanishes along this line of sight. Accurate subtraction of radio continuum emission is also problematic due to bright point sources in the GC region. A detailed study of the HI distribution toward the Galactic center is beyond the scope and necessity of the present analysis.

atomic hydrogen column density assuming elemental abundances typical of the ISM. At 3.5 keV, the ISM is optically thin for all but the highest column densities ($N_H \gtrsim 10^{23}$) and the maximal absorption in our region of interest is found to be less than 10%, averaging only a few percent. In addition, the morphology is not disk-like and actually slightly enhances the quadrapolar structure observed in Fig. 10.2. While molecular hydrogen column densities can be even larger in the Galactic center and more concentrated in the Galactic plane, the photoionization cross-section for H_2 at 3.5 keV is completely negligible relative to heavier elements [527]. As a final check, we recomputed the dark matter limits found in section 10.2.2 using this absorption map, finding only percent level changes in all cases. For these qualitative and quantitative reasons, we neglect absorption throughout the rest of this analysis.

We have empirically derived spatial templates for a variety of line and continuum emission in the Galactic center and Perseus fields of view. We have also generated emission profiles for dark matter templates which have been convolved with the necessary instrument response functions and analysis masks. All templates used are summarized in Table 10.1. In the case of emission line templates we also include the electron temperatures for which the corresponding transition line is at its peak intensity [51]. In the next section we use the pixel-by-pixel binned likelihood analysis in order to determine the primary emission template components associated with the 3.45-3.6 keV band.

Template	E (keV)	$T_{pk}(10^7$ K)	Template	E (keV)
Si XIII	2.183	1.0	Ctnm1	3.190-3.270
S XV	2.430	1.26	Ctnm2	3.373-3.450
Si XVI	2.620	2.0	Ctnm3	3.600-3.811†
Ar XVII	3.140	2.0	Ctnm4	4.200-4.500
Ar XVIII	3.323	3.98	Ctnm5	4.500-4.800
Ca XIX	3.861	2.51	DM	–
Ca XIX	3.902	3.16	Focused Isotropic	–
Ca XX	4.107	5.01	Flat Isotropic	–

Table 10.1: Summary of templates used. For atomic emission lines (top), we also indicate the peak emissivity temperatures taken from the `AtomDB 2.0.2` [51]. We note that the K XVIII emission peaks at 2.16 keV (2.51×10^7 K). †This continuum band includes three weak lines from Ar XVII; the limited energy resolution of the EPIC MOS CCD's prevents the lines from being cleanly separated and they are thus treated as a single broad continuum band.

10.2 Results of the Morphological Analysis

In this Section, we discuss the basic morphology of the 3.45-3.6 keV residual emission using each of our three continuum model choices (sec 10.2.1). This involves subtracting off the best-fitting continuum+isotropic templates and comparing the results against expectations for dark matter and line-like emission. Next, in sec. 10.2.2, we add a decaying DM template to the fit, finding that there is no indication for a component whose morphology follows the dark matter templates in either the Galactic center or the Perseus cluster. We then calculate upper limits on the particle decay lifetime and discuss the implications for a dark matter interpretation of the 3.5 keV line. Finally, we use the maximum likelihood technique to check for spatial correlations between the

3.5 keV band and nearby energies, uncovering strong statistical evidence in favor of an astrophysical interpretation of the 3.5 keV line (sec. 10.2.3).

10.2.1 Residual Maps

We perform a maximum likelihood analysis of the Galactic center and of the Perseus cluster X-ray observations listed above for energies between 3.45-3.6 keV, subtracting off the best-fitting linear combination of (1) isotropic templates, and (2) each of the 'All', 'Neighboring', and 'High-Energy' continuum template sets described in Section 10.1.4. Figure 10.5 shows the residual count maps for the Galactic center (top panels) and for the Perseus cluster (bottom panels) for each of the three different continuum models.

For each continuum model in the GC we observe a bright extension emanating roughly perpendicularly to the Galactic plane from the position of Sgr A* (black '+'), with a smaller bridge connecting toward the direction of the supernova remnant Sgr A East (the outer shell is represented by the black ellipse [48]) as well as a large faint bubble extending to the positive longitude edge of the field. Although this residual appears most likely associated with Sgr A* or Sgr A East, the central few parsecs are not well resolved and are known to host a large number of potential sources. The largest residual is seen when using the high-energy model, indicating that this feature is at least partially aligned with the ≈ 3.2 keV and ≈ 3.5 keV continuum. In the 'All' and 'Neighboring' models, the residual is substantially reduced and the log-likelihood is greatly increased.

In the Perseus cluster (Fig. 10.5, bottom), prominent morphological identifiers

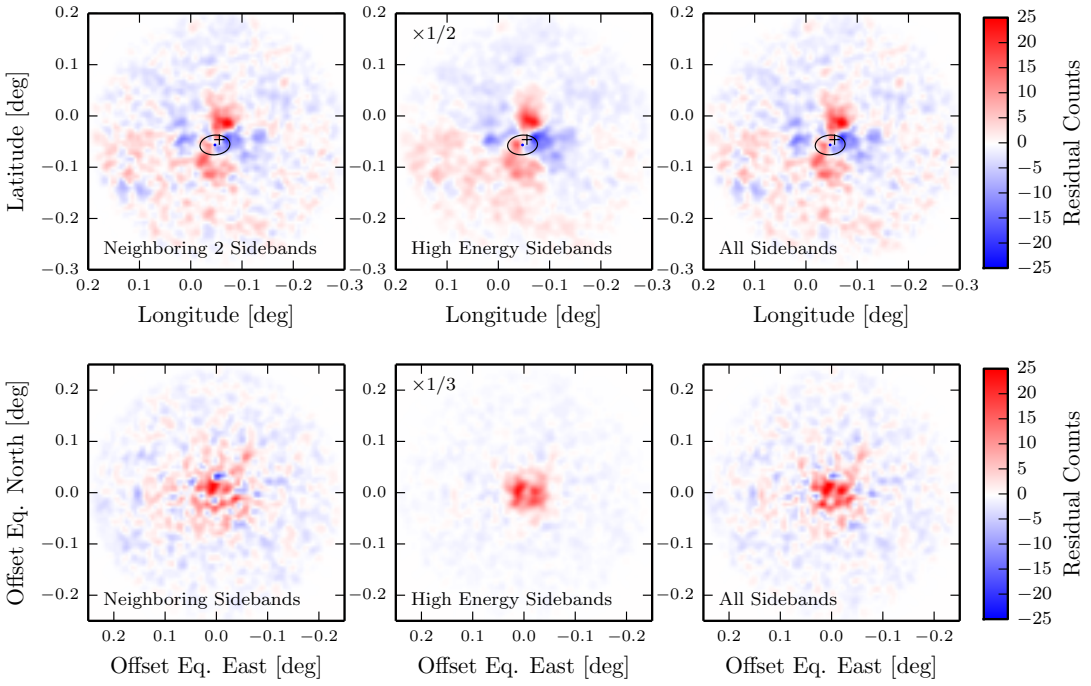

Figure 10.5: Comparisons between 3.45-3.6 keV residuals after subtracting the best fit continuum+isotropic templates for different models of the continuum near the Galactc Center (top row) and the Perseus cluster (bottom row). Black '+'s in the top row indicate Sgr A* while the shell of SNR Sgr A East is shown by the black ellipse [48]. Maps have been smoothed by a Gaussian kernel with $\sigma = 20''$. For the high-energy continuum model, the GC and Perseus cluster maps have been rescaled by a factor 1/2 and 1/3, respectively, in order to maintain visibility on a common scale.

are seen in each residual. A relatively bright core region is apparent. Extensions to large radii are also observed, similar to those observed in the hotter Calcium lines, and to a lesser extent in Ar XVIII. The clumped nature of this residual is difficult to reconcile with the much smoother distribution expected from dark matter as is the radial profile which has a much sharper gradient at the edge of the core than what expected from a decaying dark matter profile (cf. Fig. 10.4).

In Figure 10.6 we show averaged radial and azimuthal intensity profiles for each

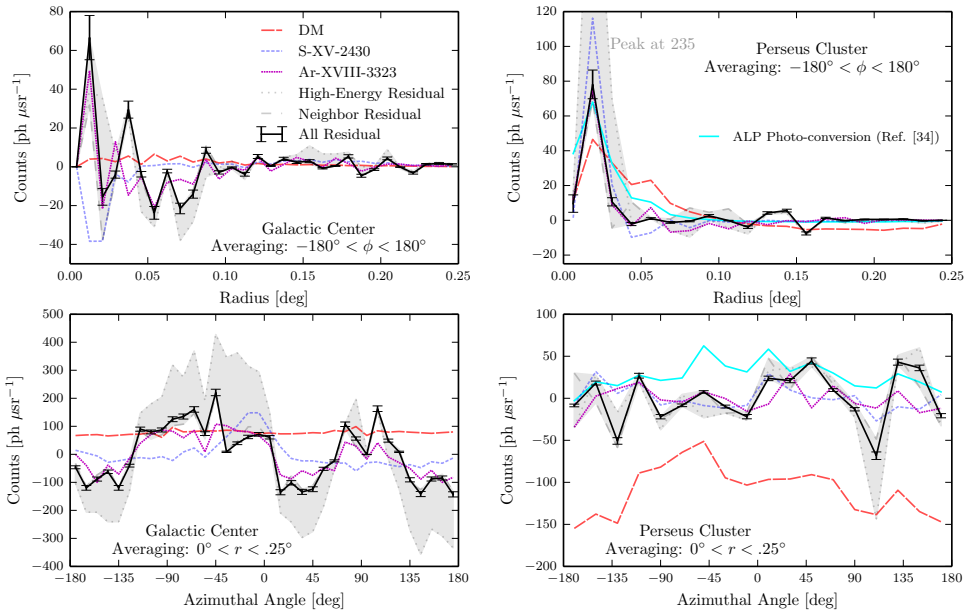

Figure 10.6: Radial and azimuthal profiles for the Galactic center (left panels) and for the Perseus cluster's (right panels) un-smoothed residual maps shown in Fig 10.5. The shaded regions bracket alternative continuum models along with the best fitting NFW template (red), S XV Line (light blue), and Ar XVIII line (magenta). Poisson error bars are shown for our 'All' model. Azimuthal profiles rotate clockwise from the line pointing from the center (Sgr A* in the GC) to positive longitudes. In the top-right panel, we also show the steepest radial profile expected from photo-conversion of axion-like-particles (solid blue), calculated using formulae in Ref. [49] and convolved with the relevant masks and instrument response.

of the residuals along with the NFW DM templates, a prototypical cool emission line (S XV at 2.43 keV), and a medium-temperature emission line (Ar XVIII at 3.32 keV), both with the 'All' continuum model already subtracted. The normalizations of lines and DM templates are determined by minimizing the total χ^2 of the binned template in question to the 'All' residual – i.e. the best fit is to the entire template rather than fitting the averaged profiles individually. Because the dark matter templates are positive everywhere, we have also included a flat isotropic degree of freedom in this case.

By visual inspection, it is evident that standard decaying dark matter does not provide a good fit to either the GC or Perseus cluster system azimuthally or radially, while the Ar XVIII line morphology shares precisely the same features as the GC residual and both the Ar XVIII and the S XV profiles share common features with the Perseus residual. The GC is characterized by a distinctly quadrupolar profile in azimuth and by a centrally peaked radial profile. The DM template is instead effectively flat in azimuth, with a slow radial falloff. Notice that the small deviations seen in the DM template are due to the combined exposure masks $\mathcal{A}(l, b)$. As noted in Sec. 10.1.6, absorption effects are negligible and are, even qualitatively, unable to account for such a morphology. The Perseus residual shows evidence of a distinct core which is truncated around $0.04^\circ \approx 50$ kpc, matching what seen for the lines. Compared with DM, this is much too sharply peaked than even the most concentrated physical NFW profile.

While the Ar XVIII line shown is detected at relatively high significance in the GC and Perseus cluster, it is substantially weaker than that of Ar XVII. The Ar XVII line morphology is similar to Ar XVIII except at the far East side of the field where a large excess is present in the GC. One must consider that a portion of any 'line' template will likely be unmodeled continuum emission. This is especially true in case of weak lines, where the continuum dominates the total flux. However, the foremost objective of this analysis is to test whether the excess emission in the 3.5 keV band traces *any* plausible astrophysical background, and whether dark matter can potentially provide a satisfactory spatial morphology. These questions will be answered quantitatively in the following sections.

For Perseus, we also overlay the steepest of the radial profiles expected from photoconversion of axion-like-particles (ALPs) in Perseus' large scale magnetic field as calculated using Eqns. (3.1) and (3.3) of Ref. [49], with a free electron density n_e taken from Ref. [528], and using the NFW parameters specified in our subsec 10.1.6. The three dimensional profile for the axion signal is then proportional to $\rho(r) \times n_e(r)^{2\eta}$ and is always steeper than the decaying DM case for a radially decaying magnetic field, as is measured in Perseus. The case shown corresponds to the steepest magnetic field profile, $\eta = 1$, while smaller values of η lead to a significant flattening. The projected skymap was then convolved with the relevant masks.

The ALP scenario is significantly steeper than the decaying DM case due to the magnetic field falloff and it visually appears marginally compatible with the morphology of the residual emission. As $\eta \to 0$, this profile asymptotes to the decaying DM case. The azimuthal profile is also reasonably compatible, though much less so than for the profiles corresponding to elemental lines. However, here we have used an idealized model for the magnetic field structure which in reality will be much more complicated and could follow an azimuthal profile similar to that of emission lines. While the steepest ALP-conversion profile morphologically traces the cluster's core, the excess emission is much better fit by adding a continuum or low energy line template (after which there is no preference for ALPs). We discuss this aspect on more quantitative grounds in the next section.

Recently, Ref. [529] also calculated the morphology expected in the Milky Way's center where the signal is expected to roughly trace the projected free electron density (see also Ref. [530]). Based on the NE2001 model for the free electron distribu-

tion [531, 532], the expected signal is (i) highly elliptical with an axis ratio of nearly 4:1 elongated in the Galactic plane, and (ii) has a peak intensity offset from the center $\approx 20'$ toward Galactic north. Neither of these features are remotely compatible with the observed excess. In fact, the orientation of an ALP-conversion excess is orthogonal to the residual shown here making it maximally incompatible with observations. A successful interpretation of the 3.5 keV line in terms of ALP photoconversion seems unlikely across both objects simultaneously. The case for an astrophysical origin of the GC 3.5 keV signal thus appears very robust.

In both systems, the 3.5 keV line makes up only a few percent of the total flux. An important caveat to above discussion is therefore to understand whether these residuals are representative of the actual 3.5 keV signal, as opposed to an energy dependent feature of the continuum that is not included in our model. The above is intended as a qualitative comparison, but in the following two sections we will draw the same conclusions, observing a stronger statistical correlation between the 3.5 keV band and, for example, the Ar-XVIII line shown in Figure 10.6, than continuum regions. Note that in what follows we do not derive limits or perform template fitting to the residuals above, but instead perform new fits allowing the normalizations of all of the included templates to vary, minimizing the impact of errors in the continuum model.

10.2.2 Fits and Limits for Decaying Dark Matter

In this section we test statistically for the presence of a dark matter component in the *spatial* distribution of photons in the 3.45-3.6 keV band. Using the method of

maximum likelihood described above, our model consists of up to eight templates: one for dark matter, one to two for flat and focused isotropic templates, and up to five more, depending on the continuum model. These template normalizations are then varied to fit to the all photons in the 3.45-3.6 keV band – i.e. *not* to the residuals found in the previous section – and similarly when calculating upper limits. Our key finding is that *there is no statistical evidence (TS≈0) for decaying dark matter in the Galactic center region for any combination of the three DM halo models or continuum models, with or without any combination of isotropic templates.*

As additional tests of the robustness of our results, we start with the 'All' continuum and an 'NFW' profile and allow the central location of the DM profile to float in the vicinity of Sgr A*, increase the size of the spatial binning, radially mask the inner 5 arcminutes, and mask the outer 5 arcminutes, finding that each variation produces no change in the (zero) statistical significance of the dark matter template. Finally, we scan the inner slope of the NFW profile between 0 and 3, finding no preferred value. Since the DM profile is a pure power-law this close to the GC, annihilating dark matter – with the intensity canonically tracing r^{-2} – is also essentially ruled out as a candidate explanation of the 3.5 keV excess from the GC at high confidence level. We reiterate that models where the signal is azimuthally flat, including e.g. eXciting dark matter [533] or annihilating dark matter scenarios (e.g. [534]), are clearly disfavored by the quadrupolar structure of the residuals from the GC.

Similarly, the morphology of the X-ray emission from Perseus also does not exhibit any evidence for a dark matter component for the default cluster NFW model

using any continuum model. Allowing the inner slope and scale factor to vary does not increase the goodness of fit, unless the relevant parameters are set to completely unphysical values (e.g. $r_s = 60$ kpc and $\gamma = 1.6$ compared to 445 kpc and 1 respectively), in which case there is a slight statistical preference. These parameters effectively try to mimic the profile of the cool inner core, making it clear that the excess emission is associated with unmodeled cool lines or with thermal continuum emission below 3 keV. We will explore this further in sec. 10.2.3.

We also test the case of ALP photoconversion for Perseus. Using the 'All' continuum model and both isotropic templates we find a TS=28 preference for the steepest ALP profile (corresponding to $\eta = 1$ in subsection 10.2.1). We note that if the 3.5 keV line is due to K XVIII, we expect to see strong correlations with the bright thermal emission below 3 keV. This continuum is not included in our three continuum models, and if we add continuum and/or line templates below 3 keV, these templates pick up TS>100 and the ALP template's TS becomes insignificant. The significance is also reduced for the shallower $\eta = 0.5$ scenario. While we cannot rule out an ALP component with robust statistical significance due to the inherent morphological similarity to the core, it is clear that an elemental origin is strongly preferred. This is also a natural interpretation given the strong incompatibility of the ALP photoconversion scenario with an excess in the Galactic Center.

We now calculate upper limits on the dark matter decay rate and sterile neutrino mixing angle. While what was described above has focused on spatially correlating the 3.5 keV excess with nearby regions of the X-ray spectrum, such analyses carry the

important caveat that they may be sensitive to the choice of background models. If the templates employed in the fit – or some combination of them – are able to mimic the emission profile of dark matter, then there would be no statistical preference for adding a (now redundant) DM template. When placing upper limits, the story is more subtle. On the one hand, as the normalization of the dark matter template is increased, additional degrees of freedom work to accommodate the 'imposed' DM component. On the other hand, if the fit is poor to begin with, a small number of critical pixels may be degenerate with a DM template; for example, within the brightest inner arcminutes of Sgr A*. In light of these competing effects we explicitly check each template combination in order to systematically assess limits.

In Table 10.2 we show the 95% confidence level lower limits on the dark matter decay lifetime for NFW, Einasto, and Burkert profiles in the Galactic center, and for the expected NFW profile for the Perseus cluster using the maximal template set: the 'All' continuum, both isotropic templates, and all lines. These have been verified to be the most conservative[11] and have also been translated into upper limits on the sterile neutrino mixing angle using Eqn. (10.2). Remarkably, our morphological analysis of the Galactic center provides the most stringent available limits. Even in the most conservative GC case, corresponding to the Burkert profile, the upper limit on the mixing angle essentially rules out preferred values for M31 in Ref. [52], while the other profiles rule these out at high significance. The GC results also rule out a standard decaying dark

[11]The sole exception is for the 'Neighboring' continuum case, where the limits weaken by a factor ~ 2 in the GC. However, if we mask the inner 2' of the DM mask, the limits become more stringent than for the 'All+Lines' case, opposite of what would happen if a true dark matter component were present.

matter interpretation of the stacked cluster analysis in Ref. [134], unless a radically different morphology is expected, as may be the case for e.g. photo-conversion of axion-like particles where emission depends also on the local transverse magnetic field structure. As shown in the previous section, even this scenario is morphologically inconsistent with observations.

The flux expected from the Perseus cluster is significantly weaker and the limits are much less stringent. In particular, the 'All' case is fully compatible with measurements of M31 from Boyarsky et al [52], but still rules out the detected mixing angle for the Perseus (MOS including core) analysis of Ref. [134]. The 'All+Lines' case is the most conservative estimate and does not limit the parameter space of interest. However, in contrast to the Galactic center case, the line templates for Perseus are broadly azimuthally symmetric, allowing them to more easily allow for a DM profile with an incorrect radial profile. For this reason, we believe these limits are likely to be overly conservative.

10.2.3 Cross-Correlating the 3.45-3.6 keV Emission

To assess the level of spatial correlation between the 3.45-3.6 keV band and different spectral regions, we compare the likelihood of a continuum only fit with that of the continuum plus a narrow 50 eV-wide "sliding window" template, which is scanned over energy. The test statistic of this template should then peak if the 3.5 keV band is correlated with all or some line emission in other regions of the spectrum. The null model used consists of the five 'All' continuum bands along with two additional low-

Target	Template Set	Profile	$\mathcal{J}$	τ	$\sin^2(2\theta)$
			(10^{18} GeV cm^{-2})	(10^{28} s)	
GC	All+Lines	NFW	6.8	>3.7	$< 1.1 \times 10^{-11}$
GC	All+Lines	Ein	8.2	>5.9	$< 7.0 \times 10^{-12}$
GC	All+Lines	Bur	1.9	>1.3	$< 3.3 \times 10^{-11}$
Perseus	All	NFW	1.4	>.55	$< 7.5 \times 10^{-10}$
Perseus	All+Lines	NFW	1.4	>.03	$< 1.5 \times 10^{-9}$

Table 10.2: $\mathcal{J}$-factors for decaying dark matter profiles and limits on a sterile neutrino's lifetime and mixing angle the Galactic center and Perseus cluster *spatial* analyses using the delta-log-likelihood method at 95% confidence level. Each of the line and continuum templates were used in deriving limits. These results exclude even the smallest value of $\sin^2(2\theta)$ from Ref. [52] at 3.4 and 4.7σ for NFW and Einasto, respectively.

energy templates covering the ranges 2.23-2.38 and 2.68-2.78 keV[12]. Next we add one more template created using photons in a 50 eV wide window (slightly lower than the FWHM energy resolution of *XMM's* MOS sensors) and scan the central energy between 1.5-5 keV, finding the maximum likelihood at each point.

In Figure 10.7 we show the test statistic as a function of the window energy (black line) for the Galactic center and Perseus cluster along with an overlay of the raw spectra for each system (light blue line with errorbars). We also indicate the 3.45-3.6 keV band (gold), continuum bands (hatched green), and spectral lines from Section 10.1.5

[12]Due to the substantial overlap of these regions with some prominent low-energy spectral lines, we have not used them previously. In what follows, however, their inclusion is a more conservative approach since any line emission 'leaking' into the continuum model will result in a lower TS for templates centered on emission lines.

(and a few extra), color coded by the ratio of their peak emissivity (electron) temperatures to that of K XVIII taken from `AtomDB 2.0.2` [51]. The width of each band corresponds to the included photon energy range while the height indicates the TS of the sliding window at the central energy of each line. The height of the continuum and 3.45-3.6 keV band are arbitrary.

Immediately, one can see a dramatic improvement to the Galactic center fit when the sliding template overlaps with any spectral line above 2.5 keV, peaking for the Ar XVII line at 3.14 keV, but also very high for the Ar XVIII and Ca XIX lines. If the Poisson uncertainty were the only source of error, the corresponding significance would be more than 10σ compared to TS=0 when adding a dark matter template. Of course, the TS becomes very large when the window overlaps with the 3.45-3.6 keV band since the fit becomes nearly perfectly autocorrelated. Contrarily, the TS runs to zero when the energy window overlaps with continuum bands already included in the fit, since little to no additional template "information" is added.

The peaks of the line emission must be compared against neighboring pseudo-continuum regions which are not included in the null model. For example, the fit improvement when the window is near 3 keV is much smaller than that of the neighboring spectral lines, indicating two things: First, the continuum emission in the 3.5 keV band is already well modeled. Since the continuum morphology changes rather slowly in energy, adding more continuum templates offers little improvement; Second, for the Galactic center the morphology of the residual emission is strongly correlated with that of atomic transition lines. Since we are using the nearby continuum as a reference point, this can

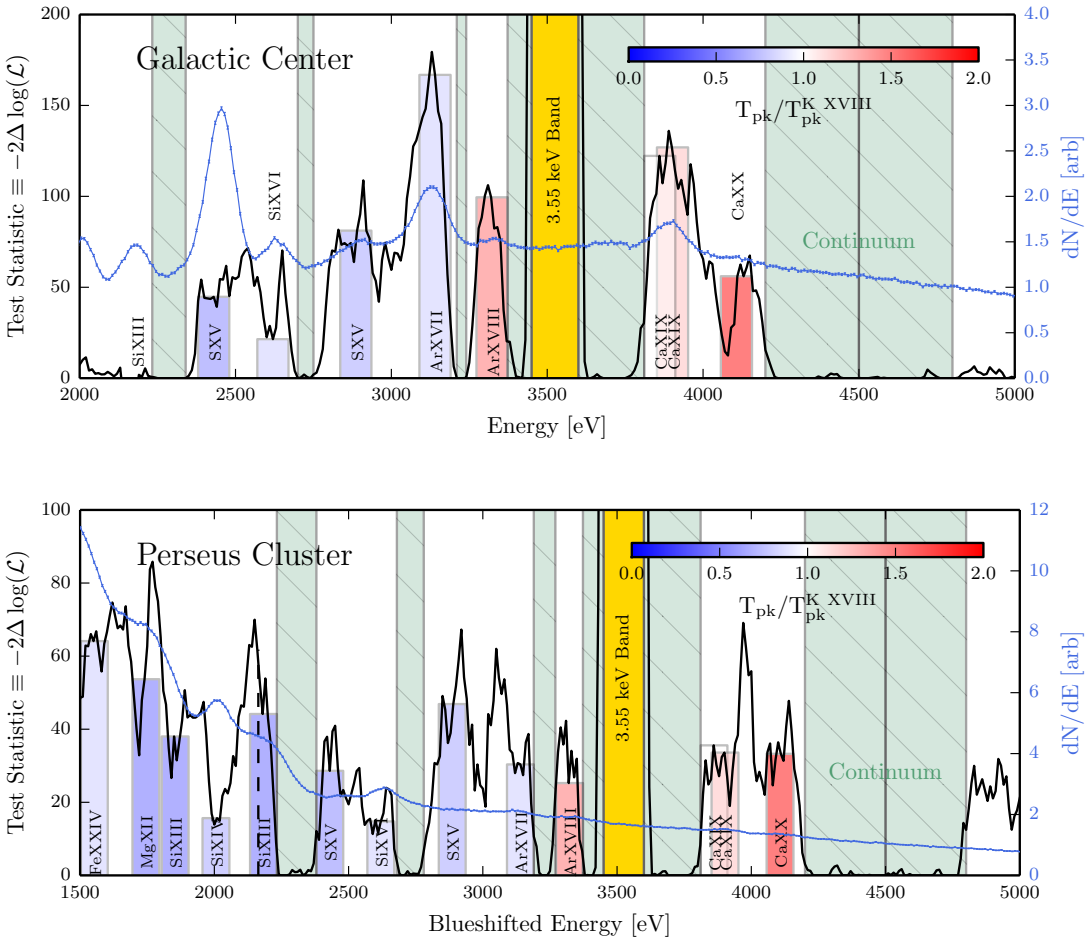

Figure 10.7: Shown in black is the test statistics corresponding to adding a sliding 50 eV-wide window template to a null model consisting of 7 continuum bands (green hatched regions). In light blue we also overlay the raw *XMM* spectrum for the Galactic center (top) and Perseus cluster (bottom). The 3.45-3.6 keV band is highlighted in gold. The brightest spectral line templates (with correct widths) are color coded according to the ratio of a given line's peak emissivity temperature to that of K XVIII. T_{peak} for K XVIII is also represented by a dashed line at 2.16 keV, visible in the Perseus plot. For both the Gaclactic center and Perseus the TS stemming from adding a dark matter template is zero.

only be attributed to the presence of a distinct emission component over a narrow en-

ergy range. The cool lines below 2.5 keV are seen to have the opposite behavior, where

the TS is instead reduced compared to the nearby continuum model. This is indicative of a negative correlation with these spectral lines, and their template normalization is preferentially driven to zero.

For each emission line, there exists a unique electron temperature where the emissivity peaks. If each element is assumed to be identically distributed, one would then expect a parallel morphology between emission lines that peak at similar temperatures. Roughly speaking, this is observed here, where the very-cool and very-hot lines do not provide a substantially improved fit. It is difficult to quantify this further for several reasons. Firstly, over the few keV energy range of interest here, the emissivity as a function of temperature changes by less than a factor two for the emission lines considered. Thus we have only weak sensitivity to the underlying plasma temperature using morphology. Secondly, it is important to note that chemical abundances are not uniform over the physical scales probed here. As noted by e.g. Ref. [48] in studying Sgr A East, heavy elements such as iron are distributed much more compactly compared with He-like elements. More generally, recent simulations of supernova explosions show that hydrodynamic instabilities can lead to highly asymmetric ejection of heavy elements [535]. These factors complicate, for example, showing a nearly perfect correlation between suspected K XVIII at 3.5 keV and a spectral line with identical peak emissivity temperatures while also showing anti-correlation with cooler and hotter transition lines.

In the lower-panel of Figure 10.7 we show results for the Perseus cluster. Here the situation is very different. The relevant physical scale is increased by more than 10^3 and emission is dominated by the approximately isothermal cool-core surrounded

by increasingly warmer and fainter radial shells. This is in contrast to the Galactic center, where the continuum flux is dominated by non-thermal emission (predominantly unresolved point sources). On this scale, entire galaxies are nearly point-like and the relative distribution of heavy elements is averaged out, depending much less on the atomic species in question. Emission lines above 2.5 keV are much weaker in Perseus, appearing only as small bumps in the spectrum. Still, distinct peaks are observed for the cooler Si XII and S XV lines while the Ar lines are more ambiguous. The hot Ca lines are now anti-correlated compared to the in-between continuum region at 4 keV.

Below 2.4 keV the flux rises very rapidly and it becomes difficult to disentangle the continuum and line emission. We note that the K XVIII line at 3.515 keV peaks at a plasma temperature of ≈2.16 keV, indicated by a vertical dashed line. In the optically thin limit, the power spectrum of the corresponding thermal bremsstrahlung is exponentially suppressed above 2.16 keV and is relatively flat below, having at most a $T_e^{-1/2}$ dependence on temperature. Since we would like to test for correlation with this very low temperature continuum, this is not included in our baseline model. The suppressed TS observed at Si line energies could therefore be interpreted as anti-correlated Si lines plus a strong continuum component due to a low temperature plasma. Such a plasma must exist, as the core temperature of Perseus has been measured to have a strong component near $kT \approx 2$ keV [519]. We note that the elemental abundances of bremsstrahlung-generating ionized hydrogen and K XVIII are likely to be different. The line structure is too dense below 2 keV to gain additional insight with such a simplistic analysis.

For the Perseus cluster, our key finding is thus that the strongest correlations are observed with the cluster's core, namely continuum emission below $\approx$ 2.16 keV and select lines that peak at similarly low electron temperatures. Such correlation is expected if the emission is due primarily to an atomic transition line of K XVIII, and is *not* expected if the emission is due to dark matter. The recent findings of Ref. [510] reveal a similar result, showing that the ratio of 3.5 keV emission in the core ($r < 6$ arcmin) to the 'confining-region' ($r > 6$ arcmin) is at least a few times too large to be compatible with decaying dark matter.

In summary, after finding no statistically significant morphological evidence for a dark matter component in Perseus or the Galactic center, we have taken a narrow window in photon energies and checked for regions of the spectrum with similar morphology to that of the 3.45-3.6 keV band. In the Galactic center the background is highly non-thermal and we see very strong statistical evidence for correlation with known spectral lines. At face value, the lines that most closely match the 3.5 keV morphology are those whose emissivity peaks at electron temperatures similar to that of K XVIII. Thermal emission from such a population of $kT_e \approx 2.1$ keV electrons is sub-dominant compared with the unresolved point source component. In the Perseus cluster, we see more ambiguous evidence of line correlated emission in the 3.5 keV band. The cool thermal emission is dominant in this system and the line fluxes above 2.6 keV are very low. Below 2.6 keV, the dense line structure also inhibits a clean correlation with continuum versus line emission. We note, however, that either of these cases could be taken as circumstantial evidence for K XVIII, or other atomic elemental emission since, for

example, a $kT_e \approx 2.1$ keV electron gas maximizes the K XVIII emission and is already measured in the core of Perseus.

10.3 Discussion of Morphological Analysis

We have examined the morphology of the X-ray emission at 3.5 keV from the Galactic center region and from the Perseus cluster of galaxies. We employed a variety of different choices to model the morphology of the continuum emission, and studied the resulting residual signal at 3.5 keV. Though it is difficult to ensure these residuals are dominated by the line signal and not mismodeling of the continuum, the azimuthal and radial distributions are strikingly different from the prediction from dark matter decay. In the case of the Galactic center, the 3.5 keV emission has a distinct quadrupolar distribution and is completely incompatible with emission from axion-like particle conversion. In the Perseus cluster 3.5 keV emission strongly overlaps with the cluster's cool core. While the ALP scenario cannot be ruled out for Perseus, it is strongly disfavored after adding even a single additional low-energy continuum or line template.

Utilizing a sliding-window template, we demonstrated that the 3.5 keV emission most prominently correlates with the morphology of strong emission lines associated with Ar and Ca transitions in the case of the Galactic center. For Perseus, the correlation is observed in lines with a comparable peak emission temperature to K XVIII ($kT_e \approx$ 2.16 keV) and/or the corresponding thermal bremsstrahlung. This is generally observed to feature a distribution overlapping with the cluster's cool core. In both the Galactic center and Perseus, we thus find strong evidence in favor of a plasma emission origin for

the observed 3.5 keV line and against a dark matter interpretation.

Finally, utilizing the same binned-likelihood approach, we set the most stringent constraints to date on the lifetime of a dark matter particle decaying into a final state including a 3.5 keV monochromatic photon. By adding a dark matter template and allowing all template normalizations to float in this process, these limits (and fits) are resilient against continuum mismodeling and robustly exclude a dark matter decay origin for the 3.5 keV line observed from clusters.

We believe that the burden of proof for a claim of discovery of any "new" physics must be set as high as reasonably possible. This includes pursuing with vigor Occam's razor, thus focusing with due diligence on any explanation that does not invoke unnecessary entities, and exploring with care the possible backgrounds and systematic errors.

Chapter 11

The WMAP-Planck Haze

Data from NASA's *Wilkinson Microwave Anistropy Probe* (WMAP) have fostered great advances in both precision cosmology and in the understanding of processes associated with the interstellar medium of our own Galaxy. WMAP also brought about unexpected observational results, including the detection of spinning dust emission [536, 537, 538, 539] and a mysterious diffuse microwave emission extending 20° around the Galactic Center, known as the "WMAP haze" [540]. While originally associated with free-free emission [540], follow-up analyses showed that the haze spectrum was too soft to be attributed to free-free emission, but too hard to match the diffuse Galactic synchrotron emission produced by relativistic cosmic ray electrons [541].

While some authors have criticized the original analysis procedure [542], or the synchrotron nature of the haze [543], both arguments have been rebutted in detail [544, 545]. Excitingly, the *Planck* mission has recently presented conclusive evidence in favor of the existence of the microwave haze [546], employing superior background

rejection methods to those available to the WMAP team. Specifically, the *Planck* data analysis proceeded along two distinct component separation techniques, one following the original WMAP template analysis of Ref. [541], and a more sophisticated Bayesian approach based on Gibbs sampling. Both techniques confirmed the existence of an anomalous diffuse haze in the Galactic Center (GC) region across multiple frequencies, with a spectral index $\beta_H = -2.55 \pm 0.05$, consistent with that found from WMAP data. Furthermore, future *Planck* studies will analyze the polarization of the haze, providing an even more stringent test of the synchrotron nature of this emission.

Several authors have considered dark matter annihilation as a possible source of the Galactic haze (see e.g. Ref. [547, 548, 549, 550, 551, 552, 553, 554, 555, 556, 557, 558, 559]) as well as in local extragalactic dark matter searches [560, 561, 562, 563, 564, 565]. The dark matter interpretation is consistent with theoretically well motivated ranges for the mass and annihilation cross section of weakly interacting massive particles, common to many extensions of the standard model of particle physics [566, 567, 568]. Furthermore, it was noted recently that the WMAP haze is consistent with the annihilations of light ($m \sim 10$ GeV) dark matter candidates which are also capable of accounting for a number of other reported observations [551], including direct detection signals from DAMA/LIBRA [569], CoGeNT [570, 571] and CRESST-II [572], as well as the spatially extended spherically symmetric excess of γ-rays observed around the GC by the Fermi-LAT [573, 456, 574], the extremely hard synchrotron spectrum observed in multiple filamentary arcs surrounding the GC [575], and the isotropic radio excess observed by the ARCADE collaboration [576] (see Ref. [577, 578] for further discussion of these

observations and experiments).

Recent observations indicate that the observed morphology of the microwave excess haze exhibits a strong correlation with a diffuse feature discovered at GeV energies by the *Fermi* Large Area Telescope, known as the Fermi bubbles [579] (previously known as "Fermi haze" [580], see also [581]). This suggests a common origin for the observed emissions at radio and gamma-ray energies [582]. Hypotheses as to the origin of this additional cosmic ray population include anomalous enhancements to the supernova activity in the relevant region and time [583], peculiar cosmic ray propagation in the region of interest, perhaps associated with Galactic winds [584], central nuclear activity fueling cosmic ray jets [585], or an additional population of cosmic ray electrons distinct from the ordinary diffuse cosmic ray population in the Galactic plane [549]. While high mass dark matter models are capable of simultaneously explaining energy *spectrum* of the WMAP haze and Fermi Bubbles, no dark matter model is capable of accommodating the sharp edges observed at high galactic latitude [550], suggesting a much more complicated story if dark matter is to remain a primary progenitor of the WMAP haze.

11.1 Testing the Dark Matter Origins of the Haze with Nearby Observations of Spiral Galaxies

In this Chapter, we point out that if the WMAP haze results from dark matter annihilation, a radio signal with a similar luminosity and morphology should be emitted from other galaxies, so long as these galaxies are comparable to our own in terms of size

and other physical characteristics. This comparison may not hold in scenarios where the haze is of astrophysical origin (e.g. in the case that the haze is powered by episodic nuclear activity in the GC). The purpose of this study is to identify a suitable set of galaxies similar to the Milky Way, estimate the radio "haze" expected from these candidate galaxies assuming a dark matter annihilation origin and benchmark values for the parameters governing the propagation of charged leptons in each galaxy, and then employ radio observations to obtain constraints on the dark matter annihilation origin of the Milky Way haze.

In order to interpret the results of this comparison, it is necessary to estimate the uncertainties in the theoretical expectation for the dark matter radio haze in external galaxies. Relatively little is known about propagation of cosmic rays, magnetic fields, or dark matter distribution in external galaxies. Any or all of these characteristics could vary considerably from galaxy-to-galaxy, even among those galaxies that are similar in size and morphology to the Milky Way. We therefore study in detail the expected range of variation in the radio luminosity of the dark matter radio haze originating from such variations.

This chapter is structured as follows. In the next section, we describe the selection criteria we employ to select the relevant set of galaxies to investigate. In Sec. 11.1.2, we address the systematic uncertainties on the estimate of the haze luminosity. In Sec. 11.1.3 we produce a Monte Carlo model indicating the expected variation in the dark matter induced synchrotron signal due to these systematic uncertainties. In Sec. 11.1.4, we compare our predictions with radio data. Lastly, we discuss implications

of our results and future directions in Sec. 11.1.6.

11.1.1 Galaxy Sample Selection

In order to identify galaxies with size and morphology similar to the Milky Way, we utilize the 1.49 GHz radio data from the Condon Atlas of Spiral Galaxies (hereafter refered to as CA) [586]. We obtain morphological information for each galaxy by cross-referencing the CA with the HyperLeda database[1], and restrict our analysis to galaxies with a morphological type $1.5 < t < 4.0$ [2], which limits the uncertainties associated with edge-on galaxies, for which morphological properties can be difficult to determine. We note that this conservative cut loosely includes type Sab-Sbc galaxies, where the Milky Way is typically classified near Sbc [587].

Apart from well-studied galaxies such as Andromeda, no specific information on the dark matter density profile is available for the galaxies in the CA. Most of these galaxies, however, have estimates for the values of the maximum rotational velocity, given by observations of 21 cm line widths. These values are highly correlated with the total enclosed mass in each galaxy. We place a cut on the maximum rotational velocity of 180 km/s$< v_{rot} <$ 280 km/s to ensure a mass and size compatible with the Milky Way, where $v_{rot} \approx 235$ [588].

After each of the above cuts is applied, the resulting sample contains 66 galaxies which are used throughout this analysis. We then rank the galaxy candidates based on the observed radio flux in two ways. First, we calculate the total radio luminosity

[1]The HyperLeda database may be found at http://leda.univ-lyon1.fr/

[2]Mapping between Hubble classification and de Vaucouleurs morphological type index may be found at http://leda.univ-lyon1.fr/leda/param/t.html

at 1.49 GHz given the total observed radio flux (S) reported in the CA and the best-fit distance estimate as given by the NASA/IPAC Extragalactic Database (NED)[3]. Second, we calculate the luminosity 2 kpc above or below the Galactic plane by using the peak flux measurement (S_P) reported by the CA, as well as the elliptical Gaussian defined by the FWHM at 1.49 Ghz along the major and minor axes, with the major axis assumed to lie along the Galactic plane as calculated by optical data. The resulting list is then sorted in ascending order of their relative luminosity, found by multiplying the flux times the square of the distance, and the two rankings are averaged. Seven of the *lowest luminosity* galaxies are analyzed in more individual detail than the full 66 galaxy sample. Ultimately, this subset of the 7 galaxies with the lowest cosmic ray background will provide the most stringent limits on a dark matter induced haze. We note that all statistical comparisons showing the percentage of galaxies which are underluminous are calculated using the full population of 66 galaxies, to remain consistent with the total distribution from which galaxies are drawn. We also note that all of our ensuing statistical statements are made by employing the large, 66 galaxy sample, but our constraints are derived from the most promising 7-galaxies sub-sample. Since we would have gotten even more stringent constraints had we considered more than the 7 most promising objects, we deem our results as conservative (i.e. they in principle can be improved upon).

In order to estimate the physical size of the cosmic ray diffusion region, we use as a proxy the projected size of the major axis of each galaxy, based on the distances

[3]The NASA/IPAC Extragalactic Database (NED) is operated by the Jet Propulsion Laboratory, California Institute of Technology, under contract with the National Aeronautics and Space Administration.

Name	Type	t	i	$v_{\rm rot}$	S	S_p	D	Rank$_L$	Rank$_{\rm 2kpc}$	Mean Rank
			[deg.]	[km/s]	[mJy]	[mJy]	[Mpc]			
NGC 4448	SBab	1.8±0.6	69.00 [589]	221.54	1	0.9	13.1	1	2	1.5
NGC 4698	Sab	1.7±1.0	73.44	201.13	0.6		21.9	2		2
NGC 4394	SBb	3 ±0.4	16.55	255.13	0.7	0.6	21.9	3	3	3
NGC 7814	Sab	2±0.2	90.00 [590]	230.9	1.1	1.1	25.8	4	6	5
NGC 1350	Sab	1.9±0.6	64.79	199.87	1.1	0.8	30.2	5	7	6
NGC 0224	Sb	3±0.4	72.17	256.7	8400	14.5	0.7	12	1	6.5
NGC 2683	Sb	3±0.3	82.79	202.92	65.9	14.6	8	13	5	9

Table 11.1: Candidate galaxies from the Condon Atlas. t, i , $v_{\rm rot}$, S, S_p, refer to the de Vaucouleurs morphological type, inclination, maximum rotational velocity, total flux, and peak flux, respectively. Rank$_L$ (Rank$_{\rm 2kpc}$) ranks the total (respectively, 2 kpc off disk) luminosity, in ascending order. Unless otherwise noted, inclination, type, and rotational velocity are from the HyperLeda database.

obtained from NED and an angular size from HyperLeda, defined as the isophotal level 25 mag/arcsec^2 in the B-band [591]. In Table 11.2, we list the mean distance for the galaxy sample, as given in the NED database. For each galaxy in the sample, we extrapolate the physical size of the Galaxy's major axes. We also report the ratio of the major-to-minor axis in the last column, although we assume cylindrical symmetry for the simulated diffusion region.

We conclude that all of our candidate galaxies have comparable diffusion region sizes, with the possible exceptions of NGC 4448 and NGC 4394, which exhibit a potentially smaller radius and a smaller major-to-minor axis ratio. These galaxies also have the largest distance uncertainties, directly affecting the reported semi-major axis.

Name	NED Distance [Mpc]	Major Axis [kpc]	Axes Ratio
NGC 0224	0.7	60.2	2.55 ± 0.29
NGC 1350	20.9	52.4	1.99 ± 0.15
NGC 2683	10.2	46.9	3.51 ± 0.42
NGC 4394	16.8	28.4	1.04 ± 0.07
NGC 4448	13.0	10.0	1.53 ± 0.15
NGC 4698	23.7	43.8	2.45 ± 0.16
NGC 7814	17.2	36.4	2.32 ± 0.14

Table 11.2: Distances and sizes of the candidate sample galaxies.

11.1.2 The Dark Matter Haze in External Spiral Galaxies

Although we employ morphological information to choose a sample of galaxies similar to the Milky Way, there are several other parameters capable of impacting the radio luminosity of a dark matter haze which can vary significantly from galaxy-to-galaxy. Generically, these parameters break down into three categories:

1. parameters that control the dark matter density profile,

2. parameters that control the diffusion of cosmic rays, and

3. parameters that control the magnetic field strength in each sample galaxy.

In Table 11.3 we show the default, maximum and minimum value for each parameter used throughout this work, and in Figure 11.2 we show the effect of changes in each individual parameter on the synchrotron luminosity due to dark matter annihilation at 1.49 GHz. In the following, we discuss the variations in the radio haze produced by of

these parameters in detail.

11.1.2.1 Dark Matter Density Profile

As the dark matter annihilation rate is proportional to the square of the dark matter density, the total synchrotron luminosity depends not only on the total dark matter mas (which can be reasonably estimated from galactic rotation measurements) but also on the density distribution of dark matter in each galaxy. In this work, we assume a generalized Navarro-Frenk-White (NFW) profile [89] with a radial density profile given by:

$$\rho(r) = \rho_s(\frac{r_s}{r})^{\alpha}(1 + \frac{r}{r_s})^{-3+\alpha} \tag{11.1}$$

where r_s is a scale radius which governs the turnover to the $r^{-\alpha}$ profile, ρ_s is a dark matter density normalization constant, and α governs the inner slope of the dark matter density. In the original NFW profile, $\alpha = 1$, in agreement with the results of certain dark matter-only simulations of structure formation, e.g. Ref. [592]. However, recent simulations which include the effects of baryons on galaxy evolution have found that the cooling and contraction of the baryonic density profile tend to steepen the dark matter density profile in the central regions [593]. This effect, known as baryonic contraction, generally leads to values of α in a range between 1.2-1.7, depending on the degree of contraction. In contrast, other numerical simulations which include a large degree of baryonic feedback have found that baryons can flatten the inner slopes of the dark matter profile, producing distributions with a flat density core as large as 1 kpc in size [594].

In our simulations we allow for r_s to change by a factor of 2 from our default choice of 22.0 kpc, and we allow α to change by a factor of 1.5 from a default value of 1.0. We normalize the dark matter density profile the dark matter density at the solar position ($R_\odot = 8.5$ kpc) to a range within a factor of 5 of the central value of 0.3 GeV cm^{-3} [595].

Figure 11.1 (top) illustrates that the haze luminosity depends strongly on the assumed value for α, increasing precipitously for profiles with $\alpha > 1$. We note that this will affect our sample producing a logarithmically asymmetric distribution in luminosity and favoring large radio fluxes. We also note only a marginal dependence on the value of r_s as the annihilation which produces the radio haze is largely confined to within the inner several kpc around the center of each galaxy.

11.1.2.2 Cosmic Ray Diffusion

As charged particles propagate through the galaxy, they are deflected by the turbulent magnetic field structure and proceed in a random walk that can be described as a standard diffusive process. Since Galactic magnetic fields are thought to be produced primarily by magnetohydrodynamic turbulence, they are highly dependent on astrophysical parameters such as the distribution of molecular clouds, ionized gas, star formation rates, etc. which vary wildly between galaxies [596]. Additionally, the nature of charged particle propagation depends sensitively on the scale of the magnetogydronamic fluctuations compared to the gyroradius of the charged particle in the magnetic field. This is a local phenomena which is not uniform across different regions of the Galaxy.

Parameter	[units]	$c_{\mathrm{f.f.}}$	Central	Min	Max
B_0	μG	2	60	30	120
r_0	kpc	2	4.0	2.0	8.0
z_0	kpc	2	1.8	0.9	3.6
D_0	$\mathrm{cm^2 s^{-1}}$	10	1.0 x 10^{29}	1.0 x 10^{28}	1.0 x 10^{30}
h_{diff}	kpc	10-2	16	1.6	32
R_{diff}	kpc	2	20	10	40
$u_{\mathrm{rad}}/u_{\mathrm{rad,MW}}$		5	1	.2	5
v_A	km $\mathrm{s^{-1}}$	1	25	25	25
γ_D		1	.33	.33	.33
ρ_0	GeV $\mathrm{cm^{-3}}$	5	0.30	0.06	1.50
r_s	kpc	2	22	11	44
α		1.5	1.0	0.67	1.5

Table 11.3: Nuisance parameters employed to estimate the range for a dark matter induced haze in external spiral galaxies. Note that we also place an additional constraint on each simulation that the diffusion height must not exceed the simulated diffusion radius. The Alfven velocity v_A and the energy dependence index, γ_D, of the diffusion coefficient are held fixed at the default values for all analyses, though the effects on the synchrotron luminosity are presented in Figure 11.1.

Although an exact solution to the diffusion equation for a galaxy is not attainable, cosmic ray propagation codes exist that allow for realistic estimates of charged particle diffusion in the Milky Way. The predictions of these codes can be tested by observable quantities such as the ratios of radioactive secondaries to primary species observed at the solar position, large scale gamma-ray emission, and other diffuse Galactic radiation backgrounds. The *Galprop* code stands at the forefront of this effort, performing numerical calculations of particle propagation and of the resulting multi-wavelength emission, taking into account effects such as the diffusion, reacceleration, and convec-

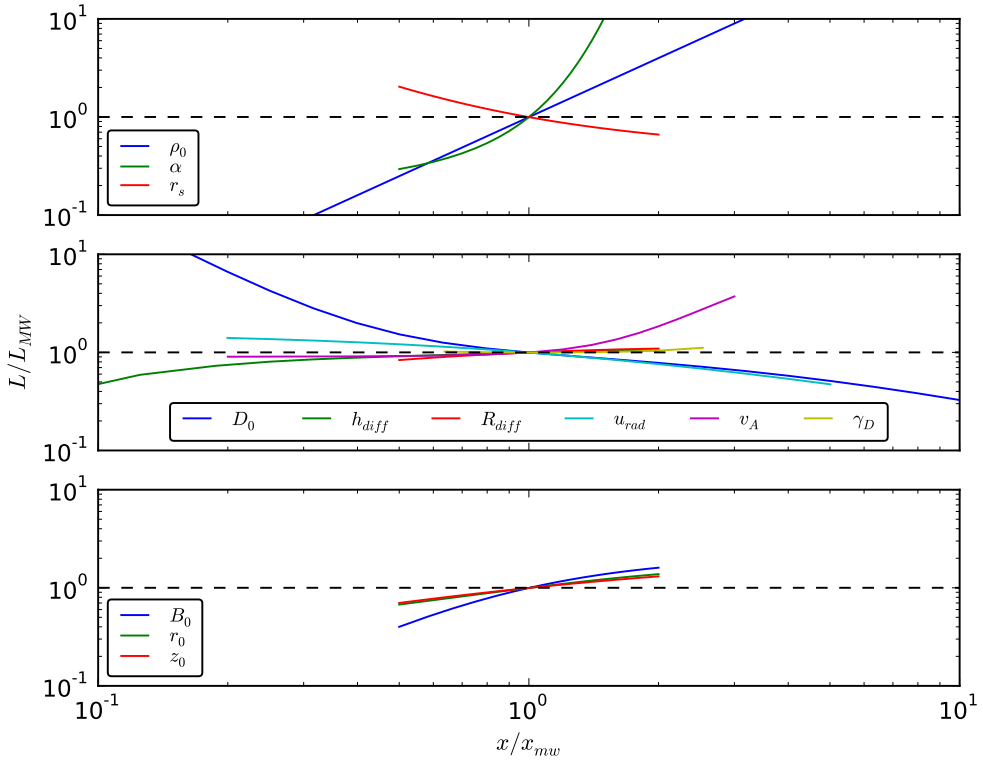

Figure 11.1: The effect of variations in the nuisance parameters on the luminosity of the dark matter synchrotron haze at 1.49 GHz in units of the benchmark value, $L_{\rm MW}$. We note that variations in h_{diff} closely floow See Table 11.3 and text for more details.

tion of cosmic rays, the intensity as well as the morphology of the Galactic magnetic and interstellar radiation fields, and the morphology of molecular gas [413]. In this analysis, we employ *Galprop* (v. 54) to study the effect of varying four parameters, which previous analyses of the WMAP haze in the Milky Way determined to have the largest effect on the synchrotron signal due to dark matter annihilation [552]. Specifically we examine changes in the mean diffusion constant, D_0, whose benchmark value we take to be 1.0×10^{29} cm^2 s^{-1}, the radius ($R_{\rm diff}$) and half-height ($h_{\rm diff}$) of the diffusion region,

which we take to be 20 kpc and 16 kpc for our central values, and the normalization of the inter-stellar radiation field, which we take to be unity in units of the default *Galprop* model.

Figure 11.1 (middle) examines the changes in the mean Milky Way luminosity for variations in our diffusion setup, finding only an minimal effect from changes in the size of the diffusion region, on the order of 10% for regions double the default size. However, changes in the diffusion constant produce a larger effect, especially in the regime of low diffusion constants where electrons created by dark matter annihilations are efficiently trapped in the galaxy. Large increases in the strength of the interstellar radiation field also greatly decrease the luminosity of the synchrotron haze, as charged leptons lose a significant fraction of their power to inverse Compton scattering as opposed to synchrotron. Variations of the default the Alfven velocity, v_A=25 km/s, show the effect the electron re-acceleration which negligibly decreases the luminosity at lower values and increases as it is raised to 100 km/s. The energy index of the diffusion coefficient, γ_D, is also shown and indicates that the default value of $\gamma_D = 0.33$ produces the minimum luminosity and variations are positive over the rest of the physical domain ($.2 \leq \gamma_D \leq 7$). Due to the inherent difficulty in constraining these parameters physically, both the Alfven velocity and the energy index of diffusion are held fixed at their conservative default choices for the remainder of this section.

11.1.2.3 Galactic Magnetic Fields

In addition to influencing the propagation of charged cosmic rays, Galactic magnetic fields also control the intensity and spectrum of synchrotron radiation produced by cosmic ray electrons as they travel through the interstellar medium. Unfortunately, the mean intensity of magnetic fields is highly uncertain, even in the case of the Milky Way. However, constraints from the rotation measures of pulsars place the mean magnetic field strength in the Milky Way to be approximately 4-6 μG [597]. In this section, we adopt the a magnetic field model described by the functional form $B(r,z) = B_0 \exp(-r/r_0) \exp(-z/z_0)$, and vary the parameters of this expression as described in Table 3.

In Figure 11.1 (bottom) we show the variation in the dark matter synchrotron luminosity for changes in the strength of the magnetic field in a given galaxy. We find only moderate changes when we shift the overall amplitude of the magnetic field, which is primarily due to the large fraction of electron energy which is lost to synchrotron for all magnetic field strengths. The dependence of the total synchrotron intensity on the radial and zenith scale of the magnetic field is even more negligible, due to the fact that the synchrotron intensity is dominated by the very inner region around each galaxies' center.

11.1.3 Monte Carlo Modeling of Systematic Uncertainties

In order to estimate a probability distribution for the luminosity of each external galaxy, we produce a Monte Carlo sample, varying each parameter listed above

within the minimum and maximum values provided in Table 3. We sample all of parameter space linearly except for the diffusion constant D_0 and the interstellar radiation density u_{rad} which are sampled logarithmically. In the case of the diffusion constant the effect of logarithmic sampling can bias the distribution toward higher luminosities as a low diffusion constant more efficiently traps electrons and positrons in the galaxy. While this does produce somewhat less conservative constraints, linear sampling would have produced unrealistically large diffusion constants on average and we find that the logarithmic results are generically more compatible with the range of values preferred by cosmic-ray data. The remaining parameters are either sub-dominant drivers of the luminosity, or are only varied by a factor of 5 or less. In these cases, we do not expect Bayesian priors to have a significant effect. We provide an additional constraint on the parameters for the dark matter density profile, specifying that the total mass enclosed within 100 kpc fall between 0.25 and 2.0 times the value for the default Milky Way Halo. This is consistent with the fact that we select galaxies in our sample within a relativity narrow mass range as fixed by our constraint on $\mathrm{v_{rot}}$.

In order to estimate a probability distribution for the luminosity of each external galaxy, we produce a Monte Carlo sample, varying each parameter listed above within the minimum and maximum values provided in Table 3. We sample all of parameter space linearly except for the diffusion constant D_0 and the interstellar radiation density u_{rad} which are sampled logarithmically. In the case of the diffusion constant the effect of logarithmic sampling can bias the distribution toward higher luminosities as a low diffusion constant more efficiently traps electrons and positrons in the galaxy.

While this does produce somewhat less conservative constraints, linear sampling would have produced unrealistically large diffusion constants on average and we find that the logarithmic results are generically more compatible with the range of values preferred by cosmic-ray data. The remaining parameters are either sub-dominant drivers of the luminosity, or are only varied by a factor of 5 or less. In these cases, we do not expect Bayesian priors to have a significant effect.

Figure 11.2 shows the distribution in the total luminosity calculated at 1.49 GHz for our Monte Carlo sample, illustrating the luminosity due both to dark matter annihilation as well as the cosmic ray luminosity for a galaxy with a cosmic ray injection rate equal to that of the Milky Way. A time-independent change in the cosmic ray injection rate would simply linearly shift the cosmic ray induced radio luminosity of a given galaxy. We also show for comparison the distribution of luminosities for all 66 "Milky-Way-like" candidates taken from the CA catalog, using the best-fitted distance given by NED. In Figure 11.3, we show the distribution of dark matter-induced luminosities as determined by our Monte Carlo as evaluated along the Galactic plane at a distance of $r = 5$ kpc from the GC (red line), and above the Galactic plane at a height $z = 1$ kpc (blue line). Also repeated for comparison is the integrated luminosity due to dark matter.

At this point, we note several key results:

1. The total synchrotron luminosity from dark matter is almost invariably found to be subdominant to that from astrophysical cosmic ray sources, typically by more than one order of magnitude. We note from Figure 11.1 that this conclusion depends primarily on the dark matter profile, as the cosmic ray injection intensity

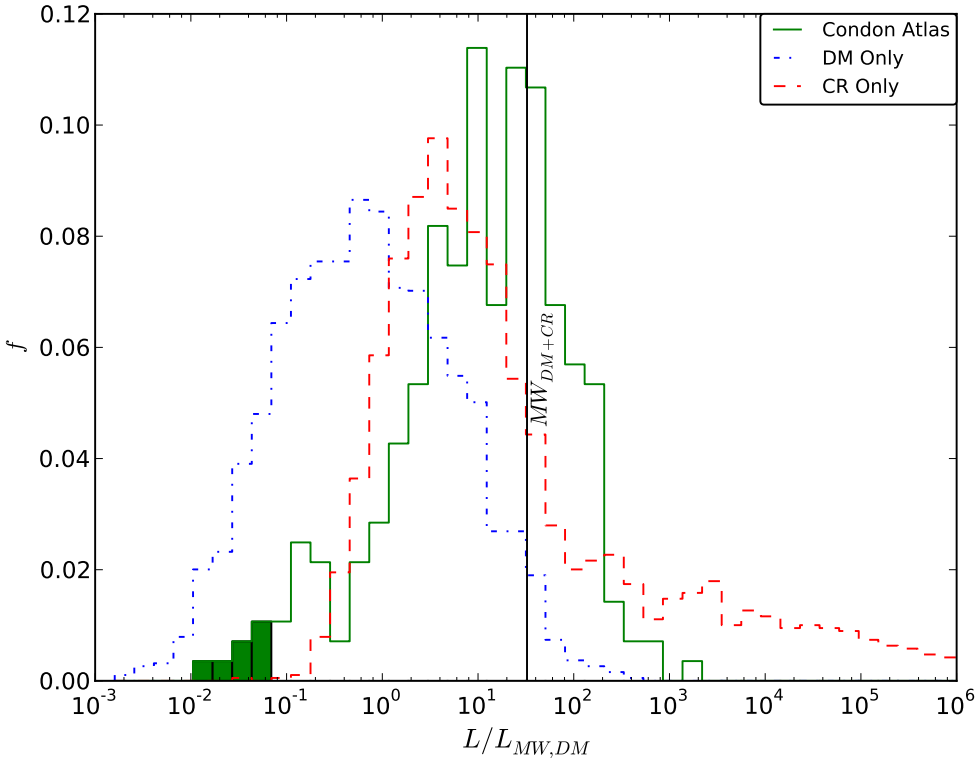

Figure 11.2: Distribution of 1.49 GHz luminosity ratio $L/L_{MW,DM}$ where L is the total integrated luminosity and $L_{MW,DM}$ is the luminosity due to dark matter for the canonical Milky Way model. The benchmark luminosity for dark matter plus cosmic rays is indicated by the vertical line. The simulated sample contains 2000 runs randomly distributed in the parameter space of tab. 11.3 with mass restricted to lie within $0.25-2$ times the mass of the Milky Way. We plot the contributions due to dark matter only (dot-dashed blue) and to cosmic rays only (dashed red) against extrapolated luminosities of 66 Condon Atlas galaxies meeting morphological cuts described in Section 11.1.1 (solid green). Only 11.2% of the simulated dark matter-induced haze luminosities are a factor 20 smaller than our benchmark value, and only 1.42% are a factor 100 smaller. Shown in shaded green are the 7 lowest background galaxies selected from the Condon Atlas.

is not altered in our simulations. This also implies that setting constraints on dark matter annihilation in external galaxies by assuming that the radio luminosity due to astrophysical sources is negligible is an extremely conservative approach, as the

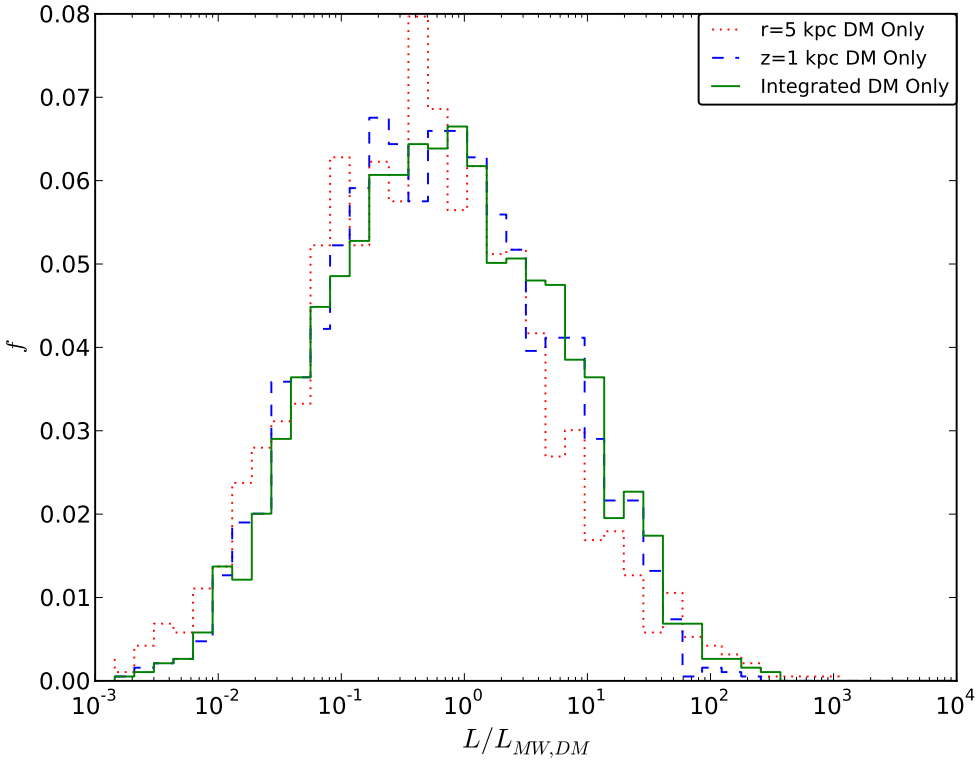

Figure 11.3: Distribution of 1.49 GHz luminosity ratio $L/L_{MW,DM}$ where L is the luminosity evaluated at a radius $r = 5$ kpc along the Galactic plane (dotted red), height $z = 1$ kpc above the Galactic Center (dashed blue) and $L_{MW,DM}$ is the luminosity due to dark matter for the canonical Milky Way model. The sample is identical to that of Figure 11.2 and we have repeated the integrated dark matter component (solid green).

radio luminosities of most galaxies is expected to be dominated by cosmic rays from astrophysical sources.

2. Our modeled astrophysical synchrotron radiation has a more pronounced high luminosity tail than is seen in the distribution of the CA galaxies, implying either that the range in the parameter space for cosmic ray diffusion is tilted towards very radio bright systems, or that the cosmic ray injection sources in our model galaxies

are typically smaller than in the Milky Way. This is not true for our distribution of dark-matter induced emission, however, which is symmetrically distributed in log-space around the luminosity of the Milky Way.

3. Only 11.2% of the simulated integrated dark matter-induced haze luminosities are a factor of 20 smaller than our benchmark value, and only 1.4% are a factor of 100 smaller. This implies that the dark matter haze is a reasonably resilient feature among a large array of dark matter density profiles and diffusion scenarios.

4. The simulated dark matter hazes can also be parameterized by the luminosity evaluated at 5 kpc along the Galactic plane and 1 kpc above the Galactic plane. In the r (z) directions, only 15.2% (12.3%) of simulations are suppressed by a factor 20 and 3.8% (1.7%) are suppressed by a factor 100. In the next section we find that the strongest constraints are typically set by comparing the flux along the major-axis. For high inclination sources this is coincident with the radial direction considered here.

11.1.4 Constraints from Radio Observations

11.1.4.1 Methodology

In addition to the above estimates of the total synchrotron power for a wide sample of values for the nuisance parameters, the *Galprop* code predicts in detail the morphology of the synchrotron emission stemming from dark matter annihilation. For each of the 7 lowest cosmic-ray background CA candidate galaxies listed in Table 11.1

this morphological information allows us to set constraints in two additional ways besides considering only the total integrated luminosity:

- First, we can set constraints by comparing the peak flux contour in each galaxy against the predicted dark matter flux at the Galactic Center.

- Second, we can compare the flux above or below the Galactic plane, where the dark matter produced haze is expected to be most significant compared to the synchrotron flux from cosmic rays. In addition we can compare the flux along the galactic plane in each direction. In order to do this, we calculate the flux at the outermost observed radio contour for each galaxy and compare it to the modeled dark matter flux. We note that Figure 11.3 shows that the scale of the luminosity distributions from our dark matter models is expected to be similar in all cases.

For the simulations presented in this section, we set all relevant parameters to the central values quoted in Table 11.3, except for the radial size of the diffusion region, which we set to the size of the major axis as given in Table 11.2. We then use *Galprop* to calculate the synchrotron emission throughout our model galaxy as a function of the radius and height, and integrate the emission over the line-of-sight based on the observed inclination of each candidate galaxy, correcting for the instrument beam-width for each galaxy. We note two subtle points in this analysis.

Firstly, the diffusion height employed in this analysis is extremely large. Although this will produce a slightly overluminous synchrotron signal, the results of Section 11.1.2 show that this is a small effect until the diffusion height becomes less than 2 kpc.

This follows from the exponential falloff of the magnetic field with a default characteristic height of 1.8kpc, which is effectively halved when considering the synchrotron luminosity ($L_{sync} \propto B^2$). We have confirmed in detail that the effect of changing the diffusion height has only an extremely suppressed effect until $h_{diff} \lesssim 2$ kpc. Very small diffusion heights can have a more pronounced effect when evaluating the off-peak flux along the radial direction because the electrons and positrons can escape through the top and bottom of the diffusion region before they are able to diffuse to large radii. For flux measurements at $r = 5$ kpc along the radial direction, the flux can vary up to $\sim 20\%$ when the diffusion height becomes less than 4 kpc. However, this is a relatively small effect occurring under special circumstances and is not expected to play a significant role in our results.

The second point is to consider the possibility of correlations between the dark matter and cosmic-ray luminosity components, i.e. does a galaxy with a low cosmic-ray signal necessarily have a low dark matter signal? To answer this we can infer from Figure 11.1 that the dark matter halo parameters produce the largest changes to the DM induced haze luminosity, with the exception of the diffusion constant D_0. We therefore expect that the DM and CR haze luminosities should be effectively decoupled, as the dark matter component depends primarily on the dark matter density parameters. Detailed checks have shown that this is indeed the case, and that these two luminosities are uncorrelated at first order[4].

[4]We thank the Referee for bringing this cross-check to our attention.

In order to compare the resulting flux contour map to observations of each CA candidate galaxy, we take into account the distance to each candidate galaxy and the related observational uncertainties. Here, we only consider the central value for the distance measurement when the flux error due to the distance uncertainty is less than 25% of the standard deviation due to the systematic uncertainties discussed in Section 11.1.2. This condition does not hold, however, for the galaxies NGC 2683, NGC 4698 and NGC 4448. For these three galaxies, we provide flux contour-maps for the average, as well as the $\pm 1\sigma$ distance measurements. We note that in the case of NGC 4448, only three distance measurements exist in the literature: we thus show results for the minimum, average, and maximum distance measurements reported in NED. For each model galaxy, we match our minimum contour to the minimum contour which is observationally reported, and then plot contours in flux increments of $2^{n/2}$ for integers n, as given by the CA catalog. For most galaxies, the lowest contour corresponds to $n = -3$, since the minimum observable flux/beam is relatively distance independent for resolved galaxies. However, the fluxes for Andromeda are reported with fluxes starting at $n = -2$.

In order to calculate the peak flux contour from our *Galprop* models, we must employ a minimum angular region in which to calculate the peak flux, and this region must exceed the size of the contour region resolved by the radio observations, or else we will set overly stringent constraints based on the smaller angular region considered in the *Galprop* models. We choose the peak flux to stem from the highest flux region with a physical size of at least 25 kpc^2, which exceeds the size of the radio beam at

our maximum distance for all galaxies. We then round the reported contour down to the next contour level, using the $2^{n/2}$ contour spacing with the minimum contour flux set by the observation. We note that this assumption is conservative, as the peak radio flux within an observed beam is always slightly higher than the average beam over the matching *Galprop* contour.

In calculations of the minimum flux contour along the minor axis of each galaxy, the anisotropy of the observed emission contours presents a challenge for any determination of the size of the candidate galaxies' minor axis. In order to conservatively estimate the size of the minor axis, we first calculate the direction orthogonal to the observed Galactic plane of each galaxy, and then calculate the smallest minor axis which includes all contours within 10° of the minor axis. We note that in the case of NGC 2683 and NGC 7814, secondary sources are observed in the -z direction, and thus only the +z measurement is used to set contour constraints. This method effectively chooses the largest possible minor axis which is consistent with the flux data.

In order to verify that our dark matter models are being correctly overlaid onto the radio halo, we also overlay the predicted dark matter contours onto optical images obtained by the STScI Digitized Sky Survey in Figure 11.4. In this case, we consider contours only for the central values of the distance to each candidate galaxy. We observe a strong morphological similarity, which serves to confirm our choices for both the size and orientation of the diffusion region.

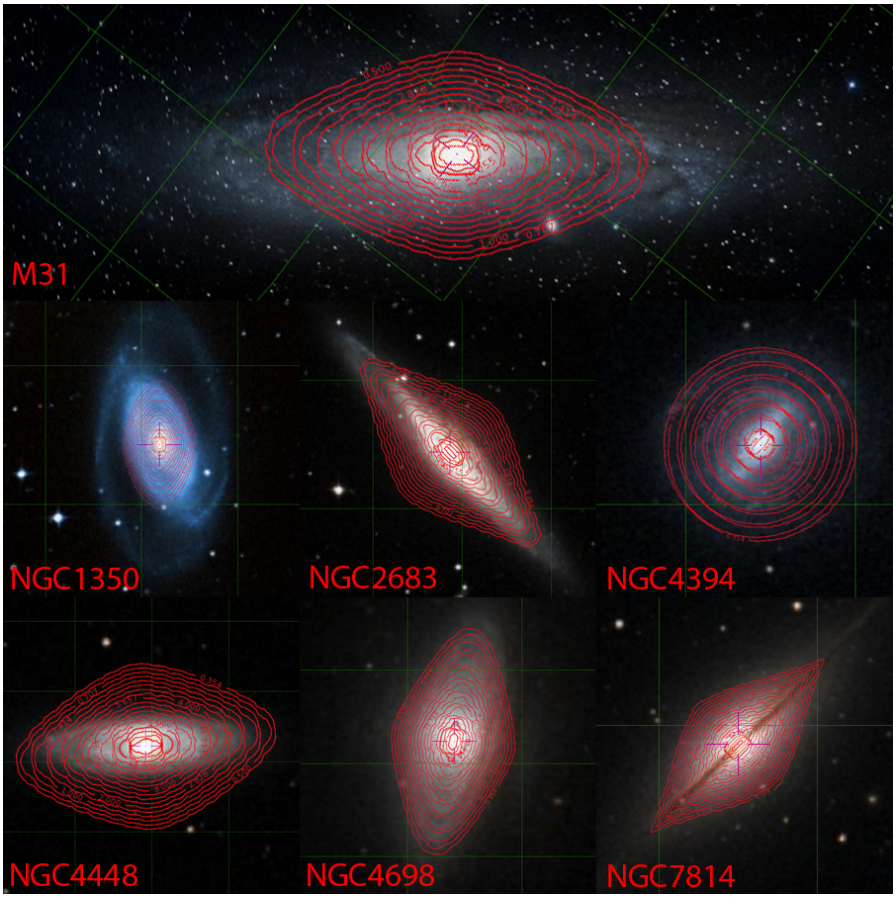

Figure 11.4: Overlays of dark matter only contours from *Galprop* onto optical images obtained from the STScI Digitized Sky Survey. Units are mJy beam^{-1}. Contours are logarithmically spaced at levels $2^{n/2}$ for integer values n with outermost contours $n = -2$ for M31 and $n = -3$ for all others. With the exception of NGC 4448, which has very large distance uncertainties, the optical dimensions are similar or slightly exceed those of the lowest detectable radio contours. The diffusion zone has been matched to the estimated physical axis size.

11.1.4.2 Constraints from the Integrated Flux

In Table 11.4 we show the distance, integrated flux, and the estimate for the dark matter-induced radio haze flux as calculated using *Galprop* for our central parameter values. Also given is the ratio between the observed and simulated flux between

1.49-15 Ghz (R_{int}) for each candidate galaxy. Ratios smaller than one, which we highlight in red, indicate that the observed flux is smaller than what we predict *from dark matter annihilation alone*. For galaxies with non-negligible distance uncertainties, the uncertainty in the distance, *Galprop* flux, and R_{int} are also given.

We note two important results: First, R_{int} falls below unity for at least 15 of the 18 galaxy observations, implying that the expected dark matter flux overproduces the entire observed radio flux from each galaxy, which presumably includes both dark matter and astrophysical sources of radio emission. While a constraint on dark matter annihilation from this simple process is difficult to quantitatively determine, we note that from Figure 11.2 it is clear that astrophysical cosmic rays usually dominate over the dark matter contribution, implying that for these 7 candidate galaxies, drawn from a larger distribution of 66 Milky-Way like galaxies, the cosmic ray contribution is extremely low.

Finally, we find that for five galaxies in our sample, $R_{\rm int}$ at 1.49 GHz is smaller than 0.05. In our simulations of the dark matter haze, we find that obtaining a dark matter haze a factor 20 smaller than the benchmark values (i.e. $R_{\rm int}$ smaller than 0.05) has a probability of 11.2%. The likelihood of having at least 5 galaxies out of a sample of 66 with an emission smaller than 0.05 corresponds to 87.9%, so we cannot derive any conclusion on the dark matter origin of the haze out of the integrated flux, barring stronger assumptions about the cosmic ray component of the radio emission. For clarity we note that by choosing only 7 samples to analyze in detail, our statistical conclusions, which are always taken from the full sample of 66 galaxies, will always be more conservative than performing an in-depth analysis of additional galaxies.

Name	Distance [Mpc]	ν [GHz]	$\Phi_{\rm Obs}$ [mJy]	$\Phi_{\rm GALPROP}$ [mJy]	$R_{\rm int}$	Ref.
M31	0.70	1.49	8400	31967	.263	[586]
		4.85	1863	7840	.238	[598]
NGC1350	20.9	1.49	1.10	36.2	.030	[586]
NGC2683	10.2 (7.96, 12.4)	1.49	65.9	139 (223, 94.0)	.472 (.295, .694)	[586]
		2.38	39±3	82.6 (137, 55.9)	.544 (.335, .805)	[599]
		4.85	27±6	34.4 (56.6, 23.3)	1.13 (.697, 1.67)	[600]
		15.0	< 0.9	22.6 (37.1, 15.3)	.040 (.025, .059)	[601]
NGC4394	16.8	1.49	.7	24.1	.029	[586]
		2.38	-1±4	14.4	.486	[599]
		15.0	$< .9$	4.01	.224	[601]
NGC4448	13.0 (9.70, 47.4)	1.49	1	70.0 (117, 5.46)	.014 (.009, .183)	[586]
		2.38	0±4	43.5 (78.1, 3.27)	.184 (.102, 2.44)	[599]
NGC4698	23.7 (16.9, 30.4)	1.49	.6	26.2 (51.1, 15.8)	.023 (.012, .038)	[586]
		2.38	2±4	15.3 (30.1, 9.29)	.654 (.334, 1.08)	[599]
		15.0	< 1.0	4.19 (8.23, 2.54)	.240 (.122, 0.394)	[601]
NGC7814	17.2	1.49	1.1	49.5	.022	[586]
		2.38	-4±5	29.0	.207	[599]
		15.0	< 0.9	7.95	.138	[601]

Table 11.4: Integrated flux limits for selected galaxies at available radio frequencies from $1.49 - 15$ GHz. First and second values in parentheses represent limits corresponding to the minimum and maximum distance variations respectively. For measurements with associated flux uncertainties, $R_{\rm int}$ was computed using the 95% confidence level upper limit. Observations providing constraints are highlighted in red.

Name	Distance [Mpc]	R_{peak}	R_z	R_r
M31	0.70	.125	.0085	.0043
NGC1350	20.9	.006	.155	.0054
NGC2683	10.2 (7.96, 12.4)	.063	8.04 (2.36, ∞)	.610 (.202, 2.05)
NGC4394	16.8	.004	.0148	.030
NGC4448	13.0 (9.70, 47.4)	.004	.043 (.0172, ∞)	.0173 (.0121, ∞)
NGC4698	23.7 (16.9, 30.4)	.004	.0265 (.0162, .107)	.0034 (.0033, .0034)
NGC7814	17.2	.008	.708	.027

Table 11.5: Contour limits for peak, major (r), and minor (z) fluxes for selected galaxies at 1.49 GHz. The first and second values in parentheses represent limits corresponding to the minimum and maximum distance variations respectively. Observations providing constraints are highlighted in red.

11.1.4.3 Constraints from Peak and Axis Fluxes

While we were not able to obtain any constraints from the total integrated radio luminosity, our dark matter radio emission simulations also allow us to investigate the signal for the galaxies in our sample by examining the peak emission (in the center of the galaxy) and off-peak emission (along and above the galactic plane). In Table 11.5 we show the flux ratios at 1.49 GHz between each observation and our models at the location of the peak (R_{peak}), the minimum observed contour within 10° of the major axis (R_r), and the minimum observed contour on within 10° the minor axis (R_z). We note four interesting results:

1. Evaluating the emission at specific locations, instead of the integrated emission, yields stronger constraints in every candidate galaxy.

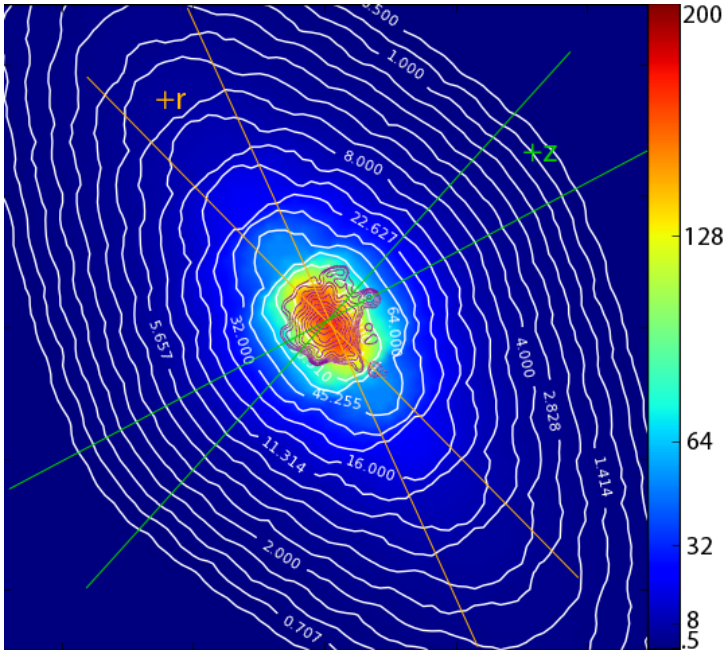

Figure 11.5: 10 Kpc square overlay for M31 of Condon Atlas 1.485 GHz radio contours displayed over dark matter only predictions from *Galprop*. Units are mJy beam^{-1} and the image has been corrected for distance, inclination, position angle, and beam solid angle. The colormap is linear while contours are logarithmically spaced at levels $2^{n/2}$ for integer values n with outermost contours at the same level $n = -2$. Contour limits are computed using the conservative case (outermost observed contour) lying within 10° major and minor axis (r, z). Although the integrated and peak flux measurements do set limits for M31, the contour limits are the most stringent, constraining a dark matter haze at the $\lesssim 1\%$ level, relative to that of the Milky Way.

2. The flux from dark matter annihilation in the majority of our candidate galaxies exceeds the observed radio flux (i.e. $R_{\rm int} < 1$) at 1.49 GHz.

3. We find that we get somewhat stronger constraints from R_r than from R_z, somewhat contrary to expectations. In the case of the Milky Way the eccentricity in the ellipse stemming from dark matter annihilation is generally smaller than that for modeled astrophysical emission, so one might expect better constraints from

off-plane observations.

In Figures 11.5 and 11.6 we show the observed 1.485 GHz radio overlays for M31 and for the remainder of our galaxy sample respectively, noting that the flux contours for each follow the form $2^{n/2}$ mJy beam^{-1} with an outermost contour of n = -2 for M31, and n = -3 for the remainder of our candidate galaxies. In Figure 11.6 we show three distance variations corresponding to the minimum and maximum NED distance measurements for NGC 4448 (2nd row) and the distance estimates corresponding to the 1σ distance error for NGC 2683 (top) and NGC 4698 (3rd row). The other three galaxies show a variation of less than 25% around the mean NED distance, and the variation is not considered.

We note that in many cases the observed flux-contours are highly anisotropic, which contrasts with the approximately symmetric contours expected from dark matter. While anisotropies could be introduced by the cosmic ray propagation parameters, the one-dimensional simulations from Figure 11.1 show that these anisotropies in the magnetic field parameters and diffusion constants have relatively minor effects on the radio luminosity, compared to the case of astrophysical injection. Instead, the odd shapes of several galaxies' contours, particularly those of NGC 4698 and NGC 7814, are highly indicative of anisotropic astrophysical cosmic ray injection. Most importantly, we do not see elliptical emission profiles for any galaxy, contrasting with our model for the Milky Way, which has a significant injection of cosmic rays in star formation regions across the Galactic plane. This means that in these radio-underluminous candidate galaxies, the elliptical extension of the expected dark matter profile in the radial direction produces

Luminosity Cut	$f_{\rm int}^{1.49\,\rm GHz}$	$f_{\rm int}^{30\,\rm GHz}$	$f_{\rm int}^{44\,\rm GHz}$	$f_{r=5\,\rm kpc}^{1.49\,\rm GHz}$	$f_{z=1\,\rm kpc}^{1.49\,\rm GHz}$
$L \leq 0.05 L_{MW,DM}$	.112	.249	.097	.152	.123
$L \leq 0.01 L_{MW,DM}$	.014	.065	.014	.038	.017
$L \leq 0.006 L_{MW,DM}$	.006	.034	.007	.023	.007

Table 11.6: Fractions of random scans with luminosity suppressed by more than a factor of 20 and 100 for a randomized sample of parameter space containing 2000 galaxies with masses restricted to $.25 \leq M/M_{MW} \leq 2$. Subscript "int" indicates the total integrated dark matter luminosity and subscript r (z) indicates the luminosity evaluated at a given distance along (above) the Galactic plane.

significantly better limits at R_r than in the direction of the minor axis.

The results of Table 11.5 indicate that for three galaxies the off-peak emission along the galaxies' major axis (r direction) is suppressed by more than a factor 100 with respect to our benchmark dark matter haze model. Our simulations, reported as the red line in Figure 11.3 and in Table 11.6, indicate that only 2.3% of the simulated galaxies are suppressed by at least .006 compared with the benchmark dark matter model. We calculate that having at least 3 galaxies out of the 66 candidates with such a suppressed radio emission has a likelihood of less than 20%. Although it is difficult to turn this estimate into a confidence level exclusion limit to the dark matter haze hypothesis, the large variations we allow in multiple physical parameters make it clear that there is some tension in the dark matter interpretation of the galactic haze with observations of external spiral galaxies.

11.1.5 Future directions

With upcoming data from the *Planck* satellite, we expect to obtain a much more robust analysis of the Milky Way's haze. *Planck* will produce all-sky observations over nine frequency bands from 30 to 857 GHz, providing a much needed spectrum with superior foreground identification and separation, as well as detailed polarization data. Having established an effective lower bound on the integrated dark matter luminosity, the availability of an all-sky *spectrum* up to higher frequencies will allow us to transcend the issues associated with complicated cosmic ray sources. With an angular resolution of 30 arcminutes at 30 GHz and 24 arcminutes at 44 GHz, *Planck* will have the ability to resolve galaxies up to roughly 5 Mpc. This encompasses the local group which contains several well studied Milky Way analogs. Galaxies at larger distances will still register as point sources. If we exclude sources with known nearby radio confusion and cross-reference against a larger galactic catalog to make morphological cuts, it should be possible to obtain integrated flux limits with substantially better statistics than those presented here.

In order to test the impact of *Planck* observations, Figure 11.7 shows the predicted total luminosity components at 30 and 44 GHz, compared to the benchmark Milky Way value for galaxies in our random parameter scan. The distribution is similar in width to that of the 1.49 GHz distribution shown in Figure 11.2. However, the synchrotron spectrum from dark matter is expected to be significantly harder than that of cosmic rays. Thus, at higher frequencies, we expect a better dark matter signal-to-cosmic ray noise ratio. Additionally, at 30 GHz (44 GHz), 6.49% (1.4%) of models produce a

haze with more than a factor 100 suppression compared to the Milky Way model. With a larger sample, higher quality data, and higher-frequency observations, it should be possible to definitively rule out dark matter annihilation as the primary progenitor of the haze, even under very conservative assumptions.

11.1.6 Discussion

If the WMAP haze is indeed produced by synchrotron emission from electrons and positrons generated via dark matter annihilation, galaxies with properties similar to those of the Milky Way should also possess an observable radio haze. High-resolution radio data allows for morphological studies in addition to peak and integrated flux comparisons against simulations. In this section, we have examined seven galaxies of size and morphological type similar to the Milky Way, and compared the available data at 1.49-15 GHz against the predicted dark matter haze, as calculated using the code *Galprop*. Our results are conservative in the sense that we did not subtract the cosmic ray-induced component of the radio emission, which is typically dominant, when setting limits on the dark matter synchrotron emission from the galaxies under consideration.

Although there are significant systematic uncertainties involved in this procedure, our analysis found that most of the galaxies under consideration are less luminous at radio frequencies than would be expected from their dark matter-induced haze, unless somewhat extreme parameters are adopted for their dark matter halo profiles, cosmic ray propagation models, or magnetic field models. In particular, to reduce the dark matter luminosity below the observed upper limits, one must simultaneously reduce the dark

matter density, increase the diffusion constant, and/or increase the interstellar radiation energy density relative to those features of the Milky Way. The size of the diffusion region and the strength of the magnetic field are less important to this problem. While most of these parameters are very poorly constrained, we have performed a Monte Carlo scan over what we consider to be a reasonable range of the parameter space, and find that the dark matter-induced haze is less than 1% as luminous as the Milky Way's haze in only about $\sim 5\%$ of the simulated galaxies.

To obtain limits on the dark matter origin of the haze, we compare observed and predicted flux densities along the semi-major and semi-minor axes, peak contour levels, and integrated flux. For six of the seven galaxies examined, a dark matter interpretation is constrained below the 5% level. We obtain stronger constraints from observations at a position of r=5 kpc along the galactic plane, where we find three galaxies which are underluminous by a factor of 100 compared to the Milky Way. Qualitatively, it is also worth noting that the radio emission from the majority of these galaxies does not closely resemble the morphology expected from dark matter annihilation, and instead appears to trace spikes in the cosmic-ray injection rate. Remarkably, one of the galaxies without evidence of a dark matter haze is our local-group neighbor, M31 (the Andromeda Galaxy). While it is difficult to turn this into a firm exclusion limit on the dark matter origin of the Milky Way haze, one would have expected Andromeda to be significantly more radio luminous in most dark matter interpretations of the WMAP haze.

An important caveat of the analysis in this section lies in the lack of experimental data on the WMAP haze below 22 GHz. It is safe to argue that for many dark matter

models the approximation of extrapolating linearly from the WMAP frequencies down to 1.49 GHz is valid. In the monochromatic approximation, the synchrotron emission peaks at

$$\nu_{\rm max} \approx \ 0.29 \nu_c \approx 4.6 {\rm MHz} \ E^2_{\rm GeV} B_{\mu {\rm G}} \tag{11.2}$$

The characteristic electron energy E_e for a dark matter particle is approximately $E_e \sim m_{\rm DM}/10$, so that for typical magnetic fields we expect the peak frequency (where the radio emission is not well-approximated by a power-law) to lie at frequencies between 500 MHz ($m_{\rm DM}$ ~10 GeV) up to 1 THz ($m_{\rm DM}$ ~1 TeV). Only for masses as large as about 10 TeV do we expect a non-trivial spectral shape for the radio emission between 1.4 GHz and the WMAP frequency range.

In addition, it is worth noting that the magnetic fields within the haze region are highly uncertain, and thus models with very different WIMP masses, may have an equivalent synchrotron spectrum for a different magnetic field structure. In the case of fits to the WMAP haze, this is often done with the intention of fitting the spectrum for WMAP emission between the 22, 33 and 41 GHz frequency bands (see e.g. [551]). In this case, the ratio of synchrotron emission at 1.4 and 22 GHz is set entirely by the fit to the WMAP data – since the Bessel function determining the synchrotron spectrum has only one degree of freedom, which must already be constrained by WMAP measurements. While this statement is necessarily true for various WIMP models annihilating through the same pathway, some minor variations are expected for models which annihilate to softer or harder final states. However, this yields only a very minor adjustment to the relative synchrotron rates, and is not considered in this work.

Upcoming data from the *Planck* space observatory will offer a much broader set of radio frequency observations (nine bands from 30 to 857 GHz). Notably, recent work from the *Planck* collaboration has already confirmed presence of the WMAP haze in the Milky Way, and found that it has a microwave edge spatially coincident with the gamma-ray bubbles detected by *Fermi*. Such a broad frequency range, and additional polarization information, will allow for much greater separation of astrophysical foregrounds, as well as reduced contamination from cosmic rays.

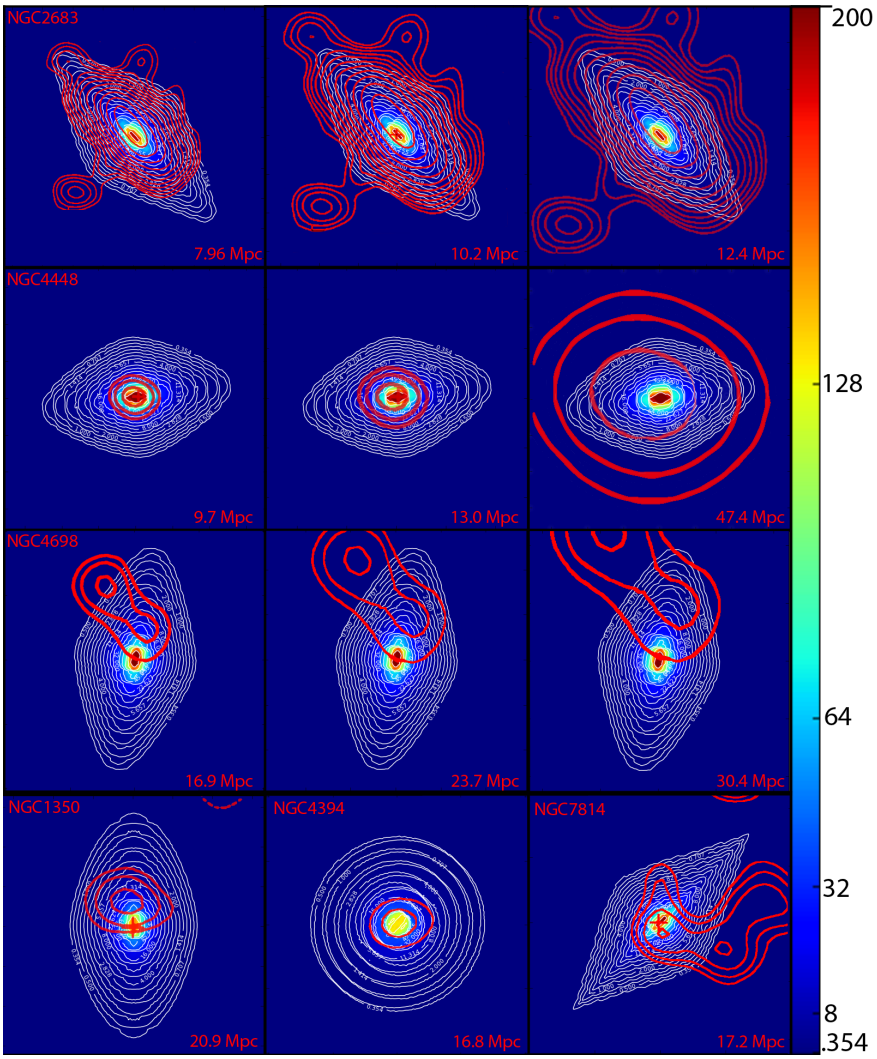

Figure 11.6: 20 kpc-square overlays of Condon Atlas 1.485 GHz radio contours onto dark matter only predictions from GALPROP. Units are mJy beam^{-1} and images have been individually corrected for distance, inclination, position angle, and beam solid angle. For NGC 4448, distance variations correspond to minimum and maximum NED measurements centered on the value from the Condon Atlas. For NGC 2683 and 4698, distances are allowed to vary by 1 standard deviation from the mean based on NED measurements. The colormap is linear while contours are logarithmically spaced at levels $2^{n/2}$ for integer values n with outermost contours at the same level $n = -3$. A dark matter haze should produce a fairly symmetric synchrotron signal. Here the irregular shapes of the observed contours often yield significant constraints along r, z, or both. Additionally, the peak predicted contours are often substantially higher than what is observed.

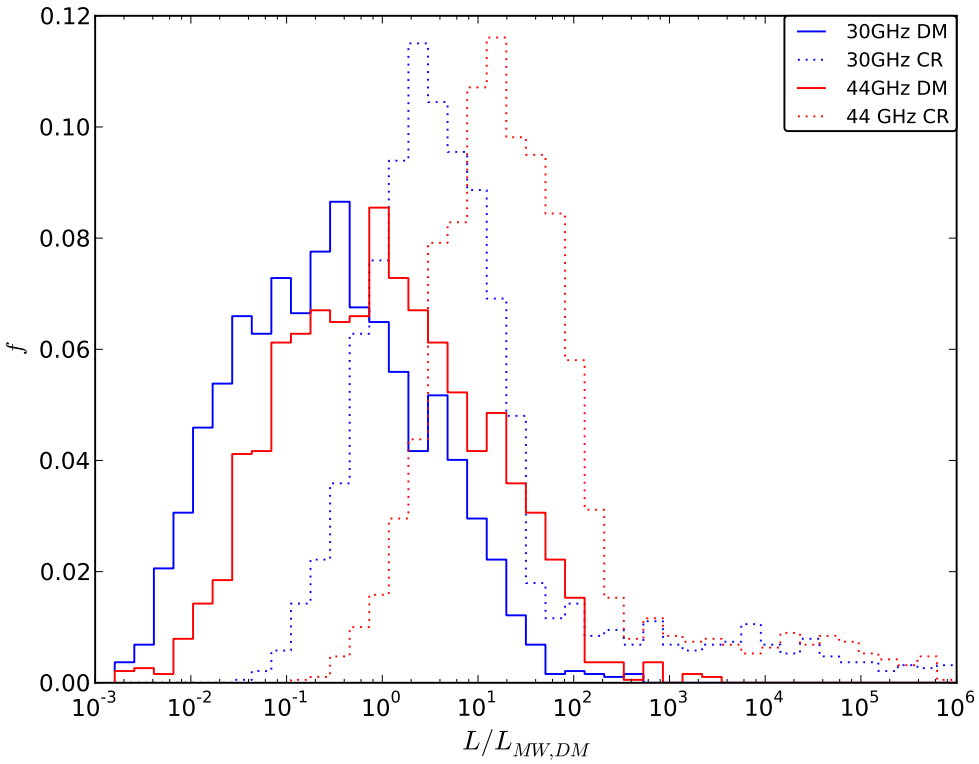

Figure 11.7: Distribution of 30 and 44 GHz luminosity ratios $L/L_{MW,DM}$ where L is the total integrated luminosity and $L_{MW,DM}$ is the luminosity due to dark matter for the canonical Milky Way model at the respective frequency. Sample contains 2000 runs randomly distributed in the parameter space of Table 11.3 with the mass restricted to lie within 0.25 to 2 times that of the Milky Way. We plot the contributions due to dark matter (solid) and cosmic rays (dashed) individually. At both 30 and 44 GHz, 6.5% and 1.4% of models show suppression greater than a factor of 100 compared to the benchmark Milky Way model respectively. This indicates that higher frequency observations from Planck will produce more robust limits on dark matter origin of the haze.

Chapter 12

Conclusions

In this dissertation we have presented a variety of new methods, models, and analyses for the indirect detection of particle dark matter in the Milky Way using cosmic and gamma rays. The status of the field remains bright, and much additional work remains before the available data is fully exploited, particularly in the astrophysical modeling of the Galactic center region, and in the incorporation of multi-wavelength/multi-messenger studies. In this chapter, we summarize the status of each sub-domain, and emphasize our contributions to the field while highlighting the most pressing future directions.

12.1 New Astrophysical Signatures

In Chapter 3, we presented details for calculating the indirect detection signals from particle dark matter annihilations and decay. Our primary contributions consisted of (i) the first calculation of the $^3\overline{\text{He}}$ flux from dark matter annihilations, and (ii) a

detailed morphological calculation for dark matter emission spawning from interactions with the Galactic interstellar medium including thermal electrons, gas, and cosmic-rays.

12.1.1 Antihelium from Dark Matter

Antihelium provides a novel and interesting potential discovery channel for dark matter owing to its negligible astrophysical backgrounds. We modified the so-called "coalescence framework" for the formation of heavy anti-nuclei with atomic number $A = 3$, as well as determining a theoretical extrapolation of the (currently unmeasured) coalescence momentum. Using Monte Carlo simulation codes and massive supercomputing clusters, we determined the injection spectrum for representative dark matter models (Sec. 3.2.4.2. In order to derive the flux at Earth, we applied new interaction cross-sections for $^3\overline{\mathrm{He}}$ on interstellar gas and applied a two-zone diffusion model combined with a force-field model of solar propagation (Sec. 5.1.3). It is clear that the current generation of experiments is very unlikely to be sensitive to primary antihelium from dark matter annihilation. Future generation satellite born experiments using a GAPS(SAT) detector, as initially proposed in Ref. [178], could potentially be sensitive to WIMPs annihilating to W^+W^- near threshold and $b\bar{b}$ at $\lesssim 10$ GeV. Unfortunately, higher masses quickly become undetectable, particularly in the W^+W^- case. If a convincing $\overline{\mathrm{d}}$ signal is observed at GAPS or AMS-02, follow-up $^3\overline{\mathrm{He}}$ observations may be needed to confidently rule out misidentified astrophysical secondaries. Refined analysis of antihelium production rates may be attainable with future collider data which directly measures antihlelium production at colliders. For now, no such (usable) data is available.

12.1.2 Dark Matter Interactions with Cosmic Rays and the ISM

In Section 3.3 we carried out a model-independent study of scenarios where diffuse electromagnetic emission originates from interactions of dark matter particles with the interstellar gas, free electrons or Galactic cosmic rays. We assumed that the relevant morphology depends on the integrated line-of-sight product of the dark matter particle density times the relevant gas/cosmic-ray density. The key motivation to consider such models is that a variety of large-scale diffuse excesses in the general direction of the Galactic center have been identified, at wavelengths ranging from radio to gamma rays, and that a variety of particle physics scenarios have been proposed that rely on dark matter interacting with Galactic gas or cosmic rays.

We considered a variety of state-of-the-art gas density models, and well-motivated cosmic ray models, utilizing several different assumed injection source distribution profiles. We produced the relevant latitudinal and longitudinal profiles, and we are making our results available publicly on the web. Finally, we compared our predictions with the emission profiles of a few selected diffuse excesses.

Generally, we find that the morphology of the 511 keV line is matched much more closely by dark matter pair-annihilation than by any of the dark matter times gas/cosmic ray models we investigated; the COMPTEL excess is reproduced by models of dark matter times gas or free electrons in the innermost regions, at low Galactic latitude, but not at large latitudes or in longitude. Finally, models advocating dark matter/cosmic-ray convolutions fail at reproducing the Fermi-LAT GeV excess, while dark matter times gas or free electrons provides a relatively good fit to the latitudinal

distribution of the signal.

12.2 Novel Statistical Methods

In Chapter 4 we discuss the current ensemble of statistical methods applied in indirect detection studies. Here our contributions include the application of the DBSCAN clustering algorithm in both (i) the discrimination of point sources from diffuse emission classes at the Galactic center (these specific findings are discussed below in Sec. 12.5 below) and (ii) the detection of unresolved point sources in sparse photon datasets. In both cases we improved the traditional algorithm in three ways. First, we utilized the well constrained point-source-function of Fermi-LAT to determine the clustering radius, second we derived an adaptive estimator for the background density, and thus clustering density thresholding (which allows scans for point sources over variable backgrounds), and finally, we employed supervised learning techniques such as boosted decision trees, to reject spurious clusters, and thus lower the point source detection threshold.

In Section 4.7, we investigated three effects that may alter the *interpretation* of the TS=8.7 excess observed in the stacked population of dSphs by the Fermi-LAT Collaboration in Ref. [50]. More generally, these methods provide improved sensitivity in Fermi Lat searches for point sources using using multiwavelength catalogs to account for unresolved point sources contamination in both regions of interest, and in blank sky calibrations. In the specific case of Fermi, we find that more than 50% of the TS>8.7 residuals observed in blank sky locations are the result of sources identified in

the BZCAT and CRATES catalogs. Recent population models of blazers, radio galaxies, and starforming galaxies lead us to expect that an even greater fraction of such residuals are the result of unresolved point sources. And although BZCAT and CRATES sources are found within 1° of 14 of the 25 dSphs analyzed in Ref. [50], the three dSphs most responsible for the observed excess (Segue 1, Ursa Major II, Willman 1) have no such sources within 0.7°, making them unlikely to be highly contaminated. Finally, for the range of dark matter masses and cross sections currently being probed by gamma-ray observations of dSphs, one expects a flux distribution of dark matter subhalos that would account for ∼5-10% of the unresolved source population. Even if all astrophysical sources are accurately modeled, these subhalos will constitute an irreducible background for gamma-ray studies of dSphs.

12.3 Modeling of Diffuse Galactic γ-rays

Throughout Chapter 7 we pushed the state-of-the-art regarding numerical models of the Milky Way's diffuse Galactic gamma-ray emission. In particular we discussed massive improvements in three domains: (1) utilizing ultra-high-resolution and fully three dimensional treatments of cosmic-ray propagation, (2) implementing a high-precision three-dimensional empirical model of galactic gas, and most importantly (3) developing a high-precision 3D model of cosmic-ray source injection which assumes injection from star-forming regions (as traced by the density of CO). While the gas model and three dimensional propagation were found to possess sub-dominant effects relative to the changing source distribution, the overall quality of the predicted diffuse Galactic

gamma-ray emission is very significantly improved when 20-25% of cosmic rays are injected in starforming regions. This is particularly true at high-latitudes and in toward the inner Galaxy. Conclusions specific to the Galactic center region are provided in Sec. 12.4.

In Sec. 5.2 we discussed several paths forward for fully 3D models of CR propagation. These include models for environmentally dependent source injection spectra based on ion-neutral damping and shock Mach numbers, anisotropic and inhomogeneous diffusion based on the local regular and random magnetic fields and turbulence structures, and models for inhomogeneous reacceleration where the propagation of magneto-hydrodynamic-turbulence depends on the magnetic field and ion density. In additoin to the improved gas and source density models above, such steps should be taken in the next generation of diffuse Galactic gamma-ray emission models.

12.4 The GeV Galactic Center Excess

In Chapter 8 we reviewed the current status of the Fermi GeV excess at the Galactic center. We have made two major contributions to this field which are the two most significant works of this dissertation. In Sec.8.1 we utilize the improved cosmic-ray injection models of Sec 8.1 to improve the modeling of the Galactic center region. In particular considering the cosmic-rays emanating form the Central Molecular Zone which harbors a plethora of high-energy sources, and has been completely neglected in the present diffuse emission models. As discussed in the following paragraphs we find that the extracted GCE signal depends senstiviely on the assumed injection model, and

that nearly all of the excess is precisely explained in terms of steady state injection of cosmic-rays from the CMZ. In Sec. 8.2 we were the first group to propose transient bursts of cosmic-ray injection as a plausible explanation for the excess.

12.4.1 GCE from Steady State Cosmic Ray Injection

The conclusive determination of the existence of genuinely *excess* diffuse emission from the inner regions of the Galaxy depends crucially on the use of *reliable* and *physically motivated* models for the Galactic diffuse emission. It is clear that in studies thus far available a critically important population of cosmic rays in the region has been neglected, with potentially dramatic implications for the determination of both the existence and the properties of any excess emission.

In Section 7.1, we proposed a physically well-motivated model for the three-dimensional Galactic cosmic-ray injection source distribution, based on a fraction $f_{\rm H2}$ of such sources being associated with relatively recent injection in star-forming regions. We employed observational data on the density of H_2 alongside a simple prescription for star-formation efficiency. In Sec. 8.1.3 it was shown that the resulting Galactic diffuse emission models with $f_{\rm H2} \sim 0.1 - 0.3$ are *statistically strongly favored* by the γ-ray data over models with $f_{\rm H2} = 0$.

Throughout Section 8.1 we explore in detail the implications of these models for the diffuse Galactic emission, and the resulting impact on the existence and properties of any Galactic center "excess". We found that the new cosmic ray population is consistent with the CMZ supernova rate (as determined by multi-wavelength observations) and

produces a significant γ-ray emission that is degenerate with many properties of the γ-ray excess. The choice of the region of interest impacts the details of this degeneracy. Specifically, without employing a GC excess template there is a strong preference for $f_{\rm H2} \sim 0.1$ in the (narrower) Galactic Center analysis, and for $f_{\rm H2} \sim 0.2$ in the (broader) Inner Galaxy and in the full-sky analyses. Including a GC excess template, but utilizing a value $f_{\rm H2} \sim 0.2$ as a *prior* in the Inner Galaxy analysis, the GC excess is strongly affected, while the Galactic Center analysis still favors the existence of a bright residual emission.

An additional important finding of is that the low-energy ($E \lesssim$20 GeV) protons and electrons are over-produced in the GC region, as determined by the negative γ-ray residuals below 1 GeV. We explored possible solutions to this issue, and argue that the most plausible solution is the addition of significant advective winds which remove the excess electron and proton populations from the central Galactic regions. We showed that the existence of such winds is physically well-motivated. The inclusion of strong Galactocentric winds significantly improves our fit to the γ-ray data both in models that include (exclude), a GCE component, at the level of $\Delta\chi^2$=605 (375) in an Inner Galaxy type analysis. For models which include a GCE component, the addition of strong Galactic winds removes the negative residuals typically absorbed by the GCE template, producing a GCE γ-ray spectrum which is physically realistic over the full energy range.

The models for the diffuse Galactic emission discussed here present a clear step forward in the current state of the art in this field. It is clear that a solid determination

of the properties of a Galactic center excess, and its association with new physical phenomena such as dark matter annihilation, hinges on further improving our modeling of the Central Molecular Zone. At present, a precision determination of diffuse emission in the Galaxy remains the most significant barrier to using high-energy gamma rays as a probe of new physics at the Galactic center.

12.4.2 GCE from Hadronic Bursts

In Sec.8.2, we presented a case for high-energy cosmic-ray protons injected in the Galactic center region as a plausible explanation to the reported Galactic center γ-ray excess over the expected diffuse background. Our study focused on whether such an explanation meets the required (i) morphology, (ii) spectrum and (iii) energetics.

We demonstrated that cosmic rays injected on the order of a mega-year ago explain the observed spherical symmetry reported from the "inner Galaxy" analysis of Ref. [43], while a more recent (on the order of a few kilo-years old) episode would possess the same morphology obtained for the innermost portions of the Galaxy in the "Galactic center" analysis of Ref. [43]

We showed that the γ-ray spectrum predicted by cosmic-ray proton energy distributions responsible for the emission observed from supernova remnants (such as broken power laws with specific spectral indexes, and exponentially suppressed power laws) provide excellent fits to the observed Galactic center excess. We pointed out that the preferred range for the break of the power law and for the spectral indexes inferred from the observed excess fall squarely in the ranges inferred from observations of

supernova remnants, as well as in the general range expected from theory considerations. We also pointed out the importance of systematic effects in spectral reconstruction due to hadronic cross sections impacting the predictions for the γ-ray spectrum from inelastic proton-proton collisions.

Finally, we inspected the time-scales, spectrum and energetics we invoked to reproduce the morphology and spectrum of the Galactic center excess in the context of one or more additional populations of cosmic-ray protons in the region. We demonstrated that the existence of such populations is motivated by a variety of observational and theoretical reasons, which were reviewed in detail.

This study provided proof of existence of a well-motivated alternative to dark matter annihilation or millisecond pulsars as an explanation to the reported Galactic center γ-ray excess. Our results indicate that conclusively claiming a signal of New Physics from γ-ray observations of the inner regions of the Galaxy must contend with a variety of additional astrophysical processes. In particular, we highlighted that one or more previously unaccounted-for populations of cosmic-ray protons in the Galactic center could potentially produce a γ-ray emission with a spectrum, morphology and intensity closely resembling those of the Galactic center γ-ray excess.

12.5 The 130 GeV Line

In Sec. 4.4 we presented the DBSCAN algorithm as a powerful discrminiator of point source versus diffuse emission sources over sparse photon datasets. Nowhere is this better exemplified as a technique than in our analysis of the 130 GeV line presneted

in Ch. 9. Barring instrumental effects, a 130 GeV line could be ascribed to either new physics, presumably a dark matter particle decaying or pair-annihilating into a 2γ (or γZ, γh etc.) final state, or to one or more pulsars featuring a cold wind with electrons with an energy at, or very close to, 130 GeV. This latter possibility, it is argued in [487], is the only "traditional" astrophysical process envisioned thus far that could produce a sharp gamma-ray line in the energy regime of interest. It is therefore of the utmost importance to discriminate between a cold pulsar wind scenario and a dark matter scenario, if indeed the line is resilient to future tests and observations.

Discriminating dark matter and pulsar interpretations of the 130 GeV line may not be possible based solely on the spectral characteristics of the Fermi-LAT data. In Chapter 9 we sought to use morphological information, i.e. the 130 GeV events' arrival direction, to establish whether the signal is likely due to multiple point sources as opposed to a truly diffuse origin. This is a meaningful question, since the signal region is much larger than the instrumental angular resolution, and it should be thus possible to discriminate a finite number of point sources, as expected in the pulsar case, from a distribution that follows a diffuse morphology, such as what expected from dark matter annihilation or decay.

To quantitatively approach the issue of discriminating pulsars versus dark matter on a morphological basis, we employed the DBSCAN algorithm which distinguishes clusters from background noise based on the local photon density. We defined a statistical significance measure, and we optimized the algorithm's two physically well-constrained parameters in order to reconstruct as accurately as possible the potential "clusters"

producing the observed γ-ray events.

As a result of our analysis of the available Fermi-LAT data, we concluded that at the 99%, 95%, 90% confidence level the data need at least 2, 3, 5 or more point sources, respectively, while the events' morphology is perfectly consistent with various dark matter density profiles. We conclude that the data strongly disfavor the hypothesis of a small number of pulsars as the origin of the signal. If the pulsar scenario is indeed the culprit for the 130 GeV events, it is necessary to postulate a relatively large population of pulsars (likely at least 4) with cold winds featuring electrons with exactly, to within the instrumental energy resolution, the same energy. This appears, to say the least, quite problematic. A diffuse origin seems therefore the most likely scenario for the 130 GeV photons. Our clustering algorithm approach, clearly, is not optimized to discriminate between different diffuse morphologies: in fact, on the basis of our results, we find that we cannot discriminate between different diffuse morphologies (like dark matter annihliation vs. decay).

We showed that present and future observatories have the potential to shed additional light on the presence and characteristics of the 130 GeV line [502]. Improvements to the H.E.S.S. telescope (H.E.S.S.-II) have reduced the γ-ray threshold to around 50 GeV, allowing for the independent determination of a line signal from the GC region. This is especially important, as the 10^4 m^2 collecting area of the H.E.S.S. telescope will quickly alleviate the low-statistics issues involved in Fermi-LAT studies [487]. Furthermore, future instruments such as Gamma-400 [503] and CTA [504] provide the necessary effective area and energy-resolution to definitively and conclusively test the diffuse or

point-like nature of high-energy gamma-ray spectral lines.

It is unfortunate that the 130 GeV line (now 135 GeV) has turned out – after the Pass 8 data release – to have been an unlucky combination of both systematic and statistical origin. Nonetheless, the methods presented here demonstrate the importance of using combined morphological and spectral information in order to maximally distinguish between competing models.

12.6 The 3.5 keV line

In Chapter 10, we examined the morphology of the X-ray line-like emission at 3.5 keV which has been detected in the Galactic center region and from the Perseus cluster of galaxies. We employed a variety of different choices to model the morphology of the continuum emission, and studied the resulting residual signal at 3.5 keV. Though it is difficult to ensure these residuals are dominated by the line signal and not mismodeling of the continuum, the azimuthal and radial distributions are strikingly different from the prediction from dark matter decay. In the case of the Galactic center, the 3.5 keV emission has a distinct quadrapolar distribution and is completely incompatible with emission from axion-like particle conversion. In the Perseus cluster 3.5 keV emission strongly overlaps with the cluster's cool clumpy core. While the ALP scenario cannot be ruled out for Perseus, it is strongly disfavored after adding even a single additional low-energy continuum or line template.

Utilizing a sliding-window template, we demonstrated that the 3.5 keV emission most prominently correlates with the morphology of strong emission lines associated with

Ar and Ca transitions in the case of the Galactic center. For Perseus, the correlation is observed in lines with a comparable peak emission temperature to K XVIII ($kT_e \approx$ 2.16 keV) and/or the corresponding thermal bremsstrahlung. This is generally observed to feature a distribution overlapping with the cluster's cool core. In both the Galactic center and Perseus, we thus find strong evidence in favor of a plasma emission origin for the observed 3.5 keV line and against a dark matter interpretation.

Finally, utilizing the same binned-likelihood approach, we set the most stringent constraints to date on the lifetime of a dark matter particle decaying into a final state including a 3.5 keV monochromatic photon. By adding a dark matter template and allowing all template normalizations to float in this process, these limits (and fits) are resilient against continuum mismodeling and robustly exclude a dark matter decay origin for the 3.5 keV line observed from clusters.

Subsequent deep XMM-Netwon observations of Draco, a nearby Milky Way satellite, have revealed no 3.5 keV line and conclusively rule out a dark matter origin in the form of sterile neutrinos [602] (although e.g. axion-like-particles may still explain the disparate line intensities across multiple objects). While the precise origins of the line remain obfuscated, several mechanisms have been proposed including charge exchange prcoesses between the neutral hydrogen and ionized sulfur atoms [603], as well as simply an understimate of the systematic uncertainties in both abundance and the multi-phase plasma model, both of which impact the line ratio predicted for the nearby K-XVIII transition. From a dark matter perspective, this signal is not as interesting as it once was, although a conclusive ruling out of exotic candidate models will have to await the

next generation of X-ray calorimeters following the destruction of the Hitomi/Astro-H instrument in March 2016.

12.7 The WMAP-Planck Haze

In Ch. 11, we tested the dark matter origins of the WMAP and Planck haze using a survey of synchrotron radiation from nearby galaxies. We showed that nearby galaxies with similar physical characteristics to the Milky Way have synchrotron intensities which are suppressed relative to our galaxy by several orders of magnitude. This implies that if dark matter is responsible for the haze, the diffusion parameters of some "Milky Way twin" galaxies must highly disfavor synchrotron emission compared to conditions of the the Milky Way. For example, neighboring galaxies would require magnetic field strengths which are an order of magnitude suppressed relative to the Milky way, as well as large diffusion constants. The large uncertainties in the diffusion parameters of both the Milky Way and neighboring galaxies make quantitative constraints on dark matter annihilation difficult. If the signal is of dark matter origin, one must reconcile the suppression in external galaxies. Astrophysical models of the WMAP haze provide a more likely scenario which is connected with the Fermi bubbles (which shares overlapping edge features), and likely related to starburst or AGN activity emanating from the Milky Way's Galactic center. In future astrophysical modeling of the Milky Way, such self consistent multi-wavelength constraints must be taken into account in order to converge on a realistic emission model.

12.8 Concluding Remarks

Of the excesses that remain viable, the Galactic center region is uniquely both the most promising and the most complex. A definitive confirmation of a dark matter origin for the GCE is unlikely to appear until the next generation of experiments can probe cleaner astrophysical systems; namely nearby dwarf galaxies. Such limits may arise from 15 year, highly improved Fermi dwarf constraints. In the meantime, the logical next step for indirect detection modeling of the Galactic center is to improve the cosmic-ray modeling, and propagation, and to incorporate full, self-consistent multiwavelength data. Diffuse emission modelling is the single largest limiting factor in extracting the properties of the GCE excess. In addition, future observatories such as Gamma-400 offer such improved angular resolution that point source interpretations may be ruled out or confirmed.

Indirect detection provides an essential and complementary probe of new physics beyond the Standard Model. As instrumentation, models, and statistical techniques continue to improve, it is likely that an increasing number of "excesses" will be reported. We should keep in mind the lessons of this dissertation, the number of misclassified signals, and take care to fully understand the background modelling being applied as well as the systematic uncertainties which are always present in the modeling of high-energy astrophysical processes. Fortunately, these mistakes inevitably lead to the discovery of interesting astrophysics and improvements in astrophysical models which can be applied to the next generation. In the theater of particle physics, the future of indirect detection

is bright, important, and uniquely positioned to discover the true nature of dark matter.

Bibliography

[1] M. G. Walker, M. Mateo, E. W. Olszewski, O. Y. Gnedin, X. Wang, B. Sen, and M. Woodroofe. Velocity Dispersion Profiles of Seven Dwarf Spheroidal Galaxies. ApJ, 667:L53–L56, September 2007.

[2] T. S. van Albada, J. N. Bahcall, K. Begeman, and R. Sancisi. Distribution of dark matter in the spiral galaxy NGC 3198. ApJ, 295:305–313, August 1985.

[3] M. Markevitch. Chandra Observation of the Most Interesting Cluster in the Universe. In A. Wilson, editor, *The X-ray Universe 2005*, volume 604 of *ESA Special Publication*, page 723, January 2006.

[4] G. Steigman, B. Dasgupta, and J. F. Beacom. Precise relic WIMP abundance and its impact on searches for dark matter annihilation. Phys. Rev. D, 86(2):023506, July 2012.

[5] M. Kuhlen, P. Madau, and J. Silk. Exploring Dark Matter with Milky Way Substructure. *Science*, 325:970, August 2009.

[6] A. A. Moiseev, M. Ajello, J. H. Buckley, R. Caputo, E. C. Ferrara, D. H. Hartmann, E. Hays, J. E. McEnery, J. W. Mitchell, R. Ojha, J. S. Perkins, J. L. Racusin, A. W. Smith, and D. J. Thompson. Compton-Pair Production Space Telescope (ComPair) for MeV Gamma-ray Astronomy. *ArXiv e-prints*, August 2015.

[7] S. Funk. Space- and Ground-Based Gamma-Ray Astrophysics. *ArXiv e-prints*, August 2015.

[8] L. A. Dal and A. R. Raklev. Alternative formation model for antideuterons from dark matter. Phys. Rev. D, 91(12):123536, June 2015.

[9] I. Yusifov and I. Kucuk. Revisiting the radial distribution of pulsars in the Galaxy. (Dm):9, 2004.

[10] Meng Su. Private Communication.

[11] Meng Su, Tracy R. Slatyer, and Douglas P. Finkbeiner. Giant gamma-ray bubbles from fermi-lat: Active galactic nucleus activity or bipolar galactic wind? *The Astrophysical Journal*, 724(2):1044, 2010.

[12] The Fermi-LAT high-latitude Survey: Source Count Distributions and the Origin of the Extragalactic Diffuse Background. *Astrophys.J.*, 720:435–453, 2010.

[13] Yoshiyuki Inoue. Contribution of the Gamma-ray Loud Radio Galaxies Core Emissions to the Cosmic MeV and GeV Gamma-Ray Background Radiation. *Astrophys.J.*, 733:66, 2011.

[14] M. Ackermann, M. Ajello, A. Allafort, L. Baldini, J. Ballet, D. Bastieri, K. Bechtol, R. Bellazzini, B. Berenji, E. D. Bloom, E. Bonamente, A. W. Borgland, A. Bouvier, J. Bregeon, M. Brigida, P. Bruel, R. Buehler, S. Buson, G. A. Caliandro, R. A. Cameron, P. A. Caraveo, J. M. Casandjian, C. Cecchi, E. Charles, A. Chekhtman, C. C. Cheung, J. Chiang, A. N. Cillis, S. Ciprini, R. Claus, J. Cohen-Tanugi, J. Conrad, S. Cutini, F. de Palma, C. D. Dermer, S. W. Digel, E. d. C. e. Silva, P. S. Drell, A. Drlica-Wagner, C. Favuzzi, S. J. Fegan, P. Fortin, Y. Fukazawa, S. Funk, P. Fusco, F. Gargano, D. Gasparrini, S. Germani, N. Giglietto, F. Giordano, T. Glanzman, G. Godfrey, I. A. Grenier, S. Guiriec,

M. Gustafsson, D. Hadasch, M. Hayashida, E. Hays, R. E. Hughes, G. Jóhannesson, A. S. Johnson, T. Kamae, H. Katagiri, J. Kataoka, J. Knödlseder, M. Kuss, J. Lande, F. Longo, F. Loparco, B. Lott, M. N. Lovellette, P. Lubrano, G. M. Madejski, P. Martin, M. N. Mazziotta, J. E. McEnery, P. F. Michelson, T. Mizuno, C. Monte, M. E. Monzani, A. Morselli, I. V. Moskalenko, S. Murgia, S. Nishino, J. P. Norris, E. Nuss, M. Ohno, T. Ohsugi, A. Okumura, N. Omodei, E. Orlando, M. Ozaki, D. Parent, M. Persic, M. Pesce-Rollins, V. Petrosian, M. Pierbattista, F. Piron, G. Pivato, T. A. Porter, S. Rainò, R. Rando, M. Razzano, A. Reimer, O. Reimer, S. Ritz, M. Roth, C. Sbarra, C. Sgrò, E. J. Siskind, G. Spandre, P. Spinelli, Ł. Stawarz, A. W. Strong, H. Takahashi, T. Tanaka, J. B. Thayer, L. Tibaldo, M. Tinivella, D. F. Torres, G. Tosti, E. Troja, Y. Uchiyama, J. Vandenbroucke, G. Vianello, V. Vitale, A. P. Waite, M. Wood, and Z. Yang. GeV Observations of Star-forming Galaxies with the Fermi Large Area Telescope. ApJ, 755:164, August 2012.

[15] Dan Hooper, Ilias Cholis, Tim Linden, Jennifer Siegal-Gaskins, and Tracy Slatyer. Pulsars Cannot Account for the Inner Galaxy's GeV Excess. *Phys.Rev.*, D88:083009, 2013.

[16] Asher Berlin and Dan Hooper. Stringent Constraints On The Dark Matter Annihilation Cross Section From Subhalo Searches With The Fermi Gamma-Ray Space Telescope. *Phys.Rev.*, D89:016014, 2014.

[17] Miguel A. Sanchez-Conde and Francisco Prada. The flattening of the concentration-mass relation towards low halo masses and its implications for the annihilation signal boost. 2013.

[18] A. Atoyan, F. Aharonian, and H. Völk. Electrons and positrons in the galactic cosmic rays. *Physical Review D*, 52(6):3265–3275, sep 1995.

[19] I. V. Moskalenko, A. W. Strong, J. F. Ormes, and M. S. Potgieter. Secondary Antipro-

tons and Propagation of Cosmic Rays in the Galaxy and Heliosphere. ApJ, 565:280–296, January 2002.

[20] R. Duperray, B. Baret, D. Maurin, G. Boudoul, A. Barrau, L. Derome, K. Protasov, and M. Buénerd. Flux of light antimatter nuclei near Earth, induced by cosmic rays in the Galaxy and in the atmosphere. Phys. Rev. D, 71(8):083013, April 2005.

[21] M. Su, T. R. Slatyer, and D. P. Finkbeiner. Giant Gamma-ray Bubbles from Fermi-LAT: Active Galactic Nucleus Activity or Bipolar Galactic Wind? ApJ, 724:1044–1082, December 2010.

[22] Gary L. Case and Dipen Bhattacharya. A New Σ D Relation and Its Application to the Galactic Supernova Remnant Distribution. *The Astrophysical Journal*, 504(2):761–772, September 1998.

[23] D. A. Green. Constraints on the distribution of supernova remnants with Galactocentric radius. MNRAS, 454:1517–1524, December 2015.

[24] D. R. Lorimer. The Galactic Population and Birth Rate of Radio Pulsars. In F. Camilo and B. M. Gaensler, editors, *Young Neutron Stars and Their Environments*, volume 218 of *IAU Symposium*, page 105, 2004.

[25] D R Lorimer, A J Faulkner, A G Lyne, R N Manchester, M Kramer, M. A. McLaughlin, G Hobbs, A Possenti, I H Stairs, F Camilo, M Burgay, N. D'Amico, A Corongiu, and F Crawford. The Parkes Multibeam Pulsar Survey - VI. Discovery and timing of 142 pulsars and a Galactic population analysis. *Monthly Notices of the Royal Astronomical Society*, 372(2):777–800, October 2006.

[26] L. Bronfman, S. Casassus, J. May, and L.-Å. Nyman. The radial distribution of OB star formation in the Galaxy. A&A, 358:521–534, June 2000.

[27] D. F. Figer, R. M. Rich, S. S. Kim, M. Morris, and E. Serabyn. An Extended Star Formation History for the Galactic Center from Hubble Space Telescope NICMOS Observations. ApJ, 601:319–339, January 2004.

[28] F. Yusef-Zadeh, J. W. Hewitt, R. G. Arendt, B. Whitney, G. Rieke, M. Wardle, J. L. Hinz, S. Stolovy, C C Lang, M G Burton, and S Ramirez. STAR FORMATION IN THE CENTRAL 400 PC OF THE MILKY WAY: EVIDENCE FOR A POPULATION OF MASSIVE YOUNG STELLAR OBJECTS. *The Astrophysical Journal*, 702(1):178–225, sep 2009.

[29] K Immer, F Schuller, A Omont, and K M Menten. Recent star formation in the inner Galactic bulge seen by ISOGAL. *Astronomy & Astrophysics*, 537:A121, jan 2012.

[30] S N Longmore, J Bally, L Testi, C R Purcell, A J Walsh, E Bressert, M Pestalozzi, S Molinari, J Ott, L Cortese, C Battersby, N Murray, E Lee, J. M. D. Kruijssen, E. Schisano, and D. Elia. Variations in the Galactic star formation rate and density thresholds for star formation. *Monthly Notices of the Royal Astronomical Society*, 429(2):987–1000, feb 2013.

[31] Timothy C Licquia and Jeffrey A Newman. Improved Estimates of the Milky WayS Stellar Mass and Star Formation Rate From Hierarchical Bayesian Meta-Analysis. *Astrophys J*, 806(1):96, 2015.

[32] R. M. Crocker, D. I. Jones, F. Aharonian, C. J. Law, F. Melia, T. Oka, and J. Ott. Wild at Heart: the particle astrophysics of the Galactic Centre. MNRAS, 413:763–788, May 2011.

[33] C. K. Rosslowe and P. a. Crowther. Erratum: Spatial distribution of Galactic Wolf-Rayet stars and implications for the global population. *Monthly Notices of the Royal Astronomical Society*, 449(3):2436–2437, apr 2015.

[34] T. A. Porter, I. V. Moskalenko, A. W. Strong, E. Orlando, and L. Bouchet. Inverse

Compton Origin of the Hard X-Ray and Soft Gamma-Ray Emission from the Galactic Ridge. ApJ, 682:400–407, July 2008.

[35] Radiation fields in the milky way and their role in high-energy astrophysics. https://indico.cern.ch/event/464471/contribution/1/attachments/1201208/1748094/rtuffs_obergurgl.ppt.

[36] F. Calore, I. Cholis, and C. Weniger. Background model systematics for the Fermi GeV excess. J. Cosmology Astropart. Phys., 3:38, March 2015.

[37] R. Trotta, G. Johannesson, I. V. Moskalenko, T. a. Porter, R. Ruiz de Austri, and a. W. Strong. Constraints on cosmic-ray propagation models from a global Bayesian analysis. 106, 2010.

[38] H.-B. Jin, Y.-L. Wu, and Y.-F. Zhou. Cosmic ray propagation and dark matter in light of the latest AMS-02 data. J. Cosmology Astropart. Phys., 9:049, September 2015.

[39] Roland M Crocker and Felix Aharonian. The Fermi Bubbles: Giant, Multi-Billion-Year-Old Reservoirs of Galactic Center Cosmic Rays. page 4, August 2010.

[40] A. W. Strong, I. V. Moskalenko, O. Reimer, S. Digel, and R. Diehl. The distribution of cosmic-ray sources in the Galaxy, γ-rays and the gradient in the CO-to-H_2 relation. A&A, 422:L47–L50, July 2004.

[41] A. W. Strong, I. V. Moskalenko, O. Reimer, S. Digel, and R. Diehl. The distribution of cosmic-ray sources in the Galaxy, γ-rays and the gradient in the CO-to-H_2 relation. *A&A*, 422:L47–L50, July 2004.

[42] M. Ajello et al. Fermi-LAT Observations of High-Energy Gamma-Ray Emission Toward the Galactic Center. 2015.

[43] Tansu Daylan, Douglas P. Finkbeiner, Dan Hooper, Tim Linden, Stephen K. N. Portillo, et al. The Characterization of the Gamma-Ray Signal from the Central Milky Way: A Compelling Case for Annihilating Dark Matter. 2014.

[44] C. Gordon and O. Macías. Dark matter and pulsar model constraints from Galactic Center Fermi-LAT gamma-ray observations. Phys. Rev. D, 88(8):083521, October 2013.

[45] Kevork N. Abazajian, Nicolas Canac, Shunsaku Horiuchi, and Manoj Kaplinghat. Astrophysical and Dark Matter Interpretations of Extended Gamma-Ray Emission from the Galactic Center. *Phys.Rev.*, D90:023526, 2014.

[46] Daniel Castro and Patrick Slane. FERMI LARGE AREA TELESCOPE OBSERVATIONS OF SUPERNOVA REMNANTS INTERACTING WITH MOLECULAR CLOUDS. *The Astrophysical Journal*, 717(1):372–378, July 2010.

[47] Ilias Cholis, Carmelo Evoli, Francesca Calore, Tim Linden, Christoph Weniger, and Dan Hooper. The Galactic Center GeV Excess from a Series of Leptonic Cosmic-Ray Outbursts. page 28, 2015.

[48] Y. Maeda, F. K. Baganoff, E. D. Feigelson, M. Morris, M. W. Bautz, W. N. Brandt, D. N. Burrows, J. P. Doty, G. P. Garmire, S. H. Pravdo, G. R. Ricker, and L. K. Townsley. A Chandra Study of Sagittarius A East: A Supernova Remnant Regulating the Activity of Our Galactic Center? ApJ, 570:671–687, May 2002.

[49] Joseph P. Conlon and Andrew J. Powell. A 3.55 keV line from DM $\to a \to \gamma$: predictions for cool-core and non-cool-core clusters. 2014.

[50] M. Ackermann et al. Dark Matter Constraints from Observations of 25 Milky Way Satellite Galaxies with the Fermi Large Area Telescope. *Phys.Rev.*, D89:042001, 2014.

[51] R. K. Smith, N. S. Brickhouse, D. A. Liedahl, and J. C. Raymond. Collisional Plasma Models with APEC/APED: Emission-Line Diagnostics of Hydrogen-like and Helium-like Ions. *ApJ Letters*, 556:L91–L95, August 2001.

[52] Alexey Boyarsky, Oleg Ruchayskiy, Dmytro Iakubovskyi, and Jeroen Franse. An unidentified line in X-ray spectra of the Andromeda galaxy and Perseus galaxy cluster. 2014.

[53] Planck Collaboration, P. A. R. Ade, N. Aghanim, M. Arnaud, M. Ashdown, J. Aumont, C. Baccigalupi, A. J. Banday, R. B. Barreiro, J. G. Bartlett, and et al. Planck 2015 results. XIII. Cosmological parameters. *ArXiv e-prints*, February 2015.

[54] G. Bertone. *Particle Dark Matter : Observations, Models and Searches*. Cambridge University Press, 2010.

[55] J. Einasto. Dark Matter. *ArXiv e-prints*, January 2009.

[56] A. Drlica-Wagner, K. Bechtol, E. S. Rykoff, E. Luque, A. Queiroz, Y.-Y. Mao, R. H. Wechsler, J. D. Simon, B. Santiago, B. Yanny, E. Balbinot, S. Dodelson, A. Fausti Neto, D. J. James, T. S. Li, M. A. G. Maia, J. L. Marshall, A. Pieres, K. Stringer, A. R. Walker, T. M. C. Abbott, F. B. Abdalla, S. Allam, A. Benoit-Lévy, G. M. Bernstein, E. Bertin, D. Brooks, E. Buckley-Geer, D. L. Burke, A. Carnero Rosell, M. Carrasco Kind, J. Carretero, M. Crocce, L. N. da Costa, S. Desai, H. T. Diehl, J. P. Dietrich, P. Doel, T. F. Eifler, A. E. Evrard, D. A. Finley, B. Flaugher, P. Fosalba, J. Frieman, E. Gaztanaga, D. W. Gerdes, D. Gruen, R. A. Gruendl, G. Gutierrez, K. Honscheid, K. Kuehn, N. Kuropatkin, O. Lahav, P. Martini, R. Miquel, B. Nord, R. Ogando, A. A. Plazas, K. Reil, A. Roodman, M. Sako, E. Sanchez, V. Scarpine, M. Schubnell, I. Sevilla-Noarbe, R. C. Smith, M. Soares-Santos, F. Sobreira, E. Suchyta, M. E. C. Swanson, G. Tarle, D. Tucker, V. Vikram, W. Wester, Y. Zhang, J. Zuntz, and DES Collaboration.

Eight Ultra-faint Galaxy Candidates Discovered in Year Two of the Dark Energy Survey. ApJ, 813:109, November 2015.

[57] Dongwon Kim and Helmut Jerjen. Horologium ii: A second ultra-faint milky way satellite in the horologium constellation. *The Astrophysical Journal Letters*, 808(2):L39, 2015.

[58] B. P. M. Laevens, N. F. Martin, R. A. Ibata, H.-W. Rix, E. J. Bernard, E. F. Bell, B. Sesar, A. M. N. Ferguson, E. F. Schlafly, C. T. Slater, W. S. Burgett, K. C. Chambers, H. Flewelling, K. A. Hodapp, N. Kaiser, R.-P. Kudritzki, R. H. Lupton, E. A. Magnier, N. Metcalfe, J. S. Morgan, P. A. Price, J. L. Tonry, R. J. Wainscoat, and C. Waters. A New Faint Milky Way Satellite Discovered in the Pan-STARRS1 3π Survey. ApJ, 802:L18, April 2015.

[59] Stphanie Ct, Claude Carignan, and Kenneth C. Freeman. The various kinematics of dwarf irregular galaxies in nearby groups and their dark matter distributions. *The Astronomical Journal*, 120(6):3027, 2000.

[60] V. C. Rubin and W. K. Ford, Jr. Rotation of the Andromeda Nebula from a Spectroscopic Survey of Emission Regions. ApJ, 159:379, February 1970.

[61] F. Zwicky. Die Rotverschiebung von extragalaktischen Nebeln. *Helvetica Physica Acta*, 6:110–127, 1933.

[62] W. A. Dawson, D. Wittman, M. J. Jee, P. Gee, J. P. Hughes, J. A. Tyson, S. Schmidt, P. Thorman, M. Bradač, S. Miyazaki, B. Lemaux, Y. Utsumi, and V. E. Margoniner. Discovery of a Dissociative Galaxy Cluster Merger with Large Physical Separation. ApJ, 747:L42, March 2012.

[63] C. R. Canizares, T. E. Jeltema, T. Fang, M. W. Bautz, M. R. Malm, H. L. Marshall, G. Bryan, M. Donahue, and G. P. Garmire. Chandra Observations of a Cluster and Two

Quasars at High Redshift. In D. M. Neumann and J. T. V. Tran, editors, *Clusters of Galaxies and the High Redshift Universe Observed in X-rays*, 2001.

[64] D. Harvey, R. Massey, T. Kitching, A. Taylor, and E. Tittley. The nongravitational interactions of dark matter in colliding galaxy clusters. *Science*, 347:1462–1465, March 2015.

[65] R. Massey, L. Williams, R. Smit, M. Swinbank, T. D. Kitching, D. Harvey, M. Jauzac, H. Israel, D. Clowe, A. Edge, M. Hilton, E. Jullo, A. Leonard, J. Liesenborgs, J. Merten, I. Mohammed, D. Nagai, J. Richard, A. Robertson, P. Saha, R. Santana, J. Stott, and E. Tittley. The behaviour of dark matter associated with four bright cluster galaxies in the 10 kpc core of Abell 3827. MNRAS, 449:3393–3406, June 2015.

[66] Dark matter density. `http://background.uchicago.edu/~whu/intermediate/driving2.html`. Accessed: 2016-04-04.

[67] K. Jedamzik and M. Pospelov. Big Bang nucleosynthesis and particle dark matter. *New Journal of Physics*, 11(10):105028, October 2009.

[68] K. M. Nollett and G. Steigman. BBN and the CMB constrain light, electromagnetically coupled WIMPs. Phys. Rev. D, 89(8):083508, April 2014.

[69] C. J. Copi, D. N. Schramm, and M. S. Turner. Big-Bang Nucleosynthesis and the Baryon Density of the Universe. *Science*, 267:192–199, January 1995.

[70] K. M. Belotsky, A. E. Dmitriev, E. A. Esipova, V. A. Gani, A. V. Grobov, M. Y. Khlopov, A. A. Kirillov, S. G. Rubin, and I. V. Svadkovsky. Signatures of primordial black hole dark matter. *Modern Physics Letters A*, 29:1440005, November 2014.

[71] Georges Aad et al. Observation of a new particle in the search for the standard model higgs boson with the atlas detector at the lhc. *Phys.Lett.*, B716:1–29, 2012.

[72] S. Chatrchyan, V. Khachatryan, A. M. Sirunyan, A. Tumasyan, W. Adam, E. Aguilo, T. Bergauer, M. Dragicevic, J. Erö, C. Fabjan, and et al. Observation of a new boson at a mass of 125 GeV with the CMS experiment at the LHC. *Physics Letters B*, 716:30–61, September 2012.

[73] S. Profumo. TASI 2012 Lectures on Astrophysical Probes of Dark Matter. *ArXiv e-prints*, 2013.

[74] D. Bauer, J. Buckley, M. Cahill-Rowley, R. Cotta, A. Drlica-Wagner, J. L. Feng, S. Funk, J. Hewett, D. Hooper, A. Ismail, M. Kaplinghat, A. Kusenko, K. Matchev, D. McKinsey, T. Rizzo, W. Shepherd, T. M. P. Tait, A. M. Wijangco, and M. Wood. Dark matter in the coming decade: Complementary paths to discovery and beyond. *Physics of the Dark Universe*, 7:16–23, March 2015.

[75] Arvind Rajaraman, William Shepherd, Tim MP Tait, and Alexander M Wijangco. Lhc bounds on interactions of dark matter. *Physical Review D*, 84(9):095013, 2011.

[76] Patrick J Fox, Roni Harnik, Joachim Kopp, and Yuhsin Tsai. Missing energy signatures of dark matter at the lhc. *Physical Review D*, 85(5):056011, 2012.

[77] Andrea De Simone, Gian Francesco Giudice, and Alessandro Strumia. Benchmarks for dark matter searches at the lhc. *arXiv preprint arXiv:1402.6287*, 2014.

[78] F. Richard, G. Arcadi, and Y. Mambrini. Searching for dark matter at colliders. *European Physical Journal C*, 75:171, April 2015.

[79] Teresa Marrodn Undagoitia and Ludwig Rauch. Dark matter direct-detection experiments. *Journal of Physics G: Nuclear and Particle Physics*, 43(1):013001, 2016.

[80] S. Profumo. *An Introduction to Particle Dark Matter*. World Scientific, 2016.

[81] K. Petraki and R. R. Volkas. Review of Asymmetric Dark Matter. *International Journal of Modern Physics A*, 28:1330028, July 2013.

[82] http://sourceforge.net/projects/galprop/, 2015.

[83] http://galprop.stanford.edu/, 2015.

[84] I. V. Moskalenko and A. W. Strong. Production and Propagation of Cosmic-Ray Positrons and Electrons. ApJ, 493:694–707, January 1998.

[85] A. W. Strong, I. V. Moskalenko, and O. Reimer. Diffuse Continuum Gamma Rays from the Galaxy. ApJ, 537:763–784, July 2000.

[86] I. V. Moskalenko, A. W. Strong, and O. Reimer. Diffuse galactic gamma rays, cosmic-ray nucleons and antiprotons. A&A, 338:L75–L78, October 1998.

[87] C. Evoli, D. Grasso, and L. Maccione. Diffuse neutrino and gamma-ray emissions of the galaxy above the TeV. J. Cosmology Astropart. Phys., 6:003, June 2007.

[88] V. R. Eke, J. F. Navarro, and M. Steinmetz. The Power Spectrum Dependence of Dark Matter Halo Concentrations. ApJ, 554:114–125, June 2001.

[89] J. F. Navarro, C. S. Frenk, and S. D. M. White. The Structure of Cold Dark Matter Halos. *ApJ*, 462:563, May 1996.

[90] J. F. Navarro, E. Hayashi, C. Power, A. R. Jenkins, C. S. Frenk, S. D. M. White, V. Springel, J. Stadel, and T. R. Quinn. The inner structure of ΛCDM haloes - III. Universality and asymptotic slopes. MNRAS, 349:1039–1051, April 2004.

[91] J. I. Read. The local dark matter density. *Journal of Physics G Nuclear Physics*, 41(6):063101, June 2014.

[92] J. J. Adams, J. D. Simon, M. H. Fabricius, R. C. E. van den Bosch, J. C. Barentine, R. Bender, K. Gebhardt, G. J. Hill, J. D. Murphy, R. A. Swaters, J. Thomas, and G. van de

Ven. Dwarf Galaxy Dark Matter Density Profiles Inferred from Stellar and Gas Kinematics. ApJ, 789:63, July 2014.

[93] J. Einasto and U. Haud. Galactic models with massive corona. I - Method. II - Galaxy. A&A, 223:89–106, October 1989.

[94] A. Burkert. The Structure of Dark Matter Halos in Dwarf Galaxies. ApJ, 447:L25, July 1995.

[95] W. J. G. de Blok, F. Walter, E. Brinks, C. Trachternach, S.-H. Oh, and R. C. Kennicutt, Jr. High-Resolution Rotation Curves and Galaxy Mass Models from THINGS. AJ, 136:2648–2719, December 2008.

[96] G. R. Blumenthal, S. M. Faber, J. R. Primack, and M. J. Rees. Formation of galaxies and large-scale structure with cold dark matter. Nature, 311:517–525, October 1984.

[97] O. Y. Gnedin, A. V. Kravtsov, A. A. Klypin, and D. Nagai. Response of Dark Matter Halos to Condensation of Baryons: Cosmological Simulations and Improved Adiabatic Contraction Model. ApJ, 616:16–26, November 2004.

[98] P. B. Tissera, S. D. M. White, S. Pedrosa, and C. Scannapieco. Dark matter response to galaxy formation. MNRAS, 406:922–935, August 2010.

[99] A. Pontzen and F. Governato. Cold dark matter heats up. Nature, 506:171–178, February 2014.

[100] M. Schaller, C. S. Frenk, T. Theuns, F. Calore, G. Bertone, N. Bozorgnia, R. A. Crain, A. Fattahi, J. F. Navarro, T. Sawala, and J. Schaye. Dark matter annihilation radiation in hydrodynamic simulations of Milky Way haloes. MNRAS, 455:4442–4451, February 2016.

[101] F. Governato, A. Zolotov, A. Pontzen, C. Christensen, S. H. Oh, A. M. Brooks, T. Quinn,

S. Shen, and J. Wadsley. Cuspy no more: how outflows affect the central dark matter and baryon distribution in Λ cold dark matter galaxies. MNRAS, 422:1231–1240, May 2012.

[102] C. Pérez de los Heros. The quest for dark matter with neutrino telescopes. *ArXiv e-prints*, November 2015.

[103] A. Geringer-Sameth, M. G. Walker, S. M. Koushiappas, S. E. Koposov, V. Belokurov, G. Torrealba, and N. W. Evans. Indication of Gamma-Ray Emission from the Newly Discovered Dwarf Galaxy Reticulum II. *Physical Review Letters*, 115(8):081101, August 2015.

[104] D. Hooper and T. Linden. On The gamma-ray emission from Reticulum II and other dwarf galaxies. J. Cosmology Astropart. Phys., 9:016, September 2015.

[105] E. Carlson, D. Hooper, and T. Linden. Improving the sensitivity of gamma-ray telescopes to dark matter annihilation in dwarf spheroidal galaxies. Phys. Rev. D, 91(6):061302, March 2015.

[106] M. Ackermann, A. Albert, B. Anderson, W. B. Atwood, L. Baldini, G. Barbiellini, D. Bastieri, K. Bechtol, R. Bellazzini, E. Bissaldi, R. D. Blandford, E. D. Bloom, R. Bonino, E. Bottacini, T. J. Brandt, J. Bregeon, P. Bruel, R. Buehler, G. A. Caliandro, R. A. Cameron, R. Caputo, M. Caragiulo, P. A. Caraveo, C. Cecchi, E. Charles, A. Chekhtman, J. Chiang, G. Chiaro, S. Ciprini, R. Claus, J. Cohen-Tanugi, J. Conrad, A. Cuoco, S. Cutini, F. D'Ammando, A. de Angelis, F. de Palma, R. Desiante, S. W. Digel, L. Di Venere, P. S. Drell, A. Drlica-Wagner, R. Essig, C. Favuzzi, S. J. Fegan, E. C. Ferrara, W. B. Focke, A. Franckowiak, Y. Fukazawa, S. Funk, P. Fusco, F. Gargano, D. Gasparrini, N. Giglietto, F. Giordano, M. Giroletti, T. Glanzman, G. Godfrey, G. A. Gomez-Vargas, I. A. Grenier, S. Guiriec, M. Gustafsson, E. Hays, J. W. Hewitt, D. Horan, T. Jogler, G. Jóhannesson, M. Kuss, S. Larsson, L. Latronico, J. Li, L. Li, M. Llena Garde, F. Longo, F. Loparco,

P. Lubrano, D. Malyshev, M. Mayer, M. N. Mazziotta, J. E. McEnery, M. Meyer, P. F. Michelson, T. Mizuno, A. A. Moiseev, M. E. Monzani, A. Morselli, S. Murgia, E. Nuss, T. Ohsugi, M. Orienti, E. Orlando, J. F. Ormes, D. Paneque, J. S. Perkins, M. Pesce-Rollins, F. Piron, G. Pivato, T. A. Porter, S. Rainò, R. Rando, M. Razzano, A. Reimer, O. Reimer, S. Ritz, M. Sánchez-Conde, A. Schulz, N. Sehgal, C. Sgrò, E. J. Siskind, F. Spada, G. Spandre, P. Spinelli, L. Strigari, H. Tajima, H. Takahashi, J. B. Thayer, L. Tibaldo, D. F. Torres, E. Troja, G. Vianello, M. Werner, B. L. Winer, K. S. Wood, M. Wood, G. Zaharijas, S. Zimmer, and Fermi-LAT Collaboration. Searching for Dark Matter Annihilation from Milky Way Dwarf Spheroidal Galaxies with Six Years of Fermi Large Area Telescope Data. *Physical Review Letters*, 115(23):231301, December 2015.

[107] MAGIC Collaboration. Limits to dark matter annihilation cross-section from a combined analysis of MAGIC and Fermi-LAT observations of dwarf satellite galaxies. J. Cosmology Astropart. Phys., 2:039, February 2016.

[108] S. Zimmer for the Fermi-LAT Collaboration. Galaxy Clusters with the Fermi-LAT: Status and Implications for Cosmic Rays and Dark Matter Physics. *ArXiv e-prints*, February 2015.

[109] M. Ackermann, M. Ajello, A. Albert, W. B. Atwood, L. Baldini, G. Barbiellini, D. Bastieri, K. Bechtol, R. Bellazzini, E. Bissaldi, E. D. Bloom, R. Bonino, E. Bottacini, T. J. Brandt, J. Bregeon, P. Bruel, R. Buehler, S. Buson, G. A. Caliandro, R. A. Cameron, R. Caputo, M. Caragiulo, P. A. Caraveo, J. M. Casandjian, E. Cavazzuti, C. Cecchi, E. Charles, A. Chekhtman, G. Chiaro, S. Ciprini, J. Cohen-Tanugi, J. Conrad, S. Cutini, F. D'Ammando, A. de Angelis, F. de Palma, R. Desiante, S. W. Digel, L. Di Venere, P. S. Drell, C. Favuzzi, S. J. Fegan, W. B. Focke, A. Franckowiak, Y. Fukazawa, S. Funk, P. Fusco, F. Gargano, D. Gasparrini, N. Giglietto, F. Giordano, M. Giroletti, T. Glanz-

man, G. Godfrey, G. A. Gomez-Vargas, I. A. Grenier, S. Guiriec, M. Gustafsson, J. W. Hewitt, A. B. Hill, D. Horan, T. E. Jeltema, T. Jogler, A. S. Johnson, M. Kuss, S. Larsson, L. Latronico, J. Li, L. Li, F. Longo, F. Loparco, M. N. Lovellette, P. Lubrano, S. Maldera, D. Malyshev, A. Manfreda, M. Mayer, M. N. Mazziotta, P. F. Michelson, T. Mizuno, M. E. Monzani, A. Morselli, I. V. Moskalenko, S. Murgia, E. Nuss, T. Ohsugi, M. Orienti, E. Orlando, J. F. Ormes, D. Paneque, J. S. Perkins, M. Pesce-Rollins, V. Petrosian, F. Piron, G. Pivato, T. A. Porter, S. Rainó, R. Rando, M. Razzano, A. Reimer, O. Reimer, M. Sánchez-Conde, A. Schulz, C. Sgró, E. J. Siskind, F. Spada, G. Spandre, P. Spinelli, E. Storm, H. Tajima, H. Takahashi, J. B. Thayer, D. F. Torres, G. Tosti, E. Troja, G. Vianello, K. S. Wood, M. Wood, G. Zaharijas, S. Zimmer, and Fermi-LAT Collaboration. Search for Extended Gamma-Ray Emission from the Virgo Galaxy Cluster with FERMI-LAT. ApJ, 812:159, October 2015.

[110] E. Storm, T. E. Jeltema, S. Profumo, and L. Rudnick. Constraints on Dark Matter Annihilation in Clusters of Galaxies from Diffuse Radio Emission. ApJ, 768:106, May 2013.

[111] The Fermi LAT Collaboration. Limits on dark matter annihilation signals from the Fermi LAT 4-year measurement of the isotropic gamma-ray background. J. Cosmology Astropart. Phys., 9:008, September 2015.

[112] Z. Li, Q. Yuan, and Y. Xu. Constraints on the dark matter annihilation from Fermi-LAT observation of M31. *ArXiv e-prints*, December 2013.

[113] M. Ackermann, A. Albert, W. B. Atwood, L. Baldini, J. Ballet, G. Barbiellini, D. Bastieri, R. Bellazzini, E. Bissaldi, E. D. Bloom, R. Bonino, T. J. Brandt, J. Bregeon, P. Bruel, R. Buehler, G. A. Caliandro, R. A. Cameron, M. Caragiulo, P. A. Caraveo, E. Cavazzuti, C. Cecchi, E. Charles, A. Chekhtman, J. Chiang, G. Chiaro, S. Ciprini, J. Cohen-Tanugi,

S. Cutini, F. D'Ammando, A. de Angelis, F. de Palma, R. Desiante, S. W. Digel, P. S. Drell, C. Favuzzi, E. C. Ferrara, W. B. Focke, A. Franckowiak, P. Fusco, F. Gargano, D. Gasparrini, N. Giglietto, F. Giordano, G. Godfrey, I. A. Grenier, M.-H. Grondin, L. Guillemot, S. Guiriec, A. K. Harding, A. B. Hill, D. Horan, G. Jóhannesson, J. Knödlseder, M. Kuss, S. Larsson, L. Latronico, J. Li, L. Li, F. Longo, F. Loparco, P. Lubrano, S. Maldera, P. Martin, M. Mayer, M. N. Mazziotta, P. F. Michelson, T. Mizuno, M. E. Monzani, A. Morselli, S. Murgia, E. Nuss, T. Ohsugi, M. Orienti, E. Orlando, J. F. Ormes, D. Paneque, M. Pesce-Rollins, F. Piron, G. Pivato, T. A. Porter, S. Rainò, R. Rando, M. Razzano, A. Reimer, O. Reimer, R. W. Romani, M. Sánchez-Conde, A. Schulz, C. Sgrò, E. J. Siskind, D. A. Smith, F. Spada, G. Spandre, P. Spinelli, D. J. Suson, H. Takahashi, J. B. Thayer, L. Tibaldo, D. F. Torres, G. Tosti, E. Troja, G. Vianello, M. Wood, and S. Zimmer. Deep view of the Large Magellanic Cloud with six years of Fermi-LAT observations. A&A, 586:A71, February 2016.

[114] R. Caputo, M. R. Buckley, P. Martin, E. Charles, A. M. Brooks, A. Drlica-Wagner, J. M. Gaskins, and M. Wood. Search for Gamma-ray Emission from Dark Matter Annihilation in the Small Magellanic Cloud with the Fermi Large Area Telescope. *ArXiv e-prints*, March 2016.

[115] D. Schoonenberg, J. Gaskins, G. Bertone, and J. Diemand. Dark matter subhalos and unidentified sources in the Fermi 3FGL source catalog. *ArXiv e-prints*, January 2016.

[116] F. Acero, M. Ackermann, M. Ajello, A. Albert, W. B. Atwood, M. Axelsson, L. Baldini, J. Ballet, G. Barbiellini, D. Bastieri, A. Belfiore, R. Bellazzini, E. Bissaldi, R. D. Blandford, E. D. Bloom, J. R. Bogart, R. Bonino, E. Bottacini, J. Bregeon, R. J. Britto, P. Bruel, R. Buehler, T. H. Burnett, S. Buson, G. A. Caliandro, R. A. Cameron, R. Caputo, M. Caragiulo, P. A. Caraveo, J. M. Casandjian, E. Cavazzuti, E. Charles, R. C. G.

Chaves, A. Chekhtman, C. C. Cheung, J. Chiang, G. Chiaro, S. Ciprini, R. Claus, J. Cohen-Tanugi, L. R. Cominsky, J. Conrad, S. Cutini, F. DAmmando, A. de Angelis, M. DeKlotz, F. de Palma, R. Desiante, S. W. Digel, L. Di Venere, P. S. Drell, R. Dubois, D. Dumora, C. Favuzzi, S. J. Fegan, E. C. Ferrara, J. Finke, A. Franckowiak, Y. Fukazawa, S. Funk, P. Fusco, F. Gargano, D. Gasparrini, B. Giebels, N. Giglietto, P. Giommi, F. Giordano, M. Giroletti, T. Glanzman, G. Godfrey, I. A. Grenier, M.-H. Grondin, J. E. Grove, L. Guillemot, S. Guiriec, D. Hadasch, A. K. Harding, E. Hays, J. W. Hewitt, A. B. Hill, D. Horan, G. Iafrate, T. Jogler, G. Jóhannesson, R. P. Johnson, A. S. Johnson, T. J. Johnson, W. N. Johnson, T. Kamae, J. Kataoka, J. Katsuta, M. Kuss, G. La Mura, D. Landriu, S. Larsson, L. Latronico, M. Lemoine-Goumard, J. Li, L. Li, F. Longo, F. Loparco, B. Lott, M. N. Lovellette, P. Lubrano, G. M. Madejski, F. Massaro, M. Mayer, M. N. Mazziotta, J. E. McEnery, P. F. Michelson, N. Mirabal, T. Mizuno, A. A. Moiseev, M. Mongelli, M. E. Monzani, A. Morselli, I. V. Moskalenko, S. Murgia, E. Nuss, M. Ohno, T. Ohsugi, N. Omodei, M. Orienti, E. Orlando, J. F. Ormes, D. Paneque, J. H. Panetta, J. S. Perkins, M. Pesce-Rollins, F. Piron, G. Pivato, T. A. Porter, J. L. Racusin, R. Rando, M. Razzano, S. Razzaque, A. Reimer, O. Reimer, T. Reposeur, L. S. Rochester, R. W. Romani, D. Salvetti, M. Sánchez-Conde, P. M. Saz Parkinson, A. Schulz, E. J. Siskind, D. A. Smith, F. Spada, G. Spandre, P. Spinelli, T. E. Stephens, A. W. Strong, D. J. Suson, H. Takahashi, T. Takahashi, Y. Tanaka, J. G. Thayer, J. B. Thayer, D. J. Thompson, L. Tibaldo, O. Tibolla, D. F. Torres, E. Torresi, G. Tosti, E. Troja, B. Van Klaveren, G. Vianello, B. L. Winer, K. S. Wood, M. Wood, and S. Zimmer. Fermi Large Area Telescope Third Source Catalog. ApJS, 218:23, June 2015.

[117] B. Bertoni, D. Hooper, and T. Linden. Is The Gamma-Ray Source 3FGL J2212.5+0703 A Dark Matter Subhalo? *ArXiv e-prints*, February 2016.

[118] L. Feng, Q. Yuan, P.-F. Yin, X.-J. Bi, and M. Li. Search for dark matter signals with Fermi-LAT observation of globular clusters NGC 6388 and M 15. J. Cosmology Astropart. Phys., 4:030, April 2012.

[119] A. A. Abdo, M. Ackermann, M. Ajello, L. Baldini, J. Ballet, G. Barbiellini, D. Bastieri, R. Bellazzini, R. D. Blandford, E. D. Bloom, E. Bonamente, A. W. Borgland, A. Bouvier, T. J. Brandt, J. Bregeon, M. Brigida, P. Bruel, R. Buehler, S. Buson, G. A. Caliandro, R. A. Cameron, P. A. Caraveo, S. Carrigan, J. M. Casandjian, E. Charles, S. Chaty, A. Chekhtman, C. C. Cheung, J. Chiang, S. Ciprini, R. Claus, J. Cohen-Tanugi, J. Conrad, M. E. Decesar, C. D. Dermer, F. de Palma, S. W. Digel, E. D. C. E. Silva, P. S. Drell, R. Dubois, D. Dumora, C. Favuzzi, P. Fortin, M. Frailis, Y. Fukazawa, P. Fusco, F. Gargano, D. Gasparrini, N. Gehrels, S. Germani, N. Giglietto, F. Giordano, T. Glanzman, G. Godfrey, I. Grenier, M.-H. Grondin, J. E. Grove, L. Guillemot, S. Guiriec, D. Hadasch, A. K. Harding, E. Hays, P. Jean, G. Jóhannesson, T. J. Johnson, W. N. Johnson, T. Kamae, H. Katagiri, J. Kataoka, M. Kerr, J. Knödlseder, M. Kuss, J. Lande, L. Latronico, S.-H. Lee, M. Lemoine-Goumard, M. Llena Garde, F. Longo, F. Loparco, M. N. Lovellette, P. Lubrano, A. Makeev, M. N. Mazziotta, P. F. Michelson, W. Mitthumsiri, T. Mizuno, C. Monte, M. E. Monzani, A. Morselli, I. V. Moskalenko, S. Murgia, M. Naumann-Godo, P. L. Nolan, J. P. Norris, E. Nuss, T. Ohsugi, N. Omodei, E. Orlando, J. F. Ormes, B. Pancrazi, D. Parent, M. Pepe, M. Pesce-Rollins, F. Piron, T. A. Porter, S. Rainò, R. Rando, A. Reimer, O. Reimer, T. Reposeur, J. Ripken, R. W. Romani, M. Roth, H. F.-W. Sadrozinski, P. M. Saz Parkinson, C. Sgrò, E. J. Siskind, D. A. Smith, P. Spinelli, M. S. Strickman, D. J. Suson, H. Takahashi, T. Takahashi, T. Tanaka, J. B. Thayer, J. G. Thayer, L. Tibaldo, D. F. Torres, G. Tosti, A. Tramacere, Y. Uchiyama, T. L. Usher, V. Vasileiou, C. Venter, N. Vilchez, V. Vitale, A. P. Waite, P. Wang, N. Webb, B. L. Winer, Z. Yang, T. Ylinen, M. Ziegler, and Fermi LAT Collaboration. A population of

gamma-ray emitting globular clusters seen with the Fermi Large Area Telescope. A&A, 524:A75, December 2010.

[120] J. Buckley, D. F. Cowen, S. Profumo, A. Archer, M. Cahill-Rowley, R. Cotta, S. Digel, A. Drlica-Wagner, F. Ferrer, S. Funk, J. Hewett, J. Holder, B. Humensky, A. Ismail, M. Israel, T. Jeltema, A. Olinto, A. Peter, J. Pretz, T. Rizzo, J. Siegal-Gaskins, A. Smith, D. Staszak, J. Vandenbroucke, and M. Wood. Cosmic Frontier Indirect Dark Matter Detection Working Group Summary. *ArXiv e-prints*, October 2013.

[121] F. D'Eramo, K. Hambleton, S. Profumo, and T. Stefaniak. Dark Matter Inelastic Up-Scattering with the Interstellar Plasma: An Exciting New Source of X-Ray Lines, including at 3.5 keV. *ArXiv e-prints*, March 2016.

[122] A. A. Abdo, M. Ajello, A. Allafort, L. Baldini, J. Ballet, G. Barbiellini, M. G. Baring, D. Bastieri, A. Belfiore, R. Bellazzini, and et al. The Second Fermi Large Area Telescope Catalog of Gamma-Ray Pulsars. ApJS, 208:17, October 2013.

[123] F. Acero, M. Ackermann, M. Ajello, L. Baldini, J. Ballet, G. Barbiellini, D. Bastieri, R. Bellazzini, E. Bissaldi, R. Blandford, E. D. Bloom, R. Bonino, E. Bottacini, J. Bregeon, P. Bruel, R. Buehler, S. Buson, G. A. Caliandro, R. A. Cameron, R Caputo, M. Caragiulo, P. A. Caraveo, J. M. Casandjian, E. Cavazzuti, C. Cecchi, A. Chekhtman, J. Chiang, G. Chiaro, S. Ciprini, R. Claus, J. M. Cohen, J. Cohen-Tanugi, L. R. Cominsky, B. Condon, J. Conrad, S. Cutini, F. D'Ammando, A. Angelis, F. Palma, R. Desiante, S. W. Digel, L. Venere, P. S Drell, A. Drlica-Wagner, C. Favuzzi, E. C. Ferrara, A. Franckowiak, Y. Fukazawa, Prof., S. Funk, Prof., P. Fusco, F. Gargano, D. Gasparrini, N. Giglietto, P. Giommi, F. Giordano, M. Giroletti, T. Glanzman, G. Godfrey, G. Gomez-Vargas, I. A. Grenier, M.-H. Grondin, L. Guillemot, S. Guiriec, M Gustafsson, D. Hadasch, A. K. Harding, M. Hayashida, E. Hays, J. W. Hewitt, A. B. Hill, D. Horan, X. Hou, G. Iafrate,

T. Jogler, G. J'ohannesson, A. S. Johnson, T. Kamae, H. Katagiri, J. Kataoka, Prof., J. Katsuta, M. Kerr, J. Knodlseder, D. Kocevski, Prof., M. Kuss, H. Laffon, J. Lande, S. Larsson, L. Latronico, M. Lemoine-Goumard, J. Li, L. Li, F. Longo, F. Loparco, M. N. Lovellette, P. Lubrano, J. Magill, S. Maldera, M. Marelli, M. Mayer, M. N. Mazziotta, P. F. Michelson, W. Mitthumsiri, T. Mizuno, A. A. Moiseev, M. E. Monzani, E. Moretti, A. Morselli, I. V. Moskalenko, S. Murgia, Prof., R. Nemmen, Prof., E. Nuss, T. Ohsugi, N. Omodei, M. Orienti, E. Orlando, J. F. Ormes, D. Paneque, J. S. Perkins, M. Pesce-Rollins, V. Petrosian, Prof., F. Piron, G. Pivato, T. Porter, S. Rain'o, R. Rando, M. Razzano, S. Razzaque, A. Reimer, O. Reimer, Prof., M. Renaud, T. Reposeur, M. Romain Rousseau, P. M. Parkinson, J. Schmid, A. Schulz, C. Sgr'o, E. J Siskind, F. Spada, G. Spandre, P. Spinelli, A. W. Strong, D. Suson, H. Tajima, H. Takahashi, T. Tanaka, J. B. Thayer, D. J. Thompson, L. Tibaldo, O. Tibolla, D. F. Torres, Prof., G. Tosti, E. Troja, Y. Uchiyama, G. Vianello, B. Wells, K. Wood, M. Wood, M. Yassine, and S. Zimmer. The 1st Fermi Lat Supernova Remnant Catalog. *ArXiv e-prints*, November 2015.

[124] P. S. Marrocchesi. CALET: a high energy astroparticle physics experiment on the ISS. *ArXiv e-prints*, December 2015.

[125] T. Bringmann, X. Huang, A. Ibarra, S. Vogl, and C. Weniger. Fermi LAT search for internal bremsstrahlung signatures from dark matter annihilation. *JCAP*, 7:54, July 2012.

[126] M. Cirelli, G. Corcella, A. Hektor, G. Hütsi, M. Kadastik, P. Panci, M. Raidal, F. Sala, and A. Strumia. PPPC 4 DM ID: a poor particle physicist cookbook for dark matter indirect detection. J. Cosmology Astropart. Phys., 3:051, March 2011.

[127] T. Sjöstrand, S. Mrenna, and P. Skands. A brief introduction to PYTHIA 8.1. *Computer Physics Communications*, 178:852–867, June 2008.

[128] M. Bähr, S. Gieseke, M. A. Gigg, D. Grellscheid, K. Hamilton, O. Latunde-Dada,

S. Plätzer, P. Richardson, M. H. Seymour, A. Sherstnev, and B. R. Webber. Herwig++ physics and manual. *European Physical Journal C*, 58:639–707, December 2008.

[129] J. F. Beacom, N. F. Bell, and G. Bertone. Gamma-Ray Constraint on Galactic Positron Production by MeV Dark Matter. *Physical Review Letters*, 94(17):171301, May 2005.

[130] L.A. Dal and A.R. Raklev. Antideuteron limits on decaying dark matter with a tuned formation model. 2014.

[131] Alejandro Ibarra and David Tran. Gamma-ray spectrum from gravitino dark matter decay. *Phys. Rev. Lett.*, 100:061301, Feb 2008.

[132] Johan Alwall, Michel Herquet, Fabio Maltoni, Olivier Mattelaer, and Tim Stelzer. MadGraph 5 : Going Beyond. *JHEP*, 1106:128, 2011.

[133] J. Knödlseder, P. Jean, V. Lonjou, G. Weidenspointner, N. Guessoum, W. Gillard, G. Skinner, P. von Ballmoos, G Vedrenne, J.-P. Roques, S Schanne, B Teegarden, V. Schönfelder, and C. Winkler. The all-sky distribution of 511 keV electron-positron annihilation emission. *Astronomy and Astrophysics*, 441(2):513–532, October 2005.

[134] Esra Bulbul, Maxim Markevitch, Adam Foster, Randall K. Smith, Michael Loewenstein, et al. Detection of An Unidentified Emission Line in the Stacked X-ray spectrum of Galaxy Clusters. 2014.

[135] D. P. Finkbeiner and N. Weiner. Exciting dark matter and the INTEGRAL/SPI 511keV signal. Phys. Rev. D, 76(8):083519, October 2007.

[136] Alexey Boyarsky, Oleg Ruchayskiy, and Mikhail Shaposhnikov. The Role of sterile neutrinos in cosmology and astrophysics. *Ann.Rev.Nucl.Part.Sci.*, 59:191–214, 2009.

[137] Tetsutaro Higaki, Kwang Sik Jeong, and Fuminobu Takahashi. The 7 keV axion dark matter and the X-ray line signal. *Phys.Lett.*, B733:25–31, 2014.

[138] Joerg Jaeckel, Javier Redondo, and Andreas Ringwald. A 3.55 keV hint for decaying axion-like particle dark matter. *Phys.Rev.*, D89:103511, 2014.

[139] Hyun Min Lee, Seong Chan Park, and Wan-Il Park. Cluster X-ray line at 3.5 keV from axion-like dark matter. 2014.

[140] Michele Cicoli, Joseph P. Conlon, M. C. David Marsh, and Markus Rummel. A 3.55 keV Photon Line and its Morphology from a 3.55 keV ALP Line. 2014.

[141] A. Ringwald. Axions and Axion-Like Particles. 2014.

[142] O. Adriani, G. C. Barbarino, G. A. Bazilevskaya, R. Bellotti, M. Boezio, E. A. Bogomolov, L. Bonechi, M. Bongi, V. Bonvicini, S. Bottai, A. Bruno, F. Cafagna, D. Campana, P. Carlson, M. Casolino, G. Castellini, M. P. de Pascale, G. de Rosa, N. de Simone, V. di Felice, A. M. Galper, L. Grishantseva, P. Hofverberg, S. V. Koldashov, S. Y. Krutkov, A. N. Kvashnin, A. Leonov, V. Malvezzi, L. Marcelli, W. Menn, V. V. Mikhailov, E. Mocchiutti, S. Orsi, G. Osteria, P. Papini, M. Pearce, P. Picozza, M. Ricci, S. B. Ricciarini, M. Simon, R. Sparvoli, P. Spillantini, Y. I. Stozhkov, A. Vacchi, E. Vannuccini, G. Vasilyev, S. A. Voronov, Y. T. Yurkin, G. Zampa, N. Zampa, and V. G. Zverev. An anomalous positron abundance in cosmic rays with energies 1.5-100GeV. Nature, 458:607–609, April 2009.

[143] L. Accardo, M. Aguilar, D. Aisa, B. Alpat, A. Alvino, G. Ambrosi, K. Andeen, L. Arruda, N. Attig, P. Azzarello, A. Bachlechner, F. Barao, A. Barrau, L. Barrin, A. Bartoloni, L. Basara, M. Battarbee, R. Battiston, J. Bazo, U. Becker, M. Behlmann, B. Beischer, J. Berdugo, B. Bertucci, G. Bigongiari, V. Bindi, S. Bizzaglia, M. Bizzarri, G. Boella, W. de Boer, K. Bollweg, V. Bonnivard, B. Borgia, S. Borsini, M. J. Boschini, M. Bourquin, J. Burger, F. Cadoux, X. D. Cai, M. Capell, S. Caroff, G. Carosi, J. Casaus, V. Cascioli, G. Castellini, I. Cernuda, D. Cerreta, F. Cervelli, M. J. Chae, Y. H. Chang, A. I. Chen, H. Chen, G. M. Cheng, H. S. Chen, L. Cheng, A. Chikanian, H. Y. Chou, E. Choumilov,

V. Choutko, C. H. Chung, F. Cindolo, C. Clark, R. Clavero, G. Coignet, C. Consolandi, A. Contin, C. Corti, B. Coste, Z. Cui, M. Dai, C. Delgado, S. Della Torre, M. B. Demirköz, L. Derome, S. Di Falco, L. Di Masso, F. Dimiccoli, C. Díaz, P. von Doetinchem, W. J. Du, M. Duranti, D. D'Urso, A. Eline, F. J. Eppling, T. Eronen, Y. Y. Fan, L. Farnesini, J. Feng, E. Fiandrini, A. Fiasson, E. Finch, P. Fisher, Y. Galaktionov, G. Gallucci, B. García, R. García-López, H. Gast, I. Gebauer, M. Gervasi, A. Ghelfi, W. Gillard, F. Giovacchini, P. Goglov, J. Gong, C. Goy, V. Grabski, D. Grandi, M. Graziani, C. Guandalini, I. Guerri, K. H. Guo, D. Haas, M. Habiby, S. Haino, K. C. Han, Z. H. He, M. Heil, R. Henning, J. Hoffman, T. H. Hsieh, Z. C. Huang, C. Huh, M. Incagli, M. Ionica, W. Y. Jang, H. Jinchi, K. Kanishev, G. N. Kim, K. S. Kim, Th. Kirn, R. Kossakowski, O. Kounina, A. Kounine, V. Koutsenko, M. S. Krafczyk, S. Kunz, G. La Vacca, E. Laudi, G. Laurenti, I. Lazzizzera, A. Lebedev, H. T. Lee, S. C. Lee, C. Leluc, G. Levi, H. L. Li, J. Q. Li, Q. Li, Q. Li, T. X. Li, W. Li, Y. Li, Z. H. Li, Z. Y. Li, S. Lim, C. H. Lin, P. Lipari, T. Lippert, D. Liu, H. Liu, M. Lolli, T. Lomtadze, M. J. Lu, Y. S. Lu, K. Luebelsmeyer, F. Luo, J. Z. Luo, S. S. Lv, R. Majka, A. Malinin, C. Mañá, J. Marín, T. Martin, G. Martínez, N. Masi, F. Massera, D. Maurin, A. Menchaca-Rocha, Q. Meng, D. C. Mo, B. Monreal, L. Morescalchi, P. Mott, M. Müller, J. Q. Ni, N. Nikonov, F. Nozzoli, P. Nunes, A. Obermeier, A. Oliva, M. Orcinha, F. Palmonari, C. Palomares, M. Paniccia, A. Papi, M. Pauluzzi, E. Pedreschi, S. Pensotti, R. Pereira, R. Pilastrini, F. Pilo, A. Piluso, C. Pizzolotto, V. Plyaskin, M. Pohl, V. Poireau, E. Postaci, A. Putze, L. Quadrani, X. M. Qi, P. G. Rancoita, D. Rapin, J. S. Ricol, I. Rodríguez, S. Rosier-Lees, L. Rossi, A. Rozhkov, D. Rozza, G. Rybka, R. Sagdeev, J. Sandweiss, P. Saouter, C. Sbarra, S. Schael, S. M. Schmidt, D. Schuckardt, A. Schulz von Dratzig, G. Schwering, G. Scolieri, E. S. Seo, B. S. Shan, Y. H. Shan, J. Y. Shi, X. Y. Shi, Y. M. Shi, T. Siedenburg, D. Son, F. Spada, F. Spinella, W. Sun, W. H. Sun, M. Tacconi, C. P. Tang, X. W. Tang, Z. C. Tang, L. Tao, D. Tescaro, Samuel C. C. Ting, S. M.

Ting, N. Tomassetti, J. Torsti, C. Türkoğlu, T. Urban, V. Vagelli, E. Valente, C. Vannini, E. Valtonen, S. Vaurynovich, M. Vecchi, M. Velasco, J. P. Vialle, V. Vitale, G. Volpini, L. Q. Wang, Q. L. Wang, R. S. Wang, X. Wang, Z. X. Wang, Z. L. Weng, K. Whitman, J. Wienkenhöver, H. Wu, K. Y. Wu, X. Xia, M. Xie, S. Xie, R. Q. Xiong, G. M. Xin, N. S. Xu, W. Xu, Q. Yan, J. Yang, M. Yang, Q. H. Ye, H. Yi, Y. J. Yu, Z. Q. Yu, S. Zeissler, J. H. Zhang, M. T. Zhang, X. B. Zhang, Z. Zhang, Z. M. Zheng, F. Zhou, H. L. Zhuang, V. Zhukov, A. Zichichi, N. Zimmermann, P. Zuccon, and C. Zurbach. High statistics measurement of the positron fraction in primary cosmic rays of 0.5˜500 gev with the alpha magnetic spectrometer on the international space station. *Phys. Rev. Lett.*, 113:121101, Sep 2014.

[144] S. Profumo. Dissecting cosmic-ray electron-positron data with Occam's razor: the role of known pulsars. *Central European Journal of Physics*, 10:1–31, February 2012.

[145] A. Ibarra, A. S. Lamperstorfer, and J. Silk. Dark matter annihilations and decays after the AMS-02 positron measurements. Phys. Rev. D, 89(6):063539, March 2014.

[146] S. Orito, T. Maeno, H. Matsunaga, K. Abe, K. Anraku, Y. Asaoka, M. Fujikawa, M. Imori, M. Ishino, Y. Makida, N. Matsui, H. Matsumoto, J. Mitchell, T. Mitsui, A. Moiseev, M. Motoki, J. Nishimura, M. Nozaki, J. Ormes, T. Saeki, T. Sanuki, M. Sasaki, E. S. Seo, Y. Shikaze, T. Sonoda, R. Streitmatter, J. Suzuki, K. Tanaka, I. Ueda, N. Yajima, T. Yamagami, A. Yamamoto, T. Yoshida, and K. Yoshimura. Precision Measurement of Cosmic-Ray Antiproton Spectrum. *Physical Review Letters*, 84:1078–1081, February 2000.

[147] T. Maeno, S. Orito, H. Matsunaga, K. Abe, K. Anraku, Y. Asaoka, M. Fujikawa, M. Imori, Y. Makida, N. Matsui, H. Matsumoto, J. Mitchell, T. Mitsui, A. Moiseev, M. Motoki, J. Nishimura, M. Nozaki, J. Ormes, T. Saeki, T. Sanuki, M. Sasaki, E. S. Seo, Y. Shikaze, T. Sonoda, R. Streitmatter, J. Suzuki, K. Tanaka, I. Ueda, J. Z. Wang, N. Yajima, T. Yam-

agami, A. Yamamoto, T. Yoshida, and K. Yoshimura. Successive measurements of cosmic-ray antiproton spectrum in a positive phase of the solar cycle. *Astroparticle Physics*, 16:121–128, November 2001.

[148] S. Haino, T. Sanuki, K. Abe, K. Anraku, Y. Asaoka, H. Fuke, M. Imori, A. Itasaki, T. Maeno, Y. Makida, S. Matsuda, N. Matsui, H. Matsumoto, J. W. Mitchell, A. A. Moiseev, J. Nishimura, M. Nozaki, S. Orito, J. F. Ormes, M. Sasaki, E. S. Seo, Y. Shikaze, R. E. Streitmatter, J. Suzuki, Y. Takasugi, K. Tanaka, K. Tanizaki, T. Yamagami, A. Yamamoto, Y. Yamamoto, K. Yamato, T. Yoshida, and K. Yoshimura. Measurements of primary and atmospheric cosmic-ray spectra with the BESS-TeV spectrometer. *Physics Letters B*, 594:35–46, July 2004.

[149] O. Adriani, G. C. Barbarino, G. A. Bazilevskaya, R. Bellotti, M. Boezio, E. A. Bogomolov, L. Bonechi, M. Bongi, V. Bonvicini, S. Bottai, A. Bruno, F. Cafagna, D. Campana, P. Carlson, M. Casolino, G. Castellini, M. P. de Pascale, G. de Rosa, D. Fedele, A. M. Galper, L. Grishantseva, P. Hofverberg, A. Leonov, S. V. Koldashov, S. Y. Krutkov, A. N. Kvashnin, V. Malvezzi, L. Marcelli, W. Menn, V. V. Mikhailov, M. Minori, E. Mocchiutti, M. Nagni, S. Orsi, G. Osteria, P. Papini, M. Pearce, P. Picozza, M. Ricci, S. B. Ricciarini, M. Simon, R. Sparvoli, P. Spillantini, Y. I. Stozhkov, E. Taddei, A. Vacchi, E. Vannuccini, G. Vasilyev, S. A. Voronov, Y. T. Yurkin, G. Zampa, N. Zampa, and V. G. Zverev. New Measurement of the Antiproton-to-Proton Flux Ratio up to 100 GeV in the Cosmic Radiation. *Physical Review Letters*, 102(5):051101, February 2009.

[150] G. Giesen, M. Boudaud, Y. Génolini, V. Poulin, M. Cirelli, P. Salati, and P. D. Serpico. AMS-02 antiprotons, at last! Secondary astrophysical component and immediate implications for Dark Matter. J. Cosmology Astropart. Phys., 9:023, September 2015.

[151] F. Donato, N. Fornengo, and P. Salati. Antideuterons as a signature of supersymmetric dark matter. Phys. Rev. D, 62(4):043003, August 2000.

[152] O. Adriani, G. C. Barbarino, G. A. Bazilevskaya, R. Bellotti, M. Boezio, E. A. Bogomolov, L. Bonechi, M. Bongi, V. Bonvicini, S. Borisov, S. Bottai, A. Bruno, F. Cafagna, D. Campana, R. Carbone, P. Carlson, M. Casolino, G. Castellini, L. Consiglio, M. P. De Pascale, C. De Santis, N. De Simone, V. Di Felice, A. M. Galper, W. Gillard, L. Grishantseva, G. Jerse, A. V. Karelin, S. V. Koldashov, S. Y. Krutkov, A. N. Kvashnin, A. Leonov, V. Malakhov, V. Malvezzi, L. Marcelli, A. G. Mayorov, W. Menn, V. V. Mikhailov, E. Mocchiutti, A. Monaco, N. Mori, N. Nikonov, G. Osteria, F. Palma, P. Papini, M. Pearce, P. Picozza, C. Pizzolotto, M. Ricci, S. B. Ricciarini, L. Rossetto, R. Sarkar, M. Simon, R. Sparvoli, P. Spillantini, Y. I. Stozhkov, A. Vacchi, E. Vannuccini, G. Vasilyev, S. A. Voronov, Y. T. Yurkin, J. Wu, G. Zampa, N. Zampa, and V. G. Zverev. PAMELA Measurements of Cosmic-Ray Proton and Helium Spectra. *Science*, 332:69–, April 2011.

[153] H. Baer and S. Profumo. Low energy antideuterons: shedding light on dark matter. *JCAP*, 12:8, December 2005.

[154] Y. Cui, J. D. Mason, and L. Randall. General analysis of antideuteron searches for dark matter. *Journal of High Energy Physics*, 11:17, November 2010.

[155] A. Ibarra and S. Wild. Determination of the cosmic antideuteron flux in a Monte Carlo approach. Phys. Rev. D, 88(2):023014, July 2013.

[156] M. Kadastik, M. Raidal, and A. Strumia. Enhanced anti-deuteron Dark Matter signal and the implications of PAMELA. *Physics Letters B*, 683:248–254, January 2010.

[157] N. Fornengo, L. Maccione, and A. Vittino. Dark matter searches with cosmic antideuterons: status and perspectives. *JCAP*, 9:31, September 2013.

[158] A. Ibarra and S. Wild. Prospects of antideuteron detection from dark matter annihilations or decays at AMS-02 and GAPS. *JCAP*, 2:21, February 2013.

[159] ALEPH Collaboration, S. Schael, R. Barate, R. Brunelière, I. de Bonis, D. Decamp, C. Goy, S. Jézéquel, J.-P. Lees, F. Martin, and et al. Deuteron and anti-deuteron production in ee collisions at the Z resonance. *Physics Letters B*, 639:192–201, August 2006.

[160] A. Monteux, E. Carlson, and J. M. Cornell. Gravitino dark matter and flavor symmetries. *Journal of High Energy Physics*, 8:47, August 2014.

[161] Glennys R. Farrar and Pierre Fayet. Phenomenology of the production, decay, and detection of new hadronic states associated with supersymmetry. *Phys.Lett.*, B76:575–579, 1978.

[162] M.C. Bento, Lawrence J. Hall, and Graham G. Ross. Generalized matter parities from the superstring. *Nucl.Phys.*, B292:400, 1987.

[163] Luis E. Ibanez and Graham G. Ross. Fermion masses and mixing angles from gauge symmetries. *Phys.Lett.*, B332:100–110, 1994.

[164] Herbi K. Dreiner, Christoph Luhn, and Marc Thormeier. What is the discrete gauge symmetry of the mssm? *Phys.Rev.*, D73:075007, 2006.

[165] Adam Alloul, Neil D. Christensen, Celine Degrande, Claude Duhr, and Benjamin Fuks. Feynrules 2.0 - a complete toolbox for tree-level phenomenology. 2013.

[166] Neil D. Christensen, P. de Aquino, N. Deutschmann, C. Duhr, B. Fuks, et al. Simulating spin-$\frac{3}{2}$ particles at colliders. *Eur.Phys.J.*, C73:2580, 2013.

[167] Benjamin Fuks. Beyond the minimal supersymmetric standard model: from theory to phenomenology. *Int.J.Mod.Phys.*, A27:1230007, 2012.

[168] Torbjorn Sjostrand, Stephen Mrenna, and Peter Z. Skands. A Brief Introduction to PYTHIA 8.1. *Comput.Phys.Commun.*, 178:852–867, 2008.

[169] L. J. Gleeson and W. I. Axford. Solar Modulation of Galactic Cosmic Rays. ApJ, 154:1011, December 1968.

[170] L.A. Dal and M. Kachelriess. Antideuterons from dark matter annihilations and hadronization model dependence. *Phys.Rev.*, D86:103536, 2012.

[171] S. T. Butler and C. A. Pearson. Deuterons from high-energy proton bombardment of matter. *Phys. Rev.*, 129:836–842, Jan 1963.

[172] A. Schwarzschild and Č. Zupančič. Production of tritons, deuterons, nucleons, and mesons by 30-gev protons on a1, be, and fe targets. *Phys. Rev.*, 129:854–862, Jan 1963.

[173] M. C. Lemaire, S. Nagamiya, S. Schnetzer, H. Steiner, and I. Tanihata. Composite particle emission in relativistic heavy ion collisions. *Physics Letters B*, 85(1):38–42, July 1979.

[174] P. Chardonnet, J. Orloff, and P. Salati. Production of anti-matter in our galaxy. *Physics Letters B*, 409:313–320, December 1997.

[175] P. Chardonnet, J. Orloff, and P. Salati. Production of anti-matter in our galaxy. *Physics Letters B*, 409:313–320, December 1997.

[176] A Bussiére, G Giacomelli, E Lesquoy, R Meunier, L Moscoso, A Muller, F Rimondi, S Zucchelli, and S Zylberajch. Particle production and search for long-lived particles in 200240 GeV/c proton-nucleon collisions. *Nuclear Physics B*, 174(1):1–15, 1980.

[177] C. Hailey, T. Aramaki, P. von Doetinchem, and R. A. Ong. Dedicated Indirect Searches for Dark Matter Using Antideuterons. *ArXiv e-prints*, May 2013.

[178] K. Mori, C. J. Hailey, E. A. Baltz, W. W. Craig, M. Kamionkowski, W. T. Serber, and

P. Ullio. A Novel Antimatter Detector Based on X-Ray Deexcitation of Exotic Atoms. ApJ, 566:604–616, February 2002.

[179] M. Cirelli and G. Giesen. Antiprotons from Dark Matter: current constraints and future sensitivities. *JCAP*, 4:15, April 2013.

[180] A. W. Strong, H. Bloemen, R. Diehl, W. Hermsen, and V. Schönfelder. COMPTEL Skymapping: a New Approach Using Parallel Computing. *Astrophysical Letters and Communications*, 39:209, 1999.

[181] Michael P. Muno, F.K. Baganoff, M.W. Bautz, E.D. Feigelson, G.P. Garmire, et al. Diffuse x-ray emission in a deep Chandra image of the Galactic center. *Astrophys.J.*, 613:326–342, 2004.

[182] Dan Hooper, Douglas P Finkbeiner, and Gregory Dobler. Evidence Of Dark Matter Annihilations In The WMAP Haze. page 4, May 2007.

[183] Planck Collaboration A Abergel, P A R Ade, N Aghanim, M Arnaud, M Ashdown, J Aumont, C Baccigalupi, and A Balbi. Special feature Planck early results . XXIV . Dust in the diffuse interstellar medium. 24:1–30, 2011.

[184] T. Daylan, D. P. Finkbeiner, D. Hooper, T. Linden, S. K. N. Portillo, N. L. Rodd, and T. R. Slatyer. The Characterization of the Gamma-Ray Signal from the Central Milky Way: A Compelling Case for Annihilating Dark Matter. *ArXiv e-prints*, February 2014.

[185] F. Calore, I. Cholis, and C. Weniger. Background model systematics for the Fermi GeV excess. *ArXiv e-prints*, August 2014.

[186] Stefano Profumo and Piero Ullio. Multi-Wavelength Searches for Particle Dark Matter. 2010.

[187] Sergio Colafrancesco, S. Profumo, and P. Ullio. Multi-frequency analysis of neutralino dark matter annihilations in the Coma cluster. *Astron.Astrophys.*, 455:21, 2006.

[188] Sergio Colafrancesco, S. Profumo, and P. Ullio. Detecting dark matter WIMPs in the Draco dwarf: A multi-wavelength perspective. *Phys.Rev.*, D75:023513, 2007.

[189] D. H. Oaknin and A. R. Zhitnitsky. 511 keV Photons from Color Superconducting Dark Matter. *Physical Review Letters*, 94(10):101301, March 2005.

[190] K. Lawson and A. R. Zhitnitsky. Diffuse cosmic gamma rays at 1-20 MeV: a trace of the dark matter? J. Cosmology Astropart. Phys., 1:022, January 2008.

[191] M. M. Forbes and A. R. Zhitnitsky. WMAP haze: Directly observing dark matter? Phys. Rev. D, 78(8):083505, October 2008.

[192] M. M. Forbes, K. Lawson, and A. R. Zhitnitsky. Electrosphere of macroscopic "quark nuclei": A source for diffuse MeV emissions from dark matter. Phys. Rev. D, 82(8):083510, October 2010.

[193] Mikhail Gorchtein, Stefano Profumo, and Lorenzo Ubaldi. Probing Dark Matter with AGN Jets. *Phys.Rev.*, D82:083514, 2010.

[194] Stefano Profumo and Lorenzo Ubaldi. Cosmic Ray-Dark Matter Scattering: a New Signature of (Asymmetric) Dark Matter in the Gamma Ray Sky. *JCAP*, 1108:020, 2011.

[195] Stefano Profumo, Lorenzo Ubaldi, and Mikhail Gorchtein. Gamma Rays from Cosmic-Ray Proton Scattering in AGN Jets: the Intra-Cluster Gas vastly outshines Dark Matter. *JCAP*, 1304:012, 2013.

[196] K. Lawson. Quark matter induced extensive air showers. Phys. Rev. D, 83(10):103520, May 2011.

[197] K. Lawson. Atmospheric radio signals from quark nugget dark matter. Phys. Rev. D, 88(4):043519, August 2013.

[198] K. Lawson and A. R. Zhitnitsky. Isotropic radio background from quark nugget dark matter. *Physics Letters B*, 724:17–21, July 2013.

[199] M. Pohl, P. Englmaier, and N. Bissantz. Three-Dimensional Distribution of Molecular Gas in the Barred Milky Way. ApJ, 677:283–291, April 2008.

[200] T. M. Dame, D. Hartmann, and P. Thaddeus. The Milky Way in Molecular Clouds: A New Complete CO Survey. ApJ, 547:792–813, February 2001.

[201] H. Nakanishi and Y. Sofue. Three-Dimensional Distribution of the ISM in the Milky Way Galaxy: I. The H I Disk. PASJ, 55:191–202, February 2003.

[202] P. M. W. Kalberla, W. B. Burton, D. Hartmann, E. M. Arnal, E. Bajaja, R. Morras, and W. G. L. Pöppel. The Leiden/Argentine/Bonn (LAB) Survey of Galactic HI. Final data release of the combined LDS and IAR surveys with improved stray-radiation corrections. A&A, 440:775–782, September 2005.

[203] Katia M. Ferriere. The Interstellar Environment of our Galaxy. page 39, June 2001.

[204] K. Ferrière, William Gillard, and Pierre Jean. Spatial distribution of interstellar gas in the innermost 3 kpc of our galaxy. *Astronomy and Astrophysics*, 467(2):611–627, May 2007.

[205] H. Nakanishi and Y. Sofue. Three-Dimensional Distribution of the ISM in the Milky Way Galaxy: II. The Molecular Gas Disk. PASJ, 58:847–860, October 2006.

[206] M. A. Gordon and W. B. Burton. Carbon monoxide in the Galaxy. I - The radial distribution of CO, H2, and nucleons. *The Astrophysical Journal*, 208:346, September 1976.

[207] John M. Dickey and Felix J Lockman. H I in the Galaxy. *Annual Review of Astronomy and Astrophysics*, 28(1):215–259, September 1990.

[208] D. Schlegel, D. Finkbeiner, and M. Davis. Application of SFD Dust Maps to Galaxy Counts and CMB Experiments. In S. Colombi, Y. Mellier, and B. Raban, editors, *Wide Field Surveys in Cosmology*, page 297, 1998.

[209] I. A. Grenier, J.-M. Casandjian, and R. Terrier. Unveiling Extensive Clouds of Dark Gas in the Solar Neighborhood. *Science*, 307:1292–1295, February 2005.

[210] M. Ackermann, M. Ajello, W. B. Atwood, L. Baldini, J. Ballet, G. Barbiellini, D. Bastieri, K. Bechtol, R. Bellazzini, B. Berenji, R. D. Blandford, E. D. Bloom, E. Bonamente, a. W. Borgland, T. J. Brandt, J. Bregeon, M. Brigida, P. Bruel, R. Buehler, S. Buson, G. a. Caliandro, R. a. Cameron, P. a. Caraveo, E. Cavazzuti, C. Cecchi, E. Charles, A. Chekhtman, J. Chiang, S. Ciprini, R. Claus, J. Cohen-Tanugi, J. Conrad, S. Cutini, A. de Angelis, F. de Palma, C. D. Dermer, S. W. Digel, E. do Couto e Silva, P. S. Drell, A. Drlica-Wagner, L. Falletti, C. Favuzzi, S. J. Fegan, E. C. Ferrara, W. B. Focke, P. Fortin, Y. Fukazawa, S. Funk, P. Fusco, D. Gaggero, F. Gargano, S. Germani, N. Giglietto, F. Giordano, M. Giroletti, T. Glanzman, G. Godfrey, J. E. Grove, S. Guiriec, M. Gustafsson, D. Hadasch, Y. Hanabata, a. K. Harding, M. Hayashida, E. Hays, D. Horan, X. Hou, R. E. Hughes, G. Jóhannesson, A. S. Johnson, R. P. Johnson, T. Kamae, H. Katagiri, J. Kataoka, J. Knödlseder, M. Kuss, J. Lande, L. Latronico, S.-H. Lee, M. Lemoine-Goumard, F. Longo, F. Loparco, B. Lott, M. N. Lovellette, P. Lubrano, M. N. Mazziotta, J. E. McEnery, P. F. Michelson, W. Mitthumsiri, T. Mizuno, C. Monte, M. E. Monzani, A. Morselli, I. V. Moskalenko, S. Murgia, M. Naumann-Godo, J. P. Norris, E. Nuss, T. Ohsugi, A. Okumura, N. Omodei, E. Orlando, J. F. Ormes, D. Paneque, J. H. Panetta, D. Parent, M. Pesce-Rollins, M. Pierbattista, F. Piron, G. Pivato, T. a. Porter, S. Rainò, R. Rando, M. Razzano, S. Razzaque, A. Reimer, O. Reimer, H. F.-W. Sadrozinski, C. Sgrò, E. J. Siskind, G. Spandre, P. Spinelli, a. W. Strong, D. J. Suson, H. Takahashi, T. Tanaka, J. G. Thayer, J. B.

Thayer, D. J. Thompson, L. Tibaldo, M. Tinivella, D. F. Torres, G. Tosti, E. Troja, T. L. Usher, J. Vandenbroucke, V. Vasileiou, G. Vianello, V. Vitale, a. P. Waite, P. Wang, B. L. Winer, K. S. Wood, M. Wood, Z. Yang, M. Ziegler, and S. Zimmer. FERMI -LAT OBSERVATIONS OF THE DIFFUSE γ-RAY EMISSION: IMPLICATIONS FOR COSMIC RAYS AND THE INTERSTELLAR MEDIUM. *The Astrophysical Journal*, 750(1):3, May 2012.

[211] JM Cordes and TJW Lazio. NE2001. I. A new model for the galactic distribution of free electrons and its fluctuations. *arXiv preprint astro-ph/0207156*, page 21, July 2002.

[212] J M Cordes and T. J. W. Lazio. NE2001. II. Using Radio Propagation Data to Construct a Model for the Galactic Distribution of Free Electrons. page 41, January 2003.

[213] J. M. Dickey, Y. Terzian, and E. E. Salpeter. Galactic neutral hydrogen emission-absorption observations from Arecibo. ApJS, 36:77–114, January 1978.

[214] N. Sartore, E. Ripamonti, A. Treves, and R. Turolla. Galactic neutron stars. I. Space and velocity distributions in the disk and in the halo. A&A, 510:A23, February 2010.

[215] M. Su, T. R. Slatyer, and D. P. Finkbeiner. Giant Gamma-ray Bubbles from Fermi-LAT: Active Galactic Nucleus Activity or Bipolar Galactic Wind? ApJ, 724:1044–1082, December 2010.

[216] E. Carlson and S. Profumo. Cosmic ray protons in the inner Galaxy and the Galactic Center gamma-ray excess. Phys. Rev. D, 90(2):023015, July 2014.

[217] J. Petrović, P. Dario Serpico, and G. Zaharijaš. Galactic Center gamma-ray "excess" from an active past of the Galactic Centre? J. Cosmology Astropart. Phys., 10:52, October 2014.

[218] BM Gaensler. The vertical structure of warm ionised gas in the Milky Way. *Publications of the ...*, pages 1–20, 2008.

[219] D. H. F. M. Schnitzeler. Modelling the Galactic distribution of free electrons. MNRAS, 427:664–678, November 2012.

[220] R. J. Reynolds. Line integrals of N[SUB]E[/SUB] and (n[SUB]E)-squared[/SUB] at high Galactic latitude. *The Astrophysical Journal*, 372:L17, May 1991.

[221] K. Ferrière. Interstellar gas within ˜10 pc of Sagittarius A. A&A, 540:A50, April 2012.

[222] K. A. Olive et al. Review of Particle Physics. *Chin. Phys.*, C38:090001, 2014.

[223] F. Feroz, M. P. Hobson, and M. Bridges. MULTINEST: an efficient and robust Bayesian inference tool for cosmology and particle physics. MNRAS, 398:1601–1614, October 2009.

[224] K. M. Górski, E. Hivon, A. J. Banday, B. D. Wandelt, F. K. Hansen, M. Reinecke, and M. Bartelmann. HEALPix: A Framework for High-Resolution Discretization and Fast Analysis of Data Distributed on the Sphere. ApJ, 622:759–771, April 2005.

[225] M. Ackermann, M. Ajello, A. Albert, W. B. Atwood, L. Baldini, J. Ballet, G. Barbiellini, D. Bastieri, K. Bechtol, R. Bellazzini, E. Bissaldi, R. D. Blandford, E. D. Bloom, E. Bottacini, T. J. Brandt, J. Bregeon, P. Bruel, R. Buehler, S. Buson, G. A. Caliandro, R. A. Cameron, M. Caragiulo, P. A. Caraveo, E. Cavazzuti, C. Cecchi, E. Charles, A. Chekhtman, J. Chiang, G. Chiaro, S. Ciprini, R. Claus, J. Cohen-Tanugi, J. Conrad, A. Cuoco, S. Cutini, F. D'Ammando, A. de Angelis, F. de Palma, C. D. Dermer, S. W. Digel, E. d. C. e. Silva, P. S. Drell, C. Favuzzi, E. C. Ferrara, W. B. Focke, A. Franckowiak, Y. Fukazawa, S. Funk, P. Fusco, F. Gargano, D. Gasparrini, S. Germani, N. Giglietto, P. Giommi, F. Giordano, M. Giroletti, G. Godfrey, G. A. Gomez-Vargas, I. A. Grenier, S. Guiriec, M. Gustafsson, D. Hadasch, K. Hayashi, E. Hays, J. W. Hewitt, P. Ippoliti, T. Jogler, G. Jóhannesson, A. S. Johnson, W. N. Johnson, T. Kamae, J. Kataoka,

J. Knödlseder, M. Kuss, S. Larsson, L. Latronico, J. Li, L. Li, F. Longo, F. Loparco, B. Lott, M. N. Lovellette, P. Lubrano, G. M. Madejski, A. Manfreda, F. Massaro, M. Mayer, M. N. Mazziotta, J. E. McEnery, P. F. Michelson, W. Mitthumsiri, T. Mizuno, A. A. Moiseev, M. E. Monzani, A. Morselli, I. V. Moskalenko, S. Murgia, R. Nemmen, E. Nuss, T. Ohsugi, N. Omodei, E. Orlando, J. F. Ormes, D. Paneque, J. H. Panetta, J. S. Perkins, M. Pesce-Rollins, F. Piron, G. Pivato, T. A. Porter, S. Rainò, R. Rando, M. Razzano, S. Razzaque, A. Reimer, O. Reimer, T. Reposeur, S. Ritz, R. W. Romani, M. Sánchez-Conde, M. Schaal, A. Schulz, C. Sgrò, E. J. Siskind, G. Spandre, P. Spinelli, A. W. Strong, D. J. Suson, H. Takahashi, J. G. Thayer, J. B. Thayer, L. Tibaldo, M. Tinivella, D. F. Torres, G. Tosti, E. Troja, Y. Uchiyama, G. Vianello, M. Werner, B. L. Winer, K. S. Wood, M. Wood, G. Zaharijas, and S. Zimmer. The Spectrum of Isotropic Diffuse Gamma-Ray Emission between 100 MeV and 820 GeV. ApJ, 799:86, January 2015.

[226] M. Ackermann, A. Albert, W. B. Atwood, L. Baldini, J. Ballet, G. Barbiellini, D. Bastieri, R. Bellazzini, E. Bissaldi, R. D. Blandford, E. D. Bloom, E. Bottacini, T. J. Brandt, J. Bregeon, P. Bruel, R. Buehler, S. Buson, G. A. Caliandro, R. A. Cameron, M. Caragiulo, P. A. Caraveo, E. Cavazzuti, C. Cecchi, E. Charles, A. Chekhtman, J. Chiang, G. Chiaro, S. Ciprini, R. Claus, J. Cohen-Tanugi, J. Conrad, S. Cutini, F. D'Ammando, A. de Angelis, F. de Palma, C. D. Dermer, S. W. Digel, L. Di Venere, E. d. C. e. Silva, P. S. Drell, C. Favuzzi, E. C. Ferrara, W. B. Focke, A. Franckowiak, Y. Fukazawa, S. Funk, P. Fusco, F. Gargano, D. Gasparrini, S. Germani, N. Giglietto, F. Giordano, M. Giroletti, G. Godfrey, G. A. Gomez-Vargas, I. A. Grenier, S. Guiriec, D. Hadasch, A. K. Harding, E. Hays, J. W. Hewitt, X. Hou, T. Jogler, G. Jóhannesson, A. S. Johnson, W. N. Johnson, T. Kamae, J. Kataoka, J. Knödlseder, D. Kocevski, M. Kuss, S. Larsson, L. Latronico, F. Longo, F. Loparco, M. N. Lovellette, P. Lubrano, D. Malyshev, A. Manfreda, F. Massaro, M. Mayer, M. N. Mazziotta, J. E. McEnery, P. F. Michelson, W. Mitthumsiri,

T. Mizuno, M. E. Monzani, A. Morselli, I. V. Moskalenko, S. Murgia, R. Nemmen, E. Nuss, T. Ohsugi, N. Omodei, M. Orienti, E. Orlando, J. F. Ormes, D. Paneque, J. H. Panetta, J. S. Perkins, M. Pesce-Rollins, V. Petrosian, F. Piron, G. Pivato, S. Rainò, R. Rando, M. Razzano, S. Razzaque, A. Reimer, O. Reimer, M. Sánchez-Conde, M. Schaal, A. Schulz, C. Sgrò, E. J. Siskind, G. Spandre, P. Spinelli, Ł. Stawarz, A. W. Strong, D. J. Suson, M. Tahara, H. Takahashi, J. B. Thayer, L. Tibaldo, M. Tinivella, D. F. Torres, G. Tosti, E. Troja, Y. Uchiyama, G. Vianello, M. Werner, B. L. Winer, K. S. Wood, M. Wood, and G. Zaharijas. The Spectrum and Morphology of the Fermi Bubbles. ApJ, 793:64, September 2014.

[227] R. Campana, E. Bernieri, E. Massaro, F. Tinebra, and G. Tosti. Minimal spanning tree algorithm for γ-ray source detection in sparse photon images: cluster parameters and selection strategies. Ap&SS, 347:169–182, September 2013.

[228] Martin Ester, Hans peter Kriegel, Jrg S, and Xiaowei Xu. A density-based algorithm for discovering clusters in large spatial databases with noise. pages 226–231. AAAI Press, 1996.

[229] A. Tramacere and C. Vecchio. gamma-ray DBSCAN: a clustering algorithm applied to Fermi-LAT gamma-ray data. I. Detection performances with real and simulated data. *ArXiv e-prints*, October 2012.

[230] Richard Bartels, Suraj Krishnamurthy, and Christoph Weniger. Strong support for the millisecond pulsar origin of the Galactic center GeV excess. 2015.

[231] W.B. Atwood et al. The Large Area Telescope on the Fermi Gamma-ray Space Telescope Mission. *Astrophys.J.*, 697:1071–1102, 2009.

[232] Alex Geringer-Sameth and Savvas M. Koushiappas. Exclusion of canonical WIMPs by the joint analysis of Milky Way dwarfs with Fermi. *Phys.Rev.Lett.*, 107:241303, 2011.

[233] M. Ackermann et al. Constraining Dark Matter Models from a Combined Analysis of Milky Way Satellites with the Fermi Large Area Telescope. *Phys.Rev.Lett.*, 107:241302, 2011.

[234] M. Ackermann et al. Search for Dark Matter Satellites using the FERMI-LAT. *Astrophys.J.*, 747:121, 2012.

[235] Dan Hooper, Chris Kelso, and Farinaldo S. Queiroz. Stringent and Robust Constraints on the Dark Matter Annihilation Cross Section From the Region of the Galactic Center. *Astropart.Phys.*, 46:55–70, 2013.

[236] M. Ackermann, M. Ajello, A. Allafort, L. Baldini, J. Ballet, G. Barbiellini, D. Bastieri, K. Bechtol, R. Bellazzini, R. D. Blandford, E. D. Bloom, E. Bonamente, A. W. Borgland, A. Bouvier, T. J. Brandt, J. Bregeon, M. Brigida, P. Bruel, R. Buehler, S. Buson, G. A. Caliandro, R. A. Cameron, P. A. Caraveo, S. Carrigan, J. M. Casandjian, C. Cecchi, E. Charles, A. Chekhtman, C. C. Cheung, J. Chiang, S. Ciprini, R. Claus, J. Cohen-Tanugi, L. R. Cominsky, J. Conrad, A. de Angelis, F. de Palma, E. d. C. e. Silva, P. S. Drell, A. Drlica-Wagner, R. Dubois, D. Dumora, Y. Edmonds, C. Farnier, C. Favuzzi, S. J. Fegan, M. Frailis, Y. Fukazawa, P. Fusco, F. Gargano, D. Gasparrini, N. Gehrels, S. Germani, N. Giglietto, F. Giordano, T. Glanzman, G. Godfrey, I. A. Grenier, S. Guiriec, M. Gustafsson, A. K. Harding, M. Hayashida, D. Horan, R. E. Hughes, T. E. Jeltema, G. Jóhannesson, A. S. Johnson, W. N. Johnson, T. Kamae, H. Katagiri, J. Kataoka, J. Knödlseder, M. Kuss, J. Lande, L. Latronico, S.-H. Lee, M. Llena Garde, F. Longo, F. Loparco, M. N. Lovellette, P. Lubrano, G. M. Madejski, A. Makeev, M. N. Mazziotta, P. F. Michelson, W. Mitthumsiri, T. Mizuno, A. A. Moiseev, C. Monte, M. E. Monzani, A. Morselli, I. V. Moskalenko, S. Murgia, P. L. Nolan, J. P. Norris, E. Nuss, M. Ohno, T. Ohsugi, N. Omodei, E. Orlando, J. F. Ormes, J. H. Panetta, M. Pepe, M. Pesce-

Rollins, F. Piron, T. A. Porter, S. Profumo, S. Rainò, M. Razzano, T. Reposeur, S. Ritz, A. Y. Rodriguez, M. Roth, H. F.-W. Sadrozinski, A. Sander, J. D. Scargle, C. Sgrò, E. J. Siskind, P. D. Smith, G. Spandre, P. Spinelli, J.-L. Starck, M. S. Strickman, D. J. Suson, H. Takahashi, T. Tanaka, J. B. Thayer, J. G. Thayer, L. Tibaldo, D. F. Torres, G. Tosti, T. L. Usher, V. Vasileiou, V. Vitale, A. P. Waite, P. Wang, B. L. Winer, K. S. Wood, Z. Yang, T. Ylinen, M. Ziegler, and Fermi LAT Collaboration. Constraints on dark matter annihilation in clusters of galaxies with the Fermi large area telescope. *JCAP*, 5:25, May 2010.

[237] L. Dugger, T. E. Jeltema, and S. Profumo. Constraints on decaying dark matter from Fermi observations of nearby galaxies and clusters. *JCAP*, 12:15, December 2010.

[238] A. A. Abdo, M. Ackermann, M. Ajello, L. Baldini, J. Ballet, G. Barbiellini, D. Bastieri, K. Bechtol, R. Bellazzini, B. Berenji, R. D. Blandford, E. D. Bloom, E. Bonamente, A. W. Borgland, A. Bouvier, J. Bregeon, A. Brez, M. Brigida, P. Bruel, T. H. Burnett, S. Buson, G. A. Caliandro, R. A. Cameron, P. A. Caraveo, S. Carrigan, J. M. Casandjian, C. Cecchi, Ö. Çelik, A. Chekhtman, C. C. Cheung, J. Chiang, S. Ciprini, R. Claus, J. Cohen-Tanugi, J. Conrad, S. Cutini, C. D. Dermer, A. de Angelis, F. de Palma, S. W. Digel, E. d. C. e. Silva, P. S. Drell, R. Dubois, D. Dumora, Y. Edmonds, C. Farnier, C. Favuzzi, S. J. Fegan, W. B. Focke, P. Fortin, M. Frailis, Y. Fukazawa, P. Fusco, F. Gargano, D. Gasparrini, N. Gehrels, S. Germani, N. Giglietto, F. Giordano, T. Glanzman, G. Godfrey, J. E. Grove, L. Guillemot, S. Guiriec, M. Gustafsson, D. Hadasch, A. K. Harding, D. Horan, R. E. Hughes, A. S. Johnson, W. N. Johnson, T. Kamae, H. Katagiri, J. Kataoka, N. Kawai, M. Kerr, J. Knödlseder, M. Kuss, J. Lande, L. Latronico, M. Llena Garde, F. Longo, F. Loparco, B. Lott, M. N. Lovellette, P. Lubrano, A. Makeev, M. N. Mazziotta, J. E. McEnery, C. Meurer, P. F. Michelson, W. Mitthumsiri, T. Mizuno, C. Monte, M. E.

Monzani, A. Morselli, I. V. Moskalenko, S. Murgia, P. L. Nolan, J. P. Norris, E. Nuss, T. Ohsugi, N. Omodei, E. Orlando, J. F. Ormes, D. Paneque, J. H. Panetta, D. Parent, V. Pelassa, M. Pepe, M. Pesce-Rollins, F. Piron, S. Rainò, R. Rando, A. Reimer, O. Reimer, T. Reposeur, A. Y. Rodriguez, M. Roth, H. F.-W. Sadrozinski, A. Sander, P. M. Saz Parkinson, J. D. Scargle, A. Sellerholm, C. Sgrò, E. J. Siskind, P. D. Smith, G. Spandre, P. Spinelli, J.-L. Starck, M. S. Strickman, D. J. Suson, H. Takahashi, T. Tanaka, J. B. Thayer, J. G. Thayer, D. F. Torres, Y. Uchiyama, T. L. Usher, V. Vasileiou, N. Vilchez, V. Vitale, A. P. Waite, P. Wang, B. L. Winer, K. S. Wood, T. Ylinen, G. Zaharijas, and M. Ziegler. Constraints on cosmological dark matter annihilation from the Fermi-LAT isotropic diffuse gamma-ray measurement. *JCAP*, 4:14, April 2010.

[239] K. N. Abazajian, P. Agrawal, Z. Chacko, and C. Kilic. Conservative constraints on dark matter from the Fermi-LAT isotropic diffuse gamma-ray background spectrum. *JCAP*, 11:41, November 2010.

[240] Ilias Cholis, Dan Hooper, and Samuel D. McDermott. Dissecting the Gamma-Ray Background in Search of Dark Matter. *JCAP*, 1402:014, 2014.

[241] Lisa Goodenough and Dan Hooper. Possible Evidence For Dark Matter Annihilation In The Inner Milky Way From The Fermi Gamma Ray Space Telescope. 2009.

[242] Dan Hooper and Lisa Goodenough. Dark Matter Annihilation in The Galactic Center As Seen by the Fermi Gamma Ray Space Telescope. *Phys.Lett.*, B697:412–428, 2011.

[243] Kevork N. Abazajian and Manoj Kaplinghat. Detection of a Gamma-Ray Source in the Galactic Center Consistent with Extended Emission from Dark Matter Annihilation and Concentrated Astrophysical Emission. *Phys.Rev.*, D86:083511, 2012.

[244] Chris Gordon and Oscar Macias. Dark Matter and Pulsar Model Constraints from Galactic Center Fermi-LAT Gamma Ray Observations. *Phys.Rev.*, D88:083521, 2013.

[245] Dan Hooper and Tracy R. Slatyer. Two Emission Mechanisms in the Fermi Bubbles: A Possible Signal of Annihilating Dark Matter. *Phys.Dark Univ.*, 2:118–138, 2013.

[246] Francesca Calore, Ilias Cholis, and Christoph Weniger. Background model systematics for the Fermi GeV excess. 2014.

[247] P. Nolan et al. Fermi Large Area Telescope Second Source Catalog. *Astrophys.J.Suppl.*, 199:31, 2012.

[248] M. Ackermann et al. Anisotropies in the diffuse gamma-ray background measured by the Fermi LAT. *Phys.Rev.*, D85:083007, 2012.

[249] Kevork N. Abazajian, Steve Blanchet, and J. Patrick Harding. The Contribution of Blazars to the Extragalactic Diffuse Gamma-ray Background and Their Future Spatial Resolution. *Phys.Rev.*, D84:103007, 2011.

[250] Tonia M. Venters. Contribution to the Extragalactic Gamma-ray Background from the Cascades of Very-high Energy Gamma Rays from Blazars. *Astrophys.J.*, 710:1530–1540, 2010.

[251] Tonia M. Venters and Vasiliki Pavlidou. The Effect of Blazar Spectral Breaks on the Blazar Contribution to the Extragalactic Gamma-ray Background. *Astrophys.J.*, 737:80, 2011.

[252] A. Cuoco, E. Komatsu, and J.M. Siegal-Gaskins. Joint anisotropy and source count constraints on the contribution of blazars to the diffuse gamma-ray background. *Phys.Rev.*, D86:063004, 2012.

[253] J. Patrick Harding and Kevork N. Abazajian. Models of the Contribution of Blazars to the Anisotropy of the Extragalactic Diffuse Gamma-ray Background. *JCAP*, 1211:026, 2012.

[254] E. Massaro, P. Giommi, C. Leto, P. Marchegiani, A. Maselli, et al. Roma-BZCAT: A multifrequency catalogue of Blazars. 2008.

[255] Stephen Edward Healey, Roger W. Romani, Gregory B. Taylor, Elaine M. Sadler, Roberto Ricci, et al. CRATES: An All-Sky Survey of Flat-Spectrum Radio Sources. *Astrophys.J.Suppl.*, 171:61–71, 2007.

[256] S. K. Lee, S. Ando, and M. Kamionkowski. The gamma-ray-flux PDF from galactic halo substructure. *"JCAP"*, 7:7, July 2009.

[257] Jennifer M. Siegal-Gaskins and Vasiliki Pavlidou. Robust identification of isotropic diffuse gamma rays from Galactic dark matter. *Phys.Rev.Lett.*, 102:241301, 2009.

[258] Volker Springel, Jie Wang, Mark Vogelsberger, Aaron Ludlow, Adrian Jenkins, et al. The Aquarius Project: the subhalos of galactic halos. *Mon.Not.Roy.Astron.Soc.*, 391:1685–1711, 2008.

[259] J. Diemand, M. Kuhlen, P. Madau, M. Zemp, B. Moore, et al. Clumps and streams in the local dark matter distribution. *Nature*, 454:735–738, 2008.

[260] L. Bergstrom. Saas-Fee Lecture Notes: Multi-messenger Astronomy and Dark Matter. *ArXiv e-prints*, February 2012.

[261] J. Buch, M. Cirelli, G. Giesen, and M. Taoso. PPPC 4 DM secondary: a Poor Particle Physicist Cookbook for secondary radiation from Dark Matter. J. Cosmology Astropart. Phys., 9:037, September 2015.

[262] F. Damiani, A. Maggio, G. Micela, and S. Sciortino. A method based on wavelet transforms for source detection in photon-counting detector images. i. theory and general properties. *The Astrophysical Journal*, 483(1):350, 1997.

[263] R. Bartels, S. Krishnamurthy, and C. Weniger. Strong Support for the Millisecond Pulsar Origin of the Galactic Center GeV Excess. *Physical Review Letters*, 116(5):051102, February 2016.

[264] S. K. Lee, M. Lisanti, B. R. Safdi, T. R. Slatyer, and W. Xue. Evidence for Unresolved γ -Ray Point Sources in the Inner Galaxy. *Physical Review Letters*, 116(5):051103, February 2016.

[265] S. K. Lee, M. Lisanti, and B. R. Safdi. Distinguishing dark matter from unresolved point sources in the Inner Galaxy with photon statistics. J. Cosmology Astropart. Phys., 5:056, May 2015.

[266] M. Selig and T. A. Enßlin. Denoising, deconvolving, and decomposing photon observations. Derivation of the D^{3}PO algorithm. A&A, 574:A74, February 2015.

[267] T. Delahaye, J. Lavalle, R. Lineros, F. Donato, and N. Fornengo. Galactic electrons and positrons at the Earth: new estimate of the primary and secondary fluxes. A&A, 524:A51, December 2010.

[268] F. Donato, D. Maurin, P. Salati, A. Barrau, G. Boudoul, and R. Taillet. Antiprotons from Spallations of Cosmic Rays on Interstellar Matter. ApJ, 563:172–184, December 2001.

[269] F. Donato, N. Fornengo, D. Maurin, P. Salati, and R. Taillet. Antiprotons in cosmic rays from neutralino annihilation. Phys. Rev. D, 69(6):063501, March 2004.

[270] G. Di Bernardo, C. Evoli, D. Gaggero, D. Grasso, and L. Maccione. Cosmic ray electrons, positrons and the synchrotron emission of the Galaxy: consistent analysis and implications. J. Cosmology Astropart. Phys., 3:036, March 2013.

[271] I. V. Moskalenko, A. W. Strong, J. F. Ormes, and M. S. Potgieter. Secondary Antiprotons and Propagation of Cosmic Rays in the Galaxy and Heliosphere. ApJ, 565:280–296, January 2002.

[272] L. C. Tan and L. K. Ng. *J. Phys. G G 9*, (9):227, 1983.

[273] M. Hillas. Is the cosmic-ray residence time $E^{-0.6}$ (spallation) or $E^{-1/3}$ (anisotropy, turbulence)? In *International Cosmic Ray Conference*, volume 4 of *International Cosmic Ray Conference*, page 225, August 1999.

[274] Daniele Gaggero, Luca Maccione, Dario Grasso, Giuseppe Di Bernardo, and Carmelo Evoli. Pamela and ams-02 e^+ and e^- spectra are reproduced by three-dimensional cosmic-ray modeling. *Phys. Rev. D*, 89:083007, Apr 2014.

[275] D. Gaggero, L. Maccione, G. Di Bernardo, C. Evoli, and D. Grasso. Three-Dimensional Model of Cosmic-Ray Lepton Propagation Reproduces Data from the Alpha Magnetic Spectrometer on the International Space Station. *Physical Review Letters*, 111(2):021102, July 2013.

[276] Andrew W Strong, Igor V Moskalenko, and Vladimir S. Ptuskin. Cosmic-Ray Propagation and Interactions in the Galaxy. *Annual Review of Nuclear and Particle Science*, 57(1):285–327, nov 2007.

[277] Pasquale Blasi. The origin of galactic cosmic rays. *The Astronomy and Astrophysics Review*, 21(1):70, nov 2013.

[278] LOC Drury. An introduction to the theory of diffusive shock acceleration of energetic particles in tenuous plasmas. *Reports on Progress in Physics*, 46(February):973–1027, 1983.

[279] M. A. Malkov, P. H. Diamond, and R. Z. Sagdeev. On the gamma-ray spectra radiated by protons accelerated in SNR shocks near molecular clouds: The case of SNR RX J1713.7-3946. *arXiv preprint astro-ph/0503403*, (Ic):11, March 2005.

[280] MA Malkov, PH Diamond, and RZ Sagdeev. Mechanism for spectral break in cosmic ray proton spectrum of supernova remnant W44. *Nature Communications*, pages 1–8, April 2011.

[281] P Blasi, G Morlino, R Bandiera, E Amato, and D Caprioli. Collisionless shocks in a partially ionized medium: I. Neutral return flux and its effects on acceleration of test particles. February 2012.

[282] Y Yuan, S Funk, G. Jóhannesson, J Lande, L Tibaldo, and Y Uchiyama. Fermi-LAT Detection of a Break in the Gamma-Ray Spectrum of the Supernova Remnant Cassiopeia A. page 18, October 2013.

[283] Yasunobu Uchiyama, Stefan Funk, Hideaki Katagiri, Junichiro Katsuta, Marianne Lemoine-Goumard, Hiroyasu Tajima, Takaaki Tanaka, and Diego Torres. Fermi-LAT Discovery of GeV Gamma-ray Emission from the Vicinity of SNR W44. *arXiv preprint arXiv: ...*, page 5, March 2012.

[284] A. et al. Giuliani. Neutral pion emission from accelerated protons in the supernova remnant W44. November 2011.

[285] C D Dermer and G Powale. Gamma Rays from Cosmic Rays in Supernova Remnants. pages 1–6, October 2012.

[286] Miguel Araya. Fermi LAT Observation of Supernova Remnant HB9. page 15, May 2014.

[287] A. J. Green, D. A. Frail, W. M. Goss, F. Yusef-Zadeh, and D. A. Roberts. Detection of OH (1720 MHz) Masers in SGR A East. In R. Gredel, editor, *The Galactic Center*, volume 102 of *Astronomical Society of the Pacific Conference Series*, page 93, 1996.

[288] K. Ferrière, W. Gillard, and P. Jean. Spatial distribution of interstellar gas in the innermost 3 kpc of our galaxy. *Astronomy & Astrophysics*, 467:611–627, May 2007.

[289] A. L. Coil and P. T. P. Ho. The Dynamics of Molecular Material within 15 PARSECS of the Galactic Center. ApJ, 533:245–259, April 2000.

[290] Mark Morris and Eugene Serabyn. THE GALACTIC CENTER ENVIRONMENT. *Annual Review of Astronomy and Astrophysics*, 34(1):645–701, September 1996.

[291] Katia Ferriere. Interstellar magnetic fields in the Galactic center region. page 16, August 2009.

[292] F. Yusef-Zadeh, J. W. Hewitt, M. Wardle, V. Tatischeff, D. A. Roberts, W. Cotton, H. Uchiyama, M. Nobukawa, T. G. Tsuru, C. Heinke, and M. Royster. Interacting Cosmic Rays with Molecular Clouds: A Bremsstrahlung Origin of Diffuse High-energy Emission from the Inner $2^\circ \times 1^\circ$ of the Galactic Center. ApJ, 762:33, January 2013.

[293] Mark Morris. The Galactic Center Magnetosphere. In *Galactic Center Workshop 2006 (GC 06): From the Center of the Milky Way to Nearby Low Luminosity Galactic Nuclei Bad Honnef, Germany, April 18-22, 2006*, 2007.

[294] Y. Sofue and T. Handa. A radio lobe over the galactic centre. Nature, 310:568, August 1984.

[295] J. Bland-Hawthorn and M. Cohen. The Large-Scale Bipolar Wind in the Galactic Center. ApJ, 582:246–256, January 2003.

[296] Y. Sofue. Bipolar Hypershell Galactic Center Starburst Model: Further Evidence from ROSAT Data and New Radio and X-Ray Simulations. ApJ, 540:224–235, September 2000.

[297] R. A. Chevalier. The Galactic center wind. ApJ, 397:L39–L42, September 1992.

[298] R. M. Crocker, D. I. Jones, F. Aharonian, C. J. Law, F. Melia, and J. Ott. γ-rays and the far-infrared-radio continuum correlation reveal a powerful Galactic Centre wind. MNRAS, 411:L11–L15, February 2011.

[299] J.-H. Zhao, M. R. Morris, and W. M. Goss. A New Perspective of the Radio Bright Zone at The Galactic Center: Feedback from Nuclear Activities. ApJ, 817:171, February 2016.

[300] A. Rodríguez-González, A. C. Raga, and J. Cantó. Low and high velocity clouds produced by young stellar clusters. A&A, 501:411–417, July 2009.

[301] E. S. Seo and V. S. Ptuskin. Stochastic reacceleration of cosmic rays in the interstellar medium. ApJ, 431:705–714, August 1994.

[302] F.A. Aharonian. *Very High Energy Cosmic Gamma Radiation: A Crucial Window on the Extreme Universe*. World Scientific, 2004.

[303] F.W. Stecker. *Cosmic gamma rays*. NASA SP. Scientific and Technical Information Office, National Aeronautics and Space Administration; [for sale by the Supt. of Docs., U.S. Govt. Print. Off.], 1971.

[304] M. S. Longair. *High energy astrophysics. Vol.1: Particles, photons and their detection*. March 1992.

[305] Charles D Dermer. Diffuse Galactic Gamma Rays from Shock-Accelerated Cosmic Rays. June 2012.

[306] C. D. Dermer, A. W. Strong, E. Orlando, L. Tibaldo, and for the Fermi Collaboration. Determining the Spectrum of Cosmic Rays in Interstellar Space from the Diffuse Galactic Gamma-Ray Emissivity. page 4, July 2013.

[307] C D Dermer, J D Finke, R J Murphy, A W Strong, F. Loparco, M. N. Mazziotta, E Orlando, T. Kamae, L. Tibaldo, J. Cohen-Tanugi, M. Ackermann, T. Mizuno, and F. W. Stecker. On the Physics Connecting Cosmic Rays and Gamma Rays: Towards Determining the Interstellar Cosmic Ray Spectrum. page 10, March 2013.

[308] T.K. Gaisser. *Cosmic Rays and Particle Physics*. Cambridge University Press, 1990.

[309] T. Kamae, N. Karlsson, T. Mizuno, T. Abe, and T. Koi. Parameterization of γ, $e^{+/-}$,

and Neutrino Spectra Produced by p-p Interaction in Astronomical Environments. ApJ, 647:692–708, August 2006.

[310] C. D. Dermer. Secondary production of neutral pi-mesons and the diffuse galactic gamma radiation. *A&A*, 157:223–229, March 1986.

[311] M. Kachelrieß and S. Ostapchenko. Deriving the cosmic ray spectrum from gamma-ray observations. Phys. Rev. D, 86(4):043004, August 2012.

[312] S. R. Kelner, F. A. Aharonian, and V. V. Bugayov. Energy spectra of gamma rays, electrons, and neutrinos produced at proton-proton interactions in the very high energy regime. *Phys. Rev. D*, 74:034018, Aug 2006.

[313] S. A. Stephens and G. D. Badhwar. Production spectrum of gamma rays in interstellar space through neutral pion decay. AASS, 76:213–233, May 1981.

[314] F. W. Stecker. Neutral-Pion Gamma Rays from the Galaxy and the Interstellar Gas Content. ApJ, 185:499–504, October 1973.

[315] Igor V. Moskalenko and Andrew W. Strong. Anisotropic Inverse Compton Scattering in the Galaxy. *The Astrophysical Journal*, 528(1):357–367, jan 2000.

[316] O. Adriani, G. C. Barbarino, G. A. Bazilevskaya, R. Bellotti, A. Bianco, M. Boezio, E. A. Bogomolov, M. Bongi, V. Bonvicini, S. Bottai, A. Bruno, F. Cafagna, D. Campana, R. Carbone, P. Carlson, M. Casolino, G. Castellini, C. De Donato, C. De Santis, N. De Simone, V. Di Felice, V. Formato, A. M. Galper, A. V. Karelin, S. V. Koldashov, S. A. Koldobskiy, S. Y. Krutkov, A. N. Kvashnin, A. Leonov, V. Malakhov, L. Marcelli, M. Martucci, A. G. Mayorov, W. Menn, M. Mergé, V. V. Mikhailov, E. Mocchiutti, A. Monaco, N. Mori, R. Munini, G. Osteria, F. Palma, P. Papini, M. Pearce, P. Picozza, C. Pizzolotto, M. Ricci, S. B. Ricciarini, L. Rossetto, R. Sarkar, V. Scotti, M. Simon, R. Sparvoli, P. Spillantini,

S. J. Stochaj, J. C. Stockton, Y. I. Stozhkov, A. Vacchi, E. Vannuccini, G. I. Vasilyev, S. A. Voronov, Y. T. Yurkin, G. Zampa, N. Zampa, and V. G. Zverev. Cosmic-ray positron energy spectrum measured by pamela. *Phys. Rev. Lett.*, 111:081102, Aug 2013.

[317] M. Aguilar, G. Alberti, B. Alpat, A. Alvino, G. Ambrosi, K. Andeen, H. Anderhub, L. Arruda, P. Azzarello, A. Bachlechner, F. Barao, B. Baret, A. Barrau, L. Barrin, A. Bartoloni, L. Basara, A. Basili, L. Batalha, J. Bates, R. Battiston, J. Bazo, R. Becker, U. Becker, M. Behlmann, B. Beischer, J. Berdugo, P. Berges, B. Bertucci, G. Bigongiari, A. Biland, V. Bindi, S. Bizzaglia, G. Boella, W. de Boer, K. Bollweg, J. Bolmont, B. Borgia, S. Borsini, M. J. Boschini, G. Boudoul, M. Bourquin, P. Brun, M. Buénerd, J. Burger, W. Burger, F. Cadoux, X. D. Cai, M. Capell, D. Casadei, J. Casaus, V. Cascioli, G. Castellini, I. Cernuda, F. Cervelli, M. J. Chae, Y. H. Chang, A. I. Chen, C. R. Chen, H. Chen, G. M. Cheng, H. S. Chen, L. Cheng, N. Chernoplyiokov, A. Chikanian, E. Choumilov, V. Choutko, C. H. Chung, C. Clark, R. Clavero, G. Coignet, V. Commichau, C. Consolandi, A. Contin, C. Corti, M. T. Costado Dios, B. Coste, D. Crespo, Z. Cui, M. Dai, C. Delgado, S. Della Torre, B. Demirkoz, P. Dennett, L. Derome, S. Di Falco, X. H. Diao, A. Diago, L. Djambazov, C. Díaz, P. von Doetinchem, W. J. Du, J. M. Dubois, R. Duperay, M. Duranti, D. D'Urso, A. Egorov, A. Eline, F. J. Eppling, T. Eronen, J. van Es, H. Esser, A. Falvard, E. Fiandrini, A. Fiasson, E. Finch, P. Fisher, K. Flood, R. Foglio, M. Fohey, S. Fopp, N. Fouque, Y. Galaktionov, M. Gallilee, L. Gallin-Martel, G. Gallucci, B. García, J. García, R. García-López, L. García-Tabares, C. Gargiulo, H. Gast, I. Gebauer, S. Gentile, M. Gervasi, W. Gillard, F. Giovacchini, L. Girard, P. Goglov, J. Gong, C. Goy-Henningsen, D. Grandi, M. Graziani, A. Grechko, A. Gross, I. Guerri, C. de la Guía, K. H. Guo, M. Habiby, S. Haino, F. Hauler, Z. H. He, M. Heil, J. Heilig, R. Hermel, H. Hofer, Z. C. Huang, W. Hungerford, M. Incagli, M. Ionica, A. Jacholkowska, W. Y. Jang, H. Jinchi, M. Jongmanns, L. Journet, L. Jungermann, W. Karpinski, G. N. Kim,

K. S. Kim, Th. Kirn, R. Kossakowski, A. Koulemzine, O. Kounina, A. Kounine, V. Koutsenko, M. S. Krafczyk, E. Laudi, G. Laurenti, C. Lauritzen, A. Lebedev, M. W. Lee, S. C. Lee, C. Leluc, H. León Vargas, V. Lepareur, J. Q. Li, Q. Li, T. X. Li, W. Li, Z. H. Li, P. Lipari, C. H. Lin, D. Liu, H. Liu, T. Lomtadze, Y. S. Lu, S. Lucidi, K. Lübelsmeyer, J. Z. Luo, W. Lustermann, S. Lv, J. Madsen, R. Majka, A. Malinin, C. Mañá, J. Marín, T. Martin, G. Martínez, F. Masciocchi, N. Masi, D. Maurin, A. McInturff, P. McIntyre, A. Menchaca-Rocha, Q. Meng, M. Menichelli, I. Mereu, M. Millinger, D. C. Mo, M. Molina, P. Mott, A. Mujunen, S. Natale, P. Nemeth, J. Q. Ni, N. Nikonov, F. Nozzoli, P. Nunes, A. Obermeier, S. Oh, A. Oliva, F. Palmonari, C. Palomares, M. Paniccia, A. Papi, W. H. Park, M. Pauluzzi, F. Pauss, A. Pauw, E. Pedreschi, S. Pensotti, R. Pereira, E. Perrin, G. Pessina, G. Pierschel, F. Pilo, A. Piluso, C. Pizzolotto, V. Plyaskin, J. Pochon, M. Pohl, V. Poireau, S. Porter, J. Pouxe, A. Putze, L. Quadrani, X. N. Qi, P. G. Rancoita, D. Rapin, Z. L. Ren, J. S. Ricol, E. Riihonen, I. Rodríguez, U. Roeser, S. Rosier-Lees, L. Rossi, A. Rozhkov, D. Rozza, A. Sabellek, R. Sagdeev, J. Sandweiss, B. Santos, P. Saouter, M. Sarchioni, S. Schael, D. Schinzel, M. Schmanau, G. Schwering, A. Schulz von Dratzig, G. Scolieri, E. S. Seo, B. S. Shan, J. Y. Shi, Y. M. Shi, T. Siedenburg, R. Siedling, D. Son, F. Spada, F. Spinella, M. Steuer, K. Stiff, W. Sun, W. H. Sun, X. H. Sun, M. Tacconi, C. P. Tang, X. W. Tang, Z. C. Tang, L. Tao, J. Tassan-Viol, Samuel C. C. Ting, S. M. Ting, C. Titus, N. Tomassetti, F. Toral, J. Torsti, J. R. Tsai, J. C. Tutt, J. Ulbricht, T. Urban, V. Vagelli, E. Valente, C. Vannini, E. Valtonen, M. Vargas Trevino, S. Vaurynovich, M. Vecchi, M. Vergain, B. Verlaat, C. Vescovi, J. P. Vialle, G. Viertel, G. Volpini, D. Wang, N. H. Wang, Q. L. Wang, R. S. Wang, X. Wang, Z. X. Wang, W. Wallraff, Z. L. Weng, M. Willenbrock, M. Wlochal, H. Wu, K. Y. Wu, Z. S. Wu, W. J. Xiao, S. Xie, R. Q. Xiong, G. M. Xin, N. S. Xu, W. Xu, Q. Yan, J. Yang, M. Yang, Q. H. Ye, H. Yi, Y. J. Yu, Z. Q. Yu, S. Zeissler, J. G. Zhang, Z. Zhang, M. M. Zhang, Z. M. Zheng, H. L. Zhuang, V. Zhukov,

A. Zichichi, P. Zuccon, and C. Zurbach. First result from the alpha magnetic spectrometer on the international space station: Precision measurement of the positron fraction in primary cosmic rays of 0.5˘350 gev. *Phys. Rev. Lett.*, 110:141102, Apr 2013.

[318] M. Werner, R. Kissmann, A.W. Strong, and O. Reimer. Spiral arms as cosmic ray source distributions. *Astroparticle Physics*, 64:18 – 33, 2015.

[319] R. Kissmann, M. Werner, O. Reimer, and A.W. Strong. Propagation in 3d spiral-arm cosmic-ray source distribution models and secondary particle production using picard. *Astroparticle Physics*, 70:39 – 53, 2015.

[320] T. Montmerle. On gamma-ray sources, supernova remnants, OB associations, and the origin of cosmic rays. *The Astrophysical Journal*, 231:95, July 1979.

[321] Thierry Montmerle. Gamma-rays from star-forming regions: from SNOBs to dark accelerators. i:1–14, 2009.

[322] J. Bally, A. A. Stark, R. W. Wilson, and C. Henkel. Galactic center molecular clouds. I - Spatial and spatial-velocity maps. ApJS, 65:13–82, September 1987.

[323] K. Ferrière, W. Gillard, and P. Jean. Spatial distribution of interstellar gas in the innermost 3 kpc of our galaxy. *Astronomy & Astrophysics*, 467:611–627, May 2007.

[324] N. Murray. Star Formation Efficiencies and Lifetimes of Giant Molecular Clouds in the Milky Way. ApJ, 729:133, March 2011.

[325] M. Schmidt. The Rate of Star Formation. ApJ, 129:243, March 1959.

[326] R. C. Kennicutt, Jr. The Global Schmidt Law in Star-forming Galaxies. ApJ, 498:541–552, May 1998.

[327] Joop Schaye and Claudio Dalla Vecchia. On the relation between the Schmidt and

Kennicutt-Schmidt star formation laws and its implications for numerical simulations. *Monthly Notices of the Royal Astronomical Society*, 383(3):1210–1222, 2008.

[328] Mark R. Krumholz and Christopher F. McKee. A general theory of turbulence-regulated star formation, from spirals to ultraluminous infrared galaxies. *The Astrophysical Journal*, 630(1):250, 2005.

[329] Andrew J. Cunningham, Richard I. Klein, Mark R. Krumholz, and Christopher F. McKee. Radiation-hydrodynamic simulations of massive star formation with protostellar outflows. *The Astrophysical Journal*, 740(2):107, 2011.

[330] M. T. Brunetti and A. Codino. Age of cosmic-ray protons computed using simple configurations of the galactic magnetic field. *The Astrophysical Journal*, 528(2):789, 2000.

[331] A. Codino. The Residence Time of Cosmic Ray Protons in the Halo of the Milky Way. *International Cosmic Ray Conference*, 4:314, 1999.

[332] K.M. Sandstrom, A.K. Leroy, F. Walter, A.D. Bolatto, K.V. Croxall, et al. The CO-to-H_2 Conversion Factor and Dust-to-Gas Ratio on Kiloparsec Scales in Nearby Galaxies. *Astrophys.J.*, 777:5, 2013.

[333] M. Heyer and T. M. Dame. Molecular Clouds in the Milky Way. ARA&A, 53:583–629, August 2015.

[334] A. D. Bolatto, M. Wolfire, and A. K. Leroy. The CO-to-H_2 Conversion Factor. ARA&A, 51:207–268, August 2013.

[335] H. Bartko, F. Martins, S. Trippe, T. K. Fritz, R. Genzel, T. Ott, F. Eisenhauer, S. Gillessen, T. Paumard, T. Alexander, K. Dodds-Eden, O. Gerhard, Y. Levin, L. Mascetti, S. Nayakshin, H. B. Perets, G. Perrin, O. Pfuhl, M. J. Reid, D. Rouan, M. Zilka, and A. Sternberg.

An Extremely Top-Heavy Initial Mass Function in the Galactic Center Stellar Disks. ApJ, 708:834–840, January 2010.

[336] U. Löckmann, H. Baumgardt, and P. Kroupa. Constraining the initial mass function of stars in the Galactic Centre. MNRAS, 402:519–525, February 2010.

[337] J. R. Lu, T. Do, A. M. Ghez, M. R. Morris, S. Yelda, and K. Matthews. Stellar Populations in the Central 0.5 pc of the Galaxy. II. The Initial Mass Function. ApJ, 764:155, February 2013.

[338] L. O'C Drury, P. Duffy, and J. G. Kirk. Limits on diffusive shock acceleration in dense and incompletely ionised media. A&A, 309:1002–1010, May 1996.

[339] Ccepted For and Publication In. Gamma-ray emission from crushed clouds in supernova remnants. (1989):1–5, 1999.

[340] K Ferrière. Global model of the interstellar medium in our galaxy with new constraints on the hot gas component. *The Astrophysical Journal*, 20, 1998.

[341] Martin Pohl. Private Communication.

[342] The Fermi-LAT Collaboration. Fermi-LAT Observations of the Diffuse Gamma-Ray Emission: Implications for Cosmic Rays and the Interstellar Medium. *ArXiv e-prints*, February 2012.

[343] P Cox, E Krügel, and PG Mezger. Principal heating sources of dust in the galactic disk. *Astronomy and Astrophysics*, 1986.

[344] L. Bronfman, R. S. Cohen, H. Alvarez, J. May, and P. Thaddeus. A CO survey of the southern Milky Way - The mean radial distribution of molecular clouds within the solar circle. ApJ, 324:248–266, January 1988.

[345] J. G. A. Wouterloot, J. Brand, W. B. Burton, and K. K. Kwee. IRAS sources beyond the solar circle. II - Distribution in the Galactic warp. A&A, 230:21–36, April 1990.

[346] J. M. Cordes and T. J. W. Lazio. NE2001.I. A New Model for the Galactic Distribution of Free Electrons and its Fluctuations. *ArXiv Astrophysics e-prints*, July 2002.

[347] J. M. Cordes and T. J. W. Lazio. NE2001. II. Using Radio Propagation Data to Construct a Model for the Galactic Distribution of Free Electrons. *ArXiv Astrophysics e-prints*, January 2003.

[348] Alex S Hill, Robert A Benjamin, Grzegorz Kowal, Ronald J. Reynolds, L. Matthew Haffner, and Alex Lazarian. The Turbulent Warm Ionized Medium: Emission Measure Distribution and MHD Simulations. *The Astrophysical Journal*, 686(1):363–378, October 2008.

[349] D. P. Finkbeiner. A Full-Sky Hα Template for Microwave Foreground Prediction. ApJS, 146:407–415, June 2003.

[350] L. M. Haffner, R. J. Reynolds, S. L. Tufte, G. J. Madsen, K. P. Jaehnig, and J. W. Percival. The wisconsin h mapper northern sky survey. *The Astrophysical Journal Supplement Series*, 149(2):405, 2003.

[351] B. Dennison, J. H. Simonetti, and G. A. Topasna. An imaging survey of northern galactic H-alpha emmission with arcminute resolution. PASA, 15:147–48, April 1998.

[352] J. E. Gaustad, P. R. McCullough, W. Rosing, and D. Van Buren. A Robotic Wide-Angle Hα Survey of the Southern Sky. PASP, 113:1326–1348, November 2001.

[353] D. P. Clemens. Massachusetts-Stony Brook Galactic plane CO survey - The Galactic disk rotation curve. ApJ, 295:422–428, August 1985.

[354] J. Roman-Duval, J. M. Jackson, M. Heyer, A. Johnson, J. Rathborne, R. Shah, and R. Si-

mon. Kinematic Distances to Molecular Clouds Identified in the Galactic Ring Survey. ApJ, 699:1153–1170, July 2009.

[355] Michal A. Kolpak, James M. Jackson, T. M. Bania, D. P. Clemens, and John M. Dickey. Resolving the kinematic distance ambiguity toward galactic h ii regions. *The Astrophysical Journal*, 582(2):756, 2003.

[356] Nicolai Bissantz, Peter Englmaier, and Ortwin Gerhard. Gas dynamics in the milky way: second pattern speed and large-scale morphology. *Monthly Notices of the Royal Astronomical Society*, 340(3):949–968, 2003.

[357] M. Tavakoli. Three Dimensional Distribution of Atomic Hydrogen in the Milky Way. *ArXiv e-prints*, July 2012.

[358] Planck Collaboration, A. Abergel, P. A. R. Ade, N. Aghanim, M. I. R. Alves, G. Aniano, C. Armitage-Caplan, M. Arnaud, M. Ashdown, F. Atrio-Barandela, and et al. Planck 2013 results. XI. All-sky model of thermal dust emission. A&A, 571:A11, November 2014.

[359] D. J. Marshall, A. C. Robin, C. Reylé, M. Schultheis, and S. Picaud. Modelling the Galactic interstellar extinction distribution in three dimensions. A&A, 453:635–651, July 2006.

[360] R. Lallement, J.-L. Vergely, B. Valette, L. Puspitarini, L. Eyer, and L. Casagrande. 3D maps of the local ISM from inversion of individual color excess measurements. A&A, 561:A91, January 2014.

[361] G. M. Green, E. F. Schlafly, D. P. Finkbeiner, H.-W. Rix, N. Martin, W. Burgett, P. W. Draper, H. Flewelling, K. Hodapp, N. Kaiser, R. P. Kudritzki, E. Magnier, N. Metcalfe, P. Price, J. Tonry, and R. Wainscoat. A Three-Dimensional Map of Milky-Way Dust. *ArXiv e-prints*, July 2015.

[362] C. Lee, A. K. Leroy, S. Schnee, T. Wong, A. D. Bolatto, R. Indebetouw, and M. Rubio. The relationship between CO emission and visual extinction traced by dust emission in the Magellanic Clouds. MNRAS, 450:2708–2726, July 2015.

[363] Roland M. Crocker, David Jones, Fulvio Melia, Jurgen Ott, and Raymond J. Protheroe. A lower limit of 50 microgauss for the magnetic field near the Galactic Centre. *Nature*, 468:65, 2010.

[364] Ronnie Jansson and Glennys R Farrar. THE GALACTIC MAGNETIC FIELD. *The Astrophysical Journal*, 761(1):L11, December 2012.

[365] A. W. Strong. Recent extensions to GALPROP. *ArXiv e-prints*, July 2015.

[366] I. V. Moskalenko, T. A. Porter, and A. W. Strong. Attenuation of Very High Energy Gamma Rays by the Milky Way Interstellar Radiation Field. ApJ, 640:L155–L158, April 2006.

[367] Richard J. Wainscoat, Martin Cohen, Kevin Volk, Helen J. Walker, and Deborah E. Schwartz. A model of the 8-25 micron point source infrared sky. *The Astrophysical Journal Supplement Series*, 83:111, 1992.

[368] S.D. Hunter, D.L. Bertsch, J.R. Catelli, T.M. Digel, S.W. Dingus, et al. EGRET observations of the diffuse gamma-ray emission from the galactic plane. *Astrophys.J.*, 481:205–240, 1997.

[369] W. de Boer, C. Sander, V. Zhukov, A.V. Gladyshev, and D.I. Kazakov. Egret excess of diffuse galactic gamma rays as tracer of dark matter. *Astron.Astrophys.*, 444:51, 2005.

[370] Andrew W. Strong, Igor V. Moskalenko, and Olaf Reimer. Diffuse galactic continuum gamma rays. A Model compatible with EGRET data and cosmic-ray measurements. *Astrophys.J.*, 613:962–976, 2004.

[371] Tuneyoshi Kamae, Toshinori Abe, and Tatsumi Koi. Diffractive interaction and scaling violation in p p ; pi0 interaction and GeV excess in galactic diffuse gamma-ray spectrum of EGRET. *Astrophys.J.*, 620:244–256, 2005.

[372] F. W. Stecker, S. D. Hunter, and D. A. Kniffen. The likely cause of the EGRET GeV anomaly and its implications. *Astroparticle Physics*, 29:25–29, February 2008.

[373] A.A. Abdo et al. The Spectrum of the Isotropic Diffuse Gamma-Ray Emission Derived From First-Year Fermi Large Area Telescope Data. *Phys.Rev.Lett.*, 104:101101, 2010.

[374] Dan Hooper and Tim Linden. On The Origin Of The Gamma Rays From The Galactic Center. *Phys.Rev.*, D84:123005, 2011.

[375] Alexey Boyarsky, Denys Malyshev, and Oleg Ruchayskiy. A comment on the emission from the Galactic Center as seen by the Fermi telescope. *Phys.Lett.*, B705:165–169, 2011.

[376] M. Chernyakova, D. Malyshev, F.A. Aharonian, R.M. Crocker, and D.I. Jones. The high-energy, Arcminute-scale galactic center gamma-ray source. *Astrophys.J.*, 726:60, 2011.

[377] Tim Linden and Stefano Profumo. Exploring the Nature of the Galactic Center Gamma-Ray Source with the Cherenkov Telescope Array. *Astrophys.J.*, 760:23, 2012.

[378] Tim Linden, Elizabeth Lovegrove, and Stefano Profumo. The Morphology of Hadronic Emission Models for the Gamma-Ray Source at the Galactic Center. *Astrophys.J.*, 753:41, 2012.

[379] K. N. Abazajian. The consistency of Fermi-LAT observations of the galactic center with a millisecond pulsar population in the central stellar cluster. *JCAP*, 3:10, March 2011.

[380] F. W. Stecker. Observations of galactic gamma-rays and their implications for galactic structure studies. ApJ, 212:60–70, February 1977.

[381] T. Linden and S. Profumo. Systematic Effects in Extracting a "Gamma-ray Haze" from Spatial Templates. *ApJ Letters*, 714:L228–L232, May 2010.

[382] O. Macias and C. Gordon. Contribution of cosmic rays interacting with molecular clouds to the Galactic Center gamma-ray excess. Phys. Rev. D, 89(6):063515, March 2014.

[383] Fermi Collaboration. Summary of the development of the model of galactic diffuse emission for use with pass 7 reprocessed lat data, October 2013.

[384] *Local HI emissivity and implications for cosmic-ray spectra*, THE ASTROPARTICLE PHYSICS CONFERENCE, Rio de Janiero, Brazil, 2013.

[385] Bei Zhou, Yun-Feng Liang, Xiaoyuan Huang, Xiang Li, Yi-Zhong Fan, Lei Feng, and Jin Chang. GeV excess in the Milky Way: The role of diffuse galactic gamma-ray emission templates. *Phys. Rev.*, D91(12):123010, 2015.

[386] Asher Berlin, Dan Hooper, and Samuel D. McDermott. Simplified Dark Matter Models for the Galactic Center Gamma-Ray Excess. *Phys. Rev.*, D89(11):115022, 2014.

[387] Prateek Agrawal, Brian Batell, Dan Hooper, and Tongyan Lin. Flavored Dark Matter and the Galactic Center Gamma-Ray Excess. *Phys. Rev.*, D90(6):063512, 2014.

[388] Alexandre Alves, Stefano Profumo, Farinaldo S. Queiroz, and William Shepherd. Effective field theory approach to the Galactic Center gamma-ray excess. *Phys. Rev.*, D90(11):115003, 2014.

[389] Mohammad Abdullah, Anthony DiFranzo, Arvind Rajaraman, Tim M. P. Tait, Philip Tanedo, and Alexander M. Wijangco. Hidden on-shell mediators for the Galactic Center γ-ray excess. *Phys. Rev.*, D90:035004, 2014.

[390] Seyda Ipek, David McKeen, and Ann E. Nelson. A Renormalizable Model for the Galactic

Center Gamma Ray Excess from Dark Matter Annihilation. *Phys. Rev.*, D90(5):055021, 2014.

[391] Francesca Calore, Ilias Cholis, Christopher McCabe, and Christoph Weniger. A Tale of Tails: Dark Matter Interpretations of the Fermi GeV Excess in Light of Background Model Systematics. *Phys. Rev.*, D91(6):063003, 2015.

[392] Qiang Yuan and Kunihito Ioka. Testing the millisecond pulsar scenario of the Galactic center gamma-ray excess with very high energy gamma-rays. *Astrophys. J.*, 802(2):124, 2015.

[393] Jovana Petrovi, Pasquale D. Serpico, and Gabrijela Zaharijas. Millisecond pulsars and the Galactic Center gamma-ray excess: the importance of luminosity function and secondary emission. *JCAP*, 1502(02):023, 2015.

[394] Ryan M. O'Leary, Matthew D. Kistler, Matthew Kerr, and Jason Dexter. Young Pulsars and the Galactic Center GeV Gamma-ray Excess. 2015.

[395] Ilias Cholis, Dan Hooper, and Tim Linden. Challenges in Explaining the Galactic Center Gamma-Ray Excess with Millisecond Pulsars. 2014.

[396] Samuel K. Lee, Mariangela Lisanti, Benjamin R. Safdi, Tracy R. Slatyer, and Wei Xue. Evidence for Unresolved Gamma-Ray Point Sources in the Inner Galaxy. 2015.

[397] E. Carlson, T. Linden, and S. Profumo. Putting Things Back Where They Belong: Tracing Cosmic-Ray Injection with H2. *ArXiv e-prints*, October 2015.

[398] Tova M. Yoast-Hull, J. S. Gallagher, and Ellen G Zweibel. The Cosmic Ray Population of the Galactic Central Molecular Zone. i(1):9, May 2014.

[399] Daniele Gaggero, Marco Taoso, Alfredo Urbano, Mauro Valli, and Piero Ullio. Towards a realistic astrophysical interpretation of the Galactic center excess. 2015.

[400] D. Gaggero, M. Taoso, A. Urbano, M. Valli, and P. Ullio. Towards a realistic astrophysical interpretation of the Galactic center excess. *ArXiv e-prints*, July 2015.

[401] Andrey V. Kravtsov. On the Origin of the Global Schmidt Law of Star Formation. *The Astrophysical Journal*, 590(1):L1–L4, June 2003.

[402] Yuexing Li, MordecaiMark Mac Low, and Ralf S. Klessen. Star Formation in Isolated Disk Galaxies. I. Models and Characteristics of Nonlinear Gravitational Collapse. *The Astrophysical Journal*, 626(2):823–843, June 2005.

[403] R.-z. Yang and F. Aharonian. On the "GeV excess" in the diffuse \gamma -ray emission towards the Galactic Center. *ArXiv e-prints*, February 2016.

[404] F. Aharonian, A. G. Akhperjanian, A. R. Bazer-Bachi, M. Beilicke, W. Benbow, D. Berge, K. Bernlöhr, C. Boisson, O. Bolz, V. Borrel, I. Braun, F. Breitling, A. M. Brown, P. M. Chadwick, L.-M. Chounet, R. Cornils, L. Costamante, B. Degrange, H. J. Dickinson, A. Djannati-Ataï, L. O. Drury, G. Dubus, D. Emmanoulopoulos, P. Espigat, F. Feinstein, G. Fontaine, Y. Fuchs, S. Funk, Y. A. Gallant, B. Giebels, S. Gillessen, J. F. Glicenstein, P. Goret, C. Hadjichristidis, D. Hauser, M. Hauser, G. Heinzelmann, G. Henri, G. Hermann, J. A. Hinton, W. Hofmann, M. Holleran, D. Horns, A. Jacholkowska, O. C. de Jager, B. Khélifi, S. Klages, N. Komin, A. Konopelko, I. J. Latham, R. Le Gallou, A. Lemière, M. Lemoine-Goumard, N. Leroy, T. Lohse, A. Marcowith, J. M. Martin, O. Martineau-Huynh, C. Masterson, T. J. L. McComb, M. de Naurois, S. J. Nolan, A. Noutsos, K. J. Orford, J. L. Osborne, M. Ouchrif, M. Panter, G. Pelletier, S. Pita, G. Pühlhofer, M. Punch, B. C. Raubenheimer, M. Raue, J. Raux, S. M. Rayner, A. Reimer, O. Reimer, J. Ripken, L. Rob, L. Rolland, G. Rowell, V. Sahakian, L. Saugé, S. Schlenker, R. Schlickeiser, C. Schuster, U. Schwanke, M. Siewert, H. Sol, D. Spangler, R. Steenkamp, C. Stegmann, J.-P. Tavernet, R. Terrier, C. G. Théoret, M. Tluczykont, C. van Eldik, G. Vasileiadis,

C. Venter, P. Vincent, H. J. Völk, and S. J. Wagner. Discovery of very-high-energy γ-rays from the Galactic Centre ridge. Nature, 439:695–698, February 2006.

[405] A. Archer et al. TeV Gamma-ray Observations of The Galactic Center Ridge By VERITAS. 2016.

[406] F. Yusef-Zadeh, J. W. Hewitt, R. G. Arendt, B. Whitney, G. Rieke, M. Wardle, J. L. Hinz, S. Stolovy, C. C. Lang, M. G. Burton, and S. Ramirez. Star formation in the central 400 pc of the milky way: Evidence for a population of massive young stellar objects. *The Astrophysical Journal*, 702(1):178, 2009.

[407] K. Yasui, S. Nishiyama, T. Yoshikawa, S. Nagatomo, H. Uchiyama, T. G. Tsuru, K. Koyama, M. Tamura, J. Kwon, K. Sugitani, R. Schödel, and T. Nagata. Number density distribution of near-infrared sources on a sub-degree scale in the Galactic center: Comparison with the Fe XXV Kα line at 6.7 keV. PASJ, 67:123, December 2015.

[408] R. Genzel, F. Eisenhauer, and S. Gillessen. The Galactic Center massive black hole and nuclear star cluster. *Reviews of Modern Physics*, 82:3121–3195, October 2010.

[409] T. Do, J. R. Lu, A. M. Ghez, M. R. Morris, S. Yelda, G. D. Martinez, S. A. Wright, and K. Matthews. Stellar Populations in the Central 0.5 pc of the Galaxy. I. A New Method for Constructing Luminosity Functions and Surface-density Profiles. ApJ, 764:154, February 2013.

[410] C. R. Purcell, S. N. Longmore, A. J. Walsh, M. T. Whiting, S. L. Breen, T. Britton, K. J. Brooks, M. G. Burton, M. R. Cunningham, J. A. Green, L. Harvey-Smith, L. Hindson, M. G. Hoare, B. Indermuehle, P. A. Jones, N. Lo, V. Lowe, C. J. Phillips, M. A. Thompson, J. S. Urquhart, M. A. Voronkov, and G. L. White. The H_2O Southern Galactic Plane Survey: NH_3 (1,1) and (2,2) catalogues. MNRAS, 426:1972–1991, November 2012.

[411] F. Guo and W. G. Mathews. The Fermi Bubbles. I. Possible Evidence for Recent AGN Jet Activity in the Galaxy. ApJ, 756:181, September 2012.

[412] H.-Y. K. Yang, M. Ruszkowski, P. M. Ricker, E. Zweibel, and D. Lee. The Fermi Bubbles: Supersonic Active Galactic Nucleus Jets with Anisotropic Cosmic-Ray Diffusion. ApJ, 761:185, December 2012.

[413] A. W. Strong, I. V. Moskalenko, and O. Reimer. Diffuse Continuum Gamma Rays from the Galaxy. ApJ, 537:763–784, July 2000.

[414] R. M. Crocker, D. I. Jones, F. Aharonian, C. J. Law, F. Melia, T. Oka, and J. Ott. Wild at Heart: the particle astrophysics of the Galactic Centre. *Monthly Notices of the Royal Astronomical Society*, 413:763–788, May 2011.

[415] R. M. Crocker, D. I. Jones, F. Aharonian, C. J. Law, F. Melia, and J. Ott. γ-rays and the far-infrared-radio continuum correlation reveal a powerful Galactic Centre wind. *Monthly Notices of the Royal Astronomical Society*, 411:L11–L15, February 2011.

[416] R. M. Crocker. Non-thermal insights on mass and energy flows through the Galactic Centre and into the Fermi bubbles. *Monthly Notices of the Royal Astronomical Society*, 423:3512–3539, July 2012.

[417] I. V. Moskalenko, A. W. Strong, J. F. Ormes, and M. S. Potgieter. Secondary Antiprotons and Propagation of Cosmic Rays in the Galaxy and Heliosphere. ApJ, 565:280–296, January 2002.

[418] B. M. Gaensler, G. J. Madsen, S. Chatterjee, and S. A. Mao. The Vertical Structure of Warm Ionised Gas in the Milky Way. *PASA*, 25:184–200, November 2008.

[419] D. J. Schlegel, D. P. Finkbeiner, and M. Davis. Maps of Dust Infrared Emission for Use

in Estimation of Reddening and Cosmic Microwave Background Radiation Foregrounds. ApJ, 500:525, June 1998.

[420] Qiang Yuan and Bing Zhang. Millisecond pulsar interpretation of the Galactic center gamma-ray excess. 2014.

[421] M et al.. The Fermi-LAT Collaboration: Ackermann. Detection of the Characteristic Pion-Decay Signature in Supernova Remnants. February 2013.

[422] R. Blandford and D. Eichler. Particle acceleration at astrophysical shocks: A theory of cosmic ray origin. *Phys. Rep.*, 154:1–75, October 1987.

[423] F. Yusef-Zadeh, J W Hewitt, M Wardle, V Tatischeff, D. Roberts, W Cotton, H Uchiyama, M Nobukawa, T G Tsuru, C Heinke, and M Royster. Interacting Cosmic Rays with Molecular Clouds: A Bremsstrahlung Origin of Diffuse High Energy Emission from the Inner 2deg by 1deg of the Galactic Center. page 51, June 2012.

[424] D. F. Figer. Massive Star Formation in the Galactic Center. pages 1–23, March 2008.

[425] M. Morris. Massive star formation near the Galactic center and the fate of the stellar remnants. ApJ, 408:496–506, May 1993.

[426] M. Chernyakova, D. Malyshev, F. A. Aharonian, R. M. Crocker, and D. I. Jones. The High-energy, Arcminute-scale Galactic Center Gamma-ray Source. ApJ, 726:60, January 2011.

[427] T. Linden, E. Lovegrove, and S. Profumo. The Morphology of Hadronic Emission Models for the Gamma-Ray Source at the Galactic Center. ApJ, 753:41, July 2012.

[428] D. Hooper and T. Linden. Origin of the gamma rays from the Galactic Center. Phys. Rev. D, 84(12):123005, December 2011.

[429] F. Aharonian and A. Neronov. High-Energy Gamma Rays from the Massive Black Hole in the Galactic Center. ApJ, 619:306–313, January 2005.

[430] W. B. Atwood, A. A. Abdo, M. Ackermann, W. Althouse, B. Anderson, M. Axelsson, L. Baldini, J. Ballet, D. L. Band, G. Barbiellini, and et al. The Large Area Telescope on the Fermi Gamma-Ray Space Telescope Mission. *ApJ*, 697:1071–1102, June 2009.

[431] F. Yusef-Zadeh, F. Melia, and M. Wardle. The Galactic Center: An Interacting System of Unusual Sources. *Science*, 287:85–91, January 2000.

[432] F. Yusef-Zadeh, W. M. Goss, D. A. Roberts, B. Robinson, and D. A. Frail. Three New Supernova Remnant OH Masers Near the Galactic Center: Evidence for Large-Scale Maser Emission from Supernova Remnants. *ApJ*, 527:172–179, December 1999.

[433] Q. D. Wang, E. V. Gotthelf, and C. C. Lang. A faint discrete source origin for the highly ionized iron emission from the Galactic Centre region. *Nature*, 415:148–150, January 2002.

[434] K. Ferrière. Interstellar gas within ˜10 pc of Sagittarius A$^?$. *AAP*, 540:A50, April 2012.

[435] R. Schödel, D. Merritt, and A. Eckart. The nuclear star cluster of the Milky Way: proper motions and mass. *AAP*, 502:91–111, July 2009.

[436] R. S. Wharton, S. Chatterjee, J. M. Cordes, J. S. Deneva, and T. J. W. Lazio. Multi-wavelength Constraints on Pulsar Populations in the Galactic Center. *ApJ*, 753:108, July 2012.

[437] D. Hooper, I. de la Calle Perez, J. Silk, F. Ferrer, and S. Sarkar. Have atmospheric Cerenkov telescopes observed dark matter? *JCAP*, 9:2, September 2004.

[438] Torsten Bringmann and Christoph Weniger. Gamma Ray Signals from Dark Matter: Concepts, Status and Prospects. *Phys.Dark Univ.*, 1:194–217, 2012.

[439] Christoph Weniger. A Tentative Gamma-Ray Line from Dark Matter Annihilation at the Fermi Large Area Telescope. *JCAP*, 1208:007, 2012.

[440] V. Springel, J. Wang, M. Vogelsberger, A. Ludlow, A. Jenkins, A. Helmi, J. F. Navarro, C. S. Frenk, and S. D. M. White. The Aquarius Project: the subhaloes of galactic haloes. *MNRAS*, 391:1685–1711, December 2008.

[441] G. R. Blumenthal, S. M. Faber, R. Flores, and J. R. Primack. Contraction of dark matter galactic halos due to baryonic infall. *ApJ*, 301:27–34, February 1986.

[442] O. Y. Gnedin, D. Ceverino, N. Y. Gnedin, A. A. Klypin, A. V. Kravtsov, R. Levine, D. Nagai, and G. Yepes. Halo Contraction Effect in Hydrodynamic Simulations of Galaxy Formation. *ArXiv e-prints*, August 2011.

[443] S. Profumo and T. Linden. Gamma-ray lines in the Fermi data: is it a bubble? *JCAP*, 7:11, July 2012.

[444] M. Su, T. R. Slatyer, and D. P. Finkbeiner. Giant Gamma-ray Bubbles from Fermi-LAT: Active Galactic Nucleus Activity or Bipolar Galactic Wind? *ApJ*, 724:1044–1082, December 2010.

[445] M. Su and D. P. Finkbeiner. Strong Evidence for Gamma-ray Line Emission from the Inner Galaxy. *ArXiv e-prints*, June 2012.

[446] E. Tempel, A. Hektor, and M. Raidal. Fermi 130 GeV gamma-ray excess and dark matter annihilation in sub-haloes and in the Galactic centre. *ArXiv e-prints*, May 2012.

[447] R.-Z. Yang, Q. Yuan, L. Feng, Y.-Z. Fan, and J. Chang. Statistical interpretation of the spatial distribution of current 130 GeV γ-ray line signal within the dark matter annihilation scenario. *Physics Letters B*, 715:285–288, September 2012.

[448] Kanishka Rao and Daniel Whiteson. Where are the Fermi Lines Coming From? 2012.

[449] M. Kuhlen, J. Guedes, A. Pillepich, P. Madau, and L. Mayer. An Off-center Density Peak in the Milky Way's Dark Matter Halo? *ArXiv e-prints*, August 2012.

[450] D. P. Finkbeiner, M. Su, and C. Weniger. Is the 130 GeV Line Real? A Search for Systematics in the Fermi-LAT Data. *ArXiv e-prints*, September 2012.

[451] Andi Hektor, Martti Raidal, and Elmo Tempel. Fermi-LAT gamma-ray signal from Earth Limb, systematic detector effects and their implications for the 130 GeV gamma-ray excess. 2012.

[452] A. Boyarsky, D. Malyshev, and O. Ruchayskiy. Spectral and spatial variations of the diffuse gamma-ray background in the vicinity of the Galactic plane and possible nature of the feature at 130 GeV. *ArXiv e-prints*, May 2012.

[453] D. Whiteson. Disentangling instrumental features of the 130 GeV Fermi line. *JCAP*, 11:8, November 2012.

[454] D. Whiteson. Searching for Spurious Solar and Sky Lines in the Fermi-LAT Spectrum. *ArXiv e-prints*, February 2013.

[455] E. Bloom, E. Charles, E. Izaguirre, A. Snyder, A. Albert, B. Winer, Z. Yang, and R. Essig. Search of the Earth Limb Fermi Data and Non-Galactic Center Region Fermi Data for Signs of Narrow Lines. *ArXiv e-prints*, March 2013.

[456] D. Hooper and T. Linden. Origin of the gamma rays from the Galactic Center. *PRD*, 84(12):123005, December 2011.

[457] A. Rajaraman, T. M. P. Tait, and D. Whiteson. Two lines or not two lines? That is the question of gamma ray spectra. *JCAP*, 9:3, September 2012.

[458] B. Shakya. A 130 GeV Gamma Ray Signal from Supersymmetry. *ArXiv e-prints*, September 2012.

[459] H. M. Lee, M. Park, and W.-I. Park. Axion-mediated dark matter and Higgs diphoton signal. *ArXiv e-prints*, September 2012.

[460] S. Baek, P. Ko, and E. Senaha. Can Zee-Babu model implemented with scalar dark matter explain both Fermi/LAT 130 GeV γ-ray excess and neutrino physics ? *ArXiv e-prints*, September 2012.

[461] J. Fan and M. Reece. A Simple Recipe for the 111 and 128 GeV Lines. *ArXiv e-prints*, September 2012.

[462] N. Weiner and I. Yavin. UV Completions of Magnetic Inelastic Dark Matter and RayDM for the Fermi Line(s). *ArXiv e-prints*, September 2012.

[463] L. Wang and X.-F. Han. 130 GeV gamma-ray line and enhancement of $h\to\gamma\gamma$ in the Higgs triplet model plus a scalar dark matter. *ArXiv e-prints*, September 2012.

[464] E. Dudas, Y. Mambrini, S. Pokorski, and A. Romagnoni. Extra U(1) as natural source of a monochromatic gamma ray line. *ArXiv e-prints*, May 2012.

[465] M. R. Buckley and D. Hooper. Implications of a 130 GeV gamma-ray line for dark matter. *PRD*, 86(4):043524, August 2012.

[466] K.-Y. Choi and O. Seto. Dirac right-handed sneutrino dark matter and its signature in the gamma-ray lines. *PRD*, 86(4):043515, August 2012.

[467] L. Bergström. The 130 GeV Fingerprint of Right-Handed Neutrino Dark Matter. *ArXiv e-prints*, August 2012.

[468] M. Garny, A. Ibarra, and D. Tran. Constraints on hadronically decaying dark matter. *JCAP*, 8:25, August 2012.

[469] Y. Bai and J. Shelton. Gamma Lines without a Continuum: Thermal Models for the Fermi-LAT 130 GeV Gamma Line. *ArXiv e-prints*, August 2012.

[470] J. M. Cline, A. R. Frey, and G. D. Moore. Composite magnetic dark matter and the 130 GeV line. *ArXiv e-prints*, August 2012.

[471] T. Li, J. A. Maxin, D. V. Nanopoulos, and J. W. Walker. A 125.5 GeV Higgs Boson in F-SU(5): Imminently Observable Proton Decay, A 130 GeV Gamma-ray Line, and SUSY Multijets & Light Stops at the LHC8. *ArXiv e-prints*, August 2012.

[472] J. M. Cline. 130 GeV dark matter and the Fermi gamma-ray line. *PRD*, 86(1):015016, July 2012.

[473] S. Tulin, H.-B. Yu, and K. M. Zurek. Three Exceptions for Thermal Dark Matter with Enhanced Annihilation to Gamma Gamma. *ArXiv e-prints*, July 2012.

[474] J.-C. Park and S. C. Park. Radiatively decaying scalar dark matter through U(1) mixings and the Fermi 130 GeV gamma-ray line. *ArXiv e-prints*, July 2012.

[475] M. T. Frandsen, U. Haisch, F. Kahlhoefer, P. Mertsch, and K. Schmidt-Hoberg. Loop-induced dark matter direct detection signals from gamma-ray lines. *ArXiv e-prints*, July 2012.

[476] I. Oda. Remarks on Two Gamma Ray Lines from the Inner Galaxy. *ArXiv e-prints*, July 2012.

[477] J. H. Heo and C. S. Kim. Cosmic ray signatures of Dipole-Interacting Fermionic Dark Matter. *ArXiv e-prints*, July 2012.

[478] T. Cohen, M. Lisanti, T. R. Slatyer, and J. G. Wacker. Illuminating the 130 GeV Gamma Line with Continuum Photons. *ArXiv e-prints*, July 2012.

[479] W. Buchmuller and M. Garny. Decaying vs Annihilating Dark Matter in Light of a Tentative Gamma-Ray Line. *ArXiv e-prints*, June 2012.

[480] N. Weiner and I. Yavin. How Dark Are Majorana WIMPs? Signals from MiDM and Rayleigh Dark Matter. *ArXiv e-prints*, June 2012.

[481] Z. Kang, T. Li, J. Li, and Y. Liu. Brightening the (130 GeV) Gamma-Ray Line. *ArXiv e-prints*, June 2012.

[482] X. Chu, T. Hambye, T. Scarna, and M. H. G. Tytgat. What if Dark Matter Gamma-Ray Lines come with Gluon Lines? *ArXiv e-prints*, June 2012.

[483] B. Samir Acharya, G. Kane, P. Kumar, R. Lu, and B. Zheng. Mixed Wino-Axion Dark Matter in String/M Theory and the 130 GeV Gamma-line "Signal". *ArXiv e-prints*, May 2012.

[484] H. M. Lee, M. Park, and W.-I. Park. Fermi Gamma Ray Line at 130 GeV from Axion-Mediated Dark Matter. *ArXiv e-prints*, May 2012.

[485] B. Kyae and J.-C. Park. 130 GeV Gamma-Ray Line from Dark Matter Decay. *ArXiv e-prints*, May 2012.

[486] Masaki Asano, Torsten Bringmann, Gunter Sigl, and Martin Vollmann. The 130 GeV gamma-ray line and generic dark matter model building constraints from continuum gamma rays, radio and antiproton data. 2012.

[487] F. Aharonian, D. Khangulyan, and D. Malyshev. Cold ultrarelativistic pulsar winds as potential sources of galactic gamma-ray lines above 100 GeV. *ArXiv e-prints*, July 2012.

[488] A. Geringer-Sameth and S. M. Koushiappas. Dark matter line search using a joint analysis of dwarf galaxies with the Fermi Gamma-ray Space Telescope. *PRD*, 86(2):021302, July 2012.

[489] A. Hektor, M. Raidal, and E. Tempel. An evidence for indirect detection of dark matter from galaxy clusters in Fermi-LAT data. *ArXiv e-prints*, July 2012.

[490] M. Su and D. P. Finkbeiner. Double Gamma-ray Lines from Unassociated Fermi-LAT Sources. *ArXiv e-prints*, July 2012.

[491] D. Hooper and T. Linden. Are Lines From Unassociated Gamma-Ray Sources Evidence For Dark Matter Annihilation? *ArXiv e-prints*, August 2012.

[492] N. Mirabal. The Dark Knight Falters. *ArXiv e-prints*, August 2012.

[493] R. M. Catchpole, P. A. Whitelock, and I. S. Glass. The Distribution of Stars Within Two Degrees of the Galactic Centre. *MNRAS*, 247:479–490, December 1990.

[494] S. Gillessen, F. Eisenhauer, S. Trippe, T. Alexander, R. Genzel, F. Martins, and T. Ott. Monitoring Stellar Orbits Around the Massive Black Hole in the Galactic Center. ApJ, 692:1075–1109, February 2009.

[495] R. Cornils, S. Gillessen, I. Jung, W. Hofmann, M. Beilicke, K. Bernlöhr, O. Carrol, S. Elfahem, G. Heinzelmann, G. Hermann, D. Horns, R. Kankanyan, A. Katona, H. Krawczynski, M. Panter, S. Rayner, G. Rowell, M. Tluczykont, and R. van Staa. The optical system of the H.E.S.S. imaging atmospheric Cherenkov telescopes. Part II: mirror alignment and point spread function. *Astroparticle Physics*, 20:129–143, November 2003.

[496] A. Abramowski, F. Acero, F. Aharonian, A. G. Akhperjanian, G. Anton, A. Barnacka, U. Barres de Almeida, A. R. Bazer-Bachi, Y. Becherini, J. Becker, B. Behera, K. Bernlöhr, A. Bochow, C. Boisson, J. Bolmont, P. Bordas, V. Borrel, J. Brucker, F. Brun, P. Brun, T. Bulik, I. Büsching, S. Carrigan, S. Casanova, M. Cerruti, P. M. Chadwick, A. Charbonnier, R. C. G. Chaves, A. Cheesebrough, L.-M. Chounet, A. C. Clapson, G. Coignet, J. Conrad, M. Dalton, M. K. Daniel, I. D. Davids, B. Degrange, C. Deil, H. J. Dickinson,

A. Djannati-Ataï, W. Domainko, L. O. '. Drury, F. Dubois, G. Dubus, J. Dyks, M. Dyrda, K. Egberts, P. Eger, P. Espigat, L. Fallon, C. Farnier, S. Fegan, F. Feinstein, M. V. Fernandes, A. Fiasson, G. Fontaine, A. Förster, M. Füßling, Y. A. Gallant, H. Gast, L. Gérard, D. Gerbig, B. Giebels, J. F. Glicenstein, B. Glück, P. Goret, D. Göring, J. D. Hague, D. Hampf, M. Hauser, S. Heinz, G. Heinzelmann, G. Henri, G. Hermann, J. A. Hinton, A. Hoffmann, W. Hofmann, P. Hofverberg, D. Horns, A. Jacholkowska, O. C. de Jager, C. Jahn, M. Jamrozy, I. Jung, M. A. Kastendieck, K. Katarzyński, U. Katz, S. Kaufmann, D. Keogh, M. Kerschhaggl, D. Khangulyan, B. Khélifi, D. Klochkov, W. Kluźniak, T. Kneiske, N. Komin, K. Kosack, R. Kossakowski, H. Laffon, G. Lamanna, D. Lennarz, T. Lohse, A. Lopatin, C.-C. Lu, V. Marandon, A. Marcowith, J. Masbou, D. Maurin, N. Maxted, T. J. L. McComb, M. C. Medina, J. Méhault, R. Moderski, E. Moulin, C. L. Naumann, M. Naumann-Godo, M. de Naurois, D. Nedbal, D. Nekrassov, N. Nguyen, B. Nicholas, J. Niemiec, S. J. Nolan, S. Ohm, J.-F. Olive, E. de Oña Wilhelmi, B. Opitz, M. Ostrowski, M. Panter, M. Paz Arribas, G. Pedaletti, G. Pelletier, P.-O. Petrucci, S. Pita, G. Pühlhofer, M. Punch, A. Quirrenbach, M. Raue, S. M. Rayner, A. Reimer, O. Reimer, M. Renaud, R. de Los Reyes, F. Rieger, J. Ripken, L. Rob, S. Rosier-Lees, G. Rowell, B. Rudak, C. B. Rulten, J. Ruppel, F. Ryde, V. Sahakian, A. Santangelo, R. Schlickeiser, F. M. Schöck, A. Schönwald, U. Schwanke, S. Schwarzburg, S. Schwemmer, A. Shalchi, M. Sikora, J. L. Skilton, H. Sol, G. Spengler, Ł. Stawarz, R. Steenkamp, C. Stegmann, F. Stinzing, I. Sushch, A. Szostek, J.-P. Tavernet, R. Terrier, O. Tibolla, M. Tluczykont, K. Valerius, C. van Eldik, G. Vasileiadis, C. Venter, J. P. Vialle, A. Viana, P. Vincent, M. Vivier, H. J. Völk, F. Volpe, S. Vorobiov, M. Vorster, S. J. Wagner, M. Ward, A. Wierzcholska, A. Zajczyk, A. A. Zdziarski, A. Zech, and H.-S. Zechlin. Search for a Dark Matter Annihilation Signal from the Galactic Center Halo with H.E.S.S. *Physical Review Letters*, 106(16):161301, April 2011.

[497] Torsten Bringmann, Francesca Calore, Gilles Vertongen, and Christoph Weniger. On the Relevance of Sharp Gamma-Ray Features for Indirect Dark Matter Searches. *Phys.Rev.*, D84:103525, 2011.

[498] T.-P. Li and Y.-Q. Ma. Analysis methods for results in gamma-ray astronomy. *ApJ*, 272:317–324, September 1983.

[499] C. Weniger. Tentative observation of a gamma-ray line at the Fermi LAT. *ArXiv e-prints*, October 2012.

[500] R. Fleysher. Discovery of Diffuse TeV Gamma Ray Emission from the Galactic Plane using Milagro Detector. In F. A. Aharonian, H. J. Völk, and D. Horns, editors, *High Energy Gamma-Ray Astronomy*, volume 745 of *American Institute of Physics Conference Series*, pages 269–274, February 2005.

[501] W. Atwood. Pass 8: A Comprehensive Revision Of The Fermi Lat Event-level Analysis. In *American Astronomical Society Meeting Abstracts*, volume 219 of *American Astronomical Society Meeting Abstracts*, page 145.18, January 2012.

[502] L. Bergström, G. Bertone, J. Conrad, C. Farnier, and C. Weniger. Investigating Gamma-Ray Lines from Dark Matter with Future Observatories. *ArXiv e-prints*, July 2012.

[503] A. M. Galper, O. Adriani, R. L. Aptekar, I. V. Arkhangelskaja, A. I. Arkhangelskiy, M. Boezio, V. Bonvicini, K. A. Boyarchuk, Y. V. Gusakov, M. O. Farber, M. I. Fradkin, V. A. Kachanov, V. A. Kaplin, M. D. Kheymits, A. A. Leonov, F. Longo, P. Maestro, P. Marrocchesi, E. P. Mazets, E. Mocchiutti, A. A. Moiseev, N. Mori, I. Moskalenko, P. Y. Naumov, P. Papini, P. Picozza, V. G. Rodin, M. F. Runtso, R. Sparvoli, P. Spillantini, S. I. Suchkov, M. Tavani, N. P. Topchiev, A. Vacchi, E. Vannuccini, Y. T. Yurkin, N. Zampa, and V. G. Zverev. Status of the GAMMA-400 Project. *ArXiv e-prints*, January 2012.

[504] T. CTA Consortium. Contributions from the Cherenkov Telescope Array (CTA) Consortium to the ICRC 2011. *ArXiv e-prints*, November 2011.

[505] Tesla E. Jeltema and Stefano Profumo. Dark matter searches going bananas: the contribution of Potassium (and Chlorine) to the 3.5 keV line. 2014.

[506] Signe Riemer-Sorensen. Questioning a 3.5 keV dark matter emission line. 2014.

[507] Tesla Jeltema and Stefano Profumo. Reply to Two Comments on "Dark matter searches going bananas the contribution of Potassium (and Chlorine) to the 3.5 keV line". 2014.

[508] D. Malyshev, A. Neronov, and D. Eckert. Constraints on 3.55 keV line emission from stacked observations of dwarf spheroidal galaxies. 2014.

[509] Michael E. Anderson, Eugene Churazov, and Joel N. Bregman. Non-Detection of X-Ray Emission From Sterile Neutrinos in Stacked Galaxy Spectra. 2014.

[510] O. Urban, N. Werner, S.W. Allen, A. Simionescu, J.S. Kaastra, et al. A Suzaku Search for Dark Matter Emission Lines in the X-ray Brightest Galaxy Clusters. 2014.

[511] A. Boyarsky, J. Franse, D. Iakubovskyi, and O. Ruchayskiy. Comment on the paper "Dark matter searches going the 3.5 keV line" by T. Jeltema and S. Profumo. 2014.

[512] Esra Bulbul, Maxim Markevitch, Adam R. Foster, Randall K. Smith, Michael Loewenstein, et al. Comment on "Dark matter searches going bananas: the contribution of Potassium (and Chlorine) to the 3.5 keV line". 2014.

[513] A. Boyarsky, J. Franse, D. Iakubovskyi, and O. Ruchayskiy. Checking the dark matter origin of 3.53˜keV line with the Milky Way center. *ArXiv e-prints*, August 2014.

[514] F. Yusef-Zadeh, M. Wardle, C. Heinke, C. D. Dowell, D. Roberts, F. K. Baganoff, and W. Cotton. Simultaneous chandra, cso, and vla observations of sgr a*: The nature of flaring activity. *The Astrophysical Journal*, 682(1):361, 2008.

[515] M. P. Muno, F. K. Baganoff, M. W. Bautz, W. N. Brandt, P. S. Broos, E. D. Feigelson, G. P. Garmire, M. R. Morris, G. R. Ricker, and L. K. Townsley. A deep chandra catalog of x-ray point sources toward the galactic center. *The Astrophysical Journal*, 589(1):225, 2003.

[516] M. P. Muno, F. K. Baganoff, M. W. Bautz, E. D. Feigelson, G. P. Garmire, M. R. Morris, S. Park, G. R. Ricker, and L. K. Townsley. Diffuse x-ray emission in a deep chandra image of the galactic center. *The Astrophysical Journal*, 613(1):326, 2004.

[517] A. C. Fabian, J. S. Sanders, S. W. Allen, C. S. Crawford, K. Iwasawa, R. M. Johnstone, R. W. Schmidt, and G. B. Taylor. A deep Chandra observation of the Perseus cluster: shocks and ripples. MNRAS, 344:L43–L47, September 2003.

[518] A. C. Fabian, J. S. Sanders, S. Ettori, G. B. Taylor, S. W. Allen, C. S. Crawford, K. Iwasawa, R. M. Johnstone, and P. M. Ogle. Chandra imaging of the complex x-ray core of the perseus cluster. *Monthly Notices of the Royal Astronomical Society*, 318(4):L65–L68, 2000.

[519] R. W. Schmidt, A. C. Fabian, and J. S. Sanders. Chandra temperature and metallicity maps of the Perseus cluster core. MNRAS, 337:71–78, November 2002.

[520] S. L. Snowden, R. F. Mushotzky, K. D. Kuntz, and D. S. Davis. A catalog of galaxy clusters observed by XMM-Newton. *Astronomy & Astrophysics*, 478:615–658, February 2008.

[521] K. D. Kuntz and S. L. Snowden. The EPIC-MOS particle-induced background spectra. *Astronomy & Astrophysics*, 478:575–596, February 2008.

[522] Palash B. Pal and Lincoln Wolfenstein. Radiative Decays of Massive Neutrinos. *Phys.Rev.*, D25:766, 1982.

[523] D. A. Buote, F. Gastaldello, P. J. Humphrey, L. Zappacosta, J. S. Bullock, F. Brighenti, and W. G. Mathews. The X-Ray Concentration-Virial Mass Relation. ApJ, 664:123–134, July 2007.

[524] T. H. Reiprich and H. Böhringer. The Mass Function of an X-Ray Flux-limited Sample of Galaxy Clusters. ApJ, 567:716–740, March 2002.

[525] N. M. McClure-Griffiths, J. M. Dickey, B. M. Gaensler, A. J. Green, J. A. Green, and M. Haverkorn. The Australia Telescope Compact Array H I Survey of the Galactic Center. ApJS, 199:12, March 2012.

[526] J. M. Dickey and F. J. Lockman. H I in the Galaxy. ARA&A, 28:215–261, 1990.

[527] J. Wilms, A. Allen, and R. McCray. On the Absorption of X-Rays in the Interstellar Medium. ApJ, 542:914–924, October 2000.

[528] E. Churazov, W. Forman, C. Jones, and H. Böhringer. XMM-Newton Observations of the Perseus Cluster. I. The Temperature and Surface Brightness Structure. ApJ, 590:225–237, June 2003.

[529] P. D. Alvarez, J. P. Conlon, F. V. Day, M. C. D. Marsh, and M. Rummel. Observational consistency and future predictions for a 3.5 keV ALP to photon line. *ArXiv e-prints*, October 2014.

[530] Joseph P. Conlon and Francesca V. Day. 3.55 keV photon lines from axion to photon conversion in the Milky Way and M31. 2014.

[531] J. M. Cordes and T. J. W. Lazio. NE2001.I. A New Model for the Galactic Distribution of Free Electrons and its Fluctuations. *ArXiv Astrophysics e-prints*, July 2002.

[532] J. M. Cordes and T. J. W. Lazio. NE2001. II. Using Radio Propagation Data to Construct

a Model for the Galactic Distribution of Free Electrons. *ArXiv Astrophysics e-prints*, January 2003.

[533] Douglas P. Finkbeiner and Neal Weiner. An X-Ray Line from eXciting Dark Matter. 2014.

[534] Emilian Dudas, Lucien Heurtier, and Yann Mambrini. Generating X-ray lines from annihilating dark matter. 2014.

[535] A. Wongwathanarat, H.-T. Janka, and E. Müller. Three-dimensional neutrino-driven supernovae: Neutron star kicks, spins, and asymmetric ejection of nucleosynthesis products. A&A, 552:A126, April 2013.

[536] B. T. Draine and A. Lazarian. Diffuse Galactic Emission from Spinning Dust Grains. *ApJL*, 494:L19, February 1998.

[537] B. T. Draine and A. Lazarian. Electric Dipole Radiation from Spinning Dust Grains. *ApJ*, 508:157–179, November 1998.

[538] A. de Oliveira-Costa, M. Tegmark, D. P. Finkbeiner, R. D. Davies, C. M. Gutierrez, L. M. Haffner, A. W. Jones, A. N. Lasenby, R. Rebolo, R. J. Reynolds, S. L. Tufte, and R. A. Watson. A New Spin on Galactic Dust. *ApJ*, 567:363–369, March 2002.

[539] D. P. Finkbeiner, G. I. Langston, and A. H. Minter. Microwave Interstellar Medium Emission in the Green Bank Galactic Plane Survey: Evidence for Spinning Dust. *ApJ*, 617:350–359, December 2004.

[540] D. P. Finkbeiner. Microwave Interstellar Medium Emission Observed by the Wilkinson Microwave Anisotropy Probe. *ApJ*, 614:186–193, October 2004.

[541] G. Dobler and D. P. Finkbeiner. Extended Anomalous Foreground Emission in the WMAP Three-Year Data. *ApJ*, 680:1222–1234, June 2008.

[542] P. Mertsch and S. Sarkar. Fermi Gamma-Ray "Bubbles" from Stochastic Acceleration of Electrons. *Physical Review Letters*, 107(9):091101, August 2011.

[543] B. Gold, C. L. Bennett, R. S. Hill, G. Hinshaw, N. Odegard, L. Page, D. N. Spergel, J. L. Weiland, J. Dunkley, M. Halpern, N. Jarosik, A. Kogut, E. Komatsu, D. Larson, S. S. Meyer, M. R. Nolta, E. Wollack, and E. L. Wright. Five-Year Wilkinson Microwave Anisotropy Probe Observations: Galactic Foreground Emission. *ApJS*, 180:265–282, February 2009.

[544] D. Pietrobon, K. M. Górski, J. Bartlett, A. J. Banday, G. Dobler, L. P. L. Colombo, S. R. Hildebrandt, J. B. Jewell, L. Pagano, G. Rocha, H. K. Eriksen, R. Saha, and C. R. Lawrence. Analysis of WMAP 7 Year Temperature Data: Astrophysics of the Galactic Haze. *ApJ*, 755:69, August 2012.

[545] G. Dobler. A Last Look at the Microwave Haze/Bubbles with WMAP. *ApJ*, 750:17, May 2012.

[546] Planck Collaboration. Planck Intermediate Results. IX. Detection of the Galactic haze with Planck. *ArXiv e-prints*, August 2012.

[547] D. P. Finkbeiner. WMAP Microwave Emission Interpreted as Dark Matter Annihilation in the Inner Galaxy. *ArXiv Astrophysics e-prints*, September 2004.

[548] D. Hooper, D. P. Finkbeiner, and G. Dobler. Possible evidence for dark matter annihilations from the excess microwave emission around the center of the Galaxy seen by the Wilkinson Microwave Anisotropy Probe. *PRD*, 76(8):083012, October 2007.

[549] T. Lin, D. P. Finkbeiner, and G. Dobler. The electron injection spectrum determined by anomalous excesses in cosmic ray, gamma ray, and microwave data. *PRD*, 82(2):023518, July 2010.

[550] G. Dobler, I. Cholis, and N. Weiner. The Fermi Gamma-Ray Haze from Dark Matter Annihilations and Anisotropic Diffusion. *ApJ*, 741:25, November 2011.

[551] D. Hooper and T. Linden. Gamma rays from the Galactic center and the WMAP haze. *PRD*, 83(8):083517, April 2011.

[552] T. Linden, S. Profumo, and B. Anderson. Morphology of the Galactic dark matter synchrotron emission with self-consistent cosmic-ray diffusion models. *PRD*, 82(6):063529, September 2010.

[553] N. Fornengo, R. Lineros, M. Regis, and M. Taoso. Cosmological radio emission induced by WIMP Dark Matter. *JCAP*, 3:33, March 2012.

[554] E. Borriello, A. Cuoco, and G. Miele. Radio constraints on dark matter annihilation in the galactic halo and its substructures. *Phys. Rev. D*, 79(2):023518, January 2009.

[555] LeZhang and G. Sigl. Dark matter signatures in the anisotropic radio sky. *JCAP*, 9:27, September 2008.

[556] M. Regis and P. Ullio. Multiwavelength signals of dark matter annihilations at the Galactic center. *Phys. Rev. Rev.*, 78(4):043505, August 2008.

[557] S. Colafrancesco, S. Profumo, and P. Ullio. Detecting dark matter WIMPs in the Draco dwarf: A multiwavelength perspective. *Phys. Rev. Rev.*, 75(2):023513, January 2007.

[558] R. Aloisio, P. Blasi, and A. V. Olinto. Neutralino annihilation at the galactic centre revisited. *JCAP*, 5:7, May 2004.

[559] P. Blasi, A. V. Olinto, and C. Tyler. Detecting WIMPs in the microwave sky. *Astroparticle Physics*, 18:649–662, March 2003.

[560] B. B. Siffert, A. Limone, E. Borriello, G. Longo, and G. Miele. Radio emission from dark

matter annihilation in the Large Magellanic Cloud. *MNRAS*, 410:2463–2471, February 2011.

[561] E. Borriello, G. Longo, G. Miele, M. Paolillo, B. B. Siffert, F. S. Tabatabaei, and R. Beck. Searching for Dark Matter in Messier 33. *Apj*, 709:L32–L38, January 2010.

[562] S. Colafrancesco, S. Profumo, and P. Ullio. Multi-frequency analysis of neutralino dark matter annihilations in the Coma cluster. *A&A*, 455:21–43, August 2006.

[563] A. Tasitsiomi, J. Gaskins, and A. V. Olinto. Gamma-ray and synchrotron emission from neutralino annihilation in the Large Magellanic Cloud. *Astroparticle Physics*, 21:637–650, September 2004.

[564] E. A. Baltz and L. Wai. Diffuse inverse Compton and synchrotron emission from dark matter annihilations in galactic satellites. *Phys. Rev. Rev.*, 70(2):023512, July 2004.

[565] N. Fornengo, R. A. Lineros, M. Regis, and M. Taoso. Galactic synchrotron emission from WIMPs at radio frequencies. *JCAP*, 1:5, January 2012.

[566] G. Bertone, D. Hooper, and J. Silk. Particle dark matter: evidence, candidates and constraints. *Physics Reports*, 405:279–390, January 2005.

[567] L. Bergström. Dark matter candidates. *New Journal of Physics*, 11(10):105006, October 2009.

[568] D. Hooper and S. Profumo. Dark matter and collider phenomenology of universal extra dimensions. *Physics Reports*, 453:29–115, December 2007.

[569] R. Bernabei, P. Belli, F. Cappella, R. Cerulli, C. J. Dai, A. D'Angelo, H. L. He, A. Incicchitti, H. H. Kuang, X. H. Ma, F. Montecchia, F. Nozzoli, D. Prosperi, X. D. Sheng, R. G. Wang, and Z. P. Ye. New results from DAMA/LIBRA. *European Physical Journal C*, 67:39–49, May 2010.

[570] C. E. Aalseth, P. S. Barbeau, N. S. Bowden, B. Cabrera-Palmer, J. Colaresi, J. I. Collar, S. Dazeley, P. de Lurgio, J. E. Fast, N. Fields, C. H. Greenberg, T. W. Hossbach, M. E. Keillor, J. D. Kephart, M. G. Marino, H. S. Miley, M. L. Miller, J. L. Orrell, D. C. Radford, D. Reyna, O. Tench, T. D. van Wechel, J. F. Wilkerson, and K. M. Yocum. Results from a Search for Light-Mass Dark Matter with a p-Type Point Contact Germanium Detector. *Physical Review Letters*, 106(13):131301, April 2011.

[571] C. E. Aalseth, P. S. Barbeau, J. Colaresi, J. I. Collar, J. Diaz Leon, J. E. Fast, N. Fields, T. W. Hossbach, M. E. Keillor, J. D. Kephart, A. Knecht, M. G. Marino, H. S. Miley, M. L. Miller, J. L. Orrell, D. C. Radford, J. F. Wilkerson, and K. M. Yocum. Search for an Annual Modulation in a p-Type Point Contact Germanium Dark Matter Detector. *Physical Review Letters*, 107(14):141301, September 2011.

[572] G. Angloher, M. Bauer, I. Bavykina, A. Bento, C. Bucci, C. Ciemniak, G. Deuter, F. von Feilitzsch, D. Hauff, P. Huff, C. Isaila, J. Jochum, M. Kiefer, M. Kimmerle, J.-C. Lanfranchi, F. Petricca, S. Pfister, W. Potzel, F. Pröbst, F. Reindl, S. Roth, K. Rottler, C. Sailer, K. Schäffner, J. Schmaler, S. Scholl, W. Seidel, M. v. Sivers, L. Stodolsky, C. Strandhagen, R. Strauß, A. Tanzke, I. Usherov, S. Wawoczny, M. Willers, and A. Zöller. Results from 730 kg days of the CRESST-II Dark Matter search. *European Physical Journal C*, 72:1971, April 2012.

[573] D. Hooper and L. Goodenough. Dark matter annihilation in the Galactic Center as seen by the Fermi Gamma Ray Space Telescope. *Physics Letters B*, 697:412–428, March 2011.

[574] K. N. Abazajian and M. Kaplinghat. Detection of a Gamma-Ray Source in the Galactic Center Consistent with Extended Emission from Dark Matter Annihilation and Concentrated Astrophysical Emission. *ArXiv e-prints*, July 2012.

[575] T. Linden, D. Hooper, and F. Yusef-Zadeh. Dark Matter and Synchrotron Emission from Galactic Center Radio Filaments. *ApJ*, 741:95, November 2011.

[576] D. Hooper, A. V. Belikov, T. E. Jeltema, T. Linden, S. Profumo, and T. R. Slatyer. The Isotropic Radio Background and Annihilating Dark Matter. *ArXiv e-prints*, March 2012.

[577] N. Fornengo, R. Lineros, M. Regis, and M. Taoso. Possibility of a Dark Matter Interpretation for the Excess in Isotropic Radio Emission Reported by ARCADE. *Physical Review Letters*, 107(26):A261302, December 2011.

[578] D. Hooper. The Empirical Case For 10 GeV Dark Matter. *ArXiv e-prints*, January 2012.

[579] M. Su, T. R. Slatyer, and D. P. Finkbeiner. Giant Gamma-ray Bubbles from Fermi-LAT: Active Galactic Nucleus Activity or Bipolar Galactic Wind? *ApJ*, 724:1044–1082, December 2010.

[580] G. Dobler, D. P. Finkbeiner, I. Cholis, T. Slatyer, and N. Weiner. The Fermi Haze: A Gamma-ray Counterpart to the Microwave Haze. *ApJ*, 717:825–842, July 2010.

[581] T. Linden and S. Profumo. Systematic Effects in Extracting a "Gamma-ray Haze" from Spatial Templates. *ApJL*, 714:L228–L232, May 2010.

[582] G. Dobler. Identifying the Radio Bubble Nature of the Microwave Haze. *ArXiv e-prints*, August 2012.

[583] P. L. Biermann, J. K. Becker, G. Caceres, A. Meli, E.-S. Seo, and T. Stanev. The WMAP Haze from the Galactic Center Region Due to Massive Star Explosions and a Reduced Cosmic Ray Scale Height. *ApJL*, 710:L53–L57, February 2010.

[584] R. M. Crocker and F. Aharonian. Fermi Bubbles: Giant, Multibillion-Year-Old Reservoirs of Galactic Center Cosmic Rays. *Physical Review Letters*, 106(10):101102, March 2011.

[585] F. Guo and W. G. Mathews. The Fermi Bubbles. I. Possible Evidence for Recent AGN Jet Activity in the Galaxy. *ApJ*, 756:181, September 2012.

[586] J. J. Condon. A 1.49 GHz atlas of spiral galaxies with B(T) = +12 or less and delta = -45 deg or greater. *ApJS*, 65:485–541, December 1987.

[587] L. Marochnik and A. Suchkov. *The Milky Way Galaxy*. 1996.

[588] J. Bovy, C. Allende Prieto, T. C. Beers, D. Bizyaev, L. N. da Costa, K. Cunha, G. L. Ebelke, D. J. Eisenstein, P. M. Frinchaboy, A. E. García Pérez, L. Girardi, F. R. Hearty, D. W. Hogg, J. Holtzman, M. A. G. Maia, S. R. Majewski, E. Malanushenko, V. Malanushenko, S. Mészáros, D. L. Nidever, R. W. O'Connell, C. O'Donnell, A. Oravetz, K. Pan, H. J. Rocha-Pinto, R. P. Schiavon, D. P. Schneider, M. Schultheis, M. Skrutskie, V. V. Smith, D. H. Weinberg, J. C. Wilson, and G. Zasowski. The Milky Way's Circular-velocity Curve between 4 and 14 kpc from APOGEE data. *ApJ*, 759:131, November 2012.

[589] G. Heald, G. Józsa, P. Serra, L. Zschaechner, R. Rand, F. Fraternali, T. Oosterloo, R. Walterbos, E. Jütte, and G. Gentile. The Westerbork Hydrogen Accretion in Local Galaxies (HALOGAS) Survey. I. Survey description and pilot observations. *A&A*, 526:A118, February 2011.

[590] F. Fraternali, R. Sancisi, and P. Kamphuis. A tale of two galaxies: light and mass in NGC 891 and NGC 7814. *A&A*, 531:A64, July 2011.

[591] G. Paturel, A. M. Garcia, P. Fouque, and R. Buta. An extragalactic database. III - Diameter reduction. *AAP*, 243:319–327, March 1991.

[592] V. Springel, J. Wang, M. Vogelsberger, A. Ludlow, A. Jenkins, A. Helmi, J. F. Navarro, C. S. Frenk, and S. D. M. White. The Aquarius Project: the subhaloes of galactic haloes. *MNRAS*, 391:1685–1711, December 2008.

[593] O. Y. Gnedin, D. Ceverino, N. Y. Gnedin, A. A. Klypin, A. V. Kravtsov, R. Levine, D. Nagai, and G. Yepes. Halo Contraction Effect in Hydrodynamic Simulations of Galaxy Formation. *ArXiv e-prints*, August 2011.

[594] F. Governato, C. Brook, L. Mayer, A. Brooks, G. Rhee, J. Wadsley, P. Jonsson, B. Willman, G. Stinson, T. Quinn, and P. Madau. Bulgeless dwarf galaxies and dark matter cores from supernova-driven outflows. *Nature*, 463:203–206, January 2010.

[595] J. Bovy and S. Tremaine. On the Local Dark Matter Density. *ApJ*, 756:89, September 2012.

[596] Y. Sofue, M. Fujimoto, and R. Wielebinski. Global structure of magnetic fields in spiral galaxies. *ARAA*, 24:459–497, 1986.

[597] H. Ohno and S. Shibata. The random magnetic field in the Galaxy. *MNRAS*, 262:953–962, June 1993.

[598] J. M. Stil, M. Krause, R. Beck, and A. R. Taylor. The Integrated Polarization of Spiral Galaxy Disks. *ApJ*, 693:1392–1403, March 2009.

[599] L. L. Dressel and J. J. Condon. The Arecibo 2380 MHz survey of bright galaxies. *ApJS*, 36:53–75, January 1978.

[600] P. C. Gregory and J. J. Condon. The 87GB catalog of radio sources covering delta between O and + 75 deg at 4.85 GHz. *ApJS*, 75:1011–1291, April 1991.

[601] N. M. Nagar, H. Falcke, and A. S. Wilson. Radio sources in low-luminosity active galactic nuclei. IV. Radio luminosity function, importance of jet power, and radio properties of the complete Palomar sample. *A&A*, 435:521–543, May 2005.

[602] T. Jeltema and S. Profumo. Deep XMM observations of Draco rule out at the 99 per cent

confidence level a dark matter decay origin for the 3.5 keV line. MNRAS, 458:3592–3596, June 2016.

[603] L. Gu, J. Kaastra, A. J. J. Raassen, P. D. Mullen, R. S. Cumbee, D. Lyons, and P. C. Stancil. A novel scenario for the possible X-ray line feature at ˜3.5 keV. Charge exchange with bare sulfur ions. A&A, 584:L11, December 2015.

Appendix A

Miscellaneous Codes

A.1 GammaLike: A Fast Binned Likelihood Analysis Package for Fermi Data

Github: https://planck.ucsc.edu/erccarls/GammaLike

GammaLike The GammaLike package is devoted to easing multi-linear template regression on gamma-ray data using a binned likelihood approach. While this library was designed to analyse Fermi-LAT data, it is easily extensible to any analysis using healpix maps. Many tutorials are provided in the tutorials folder.

The focus of this software is twofold. First, efficiency. The fermi science tools are prohibitively slow when working with large regions of interest. GammaLike can perform full-sky likelihood fits to fermi data in only a few minutes at .25 degree resolution. Second, is ease of use. After supplying flux maps, GammaLike automatically performs convolutions against instrumental response functions and supports arbitrary binning,

masking, and pixel weighting schemes. Written in pure python, it is also easy to add new functionality.

Package documentation is available at http://planck.ucsc.edu/gammalike/html/

Features include:

Fixed spectrum or bin-by-bin fitting in energy Built in support for a variety of gamma-ray structures such as the fermi bubbles or isotropic templates. Fast point source generation tool Simple interfaces to galprop output files. Multi-threading support in performance critical regions. Output models to HDF5 format. Support for Arbitrary Masking and Pixel weights. Can impose external uncertainties on components. Generate dark matter templates including common DM profiles, translations, ellipticities. This library was developed originally to study both global fits to Fermi-LAT data, and to study the GeV Galactic center excess [arxiv:1603.06584]

Modified Galprop Codes The modified Galprop codes can be found at https://github.com/erccarls/

See the README of that repository for usage information and do not forget to cite the original Galprop code http://galprop.sourceforge.net and http://galprop.stanford.edu

If you don't mind, cite us too: http://arxiv.org/abs/1510.04698 http://arxiv.org/abs/1603.06584

New Galprop Gas Maps To use our modified Galprop code you will need several additional files to be placed in the galprop_home/FITS folder:

The 3D gas maps for use in the Galprop code above can be found at: https://www.dropbox.com/sh/

The 9 galactocentric ring gas maps used for galprop can be found at: https://www.dropbox.com/s/

Finally, a conveinient script for generating Galdef files in python can be found at https://github.com/erccarls/hyades_scripts/blob/master/RunGalprop.py, although one

will want to modify this appropriately and remove the cluster submission code at the end.

New Diffuse Emission Models The emission models from http://arxiv.org/abs/1603.06584 can be found at the following links:

Mod_A from Calore et al (but with the XCO profile fitted): https://www.dropbox.com/s/r48vjnmij

The f_H2=0.2 'Canonical' emission model with no wind: https://www.dropbox.com/s/uee55f64klsr

The best fitting f_H2=0.25 model with a 600 km/s radial wind at the Galactic center: https://www.dropbox.com/s/w1oykrkqp6hdhr8/mod_v4_30_XCO_P8_corrected.hdf5?dl=0

These files are stored in HDF5 format with the templates for each Galactic diffuse component stored at the path '/templates/'. Further usage instructions can be found toward the bottom of the 'Fitting a Galprop Model.ipynb' tutorials.

If you need these in cartesian format, take a look at the script here: https://github.com/erccarls/Ga and modify as needed.

A.2 DM production of $\overline{d}$ and $^3\overline{\mathrm{He}}$ in Pythia

This includes code gist includes methods for both the coalescence mechanism and the https://gist.github.com/erccarls/d45bb81f6d66083ee8e082c464165621

A.3 GammaCAP: A Gamma-Ray Clustering Analysis Package

Project Homepage:http://planck.ucsc.edu Github:https://github.com/erccarls/GammaCAP

This package is written in pure python and provides a simple yet flexible python interface and even simpler command-line tools to compute clustering information for gamma-ray event data. It is oriented toward Fermi-LAT data set, but is also easily configured for any general data set requiring only space, time, and spectral coordinates.

At the most basic level, GammaCAP employs the clustering algorithm DBSCAN (Density Based Spatial Clustering for Applications with Noise) to detect point sources in 2 (spatial) or 2+1 (time) dimensions, given a list of event data (e.g. lat/-long/time/energy). A variety of statistics are then computed such as significance over background (which can be used as a test-statistic), centroids, and bounding ellipses. The pixel-less nature of DBSCAN provides very high sensitivity to sparse gamma-ray data which can hopefully be used to gain a better understanding of the unresolved Isotropic Gamma-Ray Background (IGRB), improve the depth of point source catalogs, and provide an additional tool for distinguishing point source from diffuse emission classes (see e.g. arXiv:1304.5524 and arXiv:1210.0522 for sample applications of the algorithm). In addition, the incorporation of timing information presents a novel method to search for transient sources that may otherwise be washed out by an integrated background signal.

Some of the other features included in GammaCAP:

-Use of Fermi instrument response functions and Diffuse Galactic and Isotropic Emission Models to automatically and adaptively tune DBSCAN parameters. -Post-processing of cluster data using Boosted Decision Tree classification to lower background contamination and improve sensitivity ***(Still in progress). -Source Ellipse Calculations using principle component analysis. -Highly optimized cluster computation rou-

tines. -Automatic parsing of Fermi-LAT data - just supply the events in the standard FITS format or directly supply coordinates. -Simple simulation tools to quickly test sensitivity to new source models (also supports the Fermi Science-Tools gtobssim). -Full PDF and online searchable HTML documentation of API. -Tutorials highlighting the primary functionality. Useful new feature requests are always appreciated!

Installation Through python setup tools (Linux/Win/OSX) Although GammaCAP is pure python and should support Windows and Mac provided the dependencies are met, it was developed and tested on Linux (Ubuntu 12.04). The easiest way to install GammaCAP is through python setup tools which will automatically install all required dependencies. If you don't have python setup tools installed, you can get it here: https://pypi.python.org/pypi/setuptools easy_install gammacap **Note that superuser privileges will be required to install on the system python.

Upgrading to the latest version is just as simple...

easy_install –upgrade gammacap

Additional Files In order to use some of the plotting functionality, the Basemap Matplotlib-Toolkit is required. Instructions for installation can be found here. On most linux distributions, this is likely included in the repository and should be installed there. On Ubuntu, the relevant command is, sudo apt-get install python-mpltoolkits.basemap

Finally, the Fermi diffuse galactic background model must be downloaded if the Fermi Science Tools are not installed. If the Fermi Science Tools are installed, and FERMI_DIR is a valid environmental variable pointing to the installation directory, then this file should be found automatically. Otherwise it can be downloaded on the Fermi

website (below) and you will need to provide the path to GammaCAP as mentioned in the tutorials.

Installation From Source If an alternative installation is needed, the latest source tarballs and windows executables are also available here

Tarballs and Executables

This package has the following dependencies.

numpy pyfits scikit-learn matplotlib Bug Reports and Feature Requests GammaCAP is being actively developed and feature requests are encouraged provided they will be useful to others. Please submit these and any bugs at the Github issues page here: https://github.com/erccarls/GammaCAP/issues

Tutorials and Documentation Documentation

GammaCAP: A Gamma-ray Clustering Analysis Package – A description/study of the DBSCAN algorithm in application to Fermi data, as well as details of the cluster properties.

Software Reference Manual (online — pdf)

Tutorials

SimTools Tutorial (online — .ipynb — .py — .pdf) – Learn how to simulate Fermi-LAT data and easily implement point source models.

DBSCAN 2D Tutorial (online — .ipynb — .py — .pdf) – Learn how to use DBSCAN to compute spatial clustering information on Fermi-LAT data and simulations.

DBSCAN 3D Tutorial (online — .ipynb — .py — .pdf) – Learn how to use DBSCAN to compute spatio-temporal clustering information on Fermi-LAT data and

simulations.

Contact Questions should be directed to Eric Carlson. Bug reports are preferentially submitted through Github here if possible, but will also be answered via email.

A.3.1 Description of GammaCAP Calculations

GammaCAP is a python software package which efficiently implements the 2 and 3-dimensional DBSCAN algorithms along with Fermi-LAT background models and data compatibility, boosted decision trees, and computation of cluster properties. It also includes easy-to-use simulation tools which include the most important of the Fermi-LAT instrument response functions with the intent of rapidly prototyping and assessing DBSCAN's sensitivity to new source models. In the following sections we describe the methods employed in detail. The package website http://planck.ucsc.edu/gammacap provides installation instructions, tutorials, and software reference manuals.

A.3.1.1 Calculating DBSCAN Parameters

As discussed above, DBSCAN has 3 parameters, $\epsilon, N_{\rm min}, \text{and } a$ (2 for the 2-Dimensional case). It should be noted that the default choices work very well, but it may be desirable to tune various settings for specific searches.

$\boldsymbol{\epsilon}$: In GammaCAP, the first parameter, ϵ is automatically determined by calculating the 68% containment radius of the point spread function at that energy as has been recommended by several previous studies. This is found by averaging the point spread function over the input energies with weights proportional to the number of events, taken

as $dN/dE \propto E^{-2.5}$. Alternatively, the package also allows for the containment fraction to be changed, or ϵ set manually.

$\boldsymbol{N}_{\rm min}$: With ϵ fixed, $N_{\rm min}$ can be automatically chosen based on evaluation of the local background. This is necessary due to the high variability of the diffuse background at low and intermediate latitudes. There are currently five built-in methods for this.

BGInt: The default option sums contributions of the Fermi Galactic Diffuse and isotropic models. In Fermi's Pass 7 release, these are separated into 31 energy bins which are integrated over input energies weighted by $dN/dE \propto E^{-2.5}$. Next the energy dependent effective area is empirically incorporated by convolving an interpolation function which globally matches the photon flux to gtobssim simulations of the isotropic and diffuse components. Finally, the template is integrated over the ϵ-neighborhood of the point of interest[1].

BGCenter: A more efficient, but less accurate method that can also be used, but does not integrate over the ϵ-neighborhood and simply uses the background rate at the point of interest. Running DBSCAN typically significantly takes longer than the BGInt method so this is rarely used.

annulus: Alternatively, the 'annulus' method evaluates the rate by counting photons in an annulus of inner and outer radii equal to 1.5 and 2.5 times ϵ. [2]

[1]For computational efficiency, the background count is actually determined by integrating the rate over a square circumscribed by a circle of radius ϵ and then multiplied by $\pi\epsilon^2$. This has been found to result in an error of less than 10% over the entire sky which is often less than uncertainty in the background model itself.

[2]Not yet implemented.

isotropic: Pass a background event density. This is only useful for isotropic backgrounds.

nMin: A single value or vector (one value for each point) for $N_{\min}$ may be directly specified, or the background density can be supplied.

The first four of these methods provide an estimate of the background rate which is then converted into $N_{\min}$ via Eqn. 4.29 where $N_{\min,\sigma}$ can be set to the desired level.

$\boldsymbol{a}$: The temporal search half-height is chosen by default by evaluating the average background density over the entire sky with the latitude interval $b \in [-5^\circ, 5^\circ]$ masked out and passing this to Eqn. 4.30. This may also be specified manually which must often be done when considering sparse data, or looking for very short pulses. The value chosen is printed when running the algorithm and can guide the necessity of this.

A.3.2 Cluster Properties

For each scan, discovered clusters are stored as an entry in the python object "ClusterResult" with a variety of properties precomputed. These details are described here.

Centroids: Spatial cluster centroids are computed by first finding the average position, called the zeroth order centroid, and then re-averaging weighted by $1/r$ where r is the points distance to the zeroth order centroid. This has been shown to provide superior centroid reconstruction for low-count sources which have coun-

terparts and well known centers in other wavelengths. For the time centroid, we simply use the mean time.

Cluster Ellipses: Spatial cluster ellipses are calculated using a Principle Component Analysis which determines the semi-major and semi-minor axes as well as position angles. From this, the 95% containment axes are reported. For times we simply determine the half-height which contains 95% of the cluster members. From the sizes, uncertainties on the centroids are given as well the geometric mean of the two as the 95% containment divided by $\sqrt{N}$.

Eccentricity: Defined as $\sqrt{1 - b^2/a^2}$ for semi-major axis a and semi-minor axis b.

Median Radius: Defined as the median distance from the cluster centroids in all three directions. This can be a size estimator more resilient to outliers.

Density Profile: A measure of the cluster profile, the densities simply calculate the percentage of cluster events in the inner, central, and outer third of the cluster radius. These are useful properties to discriminate true clusters from background fluctuations (see BDT discussion).

Significance: One of the most important properties defined by the following equation.

$$s = \sqrt{2\left(N_s \ln\left[\frac{2N_s}{N_s + N_b}\right] + N_b \ln\left[\frac{2N_b}{N_s + N_b}\right]\right)}\,. \tag{A.1}$$

where N_b and N_s are the background and signal+background counts respectively.

The background count can be estimated in one of three ways: 'BGInt' which like the determination of $N_{\min}$ presented in above integrates the background template to determine the rate and multiplies by the ellipse area. Also supports the annulus[3] and isotropic methods.

A.3.3 Simulation Tools

GammaCAP includes simple simulation tools which are much faster than gtobbsim and include easy-to-use functions for simulating background photons based and point source models. These can be very useful for tuning DBSCAN, sensitivity tests, training the boosted decision tree, or for statistical Monte-Carlo comparisons of source models, which can extraordinarily time consuming using gtobssim. The tutorials provide an overview of the functionality. The background is simulated using an accept/reject Monte-Carlo of the background template constructed in precisely the same way as with $N_{\min}$ above.

For point-sources, if a spectral distribution and flux is supplied, the distribution is convolved with the energy dependent effective area, photons sampled from the new distribution, binned by energy, and positions are modulated by the energy dependent point spread function.

A.4 Line-of-Sight Integrator with ISM Convolution

Project Homepage:http://planck.ucsc.edu/dmcr-morphology/

[3]Annulus method is implemented for significance evaluations.

Github:https://github.com/erccarls/ISMConvolve

We present supplemental material for arXiv:1504.04782. These skymaps contain spatial distribution of electromagnetic or neutrino radiation which is proportional to the product of dark matter particles with cosmic-ray electrons, cosmic-ray protons, free electrons, and interstellar gas. This product of dark matter times the matter component of interest is then integrated along the line of sight in order to obtain the projected intensity skymap. More generically, we also provide a python code which can be used to convolve an arbitrary three-dimensional distribution gas, cosmic ray, or free electron densities. Below, we briefly describe each component.

Cosmic-ray distributions are derived using the numerical code Galprop [413], under standard assumptions regarding cosmic-ray transport, and assuming several different distributions for the injection of primary cosmic-rays. Free electrons are based on the NE2001 model with corrections to the thick disk scale-height taken from Gaensler et al (2007). For the gas density (2*H2+HI+HII), we employ two models of Galactic gas. The first is based on Dickey & Lockman (1990) with corrections in the inner galaxy due to Bronfman et al (2000), and with the inner 3 kiloparsecs following Ferriere (2007). The second model utilizes velocity data from a the Leiden-Argentine-Bonn 21 cm and Dame et al (2001) surveys combined with spatial deconvolutions by Nakanishi & Sofue and Pohl, Englemier, & Martin, respectively.

As described in 3.3.2, Our implementation for the NE2001 free-electron distribution neglects components which are small outside of the Galactic center region. This should be noted before using this code to integrate against non-centrally peaked

distributions.

A.5 Modified Galprop Codes

Github: https://github.com/erccarls/galprop_diff

The modified source codes discussed throughout Section 8.1 can be found at the above github link. This is initially based on the source folder from verison Galprop v54.r2504 There are several new galdef parameters, and support files.

The second commit into this repo is the galprop version r2504, and the third commit is my modified version, so you can use the diff[4] tool to see the parts I added (also can search "ECC" in a given file typically).

Note that the variable grid spacing does not work since the transport arrays were not built for this and it was more work than it was worth to finish it. This means disregard changes in galaxy.cc, galaxy.h

There are then a handful of additional galdef keywords which control the behavior of the added functionality.

A.5.1 Source distribution parameters

1. spiral_fraction: (aka f_{H2}) A float between 0 and 1 which specifies the fraction of CR sources distributed according to our star formation model. The remaining fraction is distributed according to the usual parametrized source dist specification. The source calculation routines are in create_transport_arrays.cc since we have to

[4] https://github.com/erccarls/galprop_diff_r2504/commit/9502ee75ba9d3585ccded0c6039d758c6834f0eb

integrate over the full galaxy it was much easier than putting them elsewhere.

2. kennicutt_index: This should be called the Schmidt index which specifies the volumetric power-law dependence of SFR and gas density.

3. kennicutt_threshold: Likewise, this specifies the minimal gas density to initiate star formation (in units of cm$^-$3).

4. nuc_g1_inner etc..: Parameters to change the CMZ injection spectrum (currently hardcoded as $r_{2D} < .5$ kpc). I can't remember how normalizations are handled so be careful if using this.

A.5.2 Gas Model parameters

1. nH2_model/nHI_model: 1: use galprop default gas maps for propagation and for gamma-rays. 2: use the new PEB models for propagation and gamma-rays (but does not change source distribution). The filenames must be specified below.

2. COCube_filename: Provide the input CO gas map in cartesian coordinates (x,y,z). This gas map should be in the galprop/FITS folder containing galprop data. This is also used for source distributions with non-zero $f_{\rm H2}$ (which is the "spiral_fraction") keyword

3. HICube_filename: same as above, but for HI. You can also make your own additions to the gas/source model by modifying the fits files. The spatial info is read from the fits headers.

4. COCube_rlb and HICube_rlb: filenames of the input gas map in r,l,b coordinates. These are used if "nH2_model"=2 "nHI_model"=2 which tells the gamma-ray generation and galactic gas model (for propagation not sources) to use the new 3D models.

A.5.3 Wind parameters

1. convection: 1-3 are galprop models. 4: turn on radial 3D winds in GC as defined in our paper (1603.06584).

2. v0_conv: specified wind velocity in km/s

A.5.4 Debugging parameters

1. renorm_off: if 1, don't renormalize pixels to the gas map.

2. uniform_emiss: if 1 make CR's uniform throughout galaxy when calculating skymaps. used for debugging gas maps

3. single_component: if 1 or 2 only outputs HI or H2 contribution to the pi0 emission. There are also a few routines for calculating propagation Green's functions for dark matter injected antiprotons, but I don't remember the status of this.

A.6 Spherical Propagation Code

Github:https://gist.github.com/erccarls/fb742ae860b00008fa97e1dfc45eb1fd

The following code contains a python implementation of the ssimple spherical propagation model presented in Sec. 5.1, following the model of Ref. [18].